

MOVING FORWARD AFTER THE GOOGLE LUNAR XPRIZE, ISPACE'S PLAN FOR THE COMMERCIAL EXPLORATION AND EXPLOITATION OF THE MOON

K. Acierno¹ ispace Europe SA, 5, Rue de L'industrie, Luxembourg.

Introduction: ispace is a company whose vision is to expand and sustain humanity's presence in space by utilizing resources available on the Moon. This presentation will introduce ispace and provide details of its beginnings as Team Hakuto in the Google Lunar XPRIZE. Next, it will outline the steps ispace will take to commercialize the exploration of outer space, including an explanation of the micro-rover and lander technology that ispace is developing to prospect for resources on the Moon. Finally, it will explain its plan moving forward in Europe to work with scientists to measure, and eventually manage resources on the lunar surface.

Google Lunar XPRIZE: ispace manages Team Hakuto, a front-running team in the now closed Google Lunar XPRIZE (GLXP). ispace developed and flight qualified Team Hakuto's SORATO rover, which won the \$500K mobility milestone award. As Team Hakuto originally only planned to develop a rover, the team needed to partner with another GLXP team developing a lander in order to be transported to the Moon. Team Hakuto signed a partnership in 2017 with Team Indus, which had a validated launch and become a finalist for the \$20M Grand Prize. Unfortunately, neither Team Indus nor any other remaining team was not able to raise enough funds to pay a launch contract and Google official declared the end of the contest on January 23, 2018 [1].

Commercialization: ispace has a vision that expands beyond the GLXP. The company intends to build-upon two fundamental transport focused technologies, a rover and a lander, in order to enable the commercial exploration of the lunar surface and prepare for the establishment of in-situ resource utilization (ISRU) on the Moon.

Rover: The rover (Figure 1) will be modelled after SORATO. The rover will be scaled according to the size of the payload and necessary power. The body is built in carbon fibre and has 3D printed ULTEM wheels. The 4 HD cameras place around the rover will capture images in 360 degrees, used for localization, hazard detection and mapping.



Figure 1: SORATO rover.

Lander: The lander (Figure 2) is designed to carry from 30 to 50 kg of payload to the lunar surface. The rover in its interior is protected within the

spacecraft structure during flight. Once the lander is on the lunar surface, it opens and the rover is deployed. Other scientific and commercial payloads can also be flown on the lander.

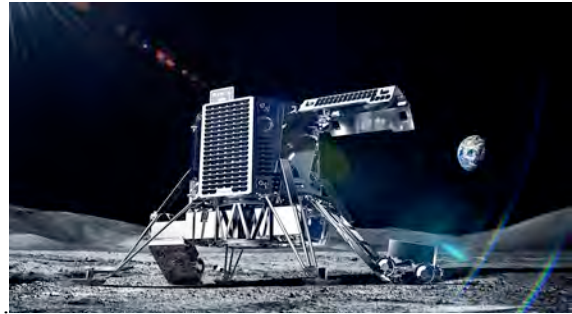


Figure 2: Concept model of ispace's lander.

ispace has a three-step plan (Figure 3) to explore for, map, measure, manage, process and eventually sell water ice and other resources on the lunar surface. First, ispace will demonstrate its rover technology during its maiden lunar missions in 2019 & 2020. Next ispace will develop its next generation transportation and landing abilities, a tethered-rover crater exploration vehicle, as well as rover with a drilling mechanism along with other ISRU techniques and process which will give the company access to the lunar sub-surface. In this phase ispace plans to partner with space agencies, scientists, and the mining community for sensor and technology development to better detect valuable deposits. In addition, ispace will offer transportation opportunities so the international community can develop and test its own technology to explore the lunar surface. Finally, depending on the location, distribution, quality and quantity of the lunar ice and other resources, ispace will develop extraction and processing methods with interested industrial partners. An ultimate goal is to convert the ice to fuel and deliver it to private companies such as the United Launch Alliance, who has offered to purchase fuel on the lunar surface for \$500/kg [2].



Figure 3: ispace's three-step approach.

References:

- [1] Google Lunar XPRIZE UPDATE, *XPRIZE* (2018)
- [2] United Launch Alliance, Space Resources Roundtable (2016)

Introduction: To realize long-term lunar explorations, ISRU is necessary to reduce risk and cost of delivering consumable and materials from the Earth, and it relies on utilization of lunar regolith that contain valuable components, such as metals, oxygen, and possibly water [1]. A large amount of the regolith can also be used as building material of lunar habitat as the regolith particles are sintered [2]. In the ISRU processes, including a drilling, sampling, storage, beneficiation, chemical processing, and sintering of the regolith, a handling technology of the particles is elementary and indispensable. Mechanical, pneumatic, electrostatic, and magnetic handling technologies of the regolith have been considered in previous studies [3-6]. Although each system has advantages in each desirable condition, it is necessary to develop a new handling technology that can be used in a wide area of ISRU without failure on the Moon. A granular handling system using vibration is one of the reliable candidates, because it has several advantages in terms of the use on the Moon, such as high tolerance to dust contamination, unnecessary of gas, simple configuration, and the ability to transport large amounts of particles regardless of the type. Some vibration systems for transporting the regolith in horizontal and slant directions have been developed [7, 8]. In this study, a granular vibration-pumping system has been developed, based on the mechanism of particle climbing in an oscillating tube [9], for transporting the lunar regolith vertically. The climbing mechanism of monodisperse spheres has been investigated in the previous study [9]. Here it was demonstrated to use the technique against the lunar regolith.

Granular Vibration-Pumping System: This system consists of two parts: one is an excitation source (LDS Small Electromagnetic Vibration Systems V721, Brüel & Kjær Sound & Vibration Measurement A/S); second is a transparent PMMA tube (inner diameter: 7 mm, outer diameter: 10 mm, Amsler & Frey AG). When the tube is inserted into a bulk of lunar regolith simulant (JSC-1A, Zybek Advanced Products Inc.) stored in a container and vibrated by the excitation, the granular can climb along the tube inside by friction with the tube surface and by granular interactions. For the sake of convenience, the large electromagnetic shaker was used in this study. It can be replaced with any small excitation source for the practical application.

Demonstration against Lunar Regolith Simulant: When a frequency and acceleration of the oscillating tube were 20 Hz and 2.8 G, the lunar regolith

began to climb inside the tube. The regolith finally reached about 300 mm height from the top surface of the bulk of regolith, as shown in Figure 1. The climbing height depends on the vibration acceleration [9]. After the vibration was turned off, the regolith remained in the same height due to frictions between particle and tube and within particles. Moreover, the tube held on the regolith after it was pulled out from the bulk of regolith, as shown in Figure 2. The regolith does not fall inside the tube easily. It is expected to use this system to sample the lunar regolith from the lunar surface and to lift the regolith in various situations of ISRU processes.

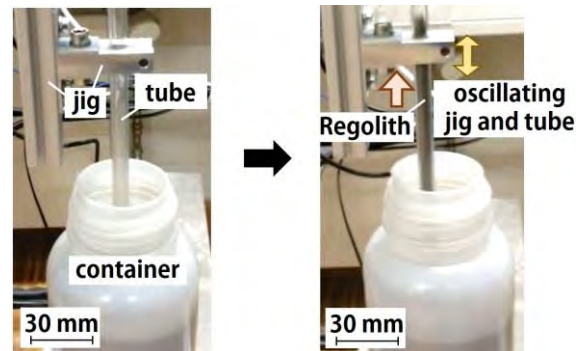


Figure 1: Climbing motions of lunar regolith simulant in the oscillating tube (20 Hz, 2.8 G).

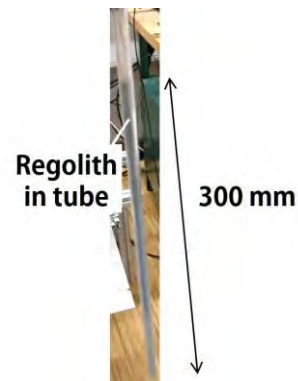


Figure 2: Lunar regolith simulant remaining inside the tube after it was pulled out from the container.

References: [1] Sanders G. B. and Larson. W. E. (2012) *J. Aerosp. Eng.* 26 (19) 5-17. [2] Sperl M., et al. (2017) *ELS 2017*. [3] Zacny K., et al. (2010) *Aerosp. Conf. 2010*, 1-7. [4] Sullivan T. A., et al. (1994) *J. Aerosp. Eng.* 7 (2) 199-208. [5] Kawamoto H. and Shirai K. (2010) *J. Aerosp. Eng.* 25 (1) 132-138. [6] Adachi M., et al. (2017) *J. Aerosp. Eng.* 31 (2) 04017095. [7] Adachi M., et al. (2017) *J. Electros.* 89, 88-98. [8] Kawamoto H., et al. (2016) *J. Aerosp. Eng.* 29 (1) 04015031. [9] Zhang F., et al. (2017) *Adv. Pow. Tech.* 28, 356-362.

THE LUNAR METEORITE VIRTUAL MICROSCOPE COLLECTION.

M. Anand^{1,2}, A. G. Tindle¹, S. P. Schwenzer¹, S. P. Kelley^{1,3} and E. K. Gibson^{1,4}. ¹Science, Technology, Engineering, & Maths Faculty, The Open University, Walton Hall, Milton Keynes, MK7 6AA, UK, [E-mail: mahesh.anand@open.ac.uk] ²Department of Earth Sciences, The Natural History Museum, London, UK. ³School of Geosciences, College of Science & Engineering, University of Edinburgh, Edinburgh EH9 3FE, UK. ⁴XI111, ARES, NASA Johnson Space Center, Houston, TX 77058. U.S.A.

Abstract: The Lunar Meteorite Virtual Microscope (VM) Collection is an Open Educational Resource which allows users to investigate the optical mineralogy and petrology of lunar meteorites. It uses a software that duplicates many of the functions of a traditional petrological microscope. The VM's may be viewed at:

<https://www.virtualmicroscope.org/content/lunar-meteorites>

Introduction: 2018 celebrates 25 years of virtual microscope work at the Open University. During this time we have created many collections based on terrestrial rock samples – Charles Darwin's Beagle Collection, UK Virtual Microscope Collection, Irish University Rock Collection, St Austell Granite Collection, Greenland Collection. We have also built a Cornish Mineral Heritage Collection based on mineral specimens in the Rashleigh Collection at the Royal Cornwall Museum in Truro, Cornwall.

When The Open University (OU), the world's largest Distance Learning Higher Education Establishment, faced the challenges of how to supply thousands of undergraduate students with an interactive petrological microscope and a personal set of thin sections, it was decided to develop a software tool called the Virtual Microscope (Figure 1). The Virtual Microscope allows users to view an entire thin section in plane polarized light, between crossed polars and also in reflected light.

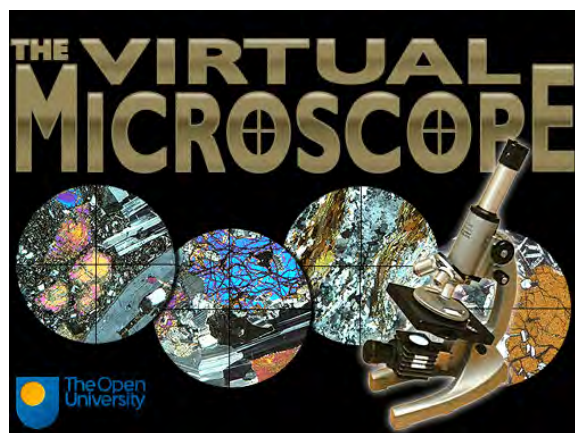


Figure 1: An early version of the Virtual Microscope produced for Open University students.

Our work is not only Earth-bound but in addition there are several stand-alone VM collections of

samples that are extra-terrestrial. The Europlanet Meteorite Collection features a spectrum of meteorite types especially including chondrites and achondrites such as eucrites and angrites. We worked with the Natural History Museum in London to create a British and Irish Meteorites Collection and with the help of many colleagues created the Martian Meteorite Collection. Finally, we have been working for the last three years on a collaborative project with NASA to create a VM collection of representative samples brought back to Earth during the Apollo Program. We have already published the bulk of this work (Apollo 11 to 16): <https://www.virtualmicroscope.org/collections/apollo> and are currently working on Apollo 17 samples.

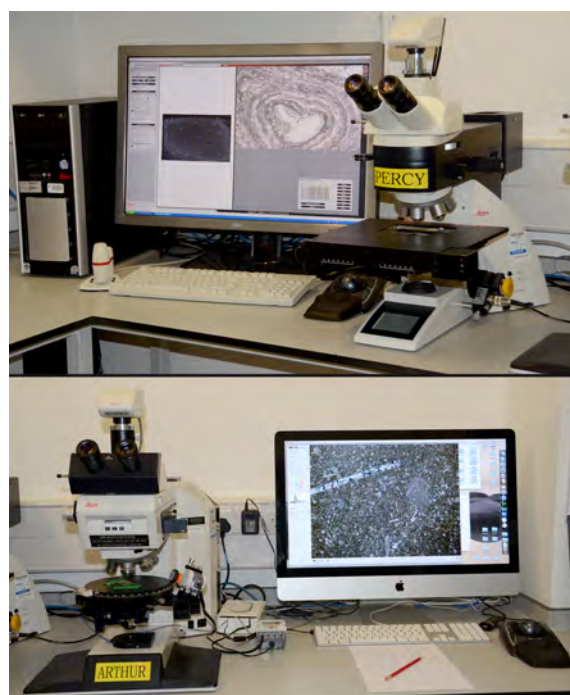


Figure 2: The VM lab at the Open University.

Method: Production of a virtual microscope dedicated to a particular theme divides into four main parts - photography, image processing, building and assembly of virtual microscope components, and publication on a website. The method used to produce the VM images has been described earlier [1, 2] and involves two Leica research microscopes (Figure 2).

We have also created virtual microscopes of a few lunar samples in an interactive book titled *Moon Rocks: An Introduction to the Geology of the Moon*. [3]. This is freely available from the Apple Bookstore.

Here, we launch our latest extra-terrestrial virtual microscope collection – Lunar Meteorites.

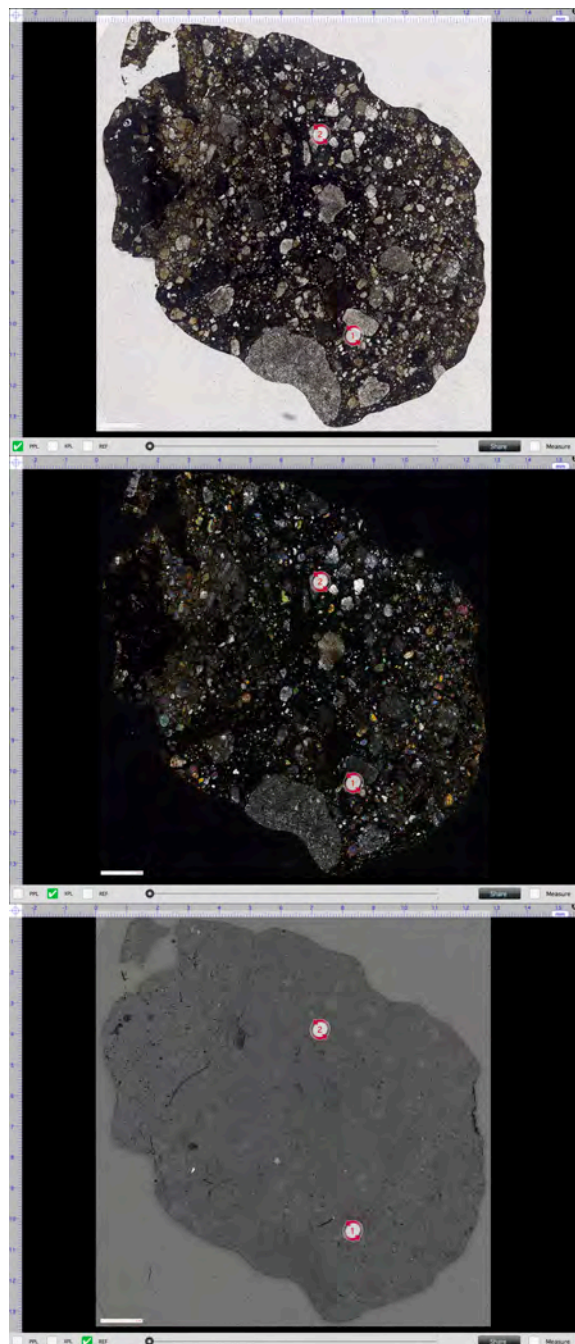


Figure 3: Screen shots from the new VM for lunar meteorite NWA 10989. Views in plane polars (top), between crossed polars (middle) and reflected light (bottom). Red circles show positions of rotation points.

Research possibilities: Although the Virtual Microscope was originally conceived as a teaching aid and was later recognised as a means of public outreach and engagement, we are increasingly realizing its potential as a high level research tool. This resource is widely used with several thousand users per week accessing the OU's VM site. The mid-week peak of visitors speaks of professional use. We note that the time visitors spend on the Apollo collection is significantly longer than for other collections, with a maximum at ~10 mins, and an average of ~5 mins (Data from Dec. 2017). The scientific return from these collections will increase exponentially as further VMs are completed and then discussed and shared between co-workers. We anticipate that our latest Lunar Meteorites Collection will serve the same purpose (Figures 3 and 4).

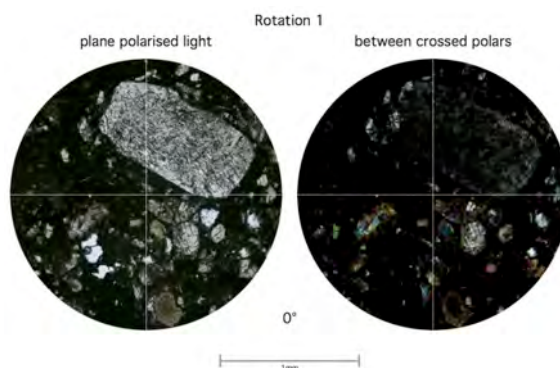


Figure 4: Screen shots of a rotation point.

References:

- [1] Gibson, E.K., Tindle, A.G, Kelley S.P. and Pillinger J.M. (2016), In LPSC XLVII, ABSTRACT #1199.
- [2] Gibson, E.K., Tindle, A.G, Kelley S.P., and Pillinger J.M. (2017), In LPSC XLVIII, ABSTRACT #1181.
- [3] Tindle, A.G and Kelley S.P., (2012) *Moon Rocks: An Introduction to the Geology of the Moon*. Apple Bookstore.

PROSPA: AN INSTRUMENT FOR LUNAR POLAR VOLATILES PROSPECTING AND IN SITU RESOURCE UTILIZATION PROOF OF CONCEPT. S. J. Barber¹, I. P. Wright¹, F. Abernethy¹, M. Anand¹, K. R. Dewar¹, M. Hodges¹, P. Landsberg¹, M. R. Leese¹, G. H. Morgan¹, A. D. Morse¹, J. Mortimer¹, H. M. Sargeant¹, I. Sheard¹, S. Sheridan¹, A. Verchovsky¹, F. Goesmann², C. Howe³, T. Morse³, N. Lillywhite⁴, A. Quinn⁴, N. Missaglia⁵, M. Pedrali⁵, P. Reiss⁶, F. Rizzi⁷, A. Rusconi⁷, M. Savoia⁷, A. Zamboni⁷, J. A. Merrifield⁸, E. K. Gibson Jr.⁹, J. Carpenter¹⁰, R. Fisackerly¹⁰, B. Houdou¹⁰, E. Sefton-Nash¹⁰ and R. Trautner¹⁰. ¹School of Physical Sciences, The Open University, Milton Keynes, MK7 6AA, UK (simeon.barber@open.ac.uk), ²Max Planck Institute for Solar System Research (MPS), Germany, ³RAL Space, UK, ⁴Airbus Defence and Space, UK, ⁵Media Lario Technologies, Italy, ⁶Technical University of Munich, Germany, ⁷Leonardo S.p.A., Italy, ⁸FGE Ltd., UK, ⁹ARES, NASA Johnson Space Center, USA, ¹⁰ESA ESTEC, Netherlands.

Introduction: Many missions are in preparation for in-situ prospecting for lunar polar volatiles and by extension the assessment of such materials as potential resources to support future exploration missions. In this context, the European Space Agency (ESA) is developing the Package for Resource Observation and in-Situ Prospecting for Exploration, Commercial exploitation and Transportation (PROSPECT). It comprises a drilling element (ProSEED – PROSPECT Sample Excavation, Extraction and Delivery) and a Sample Processing and Analysis element – ProSPA. PROSPECT is designed for high-latitude landing sites, to investigate volatiles and other resources from the perspectives of science (e.g. nature, abundance, distribution and processing of lunar volatiles) and of exploration (e.g. availability and extractability of materials for In-Situ Resource Utilization – ISRU).

Instrument Implementation: PROSPECT is part of the Roscosmos Luna-27 lander (Figure 1) planned to visit the south polar region of the Moon in 2022-3. ProSPA comprises two physical units – (1) a Solids Inlet System (SIS) comprising a series of single-use sample ovens on a rotary carousel together with a sample imager, and (2) a miniature chemical analysis laboratory incorporating two mass spectrometers and associated ancillary / control systems.

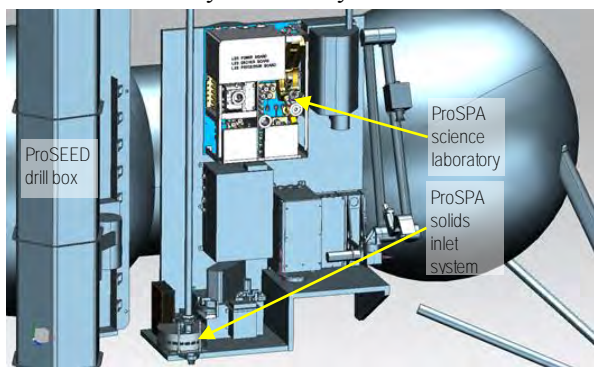


Figure 1: Location of ProSPA and ProSEED drill box on Luna-27 lander (IKI/Roscosmos)

Volatiles Preservation: At the low temperatures expected in the sampled lunar regolith (~120 to 150 K), a wide range of volatiles may exist in a variety of forms, including physically (loosely) bound and chemically (more strongly) bound species. The stability (hence rate of loss) of lunar volatiles is a strong function of temperature [1] as well as particle size [2]. To minimize the loss of volatiles before the sample is hermetically sealed within the ProSPA oven, the landing event is controlled such that instruments involved in sample acquisition and analysis face away from the Sun. Thus sample drilling, extraction and transfer to the ProSPA ovens occurs in the shade of the lander (though reflected heat is a necessary consideration). The SIS is thermally isolated from the “warm” enclosure of the chemical analysis unit, allowing the oven to be at 150 K or colder when the sample is received from the drill. After sample transfer, the carousel is rotated to place the sample-containing oven under an imager which confirms the presence of sample and enables estimation of the sample volume (up to ~60 mm³). Then the sample oven is rotated to the “tapping station” position where an actuator seals the oven to a pipe which runs to the science laboratory.

Volatiles Extraction: Volatiles are extracted from the sample through heating within the sealed sample oven. A variety of heating profiles are envisaged to accomplish a variety of analysis modes (Figure 2).

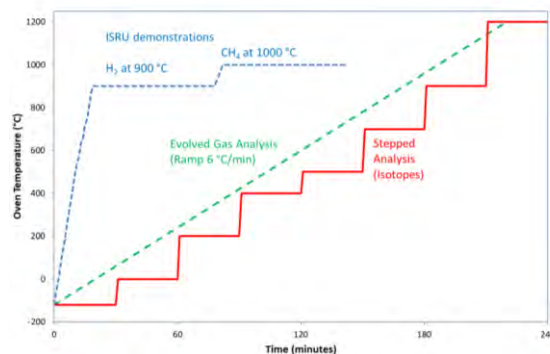


Figure 2: Example sample heating profiles

Evolved gas analysis: the oven is heated at a ramp rate of 6°C/min and the released gases are continuously analyzed by mass spectrometer to generate evolved gas analysis plots of the type previously presented for analysis of Apollo samples [3].

ISRU demonstration: the oven is heated to 900°C in the presence of added hydrogen feed gas to extract oxygen through reduction of mineral phases [4, 5]. Subsequently or alternatively, methane feed gas can effect gas-phase carbothermal reduction at 1000°C.

Stepped pyrolysis or combustion: gases released at a series of fixed temperatures from samples in vacuum or in oxygen respectively are isotopically analyzed in a magnetic sector mass spectrometer.

Volatiles Analysis: Volatiles released through the previously described extraction processes are passed to the ProSPA chemical laboratory for analysis. This comprises an ion trap device for analytical mass spectrometry (target m/z range 2-200 amu) and a magnetic sector instrument for stable isotopic analysis (~per mil level precision), together with the associated gas handling and processing components including open/closed valves, metering valves, micro-reactors, pressure sensors, reference materials etc. The chemical laboratory subsystems are shown in Figure 3.

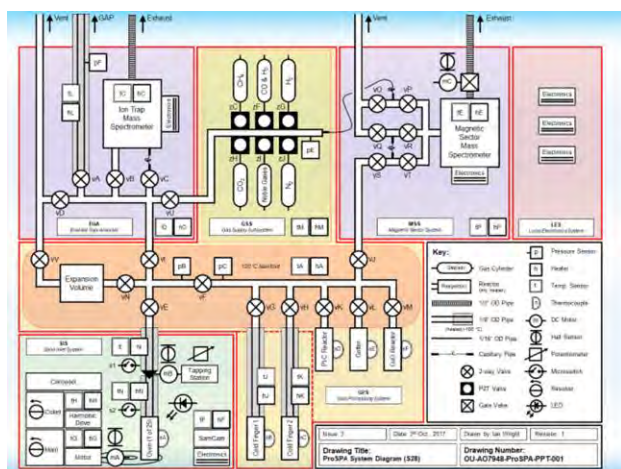


Figure 3: Schematic diagram of ProSPA Solids Inlet System (lower left) and Science Laboratory

Instrument Heritage: To minimise development timescales in line with the schedule of the Luna-27 Roscosmos-ESA mission to the lunar south pole in 2022, the ProSPA instrument draws heavily upon European heritage in flight hardware. The Solids Inlet System is based upon similar systems flown on Rosetta Philae [6] and in development for ExoMars rover [7], adapted for the lunar environment and sample nature. The ion trap mass spectrometer is based on the

lightweight (<500 gram all-in) device which made the first chemical analyses on the surface of a comet on board Rosetta Philae [8]. The magnetic sector instrument for isotopic analysis derives from that developed for the Gas Analysis Package on Beagle 2 Mars lander [9]. Further gas processing components, electronics and software share similar heritage.

The anticipated science output is the identity, quantity and isotopic composition of volatiles as a function of depth (up to 1.2 m) in the lunar surface.

Current Status: ProSPA is undergoing a Preliminary Design Review at the end of Phase B. Various technical challenges have been addressed through modelling and/or laboratory work in areas such as oven sealing in the lunar thermal and dust environments, volatiles preservation, sample imaging and volume estimation. Recent results will be presented. A prototype instrument is in construction to enable testing of the extraction profiles shown in Figure 2 and optimization of resource requirements (power, time, energy). Current predictions are that ProSPA requires 10 kg including margin and peak power of ~70 W.

Conclusions: ProSPA is a powerful and versatile scientific laboratory for analyzing lunar volatiles and testing thermo-chemical extraction processes relevant to ISRU. Using techniques developed in the laboratory and refined in previous missions it will identify, quantify and isotopically characterize (D/H, $\delta^{13}\text{C}$, $\delta^{15}\text{N}$, $\delta^{18}\text{O}$) samples extracted from up to 1.2 m depth by the ProSEED drill. The acquisition of contextual images of the samples and the use of on-board reference materials will enable the results from ProSPA to be interpreted in the context of existing lunar datasets. ProSPA will provide ground truth for remote sensing data and inform future plans for lunar exploration and ISRU.

Acknowledgement: ProSPA is being developed by a consortium led by The Open University, UK, under contract to the PROSPECT prime contractor Leonardo S.p.A., Italy, within a programme of and funded by the European Space Agency.

References:

- [1] Zhang J. A. and Paige D. A. (2009) *Geophys. Res. Lett.*, Vol. 36, L16203
- [2] Andreas E. L. (2007) *Icarus* 186 24–30
- [3] Gibson E. K., Jr. et al. (1972) *Proc. Lunar Sci. Conf.* 2029-2040
- [4] Sargeant et al. (2018) ELS, [5] Reiss et al. (2018) ELS [6] Finzi A. et al., (2007) *Sp. Sci. Rev.* 128: 281–299
- [7] Goetz, W. (2016) *Int. J. Astrobiology* 15 (3): 239–250
- [8] Wright, I. P. (2015) *Science* Vol.349 (6247), pp.aab0673
- [9] Wright, I. P. (2003) *Analyst*, 128, 1300-1303

L-DART: DIRECT ANALYSIS OF RESOURCE TRAPS WITHIN LUNAR PERMANENTLY SHADOWED REGIONS BY A PENETRATOR MISSION. S. J. Barber¹, S. Sheridan¹, H. M. Sargeant¹, I. P. Wright¹, A. Ballard², P. D. Church², P. Gould², M. D. Gupta², S. Hussain², G. H. Jones³, U. Derz⁴, M. Perkinson⁴, N. J. Murray⁵. ¹School of Physical Sciences, The Open University, Milton Keynes, MK7 6AA, UK (simeon.barber@open.ac.uk), ²QinetiQ Limited, UK, ³University College London, Mullard Space Science Laboratory, UK, ⁴Airbus Defence and Space Limited, UK, ⁵Dynamic Imaging Analytics Ltd, UK

Introduction: Lunar Direct Analysis of Resource Traps (L-DART) addresses many current knowledge gaps concerning lunar volatiles and permanently shadowed regions (PSRs), providing in-situ ground truth data to calibrate existing remote datasets.

It builds on UK expertise in developing and testing penetrator system concepts for the Moon and Europa (e.g. MOONLITE [1]). Following release of a Penetrator Descent Module in lunar orbit (Figure 1), its Penetrator Delivery System performs de-orbit and orientation before releasing the instrumented Penetrator to penetrate a few meters into target lunar surface at ~300 m/s. The penetrator itself serves as the sampling tool and an on-board mass spectrometer analyses in-situ the volatiles released both in the impact and in the subsequent thermal soak from lander to surrounding regolith. A pair of 3-axis accelerometers measure regolith structure during landing and constrain penetrator final location. Temperature sensors enable deduction of regolith thermal properties. Pre- and post-impact imagery provides context. Science is complete and data relayed to Earth within 1-2 hours, minimizing system mass and lifetime requirements.

Possible landing sites include Cabeus (for comparison with LCROSS) or Shoemaker which exhibits excess hydrogen, or areas indicated by LRO to exhibit putative surface frost. Alternatively, L-DART could target the hypothesised ancient (paleo) south pole [2] and hence potentially ancient volatiles.

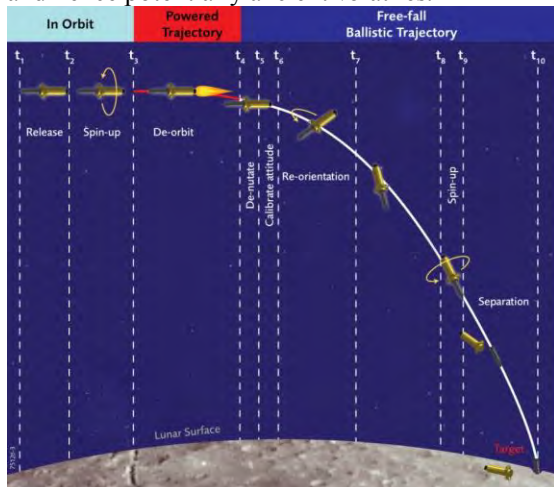


Figure 1: Typical events during penetrator delivery (credit Airbus Defence and Space)

Lunar polar volatiles and knowledge gaps:

After the lull that followed the Apollo and Luna era, many spacefaring nations are preparing new lunar missions. Many such missions target high latitudes, now understood to be very different to the largely equatorial areas sampled previously. Orbital data have revealed an extraordinary near-polar thermal environment, with the Moon's low angle of tilt meaning that topography dominates illumination conditions and temperatures in PSRs are among the lowest of any solar system body. These areas act as cold traps where a range of volatiles are thermally stable on geological timescales [3] offering a scientific treasured trove of time-integrated volatile inventory. These potentially abundant supplies of volatile resources including water, could represent a source of materials for in-situ resource utilization (ISRU). Together with nearby raised areas that offer near-constant illumination (e.g. [4]), these potentially enable sustained exploration and even a permanent human presence.

The search for lunar polar water is therefore a highly active research topic. Although a variety of instruments on orbiters have indicated the presence of hydrogen or water at or near the surface, unequivocal interpretation of orbital datasets can be problematic. The most direct evidence for lunar polar volatiles comes from the Lunar Crater Observation and Sensing Satellite (LCROSS) mission launched together with Lunar Reconnaissance Orbiter (LRO) in June, 2009 [5]. This culminated in the impact of the spacecraft's spent upper rocket stage into the permanently shadowed Cabeus crater near the lunar south pole. The impact was observed by a suite of instruments on the LCROSS shepherding spacecraft, and led to the deduction that the concentration of water ice at the impact site was $5.6 \pm 2.9\%$ by mass [6]. In addition to water, a number of other volatile species were detected by instruments on both the shepherding spacecraft and LRO (including near-infrared, visible and ultraviolet spectrometers; [6], [7]). Many of these were consistent with calculations on thermal stability [8], [9].

But still L-CROSS leaves questions unanswered. The amount of material excavated in the impact is uncertain (at least in part due to uncertainties in mechanical properties of the landing site regolith) and this propagates into uncertainties in the inferred con-

centrations of volatiles in the regolith. There is some suggestion of a delayed flash implying porosity in the target material; the sub-surface thermal environment was not measured directly. And because the observations on chemical composition of the plume were made remotely, these are subject to chemical processing that may occur within the plume hence measurements may not be fully representative of the original source materials. Notably, not only do current uncertainties relate to fundamental scientific questions, but they also involve many of the physical parameter inputs demanded by engineers seeking to design future missions.

Arguably, a rare consensus concerning lunar polar volatiles is that new landed missions are necessary, carrying suites of instruments to extract and analyze volatiles and characterize the source environment. An example is ESA's PROSPECT package [10]. At its heart is an ion trap mass spectrometer weighing only ~500 g yet capable of detecting a wide range of volatiles with high sensitivity, and with heritage of successful analogous measurements on the Rosetta comet lander [11], [12]. But its samples are supplied by a ~25 kg drill, and hence this is only suitable for deployment on a large static platform such as Luna-27 or perhaps a 250 kg-class rover. Smaller rovers in the ~25 kg class may also house such compact analysis instruments but direct regolith sampling depth may be limited to the upper ~10 cm [13].

Penetrators mission such as L-DART therefore present an ideal or even unique means through which to directly sample and analyze at depths analogous to those probed by remote sensing (i.e. the upper ~2 m), in lunar regions such as PSRs inaccessible to conventional spacecraft. Moreover, by using miniaturized and ruggedized hardware such as mass spectrometers [14] similar to those planned for landers such as Luna-27 [11], L-DART can provide valuable ground truth to aid the interpretation of remote data-sets.

Science Objectives and Instrumentation:

The science objectives of L-DART are summarized in its Science Traceability Matrix (to be presented). The focused payload of complementary and high TRL instruments comprises accelerometers, mass spectrometer, temperature sensors and imager(s). The acquired data provide unique in situ measurements of PSR volatiles and geotechnical/thermal properties. This ground truth greatly enhances existing and future remote datasets and informs future mission design. The descent imager provides wider geological context (local topography, geology, illumination) as well as images of high value for public engagement and outreach. The post-landing imager (if implemented) will provide complementary micro-scale imagery.

Current Status: The L-DART consortium is currently conducting a payload definition exercise to refine the reference payload. This will enable the updating of key payload parameters such as mass and volume to reflect recent developments in technology readiness level. In addition, preliminary results may be presented on a study by The Open University and QinetiQ (funded by UK Space Agency) aimed at increasing the understanding of the attenuation of the penetrator's UHF communications signal by any regolith overlying the onboard antenna post-landing.

The outcomes of the above activities will generate outputs ready for input to a Phase A type study in which the system design feasibility can be assessed and realistic estimates of the all-up penetrator system mass can be generated for input to more detailed mission design and cost estimating activities.

Conclusions: L-DART targets key scientific and exploration knowledge gaps concerning lunar polar volatiles, by making in situ measurements of volatiles and regolith thermal and geotechnical properties supported by contextual imaging at macro- and micro-scale. Many technological aspects have been matured in the last decade, and international partners are now actively being sought to exploit this significant potential and make the mission a reality.

Acknowledgement: The L-DART concept is being developed by a UK consortium led by The Open University (OU), with QinetiQ Limited, Airbus Defence and Space Limited and University College London, Mullard Space Science Laboratory. OU and QinetiQ gratefully acknowledge funding to SB from UK Space Agency under its CREST grant scheme.

References:

- [1] Smith, A. et al. (2008) *LPSC XXXIX*, 1238
- [2] Siegler, M. A. et al. (2016) *Nature*, 531, 480-4.
- [3] Paige, D. et al. (2010) *Science*, 330, 6003, 479-482.
- [4] Noda et al. (2008) *Geophys. Res. Lett.*, 35, L24203
- [5] Colaprete, A. et al. (2012) *Space Sci. Rev.* 167: 3. doi:10.1007/s11214-012-9880-6
- [6] Colaprete, A. et al. (2010) *Science*, 330, 463-468
- [7] Gladstone G. R. et al. (2010) *Science*, 330, 472-47
- [8] Zhang J. A. and Paige D. A. (2009) *Geophys. Res. Lett.*, Vol. 36, L16203
- [9] Zhang J. A. and Paige D. A. (2010) *Geophys. Res. Lett.*, Vol. 37, 3203
- [10] Barber, S. J. et al. (2017) *LPSC XLVIII*, 2171
- [11] Morse A. D. et al. (2015) *A&A* 583 A42
- [12] Wright I. P. et al. (2015) *Science*, 349(6247)
- [13] Urbina, D. A. et al. (2017) *Int. Astronautical Cong.* A3 2B Part 2 – LUVMI...
- [14] Sheridan et al. (2018) ELS

UNDERSTANDING THE APOLLO 15 MAGMATIC PLUMBING SYSTEM USING CRYSTAL SIZE DISTRIBUTION ANALYSIS. S. K. Bell¹, M. E. Hartley¹, K. H. Joy¹ and J. F. Pernet-Fisher¹. ¹School of Earth and Environmental Sciences, University of Manchester, Manchester, M13 9PL, UK. E-mail: samantha.bell@manchester.ac.uk.

Introduction: In 1971, the crew of Apollo 15 returned ~77 kg of lunar samples, one third of which are mare basalts. The Apollo 15 mare basalts have been chemical classified as quartz-normative or olivine-normative based on SiO₂, FeO and TiO₂ wt% [1,2]. The quartz-normative suite and the olivine-normative suite have similar eruption ages of ~3.35 and ~3.25 Ga, respectively. Bulk rock compositions of quartz-normative samples show relatively high SiO₂ contents of 47-49 wt %, with low FeO (19-20 wt. %) and TiO₂ (1-2 wt %) contents [3]. Conversely, the olivine-normative samples have bulk rock chemistries with lower SiO₂ concentrations of 44-46 wt % and comparatively higher FeO (22-23 wt %) and TiO₂ (2-3 wt %) [3].

A wide range of textures are present within the Apollo 15 mare basalt samples, from sub-ophitic to vuggy and highly vesicular rocks. However, the petrogenetic relationship and eruption histories of the two suites remains controversial. It has been suggested that the differences in major element chemistry could not be reconciled by differentiation alone and that the two suites must have originated from distinct sources within the lunar mantle [2,4]. Recent studies, nonetheless, have used major and trace element analysis to argue that the two suites can be related by complex multi-stage fractionation from a single mantle source [5]. In this scenario, the quartz-normative suite underwent a multistage cooling history with most fractional crystallization occurring within magma chambers and dikes in the lunar crust, prior to eruption. On the other hand, the olivine-normative suite predominantly underwent differentiation at low pressures in shallow crustal levels and/or in lava flows on the lunar surface [5,6,7].

Our study uses textural analysis of crystals in Apollo 15 mare basalts to further understand the petrogenetic relationship between the quartz-normative and olivine-normative suites and the magmatic processes via which they were produced.

Samples: Initial analysis has been conducted on five thin sections; Samples 15597,12 and 15597,18, 15125,6, 15475,15 and 15555, 209 (Fig.1). Samples 15597,12, 15597,18 and 15125,6 are chemically designated as parents – representing the initial magma composition from which the range of quartz-normative samples were differentiated. Sample 15475,15 is a quartz-normative fractionate sample believed to have been produced by fractional crystallisation of a parent magma and was chosen to test whether such signatures could also be determined via textural analysis. For comparison, olivine-normative

sample 15555,209 was also analysed. The chemical composition of 15555,209 is thought to represent a primitive volcanic liquid [1] and is, therefore, considered to be a parent melt sample.

Method: Crystal size distribution (CSD) analysis considers the population density of a mineral phase within different crystal size intervals and can be used as a quantitative method for determining the crystallization history of a magma. CSD plots can identify signatures of magma mixing, accumulation, fractionation and multi-stage cooling histories [8]. Backscattered electron (BSE) maps of each thin section, were collected using the FEI Quanta 650 FEG scanning electron microscope (SEM) at the University of Manchester. CSD data was then gathered by manually tracing the crystal boundaries of the mineral(s) in question from the BSE maps in CorelDraw. Crystal shapes were then analysed using ImageJ to attain properties such as major and minor axis crystal length. The 2D crystal data was then processed using CSDslice [9], to estimate true 3D crystal habit, before being stereologically converted into 3D crystal lengths in CSDcorrections [10]. CSD plots of population density against crystal length were produced for: pyroxene crystals in 15597,12, 15597,18 and 15125,6; plagioclase crystals in 15475,15; and oli-

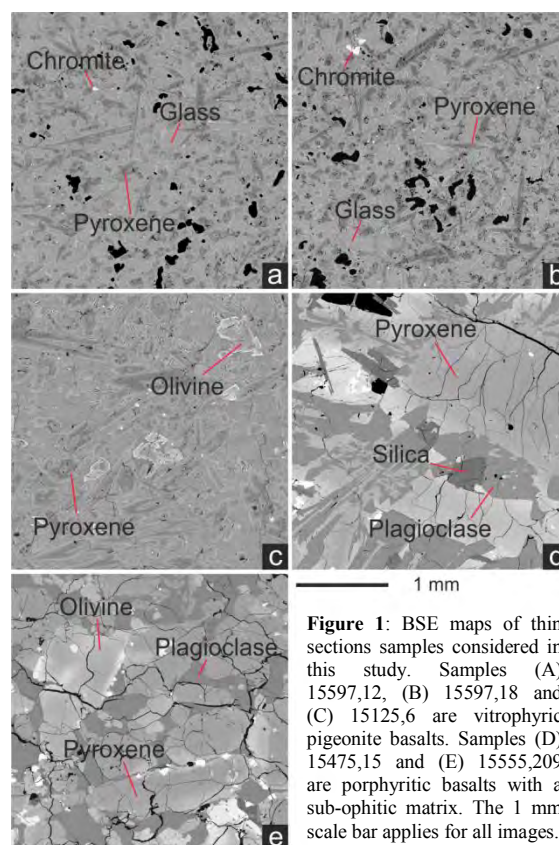


Figure 1: BSE maps of thin sections samples considered in this study. Samples (A) 15597,12, (B) 15597,18 and (C) 15125,6 are vitrophyric pigeonite basalts. Samples (D) 15475,15 and (E) 15555,209 are porphyritic basalts with a sub-ophitic matrix. The 1 mm scale bar applies for all images.

vine crystals in 15555,209. To further understand the crystal populations within the samples, aspect ratio was plotted against the square root of crystal area. Crystal residence times (akin to an average crystal growth time) were also calculated using the gradient of straight segments of the CSD plots.

Results: CSD plots for all parent samples (within this study) show similar straight trends, indicating the crystals underwent linear cooling without any accumulation, fractionation or magma mixing (Fig.2). Fractionate 15475,15 has a convex up CSD trend which is associated with accumulation, not fractionation (Fig. 2). Reasons for this signature could be due to entrainment of plagioclase crystals within a fractionate melt.

Aspect ratio vs. square root area plots for the quartz-normative parent samples display a clustered distribution suggesting a single crystal population. 15555,209 (Fig. 1e) and 15475,15 (Fig. 1d) both displayed a larger range in square root area values, which corresponds with the more variable grain size within these two sections. Calculated crystal residence times show that the average growth time for crystals within the quartz-normative samples ranged from 0.2 to 5.3 years. For olivine-normative sample 15555,209 the crystal residence time was calculated as 0.5 years.

Conclusion: Straight CSD curves and clustered aspect to square root area plots indicate a single crystal population within each quartz-normative parent sample that has undergone linear closed system cooling. A possible explanation of this trend could simply be closed system cooling within a lava flow on the lunar surface. An alternative theory could be that the quartz-normative magma was tapped from a dike or magma chamber, and crystals that had already been formed remained in the crust and were not erupted, instead crystals present within the samples grew in lava flows on the lunar surface. This scenario could also explain why sample 15475,15 does not show signatures of crystal fractionation, but may have entrained some crystals during magmatic ascent. As sample 15555,209 is the only olivine-normative sample considered here, it is only possible to speculate that analysis of other parent samples from this suite would show similar trends.

Future work will include further CSD analysis of samples within the quartz-normative and olivine-normative suites. Our work will provide new insights to lunar magmatic systems and how differences in magmatic plumbing systems may have led to the diversity seen within Apollo 15 mare basalts.

Acknowledgements: Thanks to NASA JSC curatorial team for allocation of samples and to an STFC studentship for funding.

References: [1] Chappell, B.W. and Green, D.H. (1973) *EPSL*, 18, 237–246. [2] Rhodes, J.M. and Hubbard, N.J. (1973) *LSC IV*, 2, 1127-1148. [3]

Rhodes J. M. and Hubbard N. J. (1976) *LSC VII*, 2, 1467-1489. [4] Snyder G. A., et al. (2000) *Origin of Earth and Moon*, 361-395. [5] Schnare, D.W. et al. (2008) *Geochimica et Cosmochimica Acta*, 72, 2556–2572. [6] Ryder, G. and Steele, A. (1988) *LPSC XVIII*, 273-282. [7] Ryder, G. and Schuraytz, B.C. (2001) *JGR*, 106, 1435-145. [8] Marsh, B.D. (1988) *Contrib Mineral Petrol*, 99, 277-291. [9] Morgan D. J. and Jerram, D.A. (2006) *Journal of Volcanology and Geothermal Research*, 154, 1-7. [10] Higgins, M.D. (2000) *American Mineralogist*, 85, 1105-1116.

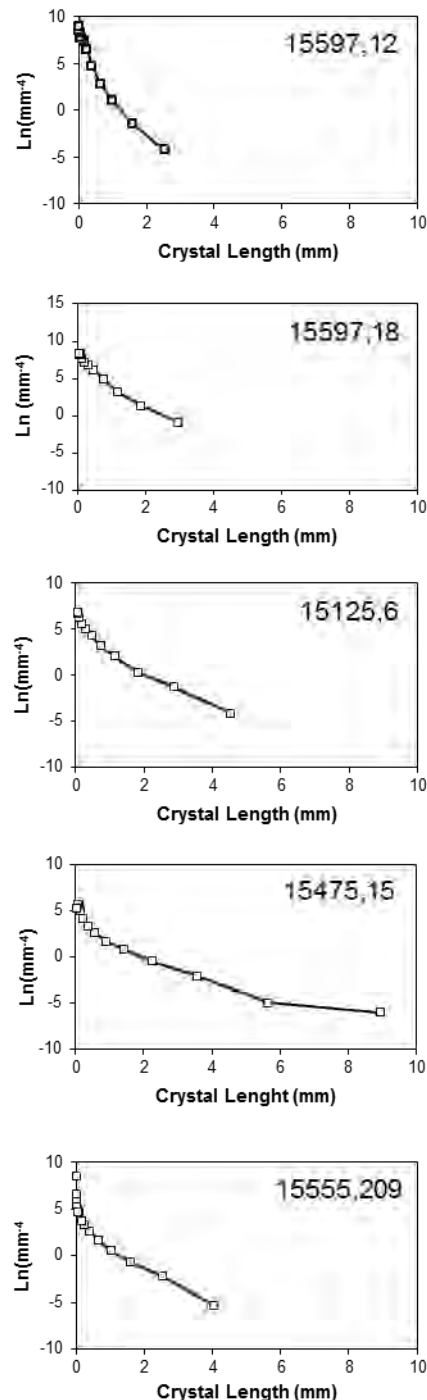


Figure 2: CSD plots of natural log of the population density (mm⁻⁴) against corrected crystal length (mm).

FUTURE LOW-COST LUNAR AND PLANETARY MISSIONS ENABLED BY COMMERCIAL SPACE COMPANIES.

Alain Berinstain¹ and Robert D. Richards², ¹Moon Express Inc., alainberinstain@moonexpress.com, 100 Spaceport Way, Cape Canaveral, Florida 32920, ²Moon Express Inc. bob@moonexpress.com.

Introduction: Science missions to the Moon need not be seen as rare and expensive opportunities. Affordable, repeated access to lunar orbit and/or the lunar surface is being made possible by innovations by commercial space companies.

Moon Express' vision is to open the lunar frontier with turn-key payload, data and services for missions to the Moon for a wide range of customers globally, including governments, NGO's, commercial enterprises, universities, and consumers.

Like the Earth, the Moon has been enriched with vast resources through billions of years of bombardment by asteroids and comets. Unlike the Earth, these resources are largely on or near the lunar surface, and therefore relatively accessible. Moon Express is blazing a trail to the Moon to seek and harvest these resources to support a new space renaissance, where economic trade between countries will eventually become trade between worlds. All Moon Express expeditions will prospect for materials on the Moon as candidates for economic development and in-situ resource utilization.

One of the greatest practical space discoveries of our generation is the presence of vast quantities of water on the Moon. Water not only supports life but its constituents, hydrogen and oxygen, are energetic and clean rocket fuel. The discovery of water on the Moon is a game changer, not just for the economic viability of lunar resources, but for the economics of humans reaching Mars and other deep space destinations. Water is the oil of the solar system, and the Moon can become a gas station in the sky to fuel human space exploration, development and settlement of the solar system. Moon Express will begin prospecting for water resources on the Moon with its very first expedition.

The MX family of spacecraft: Moon Express has developed a family of flexible, scalable robotic explorers that can reach the Moon and other solar system destinations from Earth orbit. The MX spacecraft architecture supports multiple applications, including delivery of scientific and commercial payloads to the Moon at low cost using a rideshare model, or charter science or commercial expeditions to distant worlds.

The MX robotic explorer spacecraft are optimized for launch on existing and emergent rocket systems. The payload masses quoted below assume no launcher constraints.

MX-1: A single stage spacecraft capable of delivering up to 30kg to the lunar surface.

MX-2: A dual-stage spacecraft that doubles the capability of the MX-1 and can reach the moons of Mars.

MX-5: A cis-lunar workhorse spacecraft that can deliver up to 150kg to lunar orbit or 50kg to the surface.

MX-9: A lunar prospector/harvester that can deliver up to 500kg to the lunar surface, including an embedded MX-1R spacecraft that can launch from the lunar surface and return lunar samples to Earth.

The MX spacecraft architecture supports multiple applications, including delivery of scientific and commercial payloads to the Moon at low cost using a rideshare model, or charter science expeditions to distant worlds.

Designed for Scout Class exploration capabilities starting from low Earth orbit, MX-1 delivers flexibility and performance to revolutionize access to the Moon and cis-lunar space.



MX-1 Spacecraft

Dual stage flexibility drives more payload to the lunar surface or extends the reach to deep space. Compatible with existing and emergent launch vehicles, the MX-2 delivers Scout Class possibilities for exploration and commerce at low cost.



MX-2 Spacecraft

Designed as a workhorse that can deliver 150kg to low lunar orbit from low Earth orbit, with a range of configurations to support lunar landing and cis-lunar operations, the MX-5 can also be outfitted with MX-1 or MX-2 staged systems that can bring the entire solar system within reach. Available in orbiter, lander, deep space probe and sample return configurations.



MX-5 Spacecraft

Designed for Frontier Class exploration capabilities, MX-9 will support robust lunar sample return operations. Like it's MX-5 little brother, the MX-9 can also be outfitted with MX-1 or MX-2 staged systems that can deliver over 10kms ΔV and extend its reach to span the solar system, and beyond.



MX-9 Spacecraft

Currently-Planned Lunar Missions: Our first expedition will utilize our MX-1E robotic explorer to deliver a diverse manifest of scientific and commercial payloads to the lunar surface. Our customers for this mission include the International Lunar Observatory Association, the University of Maryland, The National Laboratories of Frascati, Celestis and Google.

Following our initial “Lunar Scout” expedition next year, we will offer payload accommodations on future voyages, planned at the rate of one per year. But we can also scale up and increase the frequency of our lunar flights to meet market demand and opportunity.

Our second expedition in 2019, “Lunar Outpost”, will enable the first commercial presence and exploration of the lunar South Pole. It may in fact be the first-ever soft-landing at a lunar pole. The

primary goals of this mission are to set up the first lunar research outpost at a “peak of eternal light”, prospect for water and useful minerals, and accommodate a variety of research instruments for our expedition partners.

Our third expedition, “Harvest Moon”, will take place by 2020 and includes the first commercial sample return, beginning our business phase of lunar resource prospecting and harvesting. The samples brought back will be the only privately obtained lunar materials on Earth, and will be used to benefit science as well as commercial purposes.

Collapsing the cost of lunar missions: The paradigm of what it takes to fly a lunar mission has begun to shift. Launch costs are rapidly decreasing with emerging commercial launch providers. Commercial operators can reduce the cost of orbiters and landers by re-using designs and by innovating in ways that national space agencies are not mandated to do.

Although the current architectures for Moon Express missions involve going from Low Earth Orbit directly to Lunar orbit, then Lunar surface, or to other destinations in the solar system, integrating the MX family spacecraft into an architecture that involves the Deep Space Gateway presents new and exciting opportunities for science and for cis-lunar operations in general.

Mission concepts that assume that the DSG is available as a hub of operations in Lunar orbit can enable much larger landed masses on the lunar surface and/or continuous shuttle service for assets on the surface or for returned samples to DSG.

The Deep Space Gateway can also be a starting point for repeat robotic science and exploration missions to Mars or its moons, or to other solar system destinations. One could imagine scenarios in which refuelling of MX spacecraft could occur at DSG.

Moon Express has been able to collapse the cost of Lunar missions, and the incorporation of DSG into mission scenarios enable even lower mission costs with a workhorse for small payloads to and from the surface of the Moon, and from the Deep Space Gateway itself.

An Electronic Fieldbook supporting data collection and situational awareness during astronauts EVA geologic traverses on the lunar surface

L. Bessone¹, L. Turchi¹, F. Sauro², H. Stevenin¹, R. Pozzobon³, ¹Directorate of Human and Robotics Exploration, European Space Agency, loredana.bessone@esa.int, leonardo.turchi@mail.polimi.it, Herve.Stevenin@esa.int, ²Department of Biological, Geological and Environmental Sciences, Italian Institute of Speleology, Bologna University, [cescosauo@gmail.com](mailto:cescosauro@gmail.com), ³University of Padua, Dipartimento di Geoscienze, Via Gradenigo 6, 35131, Padova, Italy, riccardo.pozzobon@unipd.it

Introduction: During the Apollo EVA traverses astronauts gathered a variety of data, including pictures, videos, audio recordings, geographic positions and scientific data [1]. All these information have been later on associated to the samples retrieved, in order to increase their scientific value in the general geologic context. Compared to the Apollo missions, future EVA on the surface of the Moon will be supported by additional analytical tools that were not available at that time, in order to perform the most efficient science and to collect the most relevant samples to be brought back to Earth [2]. The way all these documentation and analytical data will be stored and made available in real time to crew members and scientists supporting from ground control will make a great difference in the final efficiency of scientific return of the traverses. Team Situational Awareness, both amongst crew members in the field and with the extended team in surface and orbital habitats and in ground control, will be a key asset, requiring that all and only relevant information and reference knowledge is retrieved, collected, indexed and stored in a structured way and made available in real time for fast decision making support and for later sample curation and scientific research.

Traditionally, in planetary geology analogue campaigns, data are separately captured through a multitude of devices and, mostly, stored locally at the campaign site, rarely integrated into an overall mission control and data collection and distribution system [3, 4]. In order to improve the effectiveness of operations, scientists located in a support centre control room should ideally receive in near-real time at least a relevant portion of the data acquired on the field and, after a brief analysis, provide scientific and operational guidance to the astronauts. In addition, astronaut shall have access to navigational and reference information, decision support tools, procedures to augment their effectiveness and autonomy.

With these high level requirements in mind, and in order to increase the effectiveness of their PANGAEA astronaut geological field training, the European Astronaut Center has initiated the development of an Electronic Field Book (EFB), with the main goal of integrating geological reference, traverse preparation, navigation and documentation, sampling protocols, analytical tools and of providing real time awareness to support scientists and mission control personnel. The project is ongoing, with concepts and needs verified for the first time in November 2017 during the PANGAEA-X analogue field test campaign in Lanzarote.

Electronic Fieldbook conceptual structure: The project has been structured in order to provide real time data and situation awareness to the following primary entities:

- A “field segment” (Astronauts), which primarily needs a portable tool to retrieve reference geological and navigation information, document locations, sites, samples, collect notes and drawings, attach scientific data from analytical tools and communicate with other users during a geologic traverse.



Fig. 1. The tablet is used to document the sampling site and to transfer the observations to the ground support team for evaluation

- A “ground segment” (mission team and science advisors), which needs a real-time overview execution of the traverse and of the observations and data collected, in order not only to direct or support the operations but also to provide relevant and informed scientific advice.



Fig. 2. The ground team maintains situational awareness over the overall traverse, each geological stop and sampling site, down to individual samples

The system is currently developed for a tablet (with ergonomic modifications to be usable with EVA gloves) providing the following functionalities:

- Display of pre-defined traverses and geological stops and sampling site, with retrieval of associated reference and real time information
- Marking of geological stops and sampling sites on the map
- Real-time identification of location of all field elements

- Collection and storage of geo-located relevant geological multimedial information and data analysis
- Exchange of information amongst field and ground segment
- Type of information to be retrieved, collected and exchanged includes, but is not limited to:
 - Geolocation
 - Rich text
 - Geolocated Photos
 - Audio
 - Videos and/or Panviews
 - Maps, Procedures, Geological databases

One of the main functionalities will be a continuous and automatic data flow from the field to the ground. This synchronization of data will allow to share information amongst users using two types of synchronization: one for real time transfer of compressed data, and one for safe storage of high resolution information.

The system is designed to cope with several connection losses and extended offline sessions, ensuring the availability of already synced data from a local database-replica and allowing users to continue their work transparently of provisional connection losses. The system creates a clustered P2P network to ensure the replication of data across multiple nodes, allowing two distant nodes to share a database without direct connection, relying on a series of inter-nodes to transfer replicated data (i.e. through a rover with an high-power transmitter).

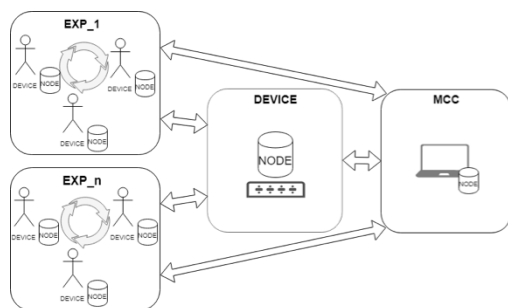


Fig. 3. The P2P network creating nodes between crew members and different crews and transferring in real time compressed data to MCC and high resolution data to a database archive.

Future implementations: the project is looking also to additional functionalities that could be added in the future to the EFB. These include the generation of panoramic images linked to samples and analytical data (i.e. analyses from portable analytical tools or rover assisted devices), the upload of existing geographic (geologic and satellite maps, etc.) and scientific databases (mineral lists, scientific relevance scales, etc.) in order to support decision making processes. All the data could then be accessed by the ground segment through real time Virtual or Augmented Reality, linking to other planetary geology

databases like the PLANMAP program of Horizon2020.

Conclusions: in future missions, science and sampling will be primary objective of astronaut and rover traverses on the surface of the Moon and Mars, before then, analogue test campaign and astronaut training will test operational concept and scenarios, and test scientific methods, operational procedures and instrumentation. The EFB project will provide a structured way to collect data during geological traverses and to made them available to the crew and ground control. This will strongly enhance the possibility of using portable analytical tools like VNIR, Raman and others as real time decision making support tools in the sampling selection, with support of scientists from mission control centres. The EFB database will also allow to record and geolocalize all the information obtained during the traverse, facilitating scientific research in the post-mission phase.

References: [1] Goddard E. N. et al. (1965) *Project Apollo Field Geology Planning Team*. [2] Hodges K. V. and Shmitt H. (1997) *Geological Society of America Special Paper 483*, 17–31. [3] Hurtado J.M et al. (2011) *Acta Astronaut.* 90(2), 344-355. [4] Young. et al. (2017) *Planetary Science Vision 2050 Workshop* (Contrib. No. 1989).

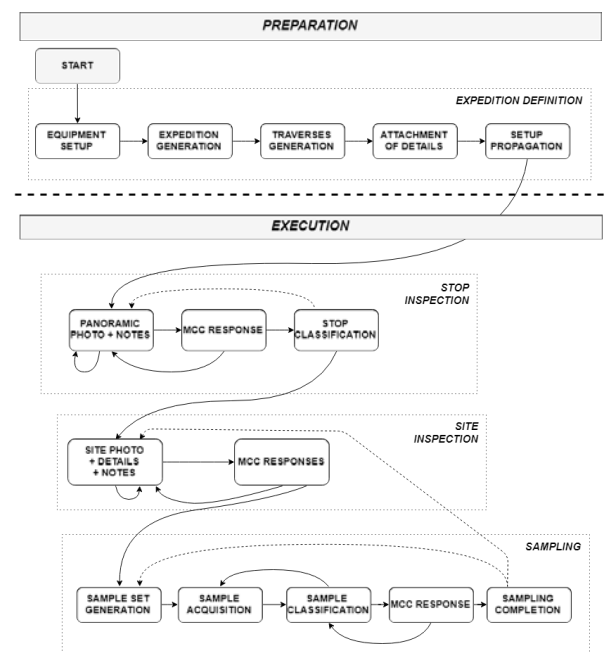


Fig. 4. Hierarchical structure of the traverse process through the Electronic Fieldbook classification. The EFB allows a continuous feedback from the Mission Control (MCC) based on the data gathered in the previous phase by the crew. The following gerarchical classification is applied: 1) “Stop” is a generic location were the crew collect PanView images and other overview information; 2) A “Stop” can be upgraded to a “Site” if the crew decides to perform a more detailed analysis of the location providing also analytical data from potential samples for evaluation; 3) A “Site” becomes a “Sampling Site” if after evaluation from MCC it is decided to proceed with the sampling phase.

Technologies and operational concepts for field geology and exploration on the Moon: the ESA PANGAEA-eXtension campaign in Lanzarote (Canary Archipelago, Spain)

L. Bessone¹, F. Sauro², M. Maurer¹, M. Piens¹, Directorate of Human and Robotics Exploration, European Space Agency, loredana.bessone@esa.int, matthias.maurer@esa.int, matthias.piens3@gmail.com, ² Department of Biological, Geological and Environmental Sciences, Italian Institute of Speleology, Bologna University, cesco-sauro@gmail.com

Introduction: After the successful implementation in the last years of the CAVES and PANGAEA training programmes [1, 2], ESA decided to develop and offer to internal actors, partner agencies, and external investigators analogue test campaigns, associated to the astronaut expeditions, focused on testing relevant technologies and operational concepts for field geology and exploration. The first campaign was called PANGAEA-eXtension and was implemented for the first time on the island of Lanzarote, Spain in November 2017, immediately following the last session of the PANGAEA astronaut planetary geology field training. The unique geological features present on this arid volcanic island, the presence of lava tubes and the extensive expertise developed within the PANGAEA astronaut training provided an ideal setting. Different sites, with specific geologic and environmental characters were made available within the Lanzarote Geopark and a complex logistic framework was set up in order to maximize efficiency and interconnection between the different experiments. The campaign was conducted with the participation of European astronauts and the assistance of ESA experts with the specific goal of evaluating potential applications and developments for future mission scenarios and to increase operational relevance of training.

Campaign goals: Two main objectives were identified for the first campaign: testing of technologies and operations for geological and geomicrobiological sampling, and testing of technologies for exploration, mapping, navigation and communication in low lighting conditions, lava tubes and rough terrain. Both these objectives are within the general aim to acquire knowledge on how to develop exploration and field geology strategies for planetary missions, with a specific focus on lunar and martian settings.

Fifteen experiments were proposed by eleven different research institutions and companies, involving four different space agencies, allowing to develop a testing programme with an ambitious set of inter-related goals, with outcomes applicable either or both to human and robotic exploration.

The PANGAEA-X experiments: The PANGAEA 2017 eXtension campaign took place from 20th to 24th November 2017. For the 5 days of field trials, interrelated activities were combined to create more valuable tests and operational scenarios. The first two days were dedicated to tests of surface geological sampling and analytical instrumentation and operations, with human-robotics interaction, taking into account mobility constraints of lunar surface sorties.

The last three days took place in low light/subterranean environments and were focused mainly on lava tube exploration and mapping. The following research projects have been implemented:

- Sampling Sequence with Constraints (SAMCO) and Operation Concept Comparison (OPSCO): the European Astronaut Center tested the use of a combination of instrumentation (Apollo tools, SPLIT, PANalytical tools) and different protocols to support alternative surface operations concepts for reconnaissance and sample collection on planetary surfaces, taking into account mobility constraints.
- Small Planetary Linear Impulse Tool (SPLIT): a geo rock-splitting tool developed by the Space Research Centre of the University of Leicester. This tool provides a new method of rock splitting through multiple very small impacts on a rock surface. Astronauts tested the operation of the tool with different type of lithologies and geologic settings, also with full integration in the OPSCO experiment.
- PANalytical (PAN): PANalytical analytical XRF and VNIR devices were tested for in-situ analysis of samples taken by the astronauts, also with integration to the OPSCO experiment.
- Environment Modelling and Navigation for Robotic Space-Exploration (ENTERN): lead by the German Research Centre for Artificial Intelligence (DFKI), this research project focused on testing a rover system for exploration of rough terrain such as lava tubes; the rover ASGUARD was tested both autonomously and in teleoperation mode to evaluate critical constraints of the environment and efficiency of the different settings.
- Microbiological Sampling Sequence (MICSS) and DNA extraction (DNAX), with the support of the Mobile Procedur Viewer (MOBIPV): the “Instituto de Recursos Naturales y Agrobiología de Sevilla” and the NASA’s Johnson Space Center provided specific instrumentation and procedures to perform microbiologic sampling and in situ DNA extraction and sequencing in a lava tube. The experiment was performed by an ESA astronaut within an operational relevant scenario, taking into account sampling protocols to avoid cross contamination, and with the support of the ESA mobIPV procedure viewer.

- Survival of Bacteria and Lichens on Mars Analogs and Space (SUBLIMAS): The Spanish “Instituto Nacional de Técnica Aeroespacial” investigated the colonisation of lichens in martian analogue geologic settings on Lanzarote using specific portable instrumentation.
- Augmented field Geology and Geophysics for Planetary Analogues (AGPA): a project of the Jacobs University Bremen and DLR with multiple experiments related to planetary geology investigation approaches and analytical tools. The AGPA team tested a geo-electric system searching subsurface features (cavities, lavatubes), an innovative LIDAR mapping system inside of the lava tube, and a passive seismometer. Drone photogrammetry was used for documenting and for 3D high resolution reconstruction of the Tinguatón testing site.
- Pegasus backpack (PEGASUS LEICA): Leica Geosystems (France) tested a combined SLAM/LIDAR systems embedded in a portable backpack for real-time mapping of lavatubes and rough terrains.

All the experiments were documented with detailed reports and the results and data obtained by the different teams were presented at the European Geoscience Conference in march 2018. The campaign was deemed by all participants a really usefull platform for validating concepts and instrumentation, mainly thanks to the integration in realistic operational scenarios and to the combination of field geology with surface and subsurface human and robotics operations (i.e. analytical tools and operational concepts).

Conclusions: The synergies created by the PANGAEA-X campaign have demonstrated to be extremely useful for ESA in the framework of future human and precursor planetary missions since it allows testing and validation of complex operational concepts and testing of exploration technologies, scientific methods and instrumentation. In addition, it fosters the exchange between research institutes, instrument developers and operational experts and thus boosts synergetically the use of novel portable analytical instrumentation and spin-in of new technologies and research into operations, as demonstrated also for other analogue testing campaign organized by NASA like Rats [3], NEEMO [4] and RIS⁴E [5]. Last but not least it provides a continuously increasingly relevant operational growth and novel scenarios for future CAVES and PANGAEA training events.

References: [1] Bessone L. et al. (2017) *Proceeding of the 17th International Congress of Speleology*. [2] Sauro F. et al. (2017) *European Lunar Symposium 2017*. [3] Hurtado J.M et al. (2011) *Acta Astronaut.* 90(2), 344-355. [4] Abercromby, A. F. et al., (2013) *43rd International Conference on Environmental System*, 3506. [5] Young. et al. (2017) *Plane-*

tary Science Vision 2050 Workshop (Contrib. No. 1989).

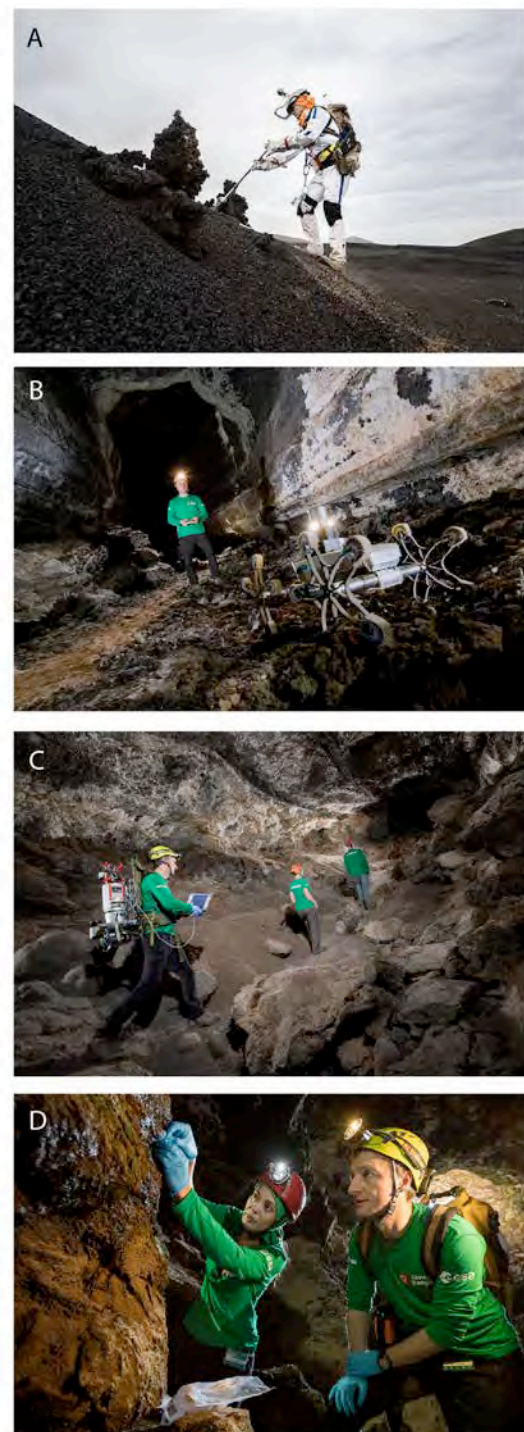


Fig. 1. ESA astronaut Matthias Maurer took part in different experiments: A) Testing of Apollo Tools during the OPSCO project (photo A. Romeo/ESA); B) Operating the ENTERN Asgard rover in the Corona Lava Tube (photo R. Shone/ESA); C) Testing of the LIDAR mobile system from AGPA-L in a Lava Tube (photo R. Shone/ESA); d) Microbiological sampling within the frame of MICSS and DNAX experiments (photo R. Shone/ESA).

MOBILE IN-SITU EXPLORATION OF LUNAR VOLATILES WITH THE LVS ON LUVMI

J. Biswas¹, P. Reiss¹, S. Sheridan², S. Barber², C. Pitcher², M. Reganaz³, L. Richter³ ¹Institute of Astronautics, Technical University of Munich, Boltzmannstr. 15, 85748 Garching, Germany, (j.biswas@tum.de), ²The Open University, Milton Keynes, MK7 6AA, UK, ³OHB System AG, Manfred-Fuchs-Str. 1, 82234 Weßling, Germany,

Introduction: Lunar volatiles are considered as a potential resource for future exploration efforts. Remote observations have confirmed the existence of volatiles deposits in permanently shadowed regions (PSRs) near the lunar poles [1], but in-situ measurements of local abundances are necessary to determine the economic viability of future exploitation. Currently existing or proposed instruments for volatiles prospecting, such as the ESA PROSPECT payload for the Luna-27 lander [2], consist of many different subsystems, like sampling drill, sample distribution systems, gas extraction ovens, and an analysis instrument suite, resulting in comparably high overall mass and complexity. The Lunar Volatiles Scout (LVS) [3,4] heats soil samples in-situ inside the drill, thus avoiding the need for extensive sample logistics and reducing the associated risks of sample degradation. Its drill can sample volatiles on the lunar surface as well as in the shallow subsurface [5] up to a depth of 20 cm. With an overall instrument mass of less than 2.0 kg, the LVS will be carried by the Lunar Volatiles Mobile Instrumentation (LUVMI) [6], a 20 – 40 kg class rover, capable of operating in and around PSRs. LUVMI is currently under development by a consortium of Space Applications Services, The Open University, Technical University of Munich, OHB Systems, and Dynamic Imaging Analytics in the European Horizon 2020 framework.

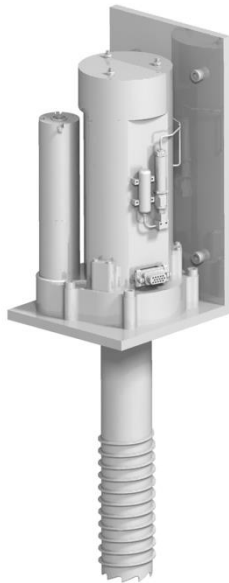


Figure 1: CAD image of the LVS

System Description: Figure 2 shows a schematic of the LVS: The hollow drill shell of the Volatiles Sampler (VS) encloses sample volume of regolith

(max. 218 cm³) and a heating rod in its center, which can heat the sample up to 400 K to extract present volatiles. Extracted gases either accumulate inside the sample volume, diffuse out through open bottom of the shell or flow through a calibrated orifice. Monitoring the pressure profile over time inside the sample volume allows the inference of the original abundance of volatiles in the sample. A miniature mass spectrometer, the Volatiles Analyser (VA), identifies the chemical species and relative concentrations for extracted volatiles with a m/z ratio between 10 and 150. The drill shell is equipped with an auger and is rotated by a brushed DC motor to ease insertion, while maintaining a low rotational speed to reduce heating through friction.

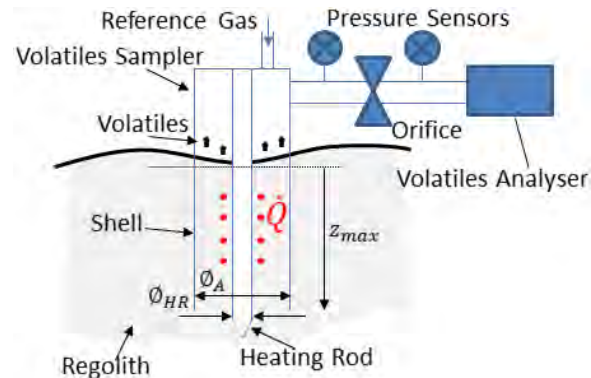


Figure 2: Schematic of the LVS

Prototypes and Testing: As part of the preparatory tests for the development of the VS, a mechanical prototype was designed and manufactured to determine the necessary vertical insertion force and the optimal drill shell geometry. It was found that no more than 30 N were required to reach a minimum depth of 10 cm. A static gas extraction prototype was built and tested in a dust tolerant (“dirty”) thermal-vacuum chamber to demonstrate gas extraction and sample preparation procedures.

Currently, an integrated prototype is being manufactured (Figure 1) that will allow end-to-end testing with cryo-cooled samples and mechanical insertion in thermal-vacuum conditions. This will allow a full characterisation of the integrated LVS in a relevant environment with the goal to raise the instrument technology readiness level to TRL 6.

Expected Results: The LVS enables in-situ extraction of volatiles from undisturbed lunar regolith samples near and inside PSRs. With the mobile platform LUVMI, a high number of repeated measurements at different locations, different depths, as well

as over longer periods of time will be possible. This allows the characterisation of volatile species



Figure 3: Static gas extraction prototype during thermal-vacuum testing

and their distribution, abundance, and variation over time. LVS on LUVMI therefore represents an ideal precursor instrument for future lunar exploration and can identify locations of interest for the exploitation of volatiles as a resource.

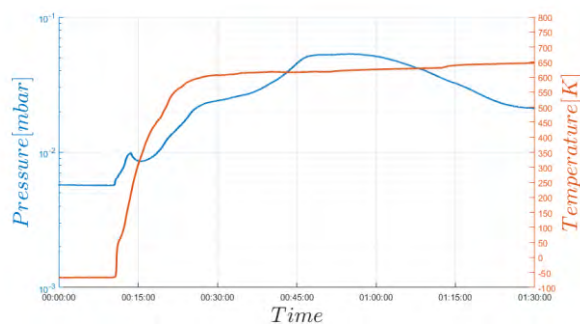


Figure 4: Exemplary gas extraction test result with a JSC-1A sample with approximately 0.25 wt% water

References: [1] Colaprete A. et al (2010) *Science*, 330, 463–468. [2] Carpenter J. et al. (2017) *European Lunar Symposium 2017*. [3] Biswas J. et al (2017) *European Lunar Symposium 2017*. [4] Reiss P. et al (2016) *European Lunar Symposium 2016*. [5] Beyer R. et al (2011) *LPSC XLII* #2735. [6] Urbina D. et al (2017) *IAC-17,A3,2B,10,X41392*

Spectral mapping and crater statistics reevaluated for all Apollo landing sites. B. Bultel¹, S. C. Werner¹, V. A. Fernandes², T. Rolf¹, ¹ Centre for Earth Evolution and Dynamics, University Oslo, Norway, benjamin.bultel@geo.uio.no, ² Museum für Naturkunde, Berlin.

Introduction: To decipher the planetary surface evolution, geologic events are dated relatively based on crater counts [1, 2]. This method has been calibrated on the Moon and adapted to other planetary bodies. A good calibration on the Moon is thus a valuable key to understand the chronology of all solid surface planetary bodies.

Crater counts are linked to isotopically-dated Apollo and Luna samples, which provides calibrated *absolute model ages (AMA)*. The observed crater size frequency distributions (CSFD) on defined surface units are fit with crater production functions, with presumably undisturbed crater size frequency distributions. These are used to derive crater density measurements, which currently have resulted in several lunar chronology models [3, 4]. The definition of a crater production function is therefore crucial for the definition of lunar cratering chronology. Indeed, the crater production function must be determined over a large crater-diameter range and over large homogeneous geologic units.

Several problems have risen regarding this method such as i) the limited number of craters on very young terrains, ii) the saturation of the cratered surface for old terrains, iii) a lack of samples with ages between 3.0 and 1.0 Gyrs, and iv) the uncertainty in linking mission samples with terrains where the crater count is obtained and used as templates [5]. This has led to uncertainties and diversities on lunar cratering rates and chronology models. We here focus on the crater size frequency of Apollo landing sites to re-evaluate lunar cratering chronology models. An example is shown here for the Apollo 11 and 17 landing sites.

Data and Method: We first analysed the Moon Mineralogical Mapper data (M3) using spectral parameters to define homogeneous units at each Apollo landing sites. The spectral parameters used are from [6] and they illustrate the different depth of absorption near 1,00 μm (with the IBD1000 parameter for the red channel), near 1,25 μm (with the IBD1250 parameter for the blue channel) and near 2,00 μm (with the IBD2000 parameter for the green channel). The spectral data are combined with the morphology to build the counting units. For each unit, areas with secondary craters have been identified and removed by combining morphologic observations and spectral mapping. We then determined CSFDs on craters with diameters in the range of 250 m to 1 km. Crater counts were done using CraterTools [7] on Kaguya Television Camera data [8] at a resolution of 10 m per pixels, and ages were determined with CraterStats [9].

Apollo 11: The first Lunar Module (LM) landed on the Moon in SW-region of Mare Tranquilitatis. From M3 data, the unit is spectrally and morphologically homogeneous. This unit is located between a fault system and a ~ 6 km diameter crater on the south and ridges on the east, west and north. The spectral signatures of the plains beyond those features have different centre and depth of absorptions near 1.00 μm , 1.25 μm and 2.00 μm as seen in Figure 1.

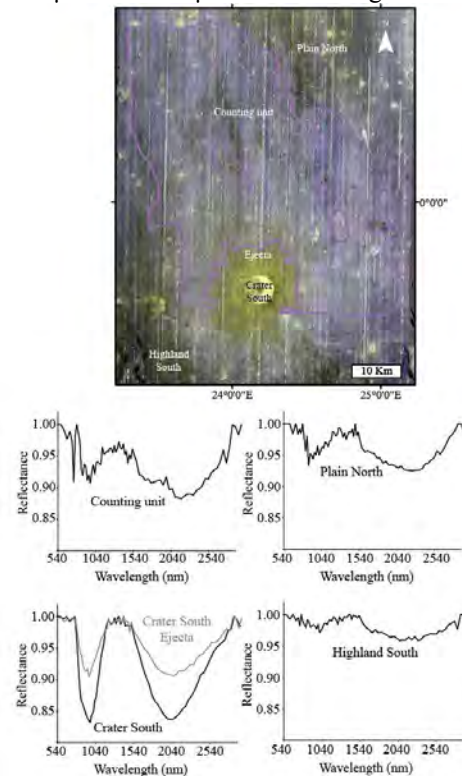


Figure 1: Apollo 11 landing site visualized by Kaguya TC data under M3 data with colour composite described in the method section. The spectra representative of the different units are shown with the continuum removed.

The CSFD obtained for the unit around the Apollo 11 LM is shown in Figure 2 as a cumulative plot [10]. A different slope is visible between the craters of a diameter <1 km and the craters of a diameter >1 km. Previous studies have already reported two distinct populations of craters, which could correspond to the two groups of ages, reported for the samples analyses [6]. The Figure 2 shows the CSFD which is lower than the previously published [11 and references therein]. One reason could be a differing interpretation of contamination due to secondary craters.

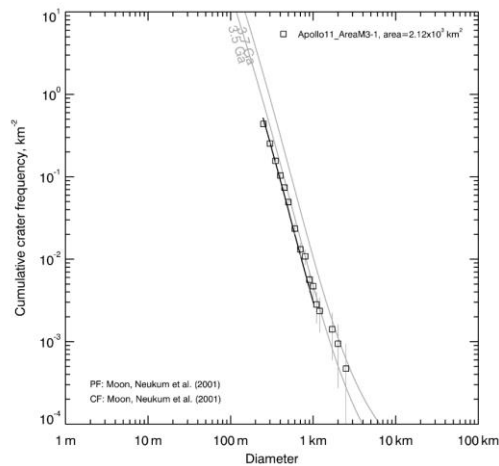


Figure 2: CSFD on the unit of the landing site of Apollo 11.

Apollo 17: The Lunar Module landed on the Moon on Mare Serenitatis in the Taurus-Littrow Valley in a cluster of secondary craters formed by the ejecta of the Tycho crater. The cluster itself was excluded from the counting area (Figure 3) that has a distinctive spectral signature as well as other geological features such as ejecta blanket material and faults that can affect cratering statistics. The CSFD for the crater diameter range of 250 m to 1 km is shown on Figure 4, and it is in line with previous studies [11 and references therein].

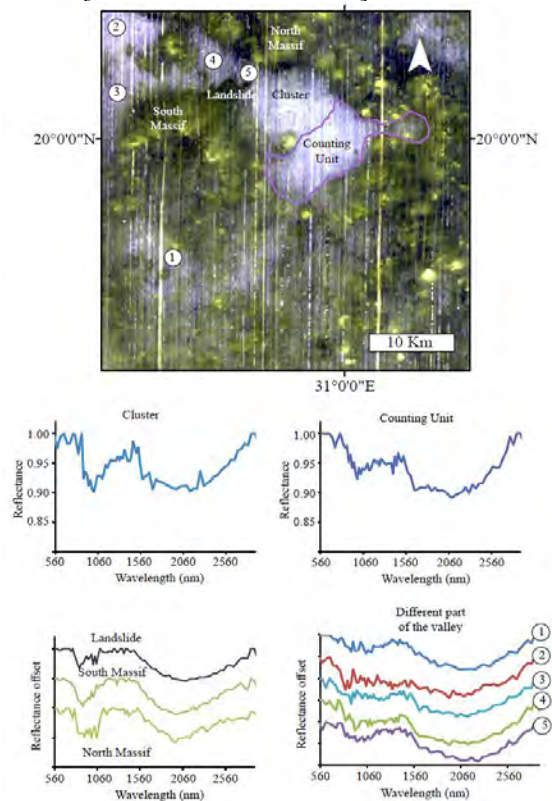


Figure 3: Top: Apollo 17 landing site visualized by Kaguya TC data under M3 data with colour composite described in method section. Bottom: Repre-

sentative spectra for the different units are shown with the continuum removed.

Work done for each Apollo Landing sites will be presented. We will compare our results to previously defined CSFDs and surface units and discuss their correspondence to K-decay constant and age of monitor-samples corrected radiometric ages obtained from Apollo and Luna samples. Our results will help to define a new lunar cratering chronology [Werner this meeting].

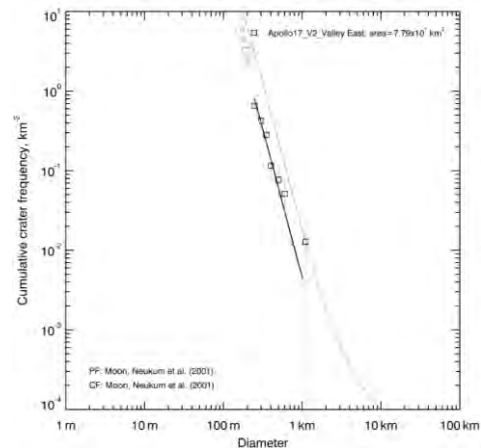


Figure 4: CSFD on the unit of the landing site of Apollo 17.

References:

[1] Öpik (1960) *Monthly Notices of the Royal Astronomical Society*, 120(5), 404-411. [2] Shoemaker, E. M. (1962). *American Scientist*, 50(1), 99-130. [3] Hartmann, W. K., & Neukum, G. (2001). Cratering chronology and the evolution of Mars. (pp. 165-194). [4] Neukum, G., Ivanov, B. A., & Hartmann, W. K. (2001). *SSR*, 96(1-4), 55-86. [5] Stöffler, D., & Ryder, G. (2001) Chronology and evolution of Mars (pp. 9-54). [6] Thiessen, F., Besse, S., Staid, M. I., & Hiesinger, H. (2014). *Planetary and Space Science*, 104, 244-252. [7] Kneissl, T., S. vanGas-selt, and G. Neukum (2011), *Planet. Space Sci.*, 59, 1243-1254 [8] Haruyama, J., T. Matsunaga, M. Ohtake, T. Morota, C. Honda, Y. Yokota, M. Torii, and Y. Ogawa, and the LISM Working Group (2008), *Earth Planets Space*, 60, 243-255. [9] Michael and Neukum (2010) *EPSL* 294. [10] Crater Analysis Techniques Working Group (1979), *Icarus*, 37, 467-474 [11] Robbins, S. J. (2014). *Earth and Planetary Science Letters*, 403, 188-198.

Acknowledgements:

This study is supported by the Research Council of Norway (235058/F20 CRATER CLOCK). The image data used are provided by PDS and JAXA. The craterstat/crater tools softwares are from the Freie Universität of Berlin. V.A.F. acknowledges financial support via a DFG-Eigenstelle FE 1523/3-1

NASA'S HUMAN EXPLORATION AND OPERATIONS MISSION DIRECTORATE'S LUNAR ACTIVITIES. D. B. J. Bussey¹ ¹NASA HQ, 300 E Street SW, Washington DC 20546 USA, ben.bussey@nasa.gov

Introduction: NASA's Human Exploration and Operations Mission Directorate (HEOMD) has a number of ongoing lunar-related activities, relating to both robotic and human exploration.

ISECG Science White Paper: Space agencies participating in the International Space Exploration Coordination Group (ISECG) are discussing an international approach for human and robotic space exploration to achieve the social, intellectual and economic benefits. The status of this work is documented in ISECG's Global Exploration Roadmap (GER). The GER reflects a coordinated international effort to prepare for collaborative space exploration missions beginning with the International Space Station and continuing to the lunar vicinity, the Moon, asteroids and Mars. While scientific research is not necessarily the main driver for human exploration, space agencies of the ISECG acknowledge the explicit stakes of scientific discovery in space exploration. Therefore, the agencies chartered the production of a Science White Paper that describes the scientific opportunities represented by near-term human exploration beyond low-Earth orbit (LEO). Specifically it considered the science enabled by human missions to three destinations. 1) A deep space habitat in the lunar vicinity, 2) the lunar surface, and 3) asteroids. The SWP was released in early 2018.

Deep Space Gateway Concept Science Workshop: Following on from the ISECG science white paper, NASA is holding a workshop in February 2018 to discuss the science that could be enabled by the presence of a deep space gateway concept in the lunar vicinity. This workshop is jointly hosted by HEOMD and NASA's Science Mission Directorate (SMD). The workshop aims to encompass a wide range of science disciplines including Earth Sciences, Heliophysics, Astrophysics, Fundamental physics, Lunar & Planetary Sciences, Life Sciences, and Space Biology. One of the goals of the workshop is to discuss what resources the gateway would have to provide in order to facilitate the types of science investigations that are proposed. To aid these discussions, there will also be crosscutting sessions covering topics such as External Payloads, Planetary Samples, Internal Payloads, Telerobotics, and use of the gateway as communication infrastructure for cubesats of lunar surface payloads.

Lunar CATALYST: Since 2014, NASA's Lunar Cargo Transportation and Landing by Soft Touchdown (Lunar CATALYST) initiative has been accelerating the development of U.S. private-sector robotic lunar landers that can enable commercial payload transportation services to the lunar surface for both public and private customers. NASA com-

petitively selected three industry partners (Astrobotic Technology, Masten Space Systems, Moon Express), and entered into no-funds-exchanged Space Act Agreements (SAA) with each of them. With NASA's support through these highly collaborative technical partnerships, each of the industry partners has made substantial progress in developing their lunar landers, while managing their respective businesses with complete autonomy. Through these government-industry partnerships, NASA has provided in-kind contributions including technical expertise, access to test facilities, software, and the loaning of equipment. Based on the significant progress each partner has made, NASA announced in November 2017 that the agency would extend and update the no-funds-exchanged Space Act Agreements with the goal of seeing the first commercial cargo deliveries to the Moon over the next few years.

Korea Pathfinder Lunar Orbiter (KPLO): HEOMD is collaborating the Korean space agency (KARI) on their KPLO lunar mission. As part of this collaboration NASA is flying the ShadowCam instrument on the KPLO spacecraft. ShadowCam is a very sensitive camera that uses light scattered from the illuminated inner rims of polar impact craters to image the floor of these craters. The expected spatial resolution of ShadowCam is better than 2 meters. ShadowCam goals include searching for spatial and temporal distribution of volatiles, monitoring movement of volatiles within permanently shadowed regions, and revealing the geomorphology, accessibility, and geotechnical characteristics of cold traps. KPLO is scheduled to launch in 2020.

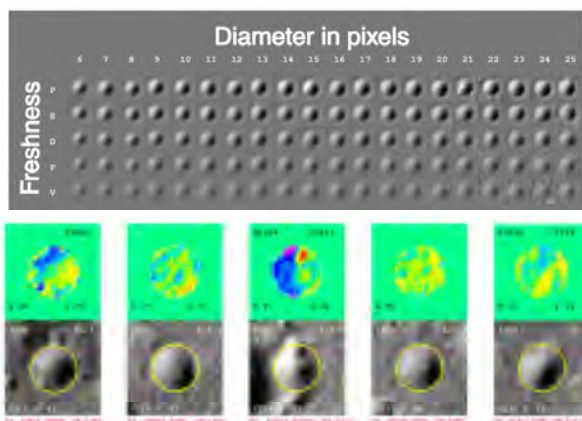
Cubesats on EM-1: The first launch of SLS will send an Orion spacecraft around the Moon. NASA is leveraging this launch to also fly 13 cubesats, several of which were selected to increase our understanding of lunar resources. Lunar Flashlight will use multiple lasers to search for volatiles in permanently shadowed craters. Lunar IceCube will look for water in sunlit regions using a spectrometer. And LunIr, by Lockheed Martin, will fly a Mid Wave Infra red sensor to study the lunar surface.

AUTOMATED COUNTING OF THE SMALLEST CRATERS AT LUNAR LANDING SITES.

Peter H Cadogan, 126 The Park, Cheltenham Glos UK GL50 2RQ – peter.cadogan@zen.co.uk

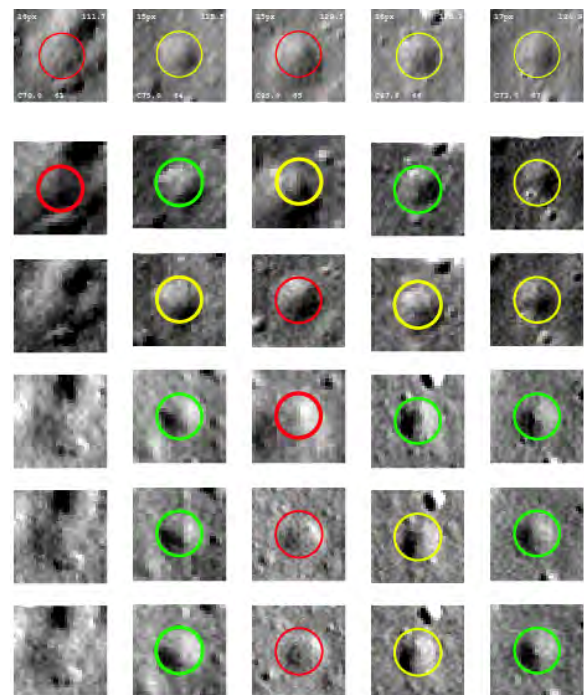
Introduction: Computerised crater counting using automatically generated templates has been shown to be capable of precise detection and measurement of small ($< 100\text{m}$) lunar craters from high resolution LROC NAC images taken under optimal illumination conditions [1]. Matching craters in other images of precisely the same area under different illumination, enables false positives to be rejected and false negatives included [2]. The numbers of craters larger than 3m in diameter is so high (typically $10^4/\text{km}^2$) that expert counting is really only practicable for small areas. Whereas counts of larger (eg $>1\text{km}$) craters enable absolute model ages of lunar surfaces to be determined [3], the distribution of the smallest lunar craters should reflect the more recent impact history of the Moon and could potentially quantify the contributions made by projectiles from different sources.

Matching craters: The methods used for automatically determining the centres and rims of craters have already been described in some detail [2]. Each crater is assigned a freshness parameter and, when all craters in an image have been found, a template is created for each combination of diameter and freshness. Each crater is matched against the corresponding template and its centre and diameter may be modified to improve the match, or else the crater may be rejected.

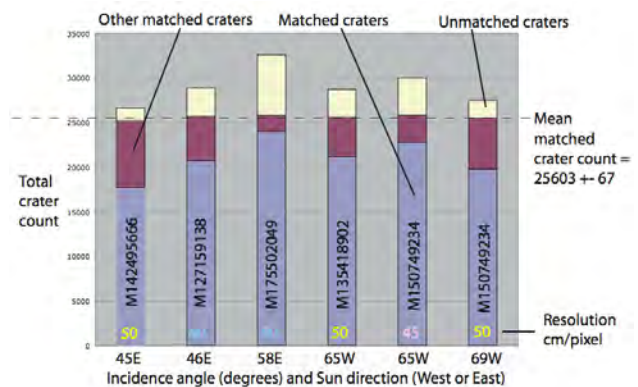


Comparing craters to templates for best fitting

LROC images of the same area on the lunar surface, once calibrated and ortho-projected, should overlap precisely and yield identical counts. In practice, this is not always the case because, under some illumination conditions, craters may be lost in deep shadows or washed out on brightly sunlit slopes. In this work, a crater is rejected as a false positive if it is not located in at least one other image. Likewise, any undetected crater that is present in at least two other images will be added as a false negative.



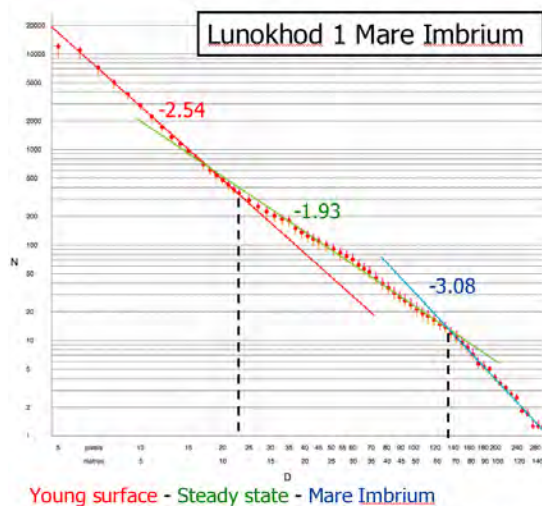
Matching craters in other images. Top row: current image. Rows below: matches in other images (green = perfect, yellow = good, red = poor)



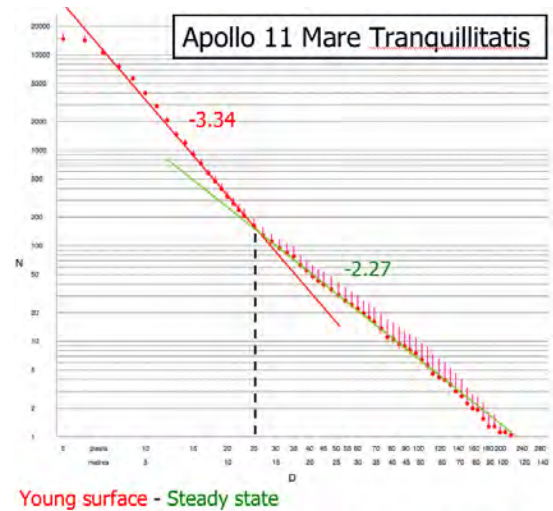
Six matching images of the Lunokhod 1 landing site, under different illumination, yield consistent results when only matched craters are included.

Crater abundances: Cumulative Size Frequency Distributions (CSFDs) plot the logarithm of counts of all craters having diameters greater than D against the logarithm of D.

In the case of the Lunokhod 1 landing site, the least squares fit straight line for craters with diameters less than 12m has the exponent of -2.54 . From 12m to 65m, the slope is shallower (-1.93), as predicted for crater saturation in this size range. Above 65 metres the slope is steeper again (-3.08), as predicted for an ancient mare surface [4].

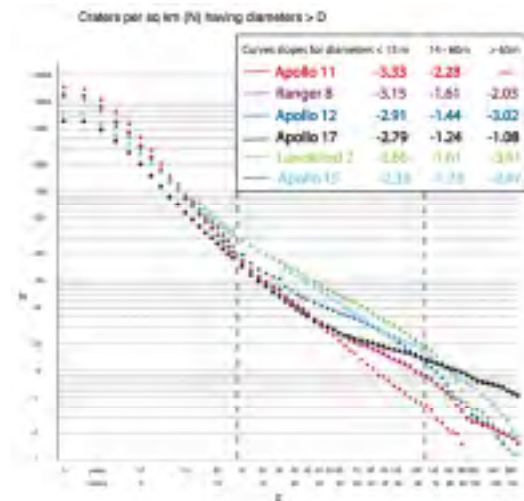


For young mare, the slope below 12 metres is shallower than at the Apollo 11 site, but steeper again above 65 metres. The steady state slope is also shallower



For this older mare, the steady state line would appear to continue beyond 130m, but the slope below 12m is steeper than at the Lunokhod 1 site

In contrast, at the Apollo 11 site, the slope for the smallest craters is steeper (-3.34), as is the slope for craters larger than 12m (-2.27). It had been anticipated that the small crater slope would be the same for all maria, so this result requires an explanation. Might there be variations in impact rates with latitude and/or longitude [5]? Or could secondary cratering be a factor [6]? To investigate this, nine mare sites have been analysed so far and the results for six of them are compared below.



There appears to be an inverse correlation between the slope for craters < 12m and the count of craters > 40m. There may also be a correlation with latitude, the slopes for the Lunokhod sites being shallower than those nearer to the equator. But such correlations appear to be complicated by the presence of secondary craters, especially from Tycho (Mare Cognitum: Apollo 13 S-IV-B) and Giordano Bruno (Mare Crisium: Luna 23/24). The test site in Mare Crisium was large enough to cover several areas affected by Giordano Bruno secondaries.



Conclusions: Automated crater detection has revealed unexpected differences between counts at nine lunar mare sites, some of which can be attributed to secondaries. A search for suitable areas in the young western (and high latitude) maria is needed so that the possible causes of these variations can be investigated further.

References: [1] Cadogan P.H. (2017) *Abstract ELS5* [2] Cadogan P.H. 2018 (*paper submitted to Icarus*) [3] Hiesinger H. et al. (2010) *JGR*, 115 E03003 [4] Moore H.J et al (1980) *Moon & Planets* 23, 231-252 [5] Speyerer E. J. et al. (2016) *Nature*, 538, 21 [6] McEwen A.S. and Bierhaus E.B (2006) *Ann. Rev. Earth and Planet. Sci.* 34, 535-67

DETECTION AND CHARACTERIZATION OF PRESENT DAY LUNAR IMPACT CRATERS WITH MINI-RF/GOLDSTONE X-BAND BISTATIC OBSERVATIONS. J.T.S. Cahill¹, G.W. Patterson¹, F.S. Turner¹, G.A. Morgan², A.M. Stickle¹, E.J. Speyerer³, R. Espiritu¹, B.J. Thomson⁴, and the Mini-RF team. ¹Johns Hopkins University Applied Physics Laboratory, Laurel, MD (Joshua.Cahill@jhuapl.edu), ²National Air and Space Museum, Smithsonian Institution, Washington, D.C., ³Arizona State University, Tempe, AZ, ⁴University of Tennessee, Knoxville, TN.

Introduction: A multi-look temporal imaging survey by Speyerer et al. [1] using the Lunar Reconnaissance Orbiter Camera (LROC) Narrow Angle Camera (NAC) has detected over 220 new resolvable impacts of at least 10 meters in diameter since NASA's Lunar Reconnaissance Orbiter (LRO) entered orbit around the Moon, at a flux that is substantially higher (33%) than anticipated from previous studies [2]. Speyerer et al. [1] also observed secondary cratering processes that they estimate churn the top two centimeters of regolith more than a hundred times faster than previous models estimated from meteoritic impacts (ten million years). This has significant implications toward an assessment of hazards for any robotic and human exploration on the surface of the Moon. It also has implications for the interpretation of crater-based chronology of the lunar surface.

The Miniature Radio Frequency (Mini-RF) instrument aboard LRO is a hybrid dual-polarized synthetic aperture radar (SAR) that now operates in concert with the Arecibo Observatory (AO) and the Goldstone deep space communications complex 34-meter antenna DSS-13 to collect S- and X-band bistatic radar data of the Moon, respectively. Here we targeted some of the larger

(>30 m) craters identified by Speyerer et al. [1] and executed bistatic X-band radar observations both to search for and, if observed, characterize the spatial extent and distribution of cm-scale scatterers in their ejecta relative to visible wavelengths. Data acquired during Mini-RF monostatic operations, when the transmitter was active, show no available coverage of the regions in question before or after two of the new impacts occurred. This makes Mini-RF and Earth-based bistatic observations all the more valuable for examination of these fresh new geologic features.

Method: Collecting bistatic radar data involves AO and/or DSS-13 illuminating the lunar surface at S-band (12.6 cm) or X-band (4.2 cm) wavelength, respectively, with a circularly polarized, chirped signal and tracking the Mini-RF antenna boresight intercept on the surface of the Moon. Transmitted pulses from AO and/or DSS-13 are 100 to 400 μ s in length and the Mini-RF receiver operates continuously, separately receiving the horizontal and vertical polarization components of the signal backscattered from the lunar surface. The resolution of the data is \sim 100 m in range and \sim 2.5 m in azimuth but can vary from observation to observation, as a function

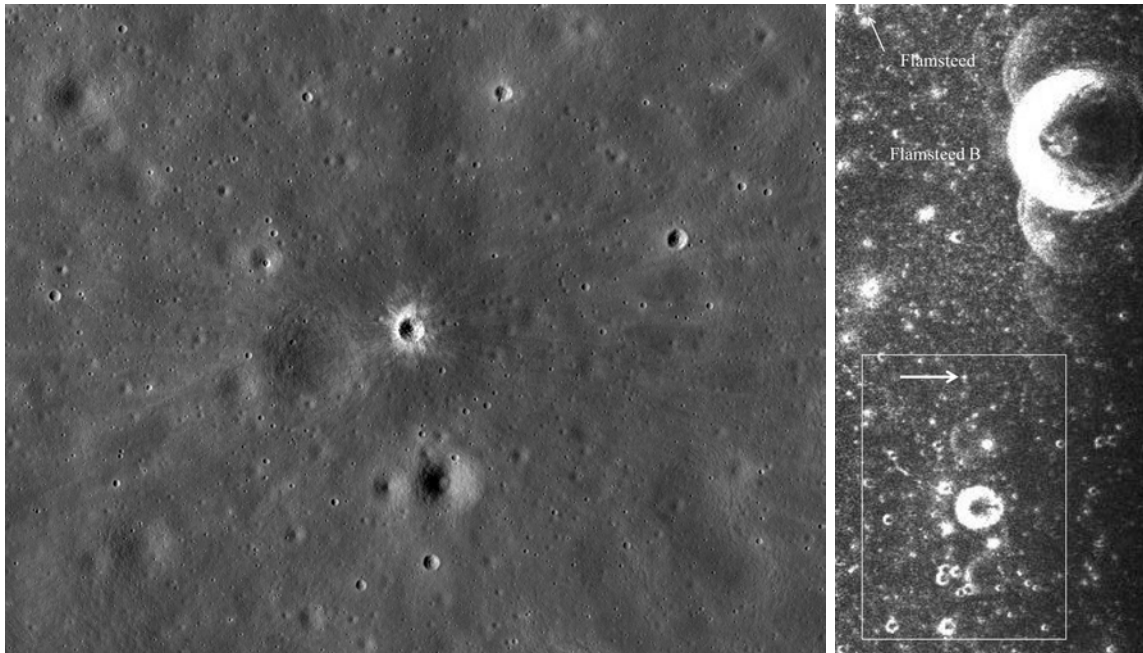


Figure 1: (Left) LROC NAC coverage at 0.5 m/pix of a 50 m diameter crater near Flamsteed and Flamsteed B craters. (Right) Mini-RF bistatic S_1 image (100 m/pix); arrow denotes crater detection.

of the viewing geometry. For analysis, the data are averaged in azimuth to provide a spatial resolution of 100

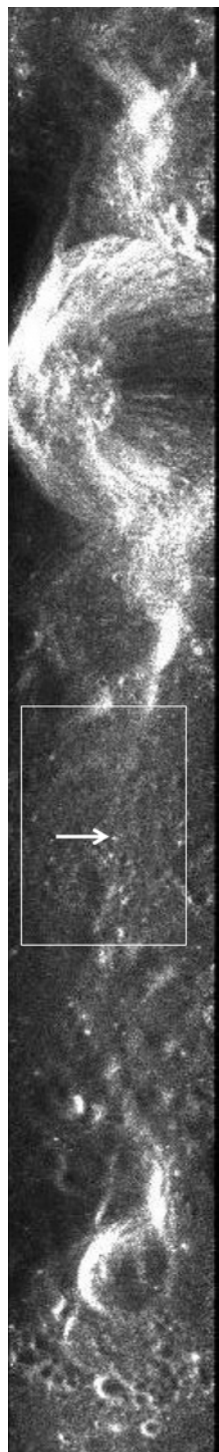


Figure 2: X-band S_1 observation of T. Mayer A crater region. Arrow denotes a new 43 m diameter crater.

m. This yields an ~ 40 -look average for each sampled location in an observation and an average $1/N^{1/2}$ uncertainty in the backscattered signal of $\pm 16\%$. In theory, this should also enable a modest improvement in along track resolution, but processing for that effort has not yet been attempted.

In a somewhat analogous fashion to a photometric analysis, we are using Mini-RF's bistatic configuration to make targeted collects of X- and S-band data at a range of phase angles. To date, we have collected one observation of the 50 m crater near the Flamsteed and Flamsteed B (Fig. 1) and two observations of the 43 m crater near T. Mayer A (Fig. 2-3).

To examine crater ejecta properties over this phase space we primarily take advantage of two basic radar parameters, the first Stokes parameter, S_1 (i.e., total backscattered power), and the circular polarization ratio, CPR, which are commonly used in analyses of planetary radar data [3-5]. Each of these parameters offer a measure of surface

roughness at the wavelength scale of the radar. Surfaces that are smooth at the wavelength scale will have lower S_1 and CPR values and surfaces that are more rough will have higher S_1 and CPR values. In this way, we intend to measure the extent of new crater ejecta observable in Mini-RF data as compared to NAC visible imagery. Average ejecta profile analyses of each are being constructed to aid in this study.

Observations: While preliminary analyses of Arecibo/Greenbank and Mini-RF/Goldstone bistatic observations are unable to resolve the new crater cavities at these localities, they do confirm lunar surface roughness changes occurred between 2008 and 2017. For example, Earth-based Arecibo/Greenbank observations (100 m/px) do not show the new 43 m crater during the early part of the LRO mission within 2013. However, Mini-RF/Goldstone bistatic observations have discerned them in 2017 (Fig. 2 and 3). It is therefore plausible some combination of Earth-based and Mini-RF orbital collects may contribute toward narrowing the timing of these occurrences in the future.

Mini-RF X-band (4.2 cm) observations of these craters indicate the presence of newly emplaced material at radial distances of 100-300 meters from each impact. Detectability at X-band further implies the proximal ejecta of these impacts contain a high proportion of scatterers in the ~ 0.5 to 50 cm size range.

Summary and On-Going Work: Mini-RF will continue to examine these and other new craters to characterize the physical properties of their ejecta and constrain them temporally.

References: [1] Speyerer et al. (2016) *Nature*, 538, 215. [2] Neukum et al. (2001) *SSR*, 96, 55. [3] Campbell et al. (2010) *Icarus*, 208, 565. [4] Raney et al. (2012) *JGR*, 117, 1. [5] Campbell (2012) *JGR*, 117, 10.1029/2012JE004061.

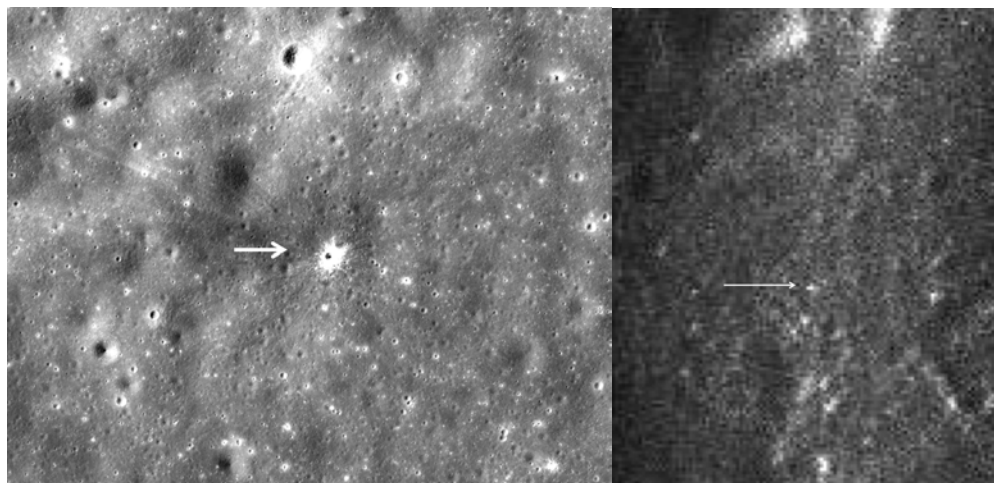


Figure 3: (Left) LROC NAC coverage at 0.5 m/pix of a 43 m diameter crater south of crater T. Mayer A. (Right) X-band S_1 detection of 43 m crater ejecta (100 m/px).

SCRUTINIZING THE PRESENCE OF LAMP IDENTIFIED LUNAR SWIRLS RELATIVE TO MODELED MAGNETIC SOURCES. J.T.S. Cahill¹, A.A. Wirth^{1,2}, A.R. Hendrix³, K.D. Retherford⁴, B.W. Denevi¹, A.M. Stickle¹, D.M. Hurley¹, K.E. Mandt¹, Y. Liu⁵, T.K. Greathouse⁴, F. Vilas³, and D.T. Blewett¹. ¹JHU/APL (Joshua.Cahill@jhuapl.edu), ²Case Western Reserve University, ³Planetary Science Institute, ⁴Southwestern Research Institute-San Antonio, and the ⁵Lunar and Planetary Institute/USRA.

Introduction: The sinuous lunar surficial markings known as ‘swirls’ are amongst the most intriguing features on the surface of the Moon [1-3]. Several hypotheses for their formation exist and include 1) magnetic shielding from solar wind [6], 2) cometary or meteorite swarm scouring of the shallow regolith [7-9], or 3) electromagnetic charge induced levitation and sorting of lunar dust [10, 11].

Three initial examinations of swirls have been performed in the ultraviolet (UV) [1, 12, 13], each one examined progressively shorter wavelengths ranges. Denevi et al. [1] mapped swirls in the Lunar Reconnaissance Orbiter Camera (LROC) Wide Angle Camera (WAC) near-UV (NUV) images, observing that the most distinguishing characteristic of swirls in this wavelength region is a low 321/415 nm ratio coupled with moderate to high 415 nm reflectance. This methodology appears

effective for differentiating swirls even within areas of high albedo. Denevi et al. [1] further note that some swirls cannot be discerned in the optical maturity index (OMAT) or band-depth images. Hendrix et al. [12] detailed examinations of the Reiner Gamma and Gerasimovich swirls using Lyman Alpha Mapping Project (LAMP) wavelengths >130 nm, noting swirls to be characterized by reddened FUV spectra. They also demonstrate that immature regolith becomes brighter (i.e., bluer) with exposure to space weathering. Finally, in a precursor to the work presented here, Cahill et al. [13], examined LAMP global Lyman- α (Ly- α) albedo (121.6 nm) maps and noted FUV evidence consisting of low albedo for swirls coincident with regions noted by Denevi et al. [1] as well as in previously undocumented areas.

In a previous report, Cahill et al. [14] leveraged the unique viewing geometry and wavelength range offered by LAMP nighttime observations to comprehensively map lunar swirls in the FUV (Fig. 1). Secondly, Cahill et al. [14] compared their observations with previous work in order to detail what can and cannot be observed in the FUV relative to the NUV, and vice versa. Here, we build upon this work comparing the results of Cahill et al. [14] with the recent modeling results of Wieczorek [4] mapping the proximity to the surface of plausible subsurface magnetic sources (Fig. 2). This is done in an effort to further scrutinize findings of plausible swirls only observed in the FUV by Cahill et al. [14].

Data Sets: LAMP continues to provide insights into the upper ~ 100 nm of the regolith. LAMP is a FUV (57-196 nm) push-broom photon-counting imaging spectrograph [15]. LAMP has also routinely collected both day and nighttime data of both polar and equatorial regions of the Moon. Here, global nighttime Lyman- α (Ly- α ; 121.6 nm) normal albedo data are examined for low-albedo features as they relate to the detection and mapping of lunar swirls (Fig. 1). This data set is unique in comparison to all other LRO data sets in that it collects reflected light from surfaces that are diffusely lit by solar Ly- α scattered off of interplanetary H atoms from all directions. The Ly- α skyglow intensity varies with respect to the motion of the solar system. Furthermore, point sources from

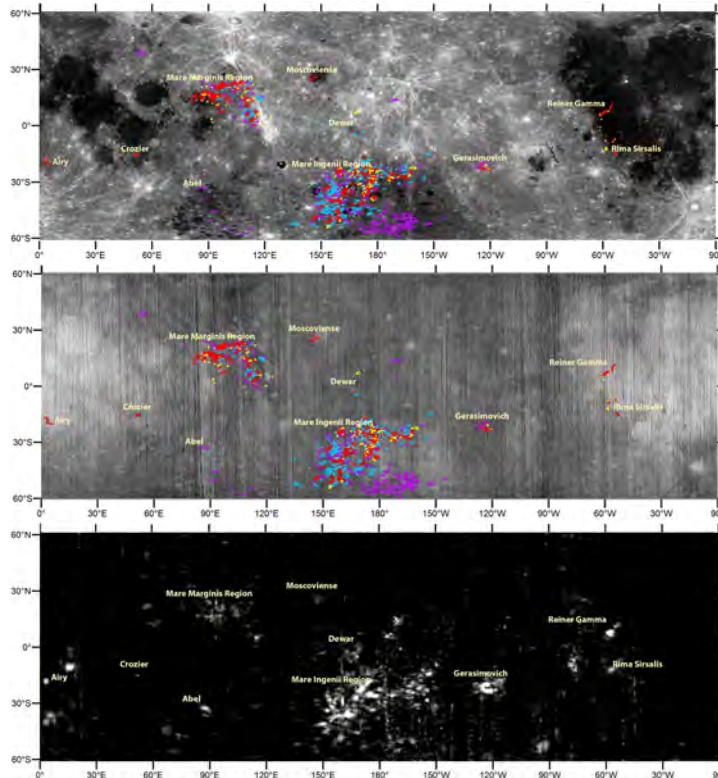


Fig. 1: (Top) WAC 415 nm, (middle) nighttime Ly- α , and (bottom) LP [B] (2-10 nT) [5]. (Red) Swirls observable independently by both FUV and NUV. (Light Blue) Swirls observed by FUV only. (Yellow) NUV identified [1] and confirmed in FUV. (Purple) Plausible LAMP-identified swirls near weak magnetic anomalies.

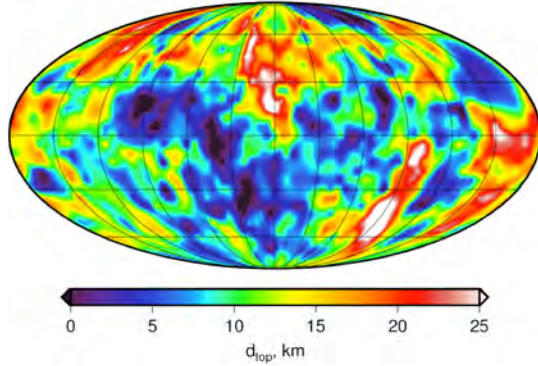


Fig. 2: Inversion results for ensembles of magnetized sills; depth to the top of the magnetized region [4].

UV-bright stars are more plentiful in the southern hemisphere owing to the Galactic plane [15, 16]. As a result, the signal-to-noise ratio of the LAMP nighttime data varies with latitude, with longer wavelength star light signals increasing from north to south. Other instrument-derived maps analyzed include the LROC WAC color [17, 18] and Lunar Prospector (LP) fluxgate magnetometer [5] data. Finally, data products derived by Wieczorek [4] of the depth to the top and bottom of plausible magnetic sources (**Fig. 2**) are also examined.

Swirls... Low-Albedo?: Unlike the NUV and visible where lunar swirls are known to show high reflectance relative to their surroundings, in Ly- α they have low albedo due to changes in material optical properties below ~ 180 nm.

Mapping Methodology: LAMP global Ly- α albedo maps were surveyed by Cahill et al. [14] for low-albedo features with sinuous ‘swirl-like’ characteristics. During this process a WAC 415 nm reflectance mosaic was used for regional context. To maintain an initial independent LAMP assessment, this initial step was taken without referring to swirl boundary maps detailed by Denevi et al. [1] or LP magnetic anomaly maps [5]. Once low-albedo regions were identified in Ly- α , they were compared to LP magnetic anomaly maps as well as WAC color composite maps. This resulted in four classes of low-albedo features, shown in **Fig. 1**: 1) Independently verified, (in red; i.e., regions identified independently by both FUV and NUV surveys, respectively), 2) Ly- α identified (in light blue; i.e., only observed in the 121.6 nm band), 3) NUV identified/FUV confirmed (in yellow; i.e., swirls not initially noticed in the initial FUV survey, but documented by Denevi et al. [1] and subsequently confirmed in Ly- α), and 4) Plausible

swirls (in purple; i.e., low-albedo features with an ambiguous morphology or setting and associated with weaker magnetic strength anomalies).

Discussion: Consistent with Denevi et al. [1], swirls are detected in LAMP Ly- α in the regions of Reiner Gamma, Mare Marginis, Rima Sirsalis, Crozier, Airy, Gerasimovich, Dewar, and South Pole-Aitken basin (**Fig. 1**). Swirls have previously been identified in all of these regions, however Ly- α often shows boundaries encompassing NUV and visible boundaries and often also show additional nearby sinuous low-albedo regions, swirls, not previously identified. That said, there are numerous areas with swirls that go initially unseen in Ly- α . Some of these (shown in yellow) are subsequently identified with additional NUV or magnetic data context, others are not. An analysis of these regions shows they have lower Ly- α albedo and higher magnetism values on average relative to their surroundings (**Fig. 2**). Swirl regions denoted by Denevi et al. [1] are consistent with these characteristics. Interestingly, low-albedo regions denoted as ‘Plausible swirls’ while showing similar average Ly- α values as swirls identified with high certainty, have lower values of total magnetic field strength (but higher magnetic field strength than ‘off swirl’ regional analyses).

References: [1] Denevi et al. (2016) *Icarus*, 10.1016/j.icarus.2016.01.017. [2] Blewett et al. (2011) *JGR*, 116, 1. [3] Kramer et al. (2011) *JGR*, 116, doi:10.1029/2010JE003729. [4] Wieczorek (2018) *JGR*, 10.1002/2017JE005418. [5] Purucker and Nicholas (2010) *JGR*, 115. [6] Hood and Schubert (1980) *Science*, 208, 49. [7] Starukhina and Shkuratov (2004) *Icarus*, 167, 136. [8] Schultz and Srnka (1980) *Nature*, 284, 22. [9] Syal and Schultz (2015) *Icarus*, 257, 194. [10] Pieters et al. (2014) *LPSC*, 45, 1408. [11] Garrick-Bethell et al. (2011) *Icarus*, 167, 136. [12] Hendrix et al. (2016) *Icarus*, 273, 68. [13] Cahill et al. (2016) *LPSC*, XXXXII. [14] Cahill et al. (2017) *LPSC*, 48, 2947. [15] Gladstone et al. (2012) *JGR*, 117, doi:10.1029/2011JE003913. [16] Pryor et al. (1992) *AJ* 394, 363. [17] Sato et al. (2014) *JGR*, 119, 1775. [18] Boyd et al. (2012), 43, 2795.

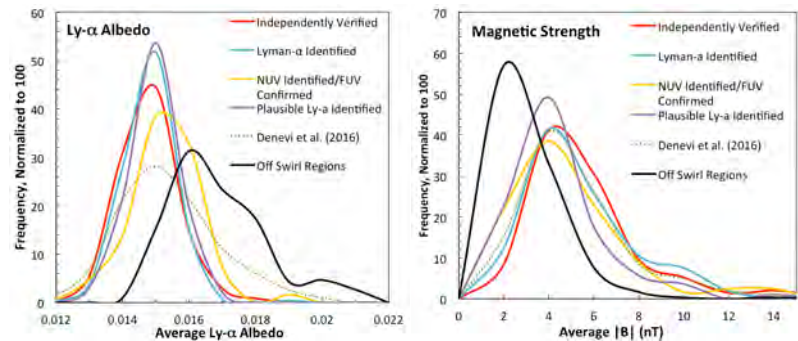


Fig. 3: Histograms of swirl characteristics detailing (Left) Ly- α , and (Right) total magnetism $|B|$. (Dotted) Study of Denevi et al. [1] mapped swirl regions. (Black) Regions nearby, but off swirl regions.

COMMERCIAL EXPLORATION OF THE MOON: ISPACE'S POLAR ICE EXPLORER

A. Calzada-Diaz¹, J-A. Lamamy¹, J.N. Raser¹ and K. Acierno¹, ¹ispace Europe. Rue de l'Industrie 5, Paul Wurth InCub, 1811 Luxembourg, Luxembourg (a-calzada@ispace-inc.com).

Introduction: ispace is a company whose vision is to expand and sustain humanity's presence in space by utilizing resources available on the Moon. In order to accomplish this vision, ispace set a 3-step roadmap as illustrated in Figure 1. The first step is the technology demonstration of ispace's rover as part of the Google Lunar XPRIZE. ispace, a finalist in the Grand Prize, developed and flight qualified the SORATO rover and won the mobility milestone award.

For Step 2, ispace intends to build-upon the rover technology to perform missions that will prepare the establishment of in-situ resource utilization (ISRU) on the Moon. With proven technologies (Step 1) and a solid understanding of the lunar environment and distribution of resources (Step 2), ispace will be ready to execute the processing and utilization of lunar resources in Step 3.

The company is headquartered in Tokyo, Japan and has subsidiaries in the NASA Ames Research Park, California and in Luxembourg. The topic of this abstract is the Polar Ice Explorer mission that is being developed by ispace Europe.

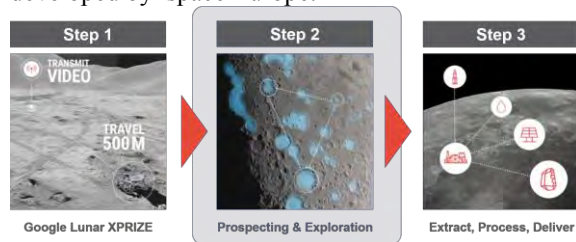


Figure 1: ispace's three-step approach.

Lunar water: Observations from the Moon Mineralogy Mapper (M3) aboard India's Chandrayaan-1, and measurements from NASA's Lunar Reconnaissance Orbiter (LRO), among others, provide with strong evidence for the presence of water ice on the Moon [1,2,3]. However, the spatial resolution of the current remote sensing datasets (tens of km) is not sufficient to understand the nature of the H molecules and bulk deposits. At this stage, there are not enough information about lunar water to start the extraction, making mandatory to send exploratory missions to perform in-situ H mapping and prospection at a local scales (from nanometers to meters).

Polar Ice Explorer (PIE) Project: The Polar Ice Explorer mission will be the first project of Step 2 for ispace Europe. It is an ISRU exploration mission that aims to identify and define the extension of the hydrogen and potential water ice deposits in lunar polar regions. This mission also will obtain valuable information on the geotechnical and trafficability properties of the polar regolith.

Four scientific mission objectives were established to address during this project:

1. To determine the local distribution and abundance of H in the subsurface regolith.
2. To characterize the form in which volatiles species containing hydrogen are present in the subsurface regolith.
3. To assess the volatile-rich contamination produced by lander exhaustion plume.
4. To obtain soil mechanics information relevant for vehicle mobility, soil penetration, and the operation and maintenance of future ISRU equipment.

Payload: Three criteria are used to identify potential instruments for the PIE.

1. The instrument fulfils at least one of the science objectives.
2. The instrument design is mature.
3. The instrument can be easily procured.

Based on these conditions several instruments have been reviewed and considered as potential payload.

Neutron Spectrometer (NS): Neutron spectrometers measure the flux of epithermal and thermal neutrons, thus providing a highly sensitive quantification of the H content of the regolith [e.g. 3,4]. This instrument will detect areas with enhanced hydrogen signatures, which may indicate the presence of subsurface water ice.

Ground Penetrating Radar (GPR): This instrument can detect, localize and characterize homogeneous stratigraphic units, such as segregated ice [5]. In combination with the NS, the GPR facilitates more accurate mapping of the subsurface water ice deposits.

Mass Spectrometer (MS): Mass spectrometry is an analytical technique that ionizes chemical species and arranges the ions based on their mass-to-charge ratio (m/z) to produce a mass spectrum. The result is a plot of the ion signal as a function of the mass-to-charge ratio. These spectra will be used to characterize the form in which the H-rich species are present in the polar regolith.

Rover: The rover (Figure 2) will be based off the innovative SORATO design. At 4 kilograms, the SORATO rover is the lightest flight-qualified planetary rover.

Lander: The Polar Ice Explorer will be delivered to the lunar surface by ispace's lander (Figure 3). This lander is currently under development, with a first launch scheduled for 2019. It is designed to carry 30 to 50 kg of payload to the lunar surface.



Figure 2: SORATO rover's camera imaging test in the field.



Figure 3: Concept model of ispace's lander.

Mission Concepts: From the combination of several of the previously described payloads, several missions concepts have emerged. Each concept fulfills at least two of the science objectives. In addition to the scientific aspects, programmatic, management and business considerations have to be taken into account in order to select the concept that provides the best cost/benefit ratio. These concepts are summarized in Table 1.

Concept	Goldcrest	Rose	Melusine	Fox
Sensing	2 NS	2 NS	2 NS	2 NS
Mapping				GPR
Sample analyses		Ion Trap MS	Magnetic Sector MS	
Objectives fulfilled	1,4	1,3,4	1,2,3,4	1,2,4

Table 1: Mission concepts for the RSP.

Landing Site: The targetted landing sites for this project are regions characterised by sufficiently low annual temperatures to maintain permafrost layers. These regions would receive some direct solar radiation for short amounts of time, but would still remain cold enough to avoid water loss via sublimation [6,7]. The region outlined in Table 2 is considered a primary area of interest for in situ exploration of water resources, as it meets the environmental constraints for permafrost, and offers the most hospitable thermal and illumination conditions for solar-powered probes.

Landing site parameters	
Latitude	>80° S
Type	Permafrost region
Deposit depth	0.1-0.5 m
LS ellipse size	>1 km
Target	Floor of impact crater Intercrater areas

Table 2: Parameters of potential landing sites for this mission.

Mission Funding: As a private company, ispace must consider new and innovative approaches to cover the costs and even make revenue from its mission. These approaches include selling access to the lunar surface for other scientific and non-scientific payloads, as well as selling the data generated by this mission. ispace intends to market its scientific and engineering data to space agencies, research institutes, and scientists interested in the most up-to-date data on the lunar surface.

Conclusions: Orbital imagery and analyses of lunar samples have indicated the presence of H-molecules that could form potential water ice deposits on certain areas of the lunar poles. However, the spatial resolution of the current remote sensing datasets (tens of km) together with the uncertainties about the lunar environment and regolith does not make possible to start water extraction right away.

This work provides the background, rationales, and the scientific objectives for the ispace Polar Ice Explorer Project, an ISRU exploratory mission that aims to provide data about the lunar polar environment that will be necessary for the prospection and utilization of lunar resources.

The most unique aspect of the PIE project is that it is run by a private space company. The company is responsible for formulating the vision and high-level goals and for tracing the success for particular objectives for the PIE project. In addition, the company must develop new and innovative ways to cover the costs associated with the mission.

References:

- [1] Hayne P. O. et al (2005) *Icarus* 255:58-69. [2] Heldmann J. L. et al. (2012) *Space Science Reviews* 167.1-4:93-140. [3] Lawrence D. J. et al. (2015) *Icarus* 255:127-134. [4] Feldman W. C. et al. (1998) *Science* 281.5382:1496-1500. [5] Ciarletti V. et al. (2017) *Astrobiology* 17.6-7:565-584. [6] Vasavada A. R. et al. (1999) *Icarus* 141.2:179-193. [7] Paige D. A. et al. (2010) *Science* 330.6003:479-482.

LUNAR EXPLORATION PLANS IN ESA. J.D. Carpenter¹, B. Hufenbach, M. Landgraf, S. de Mey, A. Borggraefe, A. Bergamasco, E. Sefton-Nash, R. Fisackerly, B. Houdou, D. de Rosa, X. Lefort, R. Trautner, D. Laurini, P. Schoonejans, S. Pastor, S. Hosseini, M. Braun, D. Parker. Directorate of Human Spaceflight and Robotic Exploration, ESA, ESTEC, Noordwijk, The Netherlands (¹james.carpenter@esa.int).

Moon is the next destination: For ESA the Moon is the next destination for human exploration after Low Earth Orbit, where we have learned to work and operate over decades [1]. ESA is now preparing for a return to the Moon for humans. This new era of lunar exploration must be achieved in a sustainable way that delivers benefits to all of humanity. To do this some fundamental capabilities must be established and delivered through partnerships.

Fundamental capabilities: Access to the Moon and sustainable operations there will involve humans and robots working together in a require that a number of fundamental capabilities are established: 1) access to the surface for both crewed and uncrewed vehicles 2) sustained and efficient operations, 3) survival of both people and equipment, 4) mobility for robots and humans, 5) reliable and widespread communications, 6) optimization of the human robotic interface, 7) the establishment of broad user communities who create benefits from lunar activities, 8) the utilization wherever possible of in situ resources.

ESA is working to establish all of these capabilities; through technology developments, through missions, through international partnerships and through partnerships with the private sector. The goal is not to get to the Moon at the earliest opportunity; but rather to get there is a way that benefits and involves everyone and ensures sustainability.

The importance of partnerships: The most robust and cost effective way to return to the Moon, and deliver the greatest benefits to Earth, is to establish partnerships. ESA is an agency with 22 member countries and so has international cooperation at its heart. ESA has also established and is establishing broader international partnerships, both bilateral and multilateral, in the area of lunar exploration. In addition new partnership models with the private sector are being explored [2]. All of these are described in more detail in the below sections.

The role of in situ resources: The potential role of lunar resources has been widely discussed and the utilization of locally sourced resources to supply lunar missions has been identified as an enabling factor for the sustainability of lunar exploration. While not on the critical path of a human lunar return it is an important capability. Establishing ISRU as a capability for the future requires several steps; 1) prospecting to characterize resource deposits, 2) technology verification and

demonstration, 3) an ISRU pilot plant integrated with human missions, 4) full implementation [3]. Through the missions in ESA's exploration roadmap and coordination with partners these steps are being addressed.

Missions:

Prospecting resources. PROSPECT is package which is in preparation to assess the resource potential of lunar regolith at any given surface location [4]. It heats samples, thermochemically extracts volatiles and analyses them. It can be used to quantify water ice deposits as well as water and oxygen extraction processes from other regolith sources. PROSPECT is in development for first flight on the Luna-27 mission in 2022 This is a Russian led partnership for which ESA is also providing precision landing and hazard avoidance capabilities to the lander (PILOT) and communications services (SPECTRUM). ESA is coordinating with other agencies to ensure that the various international missions to the lunar poles and elsewhere are utilized to greatest effect for the prospecting of resources.

Commercial partnerships. ESA is in pilot phases for two missions in preparation through commercial partnership. These commercially driven missions will establish robotic surface access, led by the Part Time Scientists [5], and produce a commercial lunar cubesat deployment and communication relay service at the Moon, led by SSTL and Goonhilly Earth Station [6].

Lunar vicinity as a staging post. ESA is providing the European Service Module [7] for NASA's Orion vehicle. This vehicle will take humans beyond low Earth orbit for the first time since Apollo and will be the basis for human exploration in the future. Once in lunar vicinity human explorers will establish and crew the Deep Space Gateway [8], humanity's first spaceship, which is currently in preparation by the agencies of the ISS partnership. This craft will be crewed for tens of days per year and could be an enabling infrastructure for sustainable lunar surface access for teleoperated robots and eventually humans.

Demonstrating in situ resource utilization. Two important aspects of sustainable exploration will be the establishment of commercial services, for landing and communications, and the demonstration of critical ISRU technologies. For this reason ESA is targeting a commercially enabled ISRU demonstration mission not later than 2025. This mission would procure commercial access to the lunar surface and commercial communication services to operate an ISRU demonstration

payload. The goal of the mission is to demonstrate the production of drinkable water or breathable oxygen at the lunar surface to prepare for a future pilot plant, implemented in the early human missions. In the process the procurement model should help to close commercial business cases, securing the commercial services that will be needed later and reducing the overall cost of the mission compared with a standard agency driven development.

Human surface exploration demonstration mission: In collaboration with CSA, and JAXA, ESA is studying the HERACLES mission (e.g. [9]), which would use the Deep Space Gateway to teleoperate a rover at the lunar surface, retrieve samples and return them to Earth. NASA supports the study in the interfaces with the Gateway and Orion. The return would be performed with Orion via the Deep Space Gateway. The mission would rehearse the key elements of a nominal human surface mission scenario and de-risk key technologies. A notional traverse, studied in the preliminary mission studies, would be in the Schroedinger basin [10].

The human mission point of departure. In the context of the International Space Exploration Group (ISECG) [11] a notional scenario for human exploration missions is under discussion. This point of departure is used as a means to coordinate strategic planning and identify potential roles and investments. This scenario includes 5 missions and the first long duration human lunar surface mission (~42 days) with long-range mobility and night operations. This would include the demonstration of re-usability (ascender, pressurized rover) and would offer unprecedented opportunities for science and applications.

Summary: ESA is preparing for the new exploration of the Moon, which will be achieved through agency programmes, international partnerships and new roles for the private sector. Driven by the missions in the ESA mission roadmap ESA is working to assure access to the capabilities needed for lunar explorations. This is achieved through technology development, development of flight systems and the establishment of partnerships with international partnerships and the commercial sector.

References: [1] ESA Space Exploration Strategy, http://esamultimedia.esa.int/multimedia/publications/ESA_Space_Exploration_Strategy, [2] www.esa.int/About_Us/Business_with_ESA/Business_Opportunities/Partners_for_Space_Exploration, [3] J. Carpenter et al. (2016) *Space Policy* 37 52-57, [4] exploration.esa.int/moon/59102-about-prospect, [5] hptscientists.com, [6] www.goonhilly.org/moon-50, [7] http://www.esa.int/Our_Activities/Human_Spaceflight/Orion, [8] [www.nasa.gov/feature/deep-space-gateway-](http://www.nasa.gov/feature/deep-space-gateway-to-open-opportunities-for-distant-destinations)

[to-open-opportunities-for-distant-destinations](http://www.nasa.gov/feature/deep-space-gateway-to-open-opportunities-for-distant-destinations), [9] M. Landgraf et al. (2015) *LEAG*, 2039, [10] E. Steenstra et al (2016) *Advances in Space Research*, 58(6), 1050-1065, [11] www.globalspaceexploration.org

PREPARING FOR IN SITU RESOURCE UTILISATION ON THE MOON. J.D. Carpenter¹, B. Hufenhach, M. Landgraf, S. de Mey, A. Borggraefe, E. Sefton-Nash, R. Fisackerly, B. Houdou, R. Trautner, A. Cowley, A. Makaya, R. Lindner, P. Rebeyre. D. Binns. ESA, ESTEC, Noordwijk, The Netherlands (james.carpenter@esa.int).

In-situ resource utilisation will be a key enabling factor for sustainable human exploration. If we have aspirations for long-term presence and sustained infrastructure at the lunar surface, and eventually elsewhere in the solar system then we are obliged to learn how to use what we find at these destinations to provide the resources we need and integrate locally sources resources into mission architectures. To achieve this requires the establishment of a detailed understanding of the ores and deposits present, the products that are needed and the processes for extraction and storage.

A process of integrating resources into future missions requires a stepwise approach from prospecting, to technology demonstration in the relevant environment to system demonstration and integration of locally produced resources into missions without dependency. Only then can missions be implemented that have a dependency on locally produced resources.

In order to ensure that Europe is able to play a role in future ISRU activities ESA is preparing a strategy for ISRU. This strategy includes:

- mission architecture and technical studies to understand the likely future opportunities and needs, and build ISRU into the planning for future human missions.
- technology development; emphasising water extraction and oxygen production, as a first likely ISRU application.
- Prospecting; including the PROSPECT system on the Russian led Luna-27 mission and international coordination activities
- Preparation of a mission to demonstrate key technologies for ISRU at the lunar surface with flight planned not later than 2025.

The mission concept aims to:

- Demonstrate the feasibility of ISRU technologies at the lunar surface
- Generate new knowledge and operational experience to inform future ISRU efforts
- Generate scientific data to support lunar science investigations
- Support the establishment of commercial lunar landing and communications services
- Facilitate new partnerships and commercial opportunities

We will report on the status of the ISRU strategy, technology and mission preparations, emphasising where there are opportunities for the science community to engage with, support and benefit from

these activities and prepare for future roles in the emerging field of lunar resources and their utilisation.

MESG - MOON ENERGY STORAGE AND GENERATION: CONCEPT DESIGN AND ANALYSIS L. Celotti¹, M. Solyga¹, M. Piskacev¹, A. Mazzetti², M. Gianotti², P. Guardabasso², G. Proffe³, M. Sperl⁴, M. Fateri⁴, A. Cowley⁵, ¹Sonaca Space GmbH (DE), Carl-Scheele-Str. 14, 12489 Berlin, ²BlueThink S.p.A., V. F. Filzi 5, 20124 Milano (I), ³OHB System AG, Universitätsallee 27-29, 28359 Bremen (DE), ⁴DLR, Linder Höhe, 51147 Köln (DE), ⁵European Space Agency European Astronaut Centre, Linder Höhe, 51147 Köln (DE).

Introduction: The return to and utilisation of the Moon, widely identified as the next logical step in implementing the global strategy for manned exploitation of the solar system, is in the focus of all the national and international space agencies.

One of the most critical points in space exploration beyond Earth's orbit, is the provision of systems which ensure the survival of both crew and technological assets, such as rovers, landers, bases.

In accordance to these two points, a project led by Sonaca Space GmbH (with BlueThink S.p.A., the German Aerospace Center - DLR and OHB System AG as partners) has been financed by ESA, with the objective to assess and design a system based on a technology's capability for efficiently storing thermal energy, and reusing it for the production of electricity in-situ to support surface operations.

In comparison to the environment of the International Space Station, which is nowadays an established working environment for mankind, the Moon is much harsher. As an example, the lunar night can last, depending on the location, for as much as 14 Earth days and the surface temperatures can vary between 100 K and 400 K. This makes any system designed for lunar applications complex and constrained by many factors. In order to address these challenges, a novel heat storage and electricity generation system is designed and studied.

A common approach of many studies is the utilization of the native regolith as a heat storage medium. The stored thermal energy within the regolith could be, at a later convenient time, released in the system for direct heating purposes, or as an input to drive a heat engine, which can then transform it into electricity. Expanding on this idea, an appropriate modified/processed lunar simulant has been used to test and to obtain the mechanical and thermal properties through characterization techniques and experiments, with the objective to identify the most suitable processing method for the fabrication of the system's thermal mass.

Multiple potential "users" for the system are assessed in order to estimate the power requirements for relevant mission scenarios (i.e. manned and unmanned missions).

The system foresees the implementation of a solar collector as a mean to collect the solar energy available on the Moon. The collected thermal energy is then transferred to the thermal mass (modified and processed regolith) for storage, completing the hot

side of the system. Together they provide the heat to the hot side of an engine. The cold side of the system, which has a function to reject the waste heat from the engine, includes heat transfer devices and a radiator.

The architecture of the system is obtained by first assessing suitable technologies for each building block of the system separately, and then analysed altogether in a complex thermal system parameterized design.

Since possible technologies for each building block may not allow a completely free selection of the other blocks (due to unavoidable dependencies or simply not optimal performances of the technology chain), three different configurations have been identified and screened for the selection of a baseline for the system.

The identified baseline compiles a solar energy concentration and collection system based on optical waveguide technology, which was already successfully demonstrated on ground in the USA under NASA contracts [1,2], and was able to minimise the size and mass of the collecting part of the system. At the same time, the system provides a simple interface with the thermal mass and an implicit switch-OFF effect during darkness periods. A Stirling engine is proposed for the heat-to-electricity building block, given the high expected efficiency as power generator. Its reliability in space applications has been flight-proven by Stirling cryocooler systems. The heat rejection segment is a simple radiator exposed to deep space. In order to transfer the heat efficiently through the different parts of the system, while at the same time keeping the system's mass at a minimum, heat pipes and loop heat pipes were selected as the ideal solution after a comparative analysis with other heat transfer systems. The system's performances and final sizing were assessed and evaluated in respect to the different users, providing promising estimations, like a slightly larger than 2.5 m³ thermal mass in order to provide sufficient electrical energy for the survival of a 115 W lander (survival operations during the night).

References:

[1] Nakamura, Takashi, et al. "Solar thermal power system for oxygen production from lunar regolith." AIP Conference Proceedings. Ed. Mohamed S. El-Genk. Vol. 969. No. 1. AIP, 2008.

[2] Gordon, Pierce EC, et al. "Thermal energy for lunar in situ resource utilization: technical challenges and technology opportunities." (2011).

ABUNDANCE AND H ISOTOPIC COMPOSITION OF WATER IN SHOCKED LUNAR APATITE FROM MG-SUITE ROCKS.

A. Černok¹, X. Zhao¹, J. Darling², L. White³, J. Dunlop², I. A. Franchi¹ and M. Anand^{1,4}.
¹Open University, School of Physical Sciences, Walton Hall, MK7 6AA, United Kingdom (ana.cernok@open.ac.uk),
²University of Portsmouth, School of Earth & Environmental Sciences, Burnaby Road Portsmouth, PO1 3QL, United Kingdom;
³Department of Natural History, Royal Ontario Museum, Toronto, Canada, M5S 2C6.
⁴Department of Earth Sciences, The Natural History Museum, London, SW7 5BD, UK.

Introduction: Apatite ($\text{Ca}_5(\text{PO}_4)_3(\text{F,Cl,OH})$) is one of the most versatile and *in situ* studied minerals among terrestrial and planetary samples [1], receiving increasingly more attention as a key tracer of the volatile budget, absolute age, oxygen fugacity, and of mineral deposits. It is a commonly used phase in studies of lunar volatiles [2] as it is found in a wide range of lunar samples, and petrogenetic environments. The focus of this study is to investigate if the shock-induced microtexture in apatite correlates with the content and distribution of H (reported from hereon in terms of equivalent H_2O) and its isotopic composition, in order to discriminate whether there is a disturbance or an enrichment taking place during the samples' impact history. This will further strengthen our understanding if the water in the Earth-Moon system has a common origin, and tackles the broad question of source of water in the Inner Solar System.

Samples: When it comes to studies of water in lunar apatite, most lunar lithologies ranging from basaltic [e.g. 3] to more evolved lithologies [4] have been thoroughly investigated. However, correspondingly little work has been done [5] on apatite in samples from lunar highlands which seem to be represented by an intermediate component in the H_2O - δD space of lunar apatite dataset. In this study, six different samples of Mg-suite norite, troctolite and gabbro were selected from the Apollo 17 collection, based on the increasing level of shock deformation: unshocked troctolite 76535, anorthositic troctolite 76335, breccia 76255 with troctolite, norite and gabbro clasts, 72255 (Civet Cat fragment), 73235 shocked troctolite, and 78236 shocked norite. All samples show a high (7-9) index of petrological pristinity. In nine different polished thin sections, we located 35 grains of apatite suitable for analyses.

Methods: The search for apatite grains in each polished thin section was performed by EDS elemental X-ray mapping using a Secondary Electron Microscope (SEM). The petrographic context was evaluated by EDS-spot analyses of the minerals surrounding apatite grains. Cathodoluminescence (CL) detector mounted on a SEM was used to investigate homogeneity or internal zoning of selected apatite grains. Lattice orientation, internal microtexture, and structural disorder of selected apatites was studied by Electron Backscatter Diffraction (EBSD). H_2O content and δD were obtained by NanoSIMS, using a previously established protocol [6].

Results: Microtexture: Two distinct types of apatite were observed. The **primary apatites** are those preserved in the primary, albeit shock-metamorphosed, mineral association. The **secondary apatites** are found associated with impact melt. They are either heavily affected and most likely recrystallized in contact with impact melt, as evident by lobate and absorbed grain boundaries, or freshly crystallized from the melt in case of euhedral apatite. Primary apatites are less abundant (a few per thin section) than the secondary ones (several dozen per thin section), and also much smaller (primary up to $\sim 50\ \mu\text{m}$ in length vs. secondary up to $\sim 200\ \mu\text{m}$). Microtexture in primary apatite shows progressively more deformation with increasing level of shock, corresponding to deformation stages from 1 (no deformation 76535) to 4 (heavily shocked, 78236). Stage 2 microtexture shows the lowest level of cataclastic deformation that involves mechanical breaking and crushing of the minerals, with initiation of subgrain formation in apatites' rim. Stage 3 apatite (see inset in Figure 1.) shows prominent subgrain formation. Stage 4 is intensively deformed, with decreasing subgrain size (see the companion abstract by Černok et al. in this symposium). Secondary apatite is a single crystal apatite, with no subgrain formation nor other evidence of deformation and it was only found in sample 76255.

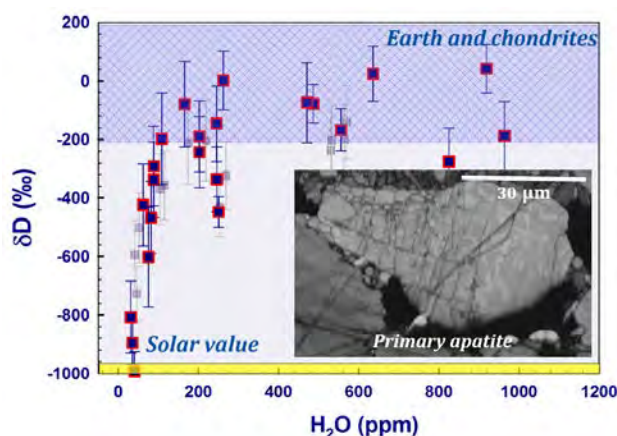


Figure 1. H_2O - δD diagram of shocked apatite from Apollo 17 Mg-suite rocks. Values highlighted by red square are those of the primary apatite, whereas the values in light grey represent secondary, impact melt apatites. The inset shows band contrast (state of crystallinity) map, as an example of shock-deformed primary apatite (stage 3). δD is corrected for cosmic ray D production.

H_2O - δD content: Apatite in shocked Apollo 17 rocks shows a wide range in water concentrations, as well as in δD values, albeit the variations within a

single sample are relatively limited. Cataclastic troctolite 76335: 166(2)-471(7) ppm H₂O, $\delta D = -336 \pm 111$ up to -74 ± 136 ‰; Impact melt breccia 76255 containing norite, troctolite and gabbro fragments: 36(1) to 964(15) ppm H₂O $\delta D = -895 \pm 74$ up to -141 ± 126 ‰; shocked *Civet Cat* norite: 31(1)-62(1) ppm H₂O $\delta D = -993 \pm 68$ up to -424 ± 141 ‰; shocked troctolite 73235: 75(2) ppm H₂O $\delta D = -602 \pm 170$ ‰; and heavily shocked norite 78236: 250(3) to 556(6) ppm H₂O $\delta D = -77 \pm 66$ up to -448 ± 53 ‰. Breccia 76255 contains three different lithologies mixed with impact melt, hence the large range of H₂O and δD values. The overall range of the water abundance and its isotopic composition follows a well-defined trend: apatite with lowest water content has very light δD , approaching solar values in case of the apatites with lowest water (~ 30 ppm). Apatite containing more water is enriched in D relative to the water-poor apatite, with most of the analysed grains showing close to terrestrial & chondritic δD values when containing ~ 100 ppm or more H₂O.

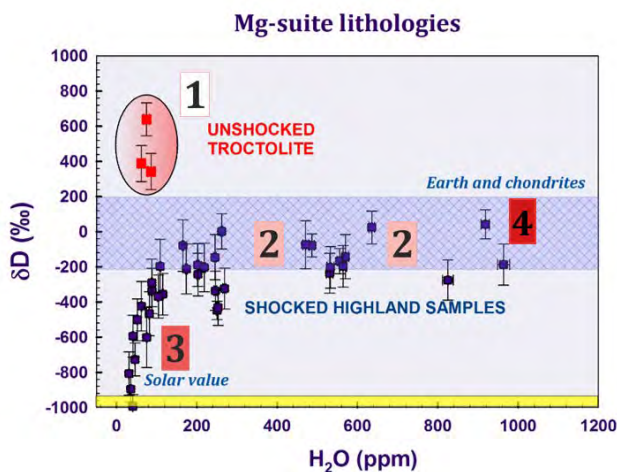


Figure 2. H₂O- δD diagram of apatite from shocked vs. unshocked [4, 5] Mg-suite samples. The numbers highlight the stage of shock deformation. δD is corrected for cosmic ray D production.

Discussion: The general H₂O- δD trend observed in the examined Mg-suite rocks does not seem to correlate with the overall level of shock deformation each sample experienced (Fig. 2). For example, the two most heavily deformed norites, 72255 *Civet Cat* and 78236, plot at the opposite ends of the observed range. Impact-melt breccia 76255 contains clasts of three different lithologies (norite, gabbro and troctolite) surrounded by fine-grained impact melt. The clasts contain primary, whilst the impact-melt rich matrix contains large secondary apatite. Although the whole sample spreads across the entire H₂O- δD range seen in this study, apatites from each individual clast and from associated impact melt have discrete H₂O- δD values, e.g. apatites within troctolite and from the melt surrounding it contain 530(9) – 964(15) ppm H₂O with $\delta D = -275 \pm 113$ up

to -142 ± 127 ‰. The melt in the sample 76255 was not formed by melting of the incorporated clasts, as these clasts are shock-deformed at pressures and temperatures insufficient for incipient melting. However, the source of the impact melt must have contained apatites of similar volatile signature, which were preferentially melted and acted as a phosphorous source or nuclei for the formation of abundant secondary apatite within the impact melt.

Our study reveals that shocked Mg-suite apatite records variable H₂O and δD , but the extent to which they were affected during an impact largely depends on their initial water abundance. Regardless of the level of shock, water-poor primary apatite exposed to shock deformation appear to show extremely low δD , most likely as a result of incorporating D-poor hydrogen. On the other hand, apatite that contains more than 100 ppm H₂O is unlikely to change its isotopic systematics significantly. The low δD , i.e. H-rich, reservoir on the Moon is the surface regolith [7], due to its long exposure to surface implantation of solar wind hydrogen. A recent study has suggested a deep source of low δD [4], based on more evolved lunar lithologies, however, it is unlikely that the Mg-suite rocks can be petrogenetically related to the same source. The regolith is extensively mixed with melt formed during an impact and can deliver abundant D-poor hydrogen. Rocks that have not been shock deformed (e.g. 76535 troctolite), preserve high δD despite being water-poor (Fig. 2).

Conclusion: We observed two distinct microtextural types of apatite in shock-deformed Mg-suite rocks: primary (shocked, granular) and secondary (impact melt related) apatites. Primary apatites show microtextural response to increasing level of shock. No obvious difference in H₂O and δD was observed between the two textural types, nor as a consequence of increasing deformation. However, shock-induced microtexture of water-poor primary apatite could potentially enhance reaction with D-poor impact melt, that is abundant in these samples and therefore reduce δD of apatite. Water-rich primary apatites, despite their complex microtextures do not show any evidence of significant reduction in their δD .

Acknowledgements: We thank NASA CAPTEM for allocation of lunar samples. The project received funding from the European Union's Horizon 2020 research and innovation programme under grant agreement No 704696. This research was partially supported by STFC grants to MA (# ST/L000776/1 and ST/P000665/1).

References: [1] Hughes J. M. (2015). *Am. Min.* 100, 1033–1039. [2] McCubbin F. et al. (2015) *Am. Min.* 100, 1668–1707. [3] Tartese et al. (2014). *Geology* 42, 363. [4] Robinson K. et al. (2016). *GCA* 188, 244–260. [5] Barnes J. et al. (2014). *EPSL* 180, 244–252. [6] Barnes et al., 2013, *Chemical Geology* 337–338, 48–55. [7] Treiman. H. A. et al. (2016) *Am. Min.* 101, 1596–1603.

SHOCK-INDUCED MICROTEXTURES IN LUNAR APATITE AND MERRILLITE. A. Černok¹, J. Darling², L. White³, J. Dunlop², and M. Anand^{1,4}. ¹Open University, School of Physical Sciences, Walton Hall, MK7 6AA, United Kingdom (ana.cernok@open.ac.uk), ²University of Portsmouth, School of Earth & Environmental Sciences, Burnaby Road Portsmouth, PO1 3QL, United Kingdom; ³Department of Natural History, Royal Ontario Museum, Toronto, Canada, M5S 2C6; ⁴Department of Earth Sciences, The Natural History Museum, London, SW7 5BD, UK.

Introduction: Apatite and merrillite are the most common phosphate minerals in lunar and meteoritic samples [e.g. 1]. They are the main host of phosphorous, volatiles and REEs in many planetary materials. Over the past two decades, apatite and merrillite have been extensively used as targets for *in situ* U-Pb and Pb-Pb age determination [2, 3], as well as for volatile budget estimations [4]. Despite the fact that most lunar and meteoritic samples show at least some evidence of impact metamorphism, not much is known about how these trace minerals behave in response to shock deformation.

In this study we aim at quantifying shock-induced deformation of apatite and merrillite and compare it with deformation in plagioclase, a well quantified shock barometer [e.g. 5]. These materials present a unique opportunity to critically understand how impact processes have affected the microstructural evolution of these key accessory phases. This can then be used to elucidate the effect of shock-induced microtextures on distribution of volatiles (see the companion abstract by Černok et al. in this symposium) and radiogenic ages (anticipated study).

Samples: Five different lunar samples of Mg-suite norite, troctolite and gabbro were selected for this study from the Apollo 17 collection, based on the increasing level of shock deformation: troctolite 76535, anorthositic troctolite 76335, Civet Cat norite fragment in 72255, and heavily shocked norite 78235 & 78236.

Methods: The search for apatites within thin section was performed by EDS elemental X-ray mapping procedure using a Scanning Electron Microscope (SEM). The petrographic context was evaluated by EDS-spot analyses of the minerals surrounding apatite. Cathodoluminescence (CL) detector was used to investigate homogeneity or internal zoning of selected phosphates, as well as for coexisting plagioclase, for comparison of the shock level. Lattice orientation, internal microtexture, and structural disorder of selected apatites and merrillites were studied by Electron Backscatter Diffraction (EBSD), and complemented by Raman Spectroscopy.

Apatite texture component

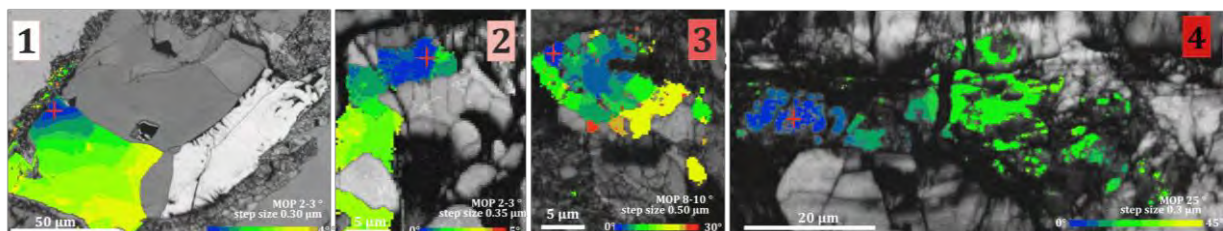


Figure 2. Band contrast images overlain with texture component maps of apatite at four different stages of deformation. Misorientation profile (MOP) within individual fragments is relative to the red cross mark.

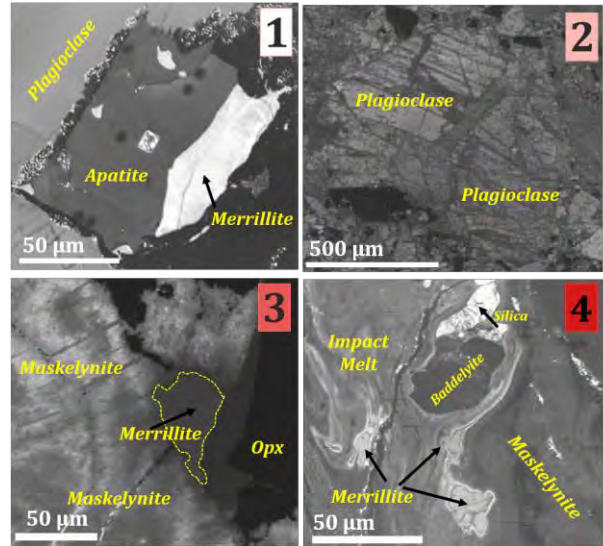


Figure 1. CL images of progressively shock-deformed plagioclase at different stages. (1) Unshocked plagioclase, surrounding apatite and merrillite; (2) striated plagioclase in cataclastic troctolite; (3) merrillite in contact with foamy/spongy maskelynite; (4) merrillite in maskelynite and impact melt.

Results: All investigated grains are apatites and merrillites of primary origin, preserved in the pristine, albeit shock-metamorphosed, Mg-suite mineral assemblages (plagioclase, Opx, Cpx, silica, baddeleyite, and other traces). Apatite and merrillite are commonly spatially associated. EDS mapping revealed ~5 to 10 apatites in each thin-section, with the largest grains having ~50 µm in the longest dimension. All apatites and merrillites have anhedral grain shape, mostly showing sub-equant crystal habit. Dataset includes high-resolution (100-500 nm step size) EBSD maps of 15 apatites and 11 merrillite grains. Microtextures in apatite and merrillite are progressively more complex and deformed with increasing level of shock. Stages of deformation ranging from 1 (no shock deformation) to 4 could be described in this set of samples, with correlation to the microtexture of the coexisting plagioclase. At stage 1 minerals show no obvious signs of deformation and

Merrillite texture component

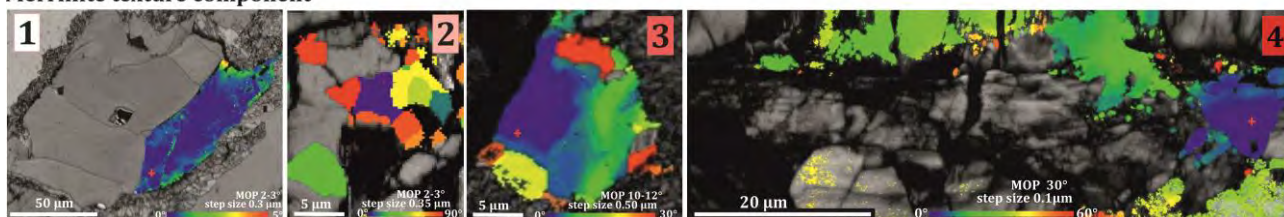


Figure 3. Band contrast images overlain with texture component maps of merrillite at four different stages of deformation. Misorientation profile (MOP) within individual fragments is relative to the red cross mark.

plagioclase seems undisturbed in CL images (Fig. 1), suggesting the sample has experienced minimal shock loading. As revealed by band contrast EBSD images (overall state of crystallinity), apatite and merrillite at stage 1 show no macro- or microscopic deformation and form large single crystals. The texture component maps reveal no more than 2° of internal crystal misorientation (Figs. 2 and 3). Stage 2 microtexture shows the lowest level of cataclastic deformation that involves mechanical breaking and crushing of all the minerals. At this stage plagioclase shows typical striation in CL images (Fig. 1) indicative of shock pressures in excess of ~ 12 GPa. Apatite and merrillite display early stage of subgrain formation, with typical irregular subgrain shape and size of several μm . However, individual subgrains remain undeformed ($2\text{--}3^\circ$ internal misorientation). Merrillite appears more prone to subgrain formation than apatite and often displays subgrains of random relative orientation. At stage 3, plagioclase is mostly maskelynitized, as evident by its foamy or spongy appearance in CL. This observation constrains the pressure experienced by the sample to > 29 GPa [5]. Subgrain formation is very prominent at this stage in both apatite and merrillite, and they appear completely granular. Size of individual subgrains is $1\text{--}5 \mu\text{m}$. Internal deformation of individual subgrains yields up to $\sim 10^\circ$ of misorientation in apatite and up to $\sim 12^\circ$ in merrillite, a sign of crystal plastic lattice deformation of individual crystals. At the highest level of deformation, maskelynite is in contact with impact melt, which shows abundant flow features. Apatite and merrillite are in contact with both impact melt and maskelynite, but also with minerals that have higher shock impedance than plagioclase, i.e. are less prone to deformation (Opx, Cpx). Band contrast of apatite reveals fine granular interior, with domains of sub- μm sized features that appear amorphous at the length scales of EBSD ($\sim 80 \times 40\text{nm}$). Texture component maps show up to 25° of misorientation within a single grain, evidence of severe crystal-plastic deformation. While these grains are heavily deformed, no signs of recrystallization of apatite are obvious. Merrillite is predominately granular, yielding randomly orientated subgrains indicative of solid-state or melt-recrystallization, with coarser granular textures clearly being evidence of a relatively late stage formation. A small number of merrillite grains

contain extensive (up to 30°) crystal lattice deformation. In both minerals, CL features show lighter cloudy regions in the areas of lower crystallinity as indexed by EBSD, indicating a high density of defects [e.g. 6]. No high pressure polymorph of any phase was detected by Raman spectroscopy. Raman spectra of all samples complement the EBSD pattern by indicating that material is well-crystallized, and not amorphous.

Conclusion: This study reveals four different stages of shock deformation in lunar apatite and merrillite. Based on the texture components maps, it can be suggested that an intermediate level of deformation between stages 2 and 3 (MOP $3\text{--}8^\circ$) should exist, as well, however it was not present in the selected set of samples. Merrillite shows lower shock impedance than apatite, i.e. more deformation at the same shock level. The internal structural complexities observed in this study cannot be visualised using backscatter electron (BSE) imaging alone. The evidence of microstructural changes in response to shock metamorphism of widely used accessory minerals should be taken into account when interpreting the volatile content and crystallization ages of lunar highland samples.

Acknowledgements: We thank NASA CAPTEM for allocation of lunar samples. The project received funding from the European Union's Horizon 2020 research and innovation programme under grant agreement No 704696. This research was partially supported by a STFC grant to MA (# ST/L000776/1 and ST/P000665/1).

References: [1] Adcock C.T. et al. (2016). *Nat-Comm.* 8:14667 [2] Snape J.F. et al. (2016) *GCA* 174, 13–29. [3] Thiessen F. et al. (2017) *MAPS* 52, 584–611. [4] McCubbin F. et al. (2015) *Am. Min.* 100, 1668–1707. [5] Rubin (2015). *Icarus* 257, 221–229. [6] Nihara et al. (2012). *EPSL* 341–344, 195–210.

Importance of impact craters: The study of the nature and distribution of materials excavated and deposited in impact craters gives information on both the composition and layering of deep-seated materials, and cratering processes. Lunar impact craters are therefore important targets for remote sensing and future field work investigations. However present remote spectral studies to infer the composition of crater materials have some limitations, and future robotic and manned in situ exploration to overcome them are not yet planned.

Impact craters expose a large variety of materials arising from both the complexity of the initial target and cratering processes. Melting occurs at different degrees and during cooling at different rates, a range of textures from glassy (“pure melt”) to coarse-grained crystalline (recrystallized melt) is likely to be found within and around the crater. Also, during the excavation process significant lithic fragments can be entrained in the melts [1]. Due to scaling effects the proportion of clasts in the impact melt is expected to be higher on the Moon than on the Earth. Hence, reflectance spectra from crater materials show complex behavior, being a function of both the starting material and the conditions of melting and/or cooling of the impacted materials. In spectra from crater materials, mineralogical features are more or less preserved through the cratering processes and impact melts play an important role which is presently not well understood.

Spectral studies of impact craters materials: Some spectral characteristics of lunar melts have been defined. For instance it has been shown that generally melt halos around many impact craters display high spectral ratio values between 0.41 and 0.76 micron (i.e., a strong red slope) [2], and lower albedo values than surrounding materials. This occurs only in a relative sense: while impact melts may be observed to be redder and darker than local soils, they are not necessarily redder and darker than soils at other locations on the Moon [3].

Also pooled impact melt in large craters [4] shows an absorption band near 1 micron suggesting the presence of significant amounts of Fe-bearing glass mixed with lithic fragments and/or recrystallized melt. The impact melt spectra also all appear to exhibit a 1.2 micron absorption feature. Experiments using crystalline and quenched glass samples of lunar samples [3] have shown that the feature observed near 1.2 micron can either be accounted for by small amounts of FeO captured within the plagioclase microcrystals [5] or a significant amount of the FeO within crystallized pyroxene [6]. An absorption near

600 nm is also observed ubiquitously in both the melt breccias and the impact melt samples attributed to the presence of submicroscopic ilmenite within a semitransparent matrix (in a transparent host typically as inclusions in plagioclase). However ilmenite is rare among pristine lunar rocks, lunar mineral separates, and lunar soils, all of which having different cooling histories. This absorption feature is therefore potentially characteristic of (but not necessarily exclusive to) fine grained, recrystallized (or devitrified) impact melt [3]. It apparently can be used to identify and map the distribution of microcrystalline impact melt as well as ilmenite-bearing pyroclastic material. Experiments also show that for glass and crystalline the most obvious spectral change is a broadening in the shape of the 1 micron absorption band with increasing glass abundance and a shifting to longer wavelengths. In both the natural and calculated mixtures, >60% glass appears necessary for its presence to be obvious in the mixture spectra.

We clearly need more experimental data to better understand the spectral behavior of impact melts deriving from crystalline materials and having textures ranging from glassy, (i.e., pure melt) to coarse-grained crystalline (recrystallized melt) as a function of the cooling history. We also need more advances in the deconvolution of the overlapping spectral absorption bands into their fundamental absorption components using the MGM (Modified Gaussian Model) model [7], taking into account not only the spectral characteristics (configurations) of crystalline mafic components but also the characteristics of impact melts at various degrees of melting, and crystalline and melt mixtures. This approach is essential for the study of impact craters where most of the initial materials are melted or at least shocked during the crater formation.

Spectral and morphological approach: Today, a first step and approach in the study of lunar impact craters can be made using the M3 (Chandrayaan-1) spectral data and the LRO high resolution imaging (morphological) data. The objectives are to link the spectral compositional information, using the MGM model, to small scale morphological observations (at metric scale) from the orbit. The morphological information is quite useful for the interpretation in terms of degree of melting of the target materials and their distribution. We conducted some studies on Aristarchus and Copernicus craters (e.g., [8, 9, 10]). From previous work based on Clementine data [11, 12] and more recent studies using M3 [9], we have for instance shown that spectral signatures showing an anorthositic with orthopyroxene (OPX) and CPX

components (unit AER in [11]) on the north-east portion of the wall (terraces) of Aristarchus, result from the presence of large boulders (up to 100 m in size for some) which are embedded in the melt during the ejection process [12]. In Aristarchus we also mapped rich olivine-bearing materials identified through the MGM model (red units in figure 1). Although olivine is the dominant component for most of these materials (red units) we identified some areas showing the presence of another component, probably a pyroxene or a Fe-bearing glass not presently modeled by the MGM. From morphological evidences the spectral signature of the olivine might predominantly be caused by the presence of prominent lithic fragments embedded in the melt and/or the presence of blocks (ejecta) on the surface [9].

Future missions inside impact craters: Remote sensing techniques (multispectral observations for composition and high resolution imaging for morphology) have their limits. In order to improve our understanding of cratering processes and the nature and origin (stratigraphy) of deep-seated materials, sampling and in situ observations conducted in different places of the crater interior, will be absolutely needed. However traverses across the floor, close to the central peak and walls (terraces) of large craters such as Aristarchus and Copernicus would be difficult either for automatic rovers or humans. The visit at the North Ray crater (1 km in diameter) by the astronauts of Apollo 16 proved that the exploration of small craters is also a very difficult task [8]. In large craters ground access and trafficability is greatly reduced for long distances.

The future in situ investigations of crater interior and ejecta, of high scientific value, by humans and/or automated means, appear to be very challenging. New techniques must be developed to conduct in situ and field work operations inside impact craters, such as vehicles having the ability to take off and hovering from place to place, with high capabilities in navigation to land in difficult but safe areas. Without the development of such techniques and new surface operations, lunar craters will remain poorly investigated, strongly limiting advances in planetary science. These techniques would also apply to the study of other formations presenting a strong interest in lunar science but difficult to explore, such as massifs surrounding the impact basins, volcanic domes and sinuous rilles. It is now time to

think and develop future missions to explore lunar craters.

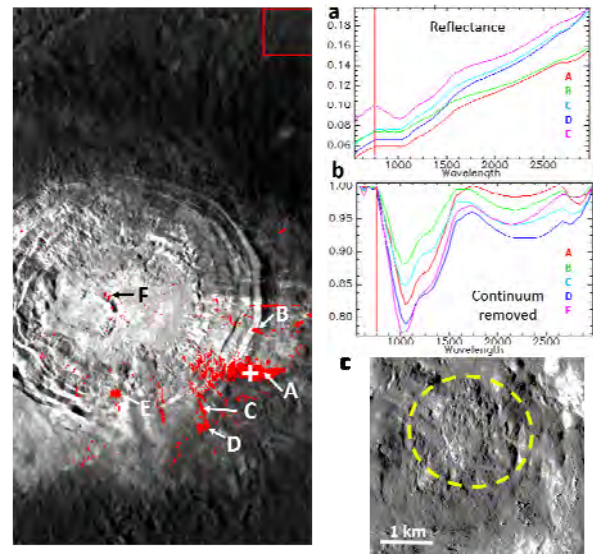


Figure 1. Left: M3 image of the crater Aristarchus (42 km in diameter). Red areas are rich olivine-bearing materials identified using the MGM model (see text). Right: Reflectance (a) and continuum removed (b) spectra of the areas shown at left; (c) LRO image (ARISTARCLOA_E237N3125_5M) at decametric resolution of area E. Yellow circle highlights a patch of impact melt on the terraced wall, displaying numerous blocs on its surface.

References: [1] Cintala M.J. and Grieve R.A.F. (1994) *Geol. Soc. of Amer. In Large meteorite impacts and planetary evolution*, ed. Dressler B ; [2] McEwen A. S. et al., (1993), *JGR* 98:17207–17231 ; [3] Tompkins S. and Carle M. Pieters (2010), *Met. & Planet. Sci.* 45, 1152–1169 ; [4] Smrekar S. and Pieters C. M. (1985), *Icarus* 63, 442–452 ; [5] Adams J. B. and Goulland L. H., (1978). *Proc. LPSC 9th*, 2901–2909 ; [6] Klima R. L. et al., (2008), *Met. & Planet. Sci.* 43, 1591–1604 ; [7] Sunshine J.M. et al. (1990) *J. Geophys. Res.*, 95, B5, 6955–6966 ; [8] Chevrel S. D. et al. (2016), abstract, European Lunar Symposium 4th ; [9] Chevrel S. D. et al. (2017), LPSC 48th, Abstract #1907 ; [10] Pinet P. C. et al. (2018), abstract, European Lunar Symposium 5th ; [11] Chevrel S. D. et al. (2009) *Icarus*, 199, 9–24 ; [12] Chevrel S. D. et al. (2015), abstract, European Lunar Symposium 3rd.

Introduction: Lunar lobate scarps are the surface expressions of low-angle thrust faults formed by contraction of the crust due to long-term interior cooling [1-7] and tidal deformation [8]. Based on their fresh morphology, the scarps are some of the youngest landforms on the Moon [4, 7, 9-12]. First scarp age estimates using Apollo panoramic camera images and crater degradation measurements on craters pre- and post-dating the scarps revealed that they formed in the last ~700 Ma [10].

Today, the Lunar Reconnaissance Orbiter Camera (LROC; [17]) provides high-resolution, 0.5 to 2 m/pixel Narrow Angle Camera (NAC) images, allowing the exploration of previously known and newly discovered scarps on a global scale [7]. Along with new imagery, techniques to derive surface ages using crater size-frequency distribution (CSFD) measurements were also developed since the study by [10] and have been tested [13] for five scarps previously studied by [10]. These recent age determinations, in addition to other work [12-16] using both traditional and buffered crater counting (BCC) CSFD measurements, revealed they were active in the late Copernican, having ages as young as 14 Ma.

Using the technique of [13], we expanded our data set to a total of 34 scarps to investigate whether there are global trends with age and distribution, how the crustal stresses developed over time, and whether scarps formed during punctuated episodes or continuously [16]. Our data also allow us to investigate the seismic record around the scarps. [13] showed that the crater record adjacent to the scarps is reset due to seismic shaking related to scarp formation. CSFDs both proximal and distal to the scarps could thus reveal information about the extent and severity of the seismic activity on the faults [13]. Here, we explore the variations in the CSFDs and derived AMAs for 34 lobate scarps.

Methods: For our study, we used the traditional CSFD method, as tested by [13] for application to lunar lobate scarps, which measures all primary craters within a single geomorphologic unit, excluding secondary and endogenic craters. Representative count areas are placed both proximal and distal (~3-4 km away) to the fault trace [12, 13]. Slopes from large craters (>1km) and regional topography are avoided since CSFDs on inclined surfaces ($\geq 10^\circ$) can result in younger apparent AMAs due to mass wasting [20, 21]. We fit the CSFDs in cumulative form with pseudo-log binning [19, 22, 23], using the lunar production function and cratering chronology

of [24]. We often measured craters smaller than the 10 m production function threshold to ensure that our dataset was complete to the limit of the image resolution.

Results: Measuring the crater population on scarp surfaces revealed that the thrust faults have been active in the last ~400 Ma and as recently as ~24 Ma. The majority of faulting events occurred in the last ~200 Ma, with an average age of 105 Ma. Of the 34 scarps, ~53% of the proximal footwall surfaces were younger than the adjacent hanging wall. Approximately 75 % of the distal count areas are older than their proximal counterparts.

Discussion: In many cases, the increase of the ages away from the scarp traces is consistent with the attenuation of seismic shaking with distance from the fault. Could an evaluation of the ranges of crater diameters reset by the event (Fig. 1) give us information about the geographic extent and severity of shaking? To answer this question, we assessed the fit ranges of the AMAs we determined that best represent each scarp age. We theorize that the erasure of larger-sized craters requires either a greater level or longer period of shaking or a larger number of events than for removal of smaller-sized craters.

Many of the ages that we fit use a minimum fit diameter of 10 m, because this is the limit allowed by the lunar production function of [24]. Thus, for the time being, 10 m is a boundary condition for our analysis until the production function can be extended to smaller crater diameters. Occasionally, the CSFDs cannot be fitted with the production function down to the 10 m boundary. Of all the CSFD measurements for scarp surfaces (111 in total), over half of the scarps that have a lower boundary above the 10 m exhibit equilibrium conditions. The largest crater diameter reset by the scarp activity minus the smallest diameter affected defines the Δ Crater diameter.

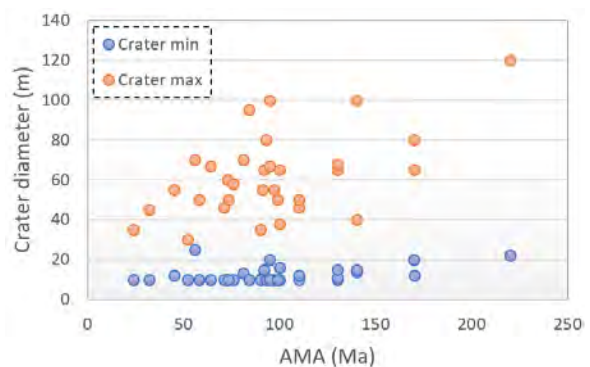


Fig 1: The maximum and minimum fitted crater diameters affected by seismic resetting events related to scarp activity at 34 lunar scarps.

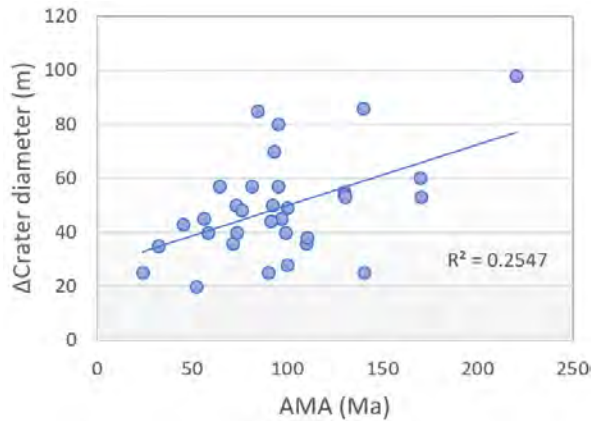


Fig 2: Δ Crater diameter range affected by seismic resetting as determined from Fig. 1 versus the derived AMA (Ma) for each of 34 studied scarps.

Δ Crater diameter vs. AMA (Fig. 2): The diameter ranges reset by the scarp activity varies from 20 to almost 100 Δ Crater diameter (m) (Fig. 2). Here, the Δ Crater diameter has a general upward trend with an increase of AMA. This might suggest that seismic activity (duration and/or magnitude) has been decreasing over the last ~250 Ma that is covered by our dataset, where smaller quakes would erase a smaller size range of craters. We do note that the trend is defined by few data points at the older ages. The addition of more scarp analyses is required to more fully evaluate the potential trend.

Δ Crater diameter vs. location (Fig. 3): As mentioned earlier, distal count areas typically yield older AMAs, presumably because of reduced seismic shaking with distance from the scarp. Using only lobate scarps where distal AMAs could be determined, we plotted how the Δ Crater diameter varies among the four count areas for the scarps (Fig 3), i.e., the proximal foot- (FWP) and hanging wall (HWP) count areas and the distal foot- (FWD) and hanging wall (HWD) count areas. First observations reveal that 60% of the scarps tend to have a wider range (e.g. a large number of crater used to derive

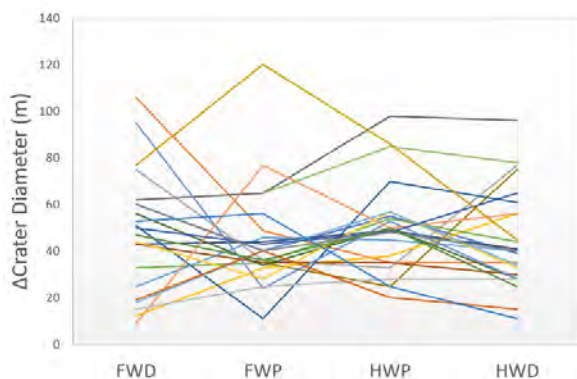


Fig 3: Δ Crater diameter range affected by seismic resetting versus the location of the count area with respect to the scarp, where FW is the footwall, HW is the hanging wall, D is for distal, and P is for proximal.

an age) of fit for the HWP than the FWP. A more detailed analysis of the data may help us determine what fault characteristics and/or local geologic settings determine the maximum fault-related shaking.

What can we learn? Beyond determining AMAs for numerous scarps, the goal of this work is to study the CSFD measurements for supplementary information about the seismic activity at and around the lobate scarps. By exploring the fits of the crater populations, we hope to uncover how seismic shaking is distributed locally, the magnitudes/duration of scarp-related moonquakes, and regional variability of crater resurfacing. More in depth studies of individual scarps [e.g., 25] could reveal more information about the formation and evolution of lunar lobate scarps

References: [1] Watters, T.R. (2003) J. Geophys. Res., 108 [2] Watters, T.R. et al., (2009) Earth Planet. Sci. Lett., 285, 285-296. [3] Watters, T.R. and Schultz, R.A. (2010) Planetary Tectonics, Cambridge Univ. Press. [4] Schultz, P.H. (1976) Moon Morphology, University of Texas Press, Austin, TX. [5] Binder, A.B. (1982) Earth, Moon, and Planets, 26, 117-133. [6] Watters, T.R. and Johnson, C.L. (2010) Planetary Tectonics, Cambridge Univ. Press, pp. 121-182. [7] Watters, T.R. et al., (2010) Science, 936-940. [8] Watters et al (2015) Geology 43, 851; [9] Lucchitta (1976) PLPSC 7, 2761; [10] Binder and Gunga (1985) Icarus 63, 421; [11] Watters et al. (2012) Nature Geo 5, 181; [12] van der Bogert et al. (2012) LPSC 43, 1847; [13] van der Bogert et al. (2018) Icarus, 10.1016/j.icarus.2018.01.019. [14] Senthil Kumar et al. (2016) JGR 121, 147 [15] Clark et al. (2017) Icarus 298, 78 [16] Clark et al. (2016) LPSC 47, 1380. [17] Robinson et al (2010) Space Sci. Rev. 150, 55. [18] Neukum (1983) Habil. Thesis NASA TM-77558. [19] Michael and Neukum (2010) EPSL 294, 223. [20] Basilevsky (1976) PLPSC7, 1005. [21] Meyer et al. (2016) LPSC 47, 2740. [22] Michael (2013) Icarus 226, 885. [23] Michael et al. (2016) Icarus 277, 279. [24] Neukum et al. (2001) Space Sci Rev 96, 55. [25] Clark et al. (2016) LPSC 47, 2956.

A Model for the Comparative Role of Impact Gardening as a Control of Near-Surface Ice on the Moon and Mercury E. S. Costello^{1,2}, R. R. Ghent^{3,4}, P. G. Lucey¹ ¹Hawaii Institute of Geophysics and Planetology, University of Hawaii, Honolulu, HI, USA, ecostello@higp.hawaii.edu; ²Dept. of Geology and Geophysics, University of Hawaii, Honolulu, HI, USA; ³University of Toronto Dept. of Earth Science, Toronto, ON, Canada; ⁴PSI, Tucson, AZ, USA.

Introduction: The Moon and Mercury have polar regions in permanent shadow that provide hospitable conditions for volatiles [1, 2, 3, 4]. While radar observations of the poles of Mercury present strong evidence for the existence of pure water ice deposits that are meters thick in permanently shadowed regions [e.g. 5, 6, 7], ice on the Moon has been less conspicuous. Workers have found traces of water or hydroxyl [e.g. 8, 9, 10, 11, 12, 13] but the Moon does not have unambiguous and extensive Mercury-like surface or shallow buried ice deposits. Mystery remains with respect to cause of the discrepancy of near-surface ice between the Moon and Mercury.

To investigate the volatile disparity between the Moon and Mercury we use an analytic model to describe the rate and magnitude of impact gardening as a function of time on both bodies. The model is based on the pioneering Apollo-era lunar regolith mixing model presented by Gault et al. (1974) [12], with updated input parameters and an expanded parameter space that allows for exploration of the rate of impact gardening as it is driven by a variety of impactor types into a variety of target materials. We take advantage of the expanded parameter space in this work, as we broaden the scope of the model beyond the Moon to calculate the rate of impact gardening on Mercury.

The model describes the maximum depth influenced by impact gardening as a function of time. Much as Gault et al. (1974) did, we assume the following: 1) the cumulative flux of objects onto the surface is a power-law, and 2) the production of craters follows a Poisson distribution, and 3) the size and shape of craters follow efficiency laws based on target material properties. We update the cratering efficiency laws and implement those presented by Holsapple (1993) [13].

Another important update to the Gault model is the inclusion of secondary cratering, which has been shown to have a significant impact on the rate of gardening on the Moon [14, 17, 18]. In our treatment of both the Moon and Mercury we implement the same treatment of secondary impacts, where secondary impactors follow a size distribution based on the McEwen et al. (2005) study of Zunil crater [19, 20].

The Moon: Our calculations suggest that secondary impacts thoroughly garden regolith to depths that are consistent with the thorough reworking of the top 3 cm of regolith calculated from the homogenous distribution of Al^{26} in Apollo cores [21] and calculated from size frequency distributions of splotches in LROC temporal pairs [22]. Gardening due to secondaries is also generally consistent with the rate at which anomalous surface features such as cold spots [23] and rays [24] are reworked into background regolith. Our calculations with secondaries included are also in better agreement than those of Gault et al. (1974) with the meter and shallower reworking of surface-correlated space weathering products (Is/FeO and cosmic ray tracks) to depth vs. isotope dating compiled from Apollo cores [25, 26].

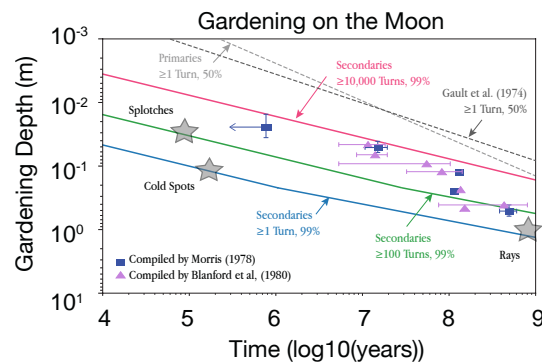


Figure 1: In comparison to the gardening rate due to primary impacts only, the secondary-driven rate is in much better agreement with the rates calculated from Apollo cores and with the residence time of surface features such as splotches, cold spots and rays.

Mercury: Marchi et al (2005) [27] present a robust model of the meteoroid flux onto the surface of Mercury, and show that the modern flux of large impactors of diameters 1 cm - 100 m is about ten times lower on Mercury than it is on the Moon. Below we present our gardening calculations with secondaries included using the Mercurial flux, gravity, and impact velocity and compare to the gardening rate on the Moon.

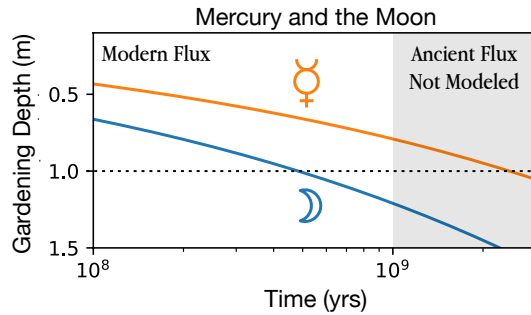


Figure 2: The gardening rate on Mercury and the Moon. Material above the contours has been gardened at least once with 99% certainty by secondary impacts.

The model describes the depth reached by impact gardening under exposure to the modern impact flux and consequent secondaries. On Mercury it would take between 2 and 3 Gyr to garden to 1 m depth. On the Moon, gardening reaches 1 m depth in about 500 Myr; gardening reworks the lunar regolith about a factor of five faster. Assuming that ice is not replenished and assuming that one gardening event obliterates all ice to the modeled depth, a 1 m thick ice deposit on Mercury would be depleted but still be present after 1 Gyr. The same 1 m ice deposit on the Moon would be erased by impacts in 500 Myr. The model suggests that if the Moon ever had a Mercury-like deposit, it may have succumbed to impact gardening.

Discussion: On Mercury, micrometeoroid bombardment is thought to be a dominant surface process [28], and Cintala (1992) [29] predict that unlike the lower flux at larger impactor sizes, the flux of micrometeoroids onto Mercury is approximately 5.5 times greater than the flux onto the Moon. In future work, we will explore the influence of micrometeorite bombardment at the micron to millimeter scale on the Moon and Mercury. Such work could help to describe the evolution of low albedo lag deposits formed by sublimation and accumulation of dark refractory material that terminate shallower than the penetration depth of radar [7] and tie into the story of thermal shielding of underlying ice.

As noted in the section on Mercury, we do not include a treatment of the flux before 1 Gyr. Such a treatment is possible using the robust crater production functions developed for the inner solar system by the unified productions function for the inner solar system by Neukum et al. (2001) [30]. By modeling gardening due to the ancient flux we may be able to better constrain the depositional age of the Mercury ice deposits and, working backwards, a potential rate of replenishment.

Secondary cratering is crucial for each of these cases and any future application of the model. Our relatively simple assumptions about secondary cratering may vary from planet to planet and even between terrains on the same planet. On Mercury, relatively high gravity and impact velocity may result in a higher number of secondary craters produced by a primary impact. The volume of material ejected by impacts is 10 to 100 times greater for ice targets than crystalline rocks [31]. Inputting a more realistic size and velocity distribution for secondary impactors that is tailored to each planetary case is an important component of ongoing work.

References: [1] Watson, K., Murray, B. C., & Brown, H. (1962). *Icarus*, 1(1-6), 317-327. [2] Vasavada, A.R., Paige, D.A., & Wood, S.E. (1999). *Icarus*, 141(2), 179-193. [3] Paige, D.A., et al. (2010). *Science*, 479-482. [4] Paige, D.A. et al. (2013). *Science*, 300-303. [5] Slade, M.A., Bryan J.B., & Duane O.M. (1992). *Science*. 635-641. [6] Harmon, J.K., et al. (1994). *Nature*. 213-215. [7] Lawrence, D. J. et al. (2013). *Science*, 292-296. [8] Nozette, S., et al. (1996). The Clementine bistatic radar experiment. [9] Colaprete, A., et al. (2010). *Science*, 463-468. [10] Zuber, M. T., et al. (2012). *Nature*, 378-381. [11] Milliken, R. E., & Li, S. (2017). *Nature Geoscience*, 10(8), 561.1 [12] Li, S., Lucey, P., & Milliken, R. (2017). *LPI Contributions*, 2041. [13] Hayne, P. O. et al. (2015). *Icarus*, 255, 58-69. [14] Gault, D. E., et al. (1974) *LPS V*, 2365-2386. [15] Holsapple, K. A. (1993) *Annu. Rev. Earth Planet. Sci.* 21:333-73. [16] Costello, E.S. et al. (2017) *LPSC XLVIII*, #1672. [17] Costello, E.S. et al. (2017) *ELS*. [18] Costello, E.S. et al. (2017) *AGU*, Poster P41D-2853. [19] McEwen, A. et al. (2005). *Icarus*, 176(2), 351-381. [20] H. Melosh, *Icarus* 59 (2) (1984) 234-260. [21] Fruchter, J S. et al. (1977). *LPS VIII* 3595-3605. [22] Speyerer, E.J. et al. (2016). *Nature*, 215-218. [23] Bandfield, J.L., et al. (2014). *Icarus*, 231, 221-231. [24] Hawke, B.R., et al. (2004). *Icarus*, 170(1), 1-16. [25] Morris, R.V. (1978). *LPS IX* 1801-1811. [26] Blanford, G. (1980). *LPS XI* 1357-1368. [27] Marchi, S., Morbidelli, A., & Cremonese, G. (2005). *Astronomy & Astrophysics*, 431(3), 1123-1127. [28] Hapke, B. (2001). *Journal of Geophysical Research: Planets*, 106(E5), 10039-10073. [29] Cintala, M. J. (1992). *Journal of Geophysical Research: Planets*, 97(E1), 947-973. [30] Neukum, G, B A Ivanov, and W K Hartmann. (2001). *Space Science Reviews* 96 (1-4). [31] Lange, M. A., & Ahrens, T. J. (1987). *Icarus*, 69(3), 506-518.

Spaceship EAC – Overview of ongoing initiative projects relating to Lunar exploration at the European Astronaut Centre A. Cowley¹, V.S. Engelschön¹, S. Cristoforetti¹, M. Fateri², M. Sperl², ¹ European Astronaut Centre EAC, European Space Agency, 51170 Köln, Germany, ² Institut für Materialphysik im Weltraum, Deutsches Zentrum für Luft- und Raumfahrt, 51170 Köln, Germany.

Introduction: The operational capabilities of the European Astronaut Centre (EAC) in terms of training and support for human spaceflight operations on the ISS are well known, and it acts as one of the major human spaceflight centres in the world. With increasing attention now being given to post-ISS human spaceflight and potential lunar exploration missions, teams at ESA-EAC are collaborating on projects that will enhance the capabilities and experience available at EAC in order to better prepare for exploration.

Spaceship EAC is a multidisciplinary innovation-driven team within the centre and beyond which aims to utilise the spaceflight experience of the centre to develop and validate operational concepts and low-TRL-level technologies in support of lunar human exploration scenarios. The initiative mission statement is to:

- *Enhance* the EAC to better prepare for human exploration of the lunar vicinity
- *Enable*, via demonstration at a low-TRL, technologies and concepts that can be valuable for future human spaceflight
- *Inspire*, via the presence of the centre, the greater public and exploration stakeholders

The individual concept/technology development and demonstration projects are coordinated with ESA centres and exploit synergies with EAC facilities as well as with the surrounding DLR campus and European research groups.

Since Spaceship EAC began, we have successfully supported research into concepts around ISRU and enhanced the centre in a number of ways. Sustainable long term manned exploration of the moons surface presumes the logical adoption of ISRU techniques. The initiative has focused on planetary fabrication approaches with ISRU, focusing on utilizing both direct microwave heating and indirect susceptor driven heating of regolith simulant in order to enable an additive manufacturing methodology using this material (following from the ESA General Studies Programme project concept proposed in 2013 [1]).

We have also been supporting the development of a large volume regolith simulant, EAC-1, for usage inside the LUNA analogue facility, and will continue to support LUNA development and utilization into the facilities future.

In this talk we will detail and provide updates on activities relating to the Spaceship EAC initiative

and activities relating to the centre's preparation for lunar exploration.



Fig. 1 – Infographic of Spaceship EAC activity areas (as of January 2018)



Fig. 2 – Image of EAC-1 simulant material in various grain sizes, the development of which has been spearheaded by Spaceship EAC.

References:

- [1] ESA GSP study on Lunar Base 3D printing: http://www.esa.int/Our_Activities/Space_Engineering_Technology/Building_a_lunar_base_with_3D_printing

Introduction:

The LUNA analogue facility is a large scale mission focused regolith testbed and attendant analogue habitat module which has been called FlexHab. The development of LUNA is a follow on from the previously completed 2016 ESA General Studies Programme (GSP) activity which recommended the establishment of such a facility at the EAC/DLR location [1]. When operational, it will provide the capability to run high-level integrated simulations, combining a habitat, lunar terrain, a Mission Control Centre (MCC) and related communication infrastructure. The planned facility will comprise of a large regolith test bed area located between the existing EAC facility and DLR EnviHab building situated in Cologne, with a half spherical fully enclosing dome structure housing the testbed. The perimeter of the structure is given with a diameter of 34m. The testbed will comprise of approximately 600t of lunar regolith simulant EAC-1. The material is shown to be a reasonably close match compositionally to published basaltic Apollo samples, and has been determined to be of sufficient practical fidelity for use in LUNA. A concept impression of the final facility can be seen in Fig. 1. The facility will provide and enable a number of features:

- ‘Mission-Focused-Analogue’, i.e. for highly integrated simulations with robots and humans in cooperative work.
- Provide a platform for human focused exploration technology demonstration and testing.
- Testing mission scenarios and simulations with a surface habitat/pressurised rover.
- Stress timelines, training and operations in an analogue environment.
- Provide an area within which to controllably demonstrate human assisted teleoperations.
- Train astronauts for lunar surface operations or in preparation for other terrestrial analogue campaigns

The FlexHab module, currently under design, will carry a number of experimental payload racks that can house potential payload demonstrators and habitat systems. The habitat will be broken into three distinct sections – a general payload and work area, an engineering compartment housing the habitat systems (electrical, data, etc), and an airlock connection module to the LUNA dome. This airlock will provide an ingress/egress capability leading directly onto the regolith simulant test bed area found in the attached LUNA.

By its design the FlexHab will support a positive pressure capability, but is not a pressure vessel in itself such as hydrospheres, etc. This slight overpressure may allow for some ECLSS systems to be investigated in a demonstration capability. Fig. 2 below shows the concept of the FlexHab module as well as a cross section showing the general work area, engineering section and airlock interface. It is important to state that the FlexHab is not designed to be space ready hardware, but rather act as a demonstration platform for testing of operational concepts, payload demonstrators and potentially EVA simulations.

The energy system for the FlexHab is also worth noting, as it comprises of a number of energy sector commercial and research partners working with EAC to create a unique solution. The energy demand of FlexHab will be met by a carbon-free stand alone power system comprised of solar panels, hydrogen electrolyzer, fuel cell system and batteries. The system, whilst constructed predominantly with terrestrial solutions, shall be representative in parts for a potential lunar energy supply scenario. This system will be established with in-kind contributions from DLR and European industry.



Fig. 1 - The LUNA facility with the habitation module, FlexHab attached. Image: O. Punch, Spaceship EAC.

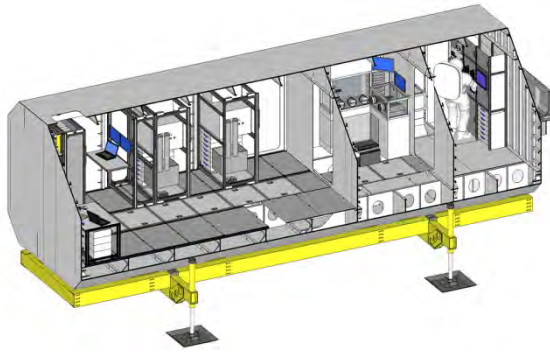


***Fig. 2** – CAD image of a cutaway of the Flex-Hab concept, showing the three main areas and payload demonstrators.*

References:

[1] T. Hoppenbrouwers. "Analogues for Preparing Robotic and Human Exploration on the Moon", SpaceOps 2016 Conference, SpaceOps Conferences, (AIAA 2016-2353)

LUNAR INDUSTRY & RESEARCH BASE. A. Degtyarev, O. Kushnar'ov, E. Baranov, G. Osinovyy, Y. Lysenko, M. Kaliapin (Yuzhnoye State Design Office, Kryvorizka 3, Dnipro, Ukraine, 49008; +38 (056) 372 00 22, info@yuzhnoye.com)

Introduction. Practical implementation of matters connected with Moon exploration by humans have started practically simultaneously with the space age beginning. Though after first successes and human landing on the Moon surface, leading space states – USSR and USA – have suspended their activities in this direction. This fact was connected with complexity and peculiarity of the tasks to be solved, high cost of their implementation, and, above all, political factor, when leadership itself was more important than economical feasibility. All these aspects postponed idea of Moon exploration for several decades.

Nowadays, leading space industry players, such as Europe, USA, Russia, China and others, are again going back to the idea of Moon exploration, including establishment of inhabited lunar base. Together with them, Yuzhnoye State Design Office (Yuzhnoye) has initiated its own activities on the development of conceptual study on lunar industrial & research base.

Objectives of Moon exploration.

Lunar industrial & research base is a testing ground for development testing of space equipment and technologies for human activities on the Moon surface, interplanetary manned flights, stepping stone for establishment of inhabited bases on the Mars and its secondary planets, asteroids exploration, etc. Establishment of lunar base will give a push to the development of humankind space activities in near and deep space, will become the first place in solar system where people will gain experience of space life-sustaining activity without support from the Earth. Pathway of humankind as an interplanetary specie will be powered through lunar exploration experience.

Concept of Yuzhnoye Lunar Industry & Research Base.

Lunar industrial & research base of Yuzhnoye design is intended to be used primarily to provide continuous presence of humans on the Moon surface. Establishment of such base will allow implementing of unique scientific researches, space technologies development testing and further on proceed with industrial resources mining and development as well as establishment of infrastructure required.

This will allow transferring to full self-dependence and provide independence from required resources' deliveries from the Earth. Implementation of this strategy will facilitate creation of the first extraterrestrial economy and further humans' expansion into space as well as will make this expansion economically feasible.

Yuzhnoye has developed step-by-step strategy of lunar industrial & research base establishment: defined its layout, identified its configuration and infrastructure for various operation phases, duration of the project implementation as well as main technical characteristics of the systems to be developed (such as space transportation system for crew and cargoes delivery to the Moon surface and return to the Earth, generic design of lunar modules, means of transportation by lunar surface).

Lunar base is one of the most global, expansive, money- and time-consuming projects that humankind faces to implement in the near future. It is reasonable to create base step-by-step and consistently, clarifying and confirming each step, each mission in order to provide extra-reliability of all components' operation.

Lunar industrial & research base is complex of modules of hermetic and nonhermetic types to be assembled into one structure after delivery to the Moon surface by separate launches.

Phase 1 Preparatory: establishment of international cooperation, exploration of Moon with unmanned vehicles, creation of the Earth-Moon-Earth space transportation system and lunar base components, preparation of take-off and landing area.

Phase 2 Establishment of base with minimal configuration: delivery of the first base modules and electric power plant; assembly of base with minimal configuration, check and testing of all systems.



Figure 1: Base with Minimal Configuration.

Phase 3 The base expansion: lunar base re-equipment, lunar surface exploration, selection and preparation of territories for expansion of industrial base and lunar observatory.



Figure 2: Base of Expansion Phase.

Phase 4 Transition to production: creation of closed-loop systems of life support, expansion of industrial base and building of lunar observatory.



Figure 3: Permanent Base.

Phase 5 Permanent base: providing of constant presence and life support of humans on the Moon, creation of space tourism complex.

Yuzhnoye State Design Office is a large scientific & industrial organization with great (more than 60-years) experience of creation of space-launch systems of various applications and space equipment, therefore number of basic elements of lunar base was designed with application of existing reliable technologies. For example, engineering study of modules' layout was performed based on mastered tank diameters and dry bays of launch vehicles of Ukrainian and European production, ultra-heavy launch vehicle is designed based on Zenit LV family, majority of liquid rocket engines used at the Earth-Moon-Earth space transportation system already exist or currently are being developed and tested, etc.

Conclusion. Implementation of the project on establishment of lunar industry & research base is a complicated and expensive scientific-technical task with high value of integrated risk due to the lack of reliable data about the Moon as well as technical risks associated with required experience lack, long-term developments and creation of separate base components.

Complexity and ambitiousness of the task to be solved encourage countries, private companies and even separate experts to create wide international

partnership that will coordinate and bring together joint efforts aimed at shared objective achievement. Establishment of multi-national agency, that will include both state companies and private enterprises, can be a possible solution.



Figure 4: Scheme of International Partnership on Lunar Base Establishment.

Global objective, set in front of the humankind will provide opportunities for the countries with low level of space technologies development take part in this ambitious challenge solution.

International partnership under such a global project with shared objective will contribute to decrease of conflicts' number, enhancement of worldwide safety and will lead to establishment of peace.

MoonLIGHT and INRRI for next lunar missions: the return of laser retroreflectors to the Moon.

S. Dell’Agnello¹, D. G. Currie², G. Delle Monache¹, E. Ciocci¹, S. Contessa¹, O. Luongo¹, M. Martini¹, C. Mondaini¹, M. Muccino¹, L. Porcelli^{1,*}, L. Salvatori¹, M. Tibuzzi¹, M. Maiello¹, R. Vittori^{3,1}, G. Bianco^{4,1}, ¹Istituto Nazionale di Fisica Nucleare - Laboratori Nazionali di Frascati (INFN-LNF), Frascati, Italy (corresponding author: luca.porcelli@lnf.infn.it), ²University of Maryland (UMD), MD, USA, ³Aeronautica Militare Italiana (AMI), Rome, Italy, ⁴Agenzia Spaziale Italiana - Centro di Geodesia Spaziale “Giuseppe Colombo” (ASI-CGS), Matera, Italy.

Introduction: Since its foundation, dating back to 2003, one of the most important objective of the INFN’s SCF_Lab (Satellite/lunar/GNSS laser ranging/altimetry and cube/microsat Characterization Facilities Laboratory) has been the development, design, manufacturing, and qualification for space flight of an ‘innovative’ LRA (laser retroreflector array) of CCRs (cube corner retroreflectors) especially intended for laser ranging operations in the Earth-Moon system; in fact, the innovation is the use of a single, large retroreflector for lunar laser ranging from MLRO (Matera Laser Ranging Observatory) for precision tests of general relativity.

The SCF_Lab Team, with support by ASI, is reaching the aforementioned goal, and is going to fly to the Moon two LRAs, namely MoonLIGHT (Moon Laser Instrumentation for General relativity High-accuracy Tests) and INRRI (INstrument for landing-Roving laser Retroreflector Investigation), after about 50 years from the last deployment of devices of the same kind on our natural satellite [1, 2].

MoonLIGHT (Figure 1) is a LRA, which makes use of a single CCR; it has got a unique and original design, aimed at compensating for the detrimental effect of lunar librations on the precision of lunar laser ranging ‘shots’ and their respective observational products, the so-called normal points [3, 4].

INRRI (Figure 2) is the microreflector array developed by INFN for ‘local’ laser ranging interrogations, from an orbiting laser down to the surface of any suitable planet, satellite, or minor body of the solar system; it has already got space heritage, and it was space qualified for the needs of interplanetary martian missions of two Agencies: ESA’s ExoMars EDM 2016 (whose unfortunate flight took place in 2016) and NASA’s InSight (whose scheduled leave to Mars is in May 2018) [5, 6].

This paper describes INFN’s unprecedented payloads, their range of possible uses, and their space qualification process for TeamIndus and Moon Express 1 missions to the Moon (Figure 3, Figure 4), which are both scheduled for 2018.

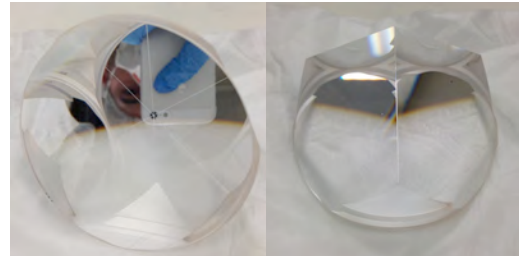


Figure 1 - Left: MoonLIGHT’s centre of reflection is indeed the vertex of the cube. Right: One of the edges of the CCR.

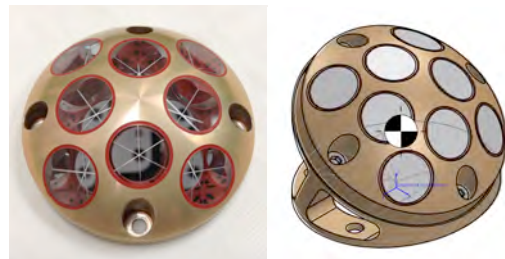


Figure 2 - Left: INRRI for TeamIndus 2018 as-built (top view, diameter of the dome = 54 mm). Right: INRRI’s assembly CAD.

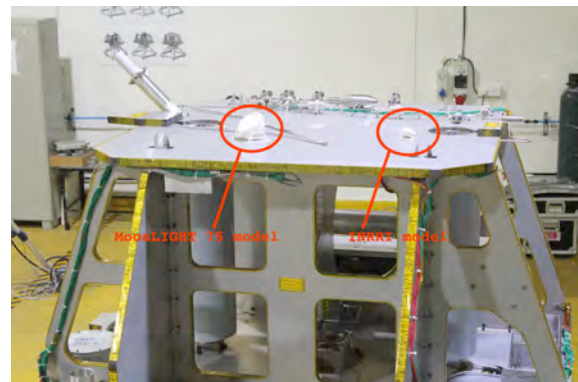


Figure 3 - Clearance assessment at TeamIndus integration site on the actual qualification model of the lander. Mounting schemes are purely indicative, and may not resemble the actual flight configurations.

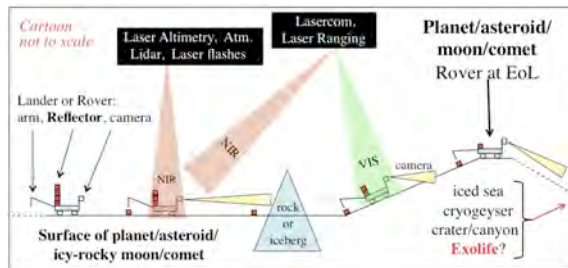


Figure 4 - Conceptual drawing, showing the deployment of microreflectors devices in the solar system (credit: INFN).

References: [1] Fournet, M., *Le reflecteur laser de Lunokhod*, Space Research XII - Akademie-Verlag, Berlin 1972. [2] Bender, P. L., Currie, D. G., Dicke, R. H., et al., The lunar laser ranging experiment, *Science* 182 (4109), 229-238, 1973. [3] Martini, M., Dell'Agnello, S., Currie, D. G., et al., MoonLIGHT: A USA-Italy lunar laser ranging retroreflector array for the 21st century, *Planetary and Space Science* 74 (2012) 276-282, doi:10.1016/j.pss.2012.09.006. [4] Ciocci, E., Martini, M., Contessa, S., et al., Performance analysis of next-generation lunar laser retroreflectors, *Advances in Space Research* 60 (2017) 1300-1306, doi:10.1016/j.asr.2017.06.005. [5] Dell'Agnello, S., Delle Monache, G., Porcelli, L., et al., INRRI-EDM/2016: the first laser retroreflector on the surface of Mars, *Advances in Space Research* 59 (2017) 645-655, doi:10.1016/j.asr.2016.10.011. [6] Dell'Agnello, S., Delle Monache, G., Ciocci, E., et al. LaRRI: Laser Retro-Reflector for InSight Mars Lander. *Space Research Today*, No. 200, Pages 25-32, December 2017.

SPACE WEATHERING AND THE STRATIGRAPHY OF THE LUNAR REGOLITH. B. W. Denevi¹, S. Klem², S. Ravi², M. S. Robinson², E. J. Speyerer², J. M. Leeburn^{1,3}, A. Duck^{1,4}, ¹Johns Hopkins University Applied Physics Laboratory, Laurel, MD 20723, USA, ²Arizona State University, Tempe, AZ 85287, USA, ³Wheaton College, Wheaton, IL 60187, USA, ⁴University of Maryland, College Park, MD 20742, USA.

Introduction: The maturity of the lunar surface is a function of its exposure to the weathering agents of the space environment, as well as the rates of regolith gardening and overturn. Regolith exposed on the surface weathers until it is buried below material delivered to the surface by impact events; weathering resumes if it is re-exposed to the surface environment by later impacts. This cycle repeats until a mature layer of some thickness develops; the stratigraphy of fresh and mature material within the upper meters of regolith provides information on the balance between space weathering and regolith gardening, and the local history of impact events and ejecta deposition.

The Apollo drill cores provide evidence of changes in maturity with depth at the Apollo 15, 16, and 17 sites (Figure 1). While the Apollo 16 core shows substantial variation, it displays a progression from mature and submature near the surface to immature at depths below ~2 m [1], consistent with a regolith that has not been reset by a recent, large impact. However, it is unclear how representative of the lunar highlands such a maturity profile is, or how much variation exists from site to site. The two mare drill cores suggest that at least within the maria, there is substantial local heterogeneity. At the Apollo 15 site, the upper ~0.35 m of the regolith is mature, and the underlying soil varies between submature and immature [2]. In contrast, the surface is submature at the Apollo 17 site, and is underlain by ~0.4 m of the most immature soil collected at any Apollo site. Below this fresh material lies >1 m of largely mature soil, and no immature soil is found even at a depth of nearly 3 m [3].

Here we seek to understand the average maturity profile of the regolith in the maria and the highlands, and to determine how typical such a profile is; i.e., the extent to which regolith stratigraphy is governed by the local impact history vs. a more homogeneous regolith gardening. From this work we seek to better understand the balance between the rates of space weathering and the rates of regolith gardening at various depths.

Methods: We employed LROC NAC images to examine the stratigraphy of fresh and mature soils at various sites across the Moon (landing sites, farside highlands, swirls). Sites ranged in size from 0.2–1 km², and all craters were identified in images with pixel scales smaller than 0.5 m, enabling a complete assessment of craters ≥2 m in diameter (>5,000 craters per site). Data collection and analysis has been completed for the Apollo 11, 16; four other sites are in progress.

The diameters of craters were measured on images with solar incidence angles of $72 \pm 5^\circ$ and emission

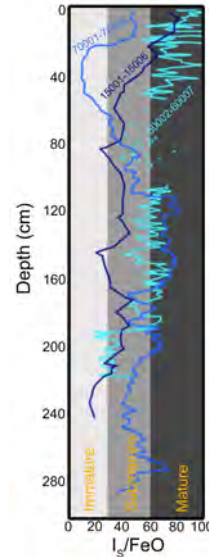


Figure 1. Profiles of I_s/FeO (a measure of soil maturity) with depth for deep drill cores from the Apollo 15, 16, and 17 landing sites. Data from Heiken et al [2], Gose and Morris [1], and Morris et al. [3].

angles $<5^\circ$. Complementary images with incidence angles $<30^\circ$ were used to determine whether the ejecta deposit of each crater was higher in reflectance than its surroundings, indicating immature material had been excavated by the impact event, or if no high-reflectance material could be identified, indicating either no immature material was excavated or the ejecta deposit experienced subsequent weathering. Craters were further classified by morphology and placed into one of three categories (1: least degraded with sharp uplifted rim, 2: minimal degradation, uplifted rim still identifiable, 3: degraded).

These data are compared to the population of craters observed to have formed during the LRO mission [4]. While the newly formed craters represent a substantially smaller population (222 impact craters ranging in diameter from 1.2–19.5 m), they have experienced no subsequent space weathering, and thus a lack of high-reflectance ejecta is unambiguously related to a failure to excavate immature material.

Apollo 11 and 16: Examining the crater populations at our two study sites, we can identify differences between the total population of impact craters and those with high-reflectance ejecta deposits related to regolith stratigraphy. The population of craters that has experienced only minimal degradation shows a clear deficit of small craters that have excavated immature regolith, manifested in the crater size–frequency distribution (CSFD) as a strong bend toward a shallower slope at small diameters for craters with high-reflectance ejecta, compared to the straight power-law slope of the CSFD of craters both with and without high-reflectance ejecta. Including more degraded craters shifts the absolute position of the

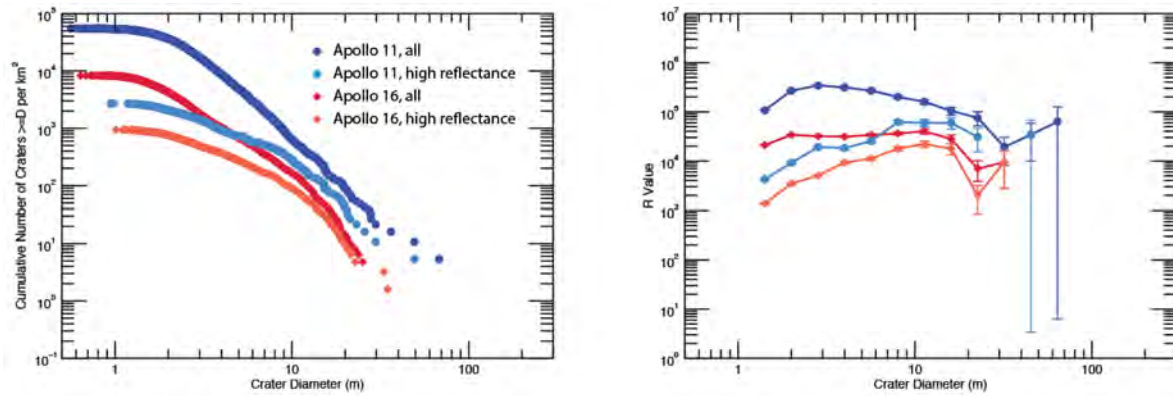


Figure 2. Left: Crater size–frequency distribution for the total and high-reflectance-only populations of craters near the Apollo 11 and Apollo 16 sites. Right: The same data, but binned and normalized to a power-law slope of -3 (R value) to highlight differences.

CSFD, but the bend in slope remains. We thus include craters of all degradation states in our initial analysis, due to concerns about the effects of target properties on crater preservation and the effects of resolution on accurate determination of the degree of degradation of the smallest craters.

From the current dataset, it is clear that there is a deficit of craters with high-reflectance ejecta at diameters smaller than ~ 8 m near the Apollo 11 landing site, and ~ 15 m near the Apollo 16 landing site (Figure 3). Assuming a depth of excavation of $\sim 1/10$ th of crater diameter, this indicates immature regolith is nearly always present at depths greater than ~ 0.8 m near the Apollo 11 site, and 1.5 m near the Apollo 16 site.

Craters that Formed During the LRO Mission:

Newly formed craters, identified via comparison of “before” and “after” LROC NAC images, were also classified by the reflectance of their proximal ejecta deposit [4]. All craters larger than 10.2 m in diameter ($n = 13$) have proximal high-reflectance ejecta, whereas below this diameter there is a mixture of craters with both high- and low-reflectance ejecta (Figure

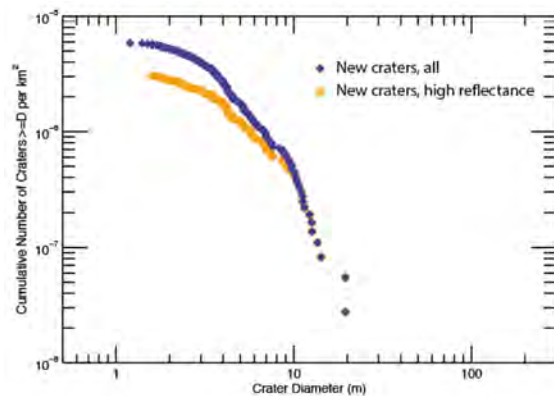


Figure 3. Crater size–frequency distribution of the population of all craters observed to have formed during the LRO mission [ref], in comparison with those that only have high-reflectance ejecta.

5). While this dataset is currently small, it yields results that are similar to those from examination of LROC images of the Apollo 11 and 16 sites – namely, immature/submature material is always present at depths greater than ~ 1 m. However, that does not indicate soils at depths >1 m are exclusively immature; craters that excavate to this depth typically have a proximal ejecta deposit that contains both high- and low-reflectance materials. If the low-reflectance regions of the proximal ejecta deposit represent excavation of mature material, as posited by Speyerer et al. [4], the observation of both mature and immature proximal ejecta suggests a large degree of lateral heterogeneity on the meter scale. The percentage of craters <5 m in diameter (excavate <0.5 m depth) that expose high-reflectance ejecta drops to 47%, in other words, half of all locations have only mature soil to depths of 50 cm.

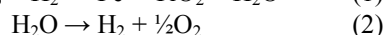
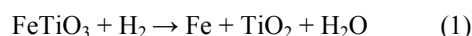
As the LRO mission progresses and more new craters are identified, we will be able to subdivide the data further, such as between mare and highland locations.

Summary: The observations here are consistent with the idea that while the uppermost regolith experiences repeated overturn (e.g., churning of the upper 2 cm of regolith in $<100,000$ years [ref]), at depths of tens of centimeters a heterogeneous stratigraphy is preserved, with both immature and mature soils being equally prevalent at depths of 50 cm. Expansion of the current dataset will allow for a more confident understanding of how representative our initial results are, and enable comparisons of estimates of the rates of regolith overturn at depths of tens of centimeters to meters with our current understanding of the rates at which materials are weathered on the surface.

References: [1] Gose W.A. and Morris R.V. (1977) *Proc. 8th Lunar Sci. Conf.*, 2909–2928. [2] Heiken G.H. et al. (1976) *Proc. Lunar Planet. Sci. Conf. 7th*, 93–111. [3] Morris R.V. et al. (1979) *Proc. 10th Lunar Planet. Sci. Conf.*, 1141–1157. [4] Speyerer E.J. et al. (2016) *Nature*, 538, 215–218.

Lunar Oxygen: One of the major challenges of future Moon missions is the supply of the spacecraft and crews with vital resources, like water, oxygen, and rocket fuel. The in-situ production of some resources on the Moon could significantly reduce the amount of mass needed to be launched from Earth.

The most needed, and at the same time most abundant resource on the Moon is oxygen. The main problem is that oxygen release requires high temperatures due to the strong chemical bonds in the minerals. The process with the most benign operating conditions is hydrogen reduction of the titanium-iron oxide mineral ilmenite (Eq. (1)) and subsequent water electrolysis (Eq. (2)) [1]:



Concentrated Solar Power: Despite of the lower efficiency, spaceflight to date has exclusively used PV for solar energy generation. One important reason is that thermodynamic cycles need huge additional cooling panels because radiation is the only way to get rid of the surplus heat. But if concentrated solar power were applied for reaction (1), the excess heat could be used for preheating of the reagents, be disposed of with the tailings, or even be stored and used as heat source in the lunar night.

Fluidized Bed: A chemical reactor for the lunar ilmenite-hydrogen reaction must meet several requirements, like continuous operation, the ability to heat and process large amounts of lunar regolith, a long solids residence time, and a good mixture with the gas reagent. All these conditions can be satisfied with a low expansion fluidized bed reactor. Fluidization is the operation by which solid particles are transformed into a fluid like state through suspension in a gas (or liquid) [2].

Solar Reactor: The Plataforma Solar de Almería (PSA), a dependency of Ciemat, is a public research centre for concentrated solar power in the south-east of Spain. In recent years, there has been developed and assembled a solar reactor for the hydrogen reduction of ilmenite (reaction (1), see fig. 1). *The goal was to build a full scale reactor for testing on Earth, demonstrating solutions for as many as possible challenges it will face on the Moon.*

The centre-piece of the reactor is a fluidized bed with a capacity of 25kg of lunar regolith. Feeding and removal of the solids is done in continuous mode by auxiliary fluidized pipes, completely avoiding moving parts in contact with the particles. The concentrated solar power enters the reactor vertically through a quartz window on the top, allowing direct heating of the particles without the need of a heat exchanger wall. The gas supply includes a recirculation pump, flow controllers, and the electrolyzer for reaction (2). Special attention has been given to the off-gas treatment. This includes cooling, hot gas cleaning from remaining fines, and separation of the desired product water from the gas stream by an active device doing sub-cooling with a Peltier element.

Despite of the complexity of the system, it can be operated by only one person due to the high level of automation of the different control features.

System Testing 2017: The option of testing with a supply of 100% hydrogen was postponed already in an early stage of the project due to safety concerns. Instead, the operation was done with argon for fluidization, and only a small amount of hydrogen (<10%) for the chemical reaction.

In the five tests of “Phase 1”, the system was operated with atmospheric air, without chemical reaction, and the temperature in the bed limited to 400°C. The goals were to learn to know in depth the behavior of the fluidized bed with the particles, to check



Fig. 1: PSA Solar Furnace with solar reactor.

the proper functioning of most of the peripheral components, to hone the data acquisition and control program, to confirm the initial predictions of the gas demand of the bed in function of the temperature, and finally to establish efficient procedures for the operation with (costly) argon.

The six tests of “Phase 2” with pure argon were to determine the operation parameters (temperatures, gas flows and pressures, solar power), and to demonstrate the ability of the system to reach the minimum nominal operation temperature of 800°C. Additional tests helped to understand the system behavior with continuous particles in- and outflow.

Finally, in “Phase 3”, hydrogen was added and the temperature further increased (up to 977°C). Fifteen tests were performed, eleven of them with hydrogen, two for particle flow / solar power tests, and two for TV interviews. The basic goal here was to demonstrate that the reaction really occurs. Further objectives were to gain initial information about the water quality, and, as a bonus, to calculate the hydrogen conversion rate. Special attention was given to guarantee that the extracted water really came from the chemical reaction, and not from other sources, e.g. hydrated minerals in the solids.

Results: All three primary goals of the campaign were successfully achieved:

1. Identify the gas flow demand of the main fluidized bed in the reactor as a function of the temperature.
2. Operate the reactor at 800-1000°C solely heated with concentrated solar power.
3. Demonstrate water production from the reaction of the ilmenite with hydrogen.

Further (secondary) goals like the demonstration and control of the continuous particle feed / removal from the reactor, or the off-gas treatment were also accomplished.

The *gas demand* at minimum fluidization can be approximated by a $\dot{V}_N \sim 1/T^{1.7}$ curve (\dot{V}_N gas volume flow at norm conditions, i.e. a mass flow). Several measurements verified the prediction. To get a meaningful turbulence and mixture in the bed, additional gas must be supplied (factor u/u_{mf}). It turned out that u/u_{mf} had to be increased continuously during operation with increasing bed temperature. This led to a new correlation, with the flow following a $\dot{V}_N \sim 1/T$ curve.

The *power balance* included the temperature change of the particles actually present in the bed, the heating of the particles entering the bed, the heating of all gas flows entering the reactor, and infrared radiation losses. Conduction through the reactor walls and the window, temperature change of the fluidized bed container walls and adjacent insulation, and the chemical reaction were neglected. Main conclusions are that insulation below the aperture cone is

needed to reduce the infrared losses (fig. 2), and that on the Moon, a concentrator [3] with a diameter of 4 to 5 meters seems reasonable.



Fig. 2: Fluidized bed (“solar lava lake”) at 900°C.

The *water production* was successfully demonstrated, but still at very limited amounts due to the low hydrogen flow rate. The water (fig. 3) contained iron in solid and dissolved form, and ions of ammonia, sulfides, and chlorides.



Fig. 3: Product water.

Outlook: After completion of the tests of 2017, some improvements were implemented in the system. They include the recalibration of the hydrogen flow controller to allow for 8x higher reaction rates, and the integration of a pre-stage for the water separation. It was observed that the already condensed water with its high heat capacity limited the ability of the Peltier-element to cool down the gas stream. At the writing of this abstract (December 2017) the planning was to perform another test campaign in spring 2018. Main goals are to achieve the design water production rate of 700g/h, and to identify the sources of the contamination of the product water.

References: [1] L. A. Taylor, W. D. Carrier (1993) *Oxygen Production on the Moon: An Overview and Evaluation*. The University of Arizona Press. [2] Kunii, D.; Levenspiel, O. (1991) *Fluidization Engineering*. Butterworth Heinemann, Boston. [3] A. González Pardo, T. Denk (2015) *A Novel Off-Axis Solar Concentrator Providing a Vertical Beam*. SolarPACES 2015, Paper-ID 36366

Introduction: Until today, photovoltaics (PV) is the only applied solar power conversion technology in space. The reasons are its simplicity and robustness, and that the power consumption requirements are often complex, what can be satisfied best with electricity. But for future ISRU activities involving the processing of large quantities of raw material from the Moon (or asteroids, Mars...), mainly heat at high temperature is needed. This raises the question if the direct application of the heat from solar radiation can lead to more efficient systems.

CSP on Earth: Concentrated solar power (CSP) Systems on Earth is a technology that is investigated since several decades. 5 GW electrical power are already installed all over the world (half of this in Spain), and another 5 GW are under construction or development [1]. Much of this technology was investigated at Europe's largest test center for concentrated solar power, the Plataforma Solar de Almería.

The *parabolic troughs* are the most common commercial technology. They are line focusing systems and reach only moderate concentrations (approx. 80-100x). Their operation temperature is limited to around 380°C, and hence they are not suitable for ISRU processes on the Moon.

Solar Towers (fig. 1) are starting to overtake the parabolic troughs because of their superior efficiency and storage capability. They are point concentration systems and reach rather high concentrations (500-2000x). They consist of a large concentrator field, composed by hundreds or even thousands of mirrors ("heliostats"), each one with a surface of 120 m². The most commonly used heat transfer fluid is molten salt, a mix of sodium and potassium nitrates (60% NaNO₃ + 40% KNO₃), operated between 265°C and 565°C. This material is cheap and can be used in large amounts for thermal heat storage. This is why solar thermal power plants can deliver electricity around the clock, with-

out the need of expensive backup systems or batteries, like it's the case for PV or wind.

Besides electricity production, CSP can also be used for *thermochemistry*. The most interesting concentrator technology for these applications at small scale (5-100kW, like it can be expected for the Moon) is the solar furnace (fig. 2). It consists of a flat heliostat for the tracking of the sun, an attenuator (shutter) for the control of the solar power, a fixed, parabolic mirror for the concentration, and a platform for the receiver. In case a vertical beam is needed, a water cooled mirror can be installed close to the focal spot. One advantage of a solar furnace over other systems is that the quality, shape, and power of the focal spot does not vary over the course of a day.

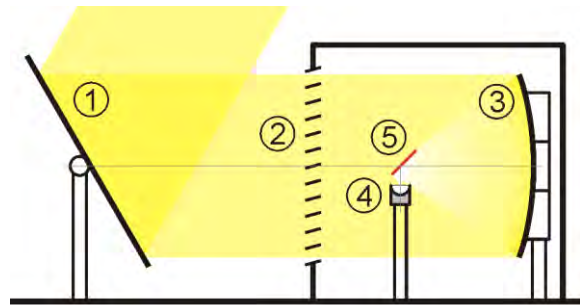


Fig. 2. Solar Furnace (optical principle). (1) Flat heliostat (2) shutter (3) fixed concentrator (4) receiver / reactor (5) diagonal mirror (cooled).

PV vs. CSP: Photovoltaics nowadays is the preferred electricity generation method in space, due to its simplicity and predictable availability without refueling need. Furthermore, it doesn't generate waste heat. The downside is the low efficiency and hence the need of large surfaces for a given power demand. This surface has to be increased further if no tracking mechanism is included.

CSP on the other hand side, when used for electricity generation, needs a cold sink to dispose of the



Fig. 1. Commercial solar tower plant.

surplus heat from the thermodynamic cycle. But when used for generation of process heat, the heat remains in the solids and no (or very little) cooling is required. There even exists the option to store the spent regolith in an insulated container and keep it as a convenient heat source for the lunar night.

CSP on the Moon: While the basic principles of concentrated solar power remain mostly the same on the Moon compared to Earth, some things differ. First is the solar radiation. On Earth, it is reflected, absorbed, and scattered by the atmosphere, leaving on the ground hardly more than 800-1000 W/m², even on very clear days. And when it's cloudy, this value can even drop down to zero. In contrast, on the Moon, the full extraterrestrial solar flux of 1367 W/m² is available from sunrise to sunset. This means that the linear size of the concentrator system can be $\frac{3}{4}$ compared to a system with the same peak performance on Earth. Next is the very slow rotation of the Moon. One day lasts 354 hours or half a month, followed by the night with the same length. This long day is an advantage for solar thermal material processing. A start-up (heating) time of several hours has only a marginal influence on the overall yield. A further difference is the absence of seasons, the Moon's axis tilt is only 1.5° against the pole of the ecliptic (Earth: 23.4°). This opens the possibility to simplify the tracking mechanism to only one axis (the right ascension), while the other axes (declination, north azimuth, elevation...) need to be adjustable only for small amounts. A further plus factor is the absence of weather (wind, rain...) and the low gravity. This allows for the construction of very lightweight structures, possibly even thin foils covered with a reflective surface. A single 1000m² optical surface to collect more than 1 MW of solar radiation should be feasible.

On the downside is the huge temperature swing on the Moon. The daytime temperature of the structures probably can be minimized simply by applying a reflective (or white) cover on the sun facing side. During night, the system possibly has to be stowed (folded) in a container, a feature that's needed in any case for the transportation of the concentrator system in the payload fairing of the rocket.

Off-axis Solar Furnace: For efficient application of CSP on the Moon, a new optical design derived from the solar furnace concept was proposed [2]. It consists of a flat heliostat (sun-tracker) and a fixed off-axis paraboloid concentrator. Both components can be manufactured in a very light weight manner using thin foils coated with a reflective surface. The heliostat can be unfolded like an umbrella, while the concentrator (dubbed “mussel” due to its appearance) can be supported by a foam structure, or maybe even by an inflatable concept [3]. The ad-

vantages of the “mussel”-concentrator are that it provides a vertical beam with only two reflections, no cooled mirror is necessary, and, maybe most important, the reactor can be installed on the ground (no platform or tower is needed). Fig. 3 gives an impression of the concept. Note the size of the reactor in comparison to the mirrors.

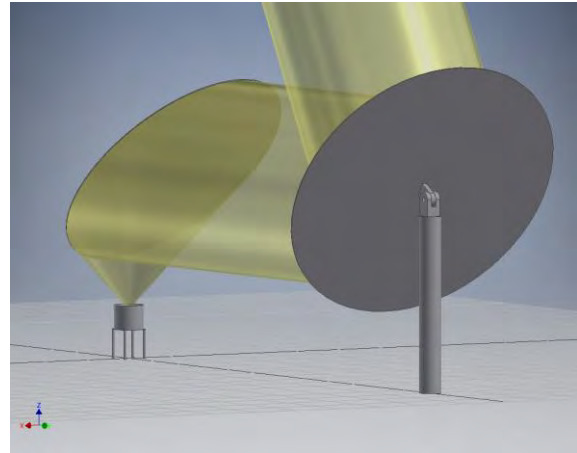


Fig. 3. Proposed off-axis concentrator concept.

Applications: The concentrator was designed with the primary goal to supply solar heat for a lunar regolith processing reactor, equipped on the top side with a quartz window. This allows the radiation to enter into the reactor, but the gaseous reactants and products remain confined.

Another potentially very attractive application could be to install the two mirrors on a rover (or two separate vehicles), with a hexapod-like, adjustable mount. Then the system could be used to literally “scan” and sinter the ground, a simple but powerful way to build dust-free streets on the Moon with concentrated solar energy!

And if such a concentrator system were installed near the poles of the Moon, it is even possible to omit the heliostat. Due to the very low elevation of the sun over the horizon at these places, tracking is possible by rotating the concentrator around the vertical axis with only slight adjustments of the pitch.

Conclusion: Concentrated solar power is a little known, but potentially interesting option for power supply in space, especially on the surface of the Moon. It can be an attractive solution for all kind of applications that need high power to generate high temperatures.

References: [1] <http://www.solarpaces.org/csp-technologies/csp-projects-around-the-world/>
[2] A. González Pardo, T. Denk (2015) *A Novel Off-Axis Solar Concentrator Providing a Vertical Beam*. SolarPACES 2015, Paper-ID 36366
[3] <https://heliovis.com/technology/>

UPDATE ON THE CHARACTERIZATION OF LUNAR HIGHLANDS REGOLITH SIMULANTS IN PREPARATION FOR DRILLING AND SAMPLING INTO THE POLAR REGOLITH BY ESA's PROSPECT PACKAGE. K. L. Donaldson Hanna¹, D. J. P. Martin², K. H. Joy², J. J. Gillis-Davis³, J. D. Carpenter⁴, E. Sefton-Nash⁴, and N. E. Bowles¹, ¹Atmospheric, Oceanic and Planetary Physics, University of Oxford, Oxford, UK (Kerri.DonaldsonHanna@physics.ox.ac.uk), ²School of Earth and Environmental Sciences, University of Manchester, Manchester, UK, ³Hawaii Institute of Geophysics and Planetology, University of Hawaii, Honolulu, HI, USA, and ⁴ESA ESTEC, Keplerlaan 1, Noordwijk, The Netherlands.

Introduction: The Package for Resource Observation and in-Situ Prospecting for Exploration, Commercial exploitation and Transportation (PROSPECT) is in development by ESA for application at the lunar surface as part of international lunar exploration missions in the coming decade, including the Russian Luna-27 mission planned for 2021. PROSPECT will search for and characterize volatiles in the lunar polar regions to answer science questions and investigate the viability of these volatiles as resources [1].

Characterizations of lunar regolith simulants are needed in order to assess their utility for mechanical property testing and ability to emulate the efficacy of scientist measurements like those that will be made by ESA PROSPECT experiment [2]. Here we present the characterization of two lunar highlands regolith simulants: NU-LHT-2M produced by the United States Geological Survey (USGS) and NU-LHT-2M produced by Zybek Advanced Products. We use a range of complementary analytical and laboratory techniques at the University of Manchester and the University of Oxford to assess the similarities and differences between the two simulants including their particle size distributions, physical properties, and mineralogical make-up.

Regolith Simulants: The USGS and Zybek NU-LHT-2M simulants investigated in this updated analyses were provided by J. Gillis-Davis (JGD) for the purpose of laboratory characterization and comparison with previous characterization of NU-LHT-2M simulants provided by Leonardo-Finmeccanica (LF; see details of [3]).

NU-LHT-2M is a lunar highlands simulant that was originally developed by the USGS to simulate the lunar highlands feldspathic regolith and has the chemical composition of the average of all Apollo 16 soils [4]. The bulk of the simulant material originated from the Stillwater Complex in Montana and included crystalline (65%) and glass (agglutinate 30% and 'good' glass 5%) components in proportions similar to the typical Apollo surface regolith value [4]. The particle size distribution of NU-LHT-2M was based on the average of 19 Apollo 16 surface soil samples and consists of particles from dust size to 1 mm [4]. As the USGS and Zybek simulants are derived from rocks of the same deposit and subject to the same milling and plasma-melting processes used to achieve the required grain size and glass compo-

nent, they would be expected to have similar physical and spectral properties.

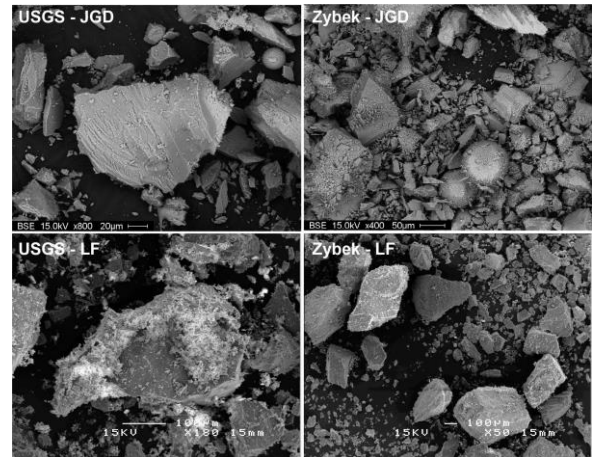


Figure 1. High magnification BSE images of the pressed grain mounts of **(Top Left)** USGS NU-LHT-2M sourced from J. Gillis-Davis (JGD), **(Bottom Left)** USGS NU-LHT-2M sourced from Leonardo-Finmeccanica (LF), **(Top Right)** Zybek NU-LHT-2M sourced from JGD and **(Bottom Right)** Zybek NU-LHT-2M sourced from LF. Note the BSE images were collected at different times so the field of view and magnification are not the same for the JGD and LF samples.

Analytical and Laboratory Techniques:

University of Manchester. The grain shapes, sizes and interactions at the sub-millimeter scale as well as their composition were analyzed using a FEI XL30 Environmental Scanning Electron Microscope (SEM) using secondary electron images (SEI), back scatter electron (BSE) images and Energy Dispersive Spectroscopy (EDS). In order to perform the SEM and EDS analyses, the regolith simulants were mounted onto SEM sample stubs via an adhesive carbon sticky pad and then carbon coated. Pressed and sprinkled grain mounts were made for each sample in a similar manner to [3].

University of Oxford. The bulk composition, dominant particle size, and thermal properties were analyzed using thermal infrared (TIR) spectroscopy. TIR emissivity measurements were made under Earth-like (ambient) and simulated lunar environment (SLE) conditions in the newest vacuum chamber at Oxford, MoonBox2. The experimental setup and calibration is similar to that of the Simulated Lunar Environment Chamber (SLEC), which has

been described previously by Thomas et al. [5]. TIR spectra were collected using a Bruker VERTEX 70v FTIR spectrometer at a resolution of 4 cm^{-1} from ~ 2400 to 200 cm^{-1} (~ 4 to $50\text{ }\mu\text{m}$).

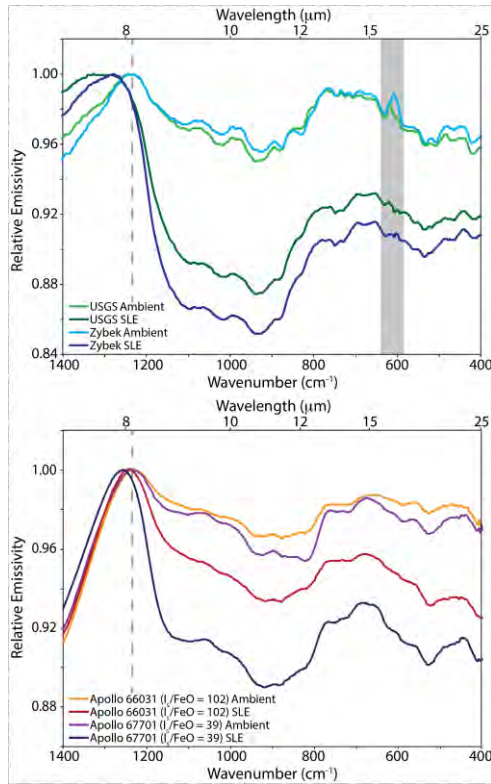


Figure 2. (Top) Ambient and SLE spectra of the two NU-LHT-2M simulants. The grey vertical box highlights a region with low SNR due to the FTIR beamsplitter. **(Bottom)** Ambient and SLE spectra of two Apollo 16 bulk lunar soils with varying maturity. The dashed line highlights the position of the CF under ambient conditions.

Results: The Zybek simulant has a greater proportion of fine material compared to the USGS simulant (Fig. 1). In addition, the USGS includes a higher abundance of small spherules that vary mineralogically in proportions of plagioclase and glass. A similar texture (angularity of clasts, small particle content and particle size) is observed when comparing the Zybek simulant analysed here with the LF provided Zybek simulant (Fig. 1 [3]). However, the USGS simulant investigated here does not contain the fibrous, fine particle size fraction observed in the Leonardo-Finmeccanica (Fig. 1. [3]) provided USGS simulant.

As seen in Fig. 2, both JGD provided simulants are of similar bulk composition to Apollo 16 soils as their Christiansen Features (CF), an emissivity maximum indicative of composition [6], are at similar frequencies as are other diagnostic features in the ambient emissivity spectra. Under SLE conditions, the emissivity spectra of the simulants show a larger shift to higher frequencies of the CF and a larger increase in the spectral contrast between the CF and the fundamental vibration bands than the Apollo 16

soils. These results suggest the thermal properties of the simulants differ from the actual Apollo 16 soils as a larger spectral contrast between the CF and the fundamental vibration bands is observed (i.e. it behaves more similar to pure minerals [7]). These results are similar to the observed spectral behavior of the LF provided simulants [3].

In addition, TIR spectra of the JGD provided USGS and Zybek simulants corroborate the SEM analysis (Fig. 1) that both are dominated by the fine particle size fraction as demonstrated by: (1) the appearance of a transparency feature near 800 cm^{-1} and (2) the increase in depth of the feature at higher frequencies than the CF. The spectra also show that the Zybek and USGS simulants are of a similar particle size fraction, and both NU-LHT-2M simulants are of coarser particle size fractions than Apollo 16 soil 66031 and 67701.

Conclusions and Future Work: We have demonstrated in this analysis that when conducting mechanical property or scientific studies of lunar simulants, a user cannot assume these properties are comparable to lunar soils even when the two are compositionally similar. Comparisons of the BSE images of the LF and JGD provided USGS simulants suggest that the LF provided simulant has been altered in some manner. Further investigation is needed to constrain these alteration processes. Further analysis is needed to better understand the repeatability of this analysis and previous analyses [3] including repeat SEM and spectral measurements of the simulants. In addition, further analysis of the finest particles is needed (e.g., constraining the particle size distributions of each simulant and EDS analyses of each simulant's finest fraction) to better understand the properties of this optically dominant fraction.

Acknowledgement: This work was supported by ESA in the context of the PROSPECT lunar volatiles package. In addition we would like to thank the UK Space Agency, UK Science and Technology Facilities Council, and the Royal Society for funding this work.

References: [1] Barber S. J. et al. (2017) 48th LPSC Abstract #2171. [2] Taylor L. A. et al. (2016) *Planet. & Space Sci.*, 126, 1-7. [3] Donaldson Hanna K. L. et al. (2017) 48th LPSC Abstract #1717. [4] Stoesser D. B. et al. (2011) NASA/TM-2010-216438, M-1287. [5] Thomas I. R. et al. (2012) *Rev. Sci. Instrum.*, 83(12), 124502. [6] Conel J. E. (1969) *JGR*, 74, 1614-1634. [7] Donaldson Hanna K. L. et al. (2017) *Icarus*, 283, 326-342.

SEISMIC VELOCITY AND CRUSTAL THICKNESS INVERSIONS: MOON AND MARS. M. Drilleau¹, J.-F. Blanchette-Guertin¹, T. Kawamura^{1,2}, P. Lognonné¹ and M. Wieczorek³, ¹Institut de Physique du Globe de Paris, Paris, France, ²National Astronomical Observatory of Japan, Iwate, Japan, ³Laboratoire Lagrange, Observatoire de la Côte d’Azur, Nice, France.

Introduction: We present results from new inversions of seismic data arrival times acquired by the Apollo active and passive experiments. Markov chain Monte Carlo inversions are used to constrain (i) 1-D lunar crustal and upper mantle velocity models and (ii) 3-D lateral crustal thickness models under the Apollo stations and the artificial and natural impact sites. A full 3-D model of the lunar crustal thickness is then obtained using the GRAIL gravimetric data, anchored by the crustal thicknesses under each Apollo station and impact site.

Method: To avoid the use of any seismic reference model, a Bayesian inversion technique is implemented [1], [2]. The advantage of such an approach is to obtain robust probability density functions of interior structure parameters governed by uncertainties on the seismic data arrival times. 1-D seismic velocities are parameterized using C1-Bézier curves, which allow the exploration of both smoothly varying models and first-order discontinuities. The parameters of the inversion include the seismic velocities of P and S waves as a function of depth, the thickness of the crust under each Apollo station and impact epicentre. The forward problem consists in a ray tracing method enabling both the relocation of the natural impact epicenters, and the computation of time corrections associated to the surface topography and the crustal thickness variations under the stations and impact sites.

Results: The results show geology-related differences between the different sites, which are due to contrasts in megaregolith thickness and to shallow subsurface composition and structure. Some of the finer structural elements might be difficult to constrain and might fall within the uncertainties of the dataset. However, we use the more precise LROC-located epicentral locations for the lunar modules and Saturn-IV upper stage artificial impacts, reducing some of the uncertainties observed in past studies.

Mars: In the framework of the NASA InSight/SEIS mission to Mars, the method developed in this study will be used to constrain the Martian crustal thickness as soon as the first data will be available (late 2018). For InSight, impacts will be located by MRO data differential analysis, which provide a known location enabling the direct inversion of all differential travel times with respect to P arrival time. We have performed resolution tests with different scenarios to investigate to what extent impact events might help us to constrain the Martian velocity structure and crustal thickness [3]. Due to

the high flexibility of the Bayesian algorithm, once the InSight lander is operational on Mars, the strategy will be to iteratively improve the interior model as more data becomes available [3], [4].

References: [1] M. Drilleau et al. (2013) *GJI*, 195, 1165-1183. [2] M. Panning et al. (2015), *Icarus*, 248, 230-242. [3] I. Daubar et al., submitted to *Space Sci. Rev.* [4] M. Panning et al. (2017), *Space Sci. Rev.*, 211, 611-650.

REMOTE CONTROLLED TELESCOPES FROM A MOON HABITAT: EUROMOONMARS PROJECT

L.C. Dubois^{1,2,4}, B.H. Foing^{1,2,3}, A. Lillo^{1,2,4}, G. A. van der Sanden^{1,2,3}, E. Clavé^{1,2,4}, P. Evellin^{1,2,5}, C. Jonglez^{1,2,4},
¹ESA/ESTEC & ²ILEWG (PB 299, 2200 AG Noordwijk, NL, louis.dubois@student.isae-superaero.fr, ³VU
Amsterdam, ⁴ISAE-SUPAERO Toulouse, ⁵ISU Strasbourg

Introduction: The International Lunar Exploration Working Group (ILEWG) and ESA/ESTEC developed together the ExoGeoLab lander [1-5]. This structure can be equipped with modular payloads, including instruments such a telescope and UV-VIS, NIR and Raman spectrometers (Fig 1). Those payloads can be remotely operated using a laptop connected with a Wi-Fi network to the Lander, and from anywhere else in the world through an internet connection. The remote control of the Lander's telescope highlights some benefits that could be offered by a larger exploitation of this technology for Moon or Mars facilities.



Figure 1 ExoGeoLab Lander on the Moon. Credits : M. Monnerie, V. Guinet, B. Jehannin, C. Jonglez.

Goals: A set of various computerized telescopes in a Moon/Mars Exo-habitat could be used to monitor the Earth and planetary bodies (Fig 2,3), the Sun's activity (Fig 2), for astrophysics, but also to monitor distant Extra-Vehicular Activities (EVAs). Therefore, the current main goals for this project are science (astrophysics, Sun surveillance, geological exploration, etc.), technology (remote control), and ergonomics (joint operation with astronauts).



Figure 2 Telescope views of the first quarter Moon, taken from ESTEC, 01/22/2018. 1.Mare Crisium, 2.Mare Feconditatis, 3.Mare Tranquilitatis, 4.Theophilus.

Known advantages: The implementation of telescopes on the Lunar surface has obvious advantages for astrophysical studies due to the absence of an atmosphere, the low-seismic activity and the slow and predictable orbital rotation [6]. The very long daylight time, especially in some “eternal light” areas, allows long exposure time for astrophysics and long Sun surveillance time. Thus, solar flares, dangerous for lunar astronauts, would be closely monitored. The very tenuous atmosphere of Mars tends also to offset its seismic activity in the frame of astrophotography, in comparison with ground-based observatories on Earth.

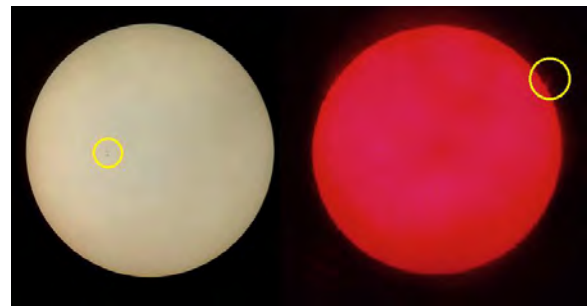


Figure 3 Sun, white light (left) and H-alpha (right), taken from ESTEC, 01/16/2018. Visible sunspots and solar prominences.

Preliminary results: The remote controlled focus and orientation of the telescope through direct Wi-Fi connection with the Lander has already been tested [5]. The telescope can also be used manually in the current analogue missions, for Sun/Moon monitoring and observations, what is perfect to simulate future use for Earth observation from Lunar facilities. Since 2017, the Lander is able, by night, to track the Moon using computer vision (Fig 4) [2-4]. These improvements could lead to an ability to target some distant points of interest unregistered on maps, like EVAs or interesting areas for geological samples. We shall present the latest results of remote control, automated tracking and orientation of the telescopes at ELS 2018.

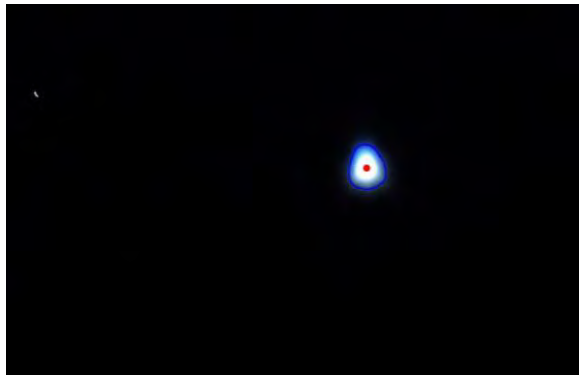


Figure 4 Contour and centre detection on a picture of the Moon taken with the webcam on the telescope's tube.

EuroMoonMars and LunAres analogue campaigns: The ExoGeoLab Lander has been deployed twice on analogue simulations in 2017, in the frame of the EuroMoonMars Workshop (July 2017, ESTEC), and in the Moon/Mars analogue environment of the LunAres base (August 2017, Piła, Poland). The telescope, as other payloads, connected to the Lander's platform, was remotely operated from the exo-habitat (ExoHab). It was operated by the analogue astronauts and remotely from ESTEC, where data were processed. We are already preparing the LunAres 2018 campaigns, procedures to be followed by crew members and tests in realistic environment (Fig 5).



Figure 5 Testing and improving the telescopes' work station in the analogue Exo-Habitat before external deployment at ESTEC.

Suggested Improvements: The next step is to enhance the former technical advancements for the control of the telescopes and the computer vision. Two major improvements are currently implemented:

1. The ability to automatically orientate and target astronomical point of interest using Moon tracking and reference sky-maps. Thus, astrophotography would be a lot easier to conduct from the –analogue or not- Exo-habitat.
2. The ability to automatically orientate and target non-astronomical marks. Such a capacity would allow, as written earlier, to monitor distant EVAs from the habitat, but also to target some interesting areas in order to send manned or unmanned exploring systems, like rovers, or drones in the case of an a Mars environment.

Acknowledgements: We thank ILEWG EuroMoonMars program.

References:

- [1] Foing B. et al, (2010), *LPI 41*, #1701.
- [2] Lillo A. et al, (2017), *ESTEC internship final report*.
- [3] Lillo A. et al, (2018), *LPSC, Improvements and telecontrol of the ExoGeoLab Lander in analogue environments*.
- [4] Evellin P. et al, (2017), *ESTEC internship final report*.
- [5] Jonglez C. et al, (2016), *ESTEC internship final report*.
- [6] Gorenstein P, (1994), *X-ray astronomy from the Moon, Astronomy and Space Science from the Moon*, Vol. 14, No. 6, 61-68.
- [7] Lillo A et al, (2017), *LPI/LEAG, Remote Operation of the ExoGeoLab Lander, 2017LPICo2041.5079L*

EAC-1A: Evaluation of a basanitic material as a novel large-volume lunar regolith simulant. V. S. Engelschön¹, S. R. Eriksson¹, A. Cowley¹, M. Fateri², A. Meurisse², Ü. Kueppers³ and M. Sperl², ¹European Astronaut Centre EAC, European Space Agency, 51170 Köln, Germany, ² Institute for Materials Physics in Space, German Aerospace Center (DLR), 51147 Köln, Germany, ³Department of Earth and Environmental Sciences, Ludwig-Maximilians-Universität (LMU) Munich, 80333 München, Germany.

Introduction:

The European Astronaut Centre is currently constructing the European Lunar Exploration Laboratory (LUNA); a large training and operations facility to be located at the DLR campus in Cologne, Germany. With an estimated lunar testbed area of approx. 660 m², a large volume of lunar regolith simulant material is needed. In this study, a basanitic sandy silt from a commercial quarry located in the Siebengebirge Volcanic Field is evaluated as a large-volume source of material.

The focus of this project has been to characterise the material to be used in the LUNA dust chamber; EAC-1A.

Characterisation:

EAC-1A is a light grey, sandy silt of <1 mm grain size. The material is delivered in three different grain size ranges which are subsequently mixed at EAC; (1) 0.02 mm – 0.2 mm, (2) 0.2 mm – 0.5 mm, (3) 0.5 mm – 1.0 mm. Physical and chemical characterisation tests have been undertaken of both granular material and hand samples from the quarry. The results of the EAC-1A tests are compared to existing lunar regolith simulants, focusing on those already available for characterisation tests at EAC and the DLR campus in Cologne. These include: JSC-1A, by Orbitec on behalf of NASA (replicating JSC-1, developed at the Johnson Space Center), JSC-2A and NU-LHT 3M, both by Zybec Advanced Products Inc., DNA, created by Monolite for ESA GSP study [1], and FJS-1, produced by researchers at JAXA (then: NASDA) [2]. Other lunar regolith simulants have also been included where published data were available, and comparisons have been made to Apollo samples for the chemical tests.

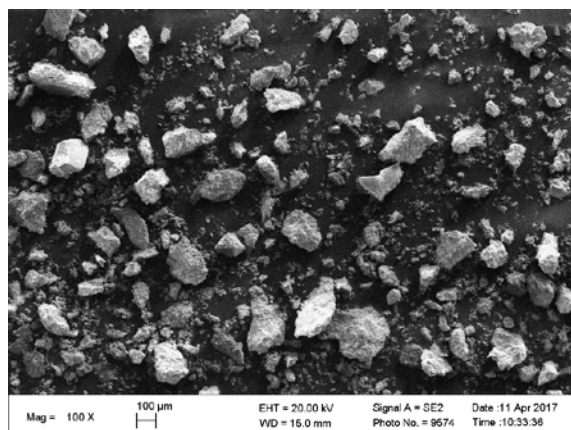


Figure 1: SEM image of unconsolidated EAC-1A.

Physical properties

EAC-1A is a poorly sorted material, with approx. 15 % of the material of a >20 µm grain size and 30% >62 µm. It is mechanically crushed and sieved by the quarry, leading to relatively angular grains (Fig. 1). The average sphericity of the EAC-1A grains was determined by using an optical microscope and calculated according to the method presented by Krumbein (1941). Only the two larger grain size fractions were selected for analysis: 0.2 mm – 0.5 mm and 0.5 mm – 1.0 mm, as the size range 0.02 mm – 0.2 mm was too small to conduct visual analysis. No large variations were found within the size fractions, with sphericity values (Ψ) of 0.601 and 0.591, respectively.

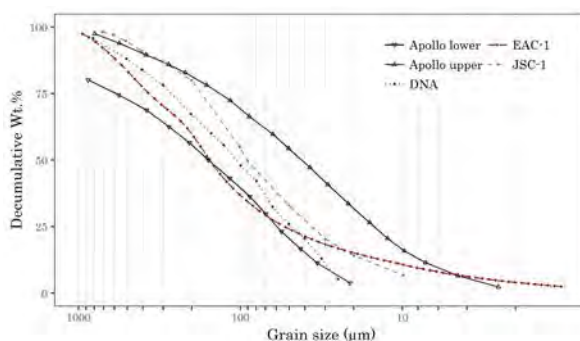


Figure 2: Grain size distribution of the EAC-1A mix.

The grain size distribution (Fig. 2) was measured using a Beckman Coulter laser diffraction particle size analyser. Various density measurements were also conducted on both bulk rock hand samples and the different size ranges of the EAC-1 granular material. EAC-1A has a compacted density of ~1.8 g/cm³.

Differential Scanning Calorimetry (DSC) measurements were carried out in an argon atmosphere in a Pegasus DSC 404 C device. The samples were heated from ambient temperature up to 1200°C by 10 K/min. EAC-1A does not have a glass transition peak, unlike JSC-1A (measured to consist of 49.3% amorphous material [3]) but similar to DNA. The thermal peak of EAC-1A was measured and found to be at ~1171 °C.

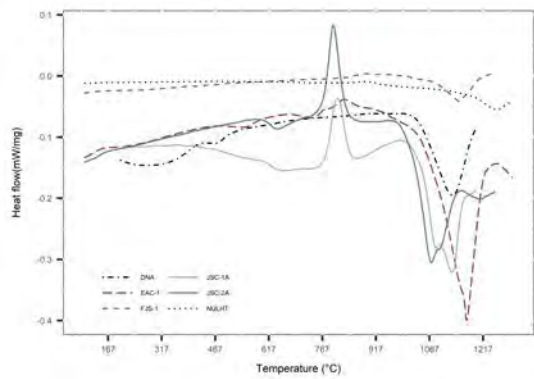


Figure 1: DSC measurements of EAC-1 and compared to other lunar regolith simulants. JSC-1A and DNA from [4].

Mineralogical analysis

Thin sections for petrographic analysis were prepared from two Siebengebirge basanite hand specimens: one from a typical homogeneously aphanitic area in the quarry, and another from a porphyritic area containing phenocrysts of olivine in an aphanitic groundmass. The samples were analysed under a polarised microscope for mineral identification and mineral volume percentage determination.

X-Ray Diffraction (XRD) analysis was conducted on the same two Siebengebirge basanite hand specimens, with the main phases identified as fayalite, forsterite, anorthite, diopside, augite and titanite. Additionally, a region of a possible alteration mineral region in a third hand specimen was analysed. Powder XRD was also acquired from the EAC-1A mixture. Scanning Electron Microscope (SEM) analysis were carried out on unconsolidated EAC-1A and on the same hand specimens that were used for the petrographical analysis.

References:

[1] Cesaretti, G. et al. (2014) *Acta Astronautica*, 93, 430-450. [2] Kanamori, H. et al. (1998) *Space*, 98, 462-468. [3] Hill, E. et al. (2007) *Journal of Geophysical Research*, 112. [4] Meurisse, A. et al. (2017) *Journal of Aerospace Engineering*, 30.

DESIGN AND DEVELOPMENT OF AN INTERFEROMETRIC READOUT FOR PLANETARY SEISMOMETERS. L. Fayon¹, H. Halloin², S. De Raucourt¹, P. Lognonné¹ ¹Institut de Physique du Globe de Paris-Sorbonne Paris Cité, Université Paris Diderot, Paris, France. ²AstroParticule et Cosmologie (APC), Université Paris Diderot, Paris, France.

Introduction: Seismometers are now likely to be placed on other planets and a seismic return on the Moon is currently considered. Indeed, the Apollo seismometers had at 0.5 Hz a resolution of about 0.5 Angstrom in ground displacement but were however unable to detect the “lunar meteoritic hum” whose amplitude has been estimated to be about 1/100 of the Apollo sensors resolution at this frequency [1]. Core seismic phases, although detected through stacking, have not also been individually recorded [2,3]. A new generation of broadband seismometers with improved performances in terms of linearity and noise level is required. A 100 to 1000 times more sensitive sensors than the Apollo ones will allow to reach the lunar seismic noise floor. The idea consists in using the gravitational waves detectors’ technology which are the reference in term of interferometric measurements at low frequency and very low noise levels. The objective is to improve the sensitivity by 2 orders of magnitude compared to the current seismometers performances (4pm at 1Hz for InSight VBBs). An optical readout system is built, based on the “Pound-Drevel-Hall” laser frequency stabilization technique. The principle of the measurement is shown, as well as the first implementation and first results.

References:

- [1] Lognonne, P. et al. (2009), *JGR*, vol. 114.
- [2] Weber R. C. et al. (2011) *Science*, vol. 331.
- [3] Garcia R. F. et al. (2011) *Elsevier*, vol. 202-203, 89–91.

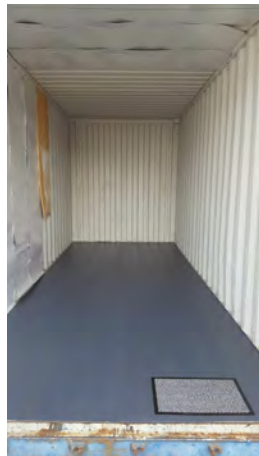
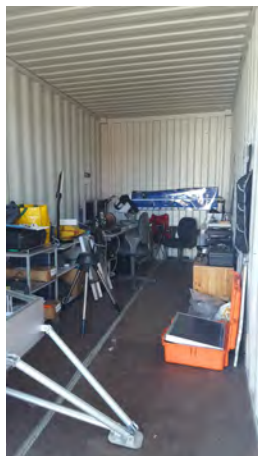
ILEWG EUROMOONMARS EXOHab 2.0

B.H. Foing^{1,2,3}, A. Lillo^{1,2,4}, P. Evellin^{1,2,5}, A. Kołodziejczyk^{1,2}, C. Heinicke^{2,3}, M. Harasymczuk^{1,2}, L. Authier^{1,2,4}, A. Blanc^{1,2,4}, C. Chahla^{1,2,5}, A. Tomic², M. Mirino^{1,2}, I. Schlacht^{2,3,6}, S. Hettrich⁷, T. Pachters⁸, ¹ESA/ESTEC & ²ILEWG (PB 299, 2200 AG Noordwijk, NL, Bernard.Foing@esa.int), ³VU Amsterdam, ⁴Supaero Toulouse, ⁵ISU Strasbourg, ⁶Extreme Design, ⁷SGAC, ⁸Puli team

Introduction: ESA provided ILEWG with a container maint for astronauts' simulation. Except the furniture were very basic, more similar to an office and nothing like a laboratory, which led to a unpractical use for the simulation. Therefore, C.Chahla managed the interior rehabilitation of the ExoLab for analog astronauts to come.

Goals of the construction work: Three weeks to embellish the container before the workshop. After finalizing the blueprints, one of the main goals was to regulate the temperature in the container in order to avoid extreme temperatures due to seasonal changes. As 220V electricity was forbidden due to risks of electrocution, we gained 4 to 5 °C differences by applying isolation to the walls.

Then we emptied the container to apply the floor layer: hydrophobic cardboards, recycled from milk bottles. Following that, we fixed wall panels, redimensioned and fixed with two essential elements: the isolation mentioned earlier, and strong magnets. The magnetic strength allows us to remove them rather easily if needed for transportation or design modifications. Yet, one really needs to pull extremely hard to remove them. It is safe enough to support shelves and other weights.



Furnishing the ExoLab : IKEA furnitures were meanwhile selected. We focused on the following needs:

-Modularity: to transform and transport as much as needed, using textiles as well.

-Height: we may lack gravity, velcro, shelves and wires on the ceiling were ideas to occupy space all around.

-Work efficiency: the more we display tools and experiments, individually and in order, the clearer and time-saving analog astronauts shall be.

-Esthetic: to feel like in outer space, the inside shall feel professional and real.



References: Interior design and pictures by Cynthia Chahla. Furnitures in final version: IKEA.



EUROMOONMARS FIELD RESULTS & MOONVILLAGE ACTIVITIES: UPDATE FOR ELS2018

B. H. Foing (1,2,3), EuroMoonMars 2017-2018 team & Moon Village Events/Workshops Organisers (G. van der Sanden, L. Dubois, E. Clavé, A. Kolodziejczyk, C. Heinicke, A. Lillo, I. Schlacht, A. Kapoglou, M. Harasymczuk, P. Evellin, V. Guinet, M. Monnerie, N. Gazda, N. Verschoor, S. Lizy-Destrez, S. Hettrich, H. Gassabian, J. Cami, V. Foing, J.L.Moro, I. Sisaid, E.Garcia Bourne, P-A. Joumel, L. Ferreira, TaiSik Lee, J. Silk, A. Decadi, A. Wendler, M. Wilde, T. Pacher, M-P.Boucher, J. Ivey, V. Beldavs, H. Rogers, J. Crisafulli, G. Reibaldi, C. Welch, O. Ben-Horin) * ¹ESA ESTEC, ²ILEWG International Lunar Exploration Working Group, ³VU Amsterdam (Bernard.Foing@esa.int)

Summary: We give an update on EuroMoonMars Field Results and Moon Village (MV) activities, with emphasis on events that took place in 2017- early 2018. The Moon Village is an open concept proposed with the goal of a sustainable human and robotic presence on the lunar surface as an ensemble where multiple users can carry out multiple activities. [1-44] .

EuroMoonMars technology & field campaigns:

ILEWG developed since 2008, "EuroMoonMars" [46-50] an evolving pilot research programme starting with a Robotic Test Bench (ExoGeoLab) and a Mobile Laboratory Habitat (ExoHab) at ESTEC, & ExoLaboratory. They can be used to validate concepts and external instruments from partner institutes. Field campaigns have been conducted in ESTEC, EAC, at Utah MDRS station, Eifel, Rio Tinto, Iceland, La Reunion, Hawaii, and LunAres base at Pila Poland in summer 2017, and are planned at ESTEC in april 2018 and Lunares in June-August 2018. We shall report on latest activities.



Fig 1: (top) ILEWG EuroMoonMars 2017 campaign crew at ESTEC (here with ExoGeoLab lander & Puli Rover) & at simulation campaigns (PMAS, LUNEX1, IcAres) at LunAres base, Poland. (below) ExoGeoLab lander at LunAres base.

Why a Moon Village? Multiple goals of the Moon Village include planetary science, life sciences, astronomy, fundamental research, resources utilisation, human spaceflight, peaceful cooperation, economical development, inspiration, training & capacity building.

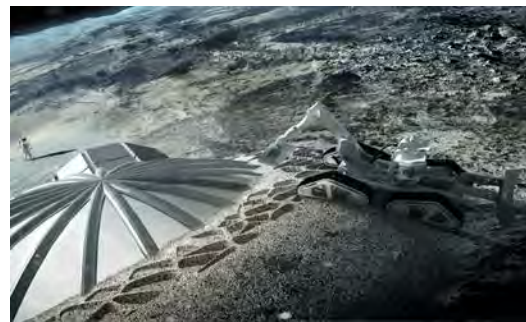


Fig 2: a possible step towards the MoonVillage using robotic with 3D printing to consolidate inflatable domes against radiation and meteorites before the arrival of astronauts

How did the Moon Village start? ESA director general has revitalized and enhanced the original concept of MoonVillage discussed in the last decade. Space exploration builds on international collaboration. COSPAR and its ILEWG International Lunar Exploration Working Group (created in 1994) have fostered collaboration between lunar missions [4-8]. A flotilla of lunar orbiters has flown in the last international lunar decade (SMART-1, Kaguya, Chang'E 1 & 2, Chandrayaan-1, LCROSS, LRO, GRAIL, LADEE). Chinese Chang'E 3 lander and Yutu rover. Upcoming other landers from 2018 (GLXP, Chang'E 4 & 5, SLIM, Luna, LRP) will form a Moon Robotic Village.

Moon Village Workshops/activities at ESA Centres:

Moon Village Workshops 2015-2016 at ESA centres in ESTEC or EAC/DLR were reported [45, 28-36]. In 2017 ESA MoonVillage ESA seminars & Euro-MoonMars workshops were held with senior experts and Young ESA professionals to discuss general topics and specific issues (habitat design, technology, science and precursor missions; public and stakeholder engagement). Dedicated ESA studies were started on mission scenarios (GO et al), building blocks (DB,ML), 3D Manufacturing & ISRU (LP, NA, MG).

Perspectives: “The Moon Village will rely both on automatic, robotic and human-tendered structures to achieve sustainable moon surface operations serving multiple purposes on an open-architecture basis.”

Moon Village community workshops in 2017/18

A number of MoonVillage talks and/or interactive jam sessions conducted at International workshops and symposia in 2016 have been reported at LPSC 2017 [45, 16-27]. In 2017, Moon Village Workshops MVWS were also conducted at international symposia or in collaboration with specific universities or institutes (we give here events, and initials of main co-organisers listed in acknowledgements*):

- *WdeKooning Acad. Arts Rotterdam: King of Moon (NV)*
- *ISU Strasbourg MVWS & design projects 6 March 2017*
- *ISAE Supaero Toulouse MVWS & design 7 March (SDM)*
- *ESTEC PMAS simulation workshop 16-18 March (SH)*
- *Paris SGAC European meeting 24-25 March (HG)*
- *London Ontario SW Uni Exploration day 4-5 April (JC)*
- *McGill Montreal Moon Village workshop 6-7 April (VF)*
- *Stuttgart Architecture Moon Village Projects April-August*
- *Cannes Innov. Centre/O'Sol MVWS 5-6 May (PS, EGB)*
- *Stuttgart Architecture MVWS & projects ESTEC 8-9 May*
- *Munich Airbus/ESA MVWS 31 May (P-A J, LF)*
- *Stuttgart Architecture MVWS & projects mid review 30 May*
- *Seoul KICT MVWS 1-2 June (TSL, BF)*
- *Paris Obs. Astronomy from Moon WS 21 June (JS, BF, AD)*
- *Salon du Bourget Air & Space 22-23 June MVWS (*
- *Torino SGAC MVWS 29 -30 June (HG)*
- *Etna ROBEX DLR campaign 29 Jun- 2 July (AW, MW)*
- *LunAres Base installation expeditions (AK, AL)*
- *LunAres Base PMAS campaign (SH, AK)*
- *LunAres Base LunEx1 campaign (AK, MH)*
- *LunAres Base IcAres campaign (AK, CH)*
- *Budapest MVWS 31 Oct (TP)*
- *VU Amsterdam/ESTEC Planetary design 9 Nov-11 Dec*
- *ESTEC, EuroMoonMars workshop 19-20 Apr 2018*
- *LunAres 1-6 2018 campaigns 2 June – 30 sept 2018*

Moon Village talks at 2017 international events

- *Global Space Congress Abu Dhabi UAE 30 Jan-1 Feb*
- *UN COPUOS Action team on Exploration 5-7 Feb 2017*
- *UN COSPAR expo workshop Vienna 25 April, 22 May*
- *European Lunar Symposium & New Views of Moon, Muenster 2-4 May (HH, CN)*
- *ISDC ST Louis (with ESA DG J. Woerner) 1-2 June*
- *GLEXP Global Exploration Conf Beijing 6-8 June*
- *Concordia U Montreal MVWS 11-12 Aug (M-P B.)*
- *Global Hands on Universe, Bowling Green 16-17 Aug*
- *Nashville Adventure Sci Center, Eclipse 19-21 Aug (JI)*
- *EPSC European Planetary Science Congress Riga, Moon Village Science, Explo. Technology Foresight 18-21 Sep*
- *Adelaide Australia IAC Intl Astronautical Congress A3 exploration symposium & plenaries 25-29 Sept*
- *Hawaii International Moon Base Alliance 1-4 Oct (HR)*
- *Columbia, LEAG Lunar Expl. Analysis Group 10-11 oct*
- *Bremen Space Tech 24-26 Oct*
- *ISU MVA MVWS 19-21 Nov (GR, CW, JM, AK)*
- *ESLAB ESTEC Extreme Habitable Worlds 4-8 Dec (ESN)*
- *MoonVillage Global Science Opera (performance over 15 countries including ESTEC event) 13 Dec (O. B.-O.)*

***Acknowledgements:** We thank Prof J. Woerner (ESA DG) for energizing the concept of MoonVillage. *We acknowledge co-conveners of MoonVillage Workshops and ILEWG EuroMoonMars field campaigns in 2016 and 2017 (including C. Jonglez, V. Guinet, M. Monnerie, A. Kleinschneider, A. Kapoglou, A. Kolodziejczyk, M. Harasymczuk, I. Schlacht, C. Heinicke, D. Esser, M. Grulich, T. Siruguet, H. Vos, M. Mirino, D. Sokolsky, J. Blamont, A. Lillo, P. Evellin, L. Authier, A. Blanc, C. Chahla, A. Tomic, M. Mirino, I. Schlacht, S. Hettrich, T. Pacher) and participants to these events. We thank A. Cowley, C. Haigneré, P. Messina, G. Ortega, S. Cristoforetti, D. Binns, M. Landgraf, M. Trovatiello, ESA colleagues involved in MoonVillage related activities. We acknowledge organisers of MoonVillage & related community workshops (identified by initials in calendar of events and including N. Verschoor, S. Lizy-Destrez, S. Hettrich, H. Gassabian, J. Cami, V. Foing, J.L. Moro, H. Lakk, I. Schlacht, I. Sisaid, E. Garcia Bourne, P-A. Joumel, L. Ferreira, Taisik Lee, J. Silk, A. Decadi, A. Wendler, M. Wilde, T. Pacher, M-P. Boucher, H. Hiesinger, C. Sallaberger, L. Ming, J. Ivey, V. Beldavs, H. Rogers, J. Crisafulli, C. Neal, G. Reibaldi, C. Welch, J. Mankins, A. Kapoglou, E. Sefton-Nash, O. Ben-Horin and others). We thank colleagues from ILEWG, Young Lunar Explorers, the International Lunar Decade Group, the Moon Village Association and Moon Village International Support Group and “MoonVillagers” at large.

References

- [1] Jan Wörner, Driving #MoonVillage <http://www.iafastro.org/events/iaf/iaf-2015/plenaryprogramme/the-moon-a-continent-and-a-gateway-for-ourfuture/> (IAC 2015)
- [2] <http://www.iafastro.org/events/iaf/iaf2016/globalnetworking-forum/making-the-moon-village-and-mars-journey-accessible-and-affordable-for-all/>
- [3] B. Foing et al, Highlights from Moon Village Workshop, ESTEC Dec 2015, <http://www.hou.usra.edu/meetings/lpsc2016/pdf/2719.pdf>, <http://www.hou.usra.edu/meetings/lpsc2016/pdf/2798.pdf>
- [4] P. Ehrenfreund et al. (PEX) “Toward a Global Space Exploration Program: A Stepping Stone Approach” (Adv Space Research, 49, n°1, January 2012)
- [5] http://www.lpi.usra.edu/leag/GER_2011.pdf
- [6] <http://sci.esa.int/ilewg/47170-gluc-iceum11-beijing-2010lunar-declaration/>
- [7] <http://www.lpi.usra.edu/meetings/leagilewg2008/>
- [8] <http://sci.esa.int/ilewg/41506-iceum9-sorrento-2007-lunar-declaration/>
- [9] Natl R Council (2007), The Scientific Context for Exploration of the Moon
- [10] P. Ehrenfreund, B.H. Foing, A. Cellino Editors, The Moon and Near Earth Objects, ASR 37, 1, pp 1-192, 2006
- [11] <http://sci.esa.int/ilewg/38863-iceum8-beijing-2006declaration/>
- [12] W. Huntress, D. Stetson, R. Farquhar, J. Zimmerman, B. Clark, W. O'Neil, R. Bourke & B. Foing, 'The next steps in exploring deep space - A cosmic study by the IAA', Acta Astr, Vol 58, Issues 6-7, 2006, p302-377
- [13] <http://sci.esa.int/ilewg/38178-iceum7-toronto-2005-declaration/>
- [14] H. Balsiger et al. Eds, Intl Lunar Workshop, 1994 May 31-June 3, Beatenberg, Switzerland. 1994. ESA-SP-1170
- [15] R.M. Bonnet et al, 'Mission to the Moon, Europe's Priorities for Scientific Exploration & Utilisation of the Moon' 1992 ESA SP-1150
- [16] <http://www.iafastro.org/events/iaf-spring-meetings/spring-meetings-2016/>
- [17] <https://www.spacesymposium.org/>
- [18] <http://www.egu2016.eu/>
- [19] <http://meetingorganizer.copernicus.org/EGU2016/session/20378>
- [20] <https://els2016.arc.nasa.gov/>
- [21] <https://nesf2016.arc.nasa.gov/>
- [22] <https://www.cospar-assembly.org/abstracted/COSPAR-16/>
- [23] <https://www.iaf2016.org/>
- [24] <http://www.hou.usra.edu/meetings/leag2016/presentations/>
- [25] <http://newworlds2016.space/>
- [26] <http://www.stx.ox.ac.uk/happ/events/history-moon>
- [27] <https://www.cranfield.ac.uk/events/events-2016/manufacturing-2075#>
- [27-36] Moon Village talks & workshops at ESA Centres
- [37-44] Moon Village workshops organised with community
- [45] Foing, B. H. 2017, LPI48, 2746
- [46] Harasymczuk, M. et al 2017, LPI48, 2997
- [47] Kolodziejczyk, A. M. et al 2017, LPICo2041, 5069
- [48] Authier L. et al 2017, LPICo2041, 5071
- [49] Foing, B. H. et al 2017, LPICo2041, 5073
- [50] Lillo, A et al 2017, LPICo2041, 5079

MOONMARS ANALOGUE SAMPLE SPECTRO-ANALYSIS IN LABORATORY & FIELD CAMPAIGNS

B.H. Foing^{1,2,3}, G.A. van der Sanden^{1,2,3}, E. Clavé^{1,2,3}, H.C. Vos^{1,2,3}, L.C. Dubois^{1,2,4}, J.Vago¹, M. Grulich^{1,2,6}, J. Lousada⁶, C. Jonglez^{1,2,4}, A. Lillo^{1,2,4}, A. Kołodziejczyk⁵, C. Heinicke^{2,3,7}, M. Harasymczuk⁵, M. Krainski¹ & ILEWG EuroMoonMars 2016, 2017 & 2018 support teams, ¹ESA/ESTEC, Postbus 299, 2200 AG Noordwijk, NL, ²ILEWG, ³Vrije Universiteit Amsterdam, ⁴ISAE Supaero, ⁵LunAres Space Garden, Poland, ⁶SGAC, ⁷ZARM

Introduction: We have analysed a set MoonMars Analogue samples from EuroMoonMars field analogue campaigns and from a petrological collection.

We have acquired samples from Utah Mars Desert Research station, Eifel volcano region, Iceland, Hawaii, La Reunion and Tenerife. Several spectroscopy analyses in the UV/VIS spectrum were performed using the remotely controlled USB4000 spectrometer in the laboratory and during field campaigns. The EuroMoonMars campaigns were rehearsed at ESTEC for feasibility. We also used other diagnostic techniques.

Spectroscopy of rocks, water, organics in the lab

The focus of these analyses (Vos et al 2017) was “the detectability of certain elements known to influence the UV/VIS spectrum such as transitional metals, but also the influences on the spectrum of minerals, water, organics and volatiles. Figure 1 shows the result from analyses whereby the influence of water was measured. the presence of water and is in accordance with known water absorption bands at 739 and 836 nm [3]. However, this influence by water is less often visible in mineral or rock analyses (due to mineral-water inreactions)”.

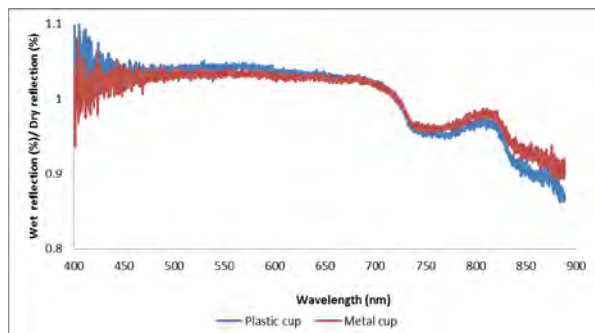


Figure 1, The influence of water on the VIS spectrum (Vos et al 2017)

Also the health of plants can be analysed using the USB4000 spectrometer. An experiment was done using different soil types to determine the influence of soil on the health and spectrum of lepidium sativum (garden cress) plants (see fig. 2) .

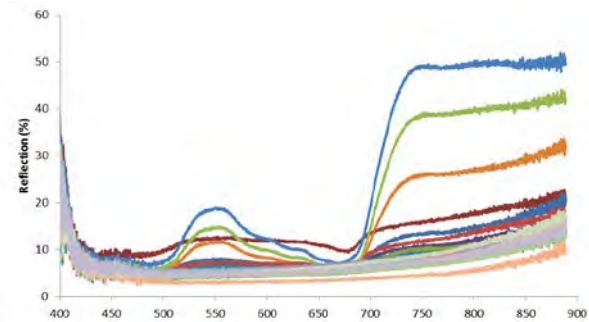


Figure 2, The spectrum of a plant (Vos et al 2017) showing Chlorophyll absorption bands at 500, 670 nm & infrared fluorescence above 720 nm

Background on ExoGeoLab lander: The field spectroscopy was also performed during a campaign following previous ILEWG EuroMoonMars campaigns [0 - 9]. The campaign was in the Eifel volcanic area in Germany at an outcrop near the Laacher See. The outcrop consisted of volcanic deposits from the Laacher See eruption from approximately 13,000 years ago. During the campaign four analogue Moon EVAs were performed. During two of these EVAs an astronaut would collect geological samples and bring them to the lander for spectrometry analyses, see figure 3.



Figure 3, Two astronauts and the ILEWG ExoGeoLab lander during an analogue Moon EVA.

Sample spectroscopy from lander: The USB4000 spectrometer was installed on the ILEWG ExoGeoLab lander and controlled remotely, see figure 4. During the field campaign sunlight was used as light source for the spectroscopy measurements.



Fig. 4, ILEWG ExoGeoLab lander with remotely controlled USB4000 spectrometer and rover

In Situ spectroscopy/ Post campaign measurements:

Figure 5 shows the reference spectrum from the sample analyses. Using ambient solar + sky incidence light is reliable in cloudless conditions. If the ratio of blue sky and cloud light changes with time this renders the reflectance spectroscopy more delicate. This is not an issue for reflectance spectrometer based on the Moon.

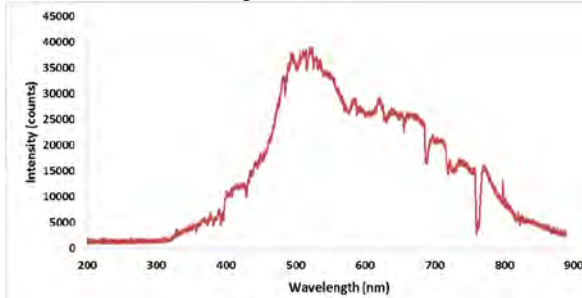


Fig. 5, The reference spectrum that was used to analyse samples during the field campaign.

The same sample that was measured during the Moon analogue mission was also analysed in a laboratory with a strong incandescence light source to prevent light contamination of the spectrum. When comparing the results from the field measurements with the laboratory measurements, some differences in the spectrum are visible. The measurements were repeated during field experiments in 2017 to determine the changes in the spectrum. By adding an extra light source near the spectrometer we improved the results from the spectroscopy analyses.

EuroMoonMars 2017 field campaigns

We have organised field campaigns using selected instruments from ExoGeoLab suite in specific locations of technical, scientific and exploration interest. Field tests have been conducted in ESTEC, EAC, at Utah MDRS station, Eifel volcano region, Rio Tinto, Ice-

land, La Reunion, Hawaii, and LunAres base at Pila Poland in summer 2017.

These were organised by ILEWG in partnership with ESTEC, VU Amsterdam, NASA Ames, GWU in Utah MDRS (EuroGeoMars 2009, and then yearly for EuroMoonMars 2010-2013).



Fig. 6: ILEWG EuroMoonMars 2017 campaign crew at ESTEC (here with ExoGeoLab lander & Puli Rover) & at simulation campaigns (PMAS, LUNEX1, IcAres) at LunAres base, Poland.

EuroMoonMars 2018 field sample analysis

For EuroMoonMars 2018 Field tests, we started the preparation at ESTEC, with reference laboratory measurements & a short reconnaissance at Tenerife (4-7 Feb). We plan an EuroMoonMars workshop & field demo at ESTEC on 19-20 april, an EAC/DLR/Eifel field volcano campaign, simulations and controlled EVAs field sampling & spectroscopy at LunAres base at Pila Poland in June-July 2018, and 2 weeks crew campaign at Utah MDRS station at end 2018/begin 2019.

We thank participants and collaborators for ILEWG EuroMoonMars 2016, 2017 & 2018 campaigns.

References:

- [0] Foing B. H. et al. (2011) *Special Issue of Int J of Astrobiology*, 10, IJA.
- [1] Ehrenfreund et al. (2011) IJA 2011, 10 (3), 239
- [2] Stoker C. et al (2011) IJA 2011, 10 (3), 269
- [3] Kotler et al. (2011) IJA 2011, 10 (3), 221;
- [4] Groemer G. et al. (2010) LPSC 41, Abstract 1680
- [5] Foing B. H. et al. (2014) LPSC 45, Abstract 2675
- [6] Foing B. H. et al. (2016) LPSC 47, Abstract 2719
- [7] Batenburg P. et al. (2016) LPSC 47, Abstract 2798
- [8] Offringa M.S. et al (2016) LPSC 47, Abstract 2522
- [9] Kamps O.M. et al (2016) LPSC 47, Abstract 2508

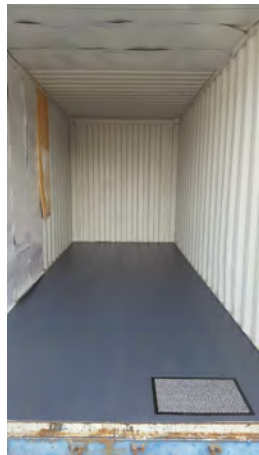
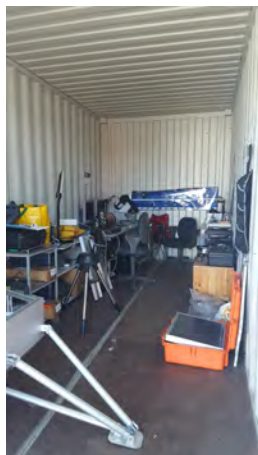
ILEWG EUROMOONMARS ExoLab 2.0

B.H. Foing, C. Chahla, A. Lillo, P. Evellin, A. Kołodziejczyk, C. Heinicke, M. Harasymczuk, L. Authier, A. Blanc, A. Tomic, M. Mirino, I. Schlacht, S. Hettrich, T. Pacher, ESA/ESTEC & ILEWG (PB 299, 2200 AG Noordwijk, NL, Bernard.Foing@esa.int), VU Amsterdam, Supaero Toulouse, ISU Strasbourg, Extreme Design, SGAC, Puli Team

Introduction: ESA provided ILEWG with a container maint for astronauts' simulation. Except the furniture were very basic, more similar to an office and nothing like a laboratory, which led to a unpractical use for the simulation. Therefore, C.Chahla managed the interior rehabilitation of the ExoLab for analog astronauts to come.

Goals of the construction work: Three weeks to embellish the container before the workshop. After finalizing the blueprints, one of the main goals was to regulate the temperature in the container in order to avoid extreme temperatures due to seasonal changes. As 220V electricity was forbidden due to risks of electrocution, we gained 4 to 5 °C differences by applying isolation to the walls.

Then we emptied the container to apply the floor layer: hydrophobic cardboards, recycled from milk bottles. Following that, we fixed wall panels, redimensioned and fixed with two essential elements: the isolation mentioned earlier, and strong magnets. The magnetic strength allows us to remove them rather easily if needed for transportation or design modifications. Yet, one really needs to pull extremely hard to remove them. It is safe enough to support shelves and other weights.



Furnishing the ExoLab : IKEA furnitures were meanwhile selected. We focused on the following needs:

-Modularity: to transform and transport as much as needed, using textiles as well.

-Height: we may lack gravity, velcro, shelves and wires on the ceiling were ideas to occupy space all around.

-Work efficiency: the more we display tools and experiments, individually and in order, the clearer and time-saving analog astronauts shall be.

-Esthetic: to feel like in outer space, the inside shall feel professional and real.



References: Interior design and pictures by Cynthia Chahla. Furnitures in final version: IKEA.



CANDIDATE SELECTION FOR CHANGE DETECTION AND DTM PRODUCTION ON THE MOON. A. M. Francis¹, J. P. Muller¹ and P. Sidiropoulos¹. ¹Mullard Space Science Laboratory, UCL

Repeat imagery of the lunar surface can be used to study surface change associated with meteoritic impacts and other as yet undiscovered processes. Under certain circumstances, a geometric combination of these images at a range of intersecting angles can be used to create Digital Terrain Models (DTMs) both from a single system, such as LROC-NAC or by use of multiple instruments such as CLEMENTINE and LROC-NAC. We demonstrate how the PDS-ODE and SPICE kernels can be employed to generate repeat coverage maps of the Lunar surface using NAC and other instruments, allowing for the automatic selection of suitable candidate sites for change detection and DTM production. These maps document the number of images taken at every point on the surface of the Moon, as well as the dates when each image was taken, and the relevant metadata including resolution, illumination conditions and SPICE-derived camera angles. We will show the selenographic distribution of candidate stereo pairs from NAC images, and demonstrate the creation of example DTMs using the UCL CASP-GO (Tao et al., PSS, in press) system in comparison with LOA 3D heights.

Introduction: Apollo sample 15426 is a friable greenish clod that was collected from the north rim of Spur Crater. The green material is the common Apollo 15 very-low Ti glass that was formed by volcanic fire-fountaining of primitive melts ~3.4 Gyrs ago [1-3]. Previous noble gas analyses indicated that the cosmic ray exposure age of 15426 glass beads varies significantly between 139 and 400 Myrs [3-5]. In addition to cosmogenic and solar wind (SW)-derived noble gases acquired during space exposure, the glasses appear to contain a 'trapped' solar-like neon and argon component, which may have been absorbed from an ambient gas phase or, alternatively, may represent primordial lunar gas [4,5]. According to this scenario, water in green glasses [6] could be of solar and/or indigenous origin.

Analytical approach and preliminary results: We have analyzed the noble gas signature of 15426 green glasses by CO₂ laser extraction static mass spectrometry in order to re-assess the proportion of different noble gas components in these samples. Noble gas (He, Ne, Ar) concentrations and isotope ratios of twelve single vitreous glass beads, between 13 and 25 (±2) micrograms in mass, were measured using the Helix MC *Plus* noble gas mass spectrometer at CRPG. Two heating steps were applied in order to separate surface-sited (implanted, adsorbed) from volume-correlated (trapped, cosmogenic) noble gas components. Neon isotopes were measured in multi-collection mode on three electron multipliers, whereas helium and argon isotopes were measured in peak-jumping mono-collection mode.

The ⁴He content of several spherules is below detection limit, indicating that the glasses experienced severe helium losses. Any remaining ⁴He and ³He is predominantly released at the first heating step. The neon and argon abundances are significantly above blank levels and vary by 2 orders of magnitude (**Fig. 1**). ²⁰Ne/²²Ne and ²¹Ne/²²Ne ratios vary between 12.5 and 1.0 and between 0.03 and 0.83, respectively, and can be explained by mixing between solar and cosmogenic neon. Similarly, ³⁸Ar/³⁶Ar ratios range from a solar-like value of ~5.5 to 0.91, which is close to the cosmogenic endmember. Strikingly, the two spherules that show the highest noble gas contents appear to release a solar-like volume-correlated component at the second heating step; this component has a slightly lower ²⁰Ne/²²Ne ratio than SW-derived neon extracted at the low-temperature step.

Discussion: Different grain size fractions of lunar regolith and glasses generally show an inverse correlation between their noble gas content and the

particle size. However, the spherules analyzed in this study are all of similar (small) size. Therefore, the highly variable neon and argon content of single 15426 glass beads found here is astonishing and indicates that the spherules experienced distinct irradiation histories. Furthermore, in addition to implanted solar gases and cosmogenic nuclides produced in situ, these glasses seem to contain a third (solar-like) noble gas component, as previously suggested by Lakatos et al. [4] and Megrue [5].

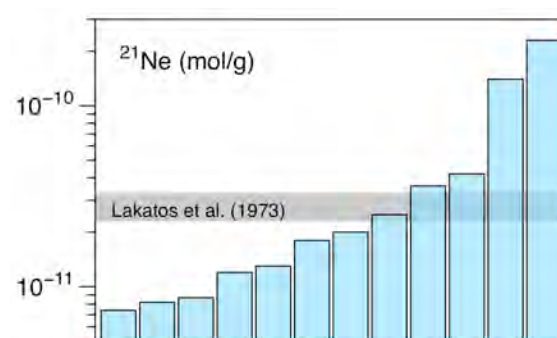


Fig.1: Total measured ²¹Ne concentrations (in mol/g) of twelve individual Apollo 15426 green glass beads. The ²¹Ne concentration range observed by Lakatos et al. [4] in five grain size fractions and two large single spherules is shown for comparison.

Conclusions: New neon and argon abundances and isotope ratios have been obtained for very small (≤300 μm) individual glass beads from Apollo sample 15426. The new results reveal that the glasses record a wide range of noble gas concentrations, likely due to variable contributions from implanted SW gas, cosmogenic nuclides, and a 'trapped' solar-like component. The nature and origin of this component remains enigmatic but it could be derived from the lunar mantle. Notably, the 15426 glasses are inferred to contain indigenous lunar water [5], and volatiles concentrated at their surfaces (e.g., Pb) are thought to be derived from an undifferentiated, volatile-rich reservoir in the mantle [1].

References: [1] Delano J.W. (1979) *Proc. Lunar Planet. Sci. Conf. 10th*, 275-300. [2] Podosek F.A. and Huneke J.C. (1973) *EPSL*, 19, 413-421. [3] Spangler R.R. and Warasila R. (1984) *Proc. 14th Lunar Planet. Sci. Conf., JGR*, 89, B487-B497. [4] Lakatos S. et al. (1973) *The Moon*, 7, 132-148. [5] Megrue G.H. (1973) *JGR*, 78, 4875-4883. [6] Saal A.E. et al. (2013) *Science*, 340, 1317-1320.

Bouillabaisse: A rich, spicy stew or soup made with various kinds of fish, originally from Provence.

KEY SCIENCES OF THE LUNAR SPACE ENVIRONMENT TO BE INVESTIGATED BY THE MISSION SELMA. Y. Futaana¹, S. Barabash¹, and the SELMA proposal team, ¹Swedish Institute of Space Physics, Box 812, Kiruna, SE-98128, Sweden.

Introduction: The Moon is an archetypical airless bodies in the solar system. It has a complex interaction between the space plasma, exosphere, dust and the surface. The mission SELMA was proposed to ESA as a medium-class (M5) mission in October 2016 [1]. SELMA uses a unique combination of remote sensing and in situ measurements. In addition, SELMA releases an impact probe to sound a magnetic anomaly down to the surface in order to sound a mini-magnetosphere. SELMA also conducts an impact experiment directly to measure the volatile content in the soil of a permanently shadowed crater. With its planned 1 year operation, SELMA investigates physics of the complex interaction, and reveals resulting influence to the lunar environment.

SELMA sciences: SELMA aims to answer four overarching scientific questions.

1. What is the origin of water on the Moon?
2. How do the volatile cycles on the Moon work?
3. How do the lunar mini-magnetospheres work?
4. What is the influence of dust on the lunar environment and surface?

Key sciences of the lunar space environment: Out of those SELMA science questions, we focus on a few scientific questions in this presentation.

Hydrogen balance at the Moon. Since the hydrogen at the lunar surface should be in an equilibrium state, the incoming hydrogen (mainly the solar wind protons) should be balanced to the outgoing flux (e.g. diffusion to the interior, release to the exosphere, or escape to space). A part of the hydrogen (in a form of H₂O molecule) is expected to be trapped in permanently shadowed craters [2]. SELMA aims to answer the question "how does the solar wind hydrogen interaction with the lunar soil" by measuring the solar wind proton as in flux, in addition to the hydrogen related molecules in the exosphere and the escaping fluxes of hydrogen in all the charge states as outflows.

Mini-magnetosphere sounding down to surface. Magnetic anomaly-solar wind interaction is of special interest for plasma physics. The interaction occurs over multiple scales from the fluid scale to the electron scale [3]. The key region to understand the interaction is the altitude below the electron scale above the surface, i.e. <100 m, where strong electric current flows determine the characteristics of mini-magnetospheres. SELMA investigate this region by measuring ion and electron spectra with ultra high time resolutions on board an impact probe. The impact probe targets one of the most famous magnetic anomalies, Reiner Gamma. SELMA establishes "the mechanisms creating small-scale plasma depletions

and deceleration of the electrons and ions associated with mini-magnetospheres."

Impact experiment and plume release. A dozen of permanently shadowed craters exist in the lunar South Polar area. Such craters are cold enough to keep the water ice at the bottom or below the surface. NASA's LCROSS mission investigated a plume caused by an impact of an upper stage rocket, and observed the water absorption lines by remote sensing in the infrared and ultraviolet wavelengths, indicating a mass fraction of water in the ejected regolith of $5.6 \pm 2.9\%$ [4]. SELMA conducts a similar impact experiment while using both in situ and remote sensing techniques. A passive impactor is released first, targeting the Shackleton crater to produce a plume. SELMA orbiter then follows the impactor to measure the volatile components in the plume. With this experiment, SELMA will answer the question "how much is the water buried in the soil of the permanently shadowed region and what is its isotope composition?"

References:

- [1] Futaana, Y., et al. (2018) *Planet. Space Sci.*, doi:10.1016/j.pss.2017.11.002.
- [2] Lord, H.C., (1968), *J. Geophys. Res.*
- [3] Kallio, E., et al. (2012) *Planet. Space Sci.*, doi:10.1016/j.pss.2012.09.012.
- [4] Colaprete, A., et al., *Science*, doi:10.1126/science.1186986.

An international team to create reference models and data sets for Moon seismology. R.F. Garcia¹, ISSI international team², ¹ISAE-SUPAERO, 10 Ave E. Belin, 31400 Toulouse (raphael.garcia@isae.fr), ²<http://www.issibern.ch/teams/internstructmoon/>

Introduction: The seismological data of Apollo missions were processed almost continuously during the past 40 years. This example of planetary data processing is unique for planetary science by its duration and the important results obtained over the years. It is currently driving many rules in planetary data collection and archiving. A consequence of such a long and continuous data processing is the availability of many internal structure models and many processed data sets (Level 2 or 3). The processed data sets are not always publicly available and there is no general agreement on the error bars of both processed data and internal structure models.

Team Goals: We present here the work performed by an internal team on Moon seismology which gathered with the support of ISSI Bern and Beijing.

Our goal is to provide to the scientific community the following elements:

- processed data sets and an analysis of their error bars
- internal structure models produced by using these processed data sets and up to date a priori information
- an analysis describing what we know and what we don't know about the internal structure of the Moon, in order to support and drive future seismological deployments.

Work presented: We will present the review work of a priori information and internal structure models, and the preliminary analysis of processed data sets (travel times, deep moonquake stacks...) performed up to know. The strategy for data analysis and reference model production will also be presented. We conclude on our statement to support future lunar internal geophysics missions.

CARACTERIZATION OF SHALLOW MOONQUAKES AND THE MEGAREGOLITH: NEW INSIGHTS FROM APOLLO DATA . K. Gillet¹, L. Margerin¹, M. Calvet¹, M. Monnereau¹, ¹IRAP, Université de Toulouse, CNRS, CNES, UPS, Observatoire Midi-Pyrénées, 14 avenue Edouard Belin, 31400 Toulouse, France

Introduction: Lunar seismic signals are notably different from usual terrestrial seismic records: the energy rise at the onset of the signal is gradual, the S-wave arrival is difficult (or impossible) to detect, the maximum of energy is broad, and the energy decay in the coda is very slow. The signal can remain noticeably above the noise level for up to two hours, compared to a few minutes on Earth for an event of the same magnitude. Soon after the beginning of the experiment, several studies have established a link between the characteristics of lunar signals and strong scattering in the heterogeneous upper lunar crust. This lunar megaregolith results of intensive meteoritic bombardment that caused cratering, cracking, distribution of ejecta and partial melting over the entire surface of the Moon. At depth, cracks close gradually with confining pressure until the crust becomes competent. The thickness of the megaregolith has been revised several times since the beginning of the analysis of Apollo data. Latham et al. [1] suggested that the characteristics of lunar seismic signals could be explained by the presence of a scattering layer with a maximum thickness of 20km due to the confining pressure. The velocity model of Lognonné et al. [2] suggests that impact-induced cracks might still be present below 30 km. Recently, the GRAIL mission collected gravity data that were used by Wieczorek et al. [3] to infer a 34–43 km deep crust with an average porosity of 12%, which supports the idea of a highly-fractured environment up to great depths. The spindle-like shape of short period lunar seismic signals supports the idea that seismic waves propagate in the multiple scattering regime, and that energy transport can be modeled using diffusion theory. Dainty et al. [4] made the first attempt at modeling the scattering processes in the Moon using diffusion theory, and inferred a thickness of 25 km for the scattering layer. However, these modeling efforts were limited to the planar case. Considering the size of the Moon and the duration of lunar seismic signals, it is essential to take sphericity into account. In this work, we consider for the first time the stratification of scattering properties and the spherical geometry [5].

Data Processing : Our dataset consists of waveforms corresponding to 62 events, including artificial and natural impacts, shallow moonquakes and deep moonquakes, recorded by the four seismometers deployed during Apollo missions 12, 14, 15 and 16. For impacts and shallow moonquakes, signals are band-pass filtered between 0.25 Hz and the Nyquist frequency (3.15 Hz for low frequency). Deep moonquake signals were provided by Garcia et al. [6]. Our final dataset is composed of 446 records distributed

as follows: 30 artificial impacts, 154 natural impacts, 143 shallow moonquakes and 119 deep moonquakes. To quantify attenuation and distinguish between elastic (scattering) and inelastic (absorption) mechanisms, we measure the time of arrival of the maximum of energy t_{\max} and the coda quality factor Q_c . The former is controlled by both scattering and absorption, while the latter is an excellent proxy for absorption. To reduce the fluctuations and facilitate the detection of the maximum, the energy envelope of the signal is smoothed by replacing the instantaneous intensity by its running average in a time window of typical duration 10 periods. We introduce a robust method of estimation of the uncertainty on the t_{\max} measurement which relies on the circular gaussian statistics property of scattered waves [7]. Figure 1a shows t_{\max} as a function of the epicentral distance for all events: (1) t_{\max} is systematically higher for impacts than for moonquakes ; (2) variation of t_{\max} for impacts shows two different slopes with a local maximum between 10° and 20°. Q_c is the coda quality factor which quantifies the rate of decay in the

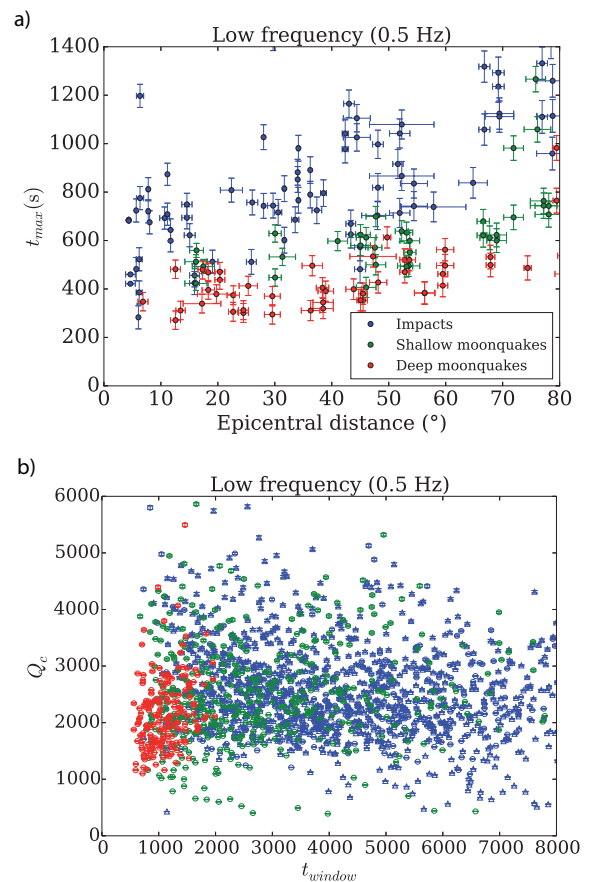


Figure 1 : (a) t_{\max} for impacts (blue dots), shallow moonquakes (green dots) and deep moonquakes (blue dots) as a function of the epicentral distance; (b) Dependence of the quality factor Q_c on the lapse-time in the coda (t_{window}).

coda [8]. Figure 1b illustrates the variation of Q_c as a function of the lapsetime in the coda. At low frequency, we do not observe any dependence of Q_c with either source depth or lapse-time. These observations confirm that the Moon is a medium with low absorption and strong scattering at the surface.

Model and Inversion procedure : We employ diffusion theory in spherical geometry to model the propagation of seismic energy in depth-dependent scattering and absorbing media. We introduce the diffusion constant $D(r)$ which may be expressed as $D(r) = c(r)^2 Q_s(r) / 3\omega$ with $c(r)$ the S-wave velocity and $Q_s(r)$ the scattering quality factor. Absorption is quantified by an absorption quality factor $Q_i(r)$. To solve numerically the diffusion equation, we use finite differences and second order alternating directions implicit (ADI) methods in axisymmetric spherical geometry. In our model, the boundary conditions of the diffusion equation are as follows: continuity of intensity I and flux $D \nabla I$ at each internal interface of the model, zero normal flux at the surface. The grid is composed of 100 radial points and 300 latitudinal points. The input parameters of the model are 1-D radial profiles of diffusivity and absorption quality factors. In order to explore the parameter space efficiently, we implement a genetic algorithm. We impose that the diffusivity be increasing with depth. Considering the absence of clear dependence of Q_c with either epicentral distance, source depth or lapsetime, a single value of Q_i is chosen for the entire Moon. We do not use shallow moonquakes in the inversion because the uncertainty on their depth location is typically as large as the thickness of the megaregolith. Including these events in the inversion may therefore strongly bias our output models.

Results : The scattering and absorption profiles that best fit the data (Figure 2) display very strong scattering attenuation ($Q_{sc} \leq 10$) or equivalently very low wave diffusivity ($D \approx 2 \text{ km}^2/\text{s}$) in the first 10 km of the Moon. These values correspond to the most heterogeneous regions on Earth, namely volcanic areas. Below this surficial layer, the diffusivity rises very slowly up to a depth of approximately 80 km where Q_{sc} and D exhibit an abrupt increase of about one order of magnitude. Below 100 km depth, Q_{sc} increases rapidly up to approximately 2000 at a depth of about 150 km, a value similar to the one found in the Earth's mantle. By contrast, the absorption quality factor on the Moon $Q_i \approx 2400$ is about one order of magnitude larger than on Earth. Our results suggest the existence of an approximately 100 km thick megaregolith, which is much larger than what was previously thought. The rapid decrease of scattering attenuation below this depth is compatible with crack healing through viscoelastic mechanisms. As cracks may well be present at greater depth than previously thought, it may have implications for the density

profile and consequently on the characterization of the lunar core (radius and density) which are partly constrained by the moments of inertia of the Moon.

Using our best attenuation model, we invert for the depth of shallow moonquakes based on the observed variation of t_{\max} with epicentral distance. On average, they are found to originate from a depth of about $50 \text{ km} \pm 20 \text{ km}$, which suggests that these earthquakes are caused by the failure of deep faults in the brittle part of the Moon. But shallow moonquakes are the most energetic events on the Moon, with magnitudes as large as 5, and are also characterized by strong stress drop [9]. In future work, the problem of the seismic stress drop will be re-examined with the aid of our new attenuation model.

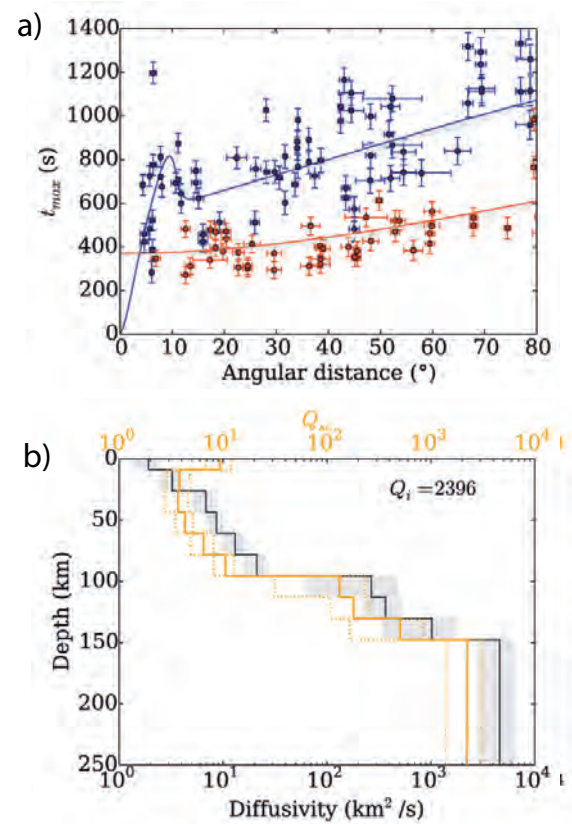


Figure 2: (a) t_{\max} as a function of the epicentral distance: solid lines are the 10 best-fitting models; (b) Diffusivity (black line) and scattering quality factor (orange line) profiles at 0.5 Hz with uncertainty limits (grey area for $D(r)$ and orange dashed lines for $Q_{sc}(r)$).

References: [1] Latham G. et al. (1972) *Moon*, 4, 373-382. [2] Lognonné P. et al. (2006) *Earth Planet. Sci. Lett.*, 211, 27-44. [3] Wieczorek M. A. et al. (2013) *Science*, 339, 671-675. [4] Dainty A. M. (1974) *Moon*, 9, 11-29. [5] Gillet K. et al. (2017) *Phys. Earth Planet. Int.*, 262, 28-40. [6] Garcia R. F. et al. (2011) *Phys. Earth Planet. Inter.*, 188, 96-113. [7] Anache-Ménier D. et al. (2009) *Phys. Rev. Lett.*, 102, 248501. [8] Aki K. and Chouet B. (1975) *J. Geophys. Res.*, 80, 3322-3342. [9] Goins N. R. et al. (1981) *J. Geophys. Res.*, 86, 378-388.

THE LAMP SPECTROGRAPH ON THE LUNAR RECONNAISSANCE ORBITER: LUNAR SCIENCE WITH ULTRAVIOLET EYES. C. Grava¹, K. D. Retherford¹, T. K. Greathouse¹, K. E. Mandt², G. R. Gladstone¹, A. R. Hendrix³, D. M. Hurley², U. Raut¹, J. T. Cahill², Y. Liu⁴. ¹Southwest Research Institute, 6220 Culebra Road, San Antonio, TX, 78238, USA (cgrava@swri.edu), ²Johns Hopkins University Applied Physics Laboratory, Laurel, MD, USA, ³Planetary Science Institute, Boulder, CO, USA, ⁴Lunar and Planetary Institute, Houston, TX, USA.

Introduction: The Lyman-Alpha Mapping Project (LAMP; [1]) UV imaging spectrograph (56-190 nm) onboard the Lunar Reconnaissance Orbiter (LRO; [2]) has demonstrated an innovative nightside observing technique, casting a new light on permanently shadowed regions (PSRs) and other features on the Moon. LAMP exploits the polar orbit of LRO and the light coming from UV-bright stars and interstellar hydrogen resonantly scattering solar photons at Lyman-alpha (121.6 nm) to look into PSRs.

The far-UV absorption edge near 165 nm is a strong indicator of water frost, providing constraints on hydration that complement infrared spectroscopy, visible imaging, neutron spectroscopy, radar, and other techniques. Water ice has been detected by LAMP in some PSRs in the polar regions [3,4], and this hydration signature has been detected by LAMP in dayside regions [5], enabling tracking of the lunar diurnal cycle of water.

By utilizing natural diffuse illumination sources on the nightside, LAMP is able to identify relative increases in porosity within the PSRs [3], and provides an additional tool for determining relative surface ages and even for detecting geologically young craters [6].

The far-UV wavelength region is also diagnostic of maturity: a bluer spectral slope indicates more space weathering. LAMP has observed lunar swirls in the far-UV for the first time and found that they are relatively less blue than surrounding terrain, indicating a difference in either composition or weathering [7].

Being such a sensitive instrument, LAMP is able to detect emission lines from the species in the tenuous lunar exosphere, such as He [8,9,10,11,12] and H₂ [13,14], and to place more stringent upper limits on several other species [15]. Moreover, LAMP detected numerous volatiles (including CO, H₂, Hg, Ca, and Mg) when the LCROSS impact occurred in a PSR in Cabeus crater, near the South Pole [16, 17]. LAMP also placed very stringent upper limits on the lunar nanodust cloud population [18].

On October 6, 2016 LAMP enacted a new, more sensitive dayside operating mode that expands its ability to search for diurnally varying hydration signals associated with different regions and features. We will discuss the strengths of the far-UV reflectance imaging spectroscopy technique with respect to several new LAMP results.

References: [1] Gladstone G. R. et al. (2010) *Sp. Sci. Rev.*, 150(1-4), 161-181. [2] Chin G. et al. (2007) *Sp. Sci. Rev.*, 129(4), 391-419. [3] Gladstone G. R. et al. (2012) *J. Geophys. Res.*, 117, E00H04. [4] Hayne, P. O. et al. (2015) *Icarus*, 255, 58-69. [5] Hendrix A. R. et al. (2012) *J. Geophys. Res.*, 117(E12). [6] Mandt, K. E. et al. (2016) *Icarus*, 273, 114-120. [7] Hendrix A. R. et al. (2016) *Icarus*, 273, 68-74. [8] Stern S. A. et al. (2012) *Geophysical Research Letters*, 39(12). [9] Feldman P. D. et al. (2012) *Icarus*, 221, 854-858. [10] Cook J. C. & Stern S. A. (2014) *Icarus*, 236, 48-55. [11] Hurley D. M. et al. (2016) *Icarus*, 273, 45-52. [12] Grava C. et al. (2016) *Icarus*, 273, 36-44. [13] Stern A. S. et al. (2013) *Icarus*, 226, 1210-1213. [14] Hurley D. M. et al. (2017) *Icarus*, 283, 31-37. [15] Cook J. C. et al. (2013) *Icarus*, 225, 681-687. [16] Gladstone G. R. et al. (2010) *Science* 330, 472-476. [17] Hurley D. M. et al. (2012) *J. Geophys. Res.* 117, E00H07. [18] Grava C. et al. (2017) *Geophysical Research Letters*, 44 (10), 4591-4598.

INVESTIGATING THERMAL EMISSION FROM THE LUNAR EPIREGOLITH. B. T. Greenhagen¹, P. Prem¹, K. L. Donaldson Hanna², N. E. Bowles², and P. G. Lucey³, ¹Johns Hopkins Applied Physics Laboratory, Laurel, MD (benjamin.greenhagen@jhuapl.edu), ²University of Oxford, Oxford, GB, ³University of Hawai'i at Mānoa, Honolulu, HI.

Introduction: On the Moon, near Earth asteroids, and the moons of Mars, the uppermost portion of regolith, the “epiregolith”, represents the boundary layer between the surface and space that dominates spectral observations from far-ultraviolet reflectance to far-infrared emission. This layer is typically less than 2 mm in thickness and is characterized by significant thermal gradients ($\sim 60\text{K} / 100\ \mu\text{m}$). These thermal gradients make spectral emission from airless bodies wholly different from Earth and Mars (where the epiregolith is essentially isothermal) and complicate the interpretation of spectral emission remote sensing data (Fig. 1). Therefore, thermal infrared (TIR) spectroscopy experiments measured in ambient laboratory conditions are not comparable to remote sensing datasets of airless bodies that contain significant emission components (Fig. 2). Here we use orbital data from the Lunar Reconnaissance Orbiter Diviner Lunar Radiometer (Diviner), experiments in simulated lunar environment, and radiative transfer models to investigate the thermal structure of and spectral emission from the epiregolith.

Diviner Lunar Radiometer: Diviner is a multi-spectral radiometer that has observed solar reflectance and TIR emission from the Moon at a wide range of illumination and viewing geometries to constrain radiative balance and spectral emission [1].

Simulated Lunar Environment: To simulate a relevant thermal environment we use the Simulated Lunar Environment Chamber (SLEC) and Planetary Analogue Surface Chamber for Asteroids and Lunar Environments (PASCALE) at University of Oxford's Planetary Spectroscopy Facility and the Simulated Airless Body Emission Laboratory (SABEL) at Johns Hopkins Applied Physics Laboratory. In these chambers, a particulate sample is heated (by conduction and/or illumination) within a cold radiation shield, and under vacuum. SLEC, PASCALE, and SABEL can create thermal gradients of variable magnitude and simulate the wide range of temperatures relevant to a wide range of studies [2-4].

Thermal models: Radiative transfer thermal models have been used to predict the behaviour observed by Diviner and laboratory experiments [5-6]. We are implementing a new approach incorporating Monte Carlo methods to approximate scattering.

Summary: Insights gained from this study will improve interpretations of infrared datasets of airless bodies and lead to improved thermal corrections of near-infrared datasets. The VORTICES node of SSERVI is specifically tasked with this type of multimodal data analysis and we hope to use our results to improve modelling of orbital and ground-based

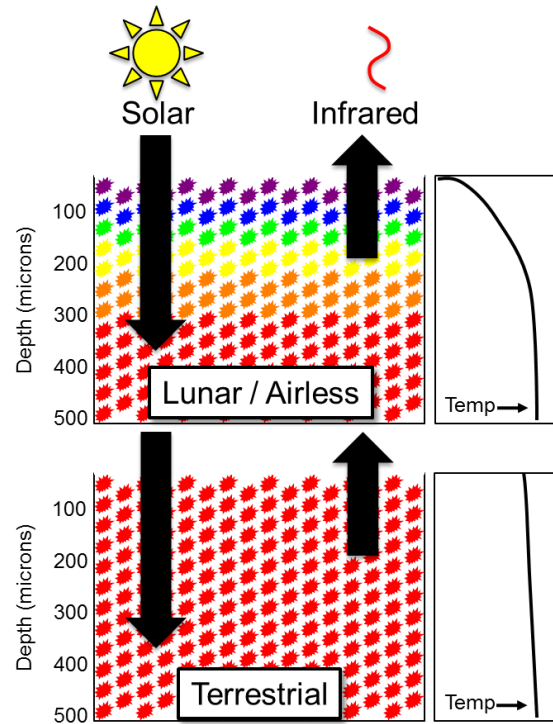


Figure 1: The lack of heat convection via atmospheric gases causes thermal gradients seen on airless bodies not found in terrestrial environments.

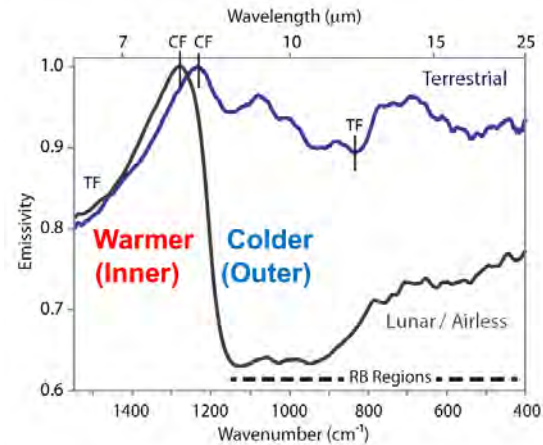


Figure 2: TIR spectral features are significantly altered by the presence of thermal gradients [after 2].

observations of the Moon, near Earth asteroids, and the moons of Mars.

References: [1] Paige D. A. et al. (2010) *SSR*, 150, 125–160. [1] Donaldson Hanna K. L. et al. (2012) *JGR*, 117, E00H05. [1] Arnold J.A. et al. (2016) *JGR*, 121, 1342–1361. [1] Donaldson Hanna K. L. et al. (2017) *Icarus*, 283, 326. [1] Henderson B. G. & B. M. Jakosky (1997) *JGR*, 99, 19063–19073. [1] Millán L. et al. (2011) *JGR*, 116, E12003.

OXYGEN ISOTOPE EVIDENCE FOR A HIGH-ENERGY MOON-FORMING GIANT IMPACT AND EARLY DELIVERY OF EARTH'S WATER.

R. C. Greenwood^{1*}, J.-A. Barrat², M. F. Miller^{1,3}, M. Anand^{1,4}, N. Dauphas⁵, I. A. Franchi¹, P. Sillard⁶, N. A. Starkey¹, ¹Planetary and Space Sciences, The Open University, Milton Keynes MK7 6AA, UK. ²Université de Bretagne Occidentale, Laboratoire Géosciences Océan (CNRS UMR 6538), Brest, France. ³British Antarctic Survey, Cambridge CB3 0ET, UK. ⁴Department of Mineralogy, The Natural History Museum, London SW7 5BD, UK. ⁵Origins Laboratory, Department of the Geophysical Sciences and Enrico Fermi Institute, The University of Chicago, Chicago IL 60637, USA. ⁶Centre de recherche en économie et statistique, 5, Av Henry Le Chatelier, 91120 Palaiseau, France. *E-MAIL : r.c.greenwood@open.ac.uk

Introduction: The canonical giant impact model envisaged an oblique impact between the proto-Earth and a Mars-sized body [1]. Numerical simulations based on this model, indicated that the Moon formed from a debris disc containing ~70 % impactor-derived material [1]. If the impactor had a different oxygen isotopic composition ($\Delta^{17}\text{O}$) to the proto-Earth, this model suggests that the Earth and Moon should show resolvable isotopic differences [2, 3]. However, with one exception [4], high-precision studies have failed to detect such a difference [5-8]. Studies of silicon [9] and titanium [10] isotopic variation also revealed no differences between the Earth and Moon. In addition, tungsten isotope studies indicate that the Earth and Moon initially had a similar ^{182}W composition [11].

The isotopic similarity between the Earth and Moon, combined with a reassessment of the angular momentum constraints, has led to the formulation of high-energy models, which invoke nearly complete mixing between the impactor and target [2, 3]. Recent modelling studies suggest that typical rocky planets may be vaporised multiple times by giant impacts [12,13]. This process results in the formation of an extended structure termed a “synestia”, initially composed principally of silicate vapour. Such a structure would involve complete isotopic equilibration for the bulk of the Earth-Moon system [13].

However, complete isotopic re-equilibration in the wake of the giant impact has been questioned by a study that detected a 12 ± 3 ppm (SEM) $\Delta^{17}\text{O}$ Earth-Moon difference [4]. Subsequently, this finding was challenged by a study which was unable to detect this isotopic difference at a level of ± 5 ppm (SEM) [5].

Lack of significant isotopic differences between the Earth and Moon has also been explained by a terrestrial accretion model, which predicts that both the impactor and proto-Earth formed from the same enstatite chondrite-like precursor materials, making large Earth-Moon isotopic differences unlikely [14].

Methods and samples: To investigate the origin and early evolution of the Earth-Moon system we have undertaken an extensive study of the oxygen isotope composition of lunar and terrestrial samples [15]. Lunar whole-rock samples ($n = 17$) covering all the main lith-

ological units, from all six Apollo landings, were analysed, as well as lunar mineral separates ($n = 14$). Terrestrial mafic rocks, comprised basalts ($n = 20$) and a mantle xenolith. The terrestrial sample set, also included our previously published olivine data [16], recalibrated against VSMOW. Full details of the samples and methods are given in [15].

Results: Lunar whole-rocks have relatively homogeneous oxygen isotope compositions, with $\delta^{18}\text{O}$ values that range from $5.64 \pm 0.02\text{‰}$ (2 SD) to $6.19 \pm 0.02\text{‰}$ (2 SD) and $\Delta^{17}\text{O}$ values from 2 to 20 ppm. In comparison, terrestrial whole-rocks show a wider spread in $\delta^{18}\text{O}$, ranging from $5.03 \pm 0.12\text{‰}$ (2 SD) to $6.27 \pm 0.15\text{‰}$ (2 SD), and have $\Delta^{17}\text{O}$ values from -4 to 15 ppm. However, the mean $\delta^{18}\text{O}$ values of the lunar and terrestrial whole-rocks are close, $5.92 \pm 0.28\text{‰}$ (2 SD) and $5.79 \pm 0.69\text{‰}$ (2 SD) respectively.

There is a 3 ppm difference between the average $\Delta^{17}\text{O}$ value of lunar and terrestrial samples, with the full suite of lunar whole-rocks and mineral separates ($n = 31$) having a mean $\Delta^{17}\text{O}$ composition of 10 ± 2 ppm (2 SEM), compared to 7 ± 2 ppm (2 SEM) for all terrestrial samples and mineral separates ($n = 37$). When terrestrial basalts ($\Delta^{17}\text{O} = 6 \pm 2$ ppm (2 SEM) ($n = 20$)), are compared to lunar whole-rocks this difference increases to 4 ppm. Statistical analysis (t tests and bootstrap analysis with 10^6 replications) indicates that this 3 to 4 ppm difference is significant at a 95% level of confidence [15].

An aubritic composition for Theia? The aubrites provide the closest match to the hypothesized reduced impactor of [17], being virtually FeO-free and having an isotopic composition that is closely similar to both the Earth and enstatite chondrites [15]. High-precision oxygen isotope data for aubrites [18], recalculated on the VSMOW scale [15], show that their oxygen isotopic composition ($\Delta^{17}\text{O} = 28 \pm 3$ ppm (2 SEM)) is close to, but fully resolvable from that of the Earth and Moon [15]. Using the canonical giant impact model [1] (10.6% impactor and 89.4% proto-Earth in the final Earth), and taking the isotopic composition of the impactor to be that of the aubrites, we have calculated the relative proportions of impactor and target material that are required in the Earth and Moon to account for the oxygen isotopic differences observed in our data. The ~4 ppm Earth-Moon difference observed between terrestrial

basalts and lunar rocks can be reproduced by a lunar impactor component of 25 to 28% of the Moon's mass, compared to the terrestrial impactor component of 10.4%. The required impactor contribution is significantly lower than the ~70% predicted by the canonical model [1], and also less than other low velocity scenarios [19].

Our analysis indicates that the 3 to 4 ppm $\Delta^{17}\text{O}$ difference between terrestrial and lunar rocks is not consistent with an aubritic impactor, unless some form of post-impact equilibration also took place. In the absence of such an equilibration event, the impactor would have had to have been much closer to the proto-Earth in its oxygen isotopic composition than the aubrites. This is not impossible, but we would argue that it is unlikely. Our results are consistent with high energy impact simulations [2, 3], which indicate a limited differential impactor component in the Moon compared to the Earth. However, if total oxygen isotopic equilibration took place in the aftermath of the giant impact, as indicated by the "synestia" model [12, 13], then the 3 to 4 ppm Earth-Moon $\Delta^{17}\text{O}$ difference requires a post-impact explanation.

Differential, post-impact, additions to the Earth and Moon: Highly siderophile element (HSE) data indicate that following the giant impact, both the Earth and Moon received an input of chondritic material, generally referred to as the late veneer [20]. However, the amounts accreted by the Earth and Moon were very different, being ~ 0.5 wt. % of the terrestrial mass and ~ 0.02 wt. % of the lunar mass, respectively [20]. This may reflect the involvement of a limited number of larger asteroids, which impacted Earth [21].

If the average lunar $\Delta^{17}\text{O}$ value is taken as representative of the post-giant impact, pre-late veneer, terrestrial composition ($\Delta^{17}\text{O} = 10 \pm 2$ ppm), the effects of adding to it various chondritic components can be assessed [15]. This analysis indicates that enstatite chondrites were likely to have been the major constituent of the late veneer, as is also shown by the results of Ru isotope analysis [22]. However, a subordinate carbonaceous chondrite (CC) component is required to explain the 4 ppm offset between terrestrial and lunar rocks revealed by our data [15].

At present, there is little consensus concerning the amount of water present in the Earth, with estimates varying between about 2 and 12 global ocean units [15, 23, 24]. In terms of hydrated CCs, both CMs and the ungrouped CC Tagish Lake have the potential to explain the 4 ppm $\Delta^{17}\text{O}$ offset between terrestrial basalts and lunar whole-rocks and also supply a proportion of Earth's water inventory.

A late veneer composition consisting of approximately 20% CM and 80% enstatite chondrite best fits the $\Delta^{17}\text{O}$ and Ru isotope constraints. However, this would provide only about 0.7 of a global ocean unit and, based on the most conservative estimates [23], represents only about 30 % of the Earth's water budget. If higher global water estimates are realistic [24], then the late veneer, at best, delivered only about 5 % of our planet's water. CV3 chondrites, which are essentially dry, would equally fulfil the $\Delta^{17}\text{O}$ constraints set by our study, but provide even less water [15].

A late veneer explanation for the 3 to 4 ppm $\Delta^{17}\text{O}$ Earth-Moon difference implies that a large fraction of the Earth's water was delivered earlier than the giant impact event. Terrestrial hydration would have been synchronous with the main phase of Earth's accretion and not the result of a late-stage delivery of water from the outer Solar System [25]. The possibility that oceans were already present on Earth at the time of the giant impact [26] is consistent with our data.

References: [1] Canup R. M. and Asphaug E (2001) *Nature* 412, 708-712. [2] Čuk M. and Stewart S. T. (2012) *Science* 338, 1047-1052. [3] Canup R. M. (2012) *Science* 338, 1052-1055. [4] Herwartz D. et al., (2014) *Science* 344, 1146-1150. [5] Young E. D. et al., (2016) *Science* 351, 493-496. [6] Wiechert U. et al., (2001) *Science* 294, 345-348. [7] Spicuzza M. L. et al., (2007) *Earth Planet. Sci. Lett.* 253, 254-265. [8] Hallis L. J. et al., (2010) *Geochim. Cosmochim. Acta* 74, 6885-6899. [9] Armytage R. M. G. et al., (2012) *Geochim. Cosmochim. Acta* 77, 504-524. [10] Zhang J. et al., (2012) *Nature Geosci.* 5, 251-255. [11] Dauphas N., et al., (2014) *Phil. Trans. Roy. Soc. Lond. A*. **372**, 20130244. [12] Lock S. J. and Stewart S. T. (2017). *JGR*, 122, 950-982. [13] Lock S. J. et al., (2018) *JGR*. DOI: 10.1002/2017JE005333. [14] Dauphas N. (2017) *Nature* 541, 521-524. [15] Greenwood et al., (2018) *Science Advances* 4, eaao5928 DOI: 10.1126/sciadv.aao592 [16] Starkey N. A. et al., (2016) *Geochim. Cosmochim. Acta* 176, 227-238. [17] Wade J. and Wood B. J. (2016). *Earth Planet. Sci. Lett.* 442, 186-193. [18] Barrat J-A et al., (2016) *Geochim. Cosmochim. Acta* 192, 29-48. [19] Reufer A. et al., (2012) *Icarus* 221, 296-299. [20] Walker R. J. et al., (2015) *Chem. Geol.* 411, 125-142. [21] Bottke W. F. et al., (2010) *Science* 330, 1527-1530. [22] Fischer-Gödde M. and Kleine T. (2017) *Nature* 541, 525-527. [23] Halliday A. N. (2013), *Geochim. Cosmochim. Acta* 105, 146-171. [24] Marty B. (2012) *Earth Planet. Sci. Lett.* 313-314, 56-66. [25] Albarède F. (2009) *Nature* 461, 1227-1233. [26] Genda H. and Abe Y. (2005) *Nature* 433, 842-844.

TEAMINDUS: COMMERCIAL LUNAR EXPLORATION MISSIONS AND FUTURE TECHNOLOGIES

N. S. Hegde^{1,2}, K. Thyagarajan,^{1,2} and A. Kothandhapani¹, ¹Axiom Research Labs Private Limited (#9, Jakkur Main Road, Bangalore – 560076, India adithya.pani@teamindus.in), ²Formerly Indian Space Research Organization

Introduction: Commercial industry has been building capacity in planetary exploration vehicles, stemming from the impetus of the global lunar science community [1].

TeamIndus' Lunar Logistics vision includes multiple lunar missions over the coming years to meet requirements of science, commercial and efforts towards building readiness for crewed missions to Mars in the global exploration roadmap.

Lunar Technologies: TeamIndus has developed various technologies towards lowering the access barrier to the lunar surface. These include: (1) Spacecraft structures & mechanisms for landing, (2) Descent Guidance, navigation and control, (3) Vision-based approach & terminal guidance for precision soft-landing; (4) Wheeled microrobots for lunar surface exploration, (5) Absolute navigation for lunar surface rovers and (6) Modular compact electronics packages to support observation platforms and scientific instrumentation. Each of these capabilities contributes towards the lunar vision from TeamIndus.

Lunar Mission-1 (LM-1): The first mission is slated for launch in 2019, with a net landed payload capacity of 50kg. The prime objective is to demonstrate autonomous precision lunar landing, and a Surface Exploration Rover - to collect data on the vicinity of the landing site. The landing site selected (29.52N, 25.68W) is in the Mare Imbrium basin, near Annegrit Crater, which is a regolith plain, with average surface slopes less than 3° and clear regions devoid of craters greater than 500m diameter.

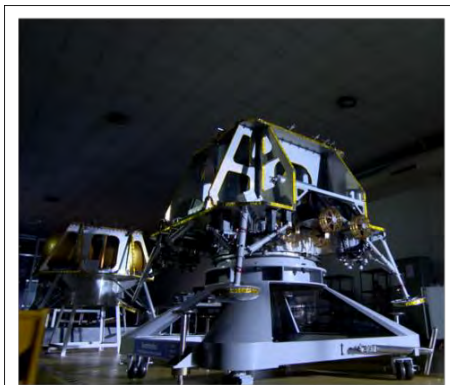


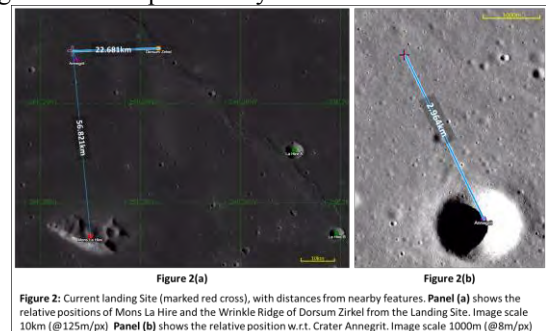
Fig-1: (Foreground) TeamIndus Lunar Lander (HHK-1) PFM at AxiomLabs integration facility, (background) Lunar Lander SQM

Lunar Lander: The lander for LM-1, designated HHK-1, has completed qualification. Landing capabilities are targeted to be at par with Chang'e-3 [3] with landing accuracy targeted to be <100m. The primary payloads on HHK-1 include: (1) ECA Lunar Rover developed by TeamIndus, (2) SORATO Lunar

Rover developed by ispace inc., (3) LUCI – Lunar Ultraviolet Cosmic Imager developed jointly by Indian Institute of Astrophysics and TeamIndus, and (4) MoonLIGHT-2, a laser retroreflector developed by Laboratori Nazionali di Frascati.

Lunar Rover: ECA-1, is a 4-wheeled micro-class exploration rover with onboard stereo-vision cameras and safeguarded autonomy software to enable reliable traverse, navigation and geo-referencing of lunar surface observations [4]. Control of the Rover from Earth is supported by a Lander communication relay which enables a traverse range of up to 500m from the Lander.

Lunar surface experiments: Six 350g scientific experiment packages designed by university teams, engineered and qualified by TeamIndus.



Enabling Technologies: In the roadmap for a sustainable lunar economy, TeamIndus is also involved in research to further the current state-of-art for technologies that can enable future missions to do more than currently possible. These include: (1) Lunar night survival [4], (2) Surface and orbital data relays, (3) Lander reusability, (4) Sample collection and encapsulation, (5) Lunar ascent, and (6) Autonomous docking.

Follow-up Missions (LM-2 and beyond): The LM-2 mission greatly re-uses technologies developed in the first mission, hence providing reliability and repeatability for scientists, commercial prospectors and financial stakeholders alike. The next-generation versions of the Lunar Lander are being developed to deliver up to 1000kg of payload to the lunar surface with a landing accuracy of $\pm 50\text{m}$ [2], thus opening up access to the challenging areas of interest (Lunar PSRs, Caves and poles) on the Moon. Technology demonstrators for non-radioactive lunar night survival and sample collection are the core technology focus areas in LM-2, apart from an increased payload capacity of 150kg to the surface.

References:

[1] NASA SServi (2016) *SServi Year 3 Report*. [2] Carson J. M. et al (2016) *AIAA Guidance, Navigation, and Control Conference, AIAA SciTech Forum, (AIAA 2016-0100)*. [3] Li, Shuang et al (2016) *Journal of Spacecraft and Rockets, Vol. 53, No. 2, pp. 258-277*. [4] Liu Zhao Q. et al (2015) *Sci. China Phys. Mech. Astron* 58:1. [5] Whitley R., Landgraf M. et al (2017) *GLEX 2017, GLEX-2017-3.2A.1*.

THE POTENTIAL LUNA-GLOB LANDING SITE: CONTRIBUTIONS OF LUNAR BASIN EJECTA MATERIALS. H. Hiesinger¹, M. A. Ivanov^{1,2}, J. H. Pasckert¹, C. H. van der Bogert¹, J. W. Head³.

¹Westfälische Wilhelms-Universität Münster, Germany, (Hiesinger@uni-muenster.de), ²Vernadsky Institute, RAS, Russia, ³Brown University, Providence, USA.

Introduction: The potential landing site of the Russian Luna-Glob (LG) mission is situated near the rim of the South Pole-Aitken (SPA) basin [1,2]. SPA is the main source of materials that constitute the megaregolith [3,4] of the potential landing area. At the landing site, mostly ancient terrains of pre-Nectarian and Nectarian ages are exposed [1]. The formation of pre-Nectarian stratigraphic units, in particular, is predominantly related to the emplacement of ejecta from SPA although ejecta from distant post-SPA basins [5-8], also contributed to the regolith formation at the LG landing zone. We assess the potential contributions of individual lunar basins to the regolith that may be encountered at the landing site in order to facilitate interpretation of the results of the LG in-situ analyses.

Modeling radial variations in ejecta thickness: In the past, numerous models of material transport and ejecta emplacement have been developed [9-16] (Fig. 1). The model of [15] is supported by topographic observations of the youngest and best-preserved lunar basin, Orientale. The model is constrained by the estimated ejecta thickness at the Cordillera rim, whereas for models of other basins, ejecta thickness estimates can be difficult to individually corroborate, potentially biasing the estimates of the ejecta radial thickness. Thus, in our study we applied the theoretical model of [13], which relates the ejecta thickness, T to the distance from the impact point, r and the radius of the crater transient cavity R by following equation:

$$T = 0.0078 \cdot R \cdot (r/R)^{-2.61}$$

We emphasize that all ejecta emplacement models do not account for the separation of the ejecta curtain into individual rays and treat the emplaced ejecta as a contiguous blanket. Consequently, model ejecta thicknesses tend to be overestimated.

Model thickness estimates for the LG landing zone: We applied the model of [17] to assess the transport and possible contributions of materials from several major remote basins to the landing zone. In particular, we constructed a $1 \times 1^\circ$ grid for the southern sub-polar region (southward of 60°S). For each grid point, we calculated the thickness of materials contributed by a specific lunar basin [18], applying the model developed by [13].

As part of our investigation of the variation of the basin ejecta thicknesses [17-20], we also considered the mixing ratio [12] of local and remote materials brought to the study area by large impacts. This is useful to estimate the depth to which the ejecta affect the original material upon emplacement. Unfortunately, because the mixing ratio is poorly constrained, its ap-

plication sometimes provides unrealistic results. For example, trying to estimate the depth of mixing for the SPA basin, we derived mixing depths as large as ~ 50 km, thus, being about six times larger than the estimated thickness of the basin ejecta. Consequently, we did not use the mixing ratio to determine the depth of mixing. Instead, we simply calculated the fractions of the materials brought to the landing site based on their respective model thicknesses. We grouped the basins according to their stratigraphic position [4] and estimated fractions of materials delivered to the Luna-Glob landing zone by the SPA basin and by the pre-Nectarian, Nectarian, and Imbrian basins separately.

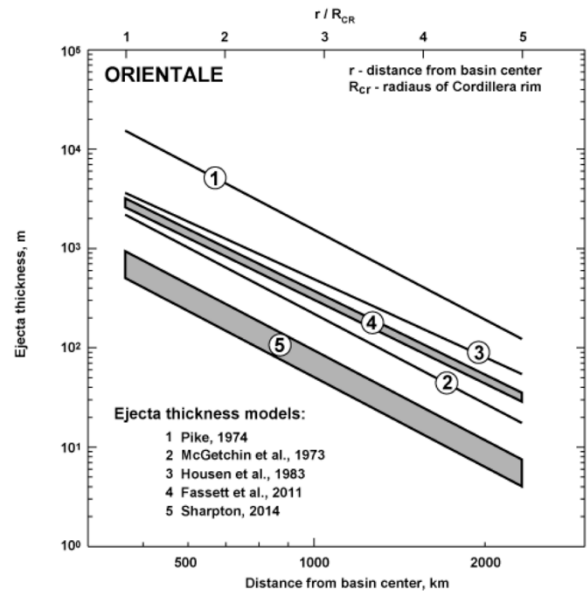


Fig. 1: Radial ejecta thickness of the Orientale basin according to different ejecta emplacement models [21].

Results and discussion: The results of our model show that the major contributor of materials to the LG landing zone is the SPA basin (Fig. 2). Near the rim of the basin transient cavity, the thickness of the ejecta is estimated to be ~ 8.1 km.

However, following a power law, the model thickness rapidly decreases away from the basin rim, resulting in an ejecta thickness of about 5.5 km at the southeast corner of the LG landing zone (the closest to the SPA) and a thickness of ~ 1.8 km at the northwest corner of the LG landing zone (most distant to SPA). We calculated a mean model thickness of the SPA ejecta within the Luna-Glob area of ~ 3.2 km, which constitutes $\sim 96\%$ of the total thickness of ejecta of all lunar basins in this region. The SPA basin is the oldest preserved lunar basin [4,22] and, thus, its ejecta likely

forms the stratigraphic base of basin ejecta deposits in the study area.

Compared to SPA, all pre-Nectarian basins have added only a small fraction of $\sim 3.6\%$, to the total thickness of basin ejecta within the Luna-Glob landing zone. Among pre-Nectarian basins, Australe (Fig. 2) appears as a particularly important source of materials. In the eastern part of the landing zone, the model ejecta blanket of Australe can be ~ 130 - 150 m thick; the mean model thickness of the Australe ejecta within the landing zone is ~ 70 m. Compared to the Australe contribution in the landing zone, the mean model ejecta thickness of other pre-Nectarian basins is a few meters at most.

According to our calculations, both Nectarian and Imbrian basins (Fig. 2) have delivered only negligible amounts (a few tens of meters) of materials to the Luna-Glob landing region, specifically when compared to the thickness of the SPA ejecta (several kilometers). Among Nectarian basins, Serenitatis and Nectaris are the most important sources of remote materials in the Luna-Glob landing zone. Although the Imbrian-age Schrödinger basin is the closest to the landing zone, we estimated its mean model thickness of ejecta to be less than one meter. According to our calculations, the main Imbrian contributor of foreign ejecta material to the landing zone is the Imbrium basin itself.

Not taking into account possible ejecta mixing, we propose that in the landing zone ejecta materials of

post-SPA basins form the upper portion of the composite layer of basins ejecta. However, gardening by subsequent impact craters, will locally affect the regional stratigraphy of basin ejecta. Thus, more detailed analyses of the local geology are needed to investigate the most probable sources of material at any specific landing site.

Acknowledgements: The work was supported by DFG grant HI 1410\12-1 and RSF grant № 17-17-01149 to MAI.

References: [1] Wilhelms et al., USGS Map I-1192, 1979. [2] Garrick-Bethell and Zuber, *Icarus*, 204, 399, 2009. [3] Moore et al., *Proc. LPSC*, 5, 71, 1974. [4] Wilhelms, USGS Spec Pap 1348, 1987. [5] Arvidson et al., *The Moon*, 13, 67, 1975. [6] Head, *The Moon*, 12, 299, 1975. [7] Haskin et al., *MPS*, 33, 959, 1998. [8] Wieczorek and Zuber, *JGR*, 106, 27853, 2001. [9] McGetchin et al., *EPSL*, 20, 226, 1973. [10] Pike, *EPSL*, 23, 265, 1974. [11] Oberbeck et al., *Proc. LPSC*, 5, 111, 1974. [12] Oberbeck, *Rev. GSP*, 13, 337, 1975. [13] Housen et al., *JGR*, 88, 2485, 1983. [14] Haskin et al., *MPS*, 38, 13, 2003. [15] Fassett et al., *GRL*, 38, L17201, 2011. [16] Sharpton, *JGR*, 119, 154, 2014. [17] Petro and Pieters, *MPS*, 43, 1517, 2008. [18] Spudis P.D. *The Geology of Multi-ring Basins*, Cambridge UP, 1993. [19] Petro and Pieters, *JGR*, 109, E06004, 2004. [20] Petro and Pieters, *JGR*, 111, E09005, 2006. [21] Ivanov et al., *LPSC*, 2018. [22] Hiesinger et al., *LPSC* 43, 2863, 2012.

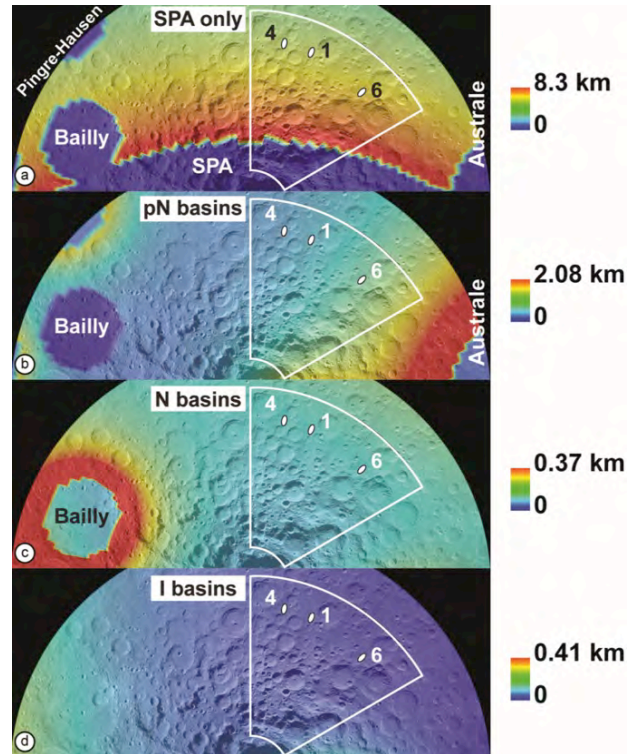


Fig. 2: The model estimates of the thicknesses of lunar basin ejecta in the LG landing zone (white polygon) with potential landing ellipses (white numbers) [21].

Lunar Science with HERACLES. Victoria Hipkin¹, Junichi Haruyama², Masanao Abe², Yuzuru Karouji², Makiko Ohtake², M. Landgraf³, James Carpenter³, and, S. DeMey³, ¹Canadian Space Agency, 6767 Route de l'Aéroport, St Hubert, QC, J3Y 8Y9, Canada (Victoria.Hipkin@Canada.ca); ²Japan Aerospace Exploration Agency, 3-1-1 Yoshinodai, Chuo-ku, Sagami-hara-shi, Kanagawa 252-5210, Japan; ³ESA/ESTEC, Postbus 299, 2201 AZ Noordwijk, 2201 The Netherlands.

Introduction: ESA, JAXA and CSA are exploring common interests in human lunar exploration, which is one of the four cornerstones of the European Exploration Envelope Programme. It is currently a shared understanding that the most affordable approach to the development of a human lunar exploration architecture is the flight-demonstration of key components of lunar vehicles (lander, rover and ascent vehicle) through a sub-scale demonstration mission, launching in the mid-2020's timeframe. Initiated by ESA as the Human-Enabled Robotic Architecture and Capability for Lunar Exploration and Science (HERACLES), advanced studies for this mission concept are being undertaken in 2018 and 2019 in a collaborative framework with ESA in the coordination role and undertaking study of the ascent module, JAXA undertaking study of the lander, and CSA, study of the rover element.

Scientific knowledge gain is recognised by the HERACLES partner agencies as a significant socio-economic benefit that can be enabled by a human lunar exploration architecture. While the primary objective of HERACLES is to demonstrate key precursor technologies, its initial surface operations scenario builds on the international science community motivation for lunar sample return [1][2] and involves landing at a site of high scientific interest and return of lunar samples of high scientific value before conducting a long distance traverse that provides further opportunities for science and exploration. Science planning for the HERACLES mission is co-led, with a multi-agency HERACLES Science Working Group responsible for developing a mission science management plan to describe science team and science payload selection processes, and data and sample policies.

The HERACLES Design Reference Mission: In the initial phase of mission planning, a HERACLES study team developed a nominal scenario with Schrödinger basin as the reference landing site, with a 70 day surface sample return mission, followed by a 1 year traverse encompassing one or more additional potential human exploration landing sites in the south pole region [3]. The reference for returned sample mass is 25kg, including container. A common reference set of mission science objectives (Table 1) was further developed by a Science Working Group in 2017, based on previous studies and agencies' consultations, and responding to the themes of the ISECG Science White Paper [4]. Cold-trapped volatiles are not included, as though these are a high scientific priority and of interest for In Situ Resource Utilisation, it was determined that a

cryogenic sample return was beyond the scope of this demonstration mission (however the technical feasibility still exists). The reference science objectives have been used, with the help of a Canadian science study team, to provide a strawman science payload (imaging, elemental composition, mineralogy, sub-surface structure, radiation sensors, possible deployment of a small payload (<1kg) to the surface)) to assess the feasibility of payload accommodation within the current HERACLES rover concept. The capability to acquire fresh rock samples has been included in the reference, but at this time a drill capability has not.

Table 1: Initial HERACLES Science Objectives (unprioritised)

Responding to ISECG Science Theme: Understanding our place in the universe	
S1	Constrain the impact chronology of the Earth-Moon system and test the cataclysm hypotheses by determining absolute ages for major impact events based on surface geological features
S2	Understand the Earth-moon impact flux by determining the abundance, composition and isotopic nature of impactor remnants in regoliths of various ages
S3	Enhance understanding of dynamic processes on airless bodies by measuring the processes of space weathering, solar wind and magnetosphere interactions and the exosphere
S4	Enhance understanding of the origin and evolution of the moon by determination of structural layering of the highland crust and mantle through in situ geophysical networks, and determination of compositional layering and solidification age through sample return
S5	Understand volcanic processes on the moon through obtaining eruption information, composition and age of silicic domes, scoria cones and holes and youngest and oldest mare material.
S6	Enhance understanding of cratering processes on the moon through study of impacts of different size, age and complexity
S7	Understand the origins of lunar volatiles trapped in ancient rock
S8	Understand solar and galactic evolution by measuring the abundance of cosmic ray generated isotopes in minerals of various exposure ages
S9	Contribute to understanding the origin of life and prebiotic chemistry through constraining Solar System Conditions when life first arose
Responding to ISECG Theme: Living and Working in Space	
L1	Determine the physical and chemical properties of dust and its toxicity
L2	Determine the composition and abundance of minerals in regolith as resources
L3	Identify the effects of exposure to the lunar radiation environment on DNA stability, mutation rates of exploration relevant microorganisms, including human cell analogues

Prioritisation of Science Investigations and Landing Site Selection: Further work is required to refine the HERACLES science scenario. The community is invited to engage in the next step of transforming the reference scenario into prioritised investigations (in-situ instrumentation and analysis of returned samples) and provide input to landing site selection.

The HERACLES partner agencies are preparing a process by which the respective science communities can engage and prepare their contributions. The next step is the creation of an international HERACLES Science Definition Team (HSDT) who will be tasked to generate a prioritised list of investigations, and make recommendations with regard to landing site selection. Sites other than Schrödinger may be considered, subject to engineering constraints and additional exploration objectives. The HSDT report will then be used in the preparation of opportunities for science team membership and science instrument proposals, should the mission be approved for launch.

NASA and Russia are currently participating as Observers in the HERACLES project. Observer status is available for agencies with common interests, with associated representation planned on the HSDT.

Summary: The HERACLES mission concept seeks to return samples from the lunar south polar region, as a potential robotic precursor mission in preparation for the return of humans to the lunar surface. Advanced studies are underway by partner agencies ESA, JAXA and CSA, and community participation is sought in further mission definition to ensure valuable science return.

References: [1] National Research Council, The Scientific Context for Exploration of the Moon, 2007 [2] Lunar Exploration Analysis Group, The Lunar Exploration Roadmap: Exploring the Moon in the 21st Century: Themes, Goals, Objectives, Investigations, and Priorities, 2016. [3] R.J. Whitley et al., Global Exploration Roadmap Derived Concept for Human Exploration of the Moon, GLEX-2017-3.2A.1, [4] International Science Exploration Coordination Group, Scientific opportunities enabled by human exploration beyond Low-Earth-Orbit (full) – An ISECG Science White Paper, https://www.globalspaceexploration.org/wordpress/wp-content/isecg/ISECG%20SWP_FINAL-web_2017-12.pdf, 2017

THE DUST ENVIRONMENT OF THE MOON. M. Horányi^{1,2}, J. R. Szalay³, X. Wang^{1,2} (¹Department of Physics and Laboratory for Atmospheric and Space Physics, U. of Colorado, CO, USA; ²NASA-SSERVI: Institute for Modeling Plasmas, Atmospheres, and Cosmic Dust (IMPACT), ³Department of Astrophysical Sciences, Princeton University, Princeton, NJ 08540, USA; e-mails: horanyi@colorado.edu; Xu.Wang@colorado.edu; and jszalay@princeton.edu)

Introduction: The Moon, as all other airless bodies in the solar system, is continually bombarded by interplanetary dust particles, and is also immersed in the solar wind plasma flow and UV radiation. There are several controversial observations from the Apollo era that can now be revisited due to new spacecraft data, and recent dedicated laboratory experiments. Hypervelocity dust impacts generate secondary dust ejecta particles, neutral and ionized gases, sustaining the recently discovered, permanently present dust cloud engulfing the moon, and contributing to the production of the dilute lunar atmosphere and ionosphere. UV and plasma exposure results in the electrostatic charging of the lunar regolith, that can lead to the mobilization, transport, and large-scale redistribution of the lunar fines. We focus on the recent results of in situ observations, as well as the latest laboratory results, a combination which resulted in a much improved understanding of the lunar dust environment.

Dust measurements in space: The Lunar Dust Experiment (LDEX) on board the Lunar Atmosphere and Dust Environment Explorer mission was designed to make in situ dust measurements while orbiting the Moon [1, 2]. Particles with radii $a \geq 0.3 \mu\text{m}$ were detected as impacts [3]. LDEX was also capable of measuring the collective signal generated from dust impacts with sizes below its single-particle detection threshold. While to date there is no evidence of high-altitude lofted dust due to electrostatic effects over the lunar surface [4], there is strong supporting evidence from recent laboratory experiments that dust charging can lead to significant effects near the surface of an airless planetary body.

Laboratory experiments: New laboratory experiments shed light on dust charging and transport that have been suggested to explain a variety of unusual phenomena on the surfaces of airless planetary bodies. Lofted large aggregates and surface mobilization are related to many space observations. New experiments have successfully shown that the emission and re-absorption of photoelectrons and/or secondary electrons at the walls of micro-cavities formed between neighboring dust particles below the surface are responsible for generating unexpectedly large negative charges and intense particle-particle repulsive forces to mobilize and lift off dust particles [5, 6].

Summary and Conclusions: This talk will summarize the LADEE/LDEX results identifying the permanently present and intermittently enhanced lunar dust ejecta cloud that is sustained by the continual bombardment by interplanetary dust particles originating from the sporadic background population, as well as the meteoroid streams [7]. The measurements indicate no electrostatically lofted high-altitude dust density enhancements over the terminator regions, as was anticipated due to possible dust charging and strong electric fields in this region. However, there is strong supporting evidence for efficient dust mobilization and transport near the surface, due to electrostatic effects a process that is likely to be responsible for the observed dust ponding on asteroids [8], and its full effect is yet to be investigated for the lunar surface.

References: [1] R. C. Elphic, et al. (2014) *Space Science Reviews*, 2014; [2] M. Horányi, et al. (2014) *Space Science Reviews*, vol. 185, pp. 93–113; [3] M. Horányi, et al., (2015) *Nature*, vol. 522, pp. 324–326; [4] J. R. Szalay and M. Horányi (2015) *Geophys. Res. Lett.*, vol. 42, no. 13, pp. 5141–5146; [5] X. Wang, et al., (2016) *Geophys. Res. Lett.*, no. DOI: 10.1002/2016GL069491; [6] J. Schwan, et al., (2017) *Geophys. Res. Lett.*, vol. 44, pp. 3059–3065; [7] Szalay et al., (2018) *MNRAS* 474, 4225–4231; [8] J. E. Colwell, et al., (2005), *Icarus*, vol. 175, pp. 159–169.

CONSTRAINTS ON LUNAR ERUPTION STYLES FROM THE MINERALOGY OF SMALL LUNAR PYROCLASTIC DEPOSITS. B. Horgan¹, L. Gaddis², M. McBride¹, K. Bennett³, J. Stopar⁴, S. Lawrence⁵.

¹Purdue University (briony@purdue.edu), ²USGS Astrogeology Science Center, ³Northern Arizona University, ⁴Lunar and Planetary Institute, ⁵NASA Johnson Space Center.

Introduction: More than 100 pyroclastic deposits have been identified across the lunar surface [1,2]. Many small lunar pyroclastic deposits (<2000 km²) are associated with vents resembling shallow, non-impact craters or irregular depressions, supporting a volcanic origin [1]. The explosive eruptions that emplaced lunar pyroclastic deposits are driven by magmatic volatiles [3], so these deposits can provide essential constraints on the volatile content and composition of lunar magmas [4-6]. Thus, the compositions and distributions of pyroclastics contribute information on the early lunar interior [7,8] and the presence of possible resources [9].

Models investigating the eruption mechanics of lunar pyroclastic deposits has suggested that “local” deposits (<1000 km² [1]) are primarily emplaced via low effusion rate Vulcanian eruptions. Volatiles slowly build up under a cooled cap, and periodically release the pressure in one or more violent eruptions excavating significant surrounding country rock [10,11]. In contrast, “regional” deposits (>1000 km²) are hypothesized to be emplaced by more energetic and sustained Hawaiian-style fire fountaining, resulting in ballistically emplaced glass-rich deposits [3,12]. Previous studies have shown that glass is present within deposits at all sizes [9, 13-15], but none have specifically demonstrated explicitly whether or not the smaller deposits are consistent with Vulcanian eruptions.

Here we present a synthesis of our recent work on the mineralogy of a subset of small lunar pyroclastic deposits in an effort to constrain the eruption styles by which they were emplaced. All mineralogy is derived from analysis of Moon Mineralogy Mapper (M³) visible/near-infrared (VNIR; 0.35-3.0 μ m) images [16], which have a resolution of 140-280 m/pixel in the global mapping mode. Distributions of Fe-bearing minerals (pyroxenes, olivines, and glass) were determined using the techniques of [17].

Alphonsus crater: Alphonsus is a pre-Imbrian floor fractured crater located in the highlands east of Mare Nubium. The 12 pyroclastic deposits of Alphonsus [18] are located within or adjacent to several floor fractures, indicating that fractures likely provided conduits for volatile accumulation and the subsequent pyroclastic eruption [19,20]. These deposits have been previously modeled as most likely emplaced via a Vulcanian eruption [11,20]. The floor of the crater is enriched in orthopyroxene, as clearly shown in the ejecta of recent impact craters, and orthopyroxene is also detected in discontinuous haloes surrounding the pyroclastic deposits. Interior to these haloes, the

pyroclastic deposits exhibit spectra consistent with a mixture of glass and orthopyroxene, with some local concentrations of glass mixed with clinopyroxene near the vents. These observations support the prediction from models that these deposits were emplaced during a Vulcanian-style eruption. The wide distribution of crater-floor-like orthopyroxene away from the vent is consistent with an initial energetic explosion, followed by fire-fountaining to form glass-rich deposits. The near-vent clinopyroxene signatures suggest longer cooling times in especially thick pyroclastic deposits, thin lava flows, or fragmented basalt from within the source dike [19].

Oppenheimer crater: Oppenheimer is a Pre-Nectarian floor fractured crater located within the South Pole-Aitken Basin. The floor fractures are associated with 15 individual pyroclastic deposits ~200-1500 km² in size [21] that have been estimated to be ~3.98 Ga in age [22]. Previous models and spectral analysis of the Oppenheimer deposits suggested that their eruptions should also have originated from a Vulcanian-style eruption [20,23]. The floor of the crater exhibits spectra consistent with an intermediate pyroxene, which sharply contrasts with all 15 pyroclastic deposits [24]. The small deposits appear to be dominated by glass; however, some of the medium and large deposits also exhibit spectra consistent with clinopyroxene and clinopyroxene-glass mixtures. Given that no country rock has been clearly detected in these deposits, this suggests that they were likely emplaced by more sustained Strombolian-style or fire fountaining eruptions. The initial eruptions could have been Vulcanian in style, but this must have been followed by more continuous eruptions in all of the deposits. Like at Alphonsus, the presence of CPX near the vent could be due to localized lava flows or fragmentation of cooled magma in the source dike [24]. Enhanced volatile content of the Oppenheimer magmas could contribute to the sustained, high effusion rate eruption that formed the deposits

Volcanic complexes: The Marius Hills volcanic complex is a collection of domes and superimposed smaller cones located within Oceanus Procellarum [25, 26]. Detailed analysis of the Marius Hills and possible relationships to the nearby Aristarchus regional pyroclastic deposit is presented in [27]. The Marius Hills are interpreted as mafic lava domes and volatile-rich cinder cone eruptions. This is consistent with the mineralogy from M³, which shows orthopyroxene signatures over the domes and glass signatures over the cinder cones [27].

The Compton-Belkovich volcanic complex is located in the highlands of the northern farside, and is a collection of domes and plateaus surrounding a central depression. The complex has been interpreted as highly viscous and silicic lava flows and caldera collapse [28]. Pyroclastic deposits may have been emplaced in association with caldera collapse and during later resurgence [29]. Previous analysis of the region showed a strong hydration signature over the volcanic complex [30], which we find is closely associated with weak 1 and 2 μm absorption bands consistent with glass. This detection is the only clear M^3 spectral signature in the volcanic complex, but is potentially consistent with silicic lava flows, since Fe-poor felsic minerals are usually not detectable in VNIR spectra.

Synthesis: Our analyses to date shows that small lunar pyroclastic deposits are mineralogically diverse, consistent with past studies [13-15]. Our detailed mineralogical analysis reveals the spatial distribution of glass, country rock, and crystalline igneous components in the deposits, which allows us to place more rigorous constraints on their eruption styles.

Small vs. large deposits: We have focused here on smaller, typically “local” lunar pyroclastic deposits. However, many of these smaller deposits are quite large and probably fall on a nearly continuous size spectrum with the larger deposits. For example, Oppenheimer U is 1500 km^2 in area [1], which is within the previously cited range for “regional” lunar pyroclastic deposits, but the deposit is clearly related to the other “local” deposits within Oppenheimer. In terms of mineralogy, the glass- and CPX-rich deposits at Oppenheimer U also appear to be intermediate between the smaller deposits, which exhibit a diverse range of both crystalline and glassy mineralogies, and the regional deposits, which are glass-rich [9,17]. Thus, this suggests that the simplistic “regional” vs. “local” designations do not reflect the range and diversity of lunar explosive volcanic eruption styles.

Relationship to effusive eruptions: In both the pyroclastic deposits of Oppenheimer and Alphonsus as well as the volcanic complexes at Marius Hills and Compton-Belkovich, spectral evidence is consistent with a combination of effusive and explosive eruptions. This complex volcanic history is consistent with typical magma evolution on the Earth, where largely explosive eruptions can be followed by effusive lavas after volatiles are largely depleted from the magma source, or where resurgence after a largely effusive eruption can lead to volatile enrichment and late-stage pyroclastic activity. Thus, the fact that both explosive and effusive deposits are found at many of these locations suggests that more detailed study of the deposits could help us understand the volatile evolution of lunar magmas.

Controls on eruption style: The diversity of mineralogies that we have detected in lunar pyroclastic deposits suggests that lunar volcanic eruption styles

are also diverse, including Vulcanian, Strombolian, Hawaiian, cinder cones, and effusive flows. We hypothesize that the diversity we observe can be explained based on source depth, geologic context, and magma composition.

Eruption style is largely determined by volatile content, which on the Moon, is modeled to be greater for magmas sourced from greater depths [31]. Thus, the primary cause of the apparent volatile enrichment in Strombolian or Hawaiian eruptions at Oppenheimer compared to the Vulcanian eruptions at Alphonsus could be a greater source depth at Oppenheimer. Geologic context is also essential, as the highly brecciated subsurface of large impact basins can aid in near-surface sill development, but intracrater dikes are more likely to directly intersect the surface and create a more localized eruption site [20]. Thus, the formation of dispersed pyroclastic deposits in floor fractured craters like Oppenheimer and Alphonsus vs. dense volcanic complexes like Marius Hills or Compton-Belkovich may have been determined by their local geologic context. Lastly, composition also clearly affects eruption style. The relatively expansive pyroclastic deposits at Compton-Belkovich compared to the localized cinder cones at Marius Hills are potentially both consistent with late stage explosive activity from an otherwise volatile-poor magma source, but with significant enhancement of the explosivity at Compton-Belkovich due to the high viscosity of the silicic magmas.

References: [1] Gaddis et al (2003) *Icarus* 161, 262. [2] Gustafson et al (2012) *JGR* 117, E00H25. [3] Wilson & Head (1981) *JGR* 86, 2971-3001. [4] Milliken & Li (2017) *Nat Geosci* 10, 561-565. [5] Heiken et al (1974) *GCA* 38, 1703. [6] Delano (1986) *JGR* 91, D201. [7] Shearer et al (2006) *RMG* 60, 365. [8] Duke et al (2006) *RMG* 60, 597. [9] Hawke et al (1989) *LPSC* 19, 255. [10] Gaddis et al. (2000) *JGR* 105, 4245-4262. [11] Head & Wilson (1979) 5th *LPSC*, 2861-2897. [12] Heiken et al (1974) *GCA* 38, 1703-1718. [13] Besse et al (2014) *JGR* 119, 355-372. [14] Jawin et al (2015) *JGR* 120, 1310-1331. [15] Trang et al (2017) *Icarus* 283, 232-253. [16] Pieters et al (2009) *Curr Sci* 96, 500-505. [17] Horgan et al (2014) *Icarus* 234, 132-154. [18] Gaddis et al (2011) *LPSC* 42, #2691. [19] Gaddis et al (2016) *LPSC* 47, #2065. [20] Jozwiak et al (2015) 248, 424-447. [21] Gaddis et al (2014) *LPSC* 45, #2383. [22] Ivanov et al (2016) *LPSC* 47, #1070. [23] Head et al (2000) *LPSC* 31, #1280. [24] Bennett et al (2016) *Icarus* 273, 296-314. [25] Lawrence et al (2013) *JGR* 118, 615-634. [26] Besse et al (2011) *JGR* 116, E00G13. [27] McBride et al (2018), this volume. [28] Jolliff et al (2011) *Nat Geosci* 4, 566-571. [29] Chauhan et al (2015) *Icarus* 253, 115-129. [30] Bhattacharya et al (2013) *Curr Sci* 105, 685-694. [31] Weitz et al (1999) *JGR* 104, 18933-18956.

STUDYING THE CRATER SIZE-FREQUENCY DISTRIBUTION OF THE APOLLO 12 LANDING SITE. W. Iqbal¹, H. Hiesinger¹, C. H. van der Bogert¹, ¹Institut für Planetologie, Westfälische Wilhelms-Universität, Wilhelm-Klemm-Str. 10, 48149, Münster, Germany, iqbalw@uni-muenster.de

Introduction: Crater size-frequency distribution (CSFD) measurements combined with radiometric and exposure ages of Luna and Apollo samples define the lunar cratering chronology, which is used to derive absolute model ages (AMAs) for geological units across the Moon and throughout the Solar System [e.g., 1-6]. Differing opinions regarding the definition of the chronology curve [3,4] have resulted in various attempts to fit the lunar cratering chronology. Here, we use new lunar datasets from both recent lunar missions and lunar sample analyses to reanalyze the calibration points [7-10].

The Apollo 12 landing site is positioned on a south-southwest oriented ray of Copernicus crater in Mare Cognitum [8,9,11]. Therefore, the samples collected from the landing site provide two important calibration points of the lunar cratering chronology: (1) age of the surface mare basalt, and (2) age of the Copernicus crater via its ray material. We reinvestigated the geology and CSFDs of the Apollo 12 landing site with Lunar Reconnaissance Orbiter Camera (LROC) images and Moon Mineralogy Mapper (M3) spectral data.

The samples collected from the landing site were organized into four groups of basalts: pigeonite basalt (3.15 Ga), ilmenite basalt (3.17 Ga), feldspathic basalt (3.20 Ga), and olivine basalt (3.22 Ga) [6]. Recently, Snape et al. (2016) [7] investigated three Apollo 12 samples: 12039 (pigeonite basalt), 12063 (ilmenite basalt), and 12038 (feldspathic basalt) and determined ages of 3.20 Ga, 3.30 Ga, and 3.28 Ga – a few million years older than the previously determined values, after eliminating the measurement errors related to the Pb isotope concentrations in the lunar samples.

Absolute model ages (AMAs) of geologic units are derived by the lunar cratering chronology; through correlating the radiometric sample ages with the cumulative number of craters ≥ 1 km in diameter; $N(1)$ [2-4,6]. Neukum (1983) [3] initially determined the AMA of the landing site as 3.60 Ga based on CSFD measurements in the area marked in blue in Figure 1. Later, Neukum et al. (2001) [4] calculated an AMA of 3.18 ± 0.10 Ga on a relatively smaller area, around the lunar module. Hiesinger et al. (2012) [8] determined an AMA of 678 Ma for the ray of Copernicus crater adjacent to the landing site.

We used recent high-resolution image data with various illumination geometries, along with topographic and multispectral data to refine our geological understanding of the landing site and to perform new detailed CSFD studies.

Methods: The CSFDs were measured on the LROC Wide Angle (WAC; 100 m/pixel) and Narrow Angle (NAC; 1.1 m/pixel) camera data with inci-

dence angles of 73-75°. ISIS-3 was used to calibrate and map-project the data [12]. The CSFDs around the landing site were measured using the ArcGIS and CraterTools [13]. Obvious secondary crater chains and clusters were avoided; later, a randomness analysis was used to detect potential contamination from unidentified secondary craters. We used the Neukum et al. (2001) [4] lunar production and chronology functions in CraterStats [13-15] to plot the CSFDs. We presented the results in cumulative and relative plots with pseudolog binning [4,15,16], for the direct comparison with the previous studies.

The differences in the geologic units surrounding the landing sites were identified via albedo, elevation, and spectral contrast on LRO WAC and NAC data, the LOLA digital elevation model, and M3 data, respectively. The astronaut traverses and the sample collection sites were remapped on the NAC data (Figure 1). Using NAC data, we defined the homogeneous red areas on the newly identified geologic units in Figure 1. The original Neukum (1983) [3] area was also mapped (in blue) and measured on the WAC mosaic. Finally, we correlated our newly determined CSFD measurements with the updated radiometric ages of the Apollo 12 samples [7].

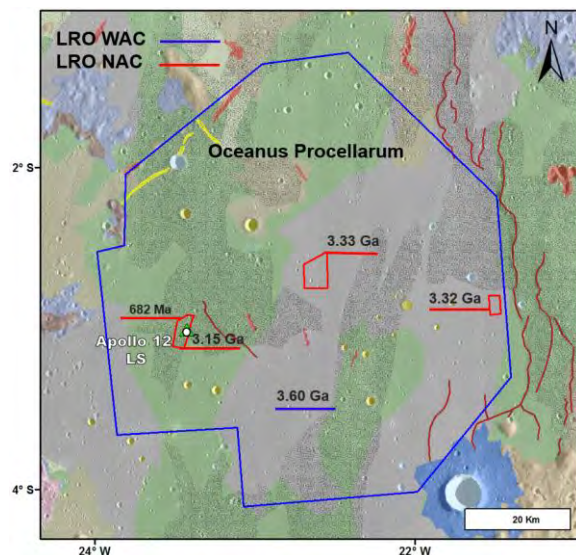


Figure 1. The count areas at the Apollo 12 landing site are marked on our updated geologic map. The blue area was recounted on LROC WAC data after Neukum (1983) for the initial calibration of the lunar chronology. The red areas are new count areas we defined using LRO NAC data.

Results and Discussion: Our newly measured CSFDs resulted in $N(1)$ values of 5.72×10^{-4} and 2.81×10^{-3} , which show two clear AMAs of 682 Ma, representing the AMA of the Copernicus crater ray, and 3.15 Ga, representing the AMA of the underlying mare unit, (Fig. 2). The 3.15 Ga AMA for the mare unit is consistent with the age of the pigeonite basalt samples [6,7]. Hiesinger et al. (2003) [17] determined an AMA of 3.32 Ga for Mare Cognitum from an $N(1)$ value of 3.30×10^{-3} measured on a Lunar Orbiter IV image. Whereas the count areas of [17] were defined on albedo and morphology only, the count area selection for this study was aided by additional Clementine color data. The different selection of the count areas likely contributes to the difference in the AMAs of the basalt units. In their later study of the lunar young craters, Hiesinger et al. (2012) [9] determined an AMA of 678 Ma from an $N(1)$ value of 5.56×10^{-4} for the Copernicus crater ray near the landing site.

The recalculated AMA of Neukum's [3] original area (Fig. 1) determined on the WAC data is 3.60 Ga, whereas the AMAs of the new areas counted on NAC data range from 682 Ma to 3.33 Ga. The results determined on the NAC data are younger than measured on WAC data for Neukum's area, possibly due to the presence of different geologic units in the larger area that influence the resulting AMA. The larger area also contains the rays and secondary chains and clusters from younger craters. Overall, the updated AMAs are consistent with the range of ages of the younger pigeonite (12039) and ilmenite basalt samples [6,7], i.e. 3.15-3.20 Ga and 3.17-3.3 Ga, respectively.

In the future, we will apply the same method of producing a new detailed geological map, comparing it to the sample collection areas, and determining the high resolution CSFDs to investigate the other landing sites. Eventually, these CSFDs will be compared with the updated radiometric ages, to potentially improve the calibration of the lunar chronology.

References: [1] Hartmann, W. K. (1970) *Icarus* 13: 299-301. [2] Neukum, G. et al. (1975) *The Moon* 12, 201-229. [3] Neukum, G. (1983) *Habil. thesis, U. of Munich*. [4] Neukum, G., et al. (2001) *Space Sci. Reviews* 96, 55-86. [5] Robbins, S. J. (2014) *Earth and Planet. Sci. Lett.* 403, 188-198. [6] Stöfler, D., et al. (2006) *Reviews in Mineral. & Geochem.* 60, 519-596. [7] Snape, J. F. (2016) *Earth and Planet. Sci. Lett.* 451, 149-158 [8] Hiesinger, H., et al. (2000) *JGR* 105, 29239-29275. [9] Hiesinger, H., et al. (2012) *JGR* 11, E00H10. [10] Hiesinger, H., et al. (2015) *LPSC* 46, #1834. [11] Team, M. E. (1970) *NASA Report MSC-01855* [12] Anderson et al. (2004) *LPSC* 35, #2039. [13] Kneissl, T., et al. (2011). *Planet. Space Sci* 59, 1243-1254. [14] Michael, G. G., et al. (2016) *Icarus* 277, 279-285. [15] Michael, G. G. et al. (2010) *Earth & Planet. Sci Lett.*

294, 223-229. [16] Group, C. A. T. W., et al. (1979) *Icarus* 37, 467-474 [17] Hiesinger, H., et al. (2003). *JGR* 108, E001985

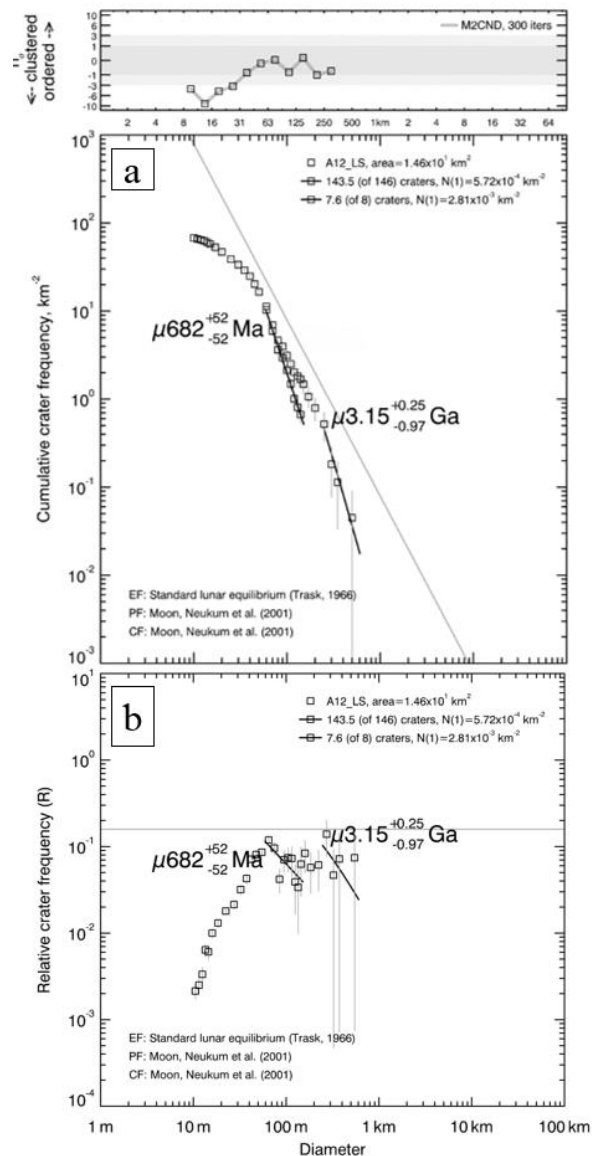


Figure 2. The NAC-scale CSFD measurements around the lunar module at the Apollo 12 landing site show two model ages for the Copernicus ray and the underlying mare unit. The results are shown as (a) cumulative form with cumulative fits for determination of absolute model ages and (b) relative crater frequency plot of the same distributions. The randomness analysis of the count area shows secondary crater contamination below 30 m (panel above). However, our results fit craters greater than 60 m in diameter and, thus, are unaffected by secondary crater contamination.

ACTIVITY REPORT ON THE LANDING SITE AND RETURN SAMPLE OF THE JAPANESE LUNAR SCIENCE COMMUNITY IN HERACLES MISSION. Y. Karouji, M. Abe, J. Haruyama, M. Ohtake, T. Sawada and N. Sato, Japan Aerospace Exploration Agency (JAXA), 3-1-1 Yoshinodai, Chuo-ku, Sagaminara-shi, Kanagawa 252-5210, Japan (karouji.yuzuru@jaxa.jp).

The space agencies of the international Space Exploration Coordination Group (ISECG) are discussing a next step of international partnership of International Space Station (ISS), and how they proceed post-ISS activities, which is proposed in the Global Exploration Roadmap (GER).

Japan Aerospace Exploration Agency (JAXA) is studying a Human-Enhanced Robotic Architecture and Capability for Lunar Exploration and Science (HERACLES) concept that is an international coordination program, which is described in the GER and led by European Space Agency (ESA). The objectives of the HERACLES study is to provide a concept of coordinated precursor architecture for future lunar missions, and set top-level technology requirements as a goal of a robotic precursor mission. Based on previous study, it is decided that the concept of HERACLES focuses on demonstrations of critical technology and risk mitigation for a future human lunar mission. HERACLES mission is going to demonstrate safe vehicle operations in cis-lunar space, in low orbit, during descent, landing, on the surface, during ascent, as well as on the surface in conditions closely representing a human surface mission. Among these architecture, a baseline concept of the HERACLES lander system is composed of a lander module, an ascent module, and a surface rover.

HERACLES mission aims a robotic sample return mission that brings samples back from the lunar surface, and we identified South Pole-Aitken (SPA) basin area near to the south pole as a landing site candidate for future manned landing missions. Exploration and sampling of the lunar material are carried out by the surface rover. After placing a sample container with the collected sample in the ascent module, the ascent module carries the sample container to the Deep Space Gateway which is a concept for a crew-tended cis-lunar space station led by the ISS partners. Then, the sample container is planned to bring back to the Earth by astronaut using crew vehicle.

As an activity of the Science Working Group (SWG), which is one of the subgroups of the HERACLES study team, we are discussing mission objectives, landing areas, requirement for the sample (mass, chemical composition and so on), requirement for in-situ observational instruments and etc.. As a reference mission, which is used for identifying required technology to achieve this type of mission, Schrödinger crater has been used as a landing area. From now on, we are planning to prioritise mission objectives suitable for this mission with landing sites

suggesting that can contribute to the progress of the lunar science by discussing international lunar science community. For this, we are planning to assembling an international science team.

In this presentation, we are going to report outcome of previous activities related to the HERACLES SWG and planned discussion within Japanese lunar science community of study in this SWG.

FUTURE SEISMIC EXPLORATION ON THE MOON: POSSIBLE LAUNCH OPPORTUNITY FROM ASIA. T. Kawamura^{1,2}, P. Lognonné², S. de Raucourt¹, R. Garcia³, J. Zhang⁴, ¹National Astronomical Observatory of Japan (2-12 Hoshigaoka-cho, Mizusawa-ku, Oshu-city, Iwate 023-0861 email: t.kawamura@nao.ac.jp), ²Institut de Physique du Globe de Paris (35 rue Hélène Brion, Case 7071 Lamarck A, 75205 Paris Cedex 13, France email: kawamura@ipgp.fr), ³Institut supérieur de l'aéronautique et de l'espace (ISAE-Supaero), Institute of Geology and Geophysics, Chinese Academy of Sciences

Introduction: Seismic observation is a powerful tool to explore the internal structure of the planet and satellites. For the Moon, Passive Seismic Experiment of Apollo observed the lunar seismic activities with 4 seismic stations and provided about 7 and a half years of seismic data stream on the Moon. Internal structure of the Moon was studied with the data and since 1980's to today and it has been one of the most important data sets to uncover the lunar interior [e.g. 1,2,3,4]. However, since the termination of Apollo observation on September, 1977, no seismic observation was made for the Moon. After decades of seismic investigations on the Moon, there is still remaining questions to be answered and there are strong demands for new seismic observation on the Moon from lunar science community. A selection of science goals of the future observations might be:

- the precise determination of the lunar core mantle boundary depth and a conclusive detection of a possible inner core [5]
- the mapping of the crustal thickness lateral variation and crustal internal layering from joint observations of seismic signals and impact flashes [6, 7]
- Detailed source analysis of the Deep Moon quakes [8]
- Detection of the Lunar normal modes and determination of a much precise lunar mantle model [9]
- Determination of the Lunar micro-seismic noise associated to continuous micro-impacting [10]

Following the termination of the Internal Space Station, international community has started to aim for the Moon as the next step. Various national space agencies started studies for the lunar missions including landing mission. Among these mission, two Asian missions are the two possible candidates to deploy seismometer on the Moon after 50 year from Apollo. These are Japanese Lunar Polar Lander and the other is the Chinese Chang'e. Here we will report the current status of the mission and the strategy to propose seismometers to these launch opportunities. In addition to this, seismic exploration with hard-landing penetrator is now under the selection in Japan. We are planning to have close scientific collaboration with the team which shall be fruitful for other future missions.

Japanese Lunar Polar Lander: Japan Aerospace eXploration Agency (JAXA) has started a study to launch a lunar polar lander which aims to land on the lunar north pole with a lander and a rover. The primary objective of the mission is to search for the lunar ice deposit and study the possibility of in-

situ resource utilization (ISRU). JAXA is currently carrying out conceptual studies to select instruments that's meets the objectives. They will be opening an application for the payloads and we are now carrying out studies to prepare for the application.

We are currently in contact with JAXA to propose two types of seismometers for the mission. The first is a very broad band seismometer developed by Institut de Physique du Globe de Paris (IPGP). While Apollo carried out seismic observation with two types of seismometers with different frequency bands, their frequency bands are limited compared to the state-of-arts seismometer. Lunar seismograms are known to have long coda due to the intense scattering of the regolith layer. It is predicted that at longer wavelength, longer than typical scale of the scatterer, the seismic signals suffer less from the scattering. One of the main reasons for the uncertainties the difficulties in identifying signal arrival times due to the scattering and the long coda. Observation at longer wave length with broad band seismometer such as VBB will significantly improve the effect of the scattering and arrival time readings accordingly. In addition, and because of better performances, they might lead to 10x more detections of quakes and impacts and therefore of several 10th per day [10,11]. Furthermore, observations at longer wavelength will enable us to study wider variety of seismic signals including surface waves and normal modes. Observations of Apollo were limited to body waves due to the limited frequency bands and the sensitivity. Detecting such seismic signals will give additional constraints on the internal structure especially at the deep interior and provides us with better understandings of the Moon. VBB is proposed as a payload on the lander. The seismometer is proposed to be deployed by the lander and carry our continuous monitoring of the lunar seismic event.

The second type of seismometer is a geophone that will be probing the subsurface layer down to few meters to search for underground ice deposits. The mission is planning to have a drilling core to dig the underground ice deposit for further analyses. JAXA is now considering several methods to probe the subsurface layer before drilling and seismic imagery is one of the candidate. The current proposal is to have 3-4 geophones on the rove to establish a micro seismic array. The rover will travel around the lander and as the rover travels, it will stop for observations to study the structure below the rover. Unlike VBB,

the instrument aims to prove the local structure around the lander and the rover in detail.

In addition to the two seismometers we are proposing an active seismic source to do active seismic experiments on the Moon. The seismic source uses an established technique in terrestrial seismology known as ACROSS (Accurately Controlled Routinely Operated Signal System). The seismic source is designed so that it can excite designed seismic signal which we can tune according to the observation target. Such type of seismic source has never been considered for the space use and the feasibility is now under investigation.

Chinese post-Chang'e Missions: No seismometers have been planned in the 4 landing Chang'e missions 4-6, despite an offer of China to CNES to install a VBB on Chang'e 4, which was incompatible with the InSight VBB activities. New perspectives are however foreseen with possible Chinese missions, to be launch in the 2020-2030 decade, which might enable to target seismology as one of the science goals of these missions around 2025. As the expected missions might re-use both the soft-landing technology and the radio-isotopic sources developed during the Chang'e program, these opportunities might allow the deployment of one, possible two VBBs for long term operations. A scientific working group lead by Institut of Geology and Geophysics from CSA and Institut de Physique du Globe de Paris has been initiated, together with several French and Chinese laboratories. Future performance tests could also be envisaged which will use the very low seismic noise of Huazhong University of Science and Technology.

Japanese Hard-Landing Penetrator Mission APPROACH: A hard-landing mission using a penetrator has a great advantage, being lightweight compared to a soft-landing system. LUNAR-A was first approved as a lunar penetrator mission, however, it was canceled in 2007 due to the delay of the penetrator development. After that, the penetrator technology was refined on the level of ground experiments in 2011. We re-design the mission to optimize small class mission using Epsilon launch vehicle and submitted to the M-class mission of JAXA as APPROACH (Advanced Penetrator Probe Applied for a Challenge of Hard landing) in January 2018. The objectives we defined are derived from one of the fundamental questions of science; "how and why life exists on the Earth and whether life is universal in the universe." Today's remaining questions in lunar science are summarized by Lunar Exploration Roadmap (Exploring the Moon in the 21st century) which was compiled by the Lunar Exploration Analysis Group (LEAG: <https://www.lpi.usra.edu/leag/>). By referring to this, we define the following three objectives and investigations of this mission;

Objective 1. Understand the physical conditions of the lunar-forming giant impact.

=> Constrain the bulk abundance of refractory elements on the Moon and understand the thermal environment of the lunar-forming disk

=> Investigate the structure of the lunar upper mantle.

Objective 2. Understand thermal evolution of the Moon.

=> Constrain the heat production in the Procellarum KREEP Terrane (PKT) region of the Moon and understand the current thermal environment of the Moon

Objective 3. Understand impact phenomena on planetary bodies.

=> Understand the energy partitioning of impacts

=> Understand the impact environment of the Earth-Moon system.

On the other hand, in order to approach the goal of the planetary technology, we define one objective as;

Objective 4. Development of a hard-landing system for the in-situ geophysical observations on the Moon.

=> Penetrator development and demonstration in space

=> Penetrator deployment and surface penetration on the Moon, and performance verification

As of now, APPROACH is basically a succession of LUNAR-A mission heritage, although the number of the penetrator is reduced to one. The science instruments onboard are seismometer and heat-flow measurement respectively to achieve the science objectives described above. In order to determine internal structure of the Moon with one station, we are also planning to deploy an onboard camera to detect impact flash with the aid of ground network observations.

References:

- [1] Nakamura, Y. (1983), *JGR*, **88**, 677–686.
- [2] Lognonné et al., (2003), *Earth Planet. Sci. Lett.*, **211**, 27–44, doi:10.1016/S0012-821X(03)00172-9.
- [3] Garcia et al., (2011) *Phys. Earth Planet. Inter.*, **188**, 96–113, doi:10.1016/j.pepi.2011.06.015.
- [4] Weber, R. et al, *Science*, **331**, 309-312, doi : [10.1126/science.1199375](https://doi.org/10.1126/science.1199375), 2011.
- [5] Yamada, R et al., *Planet. Space Sci.*, **81**, 18-31, doi : [10.1016/j.pss.2013.03.009](https://doi.org/10.1016/j.pss.2013.03.009), 2013.
- [6] Chenet et al., *Earth Planet Sci. Lett.*, **243**, 1-14, doi : [10.1016/j.epsl.2005.12.017](https://doi.org/10.1016/j.epsl.2005.12.017), 2006.
- [7] R.Yamada, et al, *Planet. Space Sci.*, doi:[10.1016/j.pss.2010.12.007](https://doi.org/10.1016/j.pss.2010.12.007), 2011
- [8] Kawamura, T., et al., *J. Geophys. Res. Planets*, **122**, 1487–1504, doi:[10.1002/2016JE005147](https://doi.org/10.1002/2016JE005147), 2017.
- [9] Lognonné, P. and C.L. Johnson, in *Treatise on Geophysics* (Second Edition), edited by Gerald Schubert., Elsevier, Oxford, Pages 65-120, ISBN 9780444538031, doi: 10.1016/B978-0-444-53802-4.00167-6, 2015.
- [10] Lognonne, P., et al. *J. Geophys. Res.*, **114**, E12003, doi:10.1029/2008JE003294.

MOON DIVER: A DISCOVERY MISSION CONCEPT FOR UNDERSTANDING THE HISTORY OF THE MARE BASALTS THROUGH THE EXPLORATION OF A LUNAR MARE PIT. L. Kerber¹, I. Nesnas¹, L. Keszthelyi², J.W. Head³, B. Denevi⁴, P.O. Hayne⁵, K. Mitchell¹, J.W. Ashley¹, J.L. Whitten⁶, A.M. Stickle⁴, M. Paton¹, K. Donaldson-Hanna⁷, R.C. Anderson¹, D. Needham⁸, P. Isaacson³, L. Jozwiak⁴, ¹Jet Propulsion Laboratory, California Institute of Technology, 4800 Oak Grove Dr., Pasadena, CA (kerber@jpl.nasa.gov), ²USGS Astrogeology Science Center, Flagstaff, AZ, ³DEEPS, Brown Univ. Providence, RI 02912, ⁴Johns Hopkins Applied Physics Laboratory, Laurel MD 20723, USA, ⁵University of Colorado, Boulder, CO, ⁶CEPS, Smithsonian Institution, MRC 315, Washington, DC 20013, ⁷AOPD University of Oxford, UK, ⁸NASA Marshall SFC, Huntsville, AL.

Introduction: Images returned by the Kaguya and Lunar Reconnaissance Orbiter missions revealed deep pits exposing tens of meters of layered stratigraphy in their walls [1-3]. Moon Diver (**Fig. 1**), a Discovery-class mission to a mare pit, would address numerous top-priority lunar science goals laid out in community reviews [4], the Decadal Survey [5], and the Lunar Exploration Roadmap [6], as follows:

(1) Virtually all mare basalt samples were collected as float rocks, without knowledge of which part of the lava flow was being sampled [6]. Lava flows, especially thick, slow-cooling flows, can differentiate or become contaminated both before their eruption onto the surface and as they flow or cool [7]. Exploring the variations in chemistry and mineralogy of an intact flow cross-section would provide vital context, and improve assessments of the probable parent melt [8]. Access to tens of meters of stratigraphy made up of numerous intact lava flows would allow intra- and interflow variability to be characterized, and could help determine whether the chemistry of the magma source(s) changed over time.

(2) The large areal extents of the mare basalts, together with their flat morphologies and sparsely identified flow fronts prompted the hypothesis that they were emplaced as “flood basalts”: quickly, with voluminous amounts of low viscosity lavas [7]. Over the last few decades, closer examination of long lava flows in Hawaii, as well as thick continental flood basalt flows, have demonstrated a large role for insulated and inflated flows [9-10]. Documenting the thicknesses and internal structures of individual mare basalt flows would illuminate whether the mare basalts were emplaced quickly or more gradually as complex flow fields with tubes and inflated sheets. In-depth characterization of the chemistry and flow textures of the layers would provide vital temperature and rheological parameters for cooling models of lunar lavas.

(3) The average mature lunar regolith differs in composition from the average basaltic lunar rock, suggesting the presence of up to 20% non-local material, as well as a greater component of agglutinates and glass [7]. A mare pit with steep walls provides access to both the regolith and its underlying basalts, allowing a direct comparison between their compositions.



Figure 1. A representation of the Axel rover rappelling into a lunar pit as part of the Moon Diver mission. This mission's exploration of mare pits with potential subsurface void spaces would address numerous top-priority lunar science goals.

(4) Potential paleoregolith layers were identified in the wall on the far side of Hadley Rille at the Apollo 15 landing site, but it was not possible to observe them up close [7]. Accessing ancient regolith preserved between basalt layers would yield insight about the intermittency of mare eruptions and the timescales for regolith formation [4].

(5) Bombardment during early Solar System times is thought to have created a deep layer of fractured bedrock blocks in the lunar highlands known as the megaregolith [11]. In the mare, a shorter exposure time and dwindling impact population have retarded megaregolith formation, yielding up to ~10 meters of fine regolith on top of seemingly coherent basalt layers [7]. Mare pits permit access to the mare regolith/bedrock interface, where the details of regolith formation, including fractures in the bedrock and compositional changes with distance from the interface, can be examined first hand.

(6) In some cases, lunar mare pits may open into subsurface void spaces or lava tubes [1-3]. Exploring and measuring these tubes would yield information about lava flux rates and the distances that insulated

lava could flow from the vent. Information about lava tubes and caves is also highly sought after for the purposes of human exploration and habitation [12-13]. Human settlements located in lava tubes would benefit from a stable, benign temperature, and would be protected from cosmic rays and micrometeorites.

For these reasons, lunar pits provide an exciting new target for lunar exploration. Before now, the desire to send a mission to these targets was tempered by the difficulty of reaching them given limitations of the vertical mobility of traditional rovers. The Axel Extreme Terrain Rover [14], developed by the Jet Propulsion Laboratory in collaboration with Caltech, has the mobility necessary to approach and rappel into this type of pit, revolutionizing our capability to access and explore in-place stratigraphy on the Moon.

The Axel Rover: The Axel rover consists of two wheels connected by a thick axle containing a winch and a tether [14]. Scientific instruments are housed inside eight deployable bays housed in the wheel wells (**Fig. 2**), which rotate independently of the wheel.



Figure 2. The Axel rover taking spectroscopic measurements on a slope of 40° (figure from [14]).

Over flat terrain (for example, from the landing site to the pit), it has mobility similar to a traditional rover. Once it reaches the pit, it can rappel down by letting out the tether stored inside its axle [14; **Fig. 2**]. This functionality allows the rover to descend and ascend steep vertical slopes. The rover can even dangle in free space and continue to let out its tether.

Axel communicates through its cable, alleviating common communication problems facing other cave-exploring robots. The rover can also receive power through its tether, meaning that it can use a solar panel on the surface to power its exploration in the dark cave below [14]. The functionality of this rover would allow a mission to examine and characterize lava layers exposed in the wall of a mare pit crater during abseil descent. Payload capability would include: morphologic measurements (provided by a camera system), mineral-

ogy (provided by a reflectance spectrometer), texture (provided by a microimager), and elemental chemistry (provided by an X-ray spectrometer). Axel's onboard cameras could record layer thicknesses and document the presence and characteristics of intervening soil layers.

Once on the floor of the pit, the Axel rover could continue to explore. If the pit opened into a lava tube or other subsurface void, the rover could attempt to negotiate the floor up to the length of its tether (currently 250-300 m, potentially up to 1 km [14]).

Axel has undergone extensive testing in terrestrial desert environments on steep slopes and various rock types [14]. Future field trials will test Axel mobility in volcanic settings with appropriate lunar pit analogs as preparation for a mission to the Moon.

Summary: Lunar mare pits represent an exciting new opportunity for lunar exploration. The Axel rover provides enhanced mobility which would enable it to land, rove to a pit or cave, enter, and explore with a suite of high-priority science instruments, with existing or highly mature technologies. The lessons learned by Moon Diver about the mare basalts would be relevant to flood basalt processes across the terrestrial planets., and its mobility technology could be easily modified to accommodate future missions in extreme terrains across the solar system.

References:

- [1] Haruyama, J., et al. (2009) *GRL* 36, L21206 [2] Robinson, M.S. et al. (2012) *PSS* 69, 18-27. [3] Wagner, R.V. and Robinson, M.S. (2014) *Icarus* 237, 52-60. [4] National Research Council (2007) *The Scientific Context for the Exploration of the Moon*. National Academies Press, Washington, DC. 120pp. [5] Squyres S. et al. (2011). *NASA Planetary Decadal Survey*. [6] Abell, P. et al. (2013) (*LEAG*) <http://www.lpi.usra.edu/leag/>. [7] Basaltic Volcanism Study Project (BVSP) (1981). *Basaltic Volcanism on the Terrestrial Planets*. New York: Pergamon, 1286pp. [8] O'Hara M.J. (2000) *J. Petrology* 41, 11, 1545-1651. [9] Cashman et al., (1998) *JGR* 103, B11, 27281-27289. [10] Keszthelyi, L. et al. (1998) *J. Geol. Soc. London*, 163, 253-264. [11] Heiken, G., Vaniman, D. & French, B. M. (eds) (1991). *Lunar Sourcebook: a User's Guide to the Moon*. Cambridge: Cambridge University Press, 736pp. [12] Haruyama, J. et al. (2012) *Moon* pp. 139-163. [13] Ashley, J. W., et al. (2013) (*LEAG*), abs. #7040. [14] Nesnas, I. et al. (2012) *J. of Field Robotics*, 29, 663-685.

Acknowledgments: This work was carried out at the Jet Propulsion Laboratory California Institute of Technology under a contract with NASA.

INTEGRATING CRYSTAL CHEMISTRY WITH LABORATORY ANALYSIS TO MODEL BOUND AND ADSORBED OH⁻ AND H₂O. R. L. Klima¹, B. Young^{1,2}, and A. S. Rivkin¹, ¹Johns Hopkins University Applied Physics Laboratory, Laurel, MD 20723, USA (Rachel.Klima@jhuapl.edu), ²Portland State University, Portland, OR.

Introduction: Investigating the specific characteristics of the H₂O/OH⁻ absorption bands near 3 microns is critical for understanding how these molecules are adhered to a remotely observed surface and for assessing their abundance. Current methods for analyzing the form and amount of water in or on rocks range from precise laboratory measurements of oriented single crystals and glasses in transmission, where individual absorptions can be modeled and examined, through more generalized band-depth analysis where a 3-micron band, observed in reflectance spectra of powdered samples in the lab or remote measurements, is treated as a single integrated absorption and compared to empirically calibrated water abundances. Understanding the relationship between the component band strengths and shapes and the bonding to the mineral also has the potential to provide a method to mathematically model terrestrial adsorbed water out of spectral measurements that were not obtained under vacuum conditions, increasing the number of laboratory spectra available for spectral analysis dramatically.

Distinguishing internal and bound water/hydroxyl: Water and/or hydroxyl detected remotely on the lunar surface may originate from several sources: 1) comets and other exogenous debris; 2) solar-wind implantation; 3) the lunar interior. While each of these sources are interesting in their own right, distinguishing among them is critical for testing hypotheses for the origin and evolution of the Moon and our solar system. Existing spacecraft observations provide limited spatial and/or spectral resolution, depending on the instrument used, to uniquely characterize the bonding energies of the hydroxyl molecules that have been detected. Because remote observations likely combine water and hydroxyl from various sources, it is important to understand whether they can be clearly distinguished from one another first in a highly controlled laboratory environment.

As part of the VORTICES SSERVI team, we are working to spectrally and mathematically characterize the distribution of energies for absorption bands caused by bound and adsorbed hydroxyl and water. To increase the amount of information that can be derived from spectra of hydrated terrains throughout the solar system, we are working to combine both transmission and reflectance spectra of a series of samples to develop a methodology for reliably separating out the specific component absorptions in the 3 micron region of reflectance spectra. For a suite of nominally anhydrous minerals, we are currently obtaining combined transmission measurements of thin sections and

powdered rock measurements in ambient air and in ultra-high vacuum. Samples are dehydrated in vacuum, resulting in a suite of spectra with a decreasing amount of adsorbed water. Transmission measurements, which are dominated by internal water/hydroxyl absorptions, are used to characterize absorption bands of any internal water present. The thin sections are then also dehydrated enabling the baseline absorption to be characterized. We will present new modeling results for analog and meteorite materials.

Sample Characterization: For our preliminary analysis, we have selected two ordinary chondrites (H and LL) as well as 8 Stillwater complex samples as analogs of lunar material. Stillwater samples include harzburgite, norite, anorthite, gabbro and orthopyroxenite. Each sample is being prepared as a double polished thin section for transmission analysis of internal water, powdered for UHV measurements, and characterized in a Hitachi Desktop SEM with a Bruker EDS attachment. Terrestrial samples have been prepared first to test our methods and to ensure that the chondrites can be handled in a way that uses the minimum amount of sample.

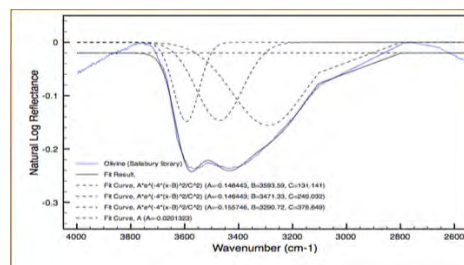


Fig. 1. Because they are due to molecular vibrations, we are initially modeling water and hydroxyl absorption using Gaussian distributions in energy space. Hydration of olivine in ambient air can be well described by three Gaussians, likely attributed to a combination of adsorbed water and more tightly bound structural water.

Spectral Measurements: Spectra of each sample are being measured in transmission to characterize the shapes and relative strengths of internal water bands. Powdered samples, with water adsorbed from the atmosphere at ambient temperature and pressure, are then measured, taken to UHV and measured again before being heated to drive the adsorbed water off. Samples are measured at progressively warmer temperatures to monitor the shapes and strengths of the absorption bands at each step. Spectra are then mod-

eled using Gaussian curves in energy space. The current objective is not to explicitly quantify the amount of water through modeling, but to determine whether the positions and shapes of bands resulting from adsorbed water are distinct enough from the water and/or hydroxyl bands in each mineral or rock type to be spectrally distinguished.

Acknowledgements: This work is supported by the NASA SSERVI grant to Johns Hopkins University/Applied Physics Laboratory.

DEPENDENCE OF ALBEDO ON SLOPE IN LUNAR HIGHLANDS: RESULTS FROM LOLA NORMAL REFLECTANCE DATA ANALYSIS. *M. A. Kreslavsky*¹, ¹Earth and Planetary Sciences, University of California – Santa Cruz, Santa Cruz, CA, 95064, USA, mkreslav@ucsc.edu.

Introduction: Steep slopes on the Moon are well known to be brighter than horizontal surfaces. It is well seen in low-phase-angle images, where albedo variations are not masked by shadows and illumination differences between tilted facets. At the first approach, the origin of this effect is understood: exposure to space weathering factors, namely, micrometeoritic bombardment and solar wind irradiation, causes regolith maturation accompanied by darkening, while on steep slopes intensive downslope transport of regolith, e.g., slides, avalanches, or intensive creep cause exposure of immature, brighter regolith. Many details of two key components of this phenomenon, regolith maturation and regolith transport, however, remain unknown. Here I report on new quantitative observations that put important constraints on those processes. I focus on highlands only, because on maria it is difficult to disentangle slope effects and effects of compositional variations due to excavation of sub-mare highland material.

Data processing: As source data on both topography and albedo I used data acquired by laser altimeter LOLA onboard LRO [1]. This excludes all possible biases related to preferential illumination direction and albedo-topography co-registration. I used only those data from the nominal mission that were not affected by the LOLA anomaly (misalignment of laser beams and the telescopes at the night side) [1], which limited my analysis to 70°S – 70°N latitudinal zone. I also excluded all off-nadir measurements. The LOLA laser radiation was split into 5 beams providing elevation measurements for 5 spots, 4 spots on 4 vertices of a square with 50 m diagonal, and 1 spot in the square centre. For each laser shot I calculated topographic gradient vector at 50 m baseline using 4 vertices, as well as the mean curvature at 50 m baseline using all 5 spots. I also calculated 4 gradient vectors at 25 m baseline using spot triplets, and discarded those laser shots, where different gradients were strongly inconsistent. In this way I excluded extremely rough sites, where surface slope is poorly defined.

I calculated the normal albedo at 1064 nm wavelength (near-infrared) from LOLA received energy in the centre spot. I applied the calibration procedure developed in [2]. I ensured independently that this calibration provided a good internal consistency of the reflectance measurements, however, the absolute calibration of the albedo is inherently inaccurate [2]. Results presented here were obtained with only one month of LOLA observations (~2×10⁷ useful data points), which excluded all problems related to gradual degradation of LOLA optics [2], despite the fact

that the calibration [2] compensates for the degradation and an order of magnitude larger source data set is potentially available. The results for that whole data set are similar and after careful bias assessment they will be published elsewhere.

Dependence of albedo on slopes: It is seen in **Fig. 1** that steep slopes have systematically higher normal albedo, as expected. The onset of a steep albedo increase occurs at ~23° slope. This angle can be interpreted as the dynamic angle of repose of the regolith: for slopes steeper than ~23° minor disturbances (e.g., micrometeoritic impacts) trigger runaway avalanches or slides that instantly expose immature regolith, while for gentler slopes no avalanches/slides is possible. The inferred dynamic angle of repose is somewhat lower than would be expected for poorly sorted regolith analogue in the terrestrial environment, which is consistent with a gentler dynamic angle of repose under lower gravity [3].

Fig. 1 also shows that in the 4° - 23° slope interval there is a weak increase of albedo with slope. This weak effect is not readily observed in the images, however, it seems reliably identifiable in the LOLA data. A possible explanation of this effect is that a relatively faster micrometeorite-induced creep at relatively steeper slopes favours exposure of less mature regolith.

A relatively sharp decrease of albedo for horizontal surfaces (from 4° to 0°) is unexpected and puzzling. I can suggest two different explanations that do not exclude each other. (1) Cryptomaria are predominantly flat and have mafic mare-type material under a thin layer of felsic highland-type material. Impact-induced admixture of mafic material from below may cause preferential darkening and/or deepening of the 1 micron absorption band on horizontal cryptomare surfaces. (2) Many small hundred(s) of metres size impact craters on highlands have been completely filled by diffusive creep of regolith. The infill material has been exposed to the space weathering on its way to the crater, therefore the horizontal crater fill is more mature.

Dependence of albedo on curvature: It is seen in **Fig. 1** that albedo of concave (right half of the plot) and convex (left half) sites differ significantly: convex sites are brighter. Diffusion creep makes the regolith thicker at the concave sites, and thinner at the convex ones. Excavation of immature material in a thinner regolith is easier, which leads to a higher albedo. The transported mature regolith already exposed to the space weathering and is piled in the local lows (concave parts of the topography) is thick and dark, and impacts capable of excavation of

bright immature material are rare. This observation indicates that the regolith transport is limited by the rate of regolith production in convex sites, e.g., at hill tops. High albedo of hill tops is seen in the low-phase images of the Moon.

Dependence of albedo on latitude and north-south slope asymmetry. A strong latitudinal trend of albedo in maria has been found in [4] and interpreted as a consequence of the latitudinal dependence of the incident solar wind flux. For highlands such a dependence is apparently absent [2], however, LOLA data show hemispherically-symmetric albedo increase at latitudes above $\sim 55^\circ$ (Fig. 3, dotted line), which also might be related to the latitudinal dependence of solar wind exposure. Albedo of tilted surfaces (Fig. 3, thick solid line) show some variations at low latitude; they are not hemispherically symmetric and may be related to compositional variations that are better expressed in immature regolith on slopes (Fig. 3, solid line) than in mature regolith at horizontal surfaces (Fig. 3, dotted line). Low albedo at 20°S – 50°S might be related to relatively Fe-rich material of South Pole – Eitken basin.

Above $\sim 40^\circ$ latitude there is a prominent north-south slope asymmetry of albedo (red and blue curves in Fig. 3): pole-facing slopes are systematically brighter, while equator-facing ones are systematically darker. This effect has been noticed in [2] with the same source data set and different analysis technique. It was naturally attributed to the difference in the solar wind exposure: pole-facing slopes at high latitudes receive much lower solar wind flux than equator-facing slopes.

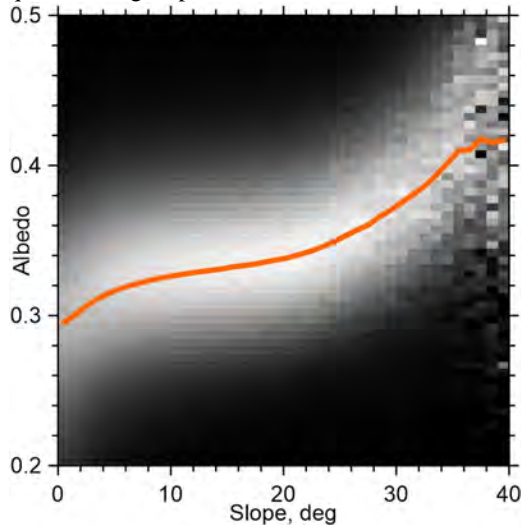


Fig. 1. Diagram Slope – Normal Albedo. Brightness denotes a proportion of data points with given albedo among those with given slope. Orange line shows the median albedo for each slope bin.

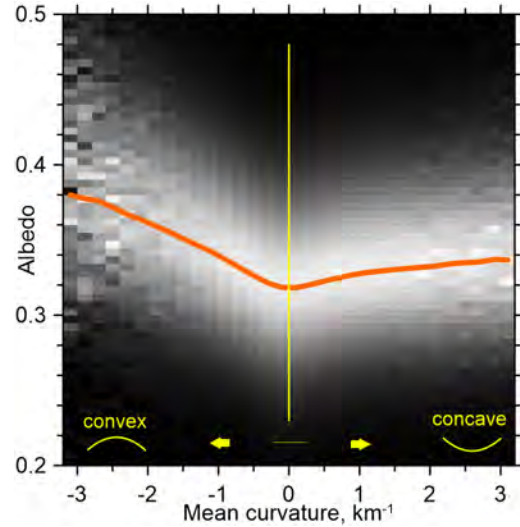


Fig. 2. Diagram Mean Curvature – Normal Albedo. Brightness denotes a proportion of data points with given albedo among those with given curvature. Orange line shows the median albedo for each curvature bin.

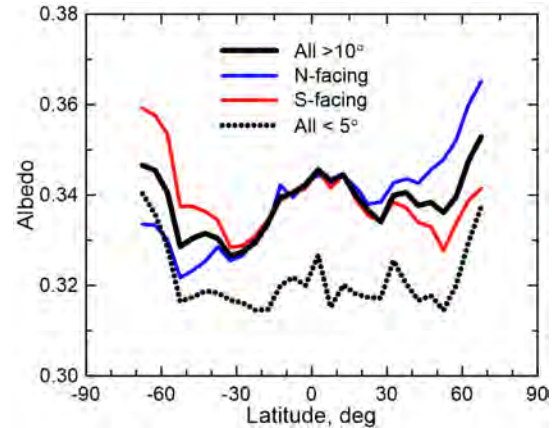


Fig. 3. Mean normal albedo as a function of latitude for all slopes gentler than 5° and steeper than 10° , and separately for north-facing and south-facing (within $\pm 22.5^\circ$ azimuth) slopes only.

Conclusions: Statistical analysis of albedo and topography showed that (1) the dynamic angle of repose of the lunar regolith is $\sim 23^\circ$; (2) regolith transport on the Moon is limited by regolith production; (3) exposure to solar wind plays a significant role in highland regolith maturation. These conclusions do not exhaust the potential of LOLA reflectance data set; further analysis looks promising.

Acknowledgements: This work was partly supported from NASA grants NNX16AQ06G and 80NSSC17K0217

References: [1] Smith D. et al. (2010) *GRL* 37, L18204. [2] Lemelin M. et al. (2016) *Icarus* 273, 315. [3] Kleinhans M. et al. (2011) *JGR* 116, E11004. [4] Hemingway D. et al. (2015) *Icarus* 261, 66.

A LUNAR SAMPLE RETURN STRATEGY FOR THE SCHRÖDINGER BASIN THAT TAPS INTO THE VOLATILE CYCLE OF THE LUNAR FAR SIDE.

David A. Kring^{1,2} and Katharine L. Robinson^{1,2},
¹Center for Lunar Science and Exploration, Lunar and Planetary Institute, Universities Space Research Association, 3600 Bay Area Blvd., Houston TX 77058 (kring@lpi.usra.edu), ²NASA Solar System Exploration Research Virtual Institute.

Introduction: The detection of water and other volatile species in Apollo samples [1,2] has provided a new tool for assessing the accretion of the Moon (e.g., [3-7]), processing of volatiles during the magmatic evolution of the lunar interior (e.g., [8]), venting at the surface [1,2,9-11], and deposition in near-surface ice caches that may be harvested to support a sustainable exploration program on the lunar surface.

Our understanding of that volatile cycle is incredibly immature. We are limited to a few nearside samples collected over a region of only 4.4% of the lunar surface [12] and confused by what appears to be a heterogeneous distribution within the lunar interior for reasons that are not yet understood [13,14]. Analyses of Apollo 17 glasses, norites, and a troctolite (**Fig. 1**) indicate that those types of samples can be used to measure H₂O abundances and isotope compositions that are key signatures of volatile sources and subsequent processing. In that case, however, the volatile cycle cannot be deciphered, because the glass came from a mantle source below the landing site, while the crystalline lithologies were derived from another mantle source and only occur at the Apollo 17 landing site because they were ejected there. The Apollo 17 norites and troctolite, if ejected from Serenitatis, travelled 61 to 375 km [15]. If they are instead ejecta from Imbrium, then they travelled 1000 km or more, so the sources of the Apollo 17 samples are likely decoupled.

To address that complexity and evaluate the volatile cycle from accretional delivery, through processing in the lunar interior, to venting at the surface, we ideally want a set of samples that taps into that system at different depths in the same location on the Moon. We also ideally want to probe the lunar far-side, for which we do not yet have any data except from meteorites without a known provenance. The Schrödinger basin is a geologically perfect site to address those issues and has already been identified as a high-priority landing site for robotic sample return missions [16-19] and human sample return missions [20-22].

Schrödinger Basin: The Schrödinger basin has a mountainous peak ring with spectacular (>72,000 m²) surface exposures of anorthositic and troctolitic rocks from mid- to lower-crustal depths down to 30 km [23] and also hosts an immense pyroclastic vent with material that erupted from estimated mantle depths of ~300 to 480 km [19]. The pyroclastic vent may be the largest indigenous source of volatiles in

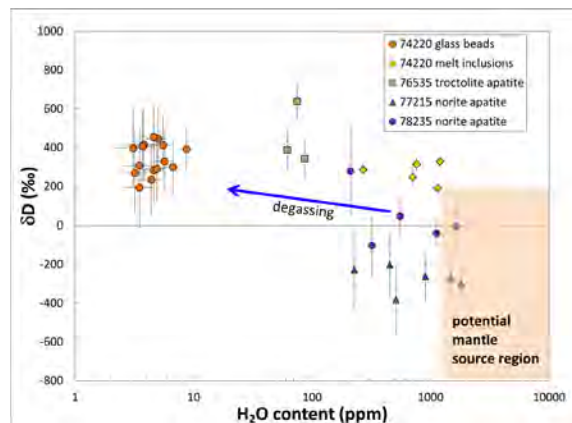


Fig. 1. Analyses of Apollo 17 samples illustrate that H₂O content and isotopic signatures can be extracted. Because of lateral transport during the impact excavation and deposition of the norites and troctolite, they may not be from the same local system as the volcanic glasses. To properly understand volatile cycling in a Moon with lateral heterogeneities of volatiles, a similar suite of samples are needed at a location, like Schrödinger, where lateral transport did not occur. Data sources are [5,13,31].

the South Polar Region during the past ~2 billion years [11], supplementing the volatiles that were vented during older mare eruptions that occurred elsewhere on the Moon [10].

Based on volatile abundances inferred from Apollo 15 and 17 pyroclastic material on the nearside [1,2,24], the Schrödinger vent produced an estimated 3.0×10^{13} to 1.6×10^{14} g of H₂O; 4.1×10^{13} to 4.1×10^{14} g CO; 7.0×10^{12} to 7.1×10^{13} g CO₂; 1.2×10^{12} to 4.6×10^{12} g F; 1.4×10^{13} to 2.6×10^{13} g S; and 0 to 2.2×10^{11} g Cl [11]. If those values are correct, then the vent produced a water mass that is significantly greater than the total water ice mass estimated in lunar permanently shadowed regions [25]. Thus, to confidently assess the sources and sinks of the portion of the volatile cycle on the lunar surface, it is essential to collect Schrödinger vent samples for return to Earth to determine if that far-side region, in proximity to potentially icy traps in the South Polar Region, produced those volatile masses.

We also note that the pyroclastic vent sits astride a graben that is part of a system of basin floor fractures. Volatiles in the rising magma may have influenced intrusions of basalt and, in turn, created the fractures [26]. Lava flows were also emplaced on the basin floor of Schrödinger, forming deposits that may provide evidence of a less-volatile rich portion of magma ascent from the same mantle source region

as the pyroclastic vent or, if a different age than the pyroclastic vent, potentially of a different mantle source region (e.g., perhaps from depths of ~130 to 250 km [19]). Thus, a set of samples from the mare flows will complement samples from the pyroclastic vent.

On the nearside, intrusive magmatic samples recovered from Apollo landing sites indicate there is an urKREEP layer at the crust-mantle boundary that may be a more concentrated reservoir of interior water than is the mantle [8]. It is not clear if the farside has that same urKREEP unit or, at least, a unit as enriched as that on the nearside. The Schrödinger impact, however, excavated material to a depth of ~19 to 24 km [23] and deposited those lithologies in a polymict breccia unit that covers most of the basin floor. Thus, if an urKREEP-derived magmatic lithology exists on that part of the farside, it could be recovered among samples of that breccia.

Collectively, a suite of samples involving pyroclastic material, peak-ring lithologies, impact breccias, and mare flows would probe volatile abundances in the lunar interior at several different depths as they were being processed and eventually vented at the surface.

Additional ISRU Opportunities: The pyroclastic vent within the Schrödinger basin was identified as an important target for in situ resource utilization (ISRU) during the Exploration Systems Mission Directorate phase of the Lunar Reconnaissance Orbiter mission. The Schrödinger vent, in addition to producing volatiles (**Fig. 2**), produced pyroclastic glass that can be easily excavated, transported, and processed. Nearby regolith can also be used for radiation shielding to protect crew or other radiation sensitive objects. Thus, the Schrödinger landing site is attractive from both a scientific and exploration perspective.

Conclusions: A key advantage of the Schrödinger landing site over other sites is that it provides probes of the volatile cycle at different depths in the same location. This is an essential element of any study of the volatile cycle, particularly if volatiles are heterogeneously distributed laterally within the lunar interior [14]. Moreover, as addressed elsewhere [16-20, 27], lunar sample missions to the Schrödinger basin can address the highest planetary science priorities of two National Research Council reports [28,29] and an astrophysical priority of a third National Research Council report [30]. The Schrödinger basin continues to grow as an exciting destination for lunar explorers.

References: [1] Saal A. E. et al. (2008) *Nature*, 454, 192–195. [2] Hauri E. H. et al. (2011) *Science*, 333, 213–215. [3] Greenwood J. P. et al. (2011) *Nat. Geosci.*, 4, 79–82. [4] Tartèse R. and Anand M. (2013) *Earth Planet. Sci. Letters*, 361, 480–486. [5] Saal A. E. et al. (2013) *Science*, 340, 1317–1320. [6] Anand M. et al. (2014) *Phil. Trans. R. Soc. A*, 372,

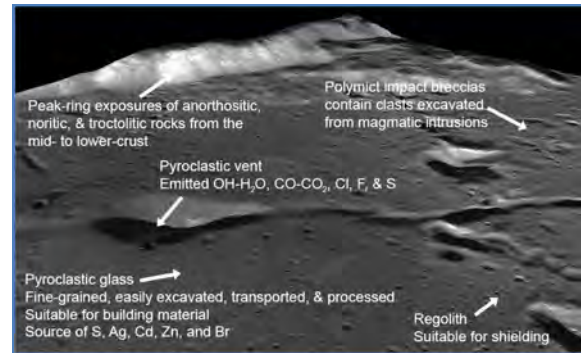


Fig. 2. A lunar sample return mission that lands between the pyroclastic vent and peak ring of the Schrödinger basin can access several samples that tap the volatile system at different depths and locations along its evolutionary path. Several ISRU opportunities exist in the same area.

doi: 10.1098/rsta.2013.0254. [7] Barnes J. J. et al. (2016) *Nat. Comm.*, 7, doi: 10.1038/ncomms11684. [8] McCubbin F. M. et al. (2015) *Am. Mineral.*, 100, 1668–1707. [9] Kring D. A. (2014) *Ann. Mtg. LEAG*, Abstract #3056. [10] Needham D. H. and Kring D. A. (2017) *Earth Planet. Sci. Letters*, 478, 175–178. [11] Kring D. A. et al. (2014) *Ann. Mtg. LEAG*, Abstract #3057. [12] Warren P. H. and Kallameyn G. W. (1991) *GCA*, 55, 3123–3138. [13] Robinson K. L. et al. (2016) *GCA*, 188, 244–260. [14] Robinson K. L. and Taylor G. J. (2014) *Nat. Geosci.*, 7, 401–408. [15] Kring D. A. et al. (2018) *LPSC XLIX*, submitted. [16] Kring D. A. and Durda D. D., eds. (2012) *A Global Lunar Landing Site Study to Provide the Scientific Context for Exploration of the Moon*, LPI Contrib. 1694, 688p. [17] Potts N. J. et al. (2015) *Adv. Space Res.*, 55, 1241–1254. [18] Hurwitz D. and Kring D. A. (2015) *Earth Planet. Sci. Letters*, 427, 31–36. [19] Steenstra E. S. et al. (2016) *Adv. Space Res.*, 58, 1050–1065. [20] O’Sullivan K. M. et al. (2011) *GSA Spec. Pap.*, 477, 117–127. [21] Bunte M. K. et al. (2011) *GSA Spec. Pap.*, 483, 533–546. [22] Ende J. J. et al. (2017) *LPS XLVIII*, Abstract #1880. [23] Kring D. A. et al. (2016) *Nat. Comm.*, 7, doi: 10.1038/ncomms13161. [24] Rutherford M. J. and Papale P. (2009) *Geology*, 37, 219–222. [25] Eke V. R. et al. (2009) *Icarus*, 200, 12–18. [26] Wilson L. and Head J. W. (2018) *Icarus*, in press. [27] Burns J. O. et al. (2013) *Adv. Space Res.*, 52, 306–320. [28] National Research Council (2007) *The Scientific Context for Exploration of the Moon*, 107p. [29] National Research Council (2011) *Vision and Voyages for Planetary Science in the Decade 2013-2022*, 382p. [30] National Research Council (2010) *New Worlds, New Horizons in Astronomy and Astrophysics*, 324p. [31] Barnes J. J. et al. (2014) *Earth Planet. Sci. Lett.*, 390, 244–252.

Introduction: Recent analyses of lunar samples have helped constrain the history of the magnetic field. The existence of a long lasting dynamo is well established between 4.2 [1] and 3.56 Ga ago [2]. A new study presents an even younger magnetized sample ~ 1 -2.5 Ga ago [3]. Paleointensity estimates suggest an early high field epoch for several 100 million years, with magnetic fields up to 100 μT (i.e., similar or larger than on present day Earth), followed by a low field epoch of several billion years and fields on the order of 1 μT or less [4].

While several processes have been studied to explain the duration and amplitude of the low field era [see 4 for a review], how to generate the early high fields remain uncertain. In this contribution, we investigate inner core nucleation and subsequent growth in more details. In particular, we use arguments from metallurgy developed by Huguet et al. [5] to investigate the effect of supercooling which suggests that nucleation does not occur when temperature reaches the liquidus, but after an additional supercooling of several 10 K.

Supercooling: When the inner core nucleates as the core reaches the melting temperature, an implicit assumption is that there is no nucleation energy barrier to form the first stable crystal. In classical nucleation theory, the first crystal formation occurs when volume free energy balances the interfacial free energy cost. This happens at a given $\Delta T/T_m$, which is experimentally about 20% for pure iron [6] (and up to 30% using molecular dynamics calculations [7]).

The lunar core is not pure iron, so more work needs to be done to constrain $\Delta T/T_m$ but the concept of supercooling itself is robust. In particular, even if the level of purity of the lunar core seems important, at slow enough cooling rate any ‘dirty’ water can be supercooled by as much as 5 K [8]. Assuming a supercooling of this order of magnitude, we propose as a proof of concept for the implications on nucleation and subsequent evolution, as suggested by [5].

Inner core nucleation and growth: To test the effect of supercooling, we use an energy balance in the outer core between latent heat generated at the crystallization front, heat conducted in the inner core and the core-mantle boundary heat flux. We assume that the transport timescale in the liquid outer core is short and that the core-mantle boundary heat flow is constant for the duration of the model (< 100 million years). The melting curve is that of an Fe-S alloy [9] and the adiabat is parameterized using the scale height defined in [10]. We then integrate forward in time for each set of model parameters and compute the power released at the ICB available to drive the dynamo.

Preliminary results: The degree of supercooling required to start nucleation is still poorly constrained and therefore test a range of values. Figure 1 shows inner core growth for those scenarios. A key result is that when considering supercooling, growth is several orders of magnitude faster than without ($\sim 10^4$ vs $\sim 10^8$ years). A direct consequence is a several orders of magnitude increase in power available to drive the dynamo (same energy released, but over a much shorter time period). The magnitude of the magnetic field depends on dissipation with the power $1/3$, therefore we expect a factor 20 to 400 increase compared to usual predictions (i.e., a surface field ~ 10 -100 μT , comparable to the observations).

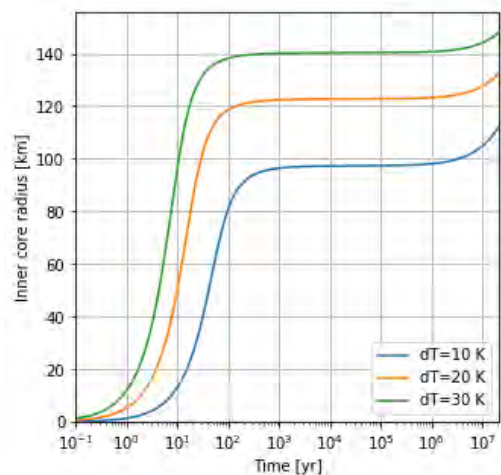


Figure 1. Inner core growth as a function of time for several initial supercooling. Note that t_0 is the onset of nucleation here, not the formation of the Moon, which could have happened several 100 Ma before.

Discussion and conclusion. We recognize that the concept of supercooling for planetary cores is still in its infancy, but we show that if it does play a role, the surface magnetic field generated during that period would be much larger than usually expected. However, such a high field will be maintained only for a very short time. Once the power source is no longer strong enough, the field decays on the ohmic timescale (one third decrease per $\sim 10^4$ years), whereas the range of ages of the high field epoch is predicted to be on the order of 100 million years.

References: [1] Garrick-Bethell et al. (2009) *Science*, [2] Suavet et al. (2013) *Proc. Natl. Acad. Sci.*, [3] Tikoo et al. (2017) *Sci. Adv.*, [4] Weiss and Tikoo (2014) *Science*, [5] Huguet et al. (2017) *AGU*, [6] Turnbull (1950) *J. App. Phys.*, [7] Zhang et al. (2015) *Phys. Earth Planet Inter.*, [8] Tan et al. (2016), *Am. J. Phys.* [9] Buono et al. (2011) *Geochim. Cosmochim. Acta*, [10] Labrosse (2003) *Phys. Earth Planet. Inter.*

LASER-INDUCED BREAKDOWN SPECTROSCOPY (LIBS): A TECHNIQUE FOR LUNAR EXPLORATION. J. Lasue¹, O. Gasnault¹, P. Pinet¹, P.Y. Meslin¹, K.H. Joy², O. Forni¹, S. Maurice¹, S. Chevrel¹, S.M. Clegg³, D.T. Vaniman⁴, R.C. Wiens³, ¹IRAP, UPS, CNRS, CNES Toulouse, France (jlase@irap.omp.eu), ²SEES, University of Manchester, Manchester, UK, ³LANL, Los Alamos, NM, USA, ⁴PSI, Boulder, CO, USA

Introduction: Laser-induced Breakdown Spectroscopy (LIBS) is an active analytical technique that makes use of a pulsed laser to ablate material of interest at a distance. The atoms in the high temperature plasma emit at specific wavelengths from the UV to near-IR and the light can be analyzed by spectrometry to determine the composition of the target [1].

Since 2012, LIBS has been successfully used under low atmospheric pressure for exploring the geology of Mars at Gale Crater with the Mars Science Laboratory rover's ChemCam instrument [2-4]. It was demonstrated from laboratory studies that LIBS also can give somewhat accurate and precise results under vacuum conditions for lunar exploration [5]. LIBS can be used to analyze single regolith mineral particles and larger rocks, giving major and minor elements composition. Moreover, LIBS is sensitive to volatile elements (H, Na, etc) that are of intrinsic interest to understand key lunar geological processes. It can also ablate dust covering rocks to allow further analysis by other instruments on the mission platform (rover, lander). The Chandrayaan 2 rover, which will be launched in 2018, will be equipped with a LIBS instrument for regolith reconnaissance around the landing site [6].

In this presentation, we review the science enabled by LIBS for lunar rock and regolith analysis by a lunar rover.

LIBS analytical capabilities: LIBS has the following capabilities that could be used advantageously to analyse lunar surface materials:

1) No sample preparation required; 2) rapid analysis; 3) operates at a distance; 4) removes dust from surfaces; 5) provides depth profiles; 6) detects many elements, and particularly the light elements (H, Li, Be, B, C, N, O, etc.)

Objectives of LIBS analyses on the Moon: The Moon provides a unique and relatively accessible body for understanding not just the Earth-Moon system and its impact history, but also the evolution of the Solar System [7-8]. As a potential stepping stone for further planetary exploration, the Moon is important for studies of potential resources and identifying hazards for future human exploration.

Early lunar exploration focused on nearside, equatorial regions. Data taken since the Clementine and Lunar Prospector missions helped to identify geochemically distinct regions such as the South Pole-Aitken (SPA) Basin, which has elevated concentrations of FeO, TiO₂, and Th consistent with the potential exposure of upper mantle material. Other anomalous regions, such as Compton-Belkovich, with its elevated Th abundance, have been discovered. It has

also been revealed that permanently shadowed craters in the lunar poles may harbour ice and frozen volatile deposits in substantial amounts (see e.g., [7] and references therein).

A LIBS instrument on-board a rover would be ideally suited for the following major scientific objectives in lunar exploration:

- 1) Continue to understand and expand the lunar rock and mineral inventory; search for a pristine lunar crust sample; assess the spatial and temporal basalt composition variability; improve the magma ocean model.
- 2) Characterize complex geological units, such as the pyroclastic units that are difficult to study by reflectance or gamma-ray spectrometry; assess the presence of KREEP basalts.
- 3) Study regolith; determine the elemental composition of the first few cms of the near-surface environment to better understand the regolith evolution processes.

Major elements quantification: The data was acquired using a pulsed (Nd:YAG) laser of 17mJ with 10ns pulses and 3 spectrometers [220-800nm]. We used 12 terrestrial rock powders and geostandards to test the LIBS capabilities in the laboratory (basalts, both altered and unaltered, andesite, and the JSC-1 lunar regolith simulant). The samples have been ground to <100µm to be homogeneous at the scale of the LIBS beam (200-300 µm diameter). These powders are compositionally roughly equivalent to lunar regolith.

The limits of detection (LOD) of the major elements was determined in [5] using the partial least squares and single lines techniques. Major elements LODs are estimated to be typically <1 wt %. The LOD of K₂O is estimated to ~1600 ppm from single line analysis. Data for Apollo soils, impact melts, high-K KREEP, regolith breccias, and lunar meteorite regolith breccias were taken from a wide range of literature references which can be found in [5].

From these data, we show that LIBS can differentiate mare basalt soils from the ones originating from the feldspathic highlands using the Al₂O₃ and FeO contents (Fig 1.a). The content of TiO₂ is used to classify mare basalts into very low Ti basalts (VLT; TiO₂ < 1 wt %), low-Ti (LT; 1 wt % < TiO₂ < 6 wt %), and high-Ti (HT; 6 wt % < TiO₂) types. The TiO₂ LOD of about 0.5 wt % allows to estimate the contributions of major classes of basalts to regolith genesis (Fig 1.b).

Finally, the K abundance is useful in determining the contribution of KREEP. Fig 1.c essentially presents a triangular array in the bottom right-hand part,

the predominance of Fe-rich mare and ferroan highland components in the bottom-left part, and the top part where KREEP sources are significant. The terrestrial analog K abundances span the whole lunar compositional range, showing that LIBS should allow estimation of the KREEP component in regolith samples (up to 8000 ppm K).

Minor elements analysis: The detection of minor elements such as K, Ba, or Zr can be further used to identify KREEP-like compositions among rocks and soils, shedding light on the petrologic evolution of the local regolith. Detections of minor elements such as Ni can be used to infer meteoritic content of the lunar regolith and associated maturation.

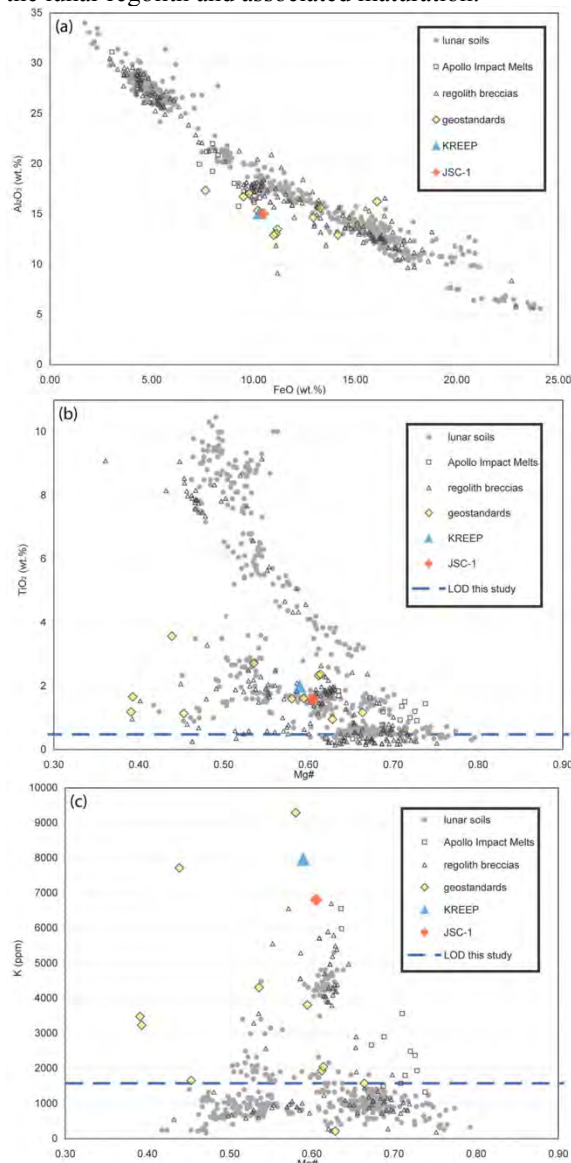


Fig. 1: Major element compositions for lunar soil samples, the geostandards and JSC-1 analogs used in this study. (a) Al_2O_3 versus FeO showing the Al-Fe mixing trends, (b) TiO_2 versus Mg\# showing the soil originating from the Mg-suite rocks and the high- to low-Ti trends, (c) K ppm versus Mg\# showing the LOD.

Of special significance, the water content of lunar soil mixed with water ice is clearly accessible with the LIBS technique at the 25 wt% H_2O level (Fig. 2). Measurements of altered basalts give a ~ 1 wt% LOD for H_2O so the LCROSS experiment content of 5.6 wt% [9] should be detectable by LIBS.

Conclusions and perspectives: This work shows the potential of LIBS analysis for rapid and accurate elemental analysis of lunar materials and characterization of potential resources for future exploration. The limits of detection determined for the major elements (typically <1 wt %) help to determine regolith parent material such as feldspathic highland rocks, rocks from the ancient magmatic high magnesian suite (Mg-suite), Fe-rich mare basalts or potassium, rare earth element, and phosphorus-rich (KREEP-rich) samples. Compositional parameters commonly used to classify lunar regoliths such as TiO_2 , Al_2O_3 , and K_2O abundances are readily determined by LIBS. Regolith analysis can also be improved: for example, Ba and Zr can be used to confirm KREEP-like composition, while quantifying the Ni content can be used to infer the amount of meteoritic material. Finally, the ice content of lunar soil produces strong H emissions with a limit of detection of about 1 wt % for H_2O content. This demonstrates that the 5.6 wt % water content detected by the recent LCROSS experiment in polar regoliths [9] should be detectable and possibly quantifiable by LIBS analysis.

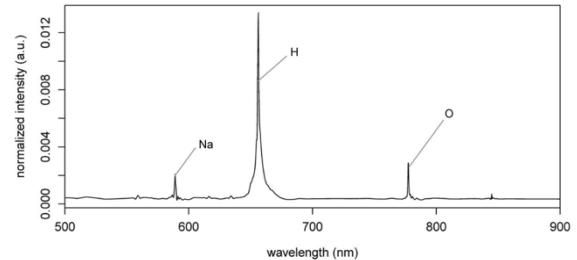


Fig. 2: VNIR spectrum of JSC-1 mixed with ~ 25 wt % of ice under vacuum with a 50 mJ laser pulse and target located 3 m from the telescope. The H and O peaks linked to water content are clearly visible.

Acknowledgments: This work was made possible by LANL and IRAP internal R&D funding.

References: [1] Cremers D.A. and Radziemski L.J. (2006) *Handbook of Laser-Induced Breakdown Spectroscopy*. [2] Wiens R.C. et al. (2012) *SSR DOI* : 10.1007/ s11214-012-9902-4. [3] Maurice S. et al. (2012) *SSR*, DOI: 10.1007/ s11214-012-9912-2. [4] Maurice S. et al. (2016) *JAAS*, DOI: 10.1039/ c5ja00417a. [5] Lasue J. (2012) *JGR*, 117, E01002 [6] Laxmiprasad et al. (2013) *ASR*, 52(2), 332 [7] Jolliff B. L. et al., eds (2006) *New Views of the Moon, Rev. Mineral. Geochem.*, vol. 60, Mineral. Soc. of Am. [8] National Research Council (NRC) (2007), *The scientific context for the exploration of the Moon, Rep. 11954*, Natl. Acad. Press. [9] Colaprete, A., et al. (2010), *Science*, 330, 463–468.

NASA'S MOON TREK: EXTENDING CAPABILITIES FOR LUNAR MAPPING AND MODELING.

E. S. Law¹ and B. H. Day², ¹ Jet Propulsion Laboratory, California Institute of Technology. M/S 168-200. 4800 Oak Grove Dr. Pasadena, CA, USA 91109. (Emily.S.Law@jpl.nasa.gov, +01-818-354-6208), ² NASA Solar System Exploration Research Virtual Institute. NASA Ames Research Center. M/S 17-1. Moffett Field, CA, USA. 94035. (Brian.H.Day@nasa.gov, +01-650-604-2605).

Introduction: NASA's Moon Trek (<https://moontrek.jpl.nasa.gov>) is the successor to and replacement for NASA's Lunar Mapping and Modeling Portal (LMMP). Released in 2017, Moon Trek features a new interface with improved ways to access, visualize, and analyse data. Moon Trek provides a web-based Portal and a suite of interactive visualization and analysis tools to enable mission planners, lunar scientists, and engineers to access mapped lunar data products from past and current lunar missions.

This presentation will provide an overview of the uses and capabilities of NASA's Moon Trek online mapping and modeling portal, and describe recent enhancements to the portal.

A Comprehensive Online Web Portal: Moon Trek provides a suite of interactive tools that incorporate observations from past and current lunar missions, creating a comprehensive lunar research Web portal. The online Web portal allows anyone with access to a computer to search through and view a vast number of lunar images and other digital products. The portal provides easy-to-use tools for browsing, data layering and feature search, including detailed information on the source of each assembled data product and links to NASA's Planetary Data System. Interactive maps, include the ability to overlay a growing range of data sets including topography, mineralogy, abundance of elements and geology. Originally designed for mission planning, Moon Trek also addresses the lunar science community, the lunar commercial community, education and outreach, and anyone else interested in accessing or utilizing lunar data. Its visualization and analysis tools allow users to measure the diameters, heights and depths of surface features, perform analyses such as lighting and local hazard assessments including slope, surface roughness and crater/boulder distribution. Moon Trek features a generalized suite of tools facilitating a wide range of activities including the planning, design, development, test and operations associated with lunar sortie missions; robotic (and potentially crewed) operations on the surface; planning tasks in the areas of landing site evaluation and selection; design and placement of landers and other stationary assets; design of rovers and other mobile assets; developing terrain-relative navigation (TRN) capabilities; deorbit/impact site visualization; and assessment and planning of science traverses. Significant advantages are afforded by Moon Trek's features facilitating collaboration among members of

distributed teams. Team members can share visualizations and add new data to be shared either with the entire Moon Trek community or only with members of their own team. Sharing of multi-layered visualizations is made easy with the ability to create and send URL-encoded visualization links. Moon Trek is also a powerful tool for education and outreach, as is exemplified by its being designated as key supporting infrastructure for NASA Science Mission Directorate's STEM Activation Initiative, and its serving of data to a growing community of digital planetariums.

Developed at NASA's Jet Propulsion Laboratory (JPL) and managed as a project of NASA's Solar System Exploration Research Virtual Institute (SSERVI) at NASA Ames Research Center, Moon Trek is a browser-based web portal. There is nothing additional to buy or install.

Moon Trek Enhancements: The Moon Trek interface provides enhanced 3D visualization and navigation. Standard keyboard gaming controls allow the user to maneuver a first-person visualization of "flying" across the surface of the Moon. User-specified bounding boxes can be used to generate STL and/or OBJ files to create physical models of surface features with 3D printers. This interface has become the standard across all of the existing and upcoming Trek products including the portals for Mars, Phobos, Vesta, Titan and more.

New tools have been added to facilitate traverse path planning, surface potential analysis, and laser retroreflector studies. A new pipeline to the PDS is facilitating the creation of NAC mosaics and NAC stereo pair DEMs. A movie generator allows the user to specify a 3D path above the surface along with camera angles in order to generate flyover movies of user-specified terrain. A new virtual reality component allows the user to draw a path using the web client, and then fly along that path in virtual reality using VR goggles.

Many new data products have been added. Resource Prospector continues to provide polar data products of particular interest for their site selection. A variety of new NAC views were added in direct response to areas of interest identified in the recent Lunar Science for Landed Missions Workshop held at NASA Ames Research Center. New mineralogy maps [1] (including polar mineralogy [2]) have been added as have maps of ice stability at depth provided by Resource Prospector based on work done by Matt Siegler.

Acknowledgments: The authors would like to thank the Planetary Science Division of NASA's Science Mission Directorate, the Science Engagement and Partnerships Division of would like to thank the Planetary Science Division of NASA's Science Mission Directorate, and the Advanced Explorations Systems Program of NASA's Human Exploration Operations Directorate and for their support and guidance in the development of Moon Trek.

References: [1] Lucey, P. G.; Lemelin, M.; Ohtake, M.; Gaddis, L. R.; Greenhagen, B. T.; Yamamoto, S.; Hare, T. M.; Taylor, J.; Martel, L.; Norman, J. (2016) American Geophysical Union, Fall General Assembly 2016, abstract id.P53A-2169. [2] Lemelin, M.; Lucey, P. G.; Trang, D.; Jha, K. (2016) American Geophysical Union, Fall General Assembly 2016, abstract id.P52B-04.

POSSIBLE IMPACT MELT LAVA TUBE SKYLIGHTS NEAR THE NORTH POLE OF THE MOON.

Pascal Lee^{1,2,3}, ¹SETI Institute, ²Mars Institute, ³NASA Ames Research Center, MS 245-3, Moffett Field, CA 94035-1000, USA. E-mail: pascal.lee@marsinstitute.net

Summary: Possible impact melt lava tube skylights are identified in Philolaus Crater near the North Pole of the Moon. If confirmed, and if the cavities harbor volatiles, they might provide access to subsurface water ice outside the lunar polar PSR (Permanently Shadowed Regions).

Introduction: *Lava Tube Skylights on the Moon.* To date, over 300 pits have been identified on the Moon in mare basalt, impact melt deposits, and highland terrain, and interpreted as volcanic lava tube skylights or post-flow features, *e.g.*, impact melt pits and impact melt lava tube skylights [1,2]. Skylights are intriguing as they represent access points to subsurface voids and potentially vast networks of subsurface cavities enjoying micro-environments distinct from conditions prevailing at the lunar surface outside the cavities [1]. While it has been hypothesized that lunar lava tubes might serve as cold traps for volatiles, all skylights positively identified to date are located outside of the polar regions of the Moon where substantial amounts of near-surface volatiles have been detected. We carried out a search for possible lava tube skylights in the North and South polar regions of the Moon using Lunar Reconnaissance Orbiter (LRO) Narrow Angle Camera (NAC) images, and reported on the identification of *candidate* impact melt lava tube skylights in Philolaus Crater near the North Pole of the Moon [3].

Philolaus Crater: Philolaus Crater (D ~ 70 km) is located at 72.1°N, 32.5°W, 540 km from the lunar North Pole, on the near side of the Moon (**Fig. 1**). Philolaus formed in the Copernican Period (< ~1.1 Ga). Impact melt deposits on its northeastern floor are among the youngest lava flows on the Moon.

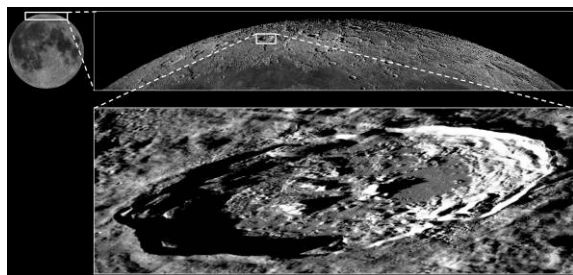


Figure 1: Philolaus Crater from Earth (NASA/LRO)

Candidate Skylights in Philolaus Crater: The impact melt deposits on the floor of Philolaus are dissected by a network of crisscrossing winding depressions, or *sinuous rilles*, typically <100 m wide. Some may be traced for several kilometers. Because of their sinuosity and the discontinuities along some sections, these rilles are interpreted as likely collapsed impact melt lava tubes interrupted by occa-

sional intact (uncollapsed or partially collapsed) sections. Some directional control of the rille network by fracturing during impact melt sheet cooling is possible. Some of the intact rille sections present short chains of discrete, round, rimless, shadowed depressions no wider than the local rille width: we interpret these as *possible* impact melt lava tube skylights. **Figure 2 E and F** shows three such pits, numbered 1 through 3, among several candidate skylights on the floor of Philolaus. The pits are near a Y junction split in the local sinuous rille network. Pits #1 and #2 are ~ 15 m across; Pit #3 is ~ 30 m wide. **Figure 3** interprets one of the highest resolution LRO images of the three pits shown in **Fig. 2E & F**.

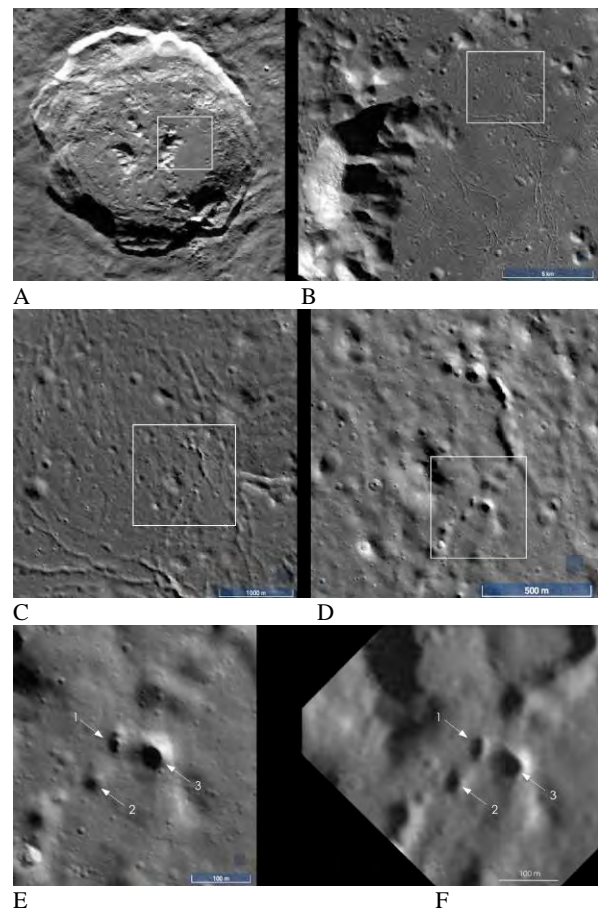


Figure 2. Candidate impact melt lava tube skylights in Philolaus Crater. Sequence of nested LRO images showing the locations of the candidate lava tube skylights identified in Philolaus Crater. **A:** Philolaus Crater (N is to the upper right); **B:** Smooth impact melt deposit on the crater's northeastern floor; **C:** Network of sinuous rilles; **D:** Discontinuous sinuous rilles with pit-like shadowed segments; **E & F:** Closeups of area boxed in D showing 3 candidate lava tube skylights numbered 1-3. (NASA/LRO/LROC/P.Lee).

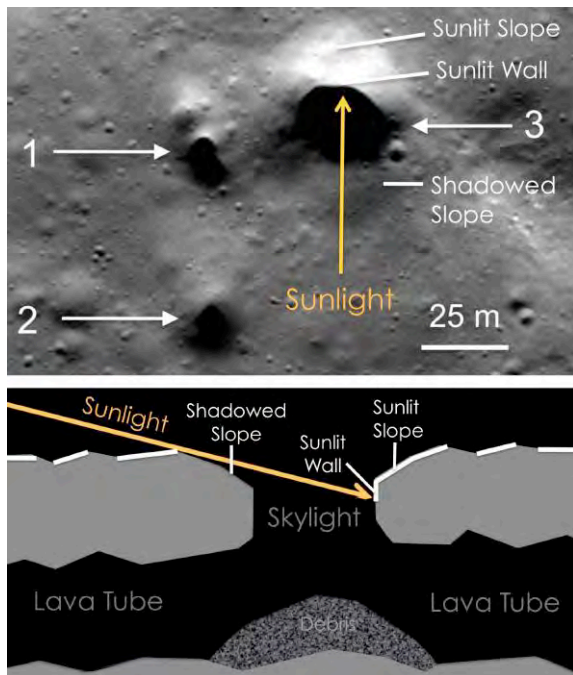


Figure 3: Illumination geometry of candidate impact melt lava tube skylights in Philolaus Crater. Lighting indicates pits are rimless. At Pit #1, brightest arc at edge of shadowed zone might be top part of skylight wall (NASA/LRO/NAC/P.Lee).

Physics of lava tube environments at Philolaus Crater: LRO Diviner measured max daytime and min nighttime temperatures on the floor of Philolaus of $T \sim 230$ K and $T \sim 80$ K, resp. Given Philolaus' high latitude (72.5°N) and typical lunar impact melt pit sizes and shapes, the cavity floor below each candidate skylight would be expected to remain permanently shadowed. In contrast to lower latitude pits reported on the Moon, sunlight would never penetrate the near-polar candidate skylights to illuminate and warm up their floors. Temperatures inside such near-polar caves might therefore remain extremely low ($T \sim 50\text{--}100$ K), close to min temperatures reached in the lunar polar PSRs ($T \sim 30$ K). Such low temperatures would allow water ice, if present, to be stable over geological timescales.

In terrestrial lava tubes in cold regions, e.g., in Lofthellir Lava Cave, Iceland, water ice may accumulate in massive form. Although water sources and thermodynamic conditions in these lava tubes are not immediately applicable to the Moon, the analogy lies in the fact that lava tubes may offer shelter and cooling compared to their outside environment.

Significance: Although the identification of impact melt lava tube skylights in Philolaus Crater remains to be confirmed, the finding is of potential significance because: a) Philolaus is relatively young; its impact melt deposits and lava tubes would be similarly young and therefore little disturbed; b) the network of lava tubes in Philolaus appears extensive; and c) near polar subsurface cavities might be cold enough to cold-trap and preserve water ice over geologic timescales, and without regolith mixing.

Mission to Philolaus Crater: A planned next step is to confirm, via high resolution orbital remote sensing, whether the shadowed depressions identified as pits in Philolaus are truly impact melt lava tube skylights. If confirmed, surface missions, robotic and/or human, to explore Philolaus and its lava tubes could follow [3]. Exploring Philolaus would represent the first *in-situ* investigation of a large lunar impact structure formed during the Copernican Period, allowing it to be dated precisely and older lunar crustal remnants excavated by the impact examined. Investigating Philolaus' impact melts would allow assessing modern lunar crustal geochemistry and volatile content. Exploration of Philolaus' relatively little-modified impact melt cavities might give access to exogenic and possibly endogenic volatiles cold-trapped and preserved in massive form over the age of the crater (up to ~ 1.1 Ga). Exploring lunar skylights and lava tubes would also help prepare for the exploration of analogous features on Mars.

Relatively smooth landing areas > 500 m wide are available on the floor of Philolaus' impact melt deposits within 1 km of the candidate lava tube skylight sites. Earth is directly visible from these sites, enabling line of sight communications. Mobility is required to effectively explore and sample the crater and its potential skylights and tubes. Robotic systems such as rovers, walkers, and hoppers have been proposed [e.g., 4]. One or more drones propelled by inert gas mini-thrusters and repeatedly deployed from a lander or rover outside the skylights (to allow recharging, refueling, and downloading of large volumes of data) might be the most effective approach considering the low T , darkness, dust, and terrain roughness anticipated inside lava tubes.

Human exploration missions could be of high value following robotic reconnaissance. If Philolaus Crater proves to be a substantial repository of subsurface ice qualifying as a resource, the site might be ideal for establishing a long-term lunar base.



Figure 4: Drone exploration of a lunar lava tube (P. Lee, composite image).

References: [1] Wagner, R. & M. Robinson (2014). *Icarus* 237, 52-60. [2] Wagner, R. & M. Robinson (2018). *NASA SSERVI Lunar Sci. for Landed Missions Wkshp*, Abstr.. [3] Lee, P. (2018). *NASA SSERVI Lunar Sci. for Landed Missions Wkshp*, Abstr.. [4] Thangavelautham, J. et al. (2017). *2nd Int'l Wkshp Instrumentation for Planet. Missions*.

Acknowledgements: This work supported in part by NASA, SETI Institute, and Mars Institute under Cooperative Agreement NNX14AT27A.

NUMERICAL MODELLING OF MICROWAVE SINTERING OF LUNAR SIMULANTS UNDER NEAR LUNAR ATMOSPHERIC CONDITION. S. Lim¹ (sungwoo.lim@open.ac.uk), V. L. Prabhu¹, M. Anand^{1,2}, J. Bowen³, A. Morse¹, and A. Holland¹, ¹School of Physical Sciences, The Open University, UK, ²Department of Earth Sciences, The Natural History Museum, London, UK, ³School of Engineering and Innovation, The Open University, UK

Introduction: The Space Instrumentation Group at The Open University has recently started investigating microwave sintering of lunar regolith/simulant as a potential fabrication method of 3D printing on the Moon to build lunar habitats. As part of this initiative, we have designed an industrial bespoke microwave heating apparatus. This apparatus will allow thorough experimental investigation of the sintering mechanism of lunar regolith/simulant in the cavity. The mechanical properties of sintered specimens produced under optimal conditions can then be explored. The experiment will also be validated using COMSOL Multiphysics simulation software.

In this contribution, we discuss the current design of the bespoke microwave heating apparatus, and how COMSOL has been employed to understand the different characteristics of lunar simulants when subjected to microwave heating.

Microwave sintering: Microwave sintering of lunar regolith as a potential fabrication method of lunar habitat construction has become one of the popular topics in recent years [1]. Previous research in this area, however, have been conducted using domestic microwaves. Figure 1 shows our initial work setting (see companion abstract by Levin-Prabhu et al. in this meeting).



Figure 1: Microwave sintering using a kitchen microwave

The picture on the left shows an infrared thermometer setting for measuring the surface temperature of specimen, the middle and right pictures show the sintered/melted lunar simulant JSC-1A. Domestic kitchen microwaves are not ideal for sintering lunar simulants for the following reasons: (i) they are not capable to withstand temperatures of up to 1,250 °C – the melting point of lunar regolith/simulant; (ii) they are not optimised to maximise microwave energy into a single hotspot; (iii) they are not able to mimic lunar atmospheric condition; (iv) it is not possible to measure sample surface temperature accurately; and (v) the frequency is fixed at 2.45 GHz which is an optimal frequency

to heat water molecules in food products but may not be optimal for inorganic solid materials such as lunar regolith.

Thus, an industrial bespoke microwave heating apparatus has been designed to overcome the current limitations. Figure 2 illustrates a design of the apparatus which includes two ports for an infrared thermometer probe and an endoscope-type digital camera, one naked-eye viewer window, and a cylindrical cavity with a flange for a vacuum pump. The ports can also be connected to a mass spectrometer, permitting extraction and analysis of volatiles while specimens are heated. Volatiles in regolith can be extracted by heating the regolith between 300 and 900 °C [2, 3]. For example, temperature of 700 °C is sufficient to obtain most of the H₂ and He [4]. Thus, the apparatus could also be used for measuring the types and amount of volatiles which could be used for propellant and life support (e.g. water). It is expected that the new apparatus would allow to (i) maximise microwave energy in a single hotspot; (ii) measure the surface temperature and phase change of specimens under near lunar atmospheric condition with more accuracy; and (iii) heating specimens of lunar simulant rapidly to be sintered/melted. This first version of apparatus does not support multiple frequencies, however, this feature is planned to be added in a future upgrade.

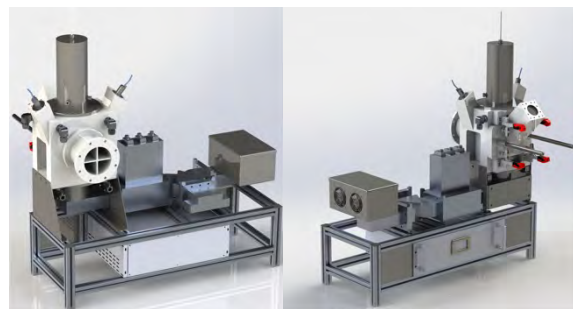


Figure 2: Industrial bespoke microwave heating apparatus

Numerical Modelling: While the actual experiment will be conducted as soon as the apparatus is installed in our lab, the experiment can also be simulated with a numerical modelling method. We have chosen COMSOL Multiphysics software (version 5.3a) [5] which has been used previously for a similar purpose [6]. COMSOL requires various parameters of material characteristics to simulate mi-

crowave heating phenomenon. Most parameters of lunar simulants have been identified, e.g., Table 1 shows the required material properties of JSC-1A for COMSOL simulation.

Table 1: Minimal material parameters of JSC-1A needed for COMSOL simulation [6]

Thermal conductivity	k	$0.35 \text{ W/m} \times \text{K}$
Specific Heat	C_p	$0.85 \text{ KJ/Kg} \times \text{K}$
Density	ρ	1.66 g/cm^3
Electrical conductivity	σ	0 S/m
Permittivity	$\epsilon' - \epsilon'' \times j$	$4 - 0.1j$
Permeability	$\mu' - \mu'' \times j$	$1 - 0.01j$

Initially, it was assumed that nanophase iron (np-Fe⁰) is key to facilitate microwave heating of lunar regolith [7], but later some experiments [8] revealed that np-Fe⁰ does not play a major role in microwave heating of lunar regolith under low magnetic field conditions and room temperature. The experiment led to another finding that the existing lunar simulants have larger absorption caused by their dielectric properties rather than magnetic properties at room temperature [9] although the finding still needs to be validated at higher temperatures.

All existing experiments, however, do not report the dielectric properties of each simulant as a function of temperature. Ideally, it would be best if we have these properties from cryogenic to the melting point of test materials in order to fully mimic the onsite fabrication on the lunar surface. As a starting point, we are measuring the dielectric properties of two lunar simulants JSC-1A and NU-LHT-3M and some powdered lunar meteorites from room temperature to 600, 800 and 950 °C; more temperature steps could be added depending upon the initial results guided by the available time and resources. The bulk density of JSC-1A powder was measured as 1.65~1.66 g/cm³ in [6, 9], however, we are making compacted pellets of simulants for which the bulk density of JSC-1A is around 2.07 g/cm³, obtained through our initial measurement of dielectric property of JSC-1A. Thus, the same value will be used for simulation.

Discussion:

Currently, we are creating a virtual cavity of the bespoke microwave apparatus in a COMSOL environment in order to conduct simulations of microwave heating in vacuum cavity with different materials, density, temperature and frequencies. With the identified full set of material data, we will be able to model more thorough mechanism of microwave heating of lunar simulant under near lunar atmospheric condition. Expected findings from the planned numerical modelling are (i) verifying the

bespoke design of the cavity that could maximise microwave energy to heat specimens; (ii) understanding the sequence of sintering phenomenon by continual simulation of the surface and internal temperature of specimens; and (iii) identifying the different effects of sintering among frequencies in terms of the time and penetration depth.

The Open University has established three Strategic Research Areas (SRA) one of which is Space. This has enabled us to integrate our existing expertise in 3D Concrete Printing [10, 11] and knowledge of lunar science and ISRU potential on the Moon [2] to perform a series of microwave sintering experiments aiming to develop a potential fabrication method of an extra-terrestrial construction process.

Acknowledgement: The authors acknowledge funding from the Open University's Space SRA.

References:

- [1] Lim, S., Prabhu V.L., Anand, M. and Taylor, L. (2017) *Adv. in Space Research J.*, 60(7), 1413-1429. [2] Anand, M., et al. (2012). *Planet. and Space Sci.*, 74(1), 42-48. [3] Ethridge, E. and Kaukler, W. (2012). *Concepts and Approaches for Mars Exploration*. [4] Crawford, I. (2015). *Progress in Physical Geography*, 39, 137-167. [5] <http://www.comsol.com>. [6] Ethridge, E. and Kaukler, W. (2012) *50th AIAA Aerospace Sci. Meeting*, AIAA2012-0801. [7] Taylor, L.A. and Meek, T.T. (2005). *J. of Aerospace Eng.* 18(3), 188-196. [8] Barmatz, M.B., et al. (2011). *42nd Lunar and Planetary Sci. Conf.*, LPI. [9] Barmatz, M.B. et al. (2012). *43rd Lunar and Planet. Sci. Conf.*, LPI. [10] Lim, S., et al. (2016). *Additive Manufacturing*, 12(B), 216-230. [11] Lim, S., et al. (2012). *Automation in Construction*, 21(1), 262-268.

THE ORIGIN OF THE HIGH-TiO₂ LUNAR BASALTS: CONSTRAINTS FROM EXPERIMENTS ON REMELTING OF SHALLOW MAGMA OCEAN CUMULATES. Yanhao Lin* and Wim van Westrenen, Department of Earth Sciences, Faculty of Science, Vrije Universiteit Amsterdam, The Netherlands (y.lin@vu.nl)

Introduction: Cooling and crystallization of the lunar magma ocean (LMO) [1,2] are thought to have led to a chemically differentiated and stratified mantle. Late crystallization of a titanium-rich cumulate layer, the so-called ilmenite bearing cumulate layer (IBCL) introduced a gravitationally unstable situation [e.g., 3], possibly resulting in large-scale overturn of the LMO cumulate pile [4]. This overturn-remelting mechanism is thought to have played a role in the formation of mare basalts [e.g., 4]. The formation process of the younger low-Ti mare basalts seems relatively straightforward, i.e. partial melting of early-formed olivine and orthopyroxene bearing LMO cumulates. In contrast, the formation mechanism of the older high-Ti basalts remains a matter great debate [e.g., 5] and overviews in refs 3, 6]. In addition, the mantle overturn model itself is controversial, due to incomplete knowledge of the rheological properties and temperatures involved [7]. As a result, the precise nature of the link between LMO crystallization, interior lunar dynamics, and mare basalt formation remains poorly resolved.

Recently, a new LMO crystallization sequence was determined by high-pressure, high-temperature experiments [8,9].

Here, re-assess the question whether high-Ti mare basalts can be formed through remelting of late-stage Ti-rich LMO cumulates assuming cumulate compositions from Lin et al. [8,9].

Experimental approach: High-pressure, high-temperature experiments were performed in a piston cylinder press using a half-inch (12.7 mm) diameter talc-pyrex cell assembly. For these experiments a hand-machined graphite bucket was filled with starting material, closed with a graphite lid and inserted in a gold-palladium (Au₈₀Pd₂₀) capsule. Pressure was 0.4 GPa in all experiments performed to date (equivalent to approximately 100 km depth in the Moon), and final target temperatures ranged from 1300 to 1130 °C. At completion of an experiment, runs were quenched by cutting power to the heater and the temperature typically dropped below the glass transition in < 10 s. Starting compositions were derived from step LBS10 of the LMO crystallization studies from our lab [8,9].

Analytical: All experiments were analyzed with JEOL electron microprobes at VU University Amsterdam or Utrecht University (15kV, 25nA for Si, Ti, Al, Fe, Mg and Ca), and checked for contamination and

iron loss. The mineral and melt proportions were determined both by mass balance calculations and area percentage using an EDAX EDS system in imaging mode.

Results: In our five experiments the mineral assemblage is orthopyroxene (Opx) ± armalcolite (Arm) ± ilmenite (Ilm) ± quartz (Qz), and melt is present in all run products.

The MgO content and Mg[#] of the melt initially remains nearly consistent during cooling from 1300 °C (5.76 wt.%, Mg[#]=29) to 1150 °C (5.47 wt.%, Mg[#]=31), and then decrease sharply to 3.86 wt.% and Mg[#]=26 at 1130 °C. SiO₂(melt) slowly increases up to 44.2 wt.% at 1150 °C from 39.8 wt.% at 1300 °C, and then increases sharply to 50.5 wt.% with the appearance of quartz at 1130 °C. Simultaneously, CaO and Al₂O₃ increase steadily to a maximum of 11.4 wt.% and 12.2 wt.% at 1130 °C, respectively. The appearance of Arm ± Ilm affects significantly the shape of the curves for the TiO₂ and FeO contents in the residual melts. The TiO₂ and FeO contents from 1300 to 1130 °C show similar evolved trends with different extent, concentrations first decreasing gradually from 14.8 to 10.1 wt.% and from 24.7 to 21.3 wt.%, respectively, until 1200 °C (Arm + Ilm), and then slightly increasing while still keeping the high-Ti (> 10 wt.%) characteristics, and finally drops sharply to 2.82 wt.% and slightly to 19.7 wt.%, respectively, at 1130 °C.

Discussion: Fig. 1 shows comparisons of mare basalt compositions among our runs, previous experimental studies and lunar samples by plotting TiO₂ versus FeO + MgO. Fig. 1 clearly shows that most quenched melts of this study fall in the range of lunar mare basalts, especially in high-Ti mare basalts, while the previous studies [10,11] reach higher-than-observed Ti contents. This shows that our starting composition and experimental conditions (low pressure, low temperature) can reproduce chemical characteristics of lunar high-Ti mare basalts, and suggests that the source of lunar high-Ti mare basalts may be the late-stage LMO cumulates in the shallow subsurface of the Moon.

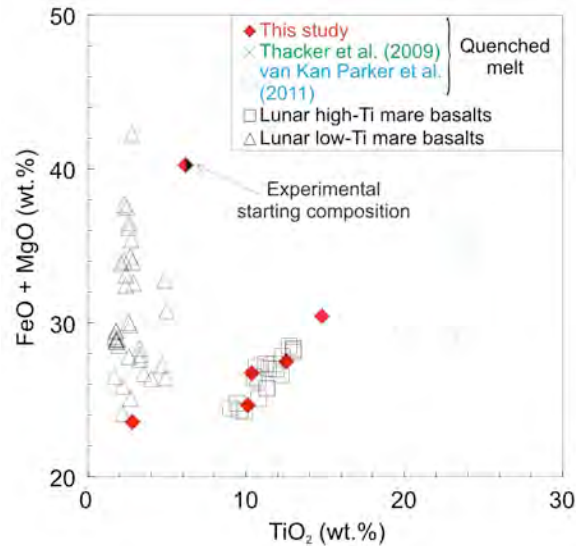


Figure 1. Comparison of experimental and lunar a) ilmenite and armalcolite, and b) quenched melt in the compositional space of TiO_2 versus $\text{FeO} + \text{MgO}$ (wt.%). Data from this study are shown as filled red diamonds and agree well with lunar basalts from [10] (green crosses), [11] (open blue circles). The literature data for lunar mare basalts are from [12] (high-Ti: open black squares, low-Ti: open black triangles).

Conclusions: Our preliminary ‘in-situ’ remelting experiments of LMO cumulates formed at ~100 km depth [8,9] indicate that shallow (not-overturned) Ti-rich cumulates could be the source of high-Ti mare basalts.

References:

- [1] Wood J. A. et al. (1970) *Proc. Apollo 11 Lunar Sci. Conf.*, 965–988.
- [2] Shearer C. K. et al. (2006) *Rev. Mineral. Geochem.* 60, 365–518.
- [3] Shearer C. K. and Papike J. J. (1999) *Am. Mineral.* 84, 1469–1494.
- [4] Hess P. C. and Parmentier E. M. (1995) *Earth Planet. Sci. Lett.* 134, 501–514.
- [5] Longhi J. et al. (1974) *Geochim. Cosmochim. Acta* 5, 447–469.
- [6] Grove T. L. and Krawczynski M. J. (2009) *Elements* 5, 29–34.
- [7] van Orman J. A. and Grove T. L. (2010) *Meteorit. Planet. Sci.* 35, 783–794.
- [8] Lin Y. et al. (2017a) *Earth Planet. Sci. Lett.* 471, 104–116.
- [9] Lin Y. et al. (2017b) *Nat. Geosci.* 10, 14–18.
- [10] Thacker C., et al. (2009) *Geochim. Cosmochim. Acta* 73, 820–836.
- [11] van Kan Parker M., et al. (2011b) *Geochim. Cosmochim. Acta* 75, 4179–4193.

[12] Wieczorek M. A. et al. (2006) *Reviews in Mineralogy and Geochemistry* 60, 221–364..

REGOLITH MIXING BY IMPACTS: LATERAL DIFFUSION OF BASIN MELT. T. Liu^{1,2} G. Michael² and J. Oberst^{1,3}, ¹Institute of Geodesy and Geoinformation Science, Technische Universität Berlin, 10623 Berlin, Germany (tiantian.liu@tu-berlin.de), ²Freie Universität Berlin, Malteserstr., 74-100, Haus D, 12249 Berlin, Germany, ³Institute of Planetary Research, German Aerospace Center (DLR), 12489 Berlin.

Introduction: Impact cratering has been the primary process to alter the distribution of lunar highland materials since the formation of a crust. The impact history – recorded in the produced impact melt that processes age as the time when it generated – may be reconstructed by combining the lunar samples with the inferred origins. However, the impact melt is exposed to the long-time gardening process (i.e. re-melting, excavating, burying, and re-excavating) by the subsequent impacts, resulting in a complex spatial distribution. To investigate this diffusion of impact melt laterally and by depth, a model is built by the means of Monte Carlo approach. The lateral melt diffusion for three late-forming basins (Serenitatis, Crisium, and Imbrium) are obtained based on the model.

Method: A band passing along the great circle is chosen for modelling. By dividing the band into cells, the ejecta volume and the portion of unheated and melted materials are recorded laterally and by depth, tracking the age of the newly-generated impact melt with progressing model time, t . There are three key aspects when modelling:

Distribution of impact events: A minimum crater diameter, D_{\min} , is chosen as 5 km for modelling. By using the Monte Carlo method, the diameter of craters, D , is generated, the size-frequency distribution of which statistically conforms to the standard production function (PF) larger than D_{\min} ^[1]. The corresponding impact centre of each event is randomly distributed along the great circle. The average time to the next impact event larger than D_{\min} in diameter, that is impact rate, is calculated from the Chronology function (CF)^[2], PF, and t ^[3].

Excavating and melting processes: The excavation depth for each simulated crater, d_{exc} , is $D_t/10$ where D_t is the diameter of the transient crater^[4]. D_t is related to D as follows: for simple craters, $D_t = 0.8D$ ^[4]; for complex craters, $D_t = (DD_Q^{0.13}/1.17)^{1/1.13}$ ^[5], where D_Q is the simple-complex transition diameter, and taken as 21 km^[6]. The corresponding volume of the excavated materials, V_{exc} , having a torus-like shape is estimated to be 1/3 of a disc with d_{exc} in thickness and D_t in diameter. For the conservation of mass, the excavation unit is assumed to be a cuboid with 1/3 D_t in length and d_{exc} in thickness located at the crater centre, and the volume of each penetrated layer in each cell is diminished. The total volume of the generated impact melt with a reset age as t is: $V_{\text{melt}} = cD_t^d$, where c and d are taken as 1.4×10^{-4} and 3.85, respectively^[7].

Distribution of melt materials: About 75% of the generated impact melt stays within the crater and the remainder is ejected. We consider the melt deposits inside the craters as ‘lens’, and the fracturing process that could lead the melt to the deeper places and the exact distribution are not taken account, both of which might be significant but difficult to estimate. About 85% of the ejected materials are deposited within five radii from crater centre and those at farther places are sporadically distributed^[8]. We, therefore, only trace the melt within five radii from crater centre. The thickness of ejecta layer decreases with distance from crater centre, r : $\delta(r) = Ar^{-3}$ ^[4], where A is varied for the craters with different D to conserve the mass and is calculated by integrating over the volume within five radii. We take the integrated volume to be V_{exc} . The quantity of impact melt in ejecta also decreases with distance: $\delta_m(r) = A_m r^{-2}$ ^[8], although the proportion of ejecta which is melt increases with distance. A_m is recalculated for craters with different size to conserve V_{melt} similar as A described above. The melt ratio, f_{melt} , at r is therefore equal to $\delta_m(r)/\delta(r)$.

Only the melt deposited in the band is traced. To conserve the mass, we assume that all the excavated materials on the band are distributed along the great circle instead of the theoretically radial ejection. It results in more melt materials locally, but compensates for the melt generated by craters outside the band that the model has not recorded.

Results: Migration occurs when large numbers of impact events strike the homogeneous target randomly. The generated craters are taken with the same D_t (40 km) to shield the effect from crater size. As can be seen from Figure 1, the generated impact melt is depleted by the re-melting process of subsequent impact events, and the melt is transported to the farther places but involving only small volumes. The total generated impact melt becomes greater with the increasing number of later impacts.

The great circle through the late-forming Imbrium, Crisium, and Serenitatis basin is chosen to investigate the melt lateral diffusion of by the giant basin-forming events. There are a total of 283 impacts with the maximum D as 118 km. The present-day distribution of impact melt by depth for three basins is shown in Figure 2. It shows that the initially generated melt is destroyed and redistributed by the subsequent impact events: the older the basin, the less the remaining melt. In addition, the ejecta materials from both Crisium and Imbrium basin cover the Serenitatis melt burying the melt to greater depth. Some of the

buried melt was re-excavated to shallow layers subjecting to the further gardening. It is obvious that the melt on the near-surface is seriously stirred by the subsequent normal-scaled (< 300 km) impacts resulting in the locally diverse distribution, which significantly influenced the scooped materials at the sampling sites.

Discussions and Conclusions: It was found that the impact melt is depleted by re-melting, spread to the farther places by excavating, and buried to deep layers by overlaying ejecta of subsequent impacts. The great volume of melt generated by the giant basin-forming events survives until present day, but the older basin melt suffers more serious gardening. The melt deposited on the near surface is stirred by the subsequent impact events causing a local heterogeneity in distribution. This may affect the outcome of scooping at sampling site in lunar landing missions.

The understanding of the transportation mecha-

nism of the impact melt is helpful for the analysis of lunar samples and may guide our choice for potential sites of future sample return missions, such as the Chinese Change'E-4 (CE-4).

References: [1] Michael G. et al. (2016) *Icarus*, 277, 279–285. [2] Neukum G. (1983) *Univ. of Munich*, 1–186. [3] Michael G. et al. (2017) *Icarus*, 302, 80–103. [4] Melosh H. (1989) *Oxford Univ.* [5] McKinnon W. et al. (1997) *Venus II: Geology, Geophysics, Atmosphere, and Solar Wind Environment*, 969. [6] Pike R. (1977) *LPSC*, 8, 3427–3436. [7] Cintala M. and Grieve R. (1998) *MPS*, 33(4), 889–912. [8] Previous talk with the group guided by Kai Wünnemann (Juliane Engelmann, Meng-Hua Zhu, and Robert Luther)

Acknowledge: The work was supported by the German Research Foundation (DFG) SFB TRR-170-1 TP A4.

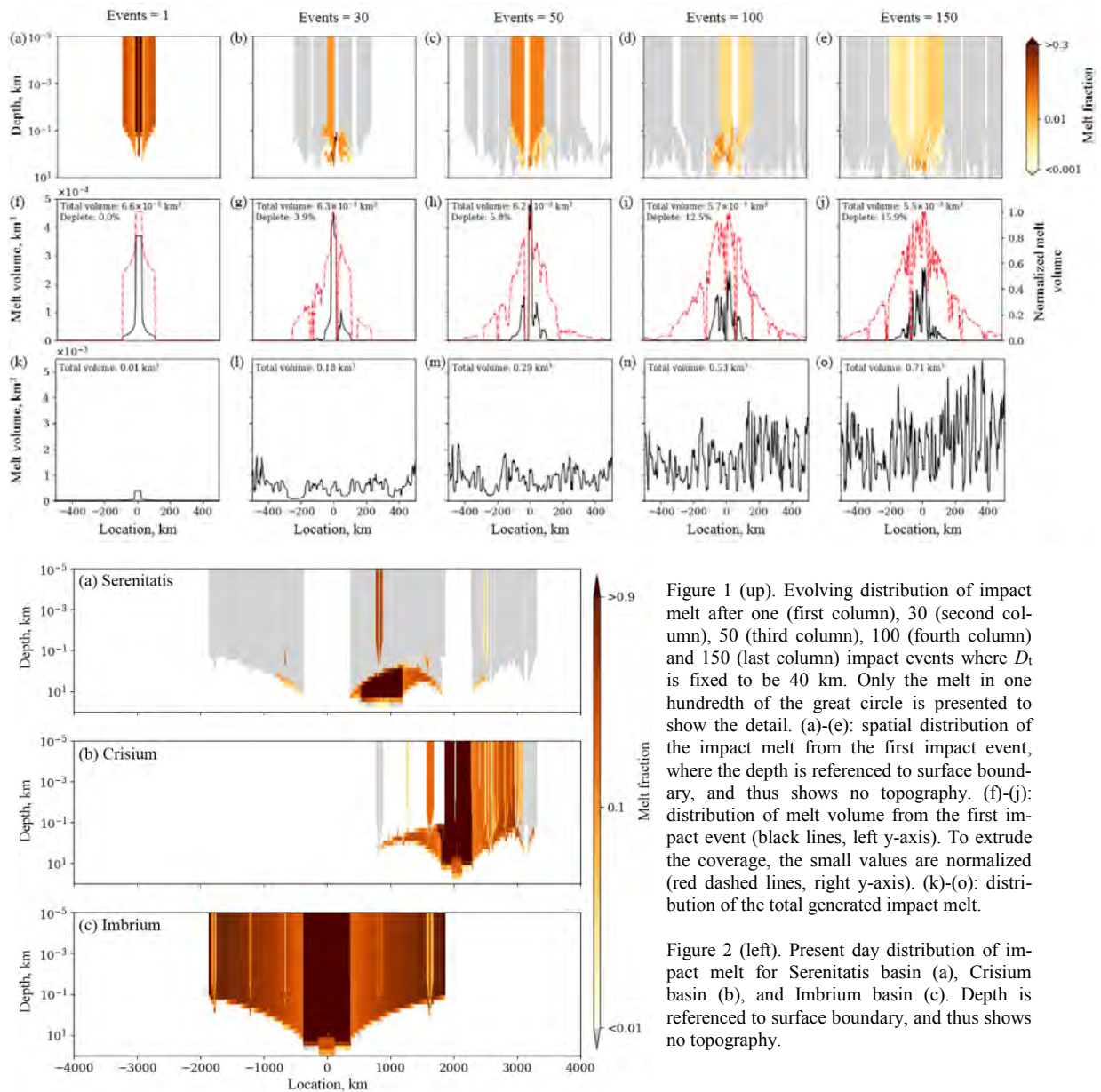


Figure 1 (up). Evolving distribution of impact melt after one (first column), 30 (second column), 50 (third column), 100 (fourth column) and 150 (last column) impact events where D_i is fixed to be 40 km. Only the melt in one hundredth of the great circle is presented to show the detail. (a)-(e): spatial distribution of the impact melt from the first impact event, where the depth is referenced to surface boundary, and thus shows no topography. (f)-(j): distribution of melt volume from the first impact event (black lines, left y-axis). To extrude the coverage, the small values are normalized (red dashed lines, right y-axis). (k)-(o): distribution of the total generated impact melt.

Figure 2 (left). Present day distribution of impact melt for Serenitatis basin (a), Crisium basin (b), and Imbrium basin (c). Depth is referenced to surface boundary, and thus shows no topography.

INVESTIGATING SIZE-DEPENDENT SMALL LUNAR CRATER DEGRADATION USING CHEBYSHEV COEFFICIENTS

P. Mahanti¹, M.S. Robinson¹, ¹Lunar Reconnaissance Orbiter Camera, School of Earth and Space Exploration, Arizona State University, Tempe, Arizona (pmahanti@asu.edu)

Introduction: Degradation of impact craters results in changes to crater shapes and leads to an overall evolution of topography on the Moon (and other bodies). Tracking degradation rates of craters is possible via simulation, by synthesizing a desired fresh crater topography and then following a model-based erosion of the topography (e.g. [1, 2, 3, 4]). Typically, a linear diffusional model is applied, whose theoretical basis relies on the assumption of a smaller impactor affecting a larger topographic area [2], leading to steady erosion of the surface. For small craters ($D < 300\text{m}$) at equilibrium, the continuous topographic evolution intuitively leads to the production, disturbance, and mixing of the upper regolith layers and rates of such processes are affected by the degradation rates of the small craters. While a complex mechanism of degradation for small craters is expected [5], our work here investigates the performance of the diffusional model for tracking the degradation for a population of small craters at the Apollo 16 and 17 landing sites. Previously, we showed that systematic degradation of lunar craters results in standardized changes in shape represented by Chebyshev coefficients [6]. In this work, we illustrate the effectiveness of using Chebyshev coefficients in characterizing size-dependent morphological degradation state for a population of small craters.

Methods: Craters were identified manually (> 2000 craters at each site, $30\text{m} < D < 250\text{m}$) from Lunar Reconnaissance Orbiter Camera Narrow Angle Camera (LROC NAC) ortho-photo mosaics, digital terrain models (DTM, $2\text{m}/\text{pixel}$) and a derived slope map [7]. Craters from two diameter bin ranges 50m to 55m ($n = 476$) and 100m to 110m ($n = 192$) were used for this work. Additionally, two sets of simple rayed craters, diameter bin ranges 7.2km to 7.5km ($n = 25$) and 5.2km to 5.7km ($n = 34$) were also included. Topographic measurements (depth, diameter, wall slope and radial elevation profile) for each crater was extracted automatically [8, 9] followed by computation of the Chebyshev coefficients from the elevation profiles.

LROC NAC images were used to visually classify craters into morphological classes A, B and C (for details see [8]) and class A craters were used to derive representative crater profiles for fresh craters in this work (at $D = 40\text{m}$ and 70m and $\frac{d}{D} = 0.2$). Radially symmetric fresh crater topography was synthesized from the representative fresh crater profile. Note that the diameter and $\frac{d}{D}$ of the synthetic fresh crater was chosen to provide a reference curve to the compare C6 (the seventh

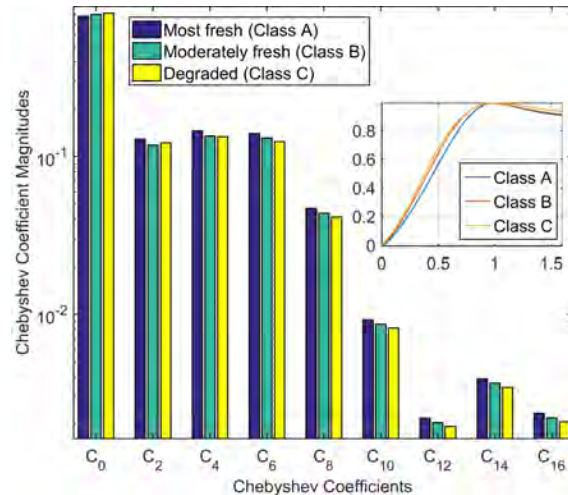


Figure 1: Chebyshev coefficients for representative (Class A, B and C) normalized crater profiles for small craters

Chebyshev coefficient) vs. $\frac{d}{D}$ from true observations (hence smaller diameters and higher $\frac{d}{D}$). Diffusion-based degradation is applied to the synthesized crater topography for 200 iterations with $\frac{d}{D}$ and Chebyshev coefficients computed from the degraded crater profile after each iteration. Coefficient C6 is used as a morphological degradation state indicator - C6 magnitude decreases with each cycle of degradation [6].

Results and Discussions: Chebyshev coefficient magnitudes computed from representative normalized profiles (same $\frac{d}{D}$) for classes A, B, and C (inset, Figure 1) for the small craters change monotonically from fresh (class A) to degraded (class C) (Figure 1). Magnitudes of higher indexed coefficients (10 and above) are smaller by an order of magnitude, so changes in shape are represented mostly by coefficients C0 to C8. For the small craters, C0, C4, C8 increase and C2, C6 decrease with increasing degradation, as crater half-profile shape changes from sigmoid to the side of an inverted cone as observed in the Apollo 16 and 17 sites [8].

The general trends (increasing or decreasing with more degradation) of coefficient magnitudes are independent of crater diameter (similar to larger craters [6]). Crater wall slope changes with crater shape, and an expected strong correlation is observed with C6 or $\frac{d}{D}$ (Figure 2). However, unlike $\frac{d}{D}$, where craters with diameters at the same scale (km-sized vs. m-sized) cluster together (Figure 2a), Chebyshev coefficients scale with crater diameter. Hence, at the same morphological degradation state, a larger crater also has larger C6 magnitude, and segregated clusters are obtained for craters from different size bins (Figure 2b). Linear fits (C6 vs.

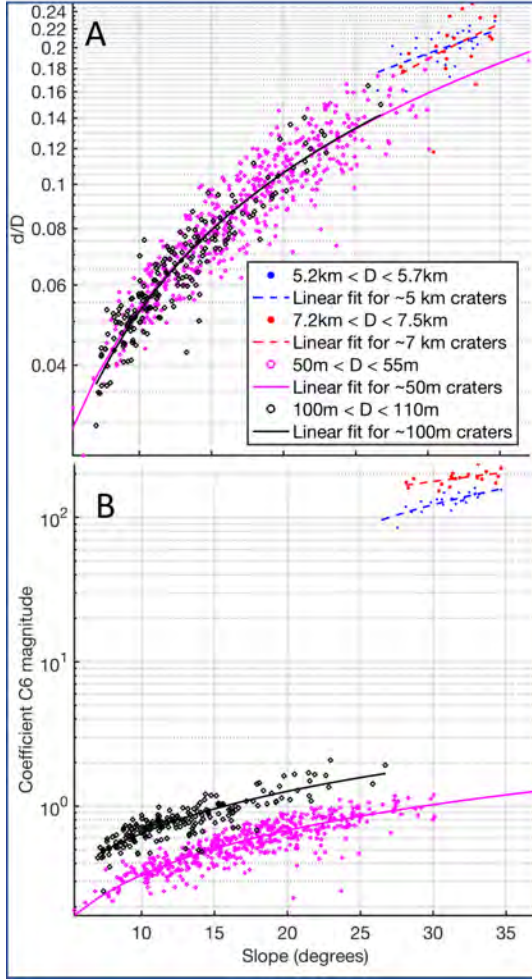


Figure 2: Relative clustering of $\frac{d}{D}$ (A) and C6 (B) values vs. wall slope for small craters of different sizes.

slope) further illustrate how de-clustered characterization of small crater degradation is possible using Chebyshev coefficients.

Assuming a linear diffusion based degradation, smaller craters degrade faster (Figure 3, inset). After the same time (e.g., 100 degradation cycles or $0.5T$) has elapsed, $\frac{d}{D}$ for the 70m crater has only reduced by 50% whereas the 40m crater is nearly obliterated. C6 magnitudes from Apollo 16 and 17 site small craters and simulated degradation (diffusion-based erosion; $D = 40\text{ m}$ and 70 m as reference) both decrease in magnitude but there is an obvious difference between the median trend-lines from observed C6 values and simulation. One possible cause for this difference is a divergence from the linear diffusion model, (e.g., anomalous diffusion [10]) for the observed craters (effect of size and equilibrium conditions). Also, a single value of $\frac{d}{D}$ ($= 0.20$) was considered (starting point) while simulating crater degradation. By combining different possible initial $\frac{d}{D}$ values at the start

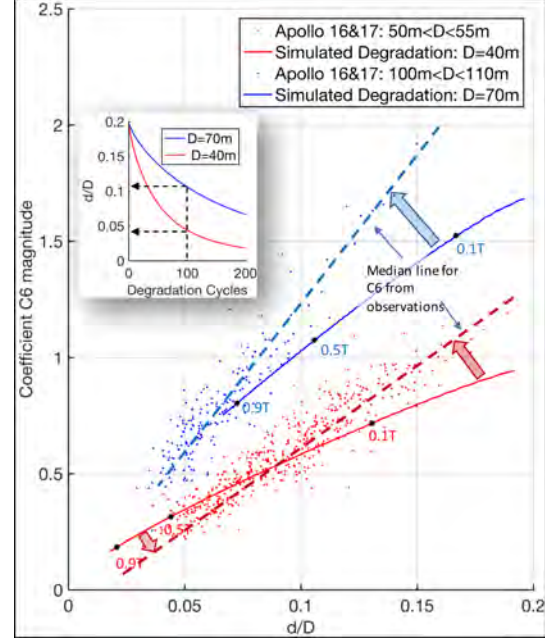


Figure 3: Magnitude of Chebyshev coefficient C6 vs. $\frac{d}{D}$ from observation and simulation

of degradation for different fresh crater sizes, different paths of crater degradation (C6 vs. $\frac{d}{D}$) are possible, which can further explain the difference between C6 values from observation and simulation. Additional analysis is also required on the choice of the initial fresh crater shape, which dictates the change in C6 magnitude during degradation.

Conclusion: Chebyshev coefficients enable efficient tracking of size-dependent morphological state for small impact craters. Difference in degradation trends is observed when the change in small crater shape (quantified by C6) vs. $\frac{d}{D}$ from Apollo 16 and 17 observations is compared to shape changes obtained from a linear diffusion based degradation model. Possible reasons include the initial fresh synthetic crater shape and/or a transition to non-linear diffusion degradation model. Our future work will study and compare degradation over a larger diameter range of craters.

References:

- [1] H. P. Ross (1968) *Journal of Geophysical Research* 73(4):1343.
- [2] L. A. Soderblom (1970) *Journal of Geophysical Research* 75(14):2655.
- [3] R. A. Craddock, et al. (2000) *Journal of Geophysical Research: Planets* (1991–2012) 105(E8):20387.
- [4] C. I. Fassett, et al. (2014) *Journal of Geophysical Research: Planets* 119(10):2255.
- [5] P. Mahanti, et al. (2014) in *LPSC Proceedings* vol. 45 1584.
- [6] P. Mahanti, et al. (2017) in *Lunar and Planetary Science Conference* vol. 48.
- [7] M. Henriksen, et al. Submitted to *Icarus*, 2015.
- [8] P. Mahanti, et al. (2018) *Icarus* 299:475.
- [9] T. Thompson, et al. (2017) *LPI Contributions* 1986.
- [10] D. Minton, et al. (2016) in *Lunar and Planetary Science Conference* vol. 47 2623.

OpenPlanetaryMap: Building the first Open Planetary Mapping and Social platform for researchers, educators, storytellers, and the general public. N. Manaud¹, A. Nass², M. Lewando³, S. van Gasselt⁴, A.P. Rossi⁵, T. Hare⁶, J. Carter⁷, H. Hargitai⁸, ¹SpaceFrog Design, Toulouse, France; nicolas@spacefrog.design, ²German Aerospace Center, Institute of Planetary Research, Berlin, Germany, ³CodeMacabre, UK, ⁴Dep. Land Economics, National Chengchi University, Taipei, Taiwan, ⁵Department of Physics and Earth Sciences, Jacobs-University Bremen, Bremen, Germany, ⁶U. S. Geological Survey, Astrogeology Team, Flagstaff, USA, ⁷Institut d’Astrophysique Spatial, Orsay, France, ⁸NASA Ames Research Center/ NPP, Moffett Field, USA.

Introduction: The popularity and ubiquity of web interactive maps constitute a powerful leverage for telling stories, educating and engaging a wide and diverse audience with planetary sciences. A few excellent planetary interactive maps [e.g. 1,2,3] exist but they are either too complex for non-experts, or they are closed-systems that do not allow for collaborative learning, social interactions, and reusability of data.

OpenPlanetaryMap (OPM) is a collaborative effort from within the OpenPlanetary community [4] and based on “Where On Mars?”, a previous outreach project to visualise ESA’s ExoMars Rover landing sites candidates [5]. OPM is supported and made possible thank to CARTO [6] and Europlanet [7] through their respective grant programmes.

Our long-term vision is to build a community around an Open Planetary Mapping and Social platform for space enthusiasts, planetary scientists, educators and storytellers. Our goal is to enable them to easily and collaboratively create and share location-based knowledge and maps of others planets of our Solar System.

Objectives: We aim to launch a first prototype version of the OpenPlanetaryMap platform at next the European Lunar Symposium in May 2018.

Web Map Interface: As part of this platform, we will develop a web map interface that will make it easy and enjoyable for novice people to discover, search, share, discuss and add their own places on Mars and the Moon (we will expand to other planets in a second stage). We aim to provide a social experience that will help creating an emotional connection with Mars and the Moon and incentives to learn and share knowledge about it.

Open Datasets Repository: A key element of the platform will be an open datasets repository containing a curated selection of location-based information and places of interest about planetary geography, topography, geology, weather, climate, scientific missions and discoveries, robotic and human exploration. These scientifically accurate data sets, along with public crowdsourced datasets, will be programmatically accessible and reusable by others to develop third-party applications for specific scientific or outreach purposes.

Basemap: We will also design and implement at least one beautifully crafted vector-based basemap of Mars and the Moon that will serve as the base layer of our web map interface and enrich its overall user experience. It will be made publicly available to foster the creation by others of theme-based planetary maps that can be easily shared on the web and social media.

Initial concepts: Initially, the places on Mars and the Moon the audience will learn about will include information from curated datasets, as well as from a public crowdsourced dataset of *Places*. These Places will either be related to a physical object or phenomenon (i.e.: crater, dune, gully, dust devil, cloud), or to a more abstract one that contributes to increasing knowledge of Mars and the Moon (i.e.: scientific publication, blog article, Wikipedia page, tweet, panoramic image, video, question, story, event). Our audience will also learn from discussions they have with each other, including with planetary scientists.

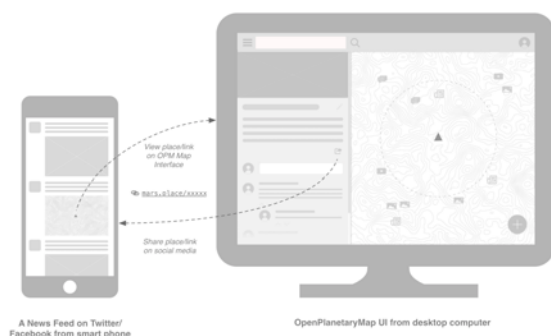


Figure 1: This illustrates the basic concept for the OPM web map interface and sharing places.

One particular requirement that is key to the success of our platform is the capability to handle multiple users and groups for our project team of planetary scientists and cartographers to collaboratively store and manage, publicly and privately share, datasets.

The OPM platform will almost entirely rely on the CARTO Engine and Builder.

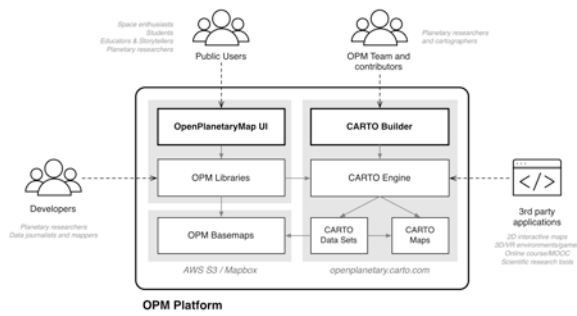


Figure 2: This illustrates how CARTO will fit into the OPM platform, and what users and applications interact with it.

Approach: We are a small interdisciplinary and international team of researchers, developers and designers passionate about planetary mapping and cartography. We started to form our team in January 2017 and held a first meeting in Berlin two months later to kick-off the project. Throughout the project, we will adopt an iterative development approach and try to follow a user-centered design process as much as possible; including user research, prototyping and testing methods. We will organize co-located hackathons at planetary data workshops and other events, to learn from potential users and experts, and stay in line with our objectives.

Being collaborative by nature, we will encourage everyone who is interested in this project to contribute [8,9] with their expertise: in planetary cartography, web development, geospatial data processing or any other areas that we haven't yet thought of.

Intended outcome and impact: We aim to make novice people feel that Mars is at their reach, both in terms of knowledge and preconceived physical proximity. We want them to use our future web application to quickly and regularly learn something about Mars, just like people head to Google Maps to find their bearings or any location-based information.

With an Open Data and Open Science philosophy in mind, we aim to encourage planetary scientists and mappers to share and collaborate on research data sets in a way that is beneficial to all parties: peers, graduate students, science communicators and the general public.

We aim to encourage science communicators, educators and storytellers to contextualise more their publications or resources by providing better location information, so as to allow their audience for further exploration and better understanding of a related topic or story.

Being an open source project, we also hope to encourage a younger audience of STEM students to apply or acquire new skills in cartography, Geographical Information System (GIS), and program-

ming, by contributing to the OPM software and platform development.

References: [1] ASU's Mars Space Flight Facility JMARS: <https://jmars.asu.edu>, [2] PDS Geosciences Node Orbital Data Explorer (ODE): <http://ode.rsl.wustl.edu>, [3] NASA Mars/MoonTrek: <https://marstrek.jpl.nasa.gov>, <https://moontrek.jpl.nasa.gov>, [4] OpenPlanetary: <http://openplanetary.co>, [5] "Where On Mars?", <http://whereonmars.co> [6] CARTO: <https://carto.com>, [7] <https://www.europlanet-eu.org>, [8] OPM website: <http://openplanetarymap.org>, [9] OPM github repository: <https://github.com/openplanetary/opm>

Acknowledgment: We warmly thank the CARTO team for believing in this project and for their outstanding support through their Grant Program. A special thanks go to: Javier de la Torre, Sergio Álvarez Leiva, Andrew Hill, Stuart Lynn, Tyler Bird, Oriol Boix, Carla Iriberry, Dani Carrión, Javi Santana, Alejandro Martínez, and Carlos Matallín.

MODAL MINERALOGY AND MATURITY ESTIMATES OF APOLLO 14, 15, AND 16 SOILS USING FTIR AND QEMSCAN TECHNIQUES. D. J. P. Martin¹, K. H. Joy¹, A. Morlok², H. Bagshaw¹, R. A. Wogelius¹, H. Hiesinger². ¹ School of Earth and Environmental Sciences, University of Manchester, Oxford Road, Manchester, M13 9PL. dayl.martin@manchester.ac.uk; ²Institut für Planetologie, Wilhelm-Klemm Strasse 10, 48149 Münster.

Introduction: Lunar regolith samples exhibit a range of physical, chemical, and mineralogical properties including grain size distribution, grain shape, modal mineralogy, bulk chemistry, maturity (often estimated via the I_s/FeO index, where I_s = amount of nanophase iron and FeO is bulk rock iron oxide content [1], or the amount of ^{36}Ar implanted from the solar wind [2]), and spectral reflectance (or emittance) profiles [3-7]. This study has employed the use of FTIR bulk- and microspectroscopy to investigate the spectral properties of unconsolidated Apollo soils (bulk and sieved fractions) and obtain modal mineralogy and maturity estimates non-destructively. QEMSCAN (an innovative new SEM phase analysis tool [8]) analysis has been used to estimate modal mineralogy from polished grain mounts, along with finding the grain size distribution and grain shape of each sample.

Sample Preparation: 7 Apollo soils (~2 grams each of 14163, 14259, 15101, 15401, 61220, 62231, and 67481) were sieved using steel-mesh sieves and a dry-brushing technique, resulting in grain size fractions of 0-25, 25-63, 63-125, 125-250, >250 μm and a bulk soil for each sample. For each size fraction, a portion was transferred into an aluminium sample cup and the edge of an aluminium spatula was scraped across the cup to obtain a flat surface. FTIR spectroscopy was then used to analyse the surface of each size fraction of each soil. Post-sieving, a portion of 3 of the soils (14259, 672, 15401, 147, and 67481, 96) were sent to JSC for mounting and polishing for QEMSCAN analysis.

FTIR Techniques: In Manchester, a PerkinElmer Spotlight-400 spectrometer with attached mapping unit was used to obtain mid-infrared (3-15 μm) images of the Apollo soils with a resolution of 25 μm per pixel. 32,000 pixels were collected per image. These measurements were made under ambient conditions. A series of band ratios were applied to the Reststrahlen Bands (RB; mineral sensitive region ~7-13 μm) of the images to identify each pixel as a specific mineral or phase, and the modal mineralogy estimates were derived from the proportions of each mineral or phase being identified per sample image. In Münster, a Bruker 70v Vertex FTIR instrument was used to obtain average spectra of each size fraction of the soils under both ambient and vacuum conditions. A shift in the Christiansen Feature (a reflectance minimum sensitive to bulk chemistry) was also used to estimate the maturity of each sample.

QEMSCAN Techniques: In Manchester, a FEI QUANTA 650 FEG ESEM was used to obtain quantitative information regarding the modal mineralogy, grain size distribution, and grain shape

properties of the polished grain mounts. A beam strength of 10 nA and step size of 2.5 μm was used (giving an effective spot size of 2.5 μm), and data was collected using the Particle Mineralogical Analysis collection mode. This was then used to identify and analyse individual particles within the polished grain mounts. The QEMSCAN software uses a Species Identification Protocol (SIP) list containing EDS data of minerals [8]. In this study, a SIP list customized for lunar samples was used to identify each 2.5 μm pixel as a specific lunar mineral or phase, and the proportions of which were used to estimate the modal mineralogy. Grain shape was also classified using the QEMSCAN software, and grain size distribution was calculated using automated particle counting (y-axis) and a series of pre-defined size bins (x-axis).

FTIR Results: The spectral properties of the soils from the same landing site were highly similar with respect to the positions of the main reflectance bands. The exception to this was soil 15401, which is a pyroclastic glass bead-rich soil and is atypical of the Apollo 15 landing site. For each soil, the positions of the diagnostic reflectance bands were also consistent between grain sizes, though a shift to shorter wavelengths of the CF position was observed in coarser grain sizes (that could not be associated with mineralogy and, by extension, bulk chemistry) along with the appearance of a Transparency Feature (TF) in the bulk soil and 0-25 μm fraction. A general reduction in reflectance of the diagnostic reflectance bands was observed with decreasing grain size. A similar decrease in %Reflectance was also observed in more highly mature samples (for example the highly mature soil 62331 with $I_s/\text{FeO} = 91$ compared to the immature soil 61220 with $I_s/\text{FeO} = 9.2$ [8]). Modal mineralogy/phase estimates were within 2-8% of those determined by previous studies [5, 9-12]. Volcanic- and impact-derived glass was identified based on their differing CF positions (impact glass is more feldspathic so has a shorter wavelength CF position). The proportions of plagioclase and agglutinate glass were found to increase with decreasing grain size (consistent with previous studies) and bulk sample results were most similar to those of the finest grain size fraction (0-25 μm).

QEMSCAN Results: Modal mineralogy estimates from QEMSCAN analyses are also within 2-8% of the proportions quoted from previous studies, and within 5% of the FTIR estimates. However, a greater range of minerals were observed in these results compared to our FTIR method, particularly oxides and sulphides, due to such minerals being IR-inactive in the RB region.

Volcanic and impact glasses were identified based on their Mg/Al ratio (>1.1 for volcanic glass) [13]. Grain size distributions of each soil size fraction generally follow bell-curve profiles, though a large number of small particles ($<5\text{ }\mu\text{m}$) are present in each sample, skewing the results toward the finer grain size fractions. As such, for the larger grain sizes ($<25\text{ }\mu\text{m}$), data from the $<5\text{ }\mu\text{m}$ fraction were discarded. Grain shapes were angular for mineral fragments and amorphous glass phases, and well-rounded for volcanic glass beads and particles $<10\text{ }\mu\text{m}$ (although the latter is due to the $2.5\text{ }\mu\text{m}$ resolution not resolving the grain boundaries in enough detail for the true grain shape to be determined).

FTIR and QEMSCAN comparison: Both techniques adequately estimate the modal mineralogy (compared with each other, Figure 1, and previous studies) of each grain size fraction. However, QEMSCAN analyses are dominated by the abundant fine particles present in each section, largely because of the small number of large particles present on a single slide (this is particularly applicable to the $>250\text{ }\mu\text{m}$ and bulk sample fractions). FTIR analyses are affected by a similar problem in that the fine particles ($<10\text{ }\mu\text{m}$) coat the surfaces of larger grains ($<50\text{ }\mu\text{m}$). Spectral mixing also occurs in samples $<25\text{ }\mu\text{m}$ due to more than 1 grain being present in a single field of view. This causes the more reflective component (in the case of lunar samples: plagioclase) to dominate a mixed spectrum, causing a skew towards greater proportions of the mineral component. This is particularly problematic in Apollo 16 samples that are plagioclase-rich, with FTIR analyses resulting in plagioclase estimates that are 10% greater than those measured by other techniques in the $0\text{--}25\text{ }\mu\text{m}$ grain size fraction. However, for the purpose of completely non-destructive (FTIR) and largely non-mineralogy, the nature of each sample (e.g. source lithology or, in the case of Apollo 14 soils, the mixed nature of the soil) can be determined, along with identification of the variety of minerals and phases present and their approximate proportions.

Maturity estimates: CF positions of the average image spectra of samples shift to lower wavelengths with increasing grain size. Such a shift is usually caused by increased feldspathic components, but this is the opposite of what would be expected (as the feldspathic component increases with decreasing grain size). Therefore, this shift is attributed to maturity effects. Given that the finest grain size fraction has the greatest surface area, space weathering (and, therefore, maturation) has the greatest effect upon this size fraction (higher surface area for solar wind argon and nanophase iron to adhere to). As such, maturation occurs at a greater rate in the finest soil fraction, resulting in a trend of increasing maturity with decreasing grain size. In terms of spectral effects, the CF position offset between the finest ($0\text{--}25\text{ }\mu\text{m}$ or Bulk

fraction) and coarsest ($>250\text{ }\mu\text{m}$) fractions would be greatest in immature samples, and lowest in highly mature samples. A comparison of this CF position offset with measured I_s/FeO values of each sample display a weak logarithmic trend ($R^2 = 0.54$). However, FTIR results of the finest fraction of Apollo 16 samples were skewed by the high plagioclase content, resulting in reduced CF position offset. When the highly immature 61220 skewed result is removed, the logarithmic fit shows a strong correlation ($R^2 = 0.91$), and a linear trend shows a fair correlation ($R^2 = 0.73$). As such, the maturity of lunar soils can be estimated using FTIR spectroscopy, though soils require sieving prior to analysis to acquire the coarse $>250\text{ }\mu\text{m}$ fraction.

Conclusions: Modal mineralogy estimates using FTIR and QEMSCAN techniques are consistent with those obtained from previous studies, with the exception of the finest fraction of some soils. The modal mineralogy proportions of soil 62231 have been estimated for the first time. Also, we highlight a non-destructive method of estimating maturity using FTIR techniques that is applicable to most samples and, potentially, could replace the destructive ferromagnetic method of estimating maturity (that is no longer used). This is important for future sample return missions to the lunar surface and to other airless bodies.

References: [1] Morris R.V. (1978) *Proc. LPSC IX*, 2287-2297 [2] Bogard D. D. and Hirsch W. C. (1975) *Proc. LPSC*, 6, 2057-2083. [3] Pieters C.M. and Taylor L. A. (1998) *LPSC XXIX*, Abstract #1840. [4] Taylor L.A. et al. (2010) *JGR:Planets*, 115, 2156-2202. [5] Apollo 15 Prel. Exam. (1972) *Science*, 175, 363-375. [6] Houck K. J. (1982) *JGR:Planets*, 87, A197-A209. [7] Ling Z. et al. (2011) *Jour. Ear. Sci.* 22, 578. [8] Sølling T. I. et al. (1983) *Proc. Int. Symp. of Soc. Core Analysts*, Abstract #37. [9] Morris R. et al. (1983) *Plan. Mat. Branch Pub.* 67, 425-914. [10] McKay, D.S., et al. (1974) *LPSC Proc.* 887-906. [11] Heiken, G., et al. (1973) *LPSC Proc.* 4, 251. [12] Apollo Soil Survey (1971) *Ear. Plan. Sci. Letters*.12, 49-54. [13] Delano J. W. and Livi K. (1981) *GCA*, 45, 2137-2149.

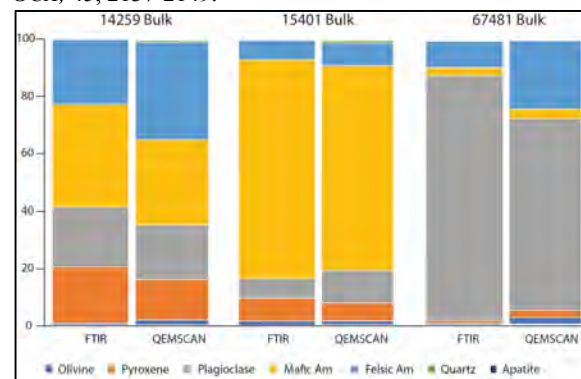


Figure 1 – A comparison of FTIR and QEMSCAN modal mineralogy estimates. Individual minerals identified through QEMSCAN were grouped for this comparison (e.g., anorthite and bytownite were combined for the plagioclase field). Am = amorphous material.

SURVEY OF THE LUNAR CRUST-MANTLE INTERFACE WITH THE MOON MINERALOGY MAPPER DATA. M. Martinot^{1,2}, J. Flahaut^{3,4}, S. Besse⁵, C. Quantin² and W. van Westrenen¹, ¹Vrije Universiteit Amsterdam, 1081HV Amsterdam, The Netherlands, email: m.martinot@vu.nl, ²LGL-TPE University of Lyon, 69622 Villeurbanne cedex, France, ³IRAP, Université de Toulouse, CNRS, CNES, UPS (Toulouse), France, ⁴CRPG, Université de Lorraine, CNRS, Nancy, France, ⁵ESAC, 28691 Villanueva de la Canada, Madrid, Spain.

Introduction: Studying the lunar crustal composition and stratigraphy can provide insight into the thermal and magmatic evolution of the Moon, *e.g.*, [1]. The Lunar Magma Ocean concept predicts the formation of an anorthositic (> 90 % plagioclase-rich) upper crust formed by floatation on a magma ocean, *e.g.*, [2,3]. The denser olivine and pyroxene minerals, formed during earlier stages of the magma ocean crystallization, sank to the bottom of the magma ocean to form the lower crust and mantle, *e.g.*, [4,5]. Spectroscopic datasets have been widely used to survey the lunar crust at a global scale, in order to provide constraints into its composition and lateral variations. Tompkins and Pieters [6] studied the mineralogy of lunar crater central peaks with Clementine data, and suggested that there is an increase of mafic content with depth. More recently, multiple surveys have highlighted evidence for lateral variations in the crustal composition [7,8]. This study aims at characterizing the lunar crust-mantle interface mineralogy and evaluate its potential vertical and horizontal variations.

Datasets: Reflectance data from the Moon Mineralogy Mapper (M³) and high resolution imagery from the Lunar Reconnaissance Orbiter (LRO) and Kaguya cameras were used on the central peak and/or peak ring of a selection of craters. M³ is a visible to near-infrared hyperspectral imager, with 85 spectral channels spanning from 430 to 3000 nm and a spatial resolution of 140 m/pixel or 280 m/pixel [9]. M³ data were selected favoring the optical period with the greatest areal coverage over the craters' central peak and/or peak ring, and with the lowest phase angle possible, in order to limit the influence of shadows. High-resolution images of the craters' central peak and/or peak ring are provided by the LRO Wide Angle Camera (WAC, resolution of 100 m/pixel) and the Kaguya Terrain Camera (TC, resolution of 10 m/pixel). Crustal thickness values are estimated from the Gravity Recovery and Interior Laboratory (GRAIL) crustal thickness models 1 and 3, derived from the gravimetric data obtained during the GRAIL mission [10].

Method: The proximity value to the crust-mantle interface was calculated for all the craters in the Lunar Impact Crater Database. The proximity value of a crater's central peak and/or peak ring is obtained by deducting the melting depth taken as a proxy for the minimum depth of origin of the material emplaced in a crater's central peak, [11]) to the pre-

impact crustal thickness, as done in [12].

The studied craters were selected based on three criteria: (1) the presence of a preserved central peak and/or peak ring; (2) good M³ coverage of all or a part of the crater's central peak and/or peak ring; (3) a proximity value to the crust-mantle interface between +10 km and -20 km. Craters embedded in other impact structures (*e.g.*, in mare basins or within SPA) were discarded from the selection, because the proximity value calculation does not apply to craters within craters [13]. Using these criteria, 36 craters located within the feldspathic highlands [14] were selected for further study. M³ data of the craters' central peak and/or peak ring are mosaicked and processed in order to remove the continuum. The study of the mineralogy of the craters' central peak and/or peak ring was performed using spectral parameter maps from the algorithm of [15] (for instance, the integrated band depth for the 1 and 2 microns absorption bands). These parameter maps were refined using filters to reduce the influence of noise, and stretched so as to highlight pixels displaying certain key spectral features. The spectra corresponding to the highlighted pixels in the color composite were then manually checked and compared to spectra from the Reflectance Experiment Laboratory (RELAB) database in order to confirm a mineralogical detection.

Results: Fig. 1 shows the global distribution of the plagioclase, pyroxene, olivine and spinel detections from our study. Our selection of craters, which are supposed to sample rocks within +10 km/-20 km of the crust-mantle interface, display a variety of mineralogical detections. Some craters display only mafic minerals (pyroxene and/or olivine, *e.g.*, Clavius) whereas other craters display mostly plagioclase signatures (*e.g.*, Humboldt, Petavius). Mixed assemblages are common, and a few craters (*e.g.*, Theophilus) display pyroxene, plagioclase, olivine and spinel detections in their central peak. To the first order, there is no correlation between the mineralogy and the proximity to the crust-mantle boundary: pyroxene as well as plagioclase are displayed in craters with all proximity values of the selected range.

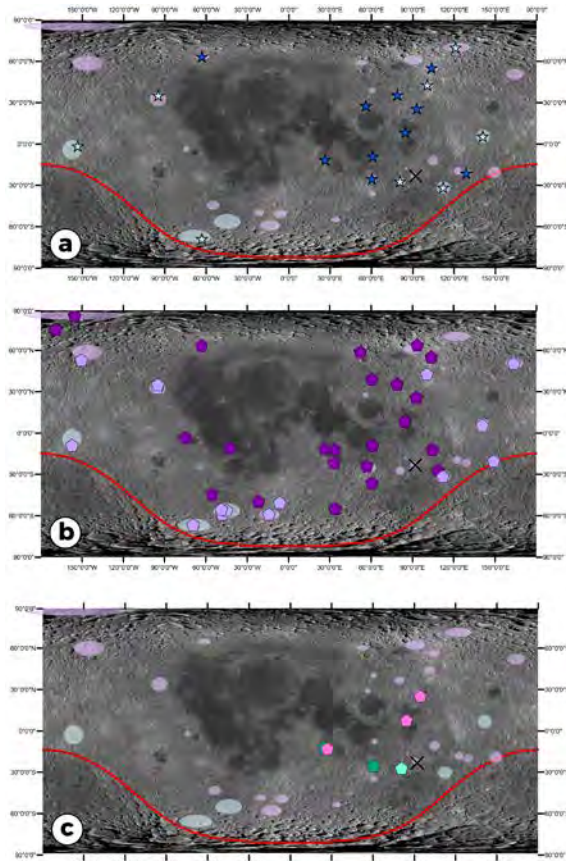


Figure 1: Global distribution of plagioclase (blue stars in **a**), pyroxene (purple pentagons in **b**) and olivine and spinel (respectively, green and pink pentagons in **c**) in the central peaks of our selected craters. The craters with a darker colored symbol display a positive proximity value, whereas the craters with a lighter colored symbol display a negative proximity value. The transparent pink and blue circles outline the selection of craters with the different GRAIL models (model 1 in pink, model 3 in blue). The crossed crater materializes the absence of a distinct mineralogical signature. The detections are overlain on the global LRO WAC mosaic, and the red outline highlights the limit of the South-Pole Aitken basin.

Discussion and Conclusions: Although the proximity value range that was used in this study highlights craters that excavate material from nearby the crust-mantle interface, no sharp changes in mineralogy, and no trends with depth are observed. Two olivine occurrences are detected in craters displaying a positive proximity value, and one in a crater displaying a negative proximity value. The spinel occurrences presented in this study are all detected in craters displaying a positive proximity value. Plagioclase is widely detected in the craters of this study, even in the craters displaying a negative proximity values. Our current observations do not allow us to identify a potential vertical stratification around the crust-mantle interface, but rather point towards the

existence of lateral heterogeneities at this depth. The occurrence of similar lithologies in specific regions (e.g., Petavius, Humboldt, Milne versus Compton, Bel’Kovich, Gauss) suggests that regional (rather than global) trends might exist. A follow-up to this study is the characterization of the pyroxene composition, which could help to identify a potential enrichment in calcium-rich pyroxene with proximity values increase (towards the upper crust).

References:

- [1] C.K. Shearer *et al.* (2006) *Reviews in Mineralogy and Geochemistry*, 60, 365–518. [2] W.M. Kaula (1979) *JGR*, 84, 999–1008. [3] P.H. Warren (1985) *Annual Review of Earth and Planetary Science*, 13, 201–40. [4] Y. Lin *et al.* (2017) *Nature Geoscience*, 1, 1–6. [5] G.A. Snyder, L.A. Taylor, C.R. Neal (1992) *Geochimica et Cosmochimica Acta*, 56, 3809–3823. [6] S. Tompkins, C.M. Pieters (1999) *Meteoritics & Planetary Science*, 34, 25–41. [7] E. Song *et al.* (2013) *JGR E: Planets*, 118, 689–707. [8] M. Lemelin *et al.* (2015) *JGR: Planets*, 120, 869–887. [9] C.M. Pieters *et al.* (2009) *Current Science*, 96, 1–6. [10] M.A. Wieczorek *et al.* (2013) *Science*, 339, 671–5. [11] M.J. Cintala, R.A.F. Grieve (1998) *Meteoritics & Planetary Science*, 33, 889–912. [12] J. Flahaut *et al.* (2012) *Advances in Space Research*, 50, 1647–1665. [13] T. Kohout *et al.* (2012) *LPI*. [14] B.L. Jolliff *et al.* (2000) *JGR: Planets*, 105, 4197–4216. [15] M. Martinot *et al.* (2018) *JGR: Planets*, 123.

PROLONGED LUNAR MAGMA OCEAN BY HEAT-PIPING FROM CUMULATE OVERTURN. M. Maurice¹, N. Tosi^{1,2}, S. Schwinger¹, D. Breuer¹, ¹German Aerospace Center (DLR), Berlin, Germany, ²Technische Universität Berlin, Germany.

Introduction: The Moon is thought to originate from a collision between the proto-Earth and a Mars-sized impactor. Such a giant impact would have left the lunar mantle largely molten, resulting in a deep magma ocean. A large part (about 80%) of the lunar magma ocean (LMO) solidifies in around 1000 years [1] by efficient radiative heat loss at its molten surface, until a solid crust forms by flotation of plagioclase. The heat is then lost by conduction through the growing crust, which is a much less efficient regime that delays the complete solidification of the LMO by a few tens of millions of years [1]. However, the lunar anorthositic crust formed over a time span of ~200 millions years [1], which is still longer than what LMO solidification models suggest. Based on the observation that the solidification time scale of the LMO is compatible with the timescale of the overturn of solid cumulates, we show that secondary melting generated by hot plumes after the onset of solid-state convection below the solidifying LMO represents an important heat source for the LMO. In fact, the extraction of hot melts from upwelling cumulates into the LMO can prolong the lifetime of the LMO and delay its complete solidification up to about 200 millions years.

Furthermore, the onset of solid-state convection in the solidifying cumulates helps to entrain the late crystallized ilmenite bearing cumulates (IBC) into the mantle. Entrainment of the IBC is needed to generate the high-Ti mare basalts and picritic glasses on the Moon's surface by secondary melting [2]. However, IBC crystallize at low temperature and remain trapped in the stagnant lid according to models where solid-state convection starts only after the whole lunar mantle is solid [3]. The onset of cumulates overturn during LMO solidification provides a mechanism to entrain IBC in the mantle compatible with a realistic rheology.

Model: We use the model described in [4] to perform 2D and 3D simulations of solid-state convection in the cumulates below a self-consistently solidifying LMO. The initial structure of the mantle is computed from fractional crystallization of a global LMO using alphaMELTS. The solidification of the LMO and the growth of the flotation crust are parametrized by solving the energy conservation equilibrating the outgoing heat flux through the crust with the incoming conductive and "heat piping" heat fluxes as well as with the internal heating of the LMO due to radioactive decay. Figure 1 shows how the different reservoirs (core, solid cumulates, LMO and crust) are thermally coupled.

Results: We investigate the influence of heat piping on the LMO crystallization duration and entrainment of IBC in the lunar mantle.

LMO duration. We varied the reference viscosity of the lunar mantle, which causes different overturn time scales and convective intensities, resulting in different heat piping efficiencies. Figure 2 shows the result for two cases. When the reference viscosity is high (10^{21} Pa s), no overturn occurs during LMO solidification and the heat piping flux is low, since melting is only caused by radioactive heating of the hot cumulates. When the reference viscosity is low (10^{19} Pa s), solid-state convection sets on rapidly resulting in strong decompression melting and a high heat piping flux that causes the LMO's depth to increase when the flotation crust starts to grow, and prolongs the solidification duration.

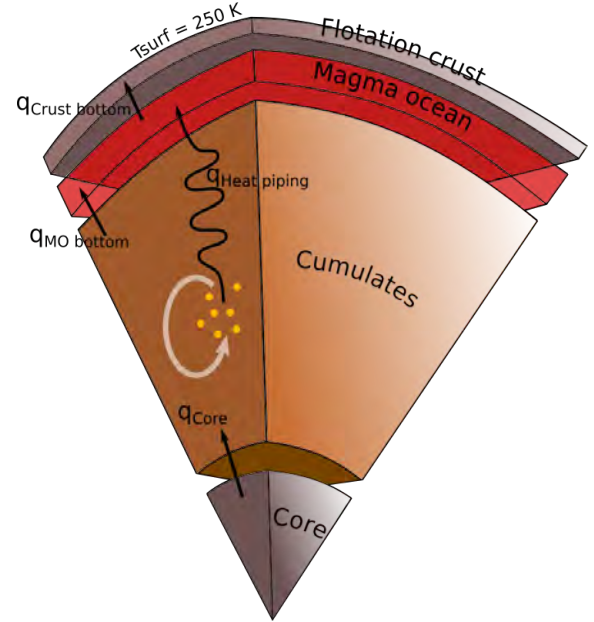


Figure 2: Thermal couplings between the different reservoirs of the system. The thermal energy is conserved for each of the four systems, the interfacial heat fluxes (black arrows) and the surface temperature providing the boundary conditions. The piping flux originates from the melting induced by solid-state convection in the cumulates (white arrow). Internal heating by radioactive decay is also included.

IBC entrainment. We showed in a previous work [4] that the onset of solid-state convection during the magma ocean solidification provides an efficient mechanism to mix composition heterogeneities inherited from fractional crystallization. The temperature at the top of the convecting domain is buffered at a high value by the overlying magma ocean, allowing the mobilization of the uppermost layers. This

mechanism applies in the case of the LMO and we show that when cumulates overturn occurs during LMO solidification, a substantial part of the IBC is entrained in the bulk convecting mantle, and ilmenite is present in re-melting plumes long after the end of the LMO solidification.

Conclusions: Cumulates overturn is likely to oc-

References:

- [1] Elkins-Tanton L. et al. (2011) *EPSL* 304, 326–336. [2] Elkins-Tanton L. et al. (2002) *EPSL* 196, 239–249. [3] Yu S. et al. (submitted). [4] Maurice M. et al. (2017) *JGR: Planets*, 122, 577–598.

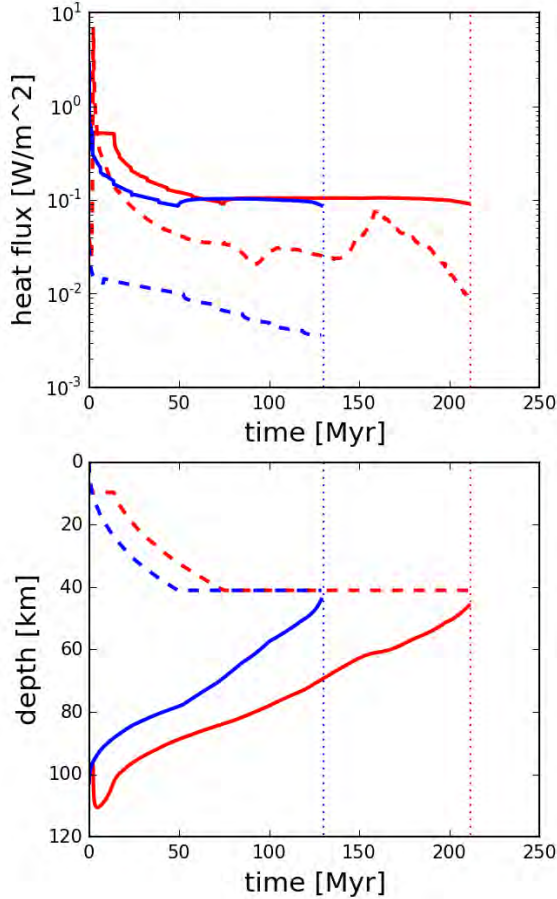


Figure 3: Evolution of the LMO for two different values of the reference viscosity of the cumulates: 10^{21} Pa s (blue) and 10^{19} Pa s (red). The top panel shows the outgoing heat flux through the crust (solid lines) and the heat piping flux (dashed lines). The bottom panel shows the depth the bottom of the LMO (solid lines) and of the bottom of the crust (dashed lines). In both panels the dotted lines represent the end of LMO crystallization time.

cur during LMO solidification and to increase the LMO solidification duration by providing a substantial quantity of heat through heat piping, resulting in a positive feedback on the solidification duration, providing a time scale that is consistent with the chronology of the anorthosite crust formation. Moreover early onset of solid-state convection provides an efficient mechanism for sinking of the late crystallized IBC, necessary to produce the observed high-Ti material on the lunar surface.

DIVERSITY OF VOLCANIC ERUPTION STYLES IN THE CENTRAL PROCELLARUM REGION OF THE MOON. M. J. McBride¹, B. H. N. Horgan¹, L. R. Gaddis², S. and S. J. Lawrence³, ¹Purdue University, 610 Purdue Mall, West Lafayette, IN 47907, ²Astrogeology Science Center, U.S. Geological Survey, Flagstaff, ³NASA Johnson Space Center (mjmcbride@purdue.edu).

Introduction: The Central Procellarum (CP) region of the Moon, located within Oceanus Procellarum (300-320°E, 9-33°N) on the western near side, is comprised of two major geologic landforms, the Aristarchus Plateau and the Marius Hills Volcanic Complex [1-5]. Copernican-aged crater Aristarchus has a diameter of 45 km and lies on the southeast corner of the Aristarchus Plateau, which is raised about 1-1.5 km above Oceanus Procellarum. The crater is known for its distinctive brightness compared to other craters of similar age. To the south of the Plateau, the Marius Hills are also located on a plateau with an area of 35,000 km² situated 100-200 m above the surrounding plains.

The CP region exhibits a diverse range of volcanic features and deposits. The Plateau is home to the largest pyroclastic deposit on the Moon, as well as a large rille hypothesized to be related to local mare emplacement [5]. Within the Marius Hills, volcanic domes, lava flows, sinuous rilles, and volcanic cones have been identified [1, 2]. These volcanic features were formed by a range of volcanic eruption styles, including both effusive and explosive eruptions. Explosivity is largely controlled by volatile content, but it is unclear whether the different apparent volatile contents in the magmas in this region were due to different magma sources or volatile evolution of the same magma sources over time. In this study, we investigate the relationship between effusive and explosive volcanic features across the CP region to constrain the magmatic history of the region.

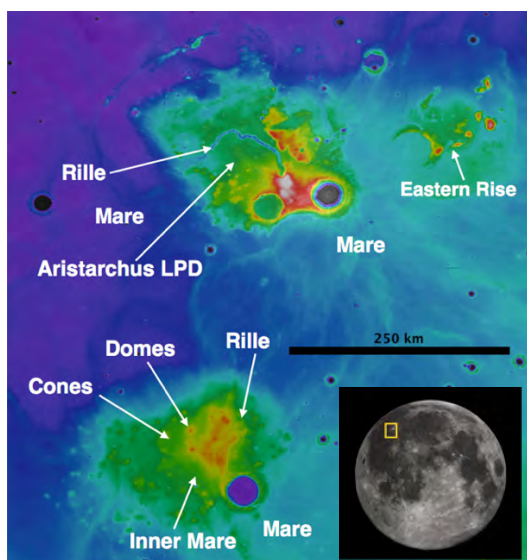


Figure 1: (inset) Location of Aristarchus and the Marius Hills on the near side of the Moon. (main image) Major volcanic features labeled on regional LOLA topography.

Previous Work: The CP region has been previously studied using visible imagery [3, 4], 9-band Clementine visible wavelengths spectral data [3, 6, and visible/near-infrared spectra from the Moon Mineralogy Mapper (M³) [6-10]. The Aristarchus Plateau is known for its spectral diversity, due to the presence of both volcanic (Fe-rich) and impact minerals. Previous M³ analysis of the Aristarchus Plateau identified olivine, and glass-rich impact melt, orthopyroxene-rich (OPX) impact ejecta, clinopyroxene (CPX) in surrounding mare basalts, and glass-rich pyroclastic deposits [4-7]. The central peak and ejecta of Aristarchus crater also exhibit spectral signatures of anorthosite [7].

Geologic units in the Marius Hills have been previously characterized by photogeologic and compositional analyses. Analysis of Clementine spectra revealed a similar composition between volcanic domes and the plateau, but differences in the spectral signatures of the cones [6]. Three different morphologies of volcanic cones have been identified in the Marius Hills, and many further potential volcanic cones have been detected in visible imagery. M³ spectra in the Marius Hills have been interpreted as consistent with olivine [9]. The Marius Hills is a region of interest for future lunar exploration mission because of the geological diversity.

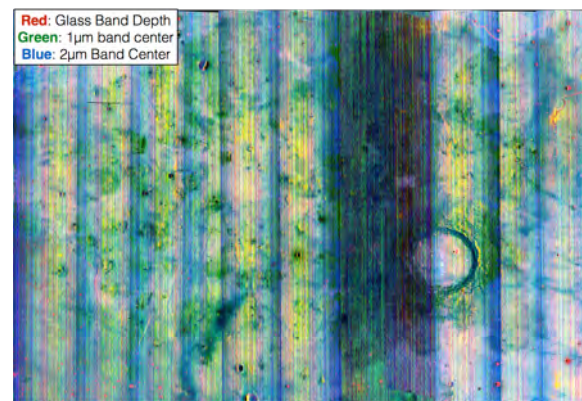


Figure 2: RGB composite from an M³ mosaic of the Marius Hills Volcanic Complex (R=glass band depth, G=1μm band center, B=2μm band center) superimposed on the LRO Wide Angle Camera (WAC) mosaic.

Methods: M³ was an imaging spectrometer on the Chandrayaan-1 lunar orbiter operating in the visible to near-infrared (0.42-3.0 μm). M³ in global mode has a resolution ranging from 140-280 m/pixel in 86 spectral channels [11]. M³ collected data during two operational periods distinguished by changes in instrument temperature, viewing orientation, and altitude. Data in this project was obtained from operational periods 1B, 2A, 2B, and 2C. Two M³ maps were

constructed with bounds 300-312°E and 9-17°N for Marius Hills and 300-320°E and 16-33°N for the Aristarchus Plateau. The continuum of each spectrum was suppressed [7, 8] using a linear convex hull with two segments between 0.6-2.6 μm . Spectral noise was reduced using a median filter and a boxcar smoothing algorithm, both with widths of 5 channels.

To investigate spectral diversity in the region, we applied spectral parameter mapping to our M^3 mosaic, as shown in Figures 2 and 3. Some of the horizontal variability across the mosaics is due to changes in resolution and sensitivity between individual observations. Our glass spectral parameter detects the wings of the glass iron absorption band, which is centered at much longer wavelengths than other Fe-bearing minerals, based on the average band depth below the continuum at 1.15, 1.18, and 1.20 μm [12]. We also calculated the position of the 1 and 2 μm iron bands, which is sensitive to mafic mineralogy [7].

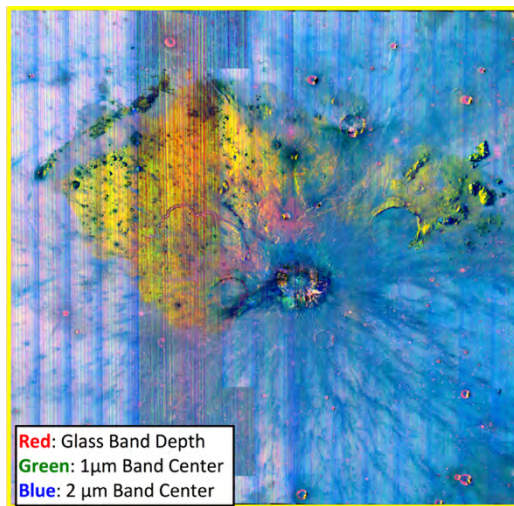


Figure 3: Composite M^3 view of the Aristarchus Plateau (R =glass band depth, G =1 μm band center, B =2 μm band center) of the MHVC superimposed on the LRO Wide Angle Camera (WAC) mosaic.

Results: Spectra consistent with high concentrations of mafic glass based on a broad 1000nm band in addition to a broad 2000 nm band have been found in both the Aristarchus pyroclastics and the Marius Hills cinder cones (Figure 4, green)[13-15]. Both of these deposits were likely comprised of quickly quenched pyroclasts due to high volatile interaction or small pyroclast size, which would increase glass content and decrease the crystalline component.

Volcanic domes are formed through the constructive emplacement of effusive flows. Domes have been identified in the MHVC [1], and a potential volcanic dome has been observed in the Eastern Rise [16], east of the AP. When analyzed spectrally, the domes and the Eastern rise appear to be more orthopyroxene-rich and have only minor glass components (Figure 4, blue)[13-15]. For comparison, spectra of several mare locations and sinuous rilles in the AP and the MHVC are visible in Figure 4 (purple, red, respectively).

Summary and Future Work: The Central Procellarum area of the Moon is home to a wide range of volcanic deposits and morphologies, with evidence for both effusive and explosive volcanic activity. All of the volcanic features analyzed in the Central Procellarum are comprised of either orthopyroxene or glass. There is no evidence for olivine or clinopyroxene in the spectra. The effusive features, including the Eastern Rise and Marius Hill domes, exhibit orthopyroxene signatures[13-15], consistent with primitive mantle-like melts, while the explosive features including the Aristarchus lunar pyroclastic deposit and Marius Hills cinder cones are similar to the volcanic Apollo 17 orange glasses [17]. Our results suggest that magma sources in Aristarchus and Marius Hills may be sourced from the same mantle sources. There is no clear correlation of mineralogy between the Aristarchus and Marius Hills deposits to the surrounding mare, suggesting that these eruptions all significantly predated the mare and may not be related to mare emplacement.

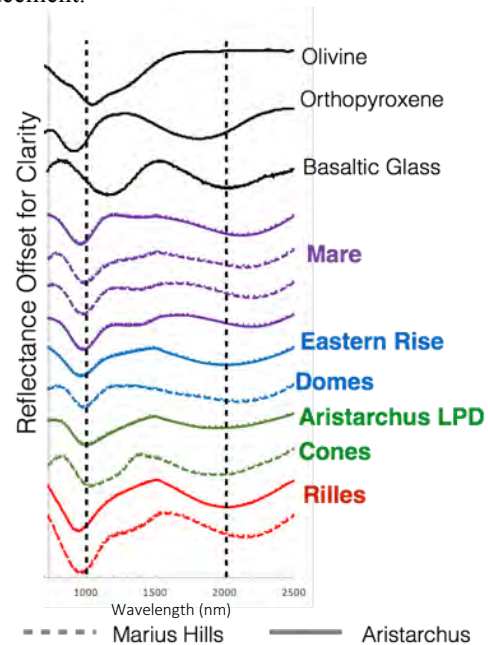


Figure 4: Spectra collected from volcanic deposits within the MHVC and Aristarchus. These spectra can be compared to the lab spectra of olivine, orthopyroxene, and basaltic glass. The location of the 1000 and 2000 nanometer bands can be used as reference points for changing mineralogy.

References: [1] Whitford-Stark and Head (1977) 8th PLPSC, 2705-2724. [2] McCauley (1967) U.S. Geol. Surv. Misc. Invest. [3] Gustafson et al. (2012) J. Geophys. Res. Planets, 116(E6), E00G13 [4] Lawrence et al. (2013) J. Geophys. Res. Planets, 118, 615-634. [5] Gaddis et al. (2003) Icarus 161:2, 262-280. [6] Weitz et al. (1999), J. Geophys. Res. Planets, 104(E8), 18933-18956. [7] Horgan et al. (2014) Icarus 234(C), 132-154. [8] Bennett et al. (2016) Icarus 273, 296-314. [9] Besse et al. (2011), JGR, 116, E00G13. [10] Heather et al. (2003), JGR, 108(E3), 5017 [11] Pieters et al. (2009) Curr. Sci. 96:4, 500-505 [12] Gaddis et al. (2016) LPSC 47, 2065. [13] McBride et al. (2016) LPSC 47, 3052. [14] McBride et al. (2017), LPSC 48, 2989. [15] McBride et al. (2018) LPSC 49, 2798. [16] Jawin et al. (2017) LPSC 48, 1184. [17] Adams et al. (1974), Fifth Lunar Conference. 171-186.

RADON AND POLONIUM AS TRACERS OF LUNAR OUTGASSING, VOLATILES AND DUST. P.Y. Meslin¹, J.-F. Pineau², G. Deprez³, J.C. Sabroux⁴, O. Gasnault¹, N. Yamashita⁵, P. Richon⁶, O. Forni¹, S. Maurice¹, J. Lasue¹, ¹IRAP, UPS, CNRS, CNES Toulouse, France (pmeslin@irap.omp.eu), ²Albedo Technologies, Saint-Sylvestre, ³LATMOS, Guyancourt, ⁴IRSN, Saclay, ⁵PSI, Tucson, AZ, ⁶CEA, DAM, DIF, Arpajon.

Historical overview: Since the early stages of the lunar exploration, radon-222 and its progeny (^{218}Po , ^{214}Po , ^{210}Pb and ^{210}Po) have been identified as key tracers of the present-day lunar seismic and venting activity. Measurements of their concentration performed both on the surface of the Moon (alpha-scattering experiments on Surveyor 5, 6 and 7) [1], from the orbit (Alpha or Charged Particle Spectrometers onboard Explorer 35, Apollo 15 and 16 command modules and Lunar Prospector) [2-4], and on returned samples (lunar fines from Apollo 11, 14 and 15, camera visor from the Surveyor 3 spacecraft and solar-wind composition foils from Apollo 12, 14, 15 and 16) [e.g., 5] have revealed temporal variations and large disparities in their spatial distribution, which were attributed to the presence of active degassing spots, of time-variable outgassing intensities, which radon and its progeny can help locate. Enrichment of ^{210}Po at the Mare/Highlands boundary and ^{222}Rn anomalies over young craters (Aristarchus, Grimaldi, Kepler) have been observed. More recently, a statistical analysis has revealed a strong correlation between the locations of ^{222}Rn and ^{210}Po anomalies and regions where Transient Lunar Phenomena (TLP) have been observed [6], which suggests that these TLPs could be caused by the sporadic release of gases and dust from the lunar interior. This analysis also reveals a correlation between the locations of deep and shallow moonquakes and the Mare/Highlands boundary. Together with the correlation that exists between the ^{40}Ar degassing rate and the occurrence of shallow moonquakes [7], there is converging evidence that the present day lunar degassing activity may be controlled by seismicity and/or the presence of fractures, which can help radon and other gases transit rapidly from the lunar interior. More recently, lunar radon gained renewed international interest with the Kaguya-Selene (Alpha Radon Detector, ARD) and Chandrayaan-1 (High-Energy X-Ray Spectrometer, HEX) missions. Although both suffered from instrumental problems, the ARD showed, once again, radon time variations and radon anomalies associated with the Aristarchus and Kepler craters [8].

Another important result of these observations was the strong difference between the exhalation rate of radon on the Earth and on the Moon, attributed to the dryness of the lunar regolith [9]. This is also illustrated by the very low (< 1%) emanation factors characterizing returned lunar samples [10].

Motivation for measuring radon and its progeny at the lunar surface: Radon and its progeny are ideal tracers of the lunar regolith-exosphere exchanges. This is in part due to: a well-identified

source term (uranium), mapped from the orbit [11]; a well-identified loss term (radioactive decay); a limited half-life, limiting its transport around its emission zone; the absence of exogenous contamination. However, despite the number of experiments that brought information on this gas, it is still presently difficult to have a fully consistent and comprehensive picture of radon outgassing on the Moon from all these datasets. In situ experiments were not optimized to measure them, and analyses of returned samples pertained to the long-lived decay product ^{210}Po [5], which only gives access to time-integrated (~20 years) information, in contrast to ^{222}Rn that could allow variations of a few-day timescale to be monitored. Analyses of data acquired from the orbit had a large footprint and limited temporal coverage (from ~70 hours of prime data for Apollo 16 to ~230 days for the APS and ~6 months of nominal mode for the ARD). Moreover, some of these measurements were made difficult and were possibly subject to systematic errors due to a contamination of the detectors by ^{210}Po or ^{241}Am sources used for their calibration prior to the mission. The ARD suffered from noise in some of its channels and its anticoincidence detectors dysfunctioned. The HEX instrument also had anticoincidence and thermal control issues [12].

Long-term monitoring of the radon cycle on the surface of the Moon would thus provide valuable ground truth for orbital measurements and would help address several key issues related to the transport of lunar volatiles and dust:

- 1) Study of the transport of gases through the lunar regolith: After being produced by the decay of radium-226, radon can eventually escape from its mineral host by recoil, with an efficiency that depends on grain size, surface area and radium distribution [9,13]. Once mobilized in the pore space, its transport to the surface by diffusion is controlled by the structural properties of the porous medium and by its adsorption onto the soil matrix, which is a temperature dependent process (and among noble gases, radon is most subject to this effect). Its exhalation rate at the surface is therefore modulated by variations of the surface temperature, and thus by the diurnal cycle. Monitoring its exhalation rate would therefore enable us to study the thermal “breathing” of the uppermost meters of the lunar regolith, and thus help understand the dynamics of the exchange of gases between the regolith and the lunar exosphere. Measuring the exhalation rate of radon and its variations, possibly in conjunction with the measurement of other endogenic gases by mass spectrometry, would make it possible

to constrain their transit times through the lunar regolith and the thickness of their production layer.

2) Monitoring of the venting activity of the Moon and identification of active outgassing spots: In addition to transport by diffusion, radon can also be liberated sporadically from the subsurface by advection along with other gases such as argon, possibly triggered by moonquakes or by the sagging of mare basalt plains, stresses from tides or mascons interacting with overlying crust, or in connection to contemporary impact events. To this respect, its measurement would perfectly fit with seismic and mass spectrometry experiments. If such an event were to occur during the timeframe of a mission, an anomaly could be measured at the landing site. Modelling its transport in the lunar exosphere would then help locate its emission site. The detection of active outgassing spots or fracture networks can help identify key targets for future exploration missions. Particularly, some radon anomalies are known, on Earth, to be correlated with helium outgassing and can thus be used for helium sources tracking [14,15].

3) Study of the transport of volatiles in the lunar exosphere: Radon atoms, released into the lunar exosphere, follow ballistic trajectories until they disintegrate, and are slowed down in this dispersion process by adsorption and reincorporation into the regolith pore space [16]. The adsorption process being controlled by surface temperatures, strong synodic variations of the exospheric concentration are expected, just like those observed for argon by Apollo 17 [7]. Understanding the time variability of ^{222}Rn would constitute a reference to study the transport of other gases. The trapping efficiency of cold traps could also be characterized remotely (e.g., from the rim of shadowed craters) by alpha spectroscopy.

4) Study of the transport of lunar dust: The ^{210}Po surficial activity measured at any given time integrates both the variations of the radon exhalation rate and the effects of dust motion over a timescale of a few decades. Over this period of time, churning processes (from micro-impacts or solar-wind induced electrostatic effects) may involve dust thicknesses comparable to the range of characteristic ^{210}Po alpha particles. This process should thus affect the measured signal and lead to disequilibrium between the ^{210}Po surface distribution and the time-integrated ^{222}Rn signal [1].

Modeling of radon transport: In order to simulate the lunar radon cycle, we have developed a 3D thermal model of the lunar subsurface, coupled to a diffusion-adsorption gas transport model. It uses as inputs the Kaguya uranium map [11], the regolith thickness map of [17], the radon emanation factor and adsorption coefficient measured by [10] and [13,18], respectively. Its output (time-variable map of the exhalation rate, Fig. 1) is injected into a Monte-Carlo code simulating the exospheric transport of radon (incl. surface adsorption) and the escape or implantation of its decay products into the surface. A strong diurnal cycle is observed (Fig. 2). This model can be

used to predict its exospheric activity, to be compared to past and future measurements.

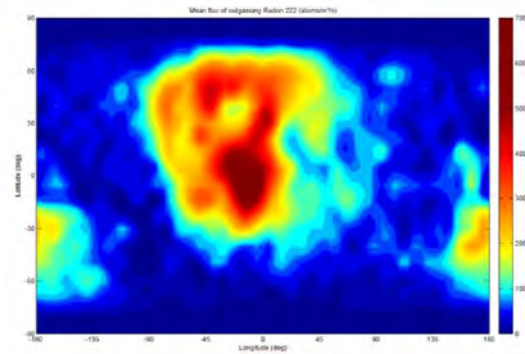


Fig. 1: Predicted map of radon exhalation rate (diffusion only)

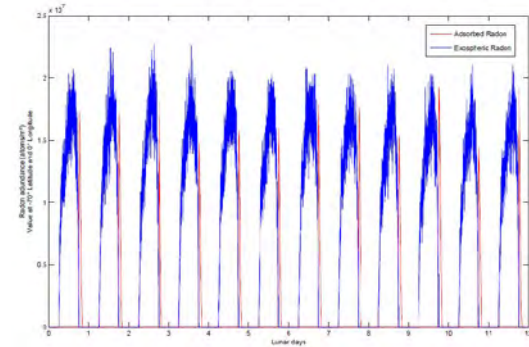


Fig. 2: Radon diurnal cycle (exospheric and adsorbed) at -70° lat., 0° long.

The DORN instrument: We developed a prototype of the DORN instrument (for “Detection of Outgassing Radon”, after the name of the physicist Friedrich Dorn, who discovered radon), a light, simple sensor aimed at measuring ^{222}Rn , ^{220}Rn and their decay products by alpha spectroscopy in the 5–10 MeV energy range with sets of silicon detectors. Each detection unit (DU) is made of a series of 6 cm^2 detectors that are paired to provide efficient background rejection of cosmic rays by anticoincidence. The instrument suite can be split into two modular and independent subsystems: DORN-1 (~ 1 kg) is made of 2 DU aimed at measuring radon and polonium atoms around the lander. This is an “exospheric” instrument: located near the rim of the lander platform, it points toward the ground, either in the close vicinity of the lander or toward remote targets, to measure atoms adsorbed on the surface. DORN-2 (~ 0.7 kg) is made of a small alpha detector aimed at measuring the subsurface flux of radon at the landing site. This is a contact instrument, which is intended to trap atoms released from the ground before they escape, using an accumulation volume and a “cold finger” (~ 95 K, reached by means of a small 185g Stirling micro-cooler). The instrument requires only 1.1 W for operation.

References: [1] Turkevich et al. (1970), *Science*, 167. [2] Gorenstein and Bjorkholm (1973), *Science*, 179. [3] Bjorkholm et al. (1973), *Science*, 180. [4] Lawson et al. (2005), *JGR*, 110. [5] Lambert et al. (1973), 4th LSC. [6] Crotts (2008), *ApJ*, 687. [7] Hodges (1977), *Phys. Earth & Plan. Int.*, 14. [8] Kinoshita et al. (2016), 47th LPSC. [9] Tanner (1980), US DOE, Conf-780422. [10] Adams et al. (1973), 4th LSC. [11] Yamashita et al. (2010), *GRL*, 37. [12] Vadawale et al. (2014), *ASR*, 54. [13] Meslin et al. (2011), *GCA*, 75. [14] Sabroux (1998), in *Le radon de l'environnement à l'homme*, EDP Sciences. [15] Ghose et al. (2003), *Radiation Meas.*, 36. [16] Gasnault and Meslin (2009), *EPSC*, 4, 578. [17] Fa and Jin (2010), *Science in China : Information Sciences*, 53. [18] Friesen and Adams (1976), *GCA*, 40.

OBSERVATIONS FROM A NEW GLOBAL MAP OF LIGHT PLAINS FROM THE LUNAR RECONNAISSANCE ORBITER CAMERA. H. M. Meyer¹, M. S. Robinson¹, B. W. Denevi², and A. K. Boyd¹, ¹School of Earth and Space Exploration, Arizona State University, Tempe, AZ 85281 USA (hmmeyer1@asu.edu), ²Johns Hopkins University Applied Physics Laboratory, Laurel, MD 20723 USA.

Introduction: The origin of lunar light plains has long been debated, particularly since the return of Apollo 16 impact breccias [e.g., 1]. Conflicting relative age estimates and geologic context suggest all light plains are ejecta from the Orientale and Imbrium basins [1-3], from many impact events [4-6], or even from volcanic eruptions [7-8]. However, the presence of cryptomaria beneath some light plains is well established [e.g., 9-10], and many previously identified light plains deposits have been interpreted as impact melt, meaning that not all light plains are formed by the same mechanism. It is not clear how much of the light plains are the result of primary ejecta emplaced on pre-existing smooth surfaces, ponding of impact melt, or debris from secondaries. In order to distinguish between the various origins of light plains deposits both at the local and global scale, a consistent global map of light plains is required.

Previous maps that included light plains [8, 11-15] relied on Lunar Orbiter, Zond 7 and 8, Mariner 10, and Apollo images, but inconsistent resolution and illumination conditions made it difficult to identify and compare units at the global scale. The Lunar Reconnaissance Orbiter Camera (LROC) [16] has captured images of the surface at ~100 m/pixel with the Wide Angle Camera (WAC), and the LROC team produced global mosaics with near-constant illumination and resolution. Here, we present a new global map of lunar light plains mapped from these new WAC mosaics (**Fig. 1**).

Data and Methods: Light plains were mapped

based on criteria of Eggleton and Schaber [1] and Scott et al. [12] as implemented by Meyer et al. [17] (ArcGIS at a scale of 1:300,000). Two LROC WAC monochrome mosaics of opposite illumination directions were used to identify smooth and relatively flat to undulatory terrain with distinct margins. The standard deviation of slopes calculated from the WAC topography (GLD100) [18] over three different baselines (1000, 667, and 333 meters) were used to evaluate the roughness of mapped plains. Smooth plains included in our map were discriminated from mare deposits using the global mare shapefile [19].

Images from the LROC Narrow Angle Camera (NAC) [16] at a pixel scale of ~50 cm and from the Kaguya Terrain Camera (TC) [20] at a pixel scale of ~10 m were used to identify stratigraphic relationships and to look for small-scale features to aid in the interpretations of origin. A Clementine FeO map [21] was used to identify compositional characteristics as well as delineate between externally emplaced and locally derived material where possible.

Observations: Light plains occupy ~9.5% of the surface: ~9 % of the farside and 10% of the nearside. Distinct ray-like clustering within ~4 radii of the Orientale and Imbrium basins suggests that the bulk of light plains are related to the formation of the basins, consistent with previous interpretations [1-3, 17]. However, many farside light plains deposits likely formed on pre-existing smooth surfaces or with more regional to local impacts (e.g., ancient impact melt, SPA mare deposits, or light plains). On the nearside, there is a cluster of light plains to the

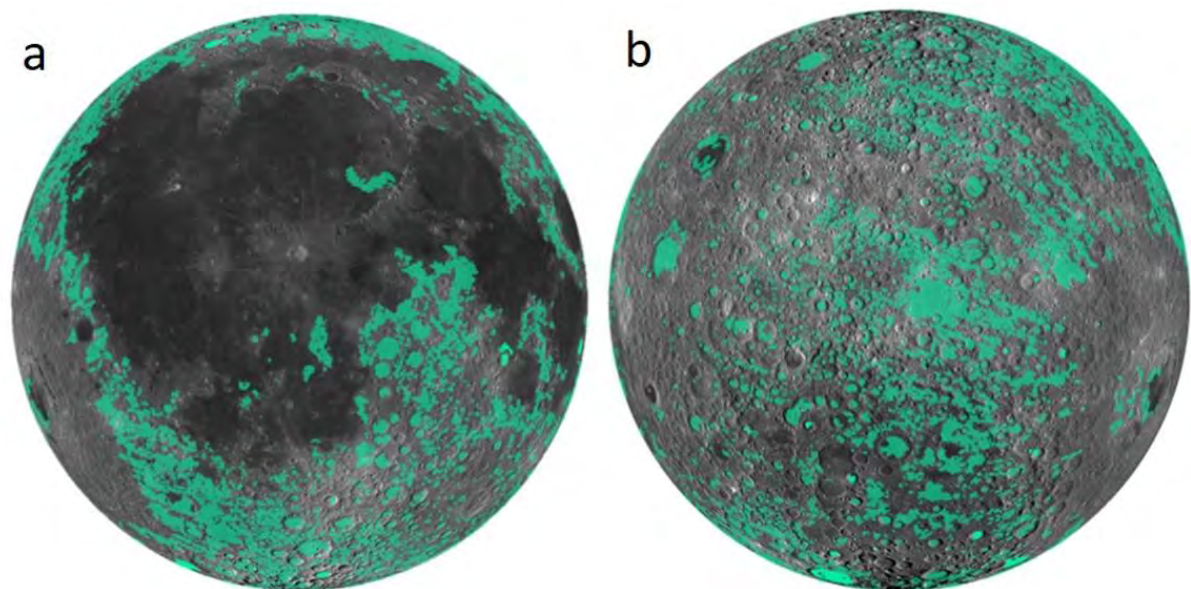


Fig. 1. Orthographic views of the (a) nearside (0°N 0°E) and (b) farside (2.7°S 168.7°W) light plains (green) overlain on the LROC WAC morphology basemap.

southeast of Orientale, many of which have been identified as Orientale ejecta overlying mare [10]. Mare flooding subsequent to the formation of Orientale and Imbrium obscures much of the nearside terrain where light plains are expected.

Orientale formed on the boundary of the highlands and the lowlying nearside, so it is likely that pre-existing topography played a significant role in the distribution of deposits associated with the basin. Low-lying topography as well as pre-existing smooth surfaces may explain why the deposits to the southeast are more continuous and larger than the patchier and radially aligned deposits in the northwest. Light plains beyond ~ 2 radii from the western rim of Imbrium are oriented radially to Orientale rather than Imbrium. Distinctive ray-like clustering is not observed around basins older than the Imbrium basin. However, smooth terrain identified roughly concentric to Nectaris (~ 4 radii from Imbrium) may be an example of ancient light plains. This smooth terrain was not included in the global map of light plains due to a lack of mappable boundaries.

The South Pole-Aitken (SPA) basin is of particular interest because Orientale light plains affected a significant portion of the SPA terrain. Similar to the southeast of Orientale, many of the light plains within SPA form large, continuous deposits and may be distinct in origin from the smaller, patchier deposits that cluster along radial paths northwest of Orientale. Alternatively, pre-existing smooth surfaces could have allowed material mobilized by Orientale to spread laterally to form more expansive deposits. In the FeO map, the light plains within SPA are distinctly enriched in FeO (red in **Fig. 2**) with respect to light plains outside SPA (yellow in **Fig. 2**), which is expected if the deposits are primarily derived from local material as suggested by [4].

Flow lobes were identified within many light plains deposits using Kaguya TC images and NAC images. These flows display a range of morphologies and sizes, and some are more heavily cratered than the terrain they embay. When compared with flows of known origins (e.g., impact melt or landslides), these smooth plains related flows may yield crucial insight into the physical properties and emplacement mechanisms of light plains.

Implications: Ray-like clustering radial from Orientale within ~ 2 radii of Imbrium suggests that extensive modification from the Orientale event largely erased any trend in light plains distribution associated with Imbrium in that region. Smooth terrain south of Nectaris may be light plains that survived resurfacing by both Imbrium and Orientale due to its location ≥ 4 radii from both basins. This suggests that light plains within ~ 2 or 3 radii of superposed basins are largely destroyed. Collectively, $\sim 70\%$ of all light plains may be related to the Imbri-

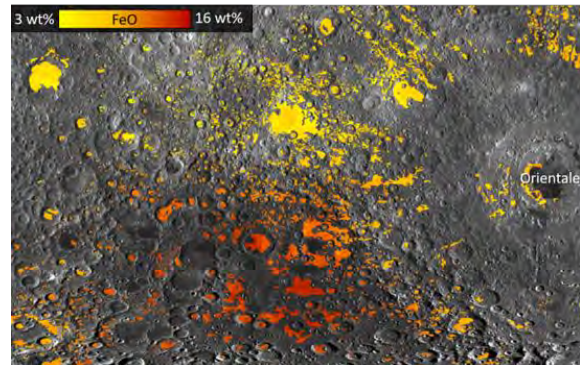


Fig. 2. FeO abundance for light plains deposits overlain on an LROC WAC mosaic.

um and Orientale basins; a detailed quantitative assessment is underway.

If SPA (~ 2400 km in diameter) produced the same amount of light plains relative to its size as the Orientale basin-forming impact, then it significantly affected ~ 30 million km^2 , or nearly 80% of the lunar surface, including the area of the basin itself, continuous ejecta (assuming an average extent of one radius), and associated light plains. If all large basins modify the surface in a manner and degree similar to the Orientale and Imbrium basins, then special care must be taken to avoid regions affected by light plains formation when deriving absolute model ages in the highlands due to the preferential destruction of small craters, particularly in topographic lows where light plains accumulate.

References: [1] Eggleton R. E. and Schaber G. G. (1972), NASA Apollo 16 Prelim. Sci. Rep., 29-7–29-16., [2] Chao et al. (1973), Lunar Science IV, p127-128., [3] Howard et al. (1974), Rev. Geophys, Space Phys. 12(3), 309-327., [4] Oberbeck et al. (1974), LPSC 5, 111-136., [5] Oberbeck, V.R. et al. (1975), The Moon 12, 19–54., [6] Head (1974), The Moon 11(1-2), 77-99., [7] Milton, D.J. (1964), Astrogeol. Studies Ann. Prog. Rept., July 1963 to July 1964, pt. A, pp. 17–27., [8] Wilhelms and McCauley (1971), USGS I-703., [9] Schultz and Spudis (1979), LPSC 10, 2899-2918., [10] Whitten and Head (2015), Icarus, 247, 150-171., [11] Wilhelms and El-Baz (1977), USGS I-948., [12] Scott et al. (1977), USGS I-1034., [13] Stuart-Alexander (1978), USGS I-1047., [14] Lucchitta (1978), USGS I-1062., [15] Wilhelms, D.E. et al. (1979), USGS I-1162., [16] Robinson M. S. et al. (2010), Space Sci. Rev. 150, 81 -124., [17] Meyer et al. (2016), Icarus, 273, 135-145., [18] Scholten F. et al. (2011), JGR, 117, doi:10.1029/2011JE003926., [19] Nelson et al. (2014), LPSC 45, #2861., [20] Huruyama et al. (2008), EPS 60(4), 243-255., [21] Lucey, P. et al. (2000), JGR, 105(E8), 20297–20305.

EVOLUTION OF THE PRESENCE OF IMPACT MELT AT THE NEAR-SURFACE OF THE MOON

G. G. Michael¹, A. T. Basilevsky², G. Neukum¹ and T. Liu³, ¹Freie Universität Berlin, Institut für Geologische Wissenschaften, Malteserstr. 74-100, 12249 Berlin, Germany. ²Vernadsky Institute of Geochemistry and Analytical Chemistry, RAS, Kosygin Str., 19, 119991 Moscow, Russia. ³Technical University Berlin, Straße des 17 Juni 135, 10623 Berlin, Germany.

Introduction: We aim to understand the cumulative effect of the impact gardening process on the presence of impact melt of different ages at the near-surface of the Moon. Estimating the amount of melt produced by impact events of differing scales together with the depth of excavation and quantity of unheated material which is redistributed at the surface, we reconstruct the effect of a sequence of impacts representing the observable history of the Moon. We compare the model's predictions for the ages of near-surface melt components with what is found in real samples.

Methods: The essence of the model is the following:

1. An initial volume, with a surface area equivalent to that of the Moon is denoted with a nominal starting age of T_0 (typically 4.5 Ga), and a minimum crater size for the simulation is chosen, D_{\min} .
2. From the lunar chronology function [3], an impact rate is found for the current model time, T , which corresponds to craters of 1 km in diameter. By means of the crater production function (PF), the equivalent rate for craters of size D_{\min} is found.
3. The rate gives the average time to the next impact event producing a crater larger than D_{\min} . With a Monte Carlo approach, we can use a Poisson function to find realistically distributed time intervals, although for the large number of events being simulated, it can be sufficient to employ an averaged interval.
4. The diameter of the crater formed is generated using the Monte Carlo method in such a way that conforms to the portion of the production function larger than D_{\min} .
5. For each crater produced, the penetration depth is taken as $D/10$ [1,2] and the volume of excavated material is approximated as the volume of the transient crater.
6. A portion of this excavated volume is considered to have been melted (or heated above the point required to reset the Ar-Ar clock): $r_{\text{melt}} = cD_{\text{tc}}^d/V_{\text{tc}}$, where D_{tc} and V_{tc} are the diameter and volume of the transient crater, and c and d are taken as 2×10^{-4} and 3.85, respectively (after [2]). The melted material is marked in the simulation with the current clock time, T .
7. The excavated material, together with the new melt, is redistributed evenly over the entire surface of the body. This is a simplification of the real situation, but in an average sense—because of the relative frequency of smaller impacts whose ejecta do not travel so far—it provides a reasonable reflection of the amount of ejecta sourced from craters of differing sizes at any point of the surface.

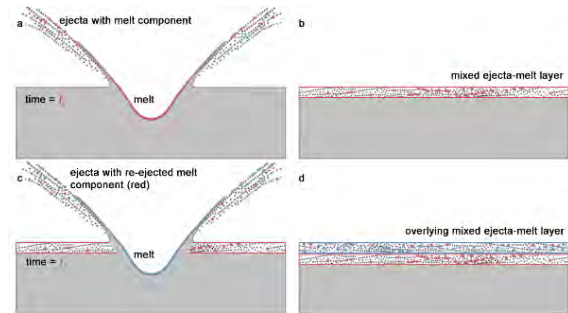


Figure 1. Schematic of the simulations showing a) impact event causing ejection of both unheated and melted material, b) the deposition of a mixed layer of unheated ejecta and melt, c) a subsequent impact event, ejecting material from both the previous layer and beneath, melting a fraction of both, and d) depositing a new layer containing both new melt and a component of re-excavated melt from the previous event.

Results: Results for an impact rate scenario as described by [3], with the rate being constant back to 3 Ga, and exponentially increasing before then are shown in Fig. 2, in comparison with those for the same scenario with the addition of a cataclysmic peak in the rate function (Fig. 3).

The near-surface melt is dominated by the most recent impacts; further back in time, it is the largest impacts which dominate: it is notable that they produce sufficient melt to leave a permanent signature in the upper layers. Later impacts of lesser scale either penetrate to the original ejecta layer to bring up more of its melt, or recycle the same aged melt nearer the surface. Eventually the melt from these events becomes present at every depth down to its source ejecta layer.

Conclusion: If there was a lunar cataclysm or late heavy bombardment, we would expect its form to be observable today in the histogram of melt ages from surface samples, both those returned from the Moon by manned and unmanned spacecraft and those delivered to the Earth in the form of meteorites (Fig. 4).

References: [1] M.R. Dence, *Meteoritics* 8 (1973) 343. [2] M.J. Cintala, R.A.F. Grieve, *Meteoritics and Planetary Science* 33 (1998) 889. [3] G. Neukum, *Meteorite bombardment and dating of planetary surfaces* (English translation, 1984).

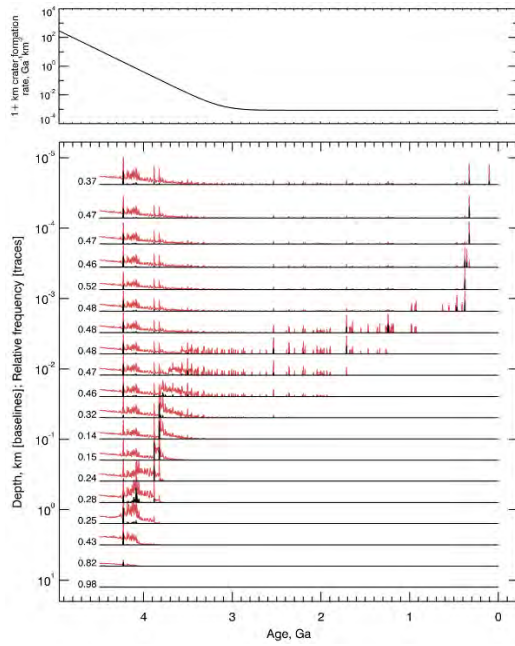


Figure 2. Simulation using craters of random size larger 30 km conforming to the size–frequency distribution described by the Neukum (1983) production function over a period of 4.5 Ga using a realistic impact rate function (plotted above) and incorporating basin-forming events. The horizontal axis indicates the age of the melt. Each trace in the plot represents a histogram of the presence of differing melt ages, the baseline of the trace being plotted at the layer's depth below the surface according to the vertical axis scale. The histograms are plotted twice: in black – with all traces using the same normalisation; in grey – with exaggerated small values. The numbers at the left side of each trace show the fraction of material of age T_0 that has never been melted during the simulation (this fraction is excluded from the histogram, since it would plot much higher). The four prominent peaks present in both runs represent South-Pole–Aitken at 4.23 Ga, Crisium at 4.08 Ga, Imbrium at 3.88 Ga and Orientale at 3.82 Ga.

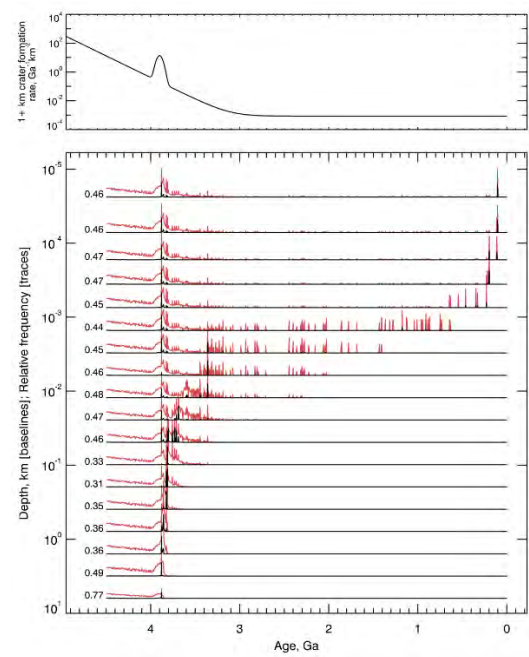


Figure 3. Simulation using craters of random size larger 30 km conforming to the size–frequency distribution described by the Neukum (1983) production function over a period of 4.5 Ga using a hypothetical impact rate function with a cataclysmic peak (plotted above) and incorporating basin-forming events. The four prominent peaks again represent South-Pole–Aitken, Crisium, Imbrium and Orientale, but have been compressed into a cataclysmic peak centred on 3.9 Ga.

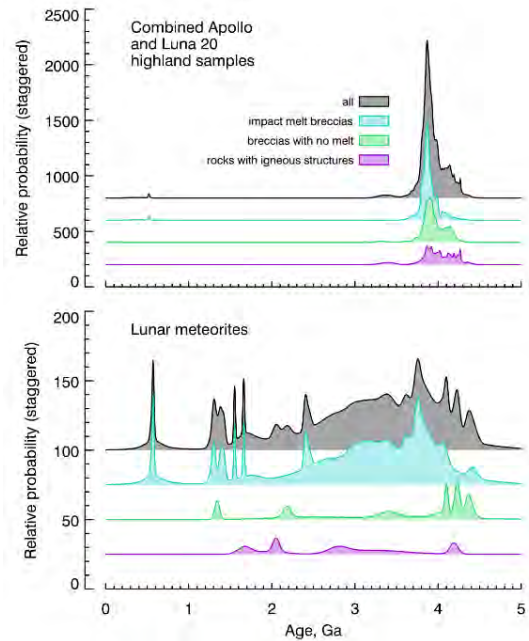


Figure 4. Relative probability plots for highland rock K-Ar ages aggregated over the Apollo-Luna sites (subdivided by lithologies). Same for lunar meteorites.

THE FOUR COMPOSITIONAL ZONES OF THE SOUTH POLE - AITKEN BASIN REVEALED BY MOON MINERALOGY MAPPER DATA. D. P. Moriarty¹, N. E. Petro¹, ¹NASA GSFC [daniel.p.moriarty@nasa.gov]

Introduction: The South Pole - Aitken Basin (SPA) is an ancient ~2500 km impact structure on the lunar farside. Understanding the Moon's oldest and largest basin is central to several critical lunar science questions relevant to (1) basin chronology, (2) lower crust/upper mantle stratigraphy and composition, (3) large impact processes, (4) lunar formation/thermal evolution, and (5) lunar volcanism. In a recent paper[1], we used Moon Mineralogy Mapper (M³) data to evaluate the compositional structure of the basin, identifying four distinct zones. Here, we discuss the properties of these zones, as well as the implications for understanding the formation and evolution of SPA.

Identification and Properties of Compositional Zones across SPA: M³ data reveal regular patterns of compositional diversity across SPA. Using the Parabolas and two-part Linear Continuum technique (PLC) validated in [2], we map the diagnostic properties of the 1 μ m and 2 μ m spectral absorption bands. Band depths (sensitive to pyroxene abundance) are shown in Fig. 1. Band centers (sensitive to pyroxene composition) are shown in Fig. 2. Based on these maps, four distinct compositional zones are identified. The properties of these zones are as follows:

SPA Compositional Anomaly (SPACA): SPACA is an approximately ~700 km unit located in the central portion of SPA, within the Pyroxene-Bearing Zone. As observed throughout the Pyroxene-Bearing Zone, SPACA exhibits a pervasive elevated pyroxene abundance. However, the surface composition is dominated by a distinct pyroxene composition, intermediate to

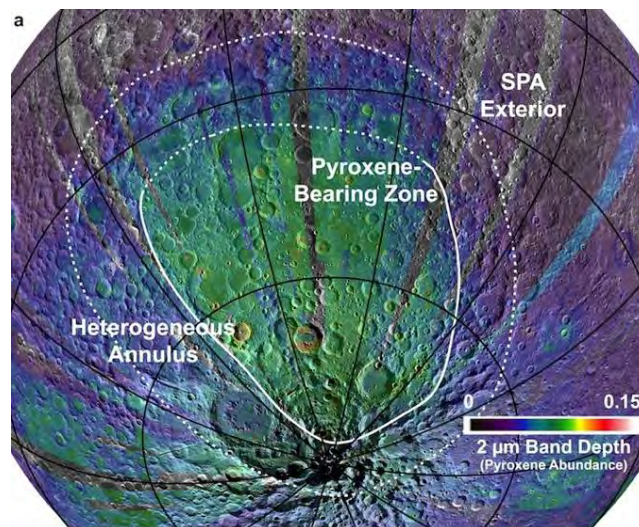


Fig. 1: 2 μ m band depths (sensitive to pyroxene abundance). Three distinct pyroxene abundance zones are evident.

mare basalts and Mg-pyroxenes. Within SPACA, this non-mare high-Ca pyroxene is observed at structures such as Mafic Mound[3], the walls of Finsen, Bhabha, Bose, White, and Stoney, and the central peaks of White and Stoney. However, several large complex craters within SPACA (Bhabha, Finsen, Stoney) exhibit distinctly Mg-rich pyroxenes in their central peaks (Fig. 3). Since central peaks represent the deepest material exposed in any

given crater, this suggests a two-layer stratigraphy. Initial analyses suggest the presence of Mg-pyroxenes at depths >5 km, underlying a several-km thick surface layer.

Mg-Pyroxene Annulus: The Mg-Pyroxene Annulus surrounding SPACA also exhibits an elevated pyroxene abundance. However, Mg-rich pyroxene compositions dominate this zone. The Mg-Pyroxene Annulus lies directly outside of the SPACA, and represents the remainder of the prominent Pyroxene-Bearing Zone (~1000 km across in total). Mg-pyroxenes dominate crater structures over a wide range of crater sizes, indicating the presence of laterally and vertically extensive Mg-Pyroxene-bearing materials.

Heterogeneous Annulus: The Heterogeneous Annulus is associated with the outer reaches of SPA interior. It is dominated by feldspathic materials, but exhibits localized pyroxene-bearing exposures and a variable but typically small mafic component in soils. In general, non-mare mafic materials found within the Heterogeneous Annulus are dominated by Mg-pyroxene.

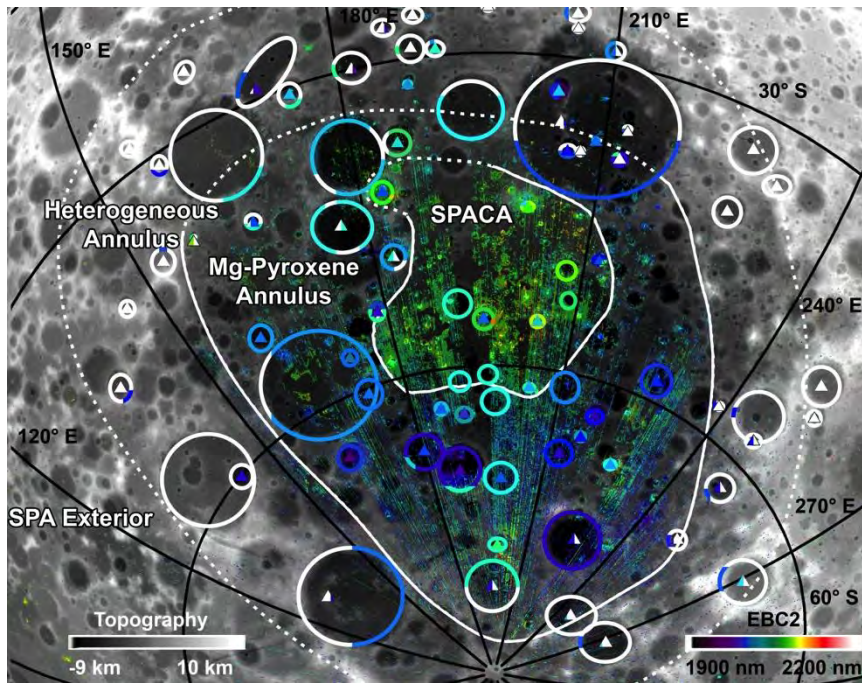


Fig. 2: Colored pixels represent 2 μ m band centers. Shorter wavelengths (purple/blue) indicate Mg-rich pyroxenes; longer wavelengths (yellow/red), Fe,Ca-rich pyroxenes. Mare basalt regions have been removed to emphasize variations in non-mare areas. A survey of large impact structures was performed to assess materials exposed from depth. The overlaid colored ellipses and triangles correspond to the dominant pyroxene compositions observed in these crater walls/rims and central peaks (white symbols represent feldspathic structures). From band centers, the Pyroxene-Bearing Zone from Fig. 1 is further classified into the SPA Compositional Anomaly (SPACA) and Mg-Pyroxene Annulus. Basemap: LOLA topography.

SPA Exterior: Other than isolated mare basalts, the SPA Exterior is highly feldspathic and appears mostly mafic-free.

Implications: The four compositional zones across SPA result from geologic processes related to basin formation and evolution. Insight into these processes can be gained by understanding the extent, composition, and inferred origin of each zone.

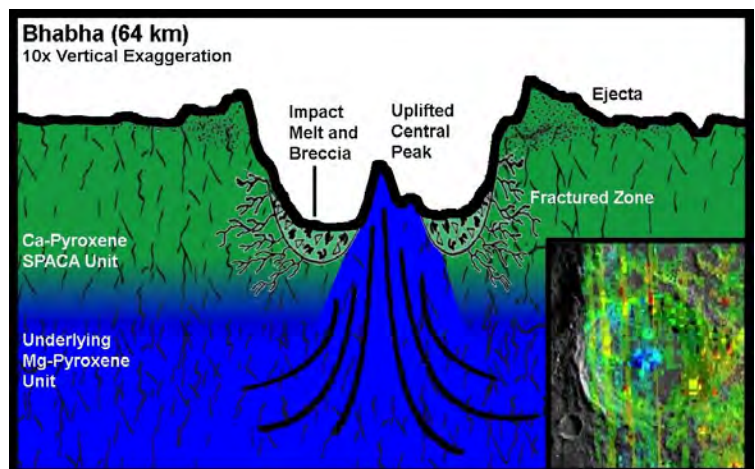
SPACA exhibits a surface composition dominated by non-mare HCP. From the estimated local stratigraphy at Bhabha (Fig. 3) and several other complex craters (Finsen, Stoney, White, Bose, etc.), this composition persists to depths of >5 km in places and is underlain by Mg-pyroxene-bearing material. SPACA exhibits a paucity of impact craters[4], an abundance of modified/filled craters[3], and is associated with the unusual volcanic construct known as Mafic Mound[3], which is identical in composition to SPACA surface materials. While these factors point to extensive volcanic resurfacing, it is unclear if volcanism alone can account for the ~5 km thickness of the SPACA surface layer. It is possible that additional processes such as impact melt differentiation or post-SPA basin ejecta may also contribute to layered stratigraphy.

Fig. 3: Schematic cross section of Bhabha, within SPACA, inferred from 2 μ m band center values (inset). The walls and floor exhibit non-mare HCP excavated from depths <~5 km, whereas the central peak exhibits Mg-rich pyroxenes from depths >~5 km.

Across the *Mg-Pyroxene Annulus*, craters are dominated by fairly uniform Mg-rich pyroxenes within their walls, floors, and central peaks. The largest impact structures in this zone may have excavated materials from depths of 40 km or greater. The vast extent, significant depth, and relatively uniform composition of the Mg-Pyroxene Annulus suggests that this Mg-pyroxene-bearing material was the primary product excavated, ejected, and melted by the SPA-forming impact. Possible sources of this material include inherently mafic lower crust, Mg-suite materials emplaced at the base of the crust, and/or Mg-pyroxene-bearing upper mantle materials. These band center and depth analyses cannot rule out the presence of a minor olivine component within this mineral assemblage. However, there is no evidence for widespread exposures of olivine-dominated assemblages in the SPA interior. If, as expected, SPA exposed mantle materials, this mantle material is dominated by Mg-pyroxenes.

Isolated mafic exposures in the *Heterogeneous Annulus* exhibit similar pyroxene compositions to the Mg-Pyroxene Annulus. These exposures probably arise from mixing of proximal SPA ejecta with the feldspathic crust during collapse of the transient cavity, further commingling the ejecta and crust into a zone within the final topographic rim of SPA.

References: [1] Moriarty, D. P. and Pieters, C. M. (2018) *JGR*, in review. [2] Moriarty, D. P. and Pieters, C. M. (2016) *Meteoritics & Planet. Sci.*, 51, 207-234. [3] Moriarty, D. P. and Pieters, C. M. (2015) *GRL*, 42, 7907-7915. [4] Head et al. (2010) *Science* 329, 1504-1507.



UPDATE ON THE PREPARATION AND CHARACTERIZATION OF CARBONACEOUS CHONDRITE STANDARDS FOR VERIFICATION OF ESA'S 'PROSPECT' PACKAGE. James Mortimer¹, Sasha Verchovsky¹, Frédéric Moynier², Mahesh Anand^{1,3}, James Carpenter⁴. ¹School of Physical Sciences, The Open University, Walton Hall, Milton Keynes, Buckinghamshire, United Kingdom, MK7 6AA, UK. (James.Mortimer@open.ac.uk), ²Institut de Physique du Globe de Paris, France, ³The Natural History Museum, London, SW7 5BD, UK., ⁴ESA ESTEC, Keplerlaan 1, 2401 AZ, Noordwijk, The Netherlands.

Introduction: This work has been carried out in the context of a planned Russian mission to the lunar surface, near to the south pole (Luna 27/Luna-Resurs Lander), for which the European Space Agency (ESA) are providing a sample acquisition and delivery drill system (ProSEED) and a miniaturized mass spectrometer sample analysis package (ProsPA). Together, this PROSPECT package aims to drill down up to 2 m below the lunar surface, collect samples of icy regolith, and analyze the samples for water and other volatile species abundances and isotopic compositions. This will provide much-needed ground truth measurements to clarify previous orbital observations and measurements of hydrogen and water ice at the lunar surface and particularly in cold regions at the lunar south pole.

Since carbonaceous chondrites (CCs) are thought to be major contributors of volatiles to the Moon [e.g. 1-3], it was decided to use CCs to produce a set of well-defined meteorite standards, using an array of high precision/high sensitivity instruments available within a modern laboratory setting to characterize the H, O, C, N, Zn, noble gases, bulk geochemistry, and petrological characteristics of the meteorites, all from the same stones. These standards will then be used to test and refine the ProSPA bench development model (BDM) as it becomes increasingly flight-ready.

Samples: CCs are inherently chemically heterogeneous, with coarser-grained objects (chondrules, CAIs, AOAs, mineral fragments) enclosed in a finer-grained matrix. Therefore, in order to produce meaningful standards, relatively large amounts of sample were required to provide enough well-homogenized material for multiple analyses. Unfortunately, since a fundamental requirement of the mission requires that the reference materials, including standards, should be available in perpetuity following these measurements, samples could not be acquired on a loan basis from the conventional museum and university curated collections. As a result, large hand specimens of two well-studied CCs were purchased from a trusted source, thus ensuring authenticity by comparison of new results with published data. A 57.54 g stone of Murchison (CM2) and a 692 g stone of Allende (CV3) were acquired in September 2016 (Fig. 1). These sample masses are large enough to provide ample material for standard preparation and characterization, with a large

amount of material left intact for future processing and scientific analysis.



Figure 1: Two carbonaceous chondrites, Allende (CV3) and Murchison (CM2) used in this work

Analytical Techniques:

- X-Ray CT Scanning (NHM).
- Optical Petrography (OU).
- Bulk Geochemistry (NHM).
- Stepped Combustion (OU).
- Elemental Analyzer-isotope ratio mass spectrometry (EA-IRMS) (OU).
- Laser Fluorination (OU).

Some of these data were presented previously (Poster #039 (ELS 2017); Abstract #2113 (LPSC 2017)), so this abstract focuses on the latest results obtained in this project.

Continuous Heating (OU). Ramped pyrolysis of sample material from 200 °C to 1400 °C, with real-time determination of extracted gas species in the range 2-200 AMU at sub-ppm level sensitivities using a quadrupole mass spectrometer. This provides important information about the relative abundances of all of the different volatile species released from CCs, not just those for which isotopic data was collected. A heating ramp of 6 °C/min was chosen to mimic the heating regime used by previous studies [4] for better comparison of data, and was also informed by the results of initial attempts, where a more rapid heating

rate of 20-30 °C/min resulted in very complex gas-phase reactions occurring in the ‘Finesse’ analytical instrument. Use of a slower heating rate has revealed several interesting gas release patterns.

For Murchison, the pressure generated by gas release correlates well with the release pattern of H₂ at $m/z = 2$, suggesting that hydrogen is the main gas being released from this meteorite during heating (Fig. 2). By contrast, the pressure derived from gas release from Allende cannot be so easily correlated with one particular mass, although small peaks in pressure could perhaps be linked to peaks in hydrogen release.

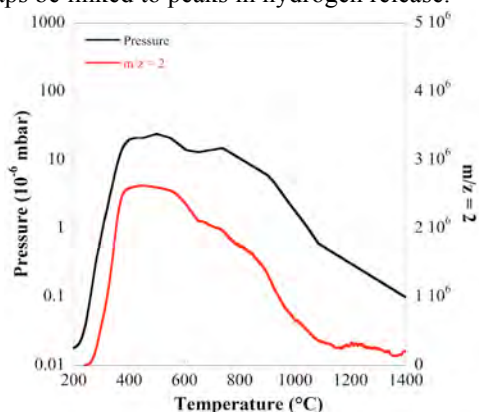


Figure 2: Pressure and H₂ release profiles: Murchison.

In addition to molecular H₂ at $m/z = 2$, water as H₂O at $m/z = 18$ is also released from both samples, although there are differences between the relationships of H₂ to H₂O in the two meteorites (Fig. 3). Both display a rapid release of H₂O as soon as the samples equilibrate with the temperature of the furnace (held at 200 °C), but in Allende, H₂O is released across a wide range of temperatures, with a peak release at 300 °C whereas in Murchison, H₂O release rapidly decreases after the initial peak at 250 °C before rising again in a broad release peak at 700 °C. However, the specific set-up of the Finesse analytical instrument means that some of the water released in the furnace condenses out in the pipework before reaching the mass spectrometer. This delays its detection, broadening the release peaks and making the release temperature appear much higher than that at which the water was actually released.

Where H₂O release from Murchison is minimal, between 300-600 °C, there is instead a large release of molecular hydrogen. In Allende, H₂ abundances are much lower and peak release occurs at 700-800 °C instead, and is correlated with a small increase in H₂O release at the same temperature.

In Murchison, an abundant, rapid release at 675 °C of $m/z = 16$ that is uncorrelated with H₂O and H₂ could be attributed to CH₄ being released.

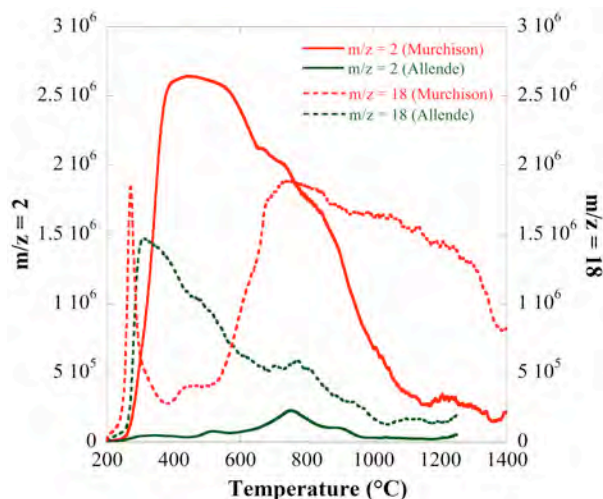


Figure 3: Continuous heating release profiles for H₂ (solid lines) and H₂O (dashed lines) in both Murchison (red) and Allende (green).

Zinc Isotopes (IPGP, Paris). Small aliquots of the finely-powdered standard materials were analysed at Institut de Physique du Globe de Paris, France for zinc isotopic analysis. Multiple-stage acid dissolution of the powdered materials was performed to isolate and purify the zinc content of the meteorites, followed by isotopic measurements using a Thermo Scientific Neptune Plus MC-ICP-MS. The results in excellent agreement with previously published Zn isotopic values for Murchison and Allende measured using the same protocols and instrumentation [5].

Summary: Results from these new CC standards are both self-consistent between different techniques, and in excellent agreement with previous literature data. An integrated approach, where multiple isotope systems are measured within the same individual stones means that the results are directly comparable to each other and can be considered together. The large sample masses purchased for these standards means that material can be available for future use, either as standards for other instrument verification studies, or in their own right as scientific samples.

Acknowledgements: This work was funded by the European Space Agency in support of the PROSPECT lunar exploration package, with the initial direction for the study provided by the PROSPECT User Group.

References: [1] Tartèse, R. and Anand M. (2013) *EPSL*, **361**, 480-486. [2] Barnes J. J. et al. (2016) *Nat. Commun.* **7**:11684 [3] Mortimer J. et al. (2016) *GCA*, **193**, 36-53. [4] Gibson, E. K. et al. (1974) *NASA Lyndon B. Johnson Space Center report*, Houston, TX. [5] Pringle, E. A. et al. (2017) *Earth Planet. Sci. Lett.* **468**, 62-71.

Introduction: The development of modern industry can not be imagined without iron alloys. Earth's native iron is found mainly in the form of Fe-Ni inclusions in metamorphic and sedimentary rocks. On the Moon, metallic iron is found in all probes of lunar soil brought to Earth, as a result of the flights of Apollo spacecraft and the automatic interplanetary stations Luna. Metal particles having crystallization nature after impact remelting correspond to meteorite origin. Therefore, the moon can be consider as the source of meteoritic iron. In this work large metal particles from Luna 20 soil samples are investigated using modern equipment.

Samples and Methods: Two metal particles (20045-544 and 2004-016) from highland region of the Moon are the objects of investigation. Particle 2004-016 have pear shape and weigh 276.4 mg. It is the largest lunar metal sample to date, over 6.3 mm in its longest dimension. Structure of samples 2004-016 and 20045-544 was study using optical microscopy and FE SEM Sigma VP with EDS and EBSD units.

Result and Discussion: The nature of metallic particles on the Moon can have a lunar or a meteoritic genesis. From the Ni-Co ratio, one can determine the origin of metallic iron on the Moon. Specific crystallization structures indicate the meteorite origin of the metal. The presence of dendrites, eutectics, and liquation gradients are characteristic features of crystallization processes in a multicomponent system. Among the studied metal samples, such structure is observed in the samples of 20045-544 and 2004-016.

Structure of 2004-016 sample contain crystallization features and satisfy condition of high-vacuum shock melting and Fe-Ni-Co-P-S alloy crystallization in case of lower gravity as compared to Earth. Cooling rate in crystallization range (approximately 0.1° C/s) was evaluated using cell size of kamacite. Despite occurred shrinkage phenomena, microporosity has not observed. This means that melt which was formed after meteorite falling to the Moon did not contain dissolved gases.

P and S enrichment result to sulfides and phosphides diversity. Six morphotypes of phosphides and three morphotypes of sulfides can be distinguished in structure of 2004-016. Also rims with Ni content up to 12.5% have been observed around all sulfide inclusion in 2004-016 (fig. 1).

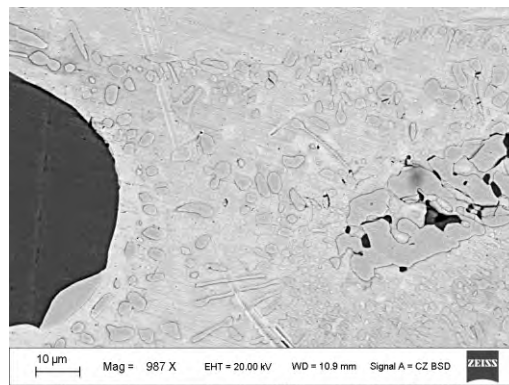


Fig. 1. BSE image of sulfide and phosphide inclusions in particle 2004-016

Particle 20045-544 have a dendrite shape with a maximum size of 1.3 mm and have bulk composition 2.3 wt. % P, 2.06 wt. % S. Particle 2004-016 have bulk composition 3.42 wt. % P, 2.28 wt. % S. According to [1] iron meteorites usually contain lower amounts of P and S. It can be explained by different interaction between meteorites with Moon and Earth. It is known that iron meteorites are the products of planetary differentiation. Fe-Ni monocrystals formed during this process could have sizes in range from one cm to several meters [2]. In sample 20045-544 one can observe an eutectic $\alpha + \text{ph}$ in interdendritic space. P and S segregated along boundaries of these crystals during cooling as phosphides and sulfides. Cracks propagate through relatively fragile phosphides and sulphides during fragmentation in the atmosphere. These inclusions disappear during ablation. But in case of absence of atmosphere unburned phosphides and sulfides enrich content of P and S in metal particles of lunar soil [3].

In work [4], the increase in P in the metal of the lunar soil is associated with their enrichment in the recovery of KREEP-basalts. The mechanism we propose is presented in a simpler and more acceptable way.

Acknowledgement: This work was supported by the Ministry of Education and Science of the Russian Federation (The projects 5.4825.2017/6.7, 5.3451.2017/4.6)

References: [1] Buchwald Vagn F. (1975) *Handbook of Iron Meteorites* 1418 pp. [2] Edward R.D. Scott, (1982) *Geochimica et Cosmochimica Acta*, 46 (5), 813–823. [3] Muftakhetdinova R.F. et al. (2015) *Meteoritics & Planet. Sci.*, 50, #5292. [4] Palme H., et al. (1982) *LPSC*, 13, 609-610.

EXPLORING NEW HORIZONS: EUROMOONMARS SIMULATION AT ESTEC 2017

A. Neklesa, B.H. Foing, A.Lillo, P.Evellin, M. Krainiski, A. Kołodziejczyk, C. Jonglez, C. Heinicke, M. Hara-symczuk, L. Authier, A. Blanc, C. Chahla, A. Tomic, M. Mirino, I. Schlacht, S. Hettrich, T. Pacher T. (anna.neklesa@network.rca.ac.uk, Bernard.Foing@esa.int) (ILEWG, ESTEC & VU Amsterdam)

Introduction: The ILEWG EuroMoonMars programme [1] conducted In July 2017 a series of workshops and the very unique analogue mission where students and professionals all over the world became one space crew. We simulated a Crew Moon landing supported by Earth control, having already ExoGeoLab lander, ExoHab, ExoLab 2.0. A media journalist (A.N.) joined the space crew and reports!

Goals: The EuroMoonMars mission simulation 2017 [2-5] set quite a few very important goals. First of all it was developing and testing it's own communication protocol between the Mission Control Center, the ExoLab and the ExoHab from both technical and verbal sides aimed to standardize and facilitate the communication. Secondly, evaluation of ergonomics of all units and the equipment needed to complete the mission. And finally, collection and analyses of samples from the Moon surface. All above was the subject of a training program in the process learning astronaut's daily routine.

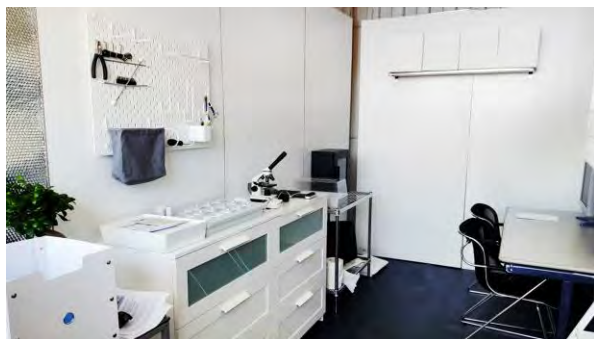


Figure 1: ExoLab 2.0 interior equipped for sample analysis and storing

Overview: After Deep Space Shuttle landed next to the already pre-landed Habitat ExoHab (the living unit), ExoLab 2.0 (the research laboratory), and the Storage Unit on the Moon, the space crew has conducted the following mandatory Health & Safety protocol:

1. Medical exam including measuring blood pressure, body and psycho check for trauma;
2. Search for a possible damage at all the pre-landed units.
3. The EVA related protocols were tested: doffing and donning, entering and exiting the ExoLab.

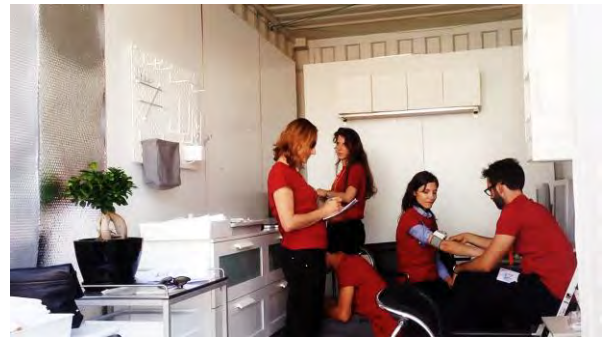


Figure 2: The Moon Crew conducting Health & Safety check at ExoLab 2.0 upon arrival.

Then the space team spread into units where ExoHab crew explored adjoining territories by using the small Rover [3] via wifi signal. Whenever something unusual was found, Lander[4] was sent to the spot for further exploration and sample collection.



Figure 3: The Rover [6] made by Mateusz Krainiski is controlled via WiFi signal by ExoHab crew in order to explore extraterrestrial sights.

Later the signal from Lander was received by the ExoHab team. It was reported to the Mission Control Center followed by two astronauts appointed to the location excavation. ExoLab and ExoHab members met next to Lander for sample collection. After one hour spent on the Moon surface both astronauts safely returned to their units.

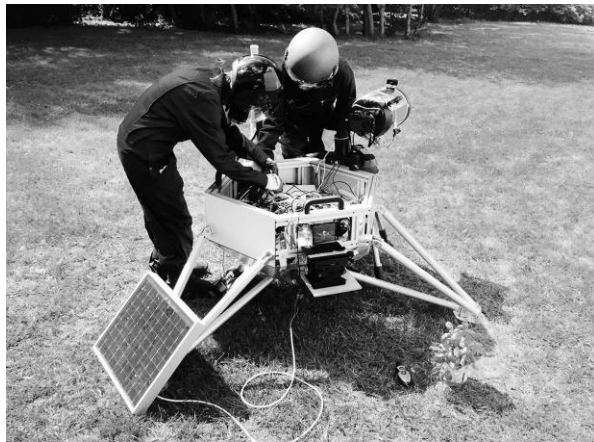


Figure 4: Astronauts collecting samples found by Lander miles away from the Moon Village.

Samples found by Lander were passed to further research at the ExoLab 2.0. According to the protocol, every step was proceeded and approved by the Mission Control Center beforehand.



Figure 5: ExoLab crew members analysing bio-samples found by Lander.

Results: From the educational point of view it was a very rich analog experience what can lay as the foundation to the future Moon/Mars behavior and communication protocols. The highly intensive mission requires

sufficient team playing where every crew member has to follow defined rules in order to complete mission successfully and provide safety all along the process. Every step has to be guided by the Mission Control Center and reports sent on a regular basis.

Summary: All the goals set by the mission control center including testing the communication protocol, operating Lander on the Moon surface, testing of ergonomics and simulating sample analysis were achieved within one day period, giving the Moon Team food for the next mission.

From the journalist perspective it was a very unique experience of witnessing real astronauts daily routine and being able to report livestream to Earth, encouraging viewers of all ages to learn more about the ESTEC Space Programme in general and current technical trends used for Moon / Mars exploration in particular. The idea of using wifi signal to control the Lander via Rover was a great success.

Acknowledgements: We thank ILEWG Euro-MoonMars programme, the Lunares team and PMAS/LUNEX astronauts.

References: [1] Foing BH (2009) LPI/LPSC 40, 2567; [2] Evellin P et al (2017) LEAG 5075; [3] Lillo A et al (2017) LEAG 5079; [4] Kolodziejczyk, A. M et al LEAG 5069; [5] Authier L et al LEAG 5071; [6] Mateusz Krański (2017).

Introduction: From a DAP 2010 overview [1] and a DAP 2017 overview on-line since 23 February 2018 [2] of published dust measurements on the lunar surface, the purpose here is to inform and assist future lunar explorations, both human and robotic, about current knowledge of movements of lunar dust *in situ*. The goal is to increase safety and cost-effective success through informed risk management of movements of fine dust on the surface of the Moon.

The first historic evidence of progress in the sciences of movements of Apollo dust is summarised in the Kuhn Cycle (Fig 2) [2] which can now be populated by 3 recent events: (i) a "Model crisis" when Chang'e-3 lunar rover Yutu was immobilised since January 2014 [4], (ii) a "Model revolution" discovery of sunrise-driven dust storms to help explain immobility of Yutu [5,2] leading to (iii) potentially a "paradigm change" in the announced revision of Chang'e-4 scientific priorities making dust top priority [4]. Transparency remains an issue, with presentations of Chang'e-3 reports on dust, each scheduled to follow our Apollo-based presentation, withdrawn in June 2017 at GLEX2017 in Beijing and in September 2017 at the 68th AIC in Adelaide. We suggest Yutu immobilisation was likely caused by friction-like effects of fine dust reported by astronaut Cernan [6] combined with high populations of dust at waist height mobilised by rocket exhausts during hovering and landing of Chang'e-3 and the 6 wheels of Yutu in its travels [4, 2]. However, conservatively we await authoritative up-to-date news about the Chang'e-4 payload.



Figure 1.

Risks. The last man on the Moon, Gene Cernan, reported that "We can overcome other physiological or physical or mechanical problems except dust" [6]. The summary of astronaut reports by Gaier in 2005 gives 9 categories of problems caused by fine dust

[7]. Most dramatic but fact-based is Gaier's conclusion "The most alarming characteristic was how quickly and irreversible (dust problems) could occur." All such astronaut observations to date have been qualitative. The 270g minimalist DDEs provide the only quantitative measurements to date of the variability of damaging dust bombardment from rocket exhausts at different distances [1]. The DDE measures both cause and effects of billions to trillions of low-energy dust particles, contrasted to traditional dust detectors measuring impacts of each individual high-speed dust particle.

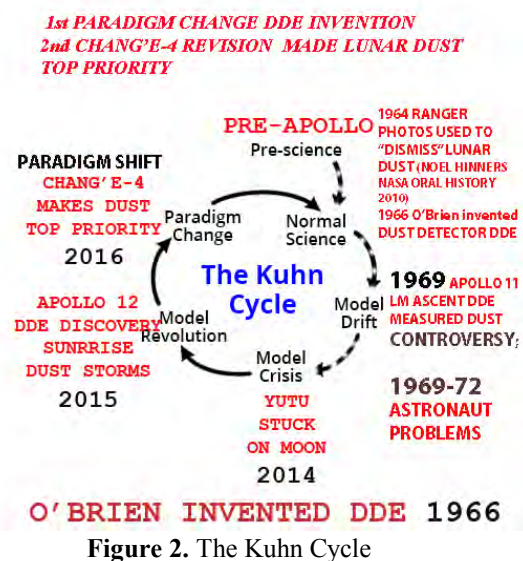


Figure 2. The Kuhn Cycle

Commercial Rewards. Rewards from DDE discoveries include helping future expeditions plan engineering, architecture and missions to minimise risks. Discoveries range from one measurement of the increment of temperature change caused by an incremental change in dust cover [1] to rich implications from discovery of dust storms during the first few sunrises after the Apollo 12 site was disrupted by rocket exhausts [5]. The resulting measurement-driven 5-step model explained 50-year mysteries of Horizon Glow, 30 years of hypotheses about levitated dust, and thus Moon Truth explanations for effects of fine dust measured at 100cm height which LADEE LDEX did not measure at 2.5 to 250km altitude. It also explains why lunar surfaces are smooth by naturally occurring phenomena despite being pock-marked by meteoritic impacts, a finding very important for the future feasibility and acceptability of In Situ Resource Utilisation (ISRU) for the Moon and large airless asteroids.

Apollo DDE solar cells also provide the longest and most varied tests to date of degradation (or efficien-

cy) of solar cell performance at 3 sites on the Moon, invaluable for solar-powered arrays planned to power future missions and Moon Villages. They provide evidence that even a lightly-shielded (0.15mm glass) solar cell shows over 6 years a greater degradation caused by dust accumulation than by radiation damage, including the August 1972 Solar Particle Event (SPE) [5].

Invitation to make Moon-Truth tests of simulated dust and simulated environments: Pre-launch testing of lunar experiments and payloads.

Payloads and experiments for soft-landing and exploratory missions on the lunar surface face two major risks (i) from 350 hours (mid-latitude) of lunar night temperatures on -170°C; and (ii) movements of lunar dust during lunar day, including the massive jolt of sunrise. To date, Pre-launch testing can be made of the cold but not the dust *in situ*. Accordingly we offered via Lunar L distribution on 30 January 2018 opportunities to help reduce this defect, by comparing lunar dust simulants and lunar environment simulations within Dirty Thermal Vacuum Chambers (DTVCs) with a 25-hour tranche of digital Apollo 12 measurements by the East-facing vertical solar cell of the Apollo 12 DDE. This test enables a low-cost Moon-Truth test over 25 hours to make a direct calibration of the variation in time (and brightness of sunlight) of adhesion to a vertical silicon surface of any simulant against the *in situ* lunar dust splashed on the Apollo 12 Dust Detector Experiment (DDE) *in situ* (see Figure 4 and discussion [8]). This may be the first such test.

Conclusions. The next 2 or 3 lunar rovers face daunting challenges which must be managed after Yutu was immobilised. The Google Lunar XPrize has been concluded, but several international and commercial planners of lunar rovers remain in developments. India Chandrasayaan-2 plans to deploy a lunar rover in 2018, as yet without a dust detector experiment, while dust experiments for Chang'e-4 in 2018 remain a work in progress. With a declaration of interest, we suggest many advantages of adding to payloads routinely a duplicate of original DDE from the slide-rule days of 1966 as simple space-proven dust experiments. They can hitch-hike with minimum impacts on planned payloads, to make immediate baseline mission-related measurements and provide international continuity of their existing 6-year provenance of unique digital data.

References: [1] O'Brien, B., doi: 10.1016/j.pss.2011.04.016 ;[2] O'Brien,B., doi: 10.1016/j.pss.2018.02.006;[3] Hinnert, Noel W., NASA Hdqs. Oral History, 2010; [4] Zou Y.L. et al. (2016) ELS 2016 Abstract #040 5; [5] O'Brien, B. and M. Hollick, doi:1015/j.pss.2015.09.018; [6] Cernan, Gene, MSC07631, 1973; [7] Gaier, James R., NASA/TM-2005-213610; [8] O'Brien, B., doi:10.1029/2008GL037116, 2009.

Introduction: In addition to the scientific interest, the Moon is considered as the next destination of human activity. The Japan Aerospace Exploration Agency (JAXA) identified lunar landing exploration as the next step for technology development in space exploration after the successful lunar orbiter SELENE (Kaguya) mission. It is carrying out a mission called Smart Lander for Investigating Moon (SLIM). The SLIM mission [1] is a technology demonstration mission targeting a pinpoint landing (landing precision is ± 100 m), which is mandatory for future lunar and any planetary explorations.

In parallel, the International Space Exploration Coordination Group, organized by the space agencies of 15 countries and regions, is discussing future space exploration plans based on international collaborations. Planning of manned lunar surface exploration via a manned cislunar space station and precursor robotic (unmanned) missions prior to the manned mission is being studied in this framework.

Lunar polar exploration is an intensely studied candidate missions of the precursor robotic mission by many countries. In this presentation, we discuss an overview of the lunar polar mission studied in Japan.

Mission objectives: Recently, it has been suggested that water ice might be present in the lunar polar region based on spectral measurements of artificial-impact-induced plumes in the permanently shadowed region, and remote sensing observation of the lunar surface using a neutron spectrometer [2], [3] and visible to infrared spectrometer [4]. In addition to the scientific interest about the origin and concentration mechanism of the water ice, there is strong interest in using water ice (if present) as an in-situ resources. Specifically, using water ice as a propellant will significantly affect future exploration scenarios and activities because the propellant generated from the water can be used for ascent from the lunar surface and can reduce the mass of the launched spacecraft of lunar landing missions.

However, currently it is unclear if water ice is really present in the polar region because of the currently limited available data. Therefore, we need to learn that by directly measuring on the lunar surface. If there is water ice, we also need to know its quantity (how much), quality (is it pure water or does it contain other phases such as CO₂ and CH₄), and usability (how deep do we need to drill or how much energy is required to derive the water) for assessing if we can use it as resources. Therefore, JAXA is studying a lunar polar exploration mission that aims to gain the above information and to establish the technology for planetary surface exploration

[5]. JAXA is also studying possibility of implementing it within the framework of international collaboration.

Spacecraft configuration: The spacecraft system comprises a lander module and rover system. The launch orbit is a geostationary transfer orbit (GTO), and the spacecraft system is transferred from GTO to lunar orbit (or the spacecraft is directly transferred to the lunar transfer orbit (LTO)) using a propulsion module. After landing onto the lunar surface, the rover is deployed using a descending ramp. The rover then prospect for water ice using observation instruments on board.

Landing site selection: Considering the mission objectives and condition of the lunar polar region, we listed the following parameters as constraints.

- 1) Presence of water
- 2) Surface topography
- 3) Communication capability
- 4) Duration of sunshine

As a first trial of the landing site selection, sunshine is simulated using digital elevation models to obtain the sunlight days per year and the number of continuous sunshine periods at each site. Also, slope and the simulated communication visibility map from the Earth are created. These conditions can be superimposed to select the landing site candidate.

Technology Development: We currently focus on developing technologies required for the exploration of polar regions and are promoting the following research and development.

- Sunshine in the polar region is from the horizontal direction, and it is affected by the local topography. Solar panels therefore need to be deployed vertically in a tower.
- Normal image based navigation is difficult in the polar region. Therefore shade image collation navigation using images of shadows created by the terrain is being studied.
- A prototype model of a rover equipped with a 1.5 m drill is being developed to examine basic functions.
- Currently, for rover deployment, we plan to develop ramps in forward and backward directions to secure redundancy. It is therefore important to develop a lightweight ramp structure.

References: [1] Sawai S. et al. (2011) *28th ISTS*, 2011-f-21. [2] Feldman W. C. et al. (1998) *Science*, 281, 1496-1500. [3] Sanin A. B. et al. (2017) *Icarus*, 283, 20-30. [4] Pieters C. M. et al. (2009) *Science*, 326, 568-572. [5] Hoshino T. et al. (2017) 68th IAC, IAC-17-A3.2B.4.

POTENTIAL LANDING SITES FOR THE CHANG'E-4 EXPLORATION MISSION TO THE APOLLO BASIN, MOON. C. Orgel¹ (orgel.csilla@fu-belin.de), M. A. Ivanov², H. Hiesinger³, J.-H. Pasckert³, C. H. van der Bogert³, G. Michael¹. ¹ Freie Universität Berlin, Department of Planetary Sciences, 12249 Berlin, Malteserstrasse 74-100, Germany, ²Vernadsky Inst., RAS, Russia, ³Westfälische Wilhelms-Universität, Münster, Germany.

Introduction: As the oldest and deepest impact structure on the Moon, the South Pole-Aitken Basin (SPA) on the lunar farside is a scientifically high priority site for human and robotic exploration [1]. The lunar farside has not been visited by any exploration missions so far, but it is the focus for Chang'e-4 robotic missions planned for the end of 2018 [2].

The Chang'e-4 mission aims to deploy a relay satellite into Halo-orbit around EM-L2 and land with a Yutu heritage rover on the lunar surface. The provisional scientific objectives of Chang'e-4 [2] are to study: (1) the interaction between the solar wind and lunar surface, (2) the formation mechanism of lunar regolith and dust, (3) the lunar-based VLF astronomical potential, (4) the regional geochemistry and subsurface, and (5) the recent impact flux of the Moon.

The most likely landing site for the Chang'e-4 robotic mission will be the 538 km-diameter Apollo basin in the NE quadrant of the SPA basin. Here, we provide a detailed analysis of three high-priority (Fig. 1 regions of interest (ROIs) with example rover traverses of 2.5 km, 5 km and 10 km radius from the center of ROIs in the central and southern mare deposits of the Apollo basin. The proposed high-priority ROIs have high scientific interest based on prioritized science concepts defined in the 2007 National Research Council (NRC) report [1] and the scientific objectives of the mission.

Science rationale: The Apollo basin has been mapped as pre-Nectarian [3-5], pre-Nectarian/Nectarian [6], and Nectarian [7]. According to CSFD measurements, its absolute model age (AMA) is 3.91 Ga [5] to 4.14 Ga [7]. Thus, the Apollo basin is one of the youngest basins inside the SPA basin.

Based on GRAIL data, the crustal thickness is less than 5 km beneath the Apollo basin [8]. The NE-E rim of the Apollo basin exposes anorthositic material from the highlands along the SPA rim and possibly impact melt and/or mantle material from the SPA interior [9]. The basin floor is mainly covered by four mare basalt provinces (center, south, west, and east), their AMAs ranging from 2.30 to 3.45 Ga [10]. The mare deposits have enhanced FeO and TiO₂ abundances compared to the immediate surroundings [11].

Data and Methods: To evaluate the potential science return of each proposed ROI, we use all available datasets from previous lunar missions and studies [11]. The terrain trafficability is determined via slope maps, and digital elevation models derived from the LOLA

instrument, at resolutions of 60 m/pix. The terrains that compose the Apollo basin are visualized using LRO WAC mosaics of 100 m/pix, and individual NAC images of 1 m/pix, and Kaguya Terrain Camera images of 7 m/pix. We use the Kaguya images as the photo-base for geologic mapping and counting craters >50m for crater size-frequency distribution analyses. Geologic maps at 1:50,000 scale are being compiled for the central and southern portions of the Apollo basin, as well as a detailed regional geologic map of the northern portion of SPA [12]. FeO and TiO₂ contents are determined using Clementine 100 m/pix global maps [13], as well as Kaguya LISM 80/pix data [14].

Selection of ROIs: The central and southern mare deposits were the main objectives of high-priority ROIs. These areas are smooth with <5° slopes and have low crater densities. The selected ROIs reflect a geologically complex area (Fig. 1), where both mare deposits are covered by younger, Copernican-aged ejecta material of various thickness and distribution, and "pure" mare is also accessible. In addition, the mare deposit has high in situ resource utilization (ISRU) potential due to relatively high FeO and TiO₂ contents ranging from 14-20 and 1-7 wt%, respectively (Tab. 1). In contrast, the younger ejecta materials have low FeO and TiO₂ contents representing material beneath the mare deposit. The origin of that material could be SPA and/or Apollo impact melt, which is a high-ranking scientific objective [1].

	ROI 1		ROI 2		ROI 3	
	FeO	TiO ₂	FeO	TiO ₂	FeO	TiO ₂
Min.	16.15	0.80	17.65	3.95	17.39	5.71
Max.	18.58	7.50	18.80	8.73	18.58	9.91
Average	17.90	4.20	18.33	6.78	18.18	7.53

Table 1: FeO and TiO₂ content of mare deposits in the ROIs based on 50 random samples within the ellipses.

Conclusion: These high-priority areas could fulfill the general engineering constraints and the scientific objectives, as well as ISRU potential of the mission. In situ observations and sample analyses can help address six of seven NRC concepts (1-3, 5-7) and provide a high ISRU potential at all selected ROIs.

Acknowledgement: This work was funded by the Deutsche Forschungsgemeinschaft (SFB-TRR 170, subproject A3-2) and Russian Science Foundation (grant 17-17-01149) to MAI.

References: [1] NRC (2007) National Academies Press. [2] Wang Q. and Liu J. (2016) *Acta Astronautica* 127, 678-683. [3] Stuart-Alexander (1978) *No. I-1047*. [4] Wilhelms et al. (1979) *No. I-1162*. [5] Hiesinger et al. (2012) *LPSC #2863*. [6] Fassett et al. (2012) *JGR* 117: E00H06. [7] Orgel et al. (2018) *LPSC #1395*. [8] Wieczorek et al. (2013) *Science* 339, 671-675. [9] Morrison D. A. and Bussy D. B.

J. (2007) LPSC #1501. [10] Pasckert et al. (2018) *Icarus* 299, 538-562. [11] Kring D.A. and Durda D.D. (2012) *LPI Contrib.* 1964.

[12] Ivanov et al. (2018) LPSC 1138. [13] Lucey et al. (2000) *JGR* 105, 20,297-20,306. [14] Lemelin et al. (2016) LPSC #2994.

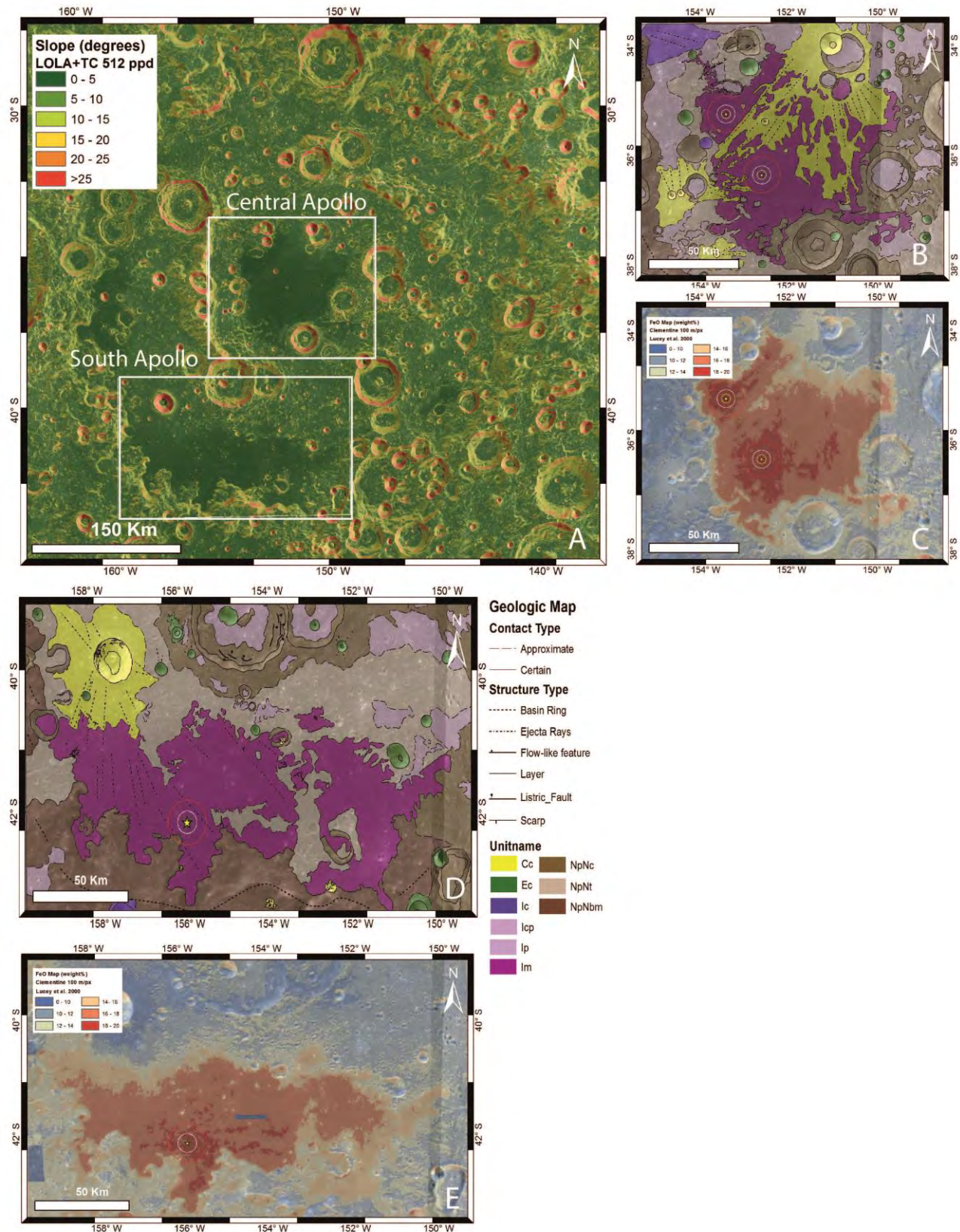


Figure 1: High-priority Region of Interests (ROI) in the Apollo basin. A/Slope map derived from LOLA and TC 60 m/pix data. White boxes indicate the location of geologic maps. B-D/Geologic maps of the central and south Apollo basin. C-E/FeO maps derived from Clementine 100 m/pix data. High-priority ROIs indicated with example rover traverses (circles) of 2.5 km (yellow), 5 km (white) and 10 km (red) radius from the center of ROIs

MINI-RF S- AND X-BAND BISTATIC RADAR OBSERVATIONS OF THE MOON. G. W. Patterson¹, L. M. Carter², A. M. Stickle¹, J. T. S. Cahill¹, M. C. Nolan², G. A. Morgan³, D. M. Schroeder⁴, and the Mini-RF team, ¹Johns Hopkins University Applied Physics Laboratory, Laurel, MD (Wes.Patterson@jhuapl.edu), ²Lunar and Planetary Laboratory, Tucson AZ, ³Planetary Science Institute, Tucson AZ, ⁴Stanford University, Stanford CA.

Introduction: NASA's Mini-RF instrument on the Lunar Reconnaissance Orbiter (LRO) is currently operating in concert with the Arecibo Observatory (AO) and the Goldstone deep space communications complex 34 meter antenna DSS-13 to collect bistatic radar data of the Moon. These data provide a means to characterize the scattering properties of the upper meter(s) of the lunar surface, as a function of bistatic angle, at S-band (12.6 cm) and X-Band (4.2 cm) wavelengths. These data are being collected to address the following driving questions for the current LRO extended mission: What is the vertical distribution of lunar water? What is the form and abundance of lunar water ice? How do impacts expose and break down rocks to produce regolith on the Moon and other airless bodies? What is the present rate of regolith gardening? How has lunar volcanism evolved over time? Is there evidence for long-lived hot-spot style volcanism?

Background: The transmitters for Mini-RF bistatic observations are AO (S-band) and DSS-13 (X-band). For each observation, the lunar surface is illuminated with a circularly polarized, chirped signal that tracks the Mini-RF antenna boresight intercept on the surface of the Moon. The Mini-RF receiver operates continuously and separately receives the horizontal and vertical polarization components of the signal backscattered from the lunar surface. The resolution of the data is ~100 m in range and ~2.5 m in azimuth but can vary from one observation to another, as a function of the viewing geometry. For analysis, the data are averaged in azimuth to provide a spatial resolution of 100 m. This yields an ~40-look average for each sampled location.

The data returned provide information on the structure (i.e., roughness) and dielectric properties of surface and buried materials within the penetration depth of the system (up to several meters for Mini-RF) [1-4]. The bistatic architecture allows examination of the scattering properties of a target surface for a variety of bistatic angles. Laboratory data and analog experiments, at optical wavelengths, have shown that the scattering properties of lunar materials can be sensitive to variations in bistatic angle [5-7].

Operations: Collecting data in the Mini-RF bistatic architecture requires significant advance planning with both the LRO operations team and ground-based facilities. As a result, no more than a few collects per month are feasible. The first Mini-RF bistatic campaign (2012-2015) included 28 AO S-band observations of the lunar surface, polar and nonpolar (Fig. 1). Those observations provided data used to suggest

the presence of water ice within floor materials of the crater Cabeus [8] and to characterize the weathering of Copernican crater ejecta [8,9].

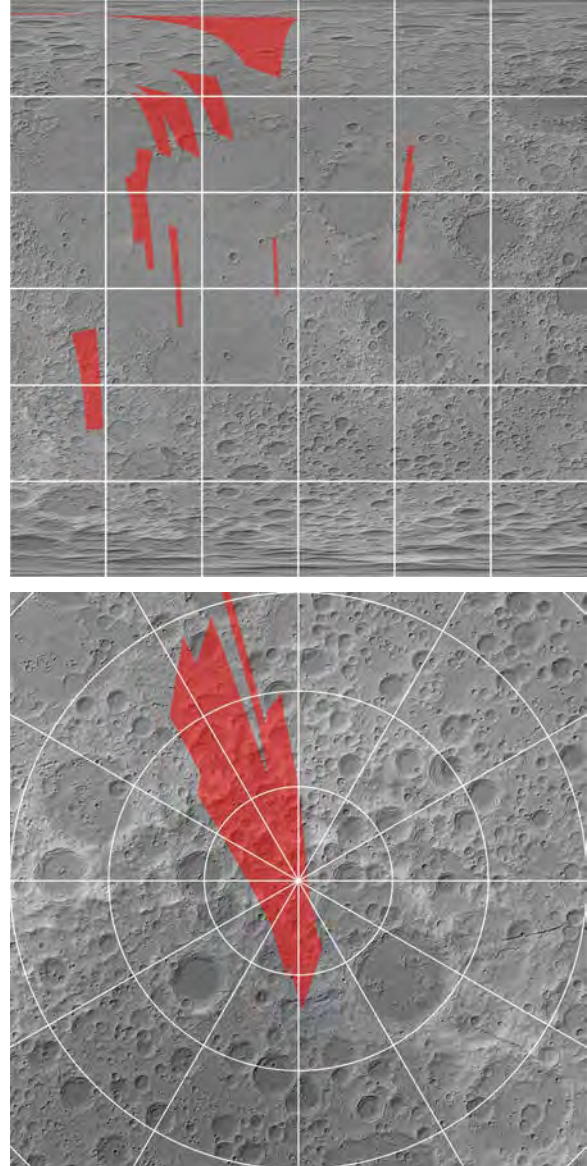


Fig. 1. S-band radar coverage in the first bistatic campaign for the lunar nearside (top; 90°W to 90°E) and south pole (bottom; 60°S to 90°S)

The current bistatic campaign (2017-present) includes an additional 4 AO S-band observations and 23 DSS-13 X-band observations of the lunar surface (Fig. 2). A variety of lunar terrains are being targeted to address science objectives for the ongoing LRO extended mission. They include collecting data of: the floors of south polar craters to search for signatures

indicative of the presence of water ice [10]; Copernican crater ejecta blankets to characterize rates of regolith breakdown/weathering [11,12]; the ejecta of newly-formed craters to characterize the size-distribution and density of wavelength-scale scatters as a function of distance from the impact [13]; mare materials within the Imbrium basin to provide important information on the locations, extents, and depths flow units and deposits [14]; and irregular mare patches (IMPs) and pyroclastic deposits to characterize their radar properties [15,16]. In concert with the collection of these data, modeling work is being conducted to characterize the response of surface materials to variations in incidence angle [17] and to address LRO science objectives with Mini-RF monostatic data [e.g., 18,19]

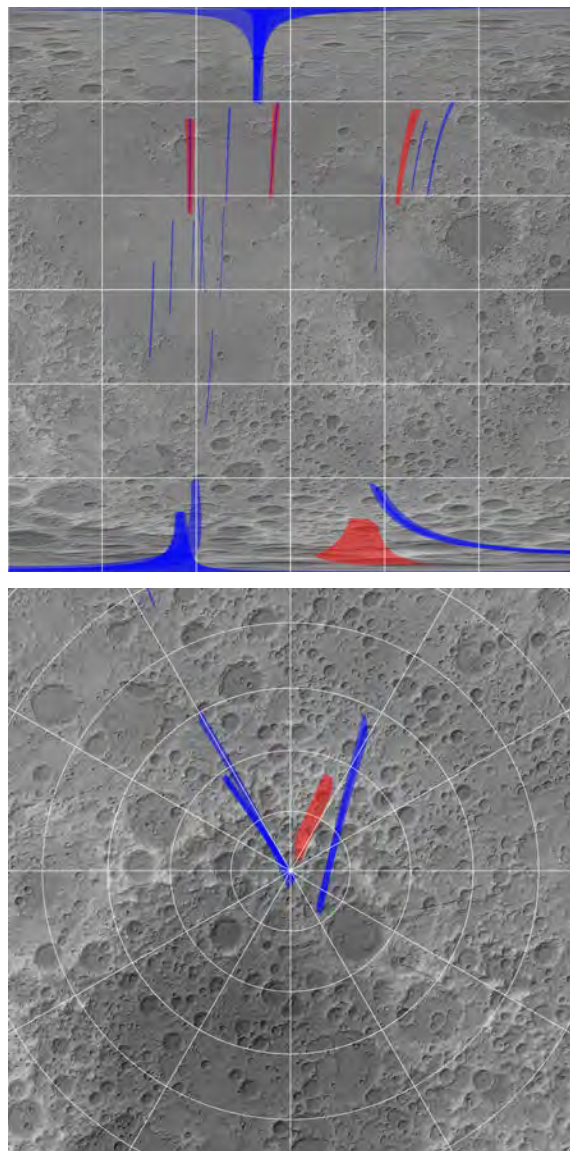


Fig. 2. S-band (red) and X-band (blue) radar coverage in the second bistatic campaign for the lunar nearside (top; 90°W to 90°E) and south pole (bottom; 60°S to 90°S)

Results: Initial analysis of south polar targets acquired at X-band [10] do not appear to show the possible water ice signature detected at S-band [8]. This would indicate that, if water ice is present in Cabeus crater floor materials, it is buried beneath ~0.5 m of regolith that does not include radar-detectable deposits of water ice. Observations of Copernican crater ejecta materials at S- and X-band wavelengths continue to show variations that can be attributed to the age of the crater [11]. Differences between S- and X-band observations of the same crater are also present, providing new insight into the size-distribution of radar scatters within the ejecta [11,12]. Two craters that formed during the LRO mission have been identified in X-band Mini-RF data acquired in the current bistatic campaign. Analysis of these data suggest enhanced wavelength-scale surface roughness to radial distances of 100s of meters from the crater centers [13]. S- and X-band observations of mare materials in the Imbrium basin and pyroclastic deposits in the Montes Carpatius, Aristarchus, and Taurus Littrow regions have been acquired and, combined with ground-based P-band observations, are providing important information on the locations, extents, and depths to individual flow units and deposits [14-16].

References: [1] Campbell et al. (2010), *Icarus*, 208, 565-573; [2] Raney et al. (2012), *JGR*, 117, E00H21; [3] Carter et al. (2012), *JGR*, 117, E00H09; [4] Campbell (2012), *JGR*, 117, E06008; [5] Hapke et al. (1998), *Icarus*, 133, 89-97; [6] Nelson et al. (2000), *Icarus*, 147, 545-558; [7] Piatek et al. (2004), *Icarus*, 171, 531-545. [8] Patterson et al. (2017), *Icarus*, 283, 2-19; [9] Stickle et al. (2016), *47th LPSC* #2928; [10] Patterson et al. (2018), *49th LPSC* #2007; [11] Stickle et al. (2018), *49th LPSC* #1585; [12] Novak et al. (2018), *49th LPSC* #2915; [13] Cahill et al. (2018), *49th LPSC* #2693; [14] Morgan et al. (2018), *49th LPSC* #1897; [15] Carter et al. (2018), *49th LPSC* #2461; [16] Sriram et al. (2018), *49th LPSC* #2496; [17] Prem et al. (2018), *49th LPSC* #2134; [18] Nypaver et al. (2018), *49th LPSC* #2560; [19] Mandt et al. (2018), *49th LPSC*.

Cryogenic Air Purification for deep space exploration.

Yan Pennec 1, James Butterworth 1, Daniele Laurini 2, Klaus Bocksthaler 3.

1: Air Liquide Advanced Technologies, 2 rue de clémencières. 38 360 Sassenage.

2: ESA – ESTEC The Netherlands.

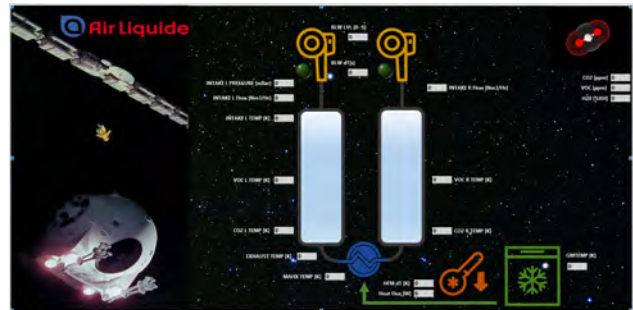
2: Airbus Defence and Space GmbH 88039 – Friedrichshafen.

Introduction:

Deep space exploration and settlement represents a new frontier for the progress of mankind. From the first stratospheric flight to the Apollo missions to the International Space Station, the occupancy and duration of flights have raised tremendously. It has put increasing demands on life support systems capabilities. Within the realm of air revitalization, several technological milestones have been witnessed from using gas bottles (O₂) or single shot chemical capture (LiOH) to current regenerative adsorbent beds (molecular sieves, amines). Looking forward, the next milestone technology must be able to provide air revitalization systems capable of handling tens of crew members for decades. Next generation systems must not only improve efficiency and reliability but they must become very low maintenance and require minimal consumables.

ALAT defends the use of capture and separation of air pollutants by cryogenic means as a promising candidate. ALAT proposal is strongly supported by its long standing experience and heritage in functional technologies (gases engineering, cryogenics) and system development (life support, cooler and distillator and separator).

In this presentation we will introduce the first results of our breadboard demonstrator targeted at the ISS and how it could be extrapolated for a lunar mission.



Introduction: The localized graceful and mysterious brightness markings found across the lunar surface called ‘lunar swirls’ (Fig. 1) continue to puzzle and awe both young and experienced lunar investigators. Their overall properties have been studied and quantified [e.g., 1,2,3,4,5]. Swirls occur in both maria and highlands; prominent magnetic anomalies are associated with swirls; no topographic variations are found for the features; swirls exhibit unusual photometric properties. More recently, the solar wind has been seen to be deflected at strong magnetic anomalies of a swirl [6] and low surface hydration is seen for swirl high albedo areas (but not the ‘dark lanes’) [7,8].

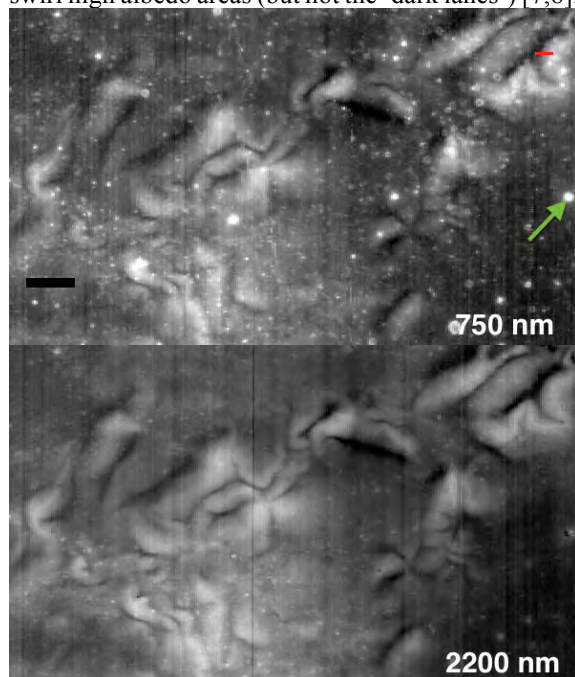


Fig. 1. A swirl trail across mare terrain SW of Reiner Gamma as imaged by M³. Since the 2200 nm wavelength image is in the middle of a pyroxene absorption band, immature basaltic soils (e.g., at craters) become largely invisible. Scale bar is 5 km.

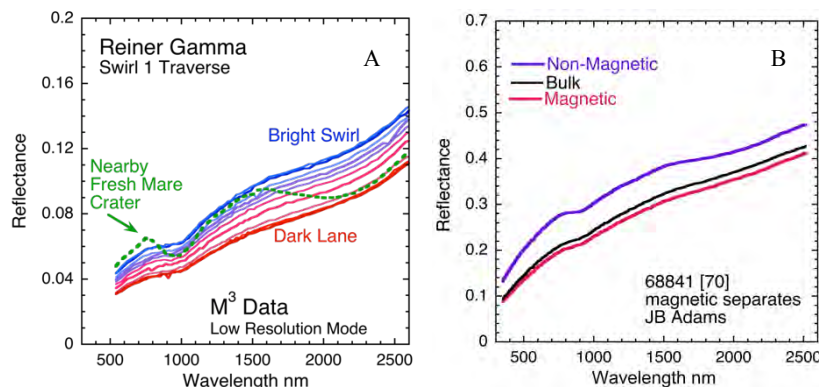


Fig. 2. [A] M³ Spectra for a traverse across the swirl shown by the red line in Fig. 1. The example immature crater is indicated with a green arrow. Background mature mare soils are comparable to dark lane spectra. [B] Example magnetic separates of mature soil, 68841. Mixtures of magnetic and non-magnetic components mimic the sequence observed across swirls.

Some form of reduced space weathering is often assumed to account for these unusual high albedo features at swirls. However, it has also been argued that the detailed spectroscopic information now available across swirls shows that their distinctive properties (a brightening across all wavelengths [9]) are quite different from observed space weathering trends [8,9,10,11]. This disconnect between swirls and normal space weathering is illustrated in Fig. 1 and 2A.

Key magnetic properties of lunar soils: It took several decades to develop an understanding of how space weathering results in strong changes of optical properties; the process is largely due to accumulation of nano-phase metallic iron (npFe⁰) on grain surfaces and within processed agglutinates [e.g., 12]. Early experiments during the Apollo era sought to concentrate space weathering products by magnetic separation for spectral analysis [13]. Although not all such spectra were of high quality, a systematic pattern emerges between the magnetic (npFe⁰-rich) and non-magnetic components of the soil and is illustrated in Fig. 2B.

Origin of swirl optical properties: The full spectral properties of the bright component of swirls in the maria are simply not consistent with immature lunar soils. Instead, they are more consistent with a soil in which the npFe⁰-rich magnetic component has been removed or has never developed. Thus, at swirls either (a) there is a continuous magnetic sorting of particles during soil evolution and gardening resulting in the pattern seen across Fig. 1, or (b) solar wind is strongly deflected on the scale of bright and dark lanes seen in Fig. 1 and is the dominant or sole stimulus of npFe⁰ formation. Although yet untested, (a) appears to be the far more probable scenario. Independent of soil evolution at these unusual sites, a major unanswered question remains concerning the origin and scale of the magnetic anomalies so clearly involved.

References:

- [1] Schultz and Srnka, 1980, *Nature*.
- [2] Hood and Schubert, 1980, *Science*.
- [3] Pinet et al., 2000 *JGR*, 105, 9457
- [4] Shkuratov et al., 2010 *Icarus* 208, 20.
- [5] Blewett et al., 2011, *JGR* 116, E02002
- [6] Wieser et al., 2010 *GRL* 37
- [7] Kramer et al., 2011, *JGR* 116, E00G18
- [8] Pieters et al. 2015 *LPSC46*-2120
- [9] Pieters et al. 2014 *LPSC45*-1408
- [10] Garrick-Bethell et al., 2011, *Icarus*.
- [11] Hemingway et al., 2015 *Icarus*
- [12] Pieters and Noble 2016 *JGR*, 121, 1865
- [13] Adams and McCord, 1973, *PLSC4th*, *GCA V1*

MINERALOGICAL MAPPING AT COPERNICUS CRATER FROM MGM DECONVOLUTION OF M3 OBSERVATIONS. P. C. Pinet¹, S. D. Chevrel¹, Y. Daydou¹, ¹IRAP, Université de Toulouse; CNRS, CNES, UPS-Observatoire Midi-Pyrénées, 14, avenue Edouard Belin, 31400 Toulouse, France (patrick.pinet@irap.omp.eu).

Introduction: Recent observations from the multiband imager and the spectral profiler onboard the Japanese SELENE spacecraft and from the Moon Mineralogy Mapper (M3) imaging spectrometer onboard the Chandrayaan mission identified in a number of lunar regions (e.g., in crater central peaks) the unambiguous occurrence of a 1.2-1.25 μm spectral feature, indicative of a crystal field absorption consistent with Fe-bearing plagioclase feldspar in anorthosite [1,2]. Olivine mineral detection has also been documented [e.g., 3,4,5]. Given the wealth of the M3 dataset, advanced hyperspectral processing appears needed to fully explore the existing variability involving plagioclase and mafic crystal field absorptions [e.g., 6], and to better constrain the lunar crust lithology and cratering process.

MGM background and testing: The principle of the Modified Gaussian Model is to deconvolve overlapping absorptions of mafic mineral spectra into their fundamental absorption components. Its specific interest is to directly account for electronic transition processes [e.g., 7]. The MGM approach is in essence able to achieve a direct detection and quantification of minerals which make up the observed surface. Spectra are modeled in the logarithm of reflectance space as a sum of modified Gaussian distributions superimposed on a baseline continuum. The resulting combinations of Gaussians can then be interpreted in terms of mineralogy. MGM can retrieve modal and/or chemical composition from an unknown spectrum in the case of simple mineralogies [8]. Several studies have shown the interest of the MGM approach for planetary surface characterization (e.g., [9,10]). However, reference studies rely on spectra acquired on controlled laboratory powder samples. More complex situations addressing mixed mineralogies (e.g., olivine and pyroxene(s) with plagioclase) and/or rock samples have been little explored and significant efforts have still to be made for improving our capability of spectroscopic modeling and interpretation when dealing with real world observations of unknown mafic rock lithologies.

Our goal here is to improve the capability of the MGM to realistically model complex mafic mineralogies when considering rock slab surfaces with coarse textures, involving plagioclase and mafic crystal field absorptions [e.g., 11]. MGM testing has been performed on slab spectra of Plg-rich rock samples from the igneous stratified Stillwater Complex [12] and on a hyperspectral cube produced on a core section from a drill in the oceanic crust (IODP Expedition 345) [13]. The composition is globally gabbroic, mostly composed of plg feldspar and cpx;

ol and opx are also present, and their variations define a modal layering, with some ol-rich layers and other ones devoid of olivine. Based on these tests, our MGM approach can properly discern the mafic minerals contribution (ol, cpx, opx), including the detection of crystalline plg, in the spectra across a complex sample such as the studied core [13]. Additional tests performed on M3 spectra acquired over Jackson crater detect Plg in the central peaks as previously found [1,2].

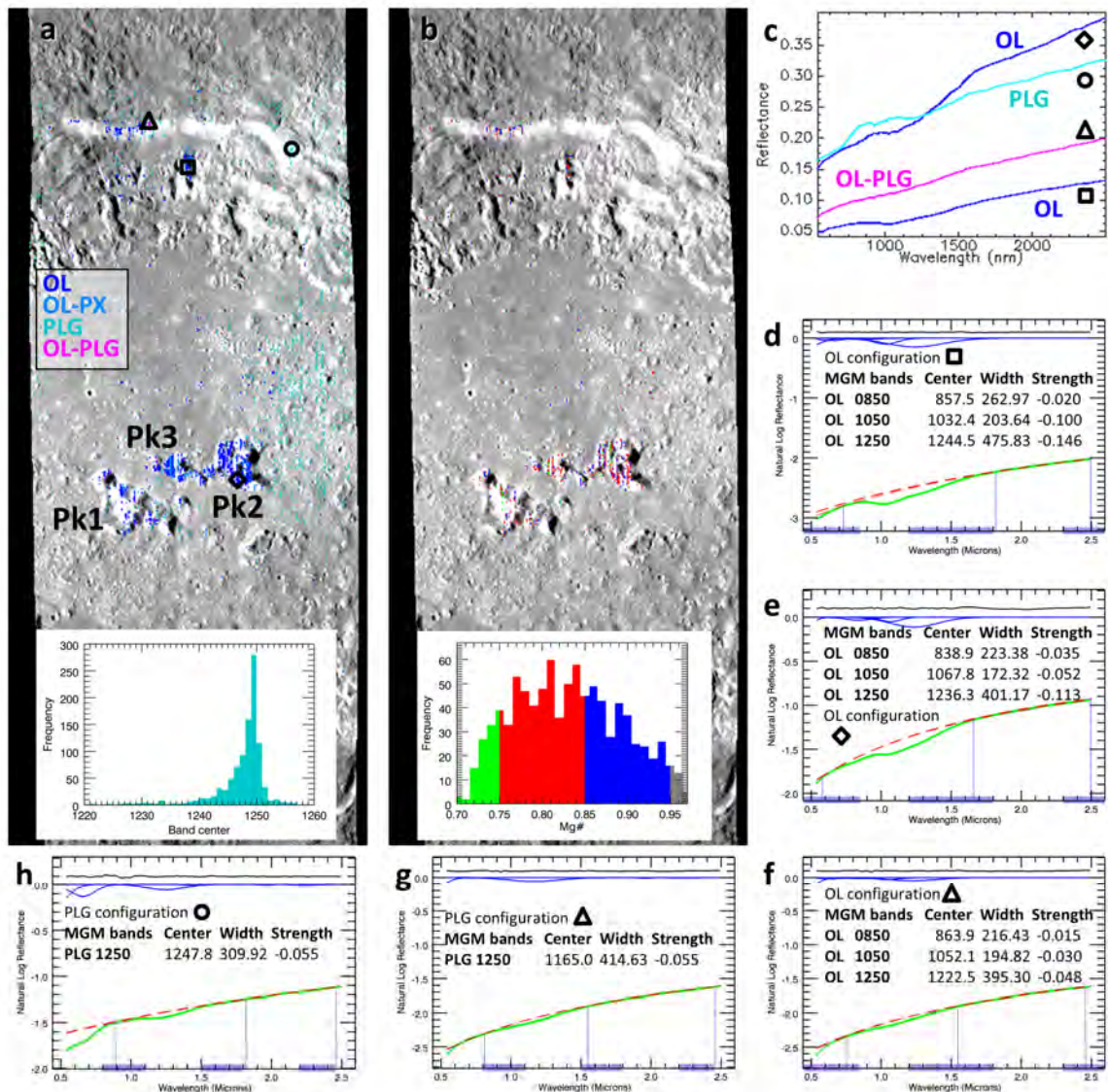
Data Analysis and Results: We now implement this hyperspectral strategy on M3 spectra with the objective of documenting the petrology at Copernicus crater through characterization of plagioclase and mafic crystal field absorptions, from exposed outcrops (e.g., central peaks, inner walls and rims). The present study has been made on a subset of the M3G20090416T122951_V01_RFL hyperspectral image (140m/pixel) acquired during the OP2A optical period. A systematic search for mineral assemblages [10] involving opx, cpx, ol and plg detects a proeminent diverse mafic mineralogy with well-developed absorption features and the presence of surface patches across the crater floor and ejecta with almost featureless signatures possibly associated with impact melts. Distinct px-rich mineralogies (Mg-pyroxenes, cpx-bearing) are found inside and outside the crater structure but not discussed here, the focus being on the ol/plg detections. Ol and plg-bearing materials identified are only found in association with the crater structure (Fig. 1.a). For the ‘olivine-only’ detections, the Mg number variation is determined and its distribution displayed (Fig. 1.b). A selection of four representative reflectance spectra associated with various ol and/or plg-rich mineralogy is shown (Fig. 1.c) with their corresponding MGM deconvolution results (see Figs. 1.d-g). This highlights the complexity in handling the composite absorption between 1.05-1.25 μm when considering ol-plg mixtures [13, 14].

Interpretation: The present results touch on the complexity of impact melt-related processes and complement findings from [3,4,5,15] concerning olivine-bearing exposures found in the central peaks, north wall and scattered blocks on the crater floor. Based on Mg#, the ol composition is Fo₇₀₋₉₀. Two central peaks (Pk2 and Pk3) appear more homogeneous than the westernmost one. Both in the north wall and on the peaks, plg-bearing exposures are found, some in association with ol mineral, possibly rejuvenating the idea of a troctolitic horizon at shallow depths [16,17]. Plg-bearing exposures are also

found scattered across the northeastern floor, the inner and outer parts of the northeastern rim. Detailed morphological investigation at high spatial resolution based on LROC data is underway [15, 18].

References: [1] Ohtake, M. et al. (2009), *Nature*, 461, 236-240 ; Pieters, C.M. et al. (2009), *Curr. Sci.*, 96 (4), 500-505. [2] Donaldson Hanna et al. (2014), *JGR*, 119, doi: 10.1002 /2013JE004476. [3] Isaacson P.J. (2011) *JGR*, 116, doi:10.1029/2010JE003731. [4] Dhingra, D. et al. (2013), *GRL*, 40, 1043-1048. [5] Dhingra, D. et al. (2015), *EPSL*, 420, 95-101. [6] Cheek, L. C. and C.M. Pieters (2014), *Am. Mineral.*, 99, 1871-1892. [7] Sunshine J.M. et al. (1990), *JGR*, 95, B5, 6955-6966. [8] Sunshine, J. and Pieters, C(1993), *JGR*, 98(E5), 9075-9087; Sunshine J. M. and C. M. Pieters (1998), *JGR*, 103, 13,675–

13,688. [9] Noble, S.K. et al. (2006), *JGR*, 111, E1 1009 ; Pompilio, L. et al. (2007), *JGR*, 112, E01004 ; Pinet, P.C. et al.(2007), *Mars Conf. 7th*, #3146. [10] Clenet, H. et al. (2011), *Icarus* 213, 404-422 ; Clenet, H. et al. (2013), *JGR*, 118, doi:10.1002/Jgre.20112. [11] Serventi, G. et al. (2016), *Icarus*, 272, 1-15. [12] Carli, C. et al (2014), *Am. Mineral.*, 99, pp. 1834-1848. [13] Pinet, P.C. et al. (2016), *Whispers 8th Conf.*, 1-4. [14] Serventi, G. and C. Carli (2017), *Icarus*, 293, 157-171. [15] Chevrel, S.D. et al. (2017), *LPSC 48th*, #1907. [16] Pieters, C.M. (1982), *Science*, 215, 59-61 ; Pieters, C.M. and D.E. Wilhelms (1985), *PLPS 15th, Part2*, *JGR*, C415-420. [17] Pinet, P.C. et al. (1993), *Science*, 260, 797-801. [18] Chevrel et al (2018), this issue, *ELS 6th*.



VOLATILE EXTRACTION AND DETECTION FROM FROZEN LUNAR REGOLITH SIMULANTS IN PREPARATION FOR THE LUVMI ROVER. C. Pitcher¹, S. Sheridan¹, S. Barber¹, D. Urbina², J. Gan-
cet², K. Kullack², E. Ceglia², H. Madakashira², J. Salinia², S. Govindaraj², L. Surdo², R. Aked², J. Biswas³, P.
Reiss³, L. Richter⁴, D. Dobrea⁴, M. Reganaz⁴, Neil Murray⁵, J. Rushton⁵ and A. Evagora⁵, ¹The Open University,
Milton Keynes, MK7 6AA, UK (craig.pitcher@open.ac.uk), ²Space Applications Services NV/SA Leu-
vensesteenweg 325, B-1932 Zaventem, Belgium, ³Institute of Astronautics, Technical University of Munich,
Boltzmannstr. 15, 85748 Garching, Germany, ⁴OHB System AG, Manfred-Fuchs-Str. 1, 82234 Weßling, Ger-
many, ⁵Dynamic Imaging Analytics Ltd, Milton Keynes, MK3 6EB, UK

Introduction: The Lunar Volatiles Mobile In-
strumentation (LUVMI) is a novel lightweight plat-
form designed for operations at the lunar South Pole.
Conducted under the EU Horizon 2020 programme
and following recommendations by the Lunar Explo-
ration Analysis Group, it is envisioned as a second-
ary payload for currently planned lunar landing mis-
sions. Comprised of the Volatiles Sampler (VS),
Volatiles Analyser (VA) and surface and sub-surface
imaging instruments upon a mobile platform,
LUVMI will prospect and extract volatiles from
permanently shadowed regions up to a depth of at
least 10cm [1].

Presented here is the work performed by the
Open University (OU) in the support of the devel-
opment of the VA, a miniature ion trap mass spec-
trometer, and the tests performed that have examined
the release and detection of volatiles embedded in
frozen lunar regolith simulants.

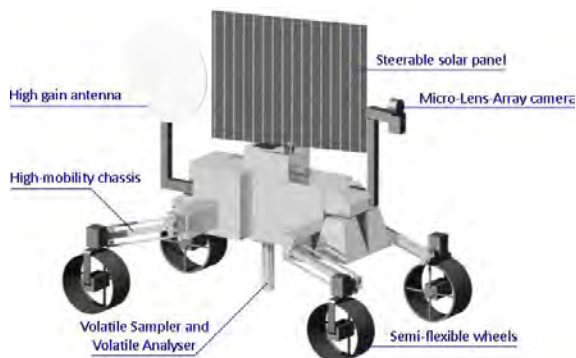


Figure 1 Model of the LUVMI rover

Extraction of Volatiles: In its final flight con-
figuration the VS will combine a hollow rotating drill
shell and heating rod to penetrate at least 10cm into
the regolith, with a goal of 20cm [2]. The heating rod
will heat the enclosed regolith to release the bound
volatiles. It is anticipated that around 50% of these
volatiles will pass through into the VA. The two in-
struments will be used together to characterise the
volatile profile of the near-surface material and pro-
vide a volatile profile with increasing depth.

Volatiles Analyser: The VA is an ion trap mass
spectrometer based upon the Ptolemy flight-proven
instrument and the MoonLite penetrator deployable
instrument. This is a low mass, compact and mechan-
ically simple device capable of rapid detection of

masses in the range of 10 – 150 m/z , enabling the
detection of volatiles, including water, that may be
released during regolith heating.

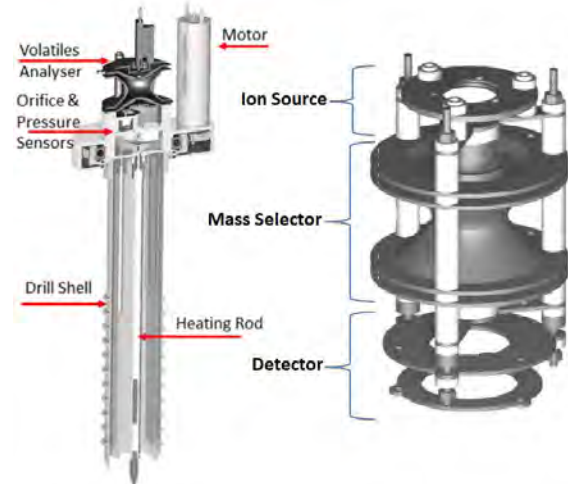


Figure 2 CAD models of the VA-VS system and the Ptolemy mass spectrometer

The VA consists of:

- An ion source, made up of an electron source that ionises the sample gases via electron bombardment
- A mass selector, formed from three hyperbolic electrodes, which create an electro potential region within the structure. Ions can be trapped or ejected by manipulating the amplitude and/or frequency of this potential
- A detector, made up of an electron multiplier that detects the individual ions leaving the mass selector
- A reference gas system developed by the OU for in-situ calibration and soil permeability measurements [3]

LUVMI Environmental test system: A thermal vacuum system for handling lunar simulant materials under representative conditions has been designed and built at the Open University. A schematic of the system is shown in Figure 3.

The sample material is contained within a liquid nitrogen cooled copper container, shown in Figure 4. The regolith temperature is monitored via embedded thermocouples and the container's temperature is managed by a Eurotherm temperature controller that opens and closes the liquid nitrogen control valve.



Figure 3 Thermal vacuum system



Figure 4 NU-LHT-2M sample held in the insulated copper container

Volatile Preservation Study: For these tests, 200g of NU-LHT-2M was used as the simulant material. This is a fine-grained (<1mm to dust) material designed to mimic the highlands regolith found at the lunar south pole, based upon core samples taken from Apollo 16 [4].

The system was initially used to evaluate the conditions similar to those seen by the LCROSS mission, where water contents of $5.6 \pm 2.6\%$ were observed in the ejecta plume created from an impactor striking the South Pole crater Cabeus [5]. A series of regolith samples were mixed with 2, 10 and 20 ml of water, giving 1%, 4.8% and 9.1% water mass contents respectively.

The doped regolith was held inside the system and cooled to -150°C in a dry nitrogen atmosphere to prevent atmospheric water being trapped in the cooling regolith. The system was then evacuated to a pressure of approximately 2×10^{-5} mbar. The sample was left under these conditions for varying lengths of time (1, 2 and 3 hours), before being brought back to atmospheric pressure. Analysis of the sample masses revealed that, when stored at temperatures below 150°C , minimal water vapour was lost (a maximum of 0.55% water mass for the 9.1% sample).

Volatile Extraction Study: Next, investigations into the ability to thermally evolve volatiles from the

frozen lunar simulant were conducted. A custom-built temperature-controlled thermal probe was designed, shown in Figure 5. Thermal control of the probe was achieved through the use of a Eurotherm temperature controller. To mimic the operation of the VA, a Hiden Analytical Halo 201 RC quadrupole mass spectrometer was used to monitor the environment within the vacuum chamber. The study was repeated with identical 200 g samples that were prepared with 2, 10 and 20 ml of water, giving 1%, 4.8% and 9.1% water mass contents respectively. The same procedure was followed as detailed previously, though the chamber was evacuated to a vacuum in the order of 10^{-7} mbar to allow operation of the quadrupole mass spectrometer. A series of background spectra measurements were taken before the heater probe was switched on, to account for outgassing of the probe as it was heated. Once it reached a target temperature of 150°C , it was lowered and embedded to a depth of approximately 45 mm into the sample. The change in spectra readings were observed, focusing on the m/z 18 peak as an indicator for the presence of water. The probe was then extracted from the sample, and the quadrupole continued taking measurements for a set time. The results of these tests will be presented.

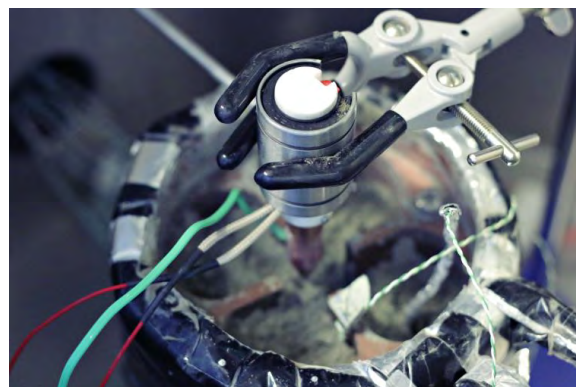


Figure 5 Heater probe set-up

Future Work: The system will be used for characterisation of the breadboard VA system prior to integration with the VS in the coming months.

Summary: The Volatiles Analyser, an ion trap mass spectrometer for the LUVMI lunar rover, is being developed by the Open University. Studies have focused on the preservation of volatiles held within a lunar regolith simulant, and the extraction and detection of said volatiles with a thermal probe.

Acknowledgments: This project is co-funded by the Horizon 2020 Framework Programme of the European Union, grant agreement 727220.

References: [1] Gancet J. et al. (2017) *ASTRA 2017*. [2] Biswas J. et al. (2017) *ELS V*. [3] Urbina D. A. et al. (2017) *IAC LXVIII* [4] Stoesser D. et al. (2010) *NASA Tech. Mem. 2010-216438*. [5] Colaprete A. et al. (2010) *Science*, 330, 463-467.

IMPACT OF MINERAL-SCALE ISOTOPIC HETEROGENEITY ON IRON ISOTOPE COMPOSITION ESTIMATES OF LUNAR IGNEOUS RESERVOIRS.

F. Poitrasson¹, T. Zambardi¹, T. Magna², C. R. Neal³, ¹GET-CNRS, 14, avenue E. Belin, 31400, Toulouse, France, ² Czech Geological Survey, Klarov 3, CZ-11821 Prague 1, Czech Republic, ³Department of Earth Sciences, 156 Fitzpatrick Hall, University Notre Dame, IN 46556, USA.

Introduction: It has always been difficult to estimate the bulk chemical and isotopic composition of the various lunar igneous reservoirs because of severe limitations in our sampling and the key absence of true lunar mantle samples. Compared to the Earth, our geographic sampling is limited to the Apollo and Luna landing sites, as well as lunar meteorites of undefined provenance. Another frequently underestimated limitation relates to the sample size available for geochemical analysis. Too small sample aliquots may turn out to be unrepresentative of coarse-grained rocks, such as anorthosites although (un)representativeness resulting from sub-optimal sample sizes has also been reported for mare basalts [1]. This is a well known issue for elements present at the ultra-trace levels such as platinum group elements (PGE) [2], but it has recently been pointed out that this can also be a problem for the currently explored field of non-traditional stable isotopes. The case for silicon stable isotope compositions has already been reported [3] and we discuss here the situation for Fe isotopes.

There is also a debate on the bulk Fe isotope composition of the Moon. Some consider $\delta^{57}\text{Fe}$ of the bulk Moon twice as high as that reported for the Earth [4], whereas others suggest irresolvable $\delta^{57}\text{Fe}$ between the Earth and Moon [5, 6]. It has even been advocated that the Earth and the Moon are lighter than previously thought, with an iron isotope composition indistinguishable relative to chondrites [7-9]. These different interpretations have obviously a severe impact on the constraints on the lunar accretion modes and/or differentiation processes where Fe isotopes may provide some important limitations.

Hence, a proper mass balance estimation of key lunar reservoirs is required. For instance, the dichotomy in $\delta^{57}\text{Fe}$ between low- and high-Ti mare basalt varieties as a consequence of differences in degree of fractional crystallization of their respective lunar mantle sources should be rigorously tested.

Results and discussion: To investigate this topic, we determined iron isotope compositions in 33 bulk lunar mare basalts and highland rocks, including KREEP-rich materials. The new data reinforce a significant Fe isotope dichotomy between high-Ti and low-Ti mare basalts, yielding mean $\delta^{57}\text{Fe}_{\text{IRMM-014}}=0.277\pm0.020\text{‰}$ and $0.127\pm0.020\text{‰}$, respectively. Assuming that lunar basalts mirror the Fe isotope composition of their respective mantle protoliths, the estimated relative proportion of the low-Ti and high-Ti mantle source suggests that the lunar upper man-

tle should be close to $\delta^{57}\text{Fe}=0.14\pm0.03\text{‰}$, in agreement with a previous estimate from Liu et al. [5]. However, it is still unclear whether the bulk lunar Fe isotope composition is indistinguishable from that of the Earth ($\delta^{57}\text{Fe}_{\text{IRMM-014}}=0.10\pm0.03\text{‰}$), when estimated solely from mare basalt data, or if it is twice as heavy relative to chondrites, as initially proposed.

Highland rocks could provide a more direct estimate of $\delta^{57}\text{Fe}$ value of the bulk Moon. However, a large scatter of the new and published data at $\delta^{57}\text{Fe}=0.08\pm0.19\text{‰}$ found for Ferroan Anorthosites (FANs), Mg-suite rocks and a KREEP basalt imparts more complexities for the global Fe isotope view of the Moon. This large scatter is stressed by the observation that different aliquot allocations of some highland rocks yield significantly different $\delta^{57}\text{Fe}$ values despite the general consistency of Fe isotope determinations performed on terrestrial silicate rock reference materials from different laboratories [10, 11].

This is likely the result of the coarse-grained nature of most highland rocks that may contain mineral phases with potentially different Fe isotope systematics, including impactor signatures as all FANs are highly brecciated. This work highlights the risk of estimating bulk planetary compositions from a handful of rocks sampled at ‘subliminal’ aliquot size (50 mg in [6]), or even on the basis of a single rock [9]. Given the limited sample size available, it is only through in situ determination of $\delta^{57}\text{Fe}$ in diverse mineral phases of highland samples that will make it possible to provide more robust estimates of the bulk rock Fe isotope composition of coarser lithologies. From there, a more reliable assessment of the Fe isotope composition of lunar highland rocks will likely be provided. This will plausibly lead to a better estimate of the Fe isotope composition of the bulk Moon, and possibly improve our knowledge about the genesis of the lunar crust itself.

References: [1] Ryder, G. and B.C. Schuraytz (2001). *Journal of Geophysical Research-Planets*, 106(E1), 1435-1451. [2] Day, J.M.D. and R.J. Walker (2015). *Earth and Planetary Science Letters*, 423, 114-124. [3] Poitrasson, F. and T. Zambardi (2015). *Geochimica et Cosmochimica Acta*, 167, 301-312. [4] Poitrasson, F., et al., (2004). *Earth and Planetary Science Letters*, 223, 253-266. [5] Liu, Y., et al., 2010) *Geochimica Et Cosmochimica Acta*, 74, 6249-6262. [6] Sossi, P.A. and F. Moynier (2017). *Earth and Planetary Science Letters*, 471, 125-135.

[7] Elardo, S.M. and A. Shahar (2017) *Nature Geoscience*, 10, 317-321. [8] Huang, S., et al. (2016) *Goldschmidt Conference*, Yokohama, Japan. p. 1196. [9] Wang, K., et al. (2015) *Earth and Planetary Science Letters*, 430, 202-208. [10] Craddock, P.R. and N. Dauphas (2011) *Geostandards and Geoanalytical Research*, 35, 101-123. [11] Poitrasson, F. (2006). *Chemical Geology*, 235: 195-200.

MICROWAVE HEATING OF LUNAR SIMULANTS JSC-1A AND NU-LHT-3M: EXPERIMENTAL AND THEORETICAL ANALYSIS

V. L. Prabhu¹ (vibha.levinprabhu@open.ac.uk), S. Lim¹, J. Bowen², A. Cowley³, J. Katrib⁴, C. Dodds⁴ and M. Anand^{1,4}

¹School of Physical Sciences, The Open University, UK, ²School of Engineering & Innovation, The Open University, UK, ³European Space Agency, European Astronaut Centre, Linder Höhe, Cologne, Germany, ⁴Faculty of Engineering, University of Nottingham, UK, ⁴Department of Earth Sciences, The Natural History Museum, London, UK.

Introduction: The future of sustained human space exploration is likely to rely on the use of local resources on the respective planetary bodies. The continuing exploration of the Moon via orbiter, lander and sample return makes it the next logical destination for setting up human outposts, laboratories, and observatories. Its proximity to Earth also makes it an ideal first destination before we explore further out in the Solar System. Lunar soil is a potential construction resource which can be melted or sintered for building structures [1].

To process the lunar soil, some form of compact, lightweight, electrically powered heat source is required and for this work microwave energy has been selected as it fulfils these criteria well. This research focusses on understanding the interaction of microwave energy with lunar soil. The heat-treated soil can then be fed into a 3D printing apparatus, enabling robotic missions to build structures on the Moon [2]. Lunar soil simulants JSC-1A (lunar mare soil simulant) and NU-LHT-3M (lunar highlands soil simulant) have been used for the experiments in this research. Lunar soil [3] is abundant in silicate minerals and glasses with traces of some other minerals. JSC-1A [4] and NU-LHT-3M [5] also has silicates, glass and other minerals. Previous research has shown that lunar soils and lunar soil simulants (LSS) melt during sustained exposure to microwave radiation at a frequency of 2.45 GHz [1, 6]. The melting of lunar soil under microwave heating is commonly attributed to the presence of nano phase Fe⁰ (np-Fe⁰) [1, 7-9]. However, JSC-1A being a terrestrially manufactured lunar soil simulant, does not contain np-Fe⁰; however, it melts under microwave heating [6].

Experimental microwave heating: A preliminary set of experiments were undertaken to assess the feasibility of heating LSS via microwaves. JSC-1A and NU-LHT-3M were exposed to 2.45 GHz incident radiation at 1kW power in a domestic microwave. Experiments began at ambient atmospheric pressure and temperature. An infra-red camera was used to monitor the temperature changes inside the cavity. The camera was adjusted to point to the sample under heating through the microwave door. It is estimated that 95% of radiation will transmit through the glass of the microwave door; the metallic mesh limits the transmission to approximately 30% on an area basis. Studies revealed that melting of different masses, different densities, and different particle

sizes of JSC-1A consistently occurred within approximately 10-17 minutes. Time-temperature profiles are generated for each of the tests and melted/sintered specimens thus obtained are characterized for their physical and chemical properties.

The experimental results provide information regarding the behaviour of LSS under microwave heating in ambient conditions, which includes the effect of heat losses by conduction and convection.

Theoretical analysis of microwave heating:

The complex permittivity of a material dictates its absorption behaviour in the presence of an incident microwave radiation at a given frequency. The permittivity of the multicomponent particulate mixture varies with mineral content, temperature, packing density, particle size, and moisture content [10]. The complex permittivity is defined as $\epsilon^* = \epsilon' - j\epsilon''$, where, ϵ^* is the complex permittivity, ϵ' is the dielectric constant, and ϵ'' is the dielectric loss [11, 12].

The complex permittivities of JSC-1A and NU-LHT-3M were assessed at microwave frequencies of 910, 1429, 1949, 2470 and 2989 MHz. Samples were heated at 20 °C and from 50 °C to 950 °C at a step temperature of 50 °C using a cavity perturbation apparatus housed adjacent to a furnace. The cavity perturbation technique allows measurement of powder samples and requires only small quantities of material [11]. The frequencies at which complex permittivity values are measured are close to the ISM (Industrial, Scientific and Medical) frequencies of 896 MHz and 2.45 GHz and are dictated by the dimensions of the cavity.

The tendency of a material to absorb microwave radiation can be estimated via three parameters: power density, power penetration depth, and temperature, all of which depend on the dielectric constant and dielectric loss. [1, 12]. Power density is the power deposited per unit volume into a material by the microwave energy [1]. Power penetration depth is defined as the depth into material at which the power has fallen to 1/e (= 0.368) of its value at the surface [12]. A theoretical model describing the time/temperature relationship under vacuum conditions has been established.

Discussion: The specimens from the experiments in ambient atmospheric condition have resulted in a molten core with sintered/partially melted layer surrounding it. This observation indicates the specimens have undergone uneven heating.

The experimental heating and the theoretical model are critically compared. We discuss the differences between performing these tests in the presence and absence of a gas phase, specifically the importance of heat loss from the sample via conduction and convection.

The preliminary finding of complex permittivity values of JSC-1A and NU-LHT-3M are shown in Figure 1 and Figure 2. The permittivity values increase with the increase in temperature for both the simulants. These are higher for lunar mare simulant than for lunar highland simulant at the given microwave frequencies. For JSC-1A (Figure 1), with the increase in frequency, dielectric constant increases up to a temperature of 600 °C. Beyond this temperature, there is significant deviation in the trend and the values corresponding to lower frequencies are higher than those corresponding to higher frequencies. The dielectric loss values of JSC-1A (Figure 1) are closer at all frequencies in the lower temperature range. Beyond 400 °C, the values continue to increase with temperature at all frequencies; however, the values are lower for higher frequencies. A sudden increase in the values of dielectric loss can be observed at all the frequencies beyond 800 °C. Ray et al. [13] have reported an endothermic peak corresponding to glass transition temperature at about 670 °C and an exothermic peak corresponding to crystallization temperature at about 880 °C for JSC-1A. These changes in the permittivity values may be attributed to the changes due to glass transition and crystallization temperatures in JSC-1A. Figure 2 shows that in NU-LHT-3M, with the increase in frequencies, the dielectric constant increases with temperature. The plot at 910 MHz does show abruptly higher values beyond 700 °C. The dielectric loss of NU-LHT-3M (Figure 2) shows the increasing value with temperature, while it shows the decreasing value with increase in frequencies. For now, there is no thermal profile obtained for NU-LHT-3M to compare the phase transformations associated with changing temperature regime. However, these values give valuable information regarding the simulant's behaviour to the microwave frequencies. Further tests will be carried out to confirm the results from this preliminary finding.

Such comparison of the microwave heating behaviour of different lunar simulants clearly suggests the challenges posed by microwave absorption characteristics of lunar soil from different locations on the surface of Moon.

As the mineral content plays a key role in determining the microwave absorption properties of a heterogeneous material, future work will assess the

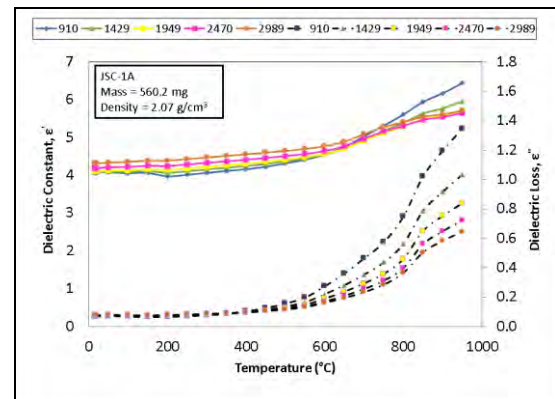


Figure 1: Dielectric constant and dielectric loss of JSC-1A.

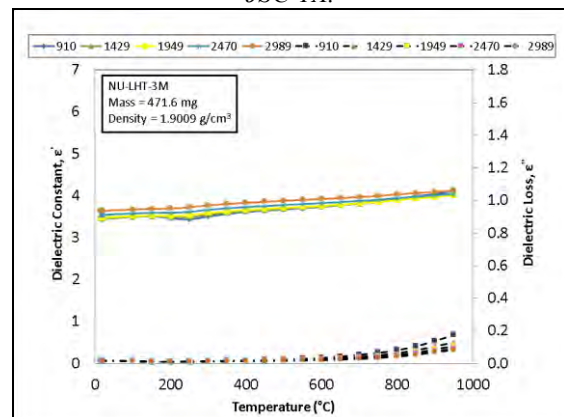


Figure 2: Dielectric constant and dielectric loss of NU-LHT-3M.

permittivity of the major mineral constituents of JSC-1A. It will highlight the major microwave absorbing phases in JSC-1A, providing information regarding why JSC-1A melts in the absence of np-Fe⁰.

References:

- [1] Taylor L. A. and Meek T. T. (2005) JAE, 18, 188-196.
- [2] Lim S., Prabhu V. L., Anand M. and Taylor L. (2017) ASR, 60, 1413-1429.
- [3] Heiken G., Vaniman D. and French B. M. (1991) CUP Archive.
- [4] JSC-1A Material safety data sheet (2005).
- [5] NU-LHT-3M Material Safety Data Sheet (2013).
- [6] Allan S. M., Merritt B. J., Griffin B. F., Hintze P. E. and Shulman H. S. (2013) JAE, 26, 874-881.
- [7] Ethridge E. C. and Kaukler W. (2009) 47th AIAA ASM.
- [8] Taylor L. A., Schmitt H. H., Carrier W. D. and Nakagawa M. (2005) 1st Space Exploration Conference: Continuing the Voyage of Discovery AIAA, 184.
- [9] Liu Y., Taylor L. A., Thompson J. R., Schnare D. W. and Park J-S. (2007) American Mineralogist, 92, 1420-1427.
- [10] Calla O. P. N. and Rathore I. S. (2012) ASR, 50, 1607-1614.
- [11] Katrib J., Folorunso O., Dodds C., Dimitrakakis G. and Kingman S. W. (2015) JMS, 50, 7591-7599.
- [12] Metaxas A. C. and Meredith R. J. (1983) IET.
- [13] Ray C. S., Reis S. T., Sen S. and O'Dell J. S. (2010) JNCS, 356, 2369-2374.

TERRACE WIDTH VARIATIONS IN FRESH LUNAR CRATERS. S. Ravi¹, P. Mahanti¹, and M.S. Robinson¹, ¹School of Earth and Space Exploration, Arizona State University, Tempe, AZ 85281, USA (sravi@ser.asu.edu)

Introduction: Lunar impact craters morphologically transition from simple to complex at diameter above ~17 km [1]. Complex craters are characterized by the presence of flat floors, central peaks, and terraces that descend from the rim along the crater wall [1]. Crater terraces have long been regarded to be a product of slumping induced by gravity when the cohesive strength of the target material is exceeded [1-4]. Hence, scaling terrace dimensions is essential to understanding complex crater formation and modification processes [5].

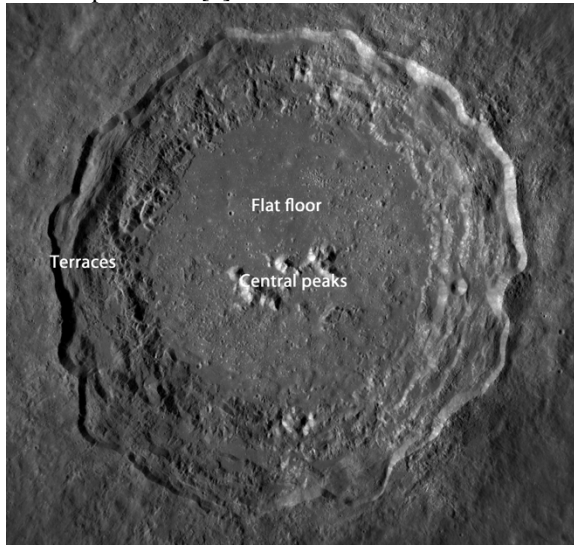


Figure 1: Copernicus (D = 93 km), a complex crater that exhibits terraces, flat floor, and central peaks (From: LROC WAC monochrome mosaic [6])

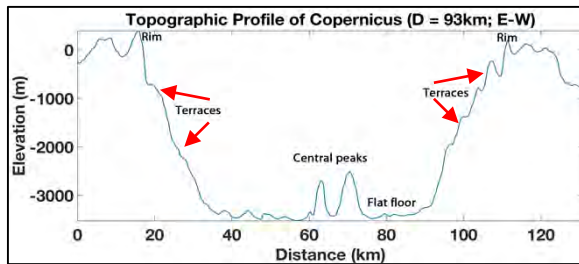


Figure 2: Topographic profile of Copernicus crater, showing the morphological characteristics of a fresh, complex crater

Pearce and Melosh [5] measured the widths of terraces closest to the crater rim of 35 fresh craters (25 km < D < 197 km) obtained from Apollo and Lunar Orbiter images and quantified the relationship between terrace width (W) and crater diameter (D) as:

$$W = 0.09D^{0.87}$$

With the availability of high-resolution images from the Lunar Reconnaissance Orbiter Camera (LROC), we present the relationship between widths of terraces of morphologically fresh complex lunar

craters (20 km < D < 90 km, 101 craters) and the diameter of the parent crater.

Methods: From our catalog of Copernican and Eratosthenian craters (D > 10 km; N ~ 2100; 6), we characterized 101 craters (N_{Copernican} = 18 and N_{Eratosthenian} = 83; 20 km < D < 90 km; 6). Terrace widths were measured from 6 topographic profiles (total number of measurements = 12; Figure 2) of each crater from LROC WAC GLD100 [7]. The median terrace width was considered for further analysis.

Results: Our complex crater dataset was divided into 2 categories – central peak craters (CP; N = 63) and craters that exhibited only terraces (T; N = 38) in order to examine the relationship, if any, between the morphological complexity of the crater and the width of the terraces (W) both as a linear (Figure 3) and as a power law regression (on a logarithmic scale) to compare with Pearce and Melosh [5] (Fig.4). The following relationships were obtained:

Linear regression:

Central peak craters (N = 63): $W = 0.01D + 0.96$

Terraced craters (N = 38): $W = 0.005D + 1.24$

All craters (N = 101): $W = 0.01D + 1.04$

Power law regression:

Central peak craters (N = 63): $W = 0.45D^{0.30}$

Terraced craters (N = 38): $W = 0.72D^{0.19}$

All craters (N = 101): $W = 0.58D^{0.24}$

Additionally, we examined if the relative age of the crater (i.e., Copernican vs. Eratosthenian) influenced terrace widths (Fig. 5).

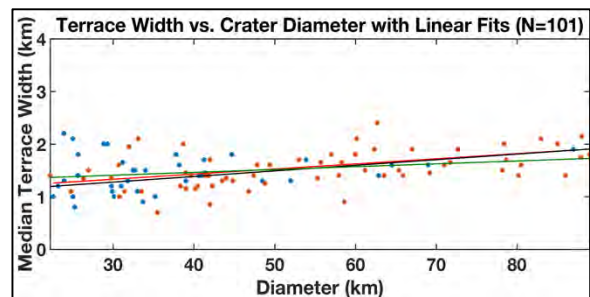


Figure 3: Median W vs. D as a linear regression. T and CP craters are shown in blue and red respectively. The red, black, and green linear fits correspond to all craters in the dataset (N = 101), central peak craters (N = 63), and terraced craters (N = 38) respectively).

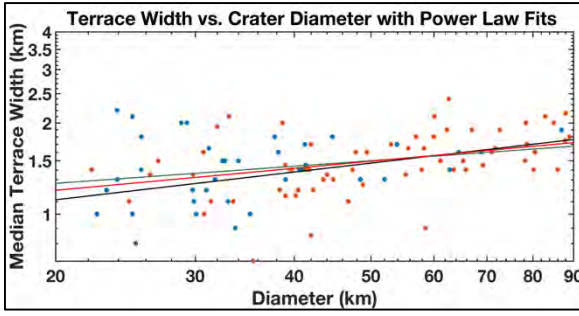


Figure 4: Median W vs. D as a power law function. T and CP craters are shown in blue and red respectively. The red, black, and green power law fits correspond to all craters in the dataset ($N = 101$), central peak craters ($N = 63$), and terraced craters ($N = 38$) respectively).

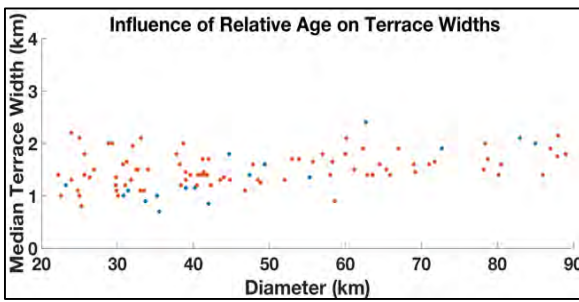


Figure 5: Influence of relative crater age on terrace widths of complex craters. Copernican and Eratosthenian craters are shown in blue and red respectively.

Discussion: We expected a positive correlation between terrace width, crater diameter, and morphology, which are proportional to the energy of impact [8]. However, the morphological complexity of craters (i.e. central peak craters vs. craters that exhibit only terraces) has no significant influence on the terrace widths (Figure. 3 and 4) measured in our work.

There is no obvious correlation between terrace widths and crater diameter when examined as a linear regression and no correlation when examined using a power law function (R -squared value = 0.2 and 0.04 respectively). However, when the dataset is limited to craters of diameter, $D \geq 60\text{km}$, we observe a significant relationship (R -squared value = 0.8) between terrace widths and crater diameter. We also do not observe any effect of relative crater ages (Copernican vs. Eratosthenian) on the terrace widths.

Conclusion: A positive correlation between terrace widths and crater diameter can be observed only when $D \geq 60\text{km}$ and/or the crater population is small ($N \sim 30 - 35$), which can also be observed in Pearce & Melosh's study [5]. This trend could be the result of larger craters excavating through to the megaregolith layer due to higher energy impacts compared to smaller craters, thereby increasing the width of terraces (as the megaregolith has a greater cohesive

strength than the regolith). In order to fully understand this trend, we will expand our study by increasing the number of craters with $D \geq 60\text{km}$ by including relatively older craters (Imbrian age) for our future work.

References: [1] Pike, R.J. (1974), *Geophys. Res. Lett.*, 291-294. [2] Quaide, W.L. et al. (1965), *Ann. N.Y. Acad. Sci.* 563-572. [3] Melosh, H.J. (1977), *Impact and Erosion Cratering*, 1245-1260. [4] Settle, M., and Head, J.W. *JGR*, 3081-3096. [5] Pearce, S.J., and Melosh, H.J. (1986), *Geophys. Res. Lett.*, 1419 – 1422. [6] Ravi et al. (2016), *AGU Fall Meeting*, #190021. [7] Scholten, F. et al. (2012), *JGR* 117, E00H17. [8] Walsh, A.M. et al. (2003), *PRL* 91, 104301.

DEMONSTRATION OF VOLATILES EXTRACTION FROM NU-LHT-2M WITH THE PROSPA INSTRUMENT BREADBOARD. P. Reiss¹, L. Grill¹, and S. Barber², ¹Institute of Astronautics, Technical University of Munich, Boltzmannstr. 15, 85748 Garching, Germany, (p.reiss@tum.de), ²The Open University, Milton Keynes, MK7 6AA, UK.

Introduction: The European Space Agency (ESA) currently develops the Package for Resource Observation and in-Situ Prospecting for Exploration, Commercial exploitation and Transportation (PROSPECT) as a payload contribution to the planned Russian Luna-27 mission to the lunar polar regions. The package contains the sample analysis instrument ProSPA (PROSPECT Sample Processing and Analysis) to investigate volatile compounds that are extracted by heating regolith samples delivered by a drill [1-4]. In support of the instrument development, the Institute of Astronautics at Technical University of Munich (TUM) has established a breadboard to study the extraction of volatiles from hydrated lunar regolith analogues in a Moon-like environment [5]. This abstract describes the results from a test campaign that was dedicated to the Volatiles Extraction Demonstration (VED) mode of ProSPA.

Breadboard: The ProSPA laboratory breadboard at TUM consists of a sample conditioning system and a volatiles extraction system briefly described in the following, based on [6].

Sample conditioning system. The preparation of lunar regolith simulants for VED is done in a stainless steel glovebox with purge gas feed, humidification/dehumidification system, and an attached vacuum airlock with a separate heater setup for sample bake-out. The glovebox has an internal volume of $\sim 0.8 \text{ m}^3$ and automatically maintains an overpressure to avoid inward leakage from the laboratory atmosphere. The humidification/dehumidification system uses dry nitrogen as a purge gas, fed either directly into the glovebox for dehumidification or through a bubbler with distilled water before entering the glovebox for humidification. Temperature as well as relative humidity and dew point are recorded by a sensor. A precision balance is installed in the glovebox for sample weighing. The airlock is equipped with a pressure gauge, evacuation line, and a feedthrough for thermocouple and power supply to power a heater for sample bake-out.

Volatiles extraction system. The experimental setup for the thermal extraction of volatiles from the sample consists of an instrumented vacuum system with two sections (Figure 1). The lower part of the system can be evacuated to 10^{-5} mbar, and includes the sample holder, a purge gas feed, a Penningvac (Leybold PTR 90) pressure gauge, and a cooling/heating system that is applied externally to the sample holder. The upper part can be evacuated to 10^{-8} mbar, and contains a quadrupole mass

spectrometer (Stanford Research Systems RGA 200) and a second Penningvac pressure gauge. Both sections are connected via a manual dosing valve, which acts as an orifice to restrict the mass flow so that the RGA filament can be operated below its maximum gas pressure of 10^{-4} mbar. The entire system is evacuated using a turbomolecular pump and an oil-free scroll pump. The vacuum system is heated to 120°C using heating wires wrapped around the tubes to enable a full bake-out and avoid condensation of the released water during operation. The sample holder is a modified stainless steel blind fitting to accommodate a sample that is 2.8 mm in diameter and 4.5 mm in height, according to the ProSPA baseline sample size.

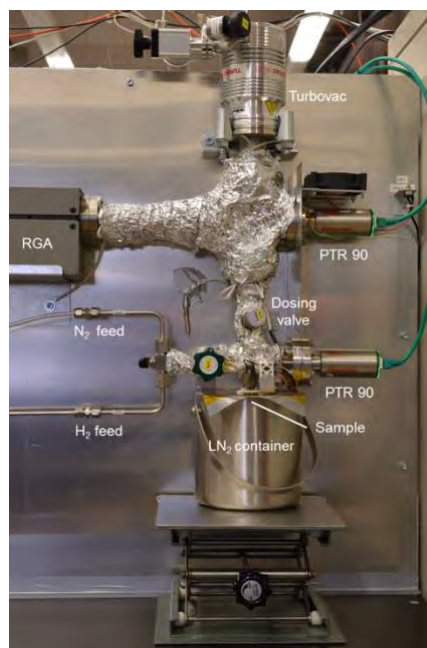


Figure 1: Detail view of the VED breadboard [6]

Procedure. Several grams of the lunar highland type regolith simulant NU-LHT-2M were placed inside the glovebox airlock and baked-out at $100\text{--}200^\circ\text{C}$ for 2 h in a medium vacuum ($\sim 10^{-1}$ mbar). The sample was then stored in the glovebox for at least 48 h to adsorb water from the humidified glovebox atmosphere. After that, a subsample of 33-36 mg (results in the ProSPA baseline sample size) was packed into the sample holder and transferred to the volatiles extraction system. After installation of the sample holder, it was cooled to -196°C using a liquid nitrogen bath. The lower section of the vacuum system was then evacuated until the sample section reached values below 10^{-5} mbar. At this time the

sample heating was started with a controlled ramp of 6 °C/min from -150 °C to 800 °C. The evolved volatiles were constantly measured with the RGA, either by repeated analogue scans of m/z 1-50 or by tracking the partial pressures of selected species. Different sample conditions and test parameters were evaluated, as described in Table 1.

Table 1: Parameters varied for the VED tests

Parameter	Value
Relative humidity for sample conditioning	1 %, 10 %, 30 %, 50 %, 70 %, saturated
Sample mass	33-36 mg, 66-72 mg, 0 mg
Particle size	70-80 μm , 100-110 μm , none
Bulk density	loose ($\sim 1.3 \text{ g/cm}^3$), compacted ($\sim 2.0 \text{ g/cm}^3$), none
Heating rate	6 °C/min, 4 °C/min

Test Results: The following describes a brief summary of the key findings from the experiments, discussed in more detail in [6]. Figure 2 shows an exemplary outgassing profile for a 33-36 mg, 70-80 μm , loose sample, conditioned at 30 % relative humidity, and heated at a rate of 6 °C/min. The outgassing of volatiles from the sample can be divided into three distinct phases, as highlighted in Figure 2:

- (1) Initial outgassing of the sample holder surface at temperatures below -50 °C (peak 'A'),
- (2) Outgassing of volatile species from the sample between -50 °C and 300 °C (peak 'B'), and
- (3) Release of mineral-bound volatiles through decomposition above 300 °C (peak 'C').

The predominant species in the gas mixture is water (m/z 18). Hydrogen (m/z 2) is present as a residual gas from the atmosphere, carbon dioxide (m/z 44) and nitrogen or carbon monoxide (m/z 28) are mainly released at higher temperatures in the third temperature phase. Fragmentation through the RGA and the present mixture of gases however means that not all of the existing species can uniquely be identified. The release of m/z 44 and 28 is due to the decomposition of carbon-bearing minerals in NU-LHT-2M, most likely calcite (CaCO_3), above 650 °C. The signal of m/z 32 is attributed to sulphur-

bearing species that are released at 550 °C, most likely due to the decomposition of pyrite (FeS_2).

The effect of different humidity levels during the storage of the samples was visible at low relative humidity between 1 % and 10 %. Above that no further increase in the partial pressure of water was detected. The smaller particle fraction as well as the larger sample mass and the higher heating rate produced a generally higher amplitude in the partial pressures. The latter was also predicted by computer simulations of the heat and mass transfer in the sample and is further explained in [7].

Lessons Learned for ProSPA: The feasibility of VED was demonstrated with an instrument-like setup under relevant ambient conditions. It was found that:

- (1) A sufficient (measurable) amount of volatiles can be released from the sample,
- (2) Volatiles reliably arrive at the gas analysis instrument,
- (3) Reproducible outgassing profiles can be created,
- (4) Qualitative differences can be seen for different sample conditions.
- (5) Mineral decomposition is detected at temperatures above 300 °C.

Furthermore, it was found that NU-LHT-2M contains a noticeable amount of carbonates, which needs to be considered when comparing the results to real lunar regolith that most likely contains no carbonates. NU-LHT-2M also releases sulphur from pyrite, while in the case of lunar regolith a possible source of sulphur would be troilite (FeS). As a basis for future studies on VED with ProSPA, reference outgassing profiles were recorded for different combinations of boundary conditions and sample preparation methods, which can be used for interpretation of future measurements.

References: [1] Barber S. J. et al. (2017) *ELS*. [2] Barber S. J. et al. (2017) *LPSC*. [3] Carpenter J. et al. (2014) *LEAG*. [4] Fisackerly R. et al. (2015) *ASTRA*. [5] Reiss P. (2017), *ELS*. [6] Reiss P. (2018), Dissertation, *TUM*. [7] Reiss, P. (2018), *Icarus*, 306C 1-15.

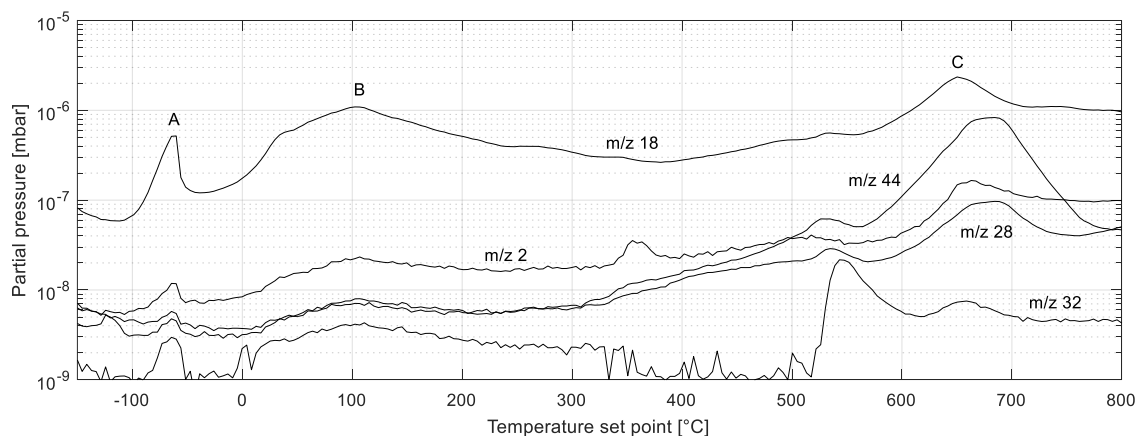


Figure 2: Exemplary partial pressure curves of selected m/z for the extraction of volatiles with 6 °C/min heating rate and a 33-36 mg, 70-80 μm , loose sample, conditioned at 30 % relative humidity [6]

IN-SITU HYDROGEN REDUCTION OF LUNAR POLAR REGOLITH: FROM PROOF OF CONCEPT EXPERIMENTS WITH PROSPA TO LARGER SCALE ISRU DEMONSTRATORS. P. Reiss¹, L. Grill¹, H. Sargeant², and S. Barber², ¹Institute of Astronautics, Technical University of Munich, Boltzmannstr. 15, 85748 Garching, Germany, (p.reiss@tum.de), ²The Open University, Milton Keynes, MK7 6AA, UK.

Introduction: The European Space Agency (ESA) currently develops the Package for Resource Observation and in-Situ Prospecting for Exploration, Commercial exploitation and Transportation (PROSPECT) as a payload contribution to the planned Russian Luna-27 mission to the lunar polar regions. The package contains the sample analysis instrument ProSPA (PROSPECT Sample Processing and Analysis) to investigate volatile compounds that are extracted by heating regolith samples delivered by a drill [1-4]. In support of the instrument development, the Institute of Astronautics at Technical University of Munich (TUM) has established a breadboard to study the capability to extract oxygen from lunar regolith for the demonstration of In-Situ Resource Utilisation (ISRU) with ProSPA. The chemical process applied for this purpose is the reduction of iron oxides in the lunar regolith using hydrogen as reducing agent. The product of this reaction is water, which in a later ISRU application could be used directly or split via electrolysis to derive oxygen and hydrogen. Similar studies have been performed at the Open University with a different breadboard [5].

Breadboard: The ProSPA laboratory breadboard at TUM allows the heating of a regolith analogue sample with 2.8 mm in diameter and 4.5 mm in height (33-36 mg at a density of 1.2-1.3 g/cm³), according to the ProSPA baseline sample size, in a high vacuum (<10⁻⁵ mbar). The breadboard design is described in detail by [6-7], a cut view of the sample container and a flow diagram are provided in Figure 1 and 2. Because the prime purpose of ProSPA is the extraction of volatile compounds from lunar regolith, the breadboard is not optimised for hydrogen reduction. As a consequence, the regolith sample is not ideally exposed to the reactant gas. As visible from Figure 1 and 2, the sample is present as a fixed bed at the end of the vacuum tubing, while the reactant gas enters and leaves the fixed bed from the top. A concern with such a configuration is that not all of the sample particles are exposed to the reactant and that the produced water accumulates in the sample, preventing further reduction.

Process: To investigate if the chemical reduction can be realised despite these concerns, several different operational modes were evaluated with the breadboard, as described in the following.

(1) Continuous gas flow: The sample is constantly purged with hydrogen at an absolute pressure of ~10¹ mbar and heated at 800 °C for 3 h. The gas mixture is permanently analysed by the RGA.

(2) Semibatch with preheating: Hydrogen is introduced into the sample compartment at an absolute pressure of ~10³ mbar and the sample is heated to 800 °C for 30 min. Subsequently, the dosing valve is opened and gas is leaked to the RGA for analysis.

(3) Semibatch without preheating: Hydrogen is introduced into the sample compartment at an absolute pressure of ~10³ mbar. The sample is heated to 800 °C and the dosing valve opened for gas analysis at the same time.

For all modes, the samples were baked-out prior to test to remove volatiles and atmospheric contamination. The samples used in the experiments were the lunar highland type regolith simulant NU-LHT-2M with standard particle size distribution and 93-96 % pure ilmenite (FeTiO₃) with a mean particle size of 174 µm. Additionally, a third run without sample was performed for each operational mode for reference.

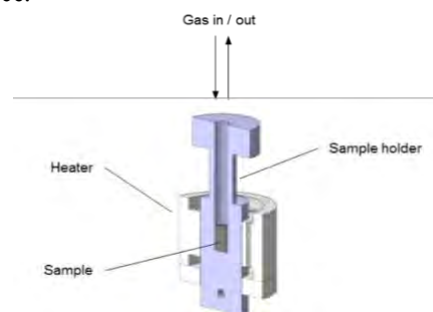


Figure 1: Cut view of the sample container

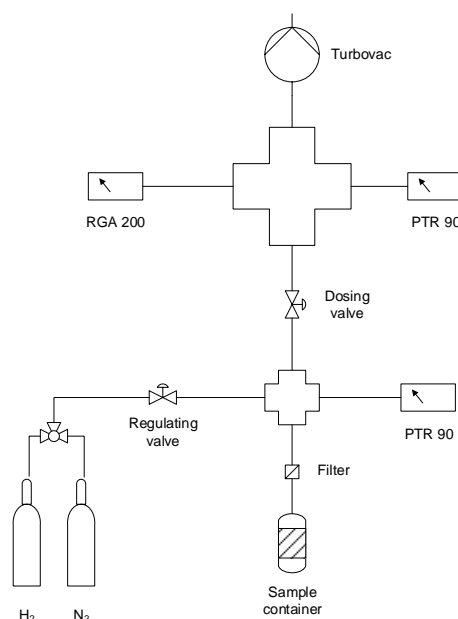


Figure 2: Flow diagram of the breadboard

Test Results: While for the first two operational modes no measurable production of water was detected, the third operational mode (semibatch without preheating) lead to a distinct raise in the partial pressure of water with the ilmenite sample. In the first 30 min of heating, the ratio of partial pressures of m/z 18 and m/z 2 (ratio of product to reactant) rises from 0.5 % to 10 % (Figure 3). For NU-LHT-2M, no significant change of this ratio was detected, comparable to the reference run without sample. An estimation of the mass of water vapour produced during the reaction, based on the temporal integration of the partial pressure, yielded values up to ~2 wt% for the ilmenite sample after a process duration of 3 h.

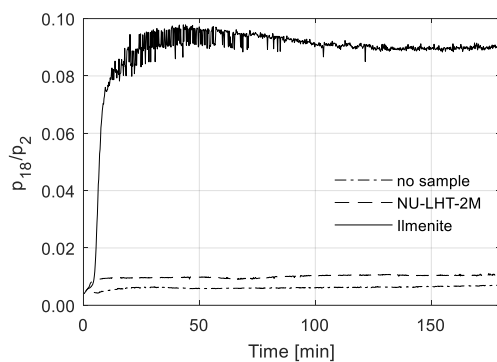


Figure 3: Partial pressure ratio water/hydrogen for the semibatch mode without preheating

Process Evaluation: The production of water from lunar regolith and its analogues is mainly done through reduction of FeO, but also TiO₂ and SiO₂. A major source of FeO that is susceptible to reduction by hydrogen is ilmenite. Lunar highland regolith typically has very low FeO and TiO₂ content (see Table 1), compared to mare regolith with FeO contents from 10-22 wt% and TiO₂ contents from 2-12 wt% [8]. As studied by [9], the oxygen yield of the present chemical reduction depends directly on the iron content: For the Apollo highland sample 62241, an oxygen yield of just over 1 % was achieved, while for the mare soils 12032 and 71131, 1.5 % and 3.5 % oxygen were achieved respectively.

Considering the above, it was expected that NU-LHT-2M would not yield a significant amount of water in the discussed experiments. However, it was not fully determined whether this was only due to low FeO content or if the non-optimised oven design has a major influence on the process efficiency. A possible risk is that the reactant gas does not diffuse through the entire sample leading to decreasing degrees of reduction over sample depth. Other risks include the resorption or reconversion of produced water within the sample.

Outlook: Based on the proof of concept studies with the ProSPA setup, further investigations will be

made that will also inform the development of scaled-up ISRU demonstrators and dedicated ISRU payloads in the near future.

ProSPA breadboard. Ongoing trade studies on the effect of several process parameters on the efficiency of the reduction are being addressed. This mainly includes the reactant gas pressure, sample temperatures, and sample type and particle size. Additional tests will be conducted to study the gas permeability of the sample and the potential of resorption or reconversion of the produced water before it leaves the sample. An improved version of the sample oven will be evaluated to assess how the current design can be optimised for ISRU purposes, for example that the reactant gas is flown through the sample.

ISRU demonstrator. The reduction of lunar regolith with hydrogen has a relatively low efficiency with oxygen yields around 2-3 wt% from pure ilmenite. The major objective for the design of future demonstrators therefore is to increase the process efficiency. Instead of using a static fixed-bed reactor such as for ProSPA or other laboratory studies [11,12], the best way of improving the reaction is to establish a continuous gas flow through the sample. This would enable better exposure of the sample to the reactant and ensure that the produced water is transported out of the sample to keep the reaction running. With larger sample quantities it is beneficial to add further sample agitation methods, such as a rotated/oscillating bed, a mixing auger [13,14], or a fluidized bed [15].

Table 1: Major oxides in Apollo 16 regolith and NU-LHT-2M (average and standard deviation in wt%)

Oxide	Apollo 16 soils and breccia [8]		NU-LHT-2M certificate of information		NU-LHT-2M material safety datasheet [10]	
	Avg.	SD	Avg.	SD	Avg.	SD
SiO ₂	44.89	0.51	47.62	0.21	46.70	0.11
Al ₂ O ₃	27.23	1.84	27.4	0.48	24.40	0.07
CaO	14.56	3.64	13.6	0.41	13.60	0.05
MgO	6.00	1.76	8.50	0.48	7.90	0.04
FeO	4.98	1.08	2.15	0.09	-	-
Fe ₂ O ₃	-	-	-	-	4.16	0.03
TiO ₂	0.53	0.14	0.33	0.02	0.41	0.02
Na ₂ O	0.47	0.08	1.43	0.03	1.26	0.02

References: [1] Barber S. J. et al. (2017) *ELS*. [2] Barber S. J. et al. (2017) *LPSC*. [3] Carpenter J. et al. (2014) *LEAG*. [4] Fisackerly R. et al. (2015) *ASTRA*. [5] Reiss P. (2017), *ELS*. [6] Sargeant H. et al (2017) *ELS*. [7] Reiss P. (2018), Dissertation, *TUM*. [8] Haskin L. and Warren P. (1991), *Lun. Sourcebook*. [9] Allen C. C. (1997), *NASA Lunar News No. 60*. [10] U.S. Geological Survey (2008), *NU-LHT-2M MSDS*. [11] Taylor L. et al. (1993), *LPSC*. [12] Yoshida H. et al (2000), 2nd Space Res. Roundtable. [13] Lee K. A. et al. (2013), *J. Aerosp. Eng.*, 26(1), 67–73. [14] Clark D. L. et al. (2009), *AIAA Sp. Conf. Expo*. [15] Taylor, L. and Carrier, W. D. (1993) *Res. of Near Earth Space*.

Spatially resolved chemical analysis using a miniature LIMS system designed for *in situ* space exploration missions. A. Riedo^{1,2}, P. Wurz², M.B Neuland³, R. Weisendanger², S. Frey², and M. Tulej²; ¹Leiden Observatory, Sackler Laboratory for Astrophysics, Leiden University, The Netherlands, riedo@strw.leidenuniv.nl; ²Physics Institute, University of Bern, Sidlerstrasse 5, 3012 Bern, Switzerland, peter.wurz@space.unibe.ch; ³Swedish Institute of Space Physics, IRF, Rymdcampus, SE - 981 28 Kiruna, Sweden.

Introduction: Instrumentation that has the measurement capabilities to deliver spatially-resolved *in situ* chemical analysis complemented by optical microscopy is of high interest to current space research and future space exploration missions. In comparison to bulk analysis, the chemical composition measurements with a spatial resolution at the micrometre level allow, e.g. detailed analysis of grain-sized samples and is avoiding the intermixing of sample material.

In this contribution we present the current figures of merit and measurement capabilities of our continuously developed miniature LIMS system (instrument name LMS) designed for *in situ* operation on planetary surfaces [1-7]. We specially set the focus on the performance demonstration to provide accurate major element abundance maps which yield the mineralogical context and measurement of element fractionation on the minor and trace element level which can deliver insights into grain formation mechanisms and geological processes including volcanism. Our studies are conducted on complex, heterogeneous materials, such as Allende [8] and Sayh al Uhaymir 169 meteorite [9] at the spatial resolution level allowing interrogating either the mechanism of solids formation in early solar system processes or processes shaping the meteoritic material.

Instrument Description: The system presented is a miniature reflectron-type time-of-flight mass spectrometer (mass analyser has a dimension of 160 mm x Ø 60 mm) that was designed for *in situ* analysis of the chemical composition of solids on planetary surfaces [1,2]. Currently, a femtosecond laser system ($\lambda = 775$ nm, $\tau \sim 190$ fs, irradiances at TW/cm² level) is coupled to the mass spectrometer, for ablation and ionisation of sample material layer by layer [3]. A beam delivery system is used to guide the laser pulses to the focussing optics installed on top of the mass analyser that focus the laser pulses through the mass analyser towards the sample surface to spot sizes of about 10 – 20 μ m in diameter. During ablation a plasma is produced and only positively charged species can enter the mass spectrometer. After passing the entrance ion optics the charged species are separated in the field free drift tube according to their mass-to-charge-ratio and are reflected at the ion mirror toward the detector system [2].

For the characterisation of the figures of merit and measurement capabilities of the miniature LIMS

system various studies on complex materials were conducted so far, ranging from semiconductor materials [5,10-11], geological samples [8-9,12-13], to samples related to astrobiology [14-15]. To date, the system has a high detection sensitivity down to the ppb level (atomic fraction) [2-3,12], a high dynamic range of about eight orders of magnitude [6], a lateral resolution of about 10 – 20 μ m (laser ablation craters), and a vertical resolution down to the nanometre level [5]. Together, these figures of merit allow e.g. the identification and localisation of e.g. microbial fossil structures embedded in a mineralogical host [15], the identification of mineral phases [14], and 3D chemical imaging of small grains [4].

In the current studies we will present the analyses of different samples of the Sayh al Uhaymir 169 meteorite, including the impact-melted breccia (K-REE-P rich lithology) and the regolith breccia. The information of the elemental mapping of the investigated meteorite areas allowed to investigate the mineralogy of the sample but also processes leading to its formation (see e.g., Fig. 1) [9]. Both the elemental mapping and the derived mineralogy of the investigated areas will be discussed in detail during the contribution.

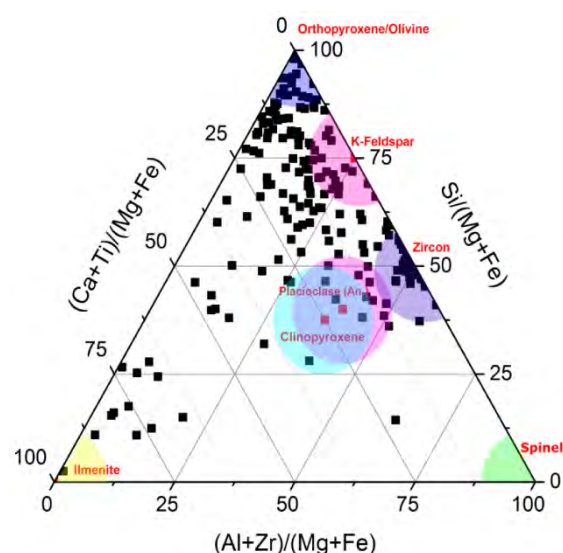


Fig. 1 Ternary diagram of an area on a K-REE-P rich sample. The diagram shows the presence of zircon, ilmenite, pyroxenes, K-feldspar and plagioclase (anorithe) [9].

In following, a detailed study of a sample of the Allende meteorite will be presented including the chemical analyses of chondrules and the matrix. Similarly to the lunar sample, we will show specific

elemental maps and corresponding mineralogies of investigated areas. One of the key finding of this study was the high degree of chemical homogeneity of the matrix, indicating that it formed independently from or in parallel to the chondrules [8]. Detailed information will be provided during the contribution.

Summary: Sensitive instrumentation that has the capabilities to investigate the chemical composition of a complex sample in situ with high spatial resolution is of high interest to current and future space exploration missions. In this contribution we demonstrate the current figures of merit of our miniature LIMS system that includes, e.g. a high detection sensitivity, a high dynamic range, and high spatial resolution. The combination of these figures of merit allows accurate quantification of elements and their isotopes, which allows subsequently studies on the mineralogy of samples, in-situ geochronology, and detection of mineral phases, among others. Although the miniature system has not the measurement performance of a large laboratory system its integration on a payload of a planetary lander could be of high benefit as various scientific questions may be answered in situ. In term of sample return missions, the system could provide valuable information on samples of interest and allows an in situ pre-selection.

References:

- [1] Rohner, U., J. Whitby, and P. Wurz, (2003) *Meas. Sci. Technol.*, 14, 2159–2164.
- [2] Riedo, A., A. Bieler, M. Neuland, M. Tulej, and P. Wurz, (2013), *J. Mass Spectrom.*, 48, 1–15.
- [3] Riedo, A., M. Neuland, S. Meyer, M. Tulej, and P. Wurz, (2013) *J. Anal. At. Spectrom.*, 28, 1256–1269.
- [4] Grimaudo, V., P. Moreno-García, A. Riedo, S. Meyer, M. Tulej, M.B. Neuland, C. Gütz, S. Waldvogel, P. Wurz, and P. Broekmann, (2017) *Anal. Chem.*, 89, 1632–1641.
- [5] Grimaudo, V., P. Moreno-García, A. Riedo, M.B. Neuland, M. Tulej, P. Broekmann, and P. Wurz, (2015) *Anal. Chem.* 87, 2037–2041.
- [6] Riedo, A., M. Tulej, U. Rohner, and P. Wurz, (2017) *Rev. Sci. Instrum.*, 88, 045114.
- [7] Riedo, A., S. Meyer, B. Heredia, M.B. Neuland, A. Bieler, M. Tulej, I. Leya, M. Iakovleva, K. Mezger, and P. Wurz, (2013) *Planet. Space Sci.*, 87, 1–13.
- [8] Neuland, M.B., K. Mezger, A. Riedo, M. Tulej, and P. Wurz, (2018) *Meteorit. Planet. Sci.*, submitted.
- [9] Frey, S., M. Neuland, R. Weisendanger, and M. Tulej, and P. Wurz, *Planet. Space Sci.*, in preparation.
- [10] Moreno-García, P., V. Grimaudo, A. Riedo, M. Tulej, M.B. Neuland, P. Wurz, and P. Broekmann, (2016) *Electrochimica Acta*, 199, 394–402.
- [11] Riedo, A., V. Grimaudo, P. Moreno-García, M.B. Neuland, M. Tulej, P. Wurz, and P. Broekmann, (2015) *J. Anal. At. Spectrom.* 30, 2371–2374.
- [12] Tulej, M., A. Riedo, M.B. Neuland, S. Meyer, D. Lasi, D. Piazza, N. Thomas, and P. Wurz, (2014) *Geostand. Geoanal. Res.*, 38, 441–466.
- [13] Neuland, M.B., S. Meyer, K. Mezger, A. Riedo, M. Tulej, and P. Wurz, (2014), *Planet. Space Sci.* 101, 196–209.
- [14] Neubeck, A., M. Tulej, M. Ivarsson, C. Broman, A. Riedo, S. McMahon, P. Wurz, and S. Bengtson, (2016) *Int. J. Astrobiol.*, 15(2), 133–146.
- [15] Tulej, M., A. Neubeck, M. Ivarsson, A. Riedo, M.B. Neuland, S. Meyer, and P. Wurz, (2015) *Astrobiol.*, 15(8), 669–682.

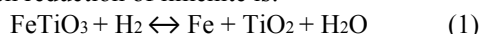
HYDROGEN REDUCTION OF ILMENITE IN A STATIC SYSTEM FOR A LUNAR ISRU

DEMONSTRATION. H.M. Sargeant¹, F. Abernethy¹, S. J. Barber¹, I. P. Wright¹, S. Sheridan¹, P. Landsberg¹, A. D. Morse¹, M. Anand^{1,2} and P. Reiss³. ¹School of Physical Sciences, The Open University, Walton Hall, Milton Keynes, ²The Natural History Museum, London, UK, ³Technical University of Munich, Germany;
E-mail: hannah.sargeant@open.ac.uk

Introduction: *In situ* Resource Utilisation (ISRU) is a concept that resources can be harvested *in situ*, enabling space exploration missions that would be otherwise economically unfeasible if solely reliant on resources from Earth. Although ISRU paper studies have been undertaken from as early as 1979 [1], more attention has been paid to laboratory and field studies in the last decade as the need for such technologies becomes critical to future exploration missions [2].

Lunar ISRU demonstration and resource prospecting missions are currently in development. ProSPA is a Sample Processing and Analysis instrument being developed at The Open University as part of ESA's Package for Resource Observation and *in situ* Prospecting for Exploration, Commercial exploitation and Transportation (PROSPECT). PROSPECT is envisaged to operate in a high latitude region of the Moon on board the Luna-27 mission in ~2022 [3]. One goal of ProSPA is to perform a proof-of-principle ISRU experiment on the lunar surface. The current work concerns the evaluation of the feasibility to carry out hydrogen reduction of ilmenite as such an experiment.

ISRU Reaction: The chemical equation for the hydrogen reduction of ilmenite is:



The reaction has been shown possible at temperatures of 700 - 1000 °C with reasonable yield of H₂O [4] which is within the temperature constraints of ProSPA. The only reactant needed is hydrogen gas which in the case of ProSPA is supplied from onboard gas tanks, and the products of the reaction are not damaging to the system. It should be noted that for full scale ISRU technologies, hydrogen gas could be sourced from lunar regolith and recycled in the reaction.

The chemical reaction is reversible so the partial pressure of water above the ilmenite must be kept sufficiently low to allow the reaction to proceed to completion. Normally this is achieved by utilising a flow of hydrogen, often by a fluidised bed system, so that as the water is produced it is transported away from the reaction site. As ProSPA is a static (non-flowing) system another technique has been proposed, in which a cold finger is used to draw any produced water away from the reaction site. As water vapour is produced it will diffuse through the system until it reaches the cold finger where it will condense. As a result, the water vapour content near the cold finger will decrease and the remaining water in

the system will continue to diffuse before ultimately condensing at the cold finger. This process will be less efficient than a flowing system in terms of quantity and speed of the removal of water from the reaction site, however 1st order modelling suggests that the diffusion of water through the hydrogen reagent gas is fast enough to allow the reaction to proceed [5].

ProSPA Breadboard Model: A breadboard model of the ISRU relevant aspects of the ProSPA system has been built at The Open University. A schematic of the breadboard is shown in Figure 1.

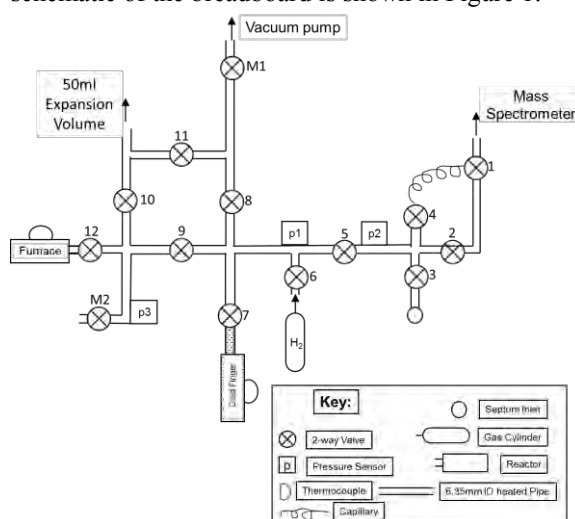


Figure 1 Schematic diagram of the ISRU demonstration breadboard model.

Water Trapping Study: The system was initially used to evaluate whether water could be trapped at the cold finger and then re-released. 0.5-5 µl samples of water were injected into the system with the cold finger operating at -180 °C for 1 hour whilst the manifold operated at 115 °C. The cold finger was then heated to 115 °C to release any trapped water into the system and pressure readings were taken in what is defined as the volatile release stage. The results are shown in Figure 2.

The results show that with increasing volumes of water, the pressure reading after heating the cold finger also increases as expected. This suggests that the system is capable of trapping water and making quantitative measurements. However, the pressure of water that can be measured is limited to ~ 120 mbar. This is likely owing the saturation vapour pressure being reached as some areas of the system are at lower temperatures because of minor imperfections in the heating system (See “Going Forward” below).

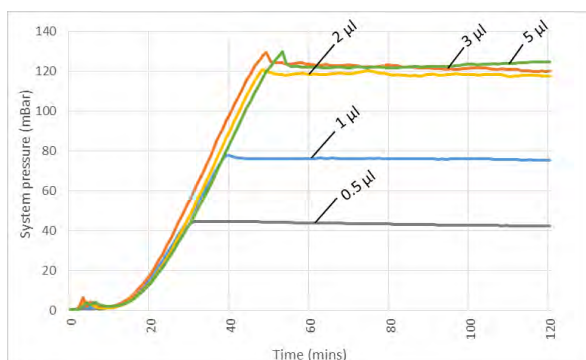


Figure 2 Pressure rise as a result of water released from the cold finger when heated to 115 °C.

Ilmenite Reduction Study: Next, the system was used to perform preliminary ilmenite reduction reactions. Since a mass spectrometer was utilised in this study (See Figure 1) this increased the operating volume of the system. A full sample expected to be collected in ProSPA ovens is ~45 mg; this was used to define 100% sample mass. A range of masses of ilmenite was studied from 0 - 100%. No other material was added to the samples. Each sample was reacted with 0.3 mmol of H_2 gas which is sufficient to completely reduce 45 mg of ilmenite. The samples were heated in the furnace to 900 °C in the presence of H_2 for 1 hour whilst the cold finger was operating at -180 °C, and the remaining manifold was heated to 115 °C. Next, any trapped water was released as in the previous study. Both pressure sensor and mass spectrometer data were recorded during the ilmenite reduction reactions.

The pressure sensor data obtained during the volatile release stage from the ilmenite reduction study shows a similar trend to the water trapping study. There is a corresponding increase in pressure with increasing ilmenite mass, albeit with a pressure limit of 18 mbar. This is likely to be a consequence of the introduction of cold spots associated with the mass spectrometer. The equivalent yield of water from each ilmenite sample was calculated assuming that the pressure increase is entirely as a result of water vapour in the system. The yield against sample mass is shown in Figure 3.

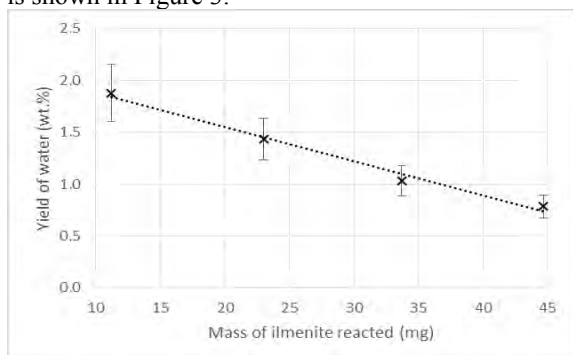


Figure 3 Estimated yield of water with corresponding sample mass as calculated from the pressure rise in the system.

Theoretically, the yield should remain constant at 11.8 wt.% across all sample sizes. The ilmenite reduction study shows that the yield decreases with larger samples with a yield significantly below the predicted value. There are a number of reasons why this could be related to completion of reaction and re-condensation of water in the system. These will be investigated further in future work.

Initial analysis of mass spectrometer data has shown that volatiles additional to water are released during the reaction, likely due to impurities in the ilmenite feedstock. The detection of mass 18 has been a challenge with the current setup due to relatively high levels of background water.

Going Forward: The ilmenite grains that were used in this study will be analysed under SEM to determine the extent of the reaction within the grains. A new breadboard model is also in development with the aim of reducing the problems highlighted in these preliminary studies, such as the non-uniform heating of the manifold and high background water signal in the mass spectrometer. The data obtained by the mass spectrometer will be used together with the pressure sensor data to quantify and characterise volatiles released during the reaction.

In terms of lunar application, one potential hindrance to the ilmenite reduction technique is the concentration of ilmenite in lunar regolith. It is thought that ilmenite concentrations in high latitude regions is <1 % [6]. Although the reaction will allow the reduction of other metal oxides, the efficiency is not well known. This will be considered along with other potential ISRU techniques.

Summary: ProSPA will perform an ISRU proof-of-principle experiment on the lunar surface. Adapting the well studied technique, hydrogen reduction of ilmenite is the primary reaction being considered to produce water from lunar regolith.

Initial results indicate that water can be trapped and re-released using a static system. Also, ilmenite reduction appears to be possible with the current setup, and the produced water can be detected.

Acknowledgements: The funding by STFC of a studentship for H.S. is acknowledged. PROSPECT is a programme of and funded by the European Space Agency.

References: [1] Rao D. B. et al. (1979) in Space Resources and Space Settlements, NASA-SP 428, NASA. 257-274. [2] Sanders G. B. and Larson W. E. (2012) *JAE*, 26.1, 5-17. [3] Barber S. J. et al. (2017) *LPS XLVII*, Abstract #2171. [4] Taylor L. A. and Carrier W. D. (1993) in Resources of near-Earth space, University of Arizona Press. 69-108.[5] Sargeant H. M. et al. (2017) *ELS* [6] Taylor L. A. et al. (2010) *JGR*, 115.E2.

COMMERCIAL LUNAR MISSION SUPPORT SERVICES. C.Saunders¹, S.Jason¹, M.Cosby², B.Hufenbach³, ¹Surrey Satellite Technology Limited, Tycho House, 20 Stephenson Road, Surrey Research Park, Guildford GU2 7YE United Kingdom c.saunders@sstl.co.uk, s.jason@sstl.co.uk ²Goonhilly Earth Station, Goonhilly Downs, Helston TR12 6LQ United Kingdom, matt.cosby@goonhilly.org, ³European Space Agency, Keplerlaan 1, 2201 AZ Noordwijk, The Netherlands, bernhard.hufenbach@esa.int

Introduction: The European Space Agency (ESA) is currently investigating ways that partnerships with commercial industry can produce benefits and gains for both agencies and industry in respect of future space exploration activities. Surrey Satellite Technology Limited (SSTL) and Goonhilly Earth Station (GES) have jointly proposed a set of Commercial Lunar Mission Support Services (CLMSS) that, in the frame of a partnership with ESA, will provide a suite of services that will provide infrastructure to support the exploration of the Moon, and ultimately the sustainable development of a Lunar economy.

The Partnership: The CLMSS partnership, is based around commercial provision of cis-lunar data relay and navigation services coupled with commercial ground station assets. SSTL and GES offer the services to any interested party. ESA may potentially act as a customer for some, or all of the services, but it also acts as an enabler bringing expertise, knowledge and support to the collaboration.

The partnership will provide services to transport payloads directly to lunar orbit, and in particular small free-flying assets such as CubeSats, enabling new classes of novel exploration missions. Opportunities for hosted payloads will also exist on the relay spacecraft. The space segment will provide proximity relay communications to both orbiting and landed assets, enabling missions to the far side of the Moon, as well as regions of high scientific interest such as the South Pole Aitken Basin. Services will be anchored via the GES ground segment which will also provide a cloud-based internet portal for principal investigators and mission managers to access data and telemetry from their exploration assets, and for users to forward commanding data.

The concept for the partnership is that a complete set of services can be purchased in the form of a ‘mission ticket’ for the execution of a particular mission, including transport directly to lunar orbit (a moderately elliptical polar orbit is targeted for payload delivery), and then provision of the supporting services needed to operate the asset, allowing the user to focus on the development and design of their system.

Initially a single satellite pathfinder mission is planned which will be the first step in the establishment of a constellation of assets orbiting the Moon, providing both communications relay and navigation services to lunar exploration users.

The relay spacecraft will be placed into a special class of frozen elliptical inclined orbit, which pro-

vides long term stability, and good coverage over the southern hemisphere of the Moon. Over time additional satellites will be placed into similar orbits to provide continual communications coverage, and to broadcast navigation signals.

Proximity relay links will be provided at UHF and S-band frequencies, with the Earth-Moon link provided through an X-band system. The CLMSS team are also currently investigating the feasibility of embarking a small optical communications terminal on the spacecraft as a European technology demonstration in support of future applications which may require increased data throughput.

Current Status: The partnership has been initiated as a phased process, and is currently in its 1st implementation phase. This will primarily implement an upgrade of the GES ground segment to full ESA deep-space antenna equivalency. This will immediately provide additional antenna capacity to support deep-space exploration and science missions. The 2nd stage, currently under pre-development, will embark the initial pathfinder mission in the 2022 timeframe, providing Cubesat delivery and initial relay services. A 3rd phase is planned for the 2025+ timeframe, in which a constellation will be built-up providing a full set of services.

Benefits: The partnership aims to provide numerous benefits to many different parties. In the frame of exploration and science the Partnership offers a framework to develop new and novel concepts for lunar science, exploration and collaboration, including new mission classes such as lunar Nano-satellites and penetrators. The Partnership can also be used de-risking of technologies and systems for other larger exploration missions.

The services offered by the Partnership also assist in the commercialisation of cis-lunar space including offering opportunities for international actors to access the Moon and develop their own business models.

There are also many opportunities for international collaboration and cooperation with exploration partners, which supports the ESA “Space 4.0” vision as articulated by the ESA Director General.

Conclusions: SSTL and GES believe that commercial industry can provide valuable services to support lunar exploration, and in partnership with ESA, are implementing a system to provide transport communications and navigation services to support the forthcoming exploration and utilisation of the Moon.

SSHADE: THE EUROPEAN SOLID SPECTROSCOPY DATABASE INFRASTRUCTURE. B. Schmitt¹, Ph. Bollard¹, A. Garenne¹, D. Albert¹, L. Bonal¹, and the SSHADE Consortium Partners² (see <https://wiki.sshade.eu/ssshade:databases>).

(1) Institut de Planétologie et Astrophysique de Grenoble (IPAG), Université Grenoble Alpes / CNRS, Grenoble, France. (bernard.schmitt@univ-grenoble-alpes.fr) (2) SSHADE Consortium partners: IPAG/UGA-CNRS (F), IAS/UPS (F), AIU Observatory (D), IRAP/U. Toulouse (F), LPG/U. Nantes (F), PGL/IGS-PAS (PL) CML/IGS-PAS (PL), WP/Unibe (CH), PIIM/U. Aix-Marseille (F), DPS/OU (GB), IAPS/INAF Roma (I), LISA/UPEC (F), CAB/INTA (E), IEM/CSIC (E), LATMOS/IPSL (F), LGL-TPE/ENS-Lyon (F), Konkoly Astro. Inst./CSFK (HU).

Introduction: Spectroscopy and spectro-imagery are increasingly used in space missions towards planets and small bodies (e.g. OMEGA/Mars Express, CRISM/MRO, VIRTIS/Rosetta, RALPH/New Horizons, MAJIS/JUICE, ...), including the Moon (NIR/Clementine, SIR/Smart-1, MI/Selene-Kaguya, SIR-2 and M3/Chandrayaan-1, IIRS/Chandrayaan-2, ...), to study the solid phases at their surface (ices, minerals or organic materials). Infrared, Raman, fluorescence and X-rays micro-spectroscopies are also used to study meteorites and cometary dusts in the laboratory and onboard some space missions (landers, rovers) for *in situ* measurements. A major contribution to the analysis of these observations is the measurement in the laboratory of UV, Visible, IR, sub-mm, Raman and XANES spectra of a variety of materials (ices, minerals, organics, ...) expected to be present at the surface of the bodies of the solar system or in their ejected grains (e.g. comets, asteroids, TNO, icy satellites, Pluto, Mars, the Moon, ...).

A large number of laboratories in Europe have developed experiments to measure and study the spectroscopic properties of a variety of solid materials of astrophysical interest, either natural (terrestrial or extra-terrestrial) or synthetics, as a function of various compositional, structural, textural or environmental (T, P, irradiations...) parameters. The amount of data collected is huge (several tens of thousands) and many of these laboratories boast leading-edge expertise in some solid spectroscopy fields. However most of the published are very difficult to access in a usable form (i.e. electronic) to compare with observations or to use in radiative transfer codes.

We thus decided in the frame of the Europlanet 2020-RI project (09/2015-08/2019) to extend our Solid Spectroscopy Data Model (SSDM) to the needs of all spectroscopy laboratories and to convert and expand the GhoSST database structure in a database infrastructure, called SSHADE, able to gather and distribute the spectroscopic data of most of the European laboratories working on solids of any types, with astrophysical and terrestrial applications.

What is SSHADE?: SSHADE ("Solid Spectroscopy Hosting Architecture of Databases and Expertise") is a project of a set of databases on solid spectroscopy that started its development in Septem-

ber 2015 and is now open to the community since 5th February 2018 (<http://www.sshade.eu>).

The SSHADE databases cover laboratory, field, airborne as well as simulated and theoretical spectral data including various levels of products (transmission, absorbance, absorption coefficient, optical constants, band list) for many different types of solids: ices, snows and molecular solids, minerals, rocks, inorganic solids, natural and synthetics organic and carbonaceous matters, meteorites, IDPs and other cosmo-materials,... They come from a wide range of measurement technics: transmission, bidirectional reflection, Raman, fluorescence, ... and over a wide range of wavelengths: from X-rays, through UV, visible, infrared to millimeter wavelengths

It is based on the GhoSST database developments (Europlanet + VAMDC 2009-2012). The SSHADE database infrastructure is hosted at the OSUG Data Center (Université Grenoble Alpes, France). The SSHADE development is part of the VESPA activity [1] within the European Europlanet-RI project of the Horizon 2020 program.

The SSHADE consortium has currently 23 partner groups in 21 laboratories from 8 different European countries (F, UK, I, D, E, HU, PL, CH), plus India and Taiwan. Information about this project can be found in the SSHADE wiki (<http://wiki.sshade.eu>)

SSHADE infrastructure: The SSHADE infrastructure has:

- A common data model: SSDM
- A common 'solid spectroscopy' interface
- A common data Import / Search / Visualization / Export engine
- A common fundamental database (species, phases, publications, objects, ...)
- A set of spectral databases: one per group/laboratory (GhoSST is one of them)

SSHADE interface: A user can currently search either spectral data or publications through two distinct forms using a simple 'Google-style' search tool that he can complement with a number of specialized filters to refine the search. For the spectral data he can filter his search according to a series of topics: by experiment, by instrument parameters, by environment, by extra-terrestrial object, by sample, by composition and/or by publication. Both tools can be combined.

Figure 2. User search page for ‘Spectra’ showing the different filters for the sample search option

The user can select and visualise a spectrum, he will then get a page with the collapsible structure of the experiment/spectra, and of the sample/layer(s)/material(s)/constituent(s). The page also display a preview of the spectrum together with the main information on the spectrum and on the measured sample.

The user can then decide either to visualize the spectrum interactively together with all its associated information, or to look at the detailed information of the experiment or of any part of the sample structure.

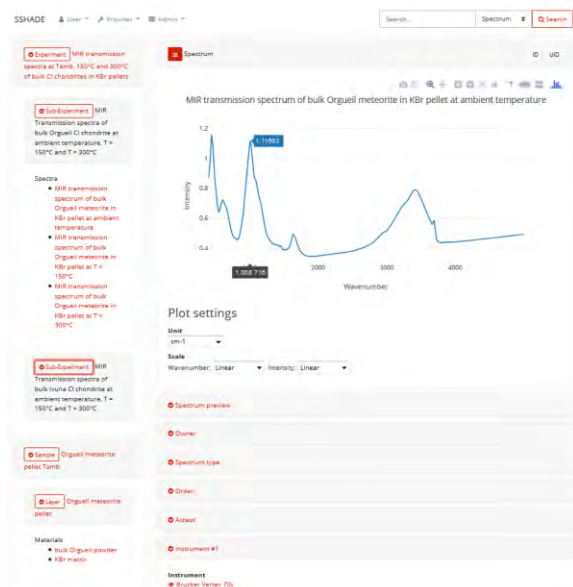


Figure 3. Display of a meteorite spectrum (dynamic), with the different categories of spectrum metadata below (left: experiment and sample structures).

The detailed page of each level of the experiment or sample structure contains all the relevant parameters values with different types of links either to another level of the structure, to other information

stored in SSHADE (such as publications) or to external pages (such as Wikipedia, WebMineral, ...).

The users can download a spectrum or an experiment from the export page for immediate and individual download. The users may also add a spectrum or an experiment in the ‘basket’ for future export.

Databases implementation: We are progressively implementing in the SSHADE infrastructure the databases of each of the 20 partners of the SSHADE consortium. 10 databases are already active in SSHADE (BYPASS, DAYS, DOCCD, FAME, GhoSST, LSD, PaSSTEL, SOSYPOL, SSTONE and STOPCODA) and one is just starting (MIA), and over 1250 spectra are already online (from 182 experiments on about 830 samples), well over what we expected for the initial delivery of the SSHADE infrastructure.

The 10 already active databases already cover a wide range of samples, spectroscopic techniques and spectral ranges.

- various types of natural and synthetic samples (ices, minerals, rocks, meteorites, carbonaceous material, micrometeorites, prebiotic and bio molecules, ...), including some made from 'soil simulants' such as JSC Mars 1.
- various types of spectral data from transmission spectra, reflectance spectra, to optical constants
- Various spectral ranges: X, Vis, NIR, MIR, FIR, sub-mm and mm.

The current contents of the 10 active databases is described in the SSHADE wiki. It also contains a SSHADE user guide and a Data search guide. (<https://wiki.sshade.eu>)

Tutorials on the use of the SSHADE database infrastructure will be organized during the Symposium.

SSHADE in Virtual Observatories: SSHADE will be soon a service for Virtual Observatories (VESPA, VAMDC, ...). In particular part of the SSHADE databases will be accessible via the EPN-TAP protocol [2], which will allow comparison with observational data and mass processing in the VESPA environment through a series of dedicated spectroscopy plotting and analysing tools [3].

References: [1] Erard et al (2014) Planetary Science Virtual Observatory architecture. *A&C* **7-8**, 71-80. [2] Erard et al (2014) The EPN-TAP protocol for the Planetary Science Virtual Observatory. *A&C* **7-8**, 52-61. [3] Erard et al (2017) Spectroscopy of planetary surfaces in a VO context (VESPA), EPSC2017

Acknowledgements: The Europlanet 2020 Research Infrastructure project has received funding from the European Union's Horizon 2020 research and innovation programme under grant agreement No 654208. We also acknowledge OSUG, INSU and CNES for additional financial supports.

CHARACTERIZATION OF LUNAR VOLCANISM FEATURES IN THE ARAGO REGION, WESTERN MARE TRANQUILITATIS. N. Schnuriger¹ (nicolas.schnuriger@gmail.com), J. Flahaut^{1,2}, M. Martinot^{3,4}, S. D. Chevrel¹, ¹IRAP, Université de Toulouse, CNRS, CNES, UPS, (Toulouse), France, ² CRPG, Université de Lorraine, CNRS, Nancy, France, ³ FALW, Vrije Universiteit Amsterdam, 1081 HV Amsterdam, The Netherlands, ⁴ Université Lyon 1, ENS-Lyon, CNRS, UMR 5276 LGL-TPE, F-69622, Villeurbanne, France.

Introduction: Mare Tranquilitatis is made of Early to Late Imbrian basaltic units filling the Tranquilitatis basin on the Moon [1]. The purpose of this study is to investigate the type, extent, duration and history of volcanism in Western Mare Tranquilitatis, using a variety of high resolution datasets. Our study area encompasses the western half of the mare (18 to 30°E, -2 to 12 °N {Figure 1, left}), near Arago and Carrel craters, where an important number of Irregular Mare Patches (nearly 40 IMPs) and eight volcanics domes have been previously reported [2,3]. The domes were previously separated into two classes, based on their morphological and spectral characteristics, which both belong to the low slope, extrusive and effusive mare domes class [2]. The IMPs were identified based on their low density of craters and tentatively interpreted as recent mare volcanism on the lunar nearside [3], although this interpretation is debated [4,5].

Methods: All the datasets available over the study area were processed, and integrated into a Geographic Information System. Our data collection includes: Kaguya TC images and associated DTM (spatial resolution 10 m/px) assembled as mosaics, LROC WAC (100 m/px) and NAC imagery (<1 m/px), LOLA topography (100 m/px), GRAIL gravity, Lunar Prospector GRS (15 km/px), and Clementine global maps. Kaguya MI data (spatial resolution of 10 to 62 m/px) were also used to build a false-color map mimicking the Clementine RGB color composite (at a greater spatial resolution), with the following bands: R = 750/415 nm, G = 750/950 nm, B = 415/750 nm. Finally, the Moon Mineralogy Mapper (M³) VNIR hyperspectral data (spatial resolution of 140 to 280 m/px) were processed with the method of [6] to provide mineralogical information over the study area.

Results: Nine candidate volcanic domes (Arago 1 to 8 + Carrel 1) were identified using the Digital Terrain Model derived from the TC images; it includes a possible domes not reported before (referred to as Arago 8 hereafter), located at 4,69° N ; 22,72°E. However, high resolution images of Carrel 1 (10.112°N; 27.096°E) reveal that the putative dome is located upon the ejecta of the crater Carrel, and close to highlands remains. Due to uncertainties about its true nature, the Carrel 1 feature was excluded from further studies. Domes Arago 1, 2, 4, 5, 6, 8 are aligned along a SE-NW trend (Figure 1B). As most domes straddle over a topographic break, it is difficult to outline their base, therefore a minimum and a maximum height and extent are given in Table 1 which also displays radius, slope, area and volume for each dome. Arago domes 1-8 range from 4.8 to 24 km in diameter, 40 to 400 m in height and their slope varies between 0.8 and 3 degrees.

Previous geologic mapping within Mare Tranquilitatis was performed by [7]. Comparison with this study reveals that the Arago domes are located onto two specific geologic units: domes Arago 2 and 3 are in the Tr3 unit (medium-Ti unit, dated at 3.67 Gy), whereas domes Arago 1, 4, 5, 6, 7, 8 are in the Tr4 unit (youngest regional unit with higher-Ti, dated at 3.59 Gy). The region is showing evidence of wrinkle ridges, one sinuous rille, and numerous extensional grabens [8] that surround, or are part of, the Tr4 unit (Figure 1, right). The load of the Tr4 unit on the mare could have led to an extensional context, resulting in the formation of the observed grabens.

Crater count dating was performed on the domes, using the Craterstats 2.0 software [9]. Three groups of ages are observed: the oldest domes are Arago 1 and 8 (respectively $3.79 \pm 0.05/0.08$ Gy and $3.71 \pm 0.10/0.38$

Dome	Coordinates		High (m)		Mean radius (m)		Slope (°)		Area (km ²)	
	Latitude (°)	Longitude (°)	Minimum	Maximum	Minimum	Maximum	Minimum	Maximum	Minimum	Maximum
Arago 1	7,703	22,066	103	159	2550,250	3146,25	2,461	2,982	17,806	24,896
Arago 2	7,570	21,563	320	398	9767,250	12021,5	1,959	1,916	240,017	395,849
Arago 3	6,158	19,938	245	397	8411,250	12048	1,685	1,896	212,899	425,414
Arago 4	8,515	21,210	38	114	2748,500	7113,25	0,820	0,931	18,357	129,185
Arago 5	8,954	20,939	46	94	3276,500	4805,5	0,814	1,149	31,871	77,379
Arago 6	9,271	20,757	84	129	3666,000	4068,25	1,408	1,842	35,451	43,1129
Arago 7	11,286	24,111	85	105	2427,750	2859,25	2,011	2,121	18,421	22,5336
Arago 8	4,696	22,717	116	213	3435,500	5240	2,538	2,616	27,963	57,967
Carrel 1W	10,112	27,096	69	129	1416,500	2350,5	2,890	3,652	12,552	26,6476
Carrel 1E			55	89	1491,500	1772,25	2,729	3,387		

Table 1: Morphologic characteristics of candidate lunar domes in the vicinity of Arago Crater.

Gy), followed by Arago 4 to 7 (ranging from $3.37 \pm 0.12/0.48$ Gy to $3.59 \pm 0.10/0.45$ Gy), and Arago 2 and 3 (respectively $2.89 \pm 0.28/0.43$ Gy and $2.70 \pm 0.41/0.55$ Gy). These estimates rely on the assumption that the domes are monogenetic, i.e., they were formed as a single volcanic event, otherwise these ages would represent the last volcanic activity for each. These ages imply that Arago 1 and 8 and Arago 4 to 7 are roughly contemporaneous to the mare unit they belong to. However, Arago 2 and 3 would be approximately 1 Gy younger than the last mare emplacement.

Furthermore, because they are all lying on the Tr4 unit (3.59 Gy), the IMPs are likely the youngest volcanic features of the region. As it is the case for the domes, some of the IMPs are aligned. IMPs align perpendicular to the extensional grabens around the mare, suggesting a strong relation to the local tectonic constraints. Also, four IMPs are situated on the dome Arago 6, implying that they formed after the dome's emplacement.

M³ spectral data reveal no major difference between the composition of the domes and the surrounding mare units, which are dominated by high calcium pyroxenes (HCP) signatures. Spectral analyses of the biggest IMPs (Sosigenes, Maclear, and those on Arago 6) show that they are also characterized by HCP signatures.

Discussion and Conclusions: The emplacement of Mare Tranquilitatis started more than 3.85 Gy (Early Imbrian) with the emplacement of the Tr1 and Tr2 geologic units. During the Late Imbrian (3.8 – 3.6 Gy), the Tr3 unit was emplaced and overlain by the small, effusive domes labelled A1 and A8.

The Tr4 unit was formed at 3.59 Gy, and because all of the IMPs are located upon it, they are contemporary to it or younger than this unit. According

to [4], the IMPs are produced by lava foams that formed slowly under a small crust, before bursting that crust and reaching the surface to spread. A similar process for the-Arago IMPs can be envisioned. The Tr4 unit expanded through the mare and its top slowly started to cool. A foam formed underneath, and through instabilities, succeeded to reach the surface locally and form the IMPs. The thickness of the unit crust might be sufficient to minimize the quantity of foam extruding and explain the small size of the IMPs.

The domes Arago 4 to 7 are slightly younger than Tr4 and thus could mark the end of the Tr4 mare emplacement from effusive eruptions along local fractures.

Finally, domes Arago 2 and 3, the largest and steepest of the domes, were emplaced at the beginning of the Eratosthenian (~ 2.9 Gy), possibly from more evolved, Si-rich magmas. The late formation of these two domes suggests long-lived volcanism in the region, which is outside the Procerallum KREEP Terrane (PKT), but is still associated to a Lunar Prospector Thorium anomaly [10]. Although it is not associated to any lunar mascon, positive anomalies in the GRAIL dataset (especially showing up 40 km south to Arago crater) [11] could indicate the presence of magmatic intrusions that fed the domes before complete cooling.

References: [1] Head (1976) Reviews of Geophysics, 14(2), 265-300. [2] Wölher et al (2007) Icarus 189, 279-307. [3] Braden et al (2014) NGeo 7, 787-791. [4] Wilson & Head (2017) JVGR 335, 113-127. [5] Qiao et al. (2017) Meteorit Planet Sci. doi:10.1111/maps.13003. [6] Martinot et al. (2018) JGR 122, doi:10.1002/2017JE005435. [7] Kodama and Yamaguchi (2003) Meteoritics & Planetary Science 38, 1461-1484. [8] Jaumann et al (2012) Planetary and Space Sciences 74, 15-41. [9] Michael and Neukum (2010) EPSL 294, 223-229. [10] Lawrence et al. (2000) JGR 105.E8, 20307-20331. [11] Zuber et al. (2013) Science 339, 6120, 668-671.

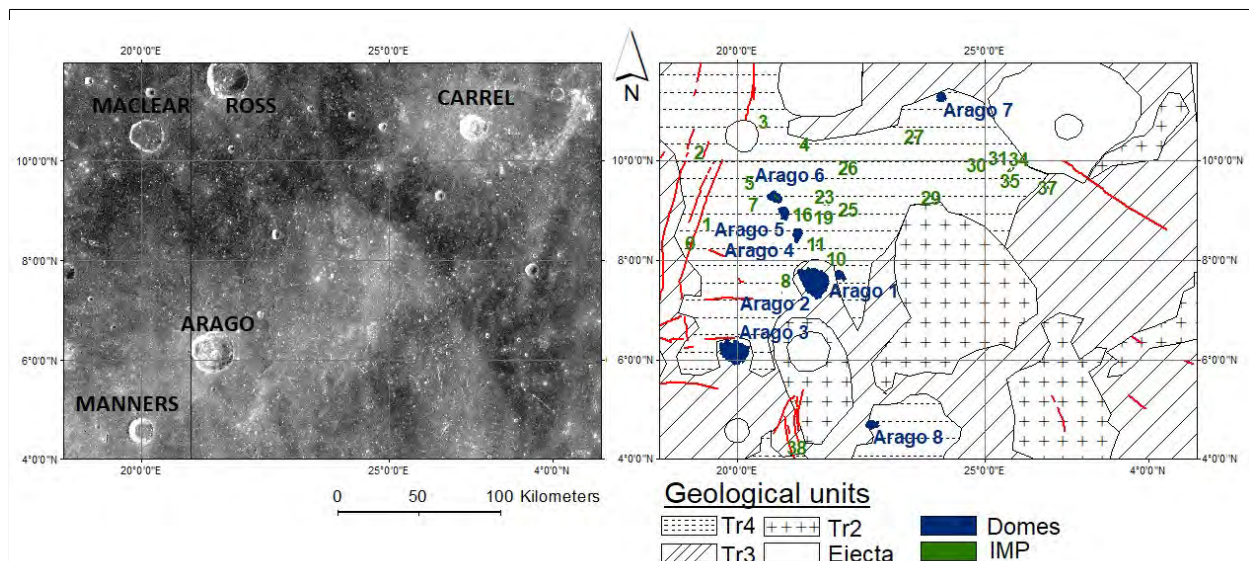


Figure 1: A: Mosaic of Kaguya TC images of the NW Mare Tranquilitatis. B: Geologic sketch map of the study area; domes are mapped in blue, IMPs in green, and grabens in red

Introduction: The compositional variations of the mare basalts on the Moon indicate that the mare basalts formed from compositionally distinct mantle reservoirs with different contents of Ti and other incompatible elements [1]. On the lunar surface, Ti-rich basalts are highly concentrated in the Procellarum region on the nearside, suggesting a local Ti enrichment of the underlying mantle. Although several scenarios have already been proposed to explain the high volume of observed Ti-rich mare basalts on the nearside of the Moon, the mechanism how to produce the Ti-enriched reservoirs within the mantle only on the nearside of the Moon is unclear. The nearside of the Moon was proposed to be a gigantic tectonomagmatic structure [2]. However, recent observations show that the farside has a layered crustal structure [3,4] and the nearside contains a large area of impact melt material (e.g., low-Ca pyroxene) [5], suggesting a giant impact occurred on the current nearside of the early Moon. A large impact event produces a thermal anomaly on the planetary scale [6] and changes the source depth and volume of magmatism [7]. Therefore, it might also induce local changes in the composition of the mantle by partial melting and heat induced mantle convection. In this work we investigate the effects of a giant impact at the Procellarum region to test if the crystallization of an impact-induced melt pool could explain the apparent Ti-enrichment of the lunar mantle underneath the Procellarum region as a potential source for the Ti-rich mare basalts on the nearside of the Moon.

Methods: *Giant Impact Modeling.* We modeled the giant impact using iSALE [8], assuming an impactor with a diameter of 780 km hitting the nearside of the Moon with a velocity of 6.4 kms⁻¹. Such a giant impact could form a mega-basin on the Procellarum region and reproduce the characteristics of the crustal dichotomy and structures comparable to those observed on the current Moon, including the nearside lowlands and the farside thick mafic-rich layer on top of the primordial anorthositic crust [9]. Using the modeled impact peak pressures, we calculated the impact induced heating to investigate the degree of partial melting.

Material Properties. We assumed a differentiated projectile with a bulk H chondritic composition and a simplified thermal stratification with a 1350 K core and 850 K mantle. The lunar mantle and crust were assumed to have formed by fractional

crystallization of a global lunar magma ocean (LMO) with main oxide contents as proposed by [10] but an elevated TiO₂ content of 0.4 wt% corresponding to the maximum estimates of other works (e.g. [11,12,13,14]). We modeled LMO crystallization with alphaMELTS [15,16,17], assuming that all crystallizing plagioclase floats to the surface to form an anorthositic crust and the remaining mantle cumulate was mixed by solid state convection. It has been shown that dense, Ti-rich, ilmenite bearing cumulates (IBC) can be partially entrained in the deeper mantle, resulting in elevated IBC concentrations both at the core mantle boundary and at the base of the crust [18]. We used this distribution of IBC in the mantle after convective overturn to calculate the TiO₂ concentrations in the lunar mantle. The mantle temperature was assumed to be at the solidus at the time of the giant impact.

Partial Melting and Melt Pool Crystallization Model. For each material considered in the impact model we determined the solidus and liquidus temperatures and the compositions of partial melts at different degrees of melting using alphaMELTS [15,16,17] and phase diagrams for iron and plagioclase. Using this information, we calculated the degree of melting and the respective composition of the partial melts in different regions of the lunar mantle depending on the local post impact temperature. We assumed that above a minimum degree of melting of 3% the partial melts could migrate to the surface and form a melt pool. The composition and volume of this melt pool was calculated by mixing the compositions of all partial melts. In order to determine the thickness of the secondary plagioclase floatation crust formed by melt pool solidification and the composition of the newly formed upper mantle, we modeled the fractional crystallization of the melt pool with alphaMELTS [15,16,17].

Results and Discussion: As a consequence of shock compression and the subsequent unloading [19], the giant impact produces partially molten material that extends almost entirely over the impact hemisphere (Fig. 1). Partially molten material reaches down to the core and extends radially to a distance of 1600 km, corresponding to the size of the mare basalt region [20] and the putative Procellarum basin [21]. About 50% of the initially 38 km thick crust in the target area is molten and the remaining solid crust is largely pushed towards the basin rim or buried deeper in the mantle. Assuming that the partial melt rises vertically towards the surface and does not penetrate any remaining crust at

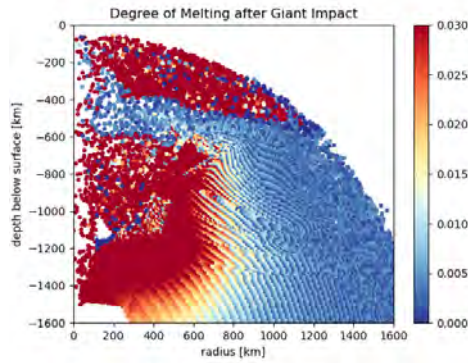


Fig. 1: Degree of melting after the giant impact. Red areas indicate the source areas of those partial melts that are assumed to form the melt pool (degree of melting $\geq 3\%$).

the basin rim, the melt forms a pool with a diameter of ~ 2900 km and a thickness of 74 km. A melt pool of this depth can be expected to crystallize within 1-10 Ma, depending on the efficiency of convective cooling during different stages of crystallization. The crust forming from this magma pool has a thickness of 21.5 km, assuming that the crust consists of pure plagioclase and that no other minerals or parts of primary crust are mixed in. This value is comparable to the average crust thickness of 25 km in the Procellarum region derived from GRAIL data [22]. Before the giant impact TiO_2 -rich materials are mostly located at the core-mantle boundary and at the base of the crust [18]. The TiO_2 contents in the upper mantle range from about 0.09 - 0.36 wt% (Fig. 2), which is similar to the TiO_2 contents that have been estimated for the mantle sources of low Ti mare basalts (0.09 - 0.34 wt%) [23]. Due to the giant impact, the mantle below the Procellarum region is partially molten and these partial melts accumulate in a melt pool at the surface. Thereby Ti is preferentially partitioned into the partial melts along with other incompatible elements, including heat producing isotopes of U, Th and K. This process results in a depletion of the mantle in incompatible elements and a complementary enrichment of that part of the upper mantle that formed by crystallization of the melt pool. Thus, the TiO_2 content in the upper 50 km of the mantle below the Procellarum region increases to an average of 0.82 wt% with local concentrations varying from 0 - 20 wt% TiO_2 if the cumulate layers are insufficiently mixed. These values are consistent with the range of TiO_2 contents up to ~ 1.5 wt% that have been estimated for the source regions of high-Ti mare basalts [23]. The TiO_2 content in the underlying mantle (depth > 50 km) decreases, respectively, from an average of about 0.15 wt% to an average of about 0.13 wt% in the region from which most of the partial melts originate (Fig. 2). In the same way inhomogeneities are produced in the mantle FeO content which is 11.3 wt% before the impact, 20.3 wt% in the solidified melt pool and 11.0 wt% in the

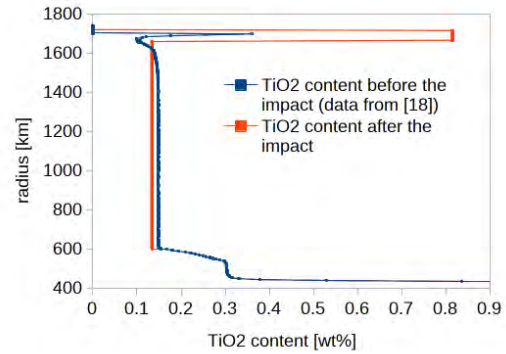


Fig. 2: TiO_2 contents of the lunar mantle below the Procellarum Basin. Blue: TiO_2 content before the impact (after overturn of the magma ocean cumulate pile as calculated by [18]). Red: Average TiO_2 contents of the depleted mantle and the solidified melt pool after the impact.

underlying mantle. These values are consistent with the range of FeO contents from ~ 12 - 20 wt% observed in mare basalts and green glasses [23].

Conclusions: In this study we demonstrate that partial melting and re-solidification of the mantle after a large impact in the Procellarum region (1) is consistent with the observed crust thickness in the Procellarum region and (2) leads to local variations of mantle Ti and FeO contents of the same order as they have been inferred from mare basalt compositions.

Acknowledgements: We gratefully acknowledge the developers of iSALE, including Gareth Collins, Kai Wünnemann, Dirk Elbeshausen, Boris Ivanov and Jay Melosh. This work was funded by the Deutsche Forschungsgemeinschaft (SFB-TRR 170, C4).

References: [1] Neal and Taylor (1992) *Geochim. Cosmochim. Acta*, 56, 2177-2211. [2] Andrews-Hanna et al. (2014) *Nature*, 514, 68-71. [3] Yamamoto et al. (2012) *GRL*, 39, L13,201. [4] Donaldson-Hanna et al. (2014) *JGR*, 119, 1,516 - 1,545. [5] Nakamura et al. (2012) *Nature Geosci.* 5, 775-778. [6] Rolf et al. (2017) *Icarus*, 286, 138-152. [7] Padovan et al. (2017) *Nature Comm.* 8, 1,945. [8] Wünnemann et al. (2006) *Icarus* 180.2, 514-527. [9] Zhu et al. (2017) *LPSC*, 1851. [10] O'Neill (1991) *Geochim. Cosmochim. Acta*, 55, 1135-1157. [11] Snyder et al. (1992) *Geochim. Cosmochim. Acta*, 56, 3809-3823. [12] Buck and Toksoz (1980) *LPSC*, 11, 1980. [13] Morgan et al. (1978) *The moon and the planets*, 18, 465-478. [14] Elkins-Tanton et al. (2011) *EPSL*, 304, 326-336. [15] Smith and Asimow (2005) *G3*, 6 (2). [16] Ghiorso and Sack (1995) *Contr. Mineral. and Petrol.*, 119, 197-212. [17] Ghiorso et al. (2002) *G3*, 3(5), 1-35. [18] Yu et al. (2017), *submitted*. [19] Pierazzo (1997) *Icarus*, 127, 408-423. [20] Jolliff et al. (2000) *JGR*, 105, 4,197-4,216. [21] Wilhelms & McCauley (1971) *I-703*, USGS. [22] Wieczorek et al. (2013) *Science*, 339, 671. [23] Lucey (1998) *JGR*, 103, 3701-3708.

ESA'S PROSPECT PACKAGE FOR EXPLORATION OF LUNAR RESOURCES: INVESTIGATION DOMAINS E. Sefton-Nash^{1*}, J. D. Carpenter¹, R. Fisackerly¹, R. Trautner¹, the ESA Lunar Exploration Team, the PROSPECT User Group and the PROSPECT Industrial Team. 1. ESA/ESTEC, Keplerlaan 1, 2201 AZ, Noordwijk, The Netherlands (e.sefton-nash@cosmos.esa.int).

Introduction: The Package for Resource Observation and in-Situ Prospecting for Exploration, Commercial exploitation and Transportation (PROSPECT) is a payload in development by ESA for application at the lunar surface as part of international lunar exploration missions.

As part of ESA's European Exploration Envelope Programme (E3P) [1] PROSPECT is part of contributions to the Russian-led Luna-Resource Lander (Luna 27) mission, which aims at exploring for the first time the South polar region of the Moon, performing an assessment of volatile inventory in near surface regolith, and an analysis to determine the abundance and origin of any volatiles discovered. Furthermore, E3P dictates that PROSPECT will build-up a European lunar exploration user community to exploit the engineering and scientific data, and the other benefits generated during the project.

Establishing the utilization potential of resources found in-situ on the Moon may be key to enabling sustainable exploration and lunar habitability in the future. The purpose of PROSPECT is to support the identification of potential resources, to assess the utilization potential of those resources at a given location and to provide information to help establish the broader distribution. PROSPECT will also perform investigations into resource extraction methodologies that maybe applied at larger scales in the future and provide data with important implications for fundamental scientific investigations on the Moon. To achieve these objectives PROSPECT is required to:

- Extract samples from depths of at least 1m.
- Extract water, oxygen and other chemicals of interest in the context of resources.
- Identify the chemical species extracted.
- Quantify the abundances of these species.
- Characterize isotopes such that the origins and emplacement processes can be established.

In the lunar polar regions PROSPECT is able to target water ice. At all locations on the Moon PROSPECT is able to extract solar wind implanted volatiles from the regolith through heating and aims to extract oxygen and other chemicals of interest as resources from minerals by a variety of techniques.

Drilling and sampling: ProSEED is the PROSPECT Sample Excavation and Extraction Drill. Once at the required depth, a tool acquires small samples, whilst preserving their temperature below limits

set to ensure volatile preservation. ProSEED then delivers samples either to the Luna 27 robotic arm for passing on to Russian analytical instruments, or to the ProSPA Solids Inlet System (SIS).

ProSEED will include sensors and equipment for making measurements of sample temperature, subsurface permittivity and recording images of the sampling operations. It will also acquire a comprehensive set of engineering data from integrated sensors that will support analysis of subsurface soil properties and engineering parameters.

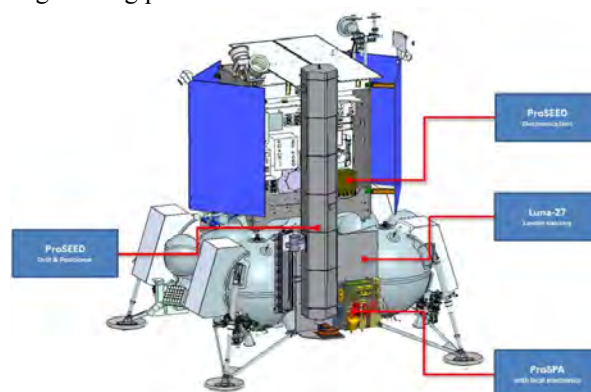


Figure 1: ProSEED and ProSPA Elements of PROSPECT on board the Luna 27 platform.

Chemical extraction and volatile analysis: The functions of ProSPA are distributed across two physical units: 1) The SIS comprises a series of single-use sample ovens (with heritage from ExoMars [2]) on a rotary carousel together with a sample imager, and 2) a miniature (37 x 27 x 13 cm) chemical analysis laboratory incorporating two mass spectrometers and associated ancillary and control systems [3].

Various heating profiles may be applied to the ovens for the purposes of addressing different science and ISRU objectives. Heating in vacuum extracts ices and solar wind implanted volatiles, and pyrolyses some volatiles from minerals. Reacting gasses may also be introduced to the ovens to extract additional chemistry of interest, including combustion with oxygen [4] and reduction using hydrogen and methane [5]. Volatiles released during a heating profile are passed to the ProSPA chemical laboratory for analysis. The laboratory comprises an ion trap device for analytical mass spectrometry (2 - 200 AMU), as well as a magnetic sector instrument for analysis of stable isotopes (D/H, $\delta^{13}\text{C}$, $\delta^{15}\text{N}$, $\delta^{18}\text{O}$) [3]. Measurements of Ar, Kr and Xe are also expected to be possible [6].

Associated ancillary and control systems comprise gas handling and processing components, including open/closed valves, metering valves, micro-reactors, pressure sensors and reference materials.

Investigation Domains: PROSPECT has objectives that lie firmly within lunar exploration and science: in-situ planetary geology, and analysis of samples and volatiles, but there exist a number of expertise domains, some related to specific hardware elements, in which scientific contributions must be focussed in order to realise these objectives:

1. Drilling, Geotechnics and Sample Handling:

Data will be returned from the ProSEED drill system that can be used to derive regolith physical properties. Sample behaviour during handling, as evidenced by relevant sensors (e.g. imagers) may also be relevant information sources. The focus of this investigation domain is therefore firmly targeted at retrieving and analysing mechanical and other relevant physical properties of lunar regolith at the landing site, to provide both context to the other measurements made and to support development of future exploration systems that also target lunar polar landing sites.

2. Imaging, Surface Modelling and Spectral Analysis: The PROSPECT payload has two cameras: 1) a drill camera to image the landing and drill site in several spectral bands, monitor drilling operations as well as robotic sample transfer operations to ProSPA's SIS and the Russian robotic arm, and 2) a sample imager that will provide multi-spectral images and allow generation of depth-maps of sample deposit surfaces after they have been deposited in ovens.

Investigations using data from the sample camera will focus on sample properties that may be derived using spectral and morphological data retrieved from images obtained in various bandpasses [7]. Data from the drill camera will also provide contextual information regarding the drill work area, boreholes and drill cuttings, as well as the landing site, allowing interpretation of local geology and local morphology/illumination conditions.

3. Permittivity: The ProSEED drill rod is planned to accommodate a permittivity sensor, which allows determination of the electrical permittivity of materials in contact with the sensor electrode, via a comparison of the electrode current measured for air/vacuum and for contact with the material of interest. Permittivity measurements of borehole materials at specific drill rotation azimuth and depth will be made during drilling operations, at periodic measurement intervals during which the drill will be stopped and non-rotating.

This will allow reconstruction of permittivity properties as a function of borehole depth and azi-

muth, leading to retrieval of profiles of H₂O content and other relevant geologic properties.

4. Thermal Environment and Volatile Loss: The ProSEED drill design includes a set of temperature sensors which provide information on sample temperature as well as mechanism temperatures. Together with engineering data on the energy used in the drilling and sampling process, the temperature data will allow the modelling of the thermal environment, and - most importantly - support the modelling and quantification of volatile losses and possible isotopic fractionation during sublimation [8], during the sampling and sample transfer processes.

5. ProSPA Sample Analysis: Volatiles released during oven heating, and optionally following reaction with reference gases, are passed to the ProSPA chemical laboratory for analysis. Volatiles could originate from ices, chemisorbed volatiles, cosmogenic volatiles, and implanted solar wind. This area of investigation focusses on analysis of the chemical composition and abundance of volatiles (using gas pressure determination and ion trap mass spectrometry) as well as isotopic analysis (using magnetic sector mass spectrometry) [3].

6. ProSPA ISRU: During ProSPA's ISRU experiment operation mode an oven may be heated to temperatures of up to 1000°C and fed with H₂ or CH₄ in order to reduce the molecules in the regolith and extract oxygen. These experiments are intended to provide an in-situ reference for terrestrial investigations into oxygen extraction processes that could be applied in future ISRU plants at the lunar surface. PROSPECT's ISRU science investigation will therefore require expertise in mineralogy and sample processing, to quantify the resource potential of lunar regolith with respect to future human and robotic missions.

References: [1] Houdou, B. and Carpenter, J. (2017), European Lunar Symposium [2] Schulte W. et al. (2010), Proceeding of i-SAIRAS. [3] Wright I.P. et al. (2012) Planetary and space science, 74, 1, p. 254 - 263. [5] Schwandt et al., (2012) Planetary and space science, 74, 1, 49-56. [3] Barber, S. J. et al. (2017), LPSC 48, Abs. 2171. [7] Schmitz, N. and Donaldson-Hanna, K. (2017), LPSC 48, Abs. 1904. [6] Curran, N. M., et al. (2017), LPSC 48, Abs. 2243. [8] Mortimer, J., et al. (2017), LPSC 48, Abs. 1945.

FAR-IR EMISSIVITY TEMPERATURE DEPENDENCE IN LUNAR SOUTH POLAR PERMANENTLY SHADED TERRAIN?

E. Sefton-Nash¹, B. Greenhagen², J.-P. Williams³ and D. A. Paige³ ¹ESTEC, European Space Agency, Keplerlaan 1, Noordwijk 2201AZ, Netherlands (e.sefton-nash@cosmos.esa.int). ²Applied Physics Laboratory, Johns Hopkins University, MD, USA. ³Department of Earth, Planetary and Space Sciences, University of California Los Angeles, USA.

Introduction: The northern floor and wall of Amundsen crater, near the lunar south pole, is a permanently shadowed region. We report on results from observations of two targets on the floor of Amundsen, one in the permanently shadowed region (PSR) and the other in the partially illuminated area (NPSR) (Figure 1), with the goal of observing relative differences in their far-IR emissivity in nighttime observations by LROs Diviner Lunar Radiometer Experiment.

A 3km radius around centers of 93.1047°E, 84.5523°S and 91.2826°E, 83.6889°S define the NPSR and PSR targets, respectively. For the PSR target this radius ensures that only observations from within the PSR boundary are included, but the size is also a balance between minimizing scatter caused by heterogeneous thermal states, while ensuring sufficient data coverage for robust statistics.

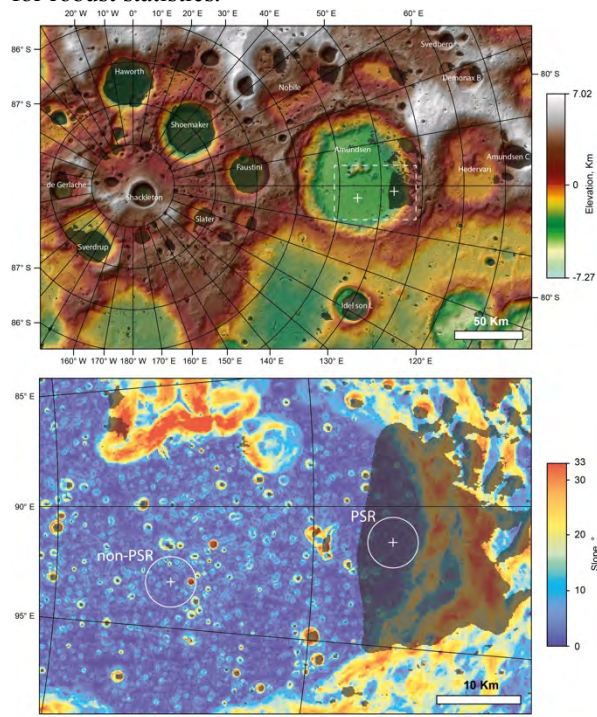


Figure 1: Study area and targets: colorized hillshade (top) and slope (bottom) from LOLA 20m/pix data. Regions in permanent shadow darkened using 120 m/pixel map [1]. Dashed box marks lower panel. 2 targets in Amundsen crater marked with white '+', encircled at 3 km radius.

The permanently shadowed target includes terrain that is reported to indicate generally brighter 1064 nm

albedo combined with annual maximum surface temperatures low enough to enable persistence of surface water ice (< 110K). Many permanently shadowed areas with similar LOLA reflectance characteristics do not show this trend [2].

This is consistent with a similar correlation of annual maximum temperature with anomalous ultraviolet radiation as measured by the LAMP instrument [3]. A patchy distribution of areas in the PSR target show a combination of off/on-band ratios > 1.2 and Lyman- α albedo < 0.03, indicating a possible water mass content of 0.1 – 2.0% [4].

Portions of our PSR target therefore indicate annual maximum temperatures, as well as ultraviolet and near-IR signatures that are anomalous compared to other south polar terrain in permanent shadow, and are consistent with the presence of surface water frost. Our method intends to quantify any effect by the presence of water frost, or by ultra-low temperatures, on emissivity in the far-IR, near their planck peak.

Method: For each orbit we bin observations onto a triangular mesh representation of a terrain model derived from LOLA 60m/pixel topography (Figure 2), incorporating effective field-of-view (EFOV) considerations [5].

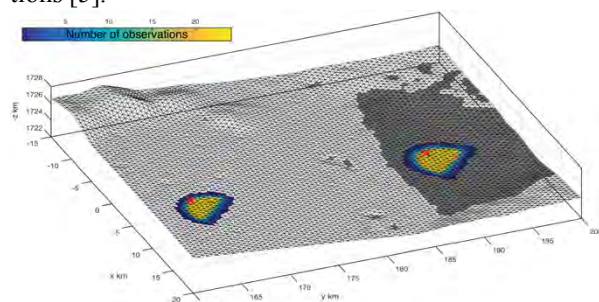


Figure 2: Cumulative diviner ch. 9 EFOVs ray-traced onto terrain model in Amundsen crater for NPSR (left, orbit 30516) and PSR (right, orbit 34194) targets. The PSR is grayed and red crosses mark target centers. For these orbits, mean boresight emission angles w.r.t. lunar sphere are 36.3° and 28.9° for NPSR and PSR targets, respectively. The vast majority of observations are almost nadir emission angles (< 5°).

Radiance received in a channel, c , is described by: $\mathcal{R}_c = \int \epsilon(\nu) f_c(\nu) B(T_s, \nu) d\nu$. Where $f_c(\nu)$ and $\epsilon(\nu)$ are the quantum efficiency and emissivity at frequency ν , respectively, and B is the black body radiance emitted at frequency ν , by a surface of temperature, T_s . This for-

mulation ignores emission angle effects, which are unimportant for night observations. For fixed T_s and known f_c , only emissivity varies. We select data from Diviner channels 7 and 8, 9; which are sensitive to photons between ~ 25 -41, 50-100 and 100-400 μm respectively, and most representative of surface brightness temperatures between 69-178, 43-69, and $< 43\text{K}$ respectively [6]. These data provide sufficient spectral coverage of radiance emitted at the expected nighttime temperatures (Figure 3).

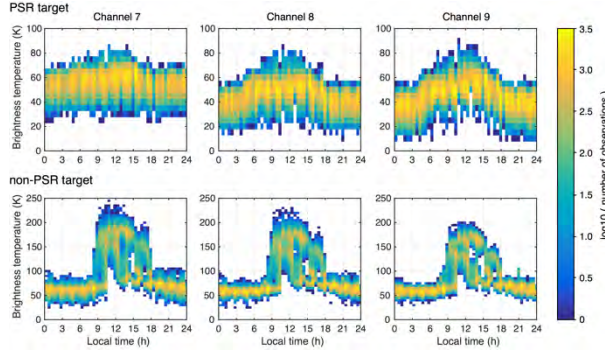


Figure 3: brightness temperatures observed for PSR (top) and NPSR (bottom) targets between Jul. 2009 – Aug. 2017) plot over local mean solar time (LMST).

We estimate the surface kinetic temperature by retrieving bolometric brightness temperature, T_{BOL} , for each terrain element where observations in all 3 channels are present. Therefore, using each observed terrain element in each orbit swath, i.e. triangle in the DEM, and over many orbits, we generate a large list of data points to populate a parameter space with dimensions: T_{BOL} , \mathcal{R}_7 , \mathcal{R}_8 , \mathcal{R}_9 , local time and emission angle. We model the band ratio $\mathcal{R}_{8/9}$ as a function of surface temperature (Figure 4), because these long wavelength channels are sensitive to PSR-relevant temperatures.

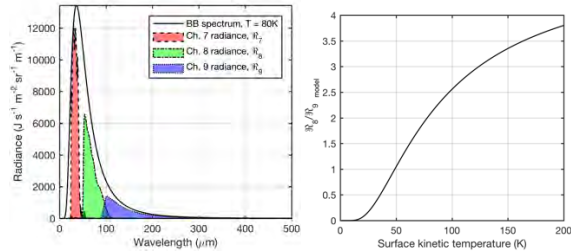


Figure 4: Left – Example of integration of quantum efficiency over wavelength $f_c(v)$ for Diviner channels 7, 8 and 9 beneath 80K Planck function to model expected signal at this temperature. Right – Ratio of radiance received in channels 8 and 9 ($\mathcal{R}_{8/9_{\text{model}}}$) expected as a function of surface temperature.

This model serves as an instrumental correction, and comparison of it to the observed $\mathcal{R}_{8/9}$ for each target allows us to plot the tentative signature of changes in apparent emissivity as a function of surface temperature (Figure 5), without assuming a value for emissivity.

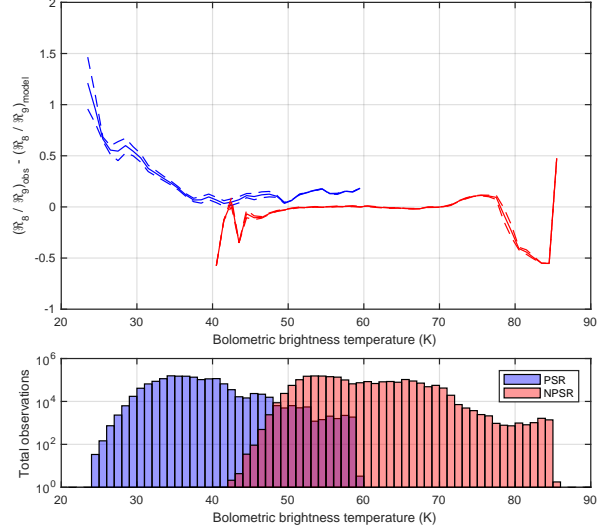


Figure 5: Band ratio model vs observations $\pm 1\sigma$ over T_{BOL} .

Discussion: The NPSR target is very well predicted by the bandpass model that assumes invariate relative emissivities, implying there is little difference between effective emissivities of channels 8 and 9 for the NPSR target in the 50-70K temperature regime. A small upturn around 75K and subsequent dramatic downturn from $\sim 77\text{K}$ upwards both coincide with reduced numbers of observations, and therefore we do not interpret these features as having significant physical meaning. The PSR target indicates a statistically significant increase from 40 to 30K, implying the model over-predicts $\mathcal{R}_{8/9}$; meaning channel 8 emissivity increases relative to 9 (or 9 lowers rel. to 8) at very low temperatures. We also find that $\mathcal{R}_{8/9}$ does not depend significantly on local time (i.e. differential nighttime cooling rates) or emission angle (i.e. non-lambertian emission).

Conclusions: The radiance ratio between Diviner channels 8 and 9, when corrected for known instrumental effects, indicates a temperature dependance in apparent emissivity in the far-IR, for a permanently shadowed target in Amundsen crater. These differences are not observed for a partially illuminated target. Possible instrumental and noise effects remain under investigation. We cannot exclude effects of temperature dependant thermal conductivity [7, 8] and differential gradients in thermophysical properties due to surface layers, possibly mediated by surface volatiles suggested in other studies.

References: [1] Marzarico et al., (2011), *Icarus* 211, p. 1066-1081. [2] Fisher, E. A. et al. (2017), *Icarus* 292, p. 74-85. [3] Gladstone, G. R. et al. (2012), *J. Geo. Res.* 117, E00H04. [4] Hayne, P. O. et al. (2015), *Icarus* 255, p. 58-69. [5] Williams, J.-P. et al., (2016), *Icarus* 273, p. 205-213. [6] Paige D. A. et al. (2010), *Space Sci. Rev.* 150, p. 125–160. [7] Woods-Robinson, R. et al. (2016) AGU, Abs. P21A-2077. [8] Siegler, M. A. et al. (2016) AGU, Abs. P24A-05.

Penetrator-deployed mass spectrometers for volatiles analysis at the moon

S Sheridan¹, S. Barber¹, A. D. Morse¹. ¹The Open University, Milton Keynes, MK7 6AA, UK (simon.sheridan@open.ac.uk),

Introduction: The polar regions of the Moon have long been known to be possible traps for solar system volatiles due to the low temperature of permanently shadowed areas. These permanently shadowed regions are cold enough to store any volatiles that enter them [1,2]. Volatiles trapped there are of interest because they record those released from the interior of the Moon during its geologic evolution, plus species derived from the solar wind, cosmic dust, and comet/asteroid bombardment. Therefore such PSRs preserve a record of the evolution of the Moon, the history of the sun, and the nature of comets/asteroids.

Arguably the most compelling evidence for lunar polar volatiles comes from the Lunar Crater Observation and Sensing Satellite (LCROSS) mission [3] where an un-instrumented spent upper rocket stage was impacted into the permanently shadowed Cabeus crater near the lunar south pole. The resulting impact was observed by instruments on LCROSS, and the results led to the deduction that the concentration of water ice at the impact site was 5.6 ± 2.9 % by mass [4]. However, many unanswered questions remain about the L-CROSS observations and arguably the next stage in understanding polar volatiles is to determine the species and their form and distribution (horizontally and vertically) through in-situ measurements. It is therefore natural that mass spectrometer based instruments will form the integral future payloads.

Penetrator deployment systems: In the near future the ESA PROSPECT package which is proposed for the Luna-27 lander [5] will perform in-situ volatile extraction and characterisation on the surface of the moon. However, PROSPECT is a complicated package and by virtue of performing its soft landing it may contaminate or modify its environment. In contrast, penetrators (Figure 1) are small probes that offer the opportunity to gain access to surface and sub-surface material at high-speed from orbit [6] without the need for drilling or excavation equipment or at low-speed from soft landers [7]. Multiple penetrators further offer geographically spaced investigations and mission redundancy.

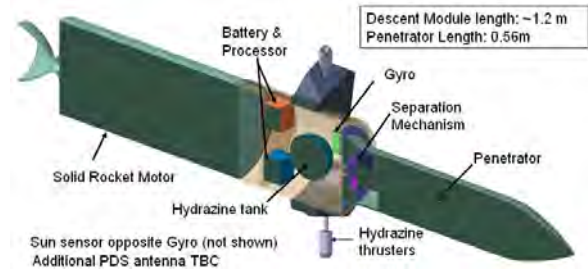


Figure 1: High-speed penetrator de-orbit and ejection system

Penetrator deployed mass spectrometers: The Ptolemy [8,9] Ion Trap mass spectrometer (Figure 2), is on-board the European Space Agency's Philae lander and returned the first in-situ volatile measurements from the surface of a comet in 2014. Due to its simple and rugged design, this type of instrument is well suited for penetrator deployment platforms. An impact tolerant version of the Ptolemy mass spectrometer has been developed by The Open University. The instrument will allow in-situ volatile characterisation following penetrator deployment. Figure 3 shows the prototype high-speed compatible instrument and a miniaturised 30 mm diameter instrument for accommodation in a low-speed ground penetrating mole device.

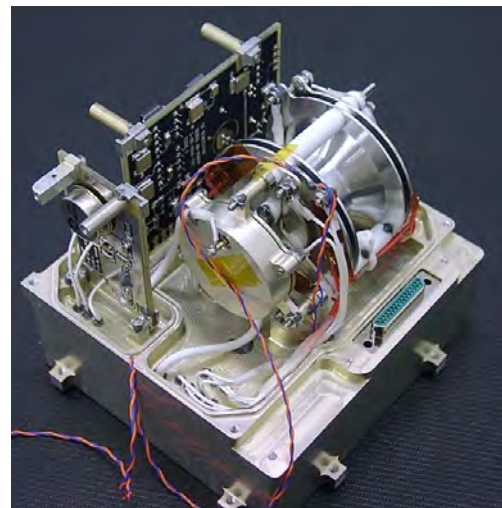


Figure 2: The Ptolemy Ion Trap Mass Spectrometer instrument



Figure 3: (left) The impact tolerant penetrator deployable mass spectrometer (right) the mole deployable mass spectrometer

Impact testing: High-speed testing of the mass spectrometer has been performed under a UK-led penetrator testing programme. The objective of these tests was to demonstrate survivability of the penetrator shell and to assess the impact on instrument sub-systems. The impact tolerant ion trap mass spectrometer was part of the payload. An Impact speed of 310 ms^{-1} was achieved with a solid rocket accelerated instrumented penetrator (Figure 4). A Penetration depth of 3.9 m into a sand target was achieved with substantial ablation to nose and belly (Figure 4)

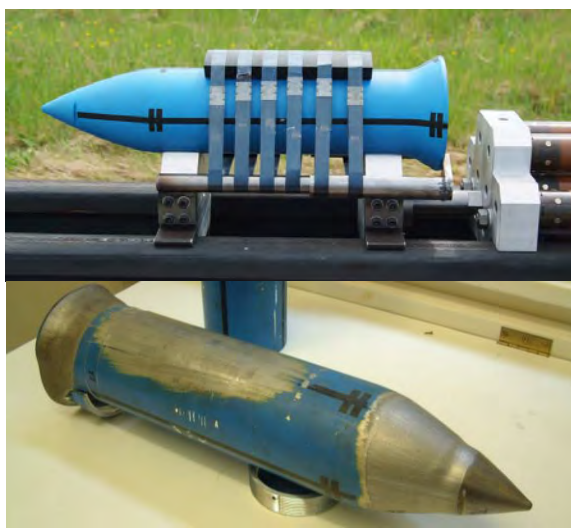


Figure 4: (Top) Instrumented penetrator prior to and (bottom) post impact penetrator shell

Results: The impact tolerant mass spectrometer survived an impact event of approximately 20000 g. Mass spectrums of PFTBA reference compound and Xenon (Figure 5) at a partial pressure of 1×10^{-7} mbar are shown following the impact testing.

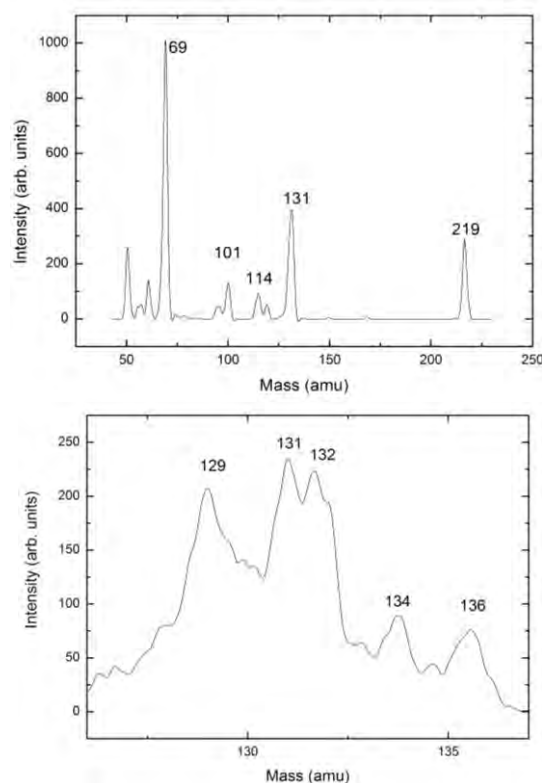


Figure 5: (Top) mass spectra of PFTBA reference compound and (bottom) Xenon

Future Work: The mass spectrometer instrument has been re-designed and miniaturised further for incorporation into a sub-surface penetrating mole device. Future testing will be carried out with low-speed mole penetrators to investigate volatile content with depth of lunar analogues

Summary: A rugged mass spectrometer has been developed, impact tested and shown to survive the forces consistent with deployment in high-speed penetrator missions such as L-DART [10]. Deployment by penetrators, either high speed or low-speed opens up the future possibility of accessing regions of the moon such as PSRs that are currently inaccessible to soft landers.

References: [1] Paige et al. (2010) *Science*, 330, 6003, 479-482. [2] Vasavada et al., (1999) *Icarus* 141: 179-193. [3] Colaprete, A. et al. (2012) *Space Sci. Rev.* 167: 3. [4] Colaprete et al. (2010) *Science*, 330, 463-468. [5] Carpenter J. et al. (2017) *European Lunar Symposium 2017*. [6] Smith et al., (2009) *Exp Astron.* 23:711-740. [7] Richter et al., (2001) *European Exo Astrobiology Workshop 2001*. [8] Todd et al. (2007) *Journal Of Mass Spectrometry*. 42 (1):1-10. [9] Wright et al., (2007) *Space Science Reviews* Volume 128, Issue 1-4, pp. 363-381. [10] Barber et al. (2018) *ELS 2018*

SOLAR SINTERING OF LUNAR REGOLITH FOR SHIELDING HABITATS ON THE MOON.
M.Sperl¹, A.Meurisse¹, M. Fateri¹, O. Lopez¹, and the RegoLight Consortium, ¹Institute of Materials Physics in Space, German Aerospace Center DLR, 51170 Cologne, Germany, Space Applications Services, Comex, Bollinger + Grohmann, Liquifer Systems Group.

Introduction: Additive Manufacturing (AM) technology is one of the most promising manufacturing techniques in the construction of a Moon village. Recent studies such as contour crafting, mixing regolith with a binder [1-2] as well as laser sintering of regolith simulant [3] proved the feasibility of AM for lunar habitats construction. The H2020 project RegoLight targets existing solar sintering techniques to reach a Technology Readiness Level (TRL) of 5 in solar based AM. In the frame of RegoLight, JSC-2A lunar simulant is sintered under ambient and vacuum conditions. The sintering results are analysed and used in a construction and architecture engineering approach to design a proper building element, habitat design and a mission scenario.

Solar sintering: Solar sintering is a cost effective process when aiming the habitat constructions. Within this project, a solar 3D printing process was developed at DLR-Cologne. A solar simulator was used in order to enable 3D printing of interlockable building elements out of JSC-2A lunar simulant under ambient and vacuum conditions, as shown in Fig. 1.

Concurrently, a mobile printing head was developed to sinter interlocking building elements using the actual sunlight.

3D printed samples were characterized mechanically and the analysed data was used to refine the design of the interlockable building element for a lunar application. An example of solar printed geometry under ambient condition is shown in Fig. 2.

Scenarios: The designed study aims at building a bearing structure for shielding a pressurised inflatable habitat from space radiation and meteorites as shown in Fig. 3. The intended structure does not require any scaffolding and is made of solar sintered interlockable building elements. This technology could also be used for paving a road or a launch-pad.



Fig. 1: Solar 3D printed setup for vacuum printing



Fig. 2: Solar 3D printed interlocking element

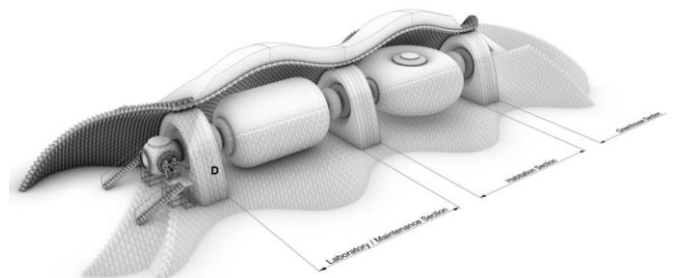


Fig.3: Inflatable lunar habitat and its shield made of 3D-printed interlockable building elements.

References:

- [1] Khoshnevis B. et al. (2005), *43rd AIAA ASM*.
- [2] Cesaretti G. et al. (2014), *Acta Astronautica*, 93, 430–450.
- [3] Fateri M. et al. (2015), *Int. J. Appl. Ceram. Technol.*, 12 [1] 46–52.

INVESTIGATING RECENT SURFACE CHANGES WITH TEMPORAL IMAGE PAIRS AND PHOTOMETRIC SEQUENCES. E. J. Speyerer¹, R. V. Wagner¹, R. Z. Povilaitis¹, A. K. Boyd¹, M. S. Robinson¹, and B. W. Denevi², ¹School of Earth and Space Exploration, Arizona State University, Tempe, AZ, ²Planetary Exploration Group, Johns Hopkins University Applied Physics Laboratory, Laurel, MD.

Introduction: The Lunar Reconnaissance Orbiter (LRO) extended mission is enabling the discovery and investigation of recent surface changes. An initial investigation led to the discovery of over 200 newly formed impact craters and 47,000 secondary surface disturbances and unresolved primary impact craters [1]. Additional temporal observations and photometric sequences acquired during the Cornerstone Mission (Sept 2016-present) are enabling us to further study these new surface features and provide insight into the cratering process and recent mass wasting events.

Temporal Imaging: The Lunar Reconnaissance Orbiter Camera (LROC) consists of a single Wide Angle Camera (WAC) and two Narrow Angle Cameras (NACs). We can identify new surface features by comparing images that cover the same surface area with nearly identical lighting conditions. We compared WAC global mosaics captured between April 2012 and January 2016 to identify several primary impact craters ranging in size between 30 and 70 m in diameter. While these craters are smaller than a single WAC pixel, the disturbance around each crater extends several km in many cases allowing us to locate them and target NAC images to confirm the formation and gather crater size statistics.

Direct comparisons of NAC images to other NAC images with similar lighting conditions (incidence angle difference $< 3^\circ$) enables us to identify hundreds of additional craters down to the resolution limit of the NAC (several meters). During the initial study [1], NAC temporal image pairs had an average time difference between observations of 1.3 years. Due to the progression of the orbit and the illumination environment, LROC started collected temporal pairs in November of 2017 with a baseline of 7.3 years. The longer baseline increases the odds of a surface change occurring over the imaged terrain and improves our coverage statistics. Additional long baseline temporal observations between 7 and 10 years will continue to be acquired during the third year of the Cornerstone Mission and the next Extended Mission.

Temporal ratio images created by dividing the after image by the before image are used to identify changes to the surface reflectance. Because the lighting and viewing geometries are similar and the images are spatially registered, the values in the temporal ratio image are close to one except in cases where a reflectance change has occurred on the surface, such as a ray forming from a new impact.

Photometric Sequences: Once a prominent new surface feature is discovered, we can target follow-up observations. For a select number of the larger, newly formed impact craters (> 30 m), we are targeting photometric sequences and geometric stereo pairs. Each month LROC can observe the newly formed crater under a different illumination environment. By comparing reflectance measurements from images acquired over many months, we can analyze the phase curve of small regions of the surface around the site. To reduce the effects of varying incidence angle, we can also target photometric sequences where images of the site are acquired on consecutive orbits (phase and emission angles vary, incidence angle remains nearly constant). In addition, sometimes as part of the same sequence, a NAC geometric stereo pair is collected. These stereo observations allow us to create digital terrain models (DTMs) to examine the topography of the site [2]. The DTMs can also be used to calculate the incidence and emission angles relative to local topography, thus allowing the effects of topography to be removed when applying a photometric correction. With the sum of these observations, we can account for the dependence of reflectance on the observational geometry (incidence, emission, and phase) and investigate how the physical properties of the regolith (such as grain size, roughness, and porosity) affect the way light is reflected [e.g., 3].

Newly Formed Impacts: To date, we have discovered over 300 newly formed craters using LROC temporal imaging. Temporal image ratios of the before and after images reveal up to 4 reflectance zones around the new impact craters [1, 4]:

- Proximal high reflectance zone (PHRZ)
- Proximal low reflectance zone (PLRZ)
- Distal high reflectance zone (DHRZ)
- Distal low reflectance zone (DLRZ)

These changes in the surface reflectance are caused by exposure of immature regolith as well as changes in the regolith properties. In addition, phase ratio images, which are collected as part of a photometric sequence, are created by taking the ratio of a low phase image over the high phase image with similar incidence angle (i.e., $p(g_1)/p(g_2)$; where $g_1 < g_2$ and $i_1 \approx i_2$) [5]. These phase ratio images allow one to assess the slope of the phase function and compare it to the surrounding, undisturbed regolith.

Figure 1 shows an example of a temporal ratio image and phase ratio image of a new 26 m crater whose impact flash was observed on Earth on 11 September 2013 [6]. In the temporal ratio, a PHRZ

and PLRZ is visible immediately adjacent to the crater. Both proximal regions in the phase ratio image appear brighter than the background, indicating a steeper phase function between 31° and 64° . In addition, there is no clear differentiation in the phase ratio image between the two distinct proximal zones visible in the temporal ratio image. The PHRZ and PLRZ are interpreted to be the immature and mature material (respectively) of the continuous ejecta blanket [1]. The steeper phase function indicates increased backscattering that could be caused by increased surface roughness. Additional bright rays in the phase ratio image extend several km from the impact site indicating increased backscattering and roughening of the regolith or an increase in the local porosity. Some of these rays correspond to the DLRZ in the temporal image pair that Speyerer et al. [1] interpret to be caused by sparse ballistic sedimentation from the primary impact event.

Recent Mass Wasting Events: Temporal image pairs have also helped us identify recent mass wasting events. Some of the landslides we identified were clearly the result of a new impact crater forming on a steep slope and causing a cascading event (Figure 2). Others show no evidence of recent impacts and originate from multiple points along the same slope face (Figure 2). These latter events could be caused by moonquakes or a seismic event caused by a nearby impact. Further mapping and classification of these mass wasting events will help us analyze the distribution and see if any correlate to hotspots for seismic events observed during the Apollo program or nearby scarps [7].

From the temporal ratio images, we can measure the extent and locate the origin of the flow. Additional geometric stereo observations enable us to measure the slopes encountered and how they compare to the angle of repose on the Moon [8]. Photometric sequences and phase ratio images indicate increased surface roughness and/or increased porosity along the flow, which is reasonable for a recent event of this type.

Ongoing work: Additional observations will enable more rigorous analysis of the phase function observed in the four different reflectance zones documented in temporal ratio images. This will help us better understand the regolith properties and the effect these events have on the regolith gardening and weathering of the lunar surface.

References: [1] Speyerer et al. (2016) *Nature*, 258, 215-218. [2] Henriksen et al. (2017) *Icarus*, 283, 122-137. [3] Hapke (2012) *Theory of Reflectance and Emittance Spectroscopy*. [4] Robinson et al. (2015) *Icarus*, 252, 229-235. [5] Kaydash (2011) *Icarus*, 211, 89-96. [6] Madieto et al. (2014) *Mon. Not. R. Astron. Soc.* 439, 2364-2369. [7] Watters et al. (2017) *LPS XLVIII*, Abstract #2569. [8] Wagner et al. (2013) *LPS XLIV*, Abstract #2924.

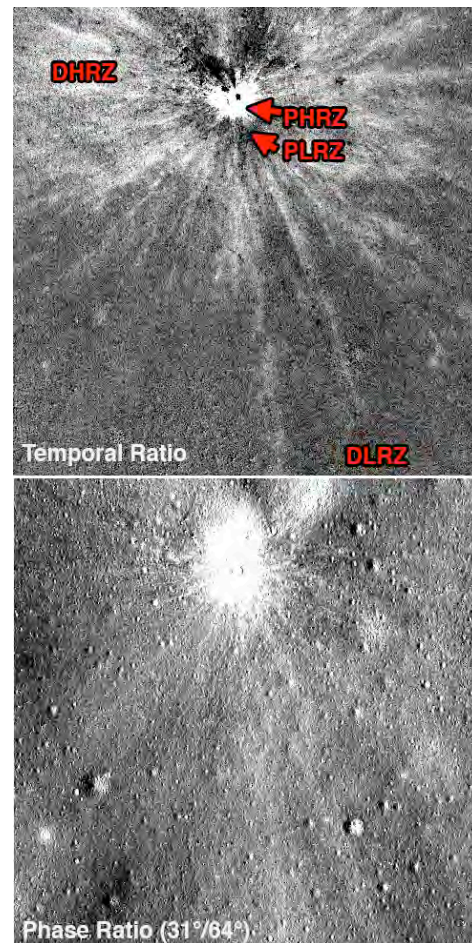


Figure 1- (Top) Temporal ratio image created by taking the ratio of M1149637354LR (2014-075) and M1119014742LR (2013-086) of a new 26 m crater. (Bottom) Phase ratio image created by taking the ratio of M1151986536LR ($i=46^\circ$, $e=17^\circ$, $g=31^\circ$) with M1152000776LR ($i=44^\circ$, $e=21^\circ$, $g=64^\circ$). Each image is 1300 m across.

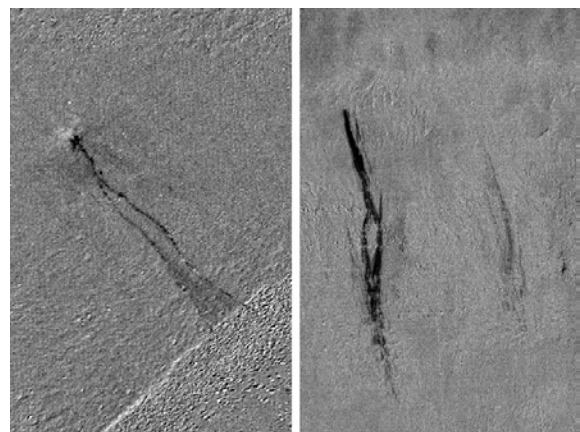


Figure 2- Example of two recent mass wasting events discovered with NAC temporal imaging. A small impact crater is visible at the top of the 350-m landslide on the left while no visible craters are seen near the origins of the landslides on the right, with the longest landslide measuring 1200 m. Both examples shown are temporal image ratios (After/Before).

ASSESSMENT OF A HIGH-ENERGY ORIGIN OF THE MOON FROM METAL-SILICATE PARTITIONING OF SIDEROPHILE ELEMENTS AT HIGH TEMPERATURES. E.S. Steenstra^{1,2}, Y. Fei², S. Matveev³, J. Berndt⁴, S. Klemme⁴, W. van Westrenen¹ ¹Faculty of Science, Vrije Universiteit Amsterdam, the Netherlands ²The Geophysical Laboratory, Carnegie Institution of Science, Washington D.C., USA ³Faculty of Geoscience, Utrecht University, the Netherlands ⁴Institute of Mineralogy, Muenster University, Germany

Introduction: Constraints on the thermal regime during lunar core-mantle differentiation are of great importance for lunar chemical and thermal evolution models and provide boundary conditions for lunar formation models [1-3]. It is now well established that the vast majority of both volatile and refractory siderophile elements are depleted in the lunar mantle relative to bulk silicate Earth (BSE), suggesting these elements partitioned into the lunar core [4-8]. Previous studies have shown that the metal-silicate partitioning behavior of Ni, Co, Cr and V is mainly a function of fO_2 , pressure (P), temperature (T) and metal composition [9-13]. Increasing geochemical evidence points to highly similar compositions of the bulk Moon and the BSE [3,14]. Assuming that the Ni, Co, Cr and V budget of the BSE is representative of the bulk Moon, Ni and Co behave far too siderophile at low T (i.e. along the mantle liquidus), relative to the inferred lunar mantle depletions [9-13,15-19]. At these same conditions, V and Cr behave insufficiently siderophile. Different fO_2 during lunar core formation cannot resolve this discrepancy because it will affect all four elements in a similar way. Although S in metal decreases the siderophile behavior of Ni, Co and increases the iron-loving tendencies of V, Cr [12,19], recent studies on S abundances in the lunar mantle in conjunction with mass balance models have indicated that the lunar core is S-poor [5,20-22].

Current lunar formation models predict that T during and shortly after the Moon-forming impact ranged anywhere between >3000–7000 K [1-2,23-25]. Lunar core formation at very high T may therefore be reflected by the unique lunar mantle depletion patterns of Ni, Co, Cr, V, as hypothesized by ref. [6]. This latter hypothesis should also be consistent with the observation that Mn is not depleted in the lunar mantle relative to BSE [16]. To test this hypothesis, high P - T experiments were conducted using a primitive lunar silicate melt to systematically study the effects of T on the metal-silicate partitioning behavior of many siderophile elements, including Ni, Co, Cr, V, and Mn. These new results can be compared with our previous partitioning results obtained at lower T using the same capsule type and starting compositions [8,12,26].

Methods: High P - T experiments were performed in a 1500-ton multi-anvil apparatus at the Geophysical Laboratory, using 18mm edge length Cr-doped MgO or ZrO₂ octahedra. Outer ZrO₂ sleeves were used as ther-

mal insulators in the MgO+Cr assemblies. All experiments were conducted at 4 GPa between 1973 – 2873 K at 100 K intervals. All experiments were conducted using C heaters, MgO spacers and 1 or 1.6 mm I.D. MgO capsules. Temperatures were measured up to 2473 K with a type C thermocouple and higher run T were constrained by linearly extrapolating well defined T – power curves obtained at 4 GPa. Starting compositions consisted of a synthetic equivalent of the A15 green glass [27] and Fe powder doped with several trace elements including Ni, Co, Cr, V and Mn. Run times varied between 15 min at 1873 K to 20s at 2873 K, which has been shown to be sufficient for metal-silicate equilibrium [28,29]. Polished experimental run products were analysed using EPMA at the Geophysical Laboratory and Utrecht University.

Results: Fig. 1 shows an example of a typical run product. Experiments yielded significant amounts of magnesiowustite crystals and substantial MgO enrichment of the silicate melt consistent with previous work [28,29]. These enrichments resulted in compositions that are similar to inferred bulk silicate Moon compositions [e.g. 2,5]. The fO_2 of the various runs are very similar and close to the lunar fO_2 range.

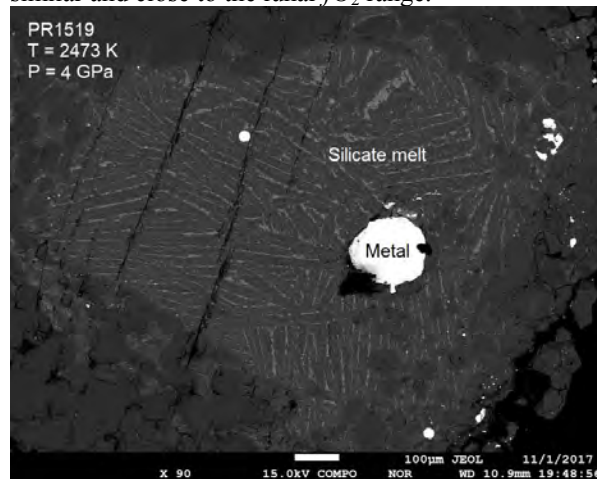


Fig. 1 BSE image of a typical run product.

Metal-silicate partitioning data was treated by consideration of the equilibrium constant K_{app} [9]:

$$\log K_{app} = \log \frac{(x_{FeO}^{silicate})^{n/2} \cdot (x_M^{metal})}{(x_{MO_{n/2}}^{silicate}) \cdot (x_{Fe}^{metal})^{n/2}} + \log \frac{(y_M^{metal})}{(y_{Fe}^{metal})^{n/2}} + \log \frac{(y_{FeO}^{silicate})^{n/2}}{(y_{MO_{n/2}}^{silicate})}$$

where the first term on the right-hand side is the exchange coefficient or K_M^D . The second and third terms relate to the activity coefficients of $M(O_{n/2})$ and $Fe(O)$. Activity coefficients were calculated using the metal activity calculator [13].

Fig. 2 shows preliminary $\log K_{app}$, Mn, Cr, Co values for the A15 green glass composition of this study and our previous work obtained at 1-2.5 GPa, as a function of T . The K_{app} values of Cr and Mn increase strongly with T , whereas those for Co decrease with T . These trends are in agreement with previous work [e.g. 11,13]. Different MgO contents cannot account for the dependency of K_{app} Cr and Mn on T , as experiments with overlapping silicate melt MgO contents still yield an increase with T . For Co, such conclusions cannot be drawn as of yet due to lack of data.

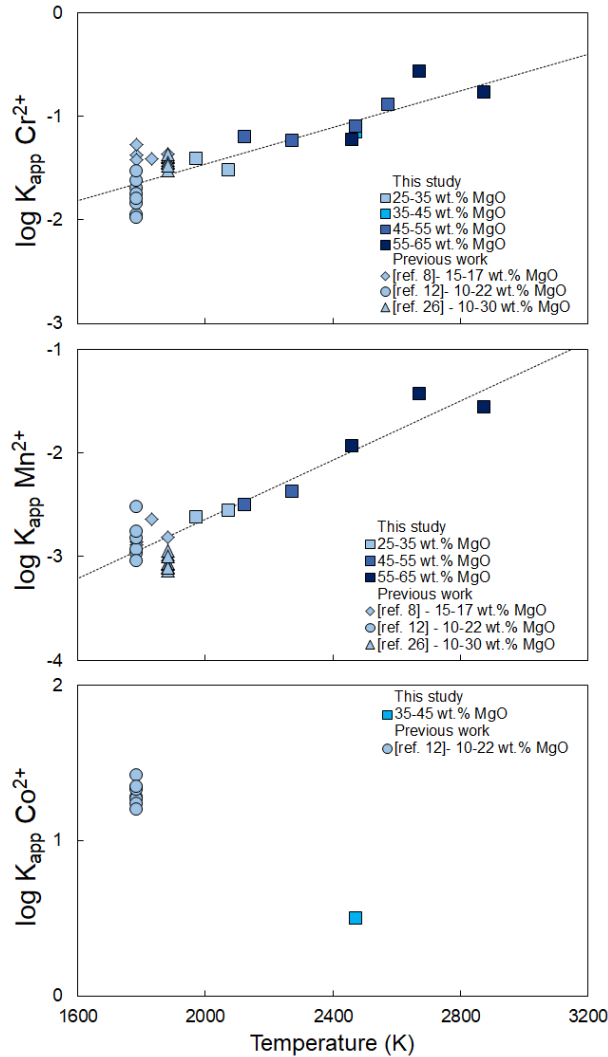


Fig. 2 K_{app} values from this study (squares) and previous work (obtained at 1-2.5 GPa) as a function of T . Also indicated are the relative MgO contents of each experiment. Lines are linear fits through data of this study only.

Finally, we found no dependency of fO_2 with T , consistent with previous work [30].

Discussion: Our preliminary results show that T indeed significantly increases the siderophile behavior of Cr, Mn. In conjunction with the negative T effects on partitioning of Co (and likely Ni), the lunar mantle depletion systematics may suggest high- T core formation in the Moon, providing tangible evidence for a giant-impact origin of the Moon. This can be fully assessed once additional analytical results are available.

Outlook: We aim to reconcile these results with new high- T data for volatile siderophile elements (VSE) at constant P . Additional experiments are currently being analysed and their results will be reported at the meeting, as well as trace element concentrations which will be measured using LA-ICP-MS at Muenster University, Germany.

References: [1] Canup (2012) *Science* 338, 1052 [2] Hauri et al (2015) *EPSL* 409, 252 [3] Zhang et al (2012) *Nat Geosci* 5, 251 [4] Righter (2002) *Icarus* 158, 1 [5] Rai & van Westrenen (2014) *EPSL* 388, 343 [6] Steenstra et al (2016) *EPSL* 441, 1 [7] Steenstra et al (2017) *AM* 102, 92 [8] Steenstra et al (2017) *Sci Rep* 7, 14552 [9] Siebert et al (2011) *GCA* 75, 1451 [10] Thibault & Walter (1995) *GCA* 59, 991 [11] Kegler et al (2008) *EPSL* 268, 28-40 [12] Steenstra et al (2017) *GCA* 212, 62 [13] Wade & Wood (2005) *EPSL* 236, 78 [14] Sossi & Moynier (2017) *EPSL* 471, 125 [15] Delano (1986) *Origin of the Moon* 231 [16] Ringwood et al (1986) *EPSL* 81, 105 [17] Jones & Palme (2000) *Origin of the Earth & Moon* 197 [18] McDonough & Sun (1995) *Chem Geol* 120, 223 [19] Wood et al (2014) *GCA* 145, 248 [20] Righter et al (2017) *EPSL* 463, 323 [21] Ding et al (2017) *GCA* 222, 319 [22] Steenstra et al (2018) *This meeting* [23] Lock et al. (2016) *LPSC #2881* [24] Wang & Jacobsen (2016) *Nature* 538, 487 [25] Čuk & Stewart (2012) *Science* 338, 1047 [26] Seegers et al (2017) *LPSC #1053* [27] Delano (1986) *JGR* 91, 201 [28] Tuff et al (2011) *GCA* 75, 673 [29] Ricolleau et al (2011) *EPSL* 310, 409 [30] Clesi et al (2016) *GCA* 192, 97

EVIDENCE FOR A SULFUR-DEPLETED LUNAR INTERIOR FROM THE SOLUBILITY OF S IN LUNAR MELTS. E.S. Steenstra^{1,2}, A.X. Seegers¹, J. Eising¹, B.G.J. Tomassen¹, F.P.F. Webers¹, J. Berndt³, S. Klemme³, S. Matveev⁴, W. van Westrenen¹ ¹Vrije Universiteit Amsterdam, the Netherlands, ²The Geophysical Laboratory, Washington D.C., United States, ³Institute of Mineralogy, Münster University, Germany ⁴Faculty of Geosciences, Utrecht University, the Netherlands (e.s.steenstra@vu.nl)

Introduction: S is a volatile element and understanding its origin, abundance, and distribution in planetary interiors is important due to the effects of the S cycle on properties of planetary crusts and atmospheres. In case of the Moon, constraining S abundances in lunar reservoirs is important to constrain the early volatile budget of, and volatile fluxes in the Earth-Moon system [1-5]. One key aspect of the lunar sulfur cycle relates to the question: was the lunar interior ever saturated in sulfide minerals? Previous studies focused mostly on determination of the S content at sulfide saturation (SCSS) for terrestrial magmas, which have distinctly lower Fe and Ti contents relative to their lunar counterpart. Only few studies determined the SCSS for some lunar melts compositions [6-8]. Determination of the SCSS for low- and high-Ti melts over a wide *P-T* and compositional range is required to assess if the source regions of lunar magmas sampled during the Apollo missions were sulfide saturated.

Methods: We quantified the SCSS for a suite of low- to high-Ti lunar melt compositions (A14 black and yellow glass, A15 green glass, A17 orange glass and a composition representative of late-stage lunar magma ocean (LMO) residual melt. The SCSS was determined as a function of *P* (1-2.5 GPa) and *T* (1683-1883 K) using a piston cylinder press at the VU high *P* laboratory. Sulfide mixtures consisted of FeS doped with 0.5 % of Se and Te. Experiments were predominantly conducted in C capsules within sealed Pt outer capsules. For these experiments, FeS powder was loaded in both the bottom and top of the C capsule to prevent significant Pt contamination [9]. Four experiments were performed in MgO capsules. Run durations varied between 30 – 120 minutes, shown to be sufficient to attain chemical equilibrium between sulfide-silicate [10]. Run products were measured for major elements with EPMA, whereas trace elements were measured with LA-ICP-MS at Münster University. The latter results were used to quantify the sulfide-silicate partitioning of 16 iron-loving elements, including Se, Te.

Results: Run products showed well-segregated sulfide blobs with a silicate melt that quenched to a heterogeneous-textured melt (high-MgO compositions) or a homogeneous glass. Some of the highest FeO-runs showed exsolved, minute FeS specks, consistent with sulfide saturation of the silicate melts [6]. Sulfides in most run products suffered no or very limited Pt contamination (<2 wt%).

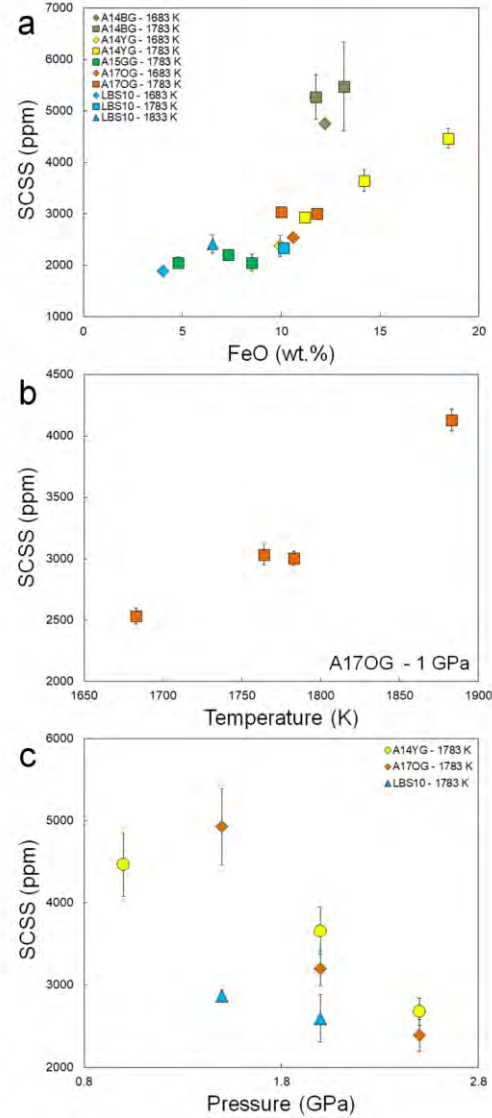


Fig. 1 SCSS versus (a) FeO at 1 GPa (b) *T* and (c) *P*.

Our new experimental data confirm previous observations of the increase of SCSS with FeO at > 5 wt% FeO and *T* and the decrease of SCSS with *P* [6,9] (Fig. 1).

Our new SCSS data is combined with previous data for high FeO (> 5 wt%) (*N* = 337) silicate melts and regressed to the following equation to obtain a model for predicting SCSS for lunar melts [6,8,11]:

$$\ln[S]_{\text{SCSS}} (\text{ppm}) = A + \frac{B}{T} + \sum C_i X_i + D X_{\text{Fe}} X_{\text{Ti}} + E \frac{P}{T} + \ln X_{\text{FeS}}^{\text{sulfide}} + \frac{F}{T} (X_{\text{NiS}}^2 + X_{\text{NiS}} X_{\text{CuS}_{0.5}}) + \frac{G}{T} (X_{\text{CuS}_{0.5}}^2 + X_{\text{NiS}} X_{\text{CuS}_{0.5}}) + \frac{H}{T} (-X_{\text{NiS}} X_{\text{CuS}_{0.5}})$$

where $A-H$ are regression coefficients, T is temperature, X_i are the molar fractions of cations Si, Al, Fe, Ca, Mg, Ti and P is pressure in GPa. Terms $X_{\text{FeS}}^{\text{sulfide}}$, X_{NiS} and $X_{\text{CuS}_{0.5}}$ are included to include the effects of sulfide composition on SCSS [11] and are defined as molar fraction ratios $\text{Fe}/(\text{Fe} + \text{Ni} + \text{Cu})$, $\text{Ni}/(\text{Ni} + \text{Fe} + \text{Cu})$ and $\text{Cu}/(\text{Cu} + \text{Fe} + \text{Ni})$, respectively. Our new model predicts the observed effects from Fig. (1) and the negative effects of Cu and Ni in sulfide on the SCSS.

We use this model to calculate the SCSS values for the various lunar low- and high-Ti melts at their proposed multiple saturation points. For (near)-primary melts (volcanic glasses and A12-A15 low-Ti basalts, the measured S abundances [4,12-14] can more or less be directly to calculated SCSS values. These results are shown in Fig. 2a. We find – even after correcting for the maximum extent of inferred degassing [4,13] – that measured S abundances for all of these samples are up to several thousand ppm lower than the predicted SCSS value. Although Cu or Ni-rich sulfides yield lower SCSS values, the existence of such sulfides in their source regions are excluded from low Cu and Ni contents in these samples [15,16].

For more evolved melts such as the A17 high-Ti basalts, calculated SCSS values cannot be directly determined with measured S contents due to the possible effects of fractional crystallization. We therefore modelled the SCSS along the liquid line of descent (LLD) determined for high-Ti basalt 70017 [17] (Fig. 2b). Note that this approach should be considered to yield a lower estimate for the SCSS, as the LLD was determined at 1 atm and associated lower T , relative to the inferred MSP's of the A17 high-Ti basalts. Most of the S contents fall below the modeled SCSS field for stoichiometric FeS, suggesting these basalts were not sulfide saturated, even when the maximum extent of degassing is assumed [4]. Some of the most evolved basalts could have been sulfide saturated, but this is highly dependent of the P - T assumed for their formation.

Discussion: Our results provide solid evidence that the source regions of the volcanic glasses and low-Ti basalts were not sulfide saturated, unless the extent of S degassing has been underestimated by several orders of magnitude. However, such significant degassing is excluded from S isotope systematics of low and high-Ti basalts [4]. This shows that (highly) siderophile element depletions determined for the lunar mantle reflect a major sequence of metal segregation, i.e. core formation. Our results also provide additional evidence for the S-poor nature of the Moon [13] and its core [1,3]. It is also consistent with the observation that the lunar mantle depletions and ratios of S, Se, Te can be reconciled with formation of a S-poor lunar core in a fully molten Moon [2].

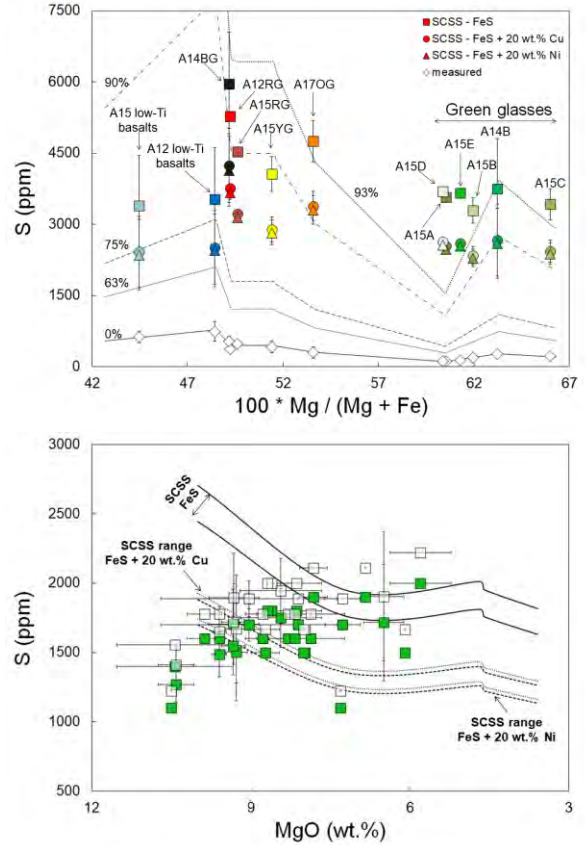


Fig. 2 (a) Modelled SCSS values for stoichiometric FeS (squares), FeS + 20 wt% Cu (circles) and FeS + 20 wt% Ni (triangles) for the different (near)-primary melts considered. Vertical lines represent different degrees of degassing **(b)** Modelled SCSS values for A17 high-Ti basalts along LLD of 70017. Open squares represent measured values corrected for 10% degassing [4]. Basalt data from [4,14].

References: [1] Righter et al (2017) *EPSL* 463, 1151 [2] Steenstra et al (2017) *Sci Rep* 7, 14552 [3] Steenstra et al (2017) *Am Min* 102, 92 [4] Wing & Farquhar (2015) *GCA* 170, 266 [5] Wang & Becker (2013) *Nature* 499, 328 [6] Ding et al (2018) *GCA* 222, 319 [7] Danckwerth et al (1979) *LPSC* 10th, 517 [8] O'Neill & Mavrogenes (2002) *J Pet* 43, 1049 [9] Wykes et al (2015) *J Pet* 56, 1407 [10] Kiseeva & Wood (2013) *EPSL* 383, 68 [11] Smythe et al (2017) *Am Min* 102, 795 [12] Delano et al (1994) *LPSC* 25, 325 [13] Hauri et al (2015) *EPSL* 409, 252 [14] Meyer (2011) Lunar sample compendium [15] Herzog et al (2009) *GCA* 73, 5884 [16] Steenstra & van Westrenen (2017) *ELS* DOI 10.1007/978-3-319-05546-6_76-1 [17] Rutherford et al (1974) *LPSC* 5, 69

ABUNDANCE AND ISOTOPIC COMPOSITION OF HYDROGEN AND CHLORINE IN APATITE FROM LUNAR METEORITE NWA 10989. A. Stephant¹, H. O. Ashcroft¹, M. Anand^{1,2}, X. Zhao¹, R.L. Korotev³, R.C. Greenwood¹, I.A. Franchi¹ and S. Strekopytov⁴. ¹School of Physical Sciences, The Open University, Milton Keynes, UK. ²Department of Earth Sciences, Natural History Museum, London, UK. ³Department of Earth & Planetary Sciences and McDonnell Center for the Space Sciences, Washington University, Saint Louis MO 63130. ⁴Imaging and Analysis Centre, The Natural History Museum, London, UK.

Introduction: NWA 10989 is a newly classified brecciated lunar meteorite of an intermediate type, based on its equal proportion of feldspathic and basaltic components [1,2]. These intermediate meteorites have FeO contents between 7-17 wt. %, and Al₂O₃ contents between 13-20 wt.%, and make up roughly 25 % of the lunar meteorites found on Earth [2]. The petrogenetic origin of these intermediate meteorites in the lunar crust is enigmatic and remains a puzzle for our understanding of the crustal evolution on the moon. A potential source region could be located near a boundary between feldspathic highlands and mare regions on the Moon. Chlorine and hydrogen isotopic ratio of NWA 10989 apatite, as well as its chlorine and hydrogen abundances, could provide insights into its origin on the Moon, as well as clues regarding the origin of lunar volatiles. Based on the combined data on H and Cl isotopic compositions of lunar apatites that have been reported to date, apatite in mare basalts generally show elevated δD ($> \sim 500\text{‰}$) [3,4] associated with a range of $\delta^{37}\text{Cl}$ of 0–15‰ [5,6]. On the other hand, apatite from the KREEP-rich, Mg- and alkali-suite lithologies from the lunar highlands have comparatively lower δD values ($< \sim 300\text{‰}$) [7,8] associated with higher $\delta^{37}\text{Cl}$ values ($> \sim 25\text{‰}$) [5,6]. Here we investigated the H and Cl isotopic values and abundances in apatite from this new lunar meteorite.

Methods: Cl abundance and $^{37}\text{Cl}/^{35}\text{Cl}$ isotopic composition were measured using the Cameca NanoSIMS 50L at the Open University (OU) using a protocol modified after [5] and [6]. Analyses were performed using a Cs⁺ primary probe current of 30 pA for ~ 5 minutes over $\sim 5 \mu\text{m} \times 5 \mu\text{m}$ areas. Secondary negative ions of $^{16}\text{OH}^-$, $^{18}\text{O}^-$, $^{19}\text{F}^-$, $^{35}\text{Cl}^-$, $^{37}\text{Cl}^-$ and $^{40}\text{Ca}^{19}\text{F}^-$ were collected simultaneously on electron multipliers. $^{16}\text{OH}^-$ was used to identify and avoid cracks or defects within the apatite crystals. Apatite Cl contents were calibrated using the measured $^{35}\text{Cl}/^{18}\text{O}$ ratios and the known Cl contents of terrestrial apatite standards which were set in an indium mount.

Hydrogen isotopes (D/H) and H₂O abundances were measured during a second session on the NanoSIMS. H, D and ^{18}O secondary ions were quantified using a Cs⁺ primary beam of ~ 500 pA. ^{13}C was also collected simultaneously to monitor possible contamination. The primary beam was rastered over a $10 \mu\text{m} \times 10 \mu\text{m}$ area but data were collected from

the central $5 \mu\text{m} \times 5 \mu\text{m}$ area during a total duration of ~ 20 min of analysis time. A H/O vs. H₂O calibration is used to calibrate H₂O concentrations for apatites, using the same standards as for chlorine. Background was monitored using nominally anhydrous, San Carlos olivine, and analyses were corrected accordingly. To avoid H contamination, analyses were performed with an analytical chamber vacuum of 4.5×10^{-10} T. The background for H₂O was estimated to be 13 ppm.

Both chlorine and hydrogen isotopes are expressed in delta notation (‰) following the equations: $\delta^{37}\text{Cl} = [(^{37}\text{Cl}/^{35}\text{Cl}_{\text{sample}}/^{37}\text{Cl}/^{35}\text{Cl}_{\text{ref}}) - 1] \times 1000$ and $\delta D = [(D/H_{\text{sample}}/D/H_{\text{SMOW}}) - 1] \times 1000$.

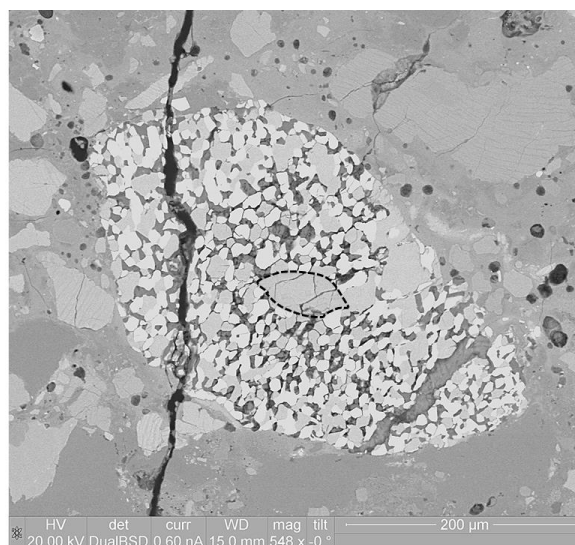


Figure 1: BSE image of an apatite (inside dashed outline) in a symplectite clast of NWA 10989.

Results : *Chlorine measurements* - 9 measurements were made on 6 apatite grains distributed throughout this meteorite matrix, except for one apatite which was located inside the symplectite clast (cf. Fig. 1). The matrix apatites show a limited range in $\delta^{37}\text{Cl}$ values between +14.4 ‰ and +18.7 ‰ with an average value of $+15.9 \pm 1.5$ ‰ (2SD). Cl contents vary between 1268 and 4884 ppm with an average of 2699 ± 1539 ppm (2SD). All the Cl results are displayed in Figure 2. The apatite grain inside the symplectite clast displayed a range in $\delta^{37}\text{Cl}$ and Cl contents. The core of the crystal exhibits $\delta^{37}\text{Cl}$ of 11.9 ± 0.9 ‰ and 2700 ± 200 ppm Cl, while the rim is more Cl rich (i.e. 6052 ± 627 ppm Cl), and shows a heavier $\delta^{37}\text{Cl}$ of 16.8 ± 1.5 ‰.

Hydrogen measurements - Hydrogen isotopic ratios and concentration were measured in 9 apatites (14 analyses in total) and results are presented in Figure 3. We measured the 6 same apatites analyzed for chlorine plus 3 more isolated apatite grains in the matrix. 7 of the 9 apatites exhibit relatively low δD , with values ranging from -423 ± 88 to 214 ± 91 ‰. Water content associated with these apatite grains show a narrow range from 262 ± 20 to 1583 ± 121 ppm H_2O . On the other hand, 2 apatite grains (4 analyses – apatite #1 and #10) show high water contents of 0.3 and 0.9-1 wt. % H_2O , respectively, along with the higher δD ever measured in a lunar meteorite apatite (from 406 ± 72 to 1006 ± 92 ‰). No spallation correction have been made on these analyses as the CRE age of NWA 10989 is not yet known. However, the relative large water content for most of the apatite should make any spallation correction almost negligible.

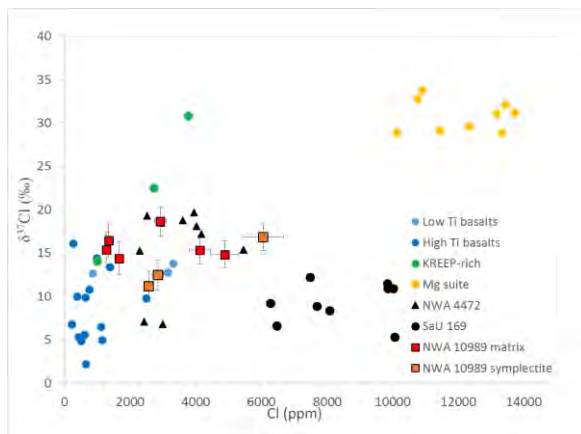


Figure 2 : $\delta^{37}Cl$ (‰) vs. Cl content (ppm) of NWA 10989 apatites, compared with literature data.[5,6]

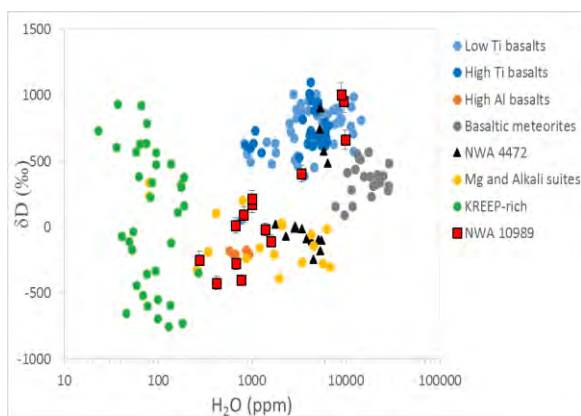


Figure 3 : δD (in ‰) vs H_2O content (ppm) of NWA 10989 apatites, compared with literature data. [3-5,7-8]

Discussion : In comparison to the Apollo samples [6], NWA apatite data exhibit slightly heavier $\delta^{37}Cl$ values compared to low Ti basalts, which averages at +13‰, along with higher Cl content in NWA 10989.

As such, the NWA apatite appear to be on a mixing line between apatites from basaltic and from Mg-suite material. Interestingly, these apatites exhibit similar Cl signature to another lunar meteorite NWA 4472 [5]. While this meteorite is also considered intermediate-iron breccia [2], its petrology differs from NWA 10989 as NWA 4472 is a KREEP-rich breccia [9].

The increase of Cl content from core to rim of the apatite in the symplectite is consistent with continued magmatic crystallization where Cl content increases due to its incompatibility in other crystallising phases. The slight increase of $\delta^{37}Cl$ observed between core and rim could be explained by magmatic degassing of metal chlorides, although the difference remains in the variation observed among apatites. The reason for heavy lunar $\delta^{37}Cl$ compared to terrestrial values was first suggested to be due to degassing of the lunar magmas [10]. More recently, several studies advocate for a mixing between 2 reservoirs: an elevated one (i.e. 25-30 ‰) from urKREEP reservoir and a lighter one (~ 0 ‰), representative of mare-basalt source regions [6,11].

In terms of hydrogen, the 7 apatites with lower δD values fall in the range of values measured either for Mg- and Alkali-suites or High-Al Apollo basalt [7-8]. Apatites #1 and #10 δD - H_2O systematics are in the range of what has been measured for Apollo mare basalts, similar to chlorine composition. Here again, the hydrogen inventory of NWA apatites is similar to NWA 4472 apatite [5]. Therefore, it seems likely that these apatites sampled the same reservoir. As a result, apatites of NWA 10989, as the rest of the mineralogy, are inferred to have sampled both highlands and mare-derived material. Some apatites, such as #10, may have sampled a reservoir similar to that for low-Ti basalts while the others appear to have sampled a low- δD reservoir similar to that proposed for Mg- and alkali-suite samples from the lunar highlands [8].

References:

- [1] Ashcroft H.O. et al. (2017) *LPSC 48th*, #1481.
- [2] Korotev E. F. et al. (2009) *Meteoritics & Planet. Sci.*, 44, 1287-1322.
- [3] Barnes J.J. et al. (2013) *Chem. Geol.*, 337-338, 48-55.
- [4] Tartese R. et al. (2013) *Geoch. et Cosmo. Acta*, 122, 58-74.
- [5] Tartese R. et al (2014) *Meteoritics & Planet. Sci.*, 49, 2266-2269.
- [6] Barnes J.J. et al. (2016) *Earth & Planet. Sci. Lett.*, 447, 84–94
- [7] Barnes J.J. et al. (2014) *Earth and Planetary Science Letters*, 390, 244-252.
- [8] Robinson K. et al. (2016) *Geoch. et Cosmo. Acta*, 188, 244-260.
- [9] Joy K.H. et al. (2008) *LPSC 39th*, #1132.
- [10] Sharp Z. (2010) *Science*, 329, 1050-1053.
- [11] Boyce J. et al. (2015) *Science Advances*, 1, 8.

REVISITING THE $^{40}\text{Ar}/^{39}\text{Ar}$ CHRONOLOGY OF LUNAR METEORITE NWA 773 PROVIDES NEW CONSTRAINTS ON ITS DIACHRONOUS GEOLOGIC HISTORY. M. M. Tremblay¹, B. E. Cohen^{1,2}, D. F. Mark^{1,3}, R. B. Ickert¹, and C. L. Smith⁴. ¹Scottish Universities Environmental Research Centre (SUERC), Rankine Avenue, East Kilbride, G75 0QF, UK (marissa.tremblay@glasgow.ac.uk), ²School of Geographical and Earth Sciences, The University of Glasgow, G12 8QQ, UK, ³Department of Earth & Environmental Science, University of St Andrews, KY16 9AJ, UK, ⁴The Natural History Museum, London, SW7 5BD, UK

Introduction: $^{40}\text{Ar}/^{39}\text{Ar}$ chronometry has been applied extensively over the last fifty years to study the geologic history of lunar materials. Specifically, $^{40}\text{Ar}/^{39}\text{Ar}$ data have been used to assess the timing of impact events that disturb this thermally-sensitive geochronological system, thereby providing absolute time constraints on relative crater counting chronologies [1]. Despite their widespread use, many lunar $^{40}\text{Ar}/^{39}\text{Ar}$ step-heating datasets exhibit complex behavior that precludes quantitative, statistically robust interpretations. This behavior may be associated with: (1) the presence and sometimes inaccurate accounting of multiple argon components, (2) partial resetting of the $^{40}\text{Ar}/^{39}\text{Ar}$ system during one or more impact events, (3) different thermal sensitivities and thermal histories recorded in multiphase, heterogeneous samples, or (4) some combination therein. Here, we demonstrate how problem (1) can be accounted for with new $^{40}\text{Ar}/^{39}\text{Ar}$ data from lunar meteorite NWA 773.

Previous chronometric constraints on the geologic history of NWA 773: NWA 773 comprises two lithologies: olivine-gabbro and regolith breccia. The regolith breccia component contains clasts of gabbro as well as of silica glass, pyroxene, and volcanic rocks. A weighted mean ^{207}Pb - ^{206}Pb baddeleyite age of 3115.6 ± 6.8 Ma (2σ , $n = 47$) was measured from the NWA 773 clan of meteorites; baddeleyite ages from gabbro and breccia components were indistinguishable [2]. A significantly younger Sm-Nd age of 2865 ± 31 Ma (2σ) was obtained for the gabbro portion of NWA 773 [3]. Fernandes et al. [4] conducted $^{40}\text{Ar}/^{39}\text{Ar}$ step heating experiments on both the gabbro and breccia components. In both cases they observed complex $^{40}\text{Ar}/^{39}\text{Ar}$ age spectra, with individual step ages ranging between 2000 and 5000 Ma and no statistically significant age plateau obtained.

Methods: We revisited the $^{40}\text{Ar}/^{39}\text{Ar}$ chronometry of NWA 773. Aliquots of pyroxene crystals and groundmass fragments from the breccia were neutron irradiated for 40 hours in the Cd-lined TRIGA reactor, Oregon State University. Argon isotopes were measured by step heating at SUERC on a MAP-215 sector-field mass spectrometer. We used an approach recently detailed by Cassata and Borg [5] to deconvolve the different components of argon (trapped, cosmogenic, radiogenic) in these neutron-irradiated experiments with independent knowledge of the cosmic ray exposure (CRE) age. Briefly, with independent constraints on the CRE

age we can subtract the fraction of ^{36}Ar that is cosmogenic from the total ^{36}Ar in each individual heating step. Then, by plotting cosmogenic-corrected $^{36}\text{Ar}/^{40}\text{Ar}$ as a function of $^{39}\text{Ar}/^{40}\text{Ar}$ for each heating step (i.e., an inverse isochron, Fig. 1), we can determine the $^{36}\text{Ar}/^{40}\text{Ar}$ of the trapped argon component (y-intercept) and both (1) determine the isochron age from the x-intercept, and (2) correct the individual step ages for trapped ^{40}Ar to obtain accurate plateau ages (Fig. 2).

Eugster and Lorenzetti [6] measured a CRE age of 160 Ma in an unirradiated fragment of NWA 773. This agrees with the CRE age calculated by Fernandes et al. [4] for the breccia component (~154 Ma), although we note that the latter CRE age was determined from ^{38}Ar measurements on an irradiated aliquot [4], and it is not clear whether reactor-produced ^{38}Ar was accounted for. Based on these two CRE age determinations, we conservatively assume a CRE age of 160 ± 16 Ma. We will confirm these CRE ages with new measurements of argon isotopes on an unirradiated aliquot of NWA 773 breccia.

Results: Using a CRE age of 160 ± 16 Ma, we corrected for the amount of cosmogenic ^{36}Ar in each heating step of the neutron-irradiated pyroxene to obtain the inverse isochron shown in Fig. 1.

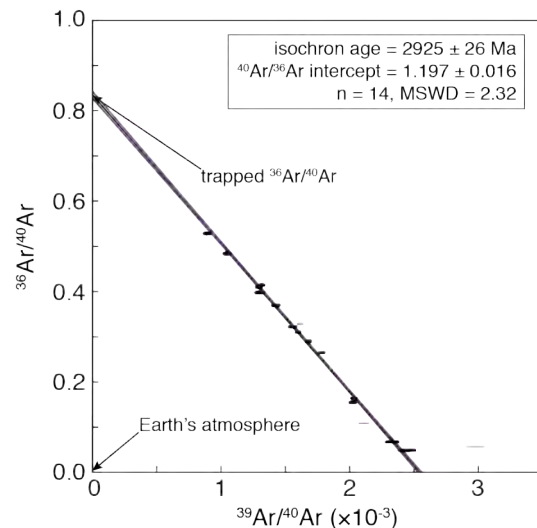


Figure 1. Inverse isochron used to define the trapped $^{36}\text{Ar}/^{40}\text{Ar}$ component and isochron age for pyroxene from NWA 773 breccia. Data in grey are not included in the linear regression.

The isochron age we obtain for NWA 773 pyroxene is 2925 ± 26 Ma (2σ). We also corrected individual step ages in both the pyroxene and groundmass step-heating experiments for the trapped component obtained from the inverse isochron ($^{40}\text{Ar}/^{36}\text{Ar} = 1.197 \pm 0.016$); these results are shown in Fig. 2. In contrast to the complex age spectra obtained by Fernandes et al. [4], with our cosmogenic corrections we observe remarkably simple age spectra with statistically significant plateau ages for both the groundmass (2956 ± 22 Ma, 94.0% ^{39}Ar , MSWD = 0.74, 19 steps) and pyroxene (2936 ± 24 Ma, 92.2% ^{39}Ar , MSWD = 0.56, 16 steps).

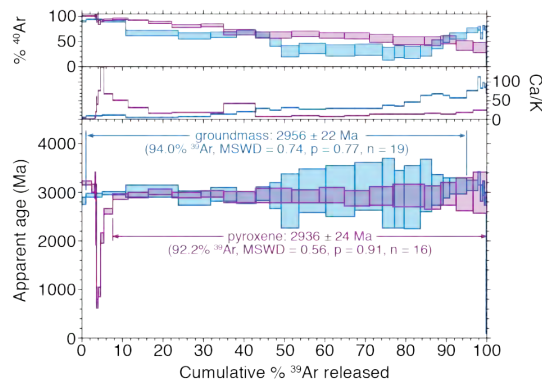


Figure 2. $^{40}\text{Ar}/^{39}\text{Ar}$ step age spectra for a pyroxene (purple) and groundmass (blue) from the breccia component of NWA 773, corrected for cosmogenic and trapped argon components using the approach of Cassata and Borg [5]. All uncertainties are reported at 2σ . Both step-heating experiments resulted in statistically significant age plateaus within uncertainty of one another, yielding a weighted mean age of 2947 ± 15 Ma.

Our weighted mean age of 2947 ± 15 Ma broadly agrees with the total gas $^{40}\text{Ar}/^{39}\text{Ar}$ age of ~ 2940 Ma reported by Fernandes et al. [4] for the breccia portion of NWA 773. Before, this integrated age was of unclear significance given the substantial over-dispersion in step ages from the Fernandes et al. [4] data. We note that if the argon isotope data from Fernandes et al. [4] were available, the same cosmogenic corrections utilized here could be applied to those data, allowing for a fully consistent comparison of these datasets.

Discussion and conclusions: The new $^{40}\text{Ar}/^{39}\text{Ar}$ ages we report are 169 ± 17 Ma younger than the ^{207}Pb - ^{206}Pb baddeleyite ages obtained by Shaulis et al. [2], and interestingly 82 ± 34 Ma older than the Sm-Nd age reported by Borg et al. [3] for the gabbro component. Fernandes et al. [4] also obtain a younger $^{40}\text{Ar}/^{39}\text{Ar}$ total gas age for the NWA 773 gabbro of ~ 2670 Ma (although as stated above the significance of this integrated age is still uncertain).

Taken collectively, these geochronologic constraints imply distinct, diachronous geologic histories for the breccia and gabbro components of NWA 773. Baddeleyite grains in the breccia came

from the gabbro during brecciation; coeval ^{207}Pb - ^{206}Pb baddeleyite ages from the breccia and gabbro components are therefore expected and represent the crystallization age of the gabbro. The Sm-Nd (2865 ± 31 Ma) and $^{40}\text{Ar}/^{39}\text{Ar}$ (~ 2670 Ma) ages in the gabbro likely reflect conductive, post-emplacement cooling of the gabbro rather than excavation-related cooling due to an impact event, which would cause synchronous ages to be recorded by these two chronometers.

Our observation of a significantly older $^{40}\text{Ar}/^{39}\text{Ar}$ age (2947 ± 15 Ma) for the breccia implies that some subcomponent(s) of the breccia cooled prior to and independently of cooling of the gabbro. A single zircon U-Pb age from the breccia component of NWA 773 (3953 ± 18 Ma) also implies an older geologic history for this portion of the meteorite [2]. Pyroxenes in the polymict breccia have a much wider range of compositions than those in gabbroic components of NWA 773 clan meteorites [2], which is also consistent with the presence of geologically distinct material in the breccia. The uniformity of step ages we observed in pyroxene and groundmass from the breccia (Fig. 2) implies rapid cooling, either associated with excavation by an impact event or extrusive crystallization.

Paired with the geochronological constraints from the gabbro, our pyroxene and groundmass $^{40}\text{Ar}/^{39}\text{Ar}$ ages constrain the timing of the impact event responsible for brecciation of NWA 773 to younger than 2865 Ma, and possibly younger than 2670 Ma. Revisiting the $^{40}\text{Ar}/^{39}\text{Ar}$ chronology of the gabbro portion of NWA 773 with the approach for deconvolving argon components used here [5] will provide better resolution on this upper temporal bound. Since the $^{40}\text{Ar}/^{39}\text{Ar}$ age spectra from the breccia exhibit no evidence for partial resetting, this also suggests that there was not substantial enough heating during the impact brecciation event to thermally disturb these systems. Future experiments to determine the kinetics of argon diffusion in these phases will be used to constrain the maximum temperature and heating duration during brecciation.

References: [1] Stöffler D. and Ryder G. (2001) *Space Sci. Rev.* 96, 9-54. [2] Shaulis B. J. et al. (2017) *GCA*, 213, 435-456. [3] Borg L. E. et al. (2004) *Nature*, 432, 209-211. [4] Fernandes V. A. (2003) *MAPS*, 38(4), 555-564. [5] Cassata W. S. and Borg L. E. (2016) *GCA*, 187, 279-293. [6] Eugster O. and Lorenzetti S. (2001), *MAPS* 36, A54.

CONSTRAINING THE AGE OF THE CRISIUM IMPACT BASIN. C. H. van der Bogert¹, H. Hiesinger¹, P. Spudis², V. A. Fernandes^{3,4}, K. D. Runyon⁵, and B. W. Denevi⁵. ¹Institut für Planetologie, Westfälische Wilhelms-Universität, Münster, Germany (vanderbogert@uni-muenster.de); ²Lunar and Planetary Institute, USRA, Houston, TX, USA; ³Museum für Naturkunde, Berlin, Germany; ⁴IDL, Univ. de Lisboa, Lisbon, Portugal; ⁵John Hopkins Applied Physics Laboratory, Laurel, MD.

Introduction: The lunar cratering chronology is used to derive absolute model ages (AMAs) of geomorphologic and structural units for which no direct samples are available [e.g., 1]. To calibrate the chronology, Stöffler and Ryder (2001) [2] and Stöffler et al. (2006) [3] sought to determine which sample ages are best related to certain lunar basins, craters, and mare units. Since this effort, many advances have been made in both sample dating techniques and crater size-frequency distribution (CSFD) measurements, motivating renewed attention to both the sample collection and remote sensing data, in addition to mission concepts and proposals for the collection and/or in situ analysis of key well-characterized lunar lithologies (e.g., South Pole-Aitken basin [4,5], young basalts [6], and Crisium/Nectaris impact melts [7]). Each sample that can be paired with corresponding CSFD measurements can be used to improve the lunar cratering chronology, as well as its application to dating other Solar System bodies.

Crisium Basin: Samples. Fragments of Crisium impact melt may have been collected by the Luna 20 sample return mission, which yielded a feldspathic sample (Fragment F, K₂O of 0.30 wt%) with a radiometric age of 3.895 ± 0.017 Ga [8]. Based on compositional considerations, Swindle et al. [8] argued that Fragment F is more likely to represent Crisium than other samples with ages of ~ 3.84 Ga that had previously been associated with Crisium [9-11]. Recently updated Apollo 17 ⁴⁰Ar/³⁹Ar sample ages, interpreted to represent Crisium, range from 3.88-3.93 Ga [12]. However, we are updating more sample ages, including those from Luna 20, using the K-decay constant of [13,14] and updated monitor sample ages [15,16], to allow renewed assessment of their origin(s) and relevance to the age of the Crisium basin. In particular, Fragment F has a relatively high K₂O content compared with typical feldspathic material and gives an updated age of 3.888 ± 0.074 Ga. Based on its lower K₂O content (<0.05 wt%), Fragment B might be a better compositional match for the expected Crisium material. Its age determined by [8] was 4.087 ± 0.021 Ga, and we assign an updated age of 4.103 ± 0.065 Ga.

Stratigraphy and Crater Size-Frequencies. Based on stratigraphic relationships, Wilhelms [9] proposed that Serenitatis is younger than Crisium, which would set the lower age limit for Crisium to older than earlier proposed sample ages for Serenitatis: 3.87 ± 0.012 Ga [17] or 3.825 ± 0.048 Ga [12]. However, recent work based on stratigraphic relationships and higher observed crater densities at Se-

renitatis [18-20] indicates that Serenitatis is older than Crisium, consistent with Baldwin's crater count and rim height observations [21,22]. Indeed, Orgel et al. [20] report an AMA for Serenitatis of 4.22 ± 0.027 - 0.033 Ga. As a result, comparisons with Serenitatis sample ages do not aid in unambiguously constraining the age of Crisium.

CSFDs measured for the Crisium basin give a range of ages. Neukum [23] reported crater densities that yield an AMA of 3.99 Ga using his 1983 chronology function, while more recently Orgel et al. [20] report an age of 4.07 ± 0.016 - 0.018 Ga from the crater rim and ejecta, using a modern buffered non-sparseness correction for CSFD measurements and the 2001 chronology function of [1]. This age is consistent with the radiometric age of Fragment B.

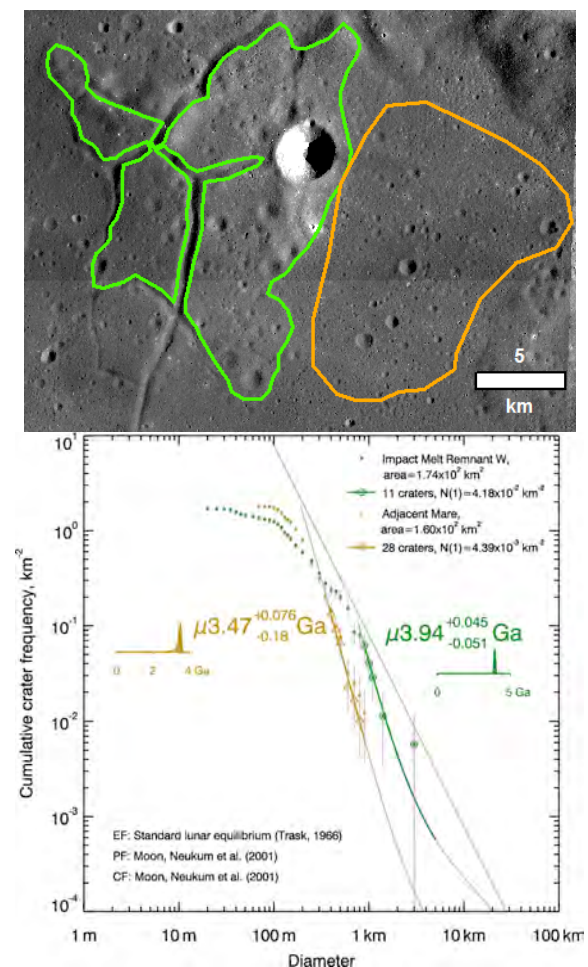


Figure 1. Count areas and corresponding fitted CSFDs, in western Crisium basin (SELENE TC mosaic), for the most prominent proposed impact melt exposure of Spudis and Sliz [24] (green, 3.94 Ga) and adjacent mare basalt (orange, 3.47 Ga).

Recent geologic mapping identified possible remnants of Crisium basin impact melt, based on morphology and composition [24]. Some of the proposed melt exposures exhibit cracked and fissured morphologies, consistent with those at both fresh craters (e.g., Tycho and King craters [25]) and older impact melts (e.g., Orientale [9,26]), and show embayment by subsequent mare basalt flows [24,27]. Clementine data indicate that the proposed impact melt remnants have less FeO (~8.3 wt. %) than the surrounding basalts (>15 wt. %), as well as highlands pyroxene compositions, attesting to their affinity to lunar highlands material [24].

Our CSFD Study: We examined the proposed impact melt exposures, as well as adjacent mare basalts, using CSFD measurements to expand our understanding of the age of the Crisium basin and its position in the basin chronology. We used Kaguya Terrain Camera (TC) [28] and Lunar Reconnaissance Orbiter Wide Angle (WAC) and Narrow Angle Camera (NAC) [29] data for our measurements and fit the CSFDs with the production and chronology functions of [1] using Poisson timing analysis [30] (*Fig. 1*).

Results and Discussion: When examined at SELENE TC and LROC NAC resolutions, some of the possible impact melt remnants appear to be secondary crater fields based on the presence of crater chains and herringbone patterns. These secondaries presumably deposited more felsic materials on Mare Crisium yielding a lower overall Clementine FeO content. Some other exposures have positive relief, but do not exhibit impact melt morphologies. One area in southern Crisium may be part of an embayed crater rim, but other areas could be megablocks of Crisium basement materials, similar to the rotated country-rock megablocks observed between the inner and outer rings of the terrestrial Ries crater [31]. These megablock exposures could nevertheless exhibit a reset crater population consistent with the timing of the Crisium impact. However, their rugged topography makes it difficult to impossible to define robust count areas. Using both traditional and buffered crater count (BCC) techniques, we were only able to derive poorly constrained ages, which are similar to the 4.07 Ga age determined by [20].

The largest and most prominent of the proposed melt deposits identified by Spudis and Sliz [24] yields an AMA of 3.94 ± 0.05 Ga (*Fig. 1*). This age is older than the oldest measured mare unit associated with Crisium (3.70 Ga) as dated by Hiesinger et al. [30] on the WAC mosaic. We also determined an AMA of 3.47 Ga for the mare unit adjacent to the proposed melt deposit, which falls into the range of ages determined for other mare basalts in Crisium [28]. An age of ~3.94 Ga is on the old side of the previously available updated radiometric ages of Apollo 17 samples thought to originate from

Crisium. However, our updated age for Luna 20 Fragment B is consistent with the CSFD measurements of [20,23] on the Crisium ejecta blanket.

The proposed impact melt exposure's morphological affinity to floor-fractured craters, as well as overprinting by ejecta from the crater Proclus [33], in combination with an AMA that is younger than derived on Crisium ejecta, might indicate that it represents the first volcanism in Crisium basin, rather than an impact melt unit. Alternately, there may be a mechanism, such as target property or self-secondary cratering effects, that causes the CSFD ejecta-based ages to be older than melt-based ages [34,35].

Conclusions and Implications: Given the uncertainty in our measurements on the megablock-like exposures, and the possibility that the westernmost exposure might be post-basin volcanism, we can constrain the age of the Crisium basin to ≥ 3.94 Ga [this work] and ≤ 4.07 Ga [20] using CSFD measurements. Our updated radiometric ages for Luna 20 Fragments B and F, may indicate that Fragment F represents a younger basin impact, while Fragment B, with a relatively low K-content and an age of 4.103 ± 0.065 Ga, would be most consistent with the AMAs for Crisium basin.

However, given the uncertainties in connecting individual fragments with large basin formation events [see also 8], our work supports the need to directly sample Crisium basin materials of more certain provenance [e.g. 7,33]. As such, an essential element of sample site selection for lunar chronology missions is not only to be able to perform a full assessment of sample provenance in the field, but also to select a landing area that meets CSFD measurement requirements to provide a meaningful calibration point for the lunar cratering chronology.

References: [1] Neukum et al. (2001) *Space Sci Rev* 96, 55. [2] Stöffler and Ryder (2001) *Space Sci Rev* 96, 9. [3] Stöffler et al. (2006) *New Views of the Moon, Rev Min Geochem* 60, 519. [4] Jolliff et al. (2010) *LEAG Meeting*, 3072. [5] Jolliff et al. (2017) *LPSC* 48, 1300. [6] Lawrence et al. (2013) *LEAG Meeting*, 7048. [7] Cohen et al. (2018) *LPSC* 49. [8] Swindle et al. (1991) *PLPSC* 21, 167. [9] Wilhelms (1987) *USGS Prof Pap* 1046-A, 71 pp. [10] Cardogan and Turner (1977) *Phil Trans R Soc London A* 284, 167. [11] Deutsch and Stöffler (1987) *GCA* 51, 1951. [12] Schmitt et al. (2017) *Icarus* 298, 2. [13] Renne et al. (2011) *GCA* 75, 5097. [14] Schwarz et al. (2011) *GCA* 75, 5094. [15] Jourdan and Renne (2007) *GCA* 71, 387. [16] Schwarz and Trierloff (2007) *Chem. Geol.* 242, 218. [17] Podosek et al. (1973) *GCA* 37, 887. [18] Spudis et al. (2011) *JGR* 116, 10.1029/2011JE003903. [19] Fassett et al. (2012) *JGR* 117, 10.1029/2011JE003951. [20] Orgel et al. (2018) *JGR*, *accepted*. [21] Baldwin (1987) *Icarus* 71, 1. [22] Baldwin (1987) *Icarus* 71, 19. [23] Neukum (1983) *NASA TM-77558*, 153 pp. [24] Spudis and Sliz (2017) *GRL*, 10.1002/2016GL071429. [25] Howard and Wilshire (1975) *J Res USGS* 3, 237. [26] Scott et al. (1978) *USGS Map* I-1034. [27] Sliz and Spudis (2016) *LPSC* 47, 1678. [28] Haruyama et al. (2008) *Earth Planet Space* 60, 243. [29] Robinson et al. (2010) *Space Sci Rev* 150, 81. [30] Michael et al. (2016) *Icarus* 277, 279. [31] Sturm et al. (2014) *MAPS* 50, 141. [32] Hiesinger et al. (2011) *LPSC* 42, 2179. [33] Runyon et al. (2018) *LPSC* 49, 1536. [34] van der Bogert et al. (2017) *Icarus* 298, 49. [35] Zanetti et al. (2017) *Icarus* 298, 64.

Optimizing Geological Exploration in an Analogue Lunar Habitat: Sub-System Analysis and Human-Factor Integration G.A. van der Sanden^{1 2}, B.H. Foing^{1 2 3}, L.C. Dubois^{2 4}, ¹Free University of Amsterdam (germaine.sanden@gmail.com), ²ESA ESTEC, ³ILEWG International Lunar Exploration Working Group (Bernard.Foing@esa.int), ⁴ISAE-SUPAERO Toulouse.

Introduction : The simulation of lunar habitats on Earth is important for furthering the understanding and integration of science, technology, human-factor and habitat design for a potential future lunar habitat, in preparation for MoonVillage [1]. Analogue habitat simulations are therefore suited to test astronaut performance, habitat integration as well as geological sample collection and on-site analysis [2-4]. A planetary habitat design consists of many sub-systems that require detailed understanding of their single-, as well as integrated functioning (used in supermarket flow analysis [5]). To optimize and construct proto-procedures for an official protocol for geological research in a planetary environment it is important to understand human behaviour and research conductions in a relatively complex habitat environment. Therefore, we focus here on the understanding of how various sub-systems function in an integrated way in a lunar habitat environment. A system-engineering perspective from a constructionism/deconstructionism point of view is applied to the lunar analogue mission to understand the temporal and spatial flux of the habitat environment. A system-engineering mindset enables study about how the habitat should be planned, designed, built and maintained for the astronaut's activities. The aim of the sub-system analyses is to optimize geological exploration in a analogue lunar habitat, as well as the overall functioning of the habitat environment. The integrated analogue missions here on Earth, will prepare humanity for the future when man may venture on other planetary bodies.

A System-Engineering Approach: A system-engineering approach towards analogue habitats is key to understand the overall performance of the habitat. The application of system-thinking superimposed upon the habitat real-time functioning enables a more detailed understanding on the sub-systems, as well as the totality of the system. Simultaneously, it will contribute to the scientific quality as well, as the well-being of the astronauts. So, system thinking not only provides the ability to look at the various components and their dependencies, but also participates in the understanding of the project in its totality [6]. A constructionism -deconstructionism system analysis will focus on the coupling and decoupling of the various sub-systems present in the analogue habitat. Every sub-system is characterized by a spatial and temporal flow, which interacts with other sub-systems and eventually creates a unified system in itself, the habitat environment. The interaction be-

tween the sub-parts that constitute the larger system consists of strong as well as weak links; which require analysis for optimization [7]. The analysis of the system-coupling and understanding the real-time motion between the astronauts, the execution of practice and the physical components, including the integration of environmental effects, are important for future habitat design (See Figure 1).

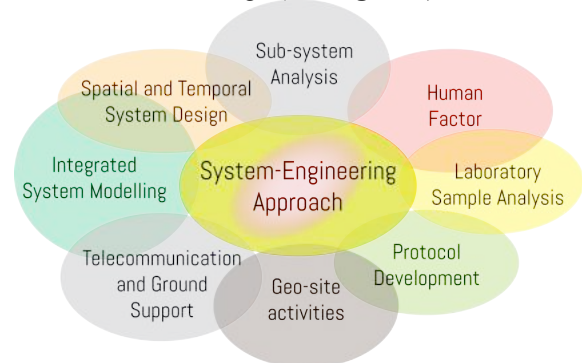


Fig 1: A system-engineering approach of human behaviour in a spatial geological exploration context

Systems Architecture: Every sub-system is characterized by its own internal structure, properties, layers, behavior and functions, this is the systems architecture. A sub-system is here defined as a set of elements, that form a unified whole or single component of a larger system. A sub-system contains a unique internal structure and interacts with other components of the system. Therefore it is an interdependent group of items interacting in a larger context. For each sub-system in the habitat an architecture description is formulated that supports the structures and behaviors of the sub-system. The system-architectural framework will contribute to a multi-layered understanding of the total system [8]. The trained astronauts will feedback on the architecture description after the analogue experiment in the lunar habitat.

Sub-system analysis: From a rather generic theory of system-analysis we will hereby create a more concrete understanding of the sub-systems in specific. The currently defined 8 sub-systems for the designed analogue environment are: the exo-habitat, the exo-laboratory, the deployable structure, the lander, the physical environment, the human-factor, the geological execution, and Earth's ground station (See Fig 2.) A system-architecture-description will be formulated for all 8 sub-systems. Subsequently, the interaction between them will be analyzed; for

the (de-)coupling and understanding of the spatial and temporal motions of the habitat:

1. **The Exo-Habitat:** The living and working space for the astronauts, which is closed off by an airlock. The exo-habitat is supported by telecommunication from Earth's Ground Station.
2. **The Exo-Laboratory:** The laboratory forms part of the working space and is essential for sample analysis. Instruments : 3-D printer; spectrometer etc.
3. **The Deployable Structure:** The deployable structure is a temporary form of architecture that functions as a shield from Earth's weather when geological investigation of the physical environment forms the activity by the astronauts.
4. **The Lander:** This remotely operated lander is composed of an aluminum body, supported by three legs. It is equipped with modular payloads including UV-VIS, NIR and Raman spectrometers, environmental sensors, a telescope, various cameras and a rover deployment system.

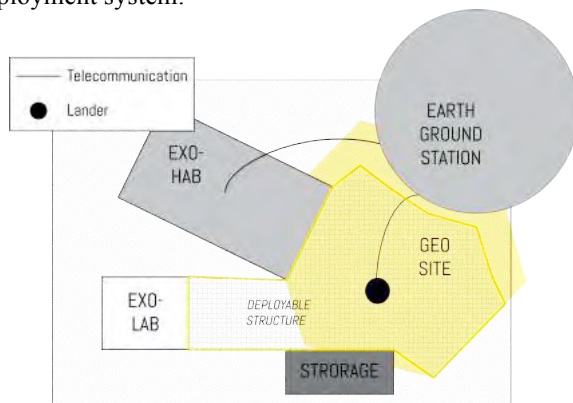


Fig.2: Visual representation of the various sub-systems that constitute the physical components involved in the analogue lunar habitat mission.

5. **The Physical Environment:** The physical environment is a natural sub-system and carrier of the total analogue habitat experiment. It enables the possibility of geological research and sample collection. It also enables In-Situ Resource Utilization (ISRU), which will in the future enable self-manufacturing of products with local materials.
6. **The Human Factor:** The analogue habitat environment will be occupied by 6 astronauts for a period of two weeks. The scientific objectives are closely related to human well-being and functioning. The human presence also offers a challenging unpredictable constraint, namely human behavior.
7. **The Geological Research:** Conducting planetary field geology forms a key element in the habitat environment and can provide new scientific insights into geological processes, exo-biology, the evolution of the planet and our solar systems, as well as other solar-systems and exoplanets. The analogue experimentation provides first-hand experience and helps

to evaluate various geological technologies. Sample collection and scientific observation can significantly contribute to current geology and may provide a wealth of lessons for further technological development for planetary field geology [8].

8. **Earth's Ground Station:** Real-time remote support for the analogue environment is provided from ESA ESTEC/VU Amsterdam.

Output in the context of Geological exploration:

I: Protocol Development for Future Habitat:

Sub-system analysis of the 8 sub-systems allows to produce a more detailed protocol or proto-official procedure for planetary geological fieldwork during Earth analogue missions or planetary missions.

II: Planetary Geospatial ArcGIS environment:

Based on the scientific fieldwork geospatial information can be uploaded into the ArcGIS environment to obtain a multi-layered visualisation of the surface map, geological samples collected by field observation, imagery, mineral detection by remote sensing data and laboratory results.

Constraints and Challenges: The system-analysis of the 8 sub-systems of the analogue habitat environment is subject to several constraints and challenges. The flows and interactions between the compartments are difficult to model or predict a priori to the actual simulation events. Monitoring is highly required, and real-time motion series can provide empirical evidence and temporal and spatial data. As expected, there will be constraints, trade-offs and bottlenecks that occur based on the system analysis. Consequently, the optimization of the habitat and geological fieldwork will likely function, in practice, below the point of optimal efficiency.

References:

- [1] Woerner, J.; Foing, B.; Moon Village International Support Group The "Moon Village" Concept and Initiative (2016) LPICo1960.5084;
- [2] Boche-Sauvan, L.; Foing, B. H.; et al ILEWG ExoHab & EuroGeoMars Campaigns: Habitability & Human Operations (2010) LPI, 41,1759;
- [3] Thiel et al Human crew-related aspects for astrobiology research (2011) IJAsB, 10, 255 ;
- [4] Peters T.H. (1998) Civil Engineering- ASCE, 68 (3), 48-51.
- [5] Mayo J.M.M. (1993) The American Grocery Store: The Business Evolution of an Architectural Spac, Connecticut.
- [6] Ashby W.R. (1991) In: Facets of Systems Science. IFSRIS SSE vol 7.
- [7] Maier M.W. and Rechtin E. (2010) The art of systems architecting (eds), Florida.
- [8] Young K. et al. (2013) Acta Astronautica, 90 (2), 332-343.

Development of Electrostatic Spacesuit Cleaner for Lunar Exploration Missions. O. Via Espinal^{1,2}, M. Adachi¹, A. Cowley², V.S. Engelschön², M. Fateri¹ and M. Sperl¹, ¹Deutsche Zentrum für Luft- und Raumfahrt, Institut für Materialphysik im Weltraum, 51147 Köln, Germany, ²European Space Agency-European Astronaut Centre, Linder Höhe, 51147 Köln, Germany.

Introduction: During the Apollo missions, the astronauts reported that the lunar regolith disturbed their extravehicular activities [1]. The electrostatically charged floating particles have a tendency to stick to the spacesuit, which caused several issues during the missions, such as clogging of mechanisms, seal malfunctions, and surface abrasions[2]. In addition, the adhered regolith was brought into the command module when astronauts came back from the extravehicular activities, irritating their eyes and lungs. Thus, the toxicity of lunar regolith is also concern for future manned explorations [3]. The regolith particles are agitated by manned and unmanned extravehicular activities, meteoroid bombardments and the electrostatic effects of cosmic rays and solar winds; they are easily suspended due to the small gravitational force and the absence of air drag. In order to ensure future astronaut activities on the Moon, the development of mitigation technologies for lunar regolith is required. In previous studies, several electrostatic mitigation systems have been developed, such as an Electrodynamic Screen for cleaning optical lenses and solar panels [4], and electrostatic spacesuit cleaners [5,6]. The use of electrostatic forces have several advantages in the lunar environment, such as the possibility to replace certain mechanical parts, a compact configuration and a low power consumption. Demonstrations of electrostatic systems have been conducted using both lunar regolith simulants and real lunar regolith in air, vacuum and low-G. The systems showed a good cleaning performance [4,5]. In this study, we have developed an electrostatic spacesuit cleaner which, considering its practical application, has been designed as small as possible in order to be easily installable and portable for the spacesuits. Subsequently, we demonstrated the cleaning performance of the set-up with lunar regolith simulant. In previous studies [5,6], the cleaning performance was mainly investigated without any motion of the substrate. However, the electrostatic spacesuit cleaner would be operated during the astronaut's extravehicular activities. The vibration from the astronaut motion could potentially affect the system performance and the regolith dynamics. Therefore, we will demonstrate the cleaning experiments under various vibrations to obtain insights on the practical performance. In addition, based on previous studies [4,5,6], it is not possible to determine the relationship between the physical and/or chemical properties of the lunar regolith, and the performance of such cleaning devices. We aim to

relate the properties of the lunar regolith simulants with the cleaning performance of the device.

Electrostatic Spacesuit Cleaner: The system consists of two parts; one is a power supply unit (Figure 1) that generates an electrodynamic traveling wave; and the other is an electrode-printed polyimide substrate which transmits the wave through its surface (Figure 2). The main components of the power supply unit are: a microcomputer, a Photo-MOS switching circuit and high-voltage amplifiers. The volume size of the power supply is approx. 150 mm³. In order to generate the electrodynamic traveling wave, the unit generates 4-phase rectangular voltage equally delayed, these delays can be controlled with the microcomputer. The microcomputer utilizes high voltage, but also an extremely low electric current, thus the power consumption is negligible comparing other devices. When the traveling wave of high voltage is applied to the electrodes, the regolith adhering to the substrate is transported by the propagating electrostatic force.

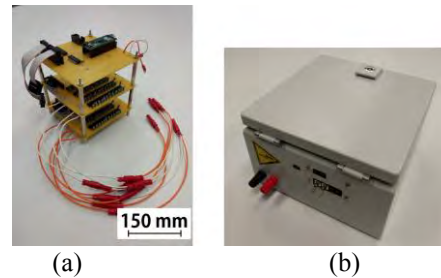


Figure 1: Portable power supply unit for electrostatic spacesuit cleaner (a) before and (b) after mounted in the insulative housing.

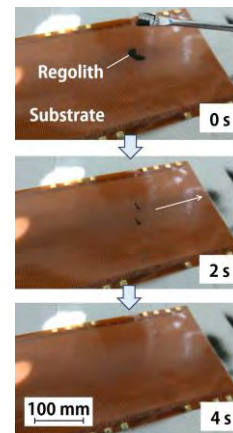


Figure 2: Removal of lunar regolith simulant on substrate when travelling wave of high voltage is applied (1800 V, 5 Hz).

Cleaning of Lunar Regolith Simulant: It is demonstrated that when a voltage of 1800 V_{p-p} and 5 Hz frequency was applied to the substrate with 1 g of the lunar regolith simulant JSC-1A, the particles are transported unidirectionally by the electrostatic force, as shown in Figure 2. After running for 4 s, most of the simulant was removed. It is foreseen to use the developed system for mitigating lunar dust in future lunar exploration missions.

Future work: There was still a small fraction of particles on the substrate after the cleaning operation, although it did not greatly affect the cleaning performance. In particular, the cleaning of small particles is difficult because of the adhesion force between the substrate and the particles increases with decreasing particle size. A use of vibration will be investigated to reduce adhesion force by agitating the contact state between particle and substrate. In addition, particle transport is affected by particle size and shape characteristics. In particular, lunar regolith has a wide range of size and shape; the effect of these properties should be investigated to improve the performance.

References: [1] Gaier, J. R. (2005) *NASA Technical Report*, TM-2005-213610. [2] Christoffersen, R., et al. (2008) *NASA Technical Report*, TM-2009-0015239. [3] Wagner, S. (2004) *NASA Technical Report*, TM-2008-0047665. [4] Calle, C. I., et al. (2011) *Acta Astronautica* 69, 11, 1082-1088. [5] Kawamoto H., et al, (2010) *J. Aerosp. Eng.* 24 (4) 442-444. [6] Manyapu, K. K., et al. (2017) *Acta Astronautica* 137, 472-481.

Lunar Cratering Chronology - Revisited. S. C. Werner¹, B. Bultel¹, V. A. Fernandes², T. Rolf¹, ¹ Centre for Earth Evolution and Dynamics, University Oslo, Norway, stephanie.werner@geo.uio.no, ² Museum für Naturkunde, Berlin.

Introduction: To decipher the planetary surface evolution, geologic events are relatively dated based on crater counts [1,2]. This method has been calibrated on the Moon and scaled to other planetary bodies. A good calibration on the Moon is thus a precious key to understand the chronology of all solid surface planetary bodies in the solar system.

Crater counts are linked to isotopically-dated Apollo and Luna samples, which provides calibrated *absolute model ages (AMA)*. The observed crater size frequency distributions (CSFD) on defined surface units are fit with crater production functions (i.e., presumed to be undisturbed crater size frequency distributions). These are used to derive crater density measurements, which have resulted in several lunar chronology models [e.g., 3,4]. The proper definition of a crater production function is therefore crucial for the definition of lunar cratering chronology. Indeed, the crater production function must be determined over a large crater diameter range and over large homogeneous units.

Several problems have risen regarding this method such as i) the limited number of craters on very young terrains, ii) the crater saturation of the cratered surface of old terrains, iii) the lack of samples with ages between 3.0 and 1.0 Gyrs, and iv) the geologic uncertainty of the relation between samples (Apollo and Luna missions) and crater count terrains used as templates [5]. This has led to uncertainties and diversities on lunar cratering rates and chronology models.

Results: We present i) an in depth evaluation of

the current crater production functions, ii) make use of newly mapped reference units based on spectral and morphologic information and the cratering statistics on these units [6], iii) the recalculated isotopic ages using more recent evaluation of age of the monitor samples [7,8] and K- and Rb-decay constants [9, 10], iv) provide the potential sequence of basin ejecta for each landing site. Jointly, these four puzzle pieces will provide the base for the discussion of current lunar cratering chronology models.

References: [1] Öpik (1960) *Monthly Notices of the Royal Astronomical Society*, 120(5), 404-411. [2] Shoemaker (1962). *American Scientist*, 50 (1), 99-130. [3] Hartmann & Neukum (2001). *Cratering chronology and the evolution of Mars*. (pp. 165-194). [4] Neukum, Ivanov, & Hartmann (2001) *SSR*, 96(1-4), 55-86. [5] Stöffler & Ryder(2001) *Chronology and evolution of Mars* (pp. 9-54). [6] Bultel et al., this meeting. [7] Jourdan & Renne. (2007) *Geochim. Cosmochim. Acta* 71, 387-402. [8] Schwarz and Tieloff (2007) *Chem. Geol.* 242, 218–231. [9] Schwarz et al. (2011) *Geochim. et Cosmochim. Acta* 75, 5094-5096. [10] Renne et al. (2011) *Geochim. et Cosmochim. Acta* 75, 5097-5100.

Acknowledgement:

This study is supported by the Research Council of Norway (235058/F20 CRATER CLOCK). V.A.F. acknowledges financial support via a DFG-Eigenstelle FE 1523/3-1.

CUBEROVER: A LOW COST, RELIABLE PLATFORM FOR PLANETARY EXPLORATION.

William “Red” Whittaker, Andrew Horchler, Fraser Kitchell, and Michael Provenzano (2515 Liberty Avenue, Pittsburgh PA 15222; red@cmu.edu), (andrew.horchler@astrobotic.com), (fraser.kitchell@astrobotic.com), and (mprovenz@tepper.cmu.edu).

Introduction and Overview: CubeRover is a lightweight planetary rover built to survive the harsh environment of the Moon. The purpose of the CubeRover platform is to develop and deliver a small rover that can serve as a platform to standardize and democratize planetary surface mobility, analogous to the transformation that CubeSats brought to the domain and economics of Low Earth Orbit. This abstract details the path to flight that the team intends to follow in order to deliver a CubeRover to customers for infusion into a lunar mission.

Identification and Significance: If successful, CubeRover stands to provide users with more access to the Moon than ever before. Countries, organizations, and universities would have affordable access to mobility platforms capable of exploring the surfaces of other worlds for the first time. The standardized format of CubeRovers will drive the space community to commoditize systems, components, and instruments, lowering costs while increasing functionality. Advancements to date have focused on the development of system design and requirements, as well as a concept of operations for a scientific mission. An engineering prototype robot has been built and is undergoing testing in preparation for a Preliminary Design Review.

Market Demand: Akin to the CubeSat revolution that standardized satellite development and pioneered low cost access to space-based data, CubeRovers are positioned to pioneer planetary exploration through standardization and at a fraction of historical costs. The form factor of a CubeRover is cross-compatible with many CubeSat parts, facilitating installation and interchange of components if desired. The CubeRover design is modifiable and scalable to support hosted payloads with minimal system changes. The CubeRover team has already engaged by large commercial and government entities to validate the platform for proposed applications.

CubeRover has been awarded a United States Small Business Innovation Research (SBIR) Phase I contract that has been successfully completed with guidance and expert support from Carnegie Mellon University and NASA Kennedy Space Center.

Separate from physical hardware sales, CubeRover plans to offer data as a service for users interested in procuring existing data without the cost of purchasing a rover. This data will be captured by the rover and communicated down through the lander platform. Some of these market segments

include, but are not limited to, 3-D terrain mapping, radiation and temperature sampling, in-situ resource utilization, and seismographic measurements.

Technical Objectives: The primary technical objective is the development of a novel, lightweight, space-rated rover, capable of performing a range of planetary science. Secondary objectives are to (1) develop an understanding of customer mission requirements and concept of operations, (2) design the rover configuration, (3) prototype and fabricate system and subsystem components, and (4) qualify flight ready rover.

CubeRover has a two-wheeled body design with a tail for low mass and mobility. The benefit of using a CubeRover is that its deployment and stowage method have been designed to fully integrate with Astrobotic’s Peregrine lander, yet its robust design can also be adapted to suit other lander services as needed.

The rover is capable of traversing distances greater than 500 m (6.6 hours roving + 6.2 hours communications + 300% margin) at speeds of up to 9 cm/s. The rover’s power systems will draw less than 10 W while roving, and less than 1.3 W while idle. The rover has a tight turning radius of less than 5 cm and can surmount obstacles up to 7.6 cm high. The design is robust to tip-over on slopes and obstacles up to 35 degrees in all orientations. Additionally, the rover has been successfully tested in 1.1-m drop tests that simulate deployment from a lander on to the lunar surface.

System Design: CubeRover, a miniature, mobile robotic platform, is a study in engineering and system trades. The most pressing challenge, determined at the outset and present in all of the engineering analyses, has been to find the balance between the constrained size and mass while answering the need for mobility, thermal and power control, and the pursuit of relevant science. An illustration of the system design is shown in Figure 1.

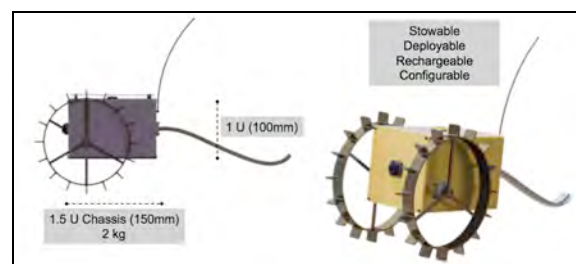


Figure 1: CubeRover 1U Concept

Concept Design. The engineering team has performed analyses and trades to solidify the CubeRover concept around the following high-level requirements:

- 2-kg deployed payload mass
- Two-wheel rover chassis with tail
- Powered by battery, with the capability to be re-charged
- WiFi for communication on lunar surface
- Teleoperation for control
- Single high-resolution camera for science and teleoperation

CubeRover has been designed for a surface mission on the lunar surface. A reference mission, based on the first mission of Astrobotic's Peregrine Lander, has been baselined to allow CubeRover's mission systems and mission operations planning to mature. As such, the Peregrine lander serves as the delivery vehicle, and the Peregrine payload concept of operations was used to guide operational analyses (e.g., defining the thermal environment during cruise) for CubeRover mission phases prior to deployment on the lunar surface. The Peregrine Interface Control Document was used in the selection of rover power, thermal, and communications interfaces and modes.

Further Technical Detail on CubeRover: Development of CubeRover will focus first on a "1U" form factor flight model, with options to grow to a 3U, 6U, or larger model for new applications and customers. See Figure 2 for a visual depiction of the intended technology roadmap.

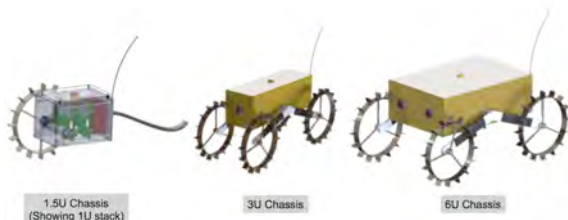


Figure 2: CubeRover Technology Roadmap

The 1U format CubeRover has a deployed mass of less than 2 kg, which includes an allotment for at least 100 grams of payload (e.g., cameras, scientific instruments). Figure 3 shows a proposed timeline for CubeRover's technology roadmap as well as significant milestones and capabilities.

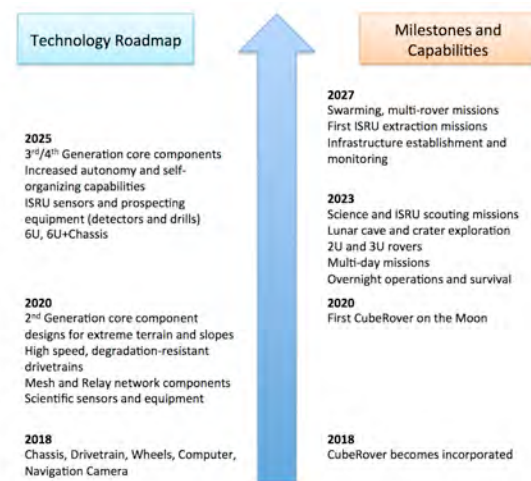


Figure 3: CubeRover Milestones and Capabilities

Timeline to Flight: CubeRover is currently planning for its first commercial launch in 2020 with Astrobotic, a lunar transportation company that delivers payloads to the moon.

Acknowledgements: We would like to thank Astrobotic for their contribution of human capital and critical resources in the completion of this SBIR Phase I contract number NNX17CK06P, launch partnership, and technical expertise.

We would like to thank NASA Kennedy Space Center for their generous contribution of financial and educational resources.

We would like to thank Carnegie Mellon University for its contribution of materials, classroom space, and subject matter expertise regarding the development of the robotic platform.

About Astrobotic: Astrobotic is a lunar logistics company that delivers payloads to the Moon for companies, governments, universities, nonprofits, and individuals. The company's spacecraft accommodates multiple customers on a single flight, offering lunar delivery at an industry-defining price. Astrobotic is a partner with NASA through a Space Act Agreement under the Lunar CATALYST program and has 23 prior and ongoing NASA contracts. Astrobotic was spun out of Carnegie Mellon University's Robotics Institute in 2007 and is headquartered in Pittsburgh, PA.

Introduction: Nearly global coverage in visible to near-infrared multispectral and hyperspectral image data allows for estimating the abundances of the main refractory elements in the lunar regolith. However, spectral parameters directly inferable from NIR spectra, such as the depths of the FeO-related absorption bands near 1 μm and 2 μm wavelength or the slope of the spectral continuum, depend not only on the FeO content of the surface material but also on its maturity [1]. Maturity-independent methods have been developed for estimating the abundances of Fe [2, 3] and Ti [2] based on spectral ratios [2] or band parameters [3] inferred from Clementine multispectral image data. Statistically-based regression models have been applied to Clementine data [4] and Chang'E-1 multispectral data [5] to estimate the abundances of Fe, Ti and further refractory elements, such as Ca, Al and Mg. As a reference, Lunar Prospector Gamma Ray Spectrometer (LP GRS) data [6] were used in [4] and laboratory measurements of returned samples in [5]. The technique of [2] was recalibrated to Kaguya multispectral image data in [7]. Visible and near-infrared hyperspectral image data acquired by the Moon Mineralogy Mapper (M³) instrument [8] on-board the Chandrayaan-1 spacecraft [9] have also been used to infer the abundances of Fe based on returned sample data as a reference [10, 11] as well as of Ti, Ca and Mg based on LP GRS data [11, 12]. However, all these algorithms are either affected by maturity and/or topography effects. This is the main motivation for the development of the new, topographically corrected and maturity-independent M³-based elemental abundance estimation algorithm described in this study.

Data and Method: The proposed algorithm is based on a regression analysis between nearly global maps of M³-derived maturity-independent spectral parameters and the corresponding LP GRS elemental abundance maps [6]. As new maturity-independent spectral parameters we defined the angular parameters A1 and A2 as

$$A1 = \arctan[BD1/(0.325 - NCSL1)]$$

$$A2 = \arctan[(BD2 - 0.004)/(0.1525 - NCSL2)],$$

where BD1 and BD2 are the depths and NCSL1 and NCSL2 the normalized continuum slopes of band I and II, with normalization at 0.750 μm and 1.579 μm for NCSL1 and NCSL2, respectively. Using an angular parameter is similar to [2], while the space in which the parameter A1 is defined is the same as in [3]. The band I and II centre wavelengths and the band I width were used as additional maturity-independent spectral parameters. All these param-

eters were extracted from a topographically and thermally corrected nearly global M³ mosaic of 2 pixels per degree resolution constructed using the framework in [12]. This regression approach is applied to Fe (excluding Fe contained in the mineral ilmenite, FeTiO₃, which is taken into account using the Ti abundance estimation algorithm in [11]), Ca and Mg.

Results: To illustrate the maturity independence of the proposed Fe abundance estimation algorithm, the Fe abundance map of a mare region east of the crater Lichtenberg is shown in Fig. 1. This region has been processed at full M³ resolution. The absence of Fe anomalies at the locations of bright, fresh craters demonstrates the maturity independence of the proposed method. Nearly global abundance maps of the elements Fe, Ti, Ca and Mg are shown in Fig. 2. These maps show the common contrast between maria and highlands but also compositional variations across different mare regions.

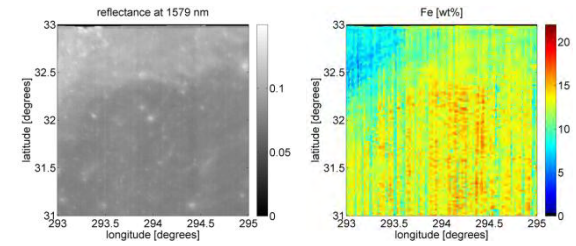


Fig. 1: Reflectance at 1.579 μm (left) and Fe abundance in wt% (right) obtained with the proposed algorithm for a region east of the lunar crater Lichtenberg.

Conclusion: In this study we have presented a new, maturity-independent method for estimating the abundances of the refractory elements Fe, Ca and Mg based on M³ hyperspectral image data.

Acknowledgements: Funding by the German Academic Exchange Service (DAAD) is gratefully acknowledged.

References: [1] Lucey, P. G. et al. (2000) JGR 105, 20377-20386; [2] Lucey, P. G. et al. (2000) JGR 105, 20297-20306; [3] LeMouélic, S. et al. (2000) JGR 105, 9445-9456; [4] Shkuratov, Y. G. et al. (2005) PSS 53, 1287-1301; [5] Wu, Y. et al. (2012) GCA 93, 214-234; [6] Elphic, R.C. et al., (1998) Science 281, 1493-1496; data download from <https://www.mapaplanet.org/explorer/moon.html>; [7] Otake, H. et al. (2012) LPSC XXXXIII, abstract #1905; [8] Pieters, C. M. et al. (2009) Current Science 96, 500-505; [9] Goswami, J. and Annadurai, M., (2009) Current Science, 96, 486-491; [10] Bhatt, M. et al. (2012) Icarus 220, 51-64; [11] Bhatt, M. et al. (2015) Icarus 248, 72-88; [12] Wöhler, C. et al. (2014) Icarus 235, 86-122.

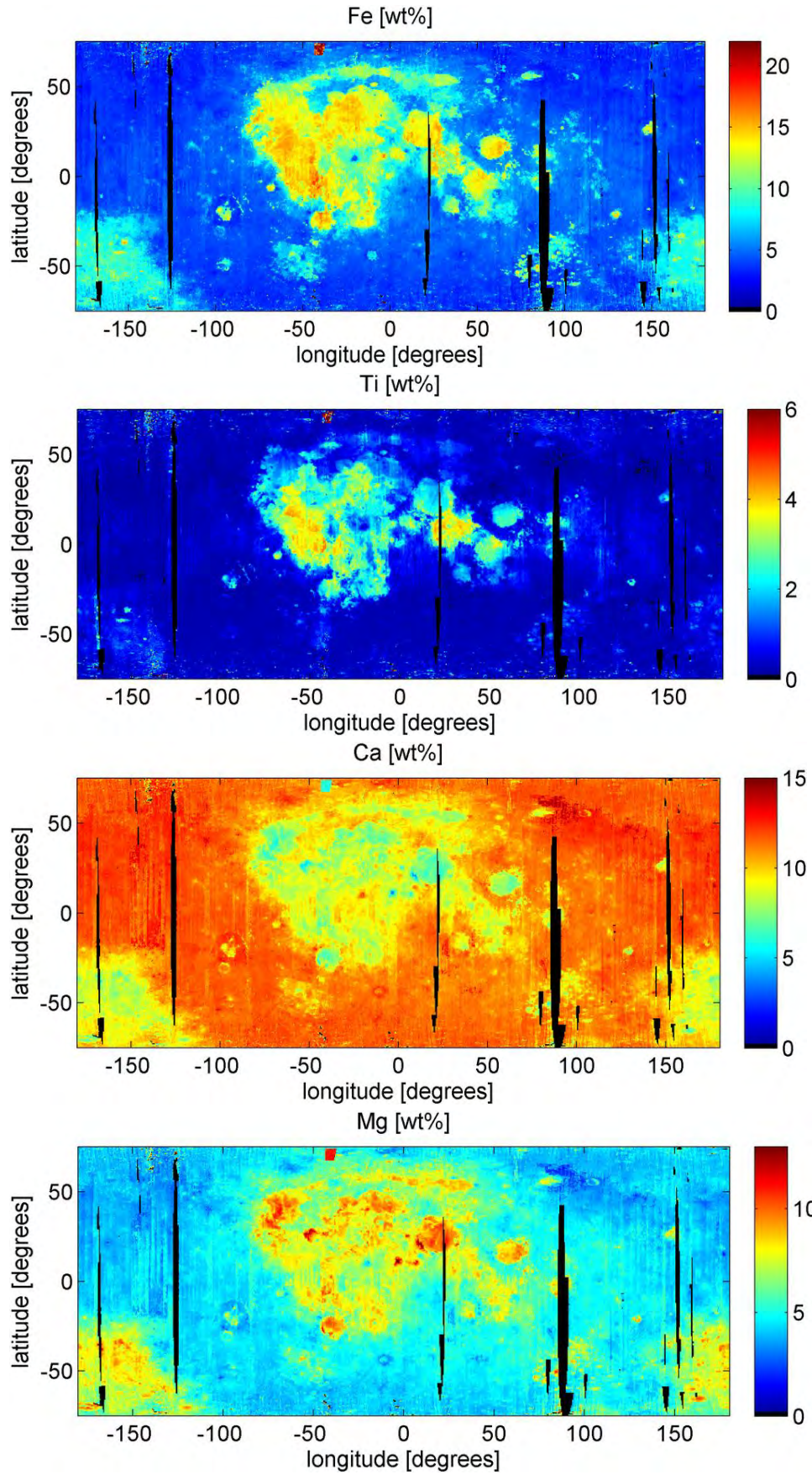


Fig. 2: M³-derived abundance maps of the elements (from top to bottom) Fe, Ti, Ca and Mg. Map resolution is 2 pixels per degree. The Fe, Ca and Mg maps were constructed using the method proposed in this study, the Ti map using the method of [10].

CORRELATION BETWEEN LUNAR SOIL COMPOSITION AND WEAKLY BOUNDED SURFICIAL OH/H₂O COMPONENT. C. Wöhler¹, A. A. Berezhnoy², A. Grumpe¹, V. V. Shevchenko², ¹Image Analysis Group, TU Dortmund University, Otto-Hahn-Str. 4, D-44227 Dortmund, Germany, {christian.woehler | arne.grumpe}@tu-dortmund.de, ²Sternberg Astronomical Institute, Universitetskij pr., 13, Moscow State University, 119234 Moscow, Russia, {ber | shev}@sai.msu.ru.

Introduction: Near-infrared spectra acquired by the Moon Mineralogy Mapper (M³) instrument [1] on Chandrayaan-1 [2] reveal an absorption band near 3 μm wavelength, indicating the presence of OH and/or H₂O in the uppermost regolith layer. Early analyses of M³ data suggested that the 3- μm band can only be observed at high latitudes beyond 50°-60° north and south [3]. More recent studies indicate that the 3- μm band is present at any time of day and is not restricted to high latitudes [4, 5].

The 3- μm band depth has been found to be time-of-day-dependent in several studies [e.g., 5-9], with the absorption band being strongest in the local morning and afternoon and weakest at midday. The analysis in [5] has shown a weaker 3- μm band at all times of day as well as a higher amplitude of the time-of-day-dependent variations for the lunar maria than for the highlands.

Based on the two-component model of lunar surficial OH/H₂O proposed in [5], we examine in this study the amplitude of the time-of-day-dependent variations of the 3- μm band depth and its dependence on the soil composition.

Analysis of the weakly bounded OH/H₂O component: A commonly accepted explanation for the occurrence of the 3- μm band is the adsorption of protons from the solar wind by the regolith, followed by reactions with O bounded in the regolith material to form OH and possibly H₂O [e.g., 3, 7, 10-12]. However, in [5] the non-vanishing 3- μm band depth at lunar midday led to the conclusion that there exists a weakly bounded and a strongly bounded component of lunar surficial OH/H₂O. The weakly bounded component is assumed to be built up in a time-of-day-dependent manner by adsorption of solar wind protons in the morning and afternoon, when the surface is cold, while it is efficiently destroyed by the sink processes of evaporation and photolysis around midday, when the surface is warm. For low latitudes, the model in [11, 12] and its extension in [13] indicate that adsorption-induced H and OH are completely removed at midday. In contrast, the strongly bounded component suggested in [5] is not affected by these sink processes and is assumed to be constant.

We make use of the nearly global 20 pixels/degree maps of the time-of-day-dependent integrated 3- μm band depth (OHIBD) presented in [5]. We assume that at low latitudes the difference between the morning and midday OHIBD level is approximately proportional to the weakly bounded

component of surficial OH/H₂O formed by adsorption of solar wind protons. We compared the resulting OHIBD difference map with M³-derived maps of 20 pixels/degree resolution of the FeO and TiO₂ content of the lunar soil obtained with the framework of [14] and [15], respectively. Here we avoided the high-latitude regions with their relatively strong time-of-day-dependent OHIBD variations in both maria and highlands, and thus focused our analysis on the latitude range of $\pm 30^\circ$, where we assume complete removal of the weakly bounded surficial OH/H₂O component at midday. Our maps are restricted to the longitude range between 120° W and 60° E due to lack of M³ data coverage acquired at local morning and midday outside this range.

Results: The OHIBD difference map is shown in Fig. 1a, revealing high OHIBD difference values in the maria (high-FeO regions in Fig. 1b). Particularly high values occur in the TiO₂-rich mare areas (e.g., Mare Tranquillitatis and western Oceanus Procellarum) apparent in Fig. 1c. The correlation coefficients between OHIBD difference vs. FeO and TiO₂ content corresponds to 0.53 and 0.59, respectively (Fig. 2).

Conclusion: Since the main carrier of lunar TiO₂ is the mineral ilmenite (FeTiO₃) [16], the positive correlation between OHIBD difference and TiO₂ content suggests a particular efficiency of ilmenite to trap OH/H₂O (possibly similar to the efficiency of ilmenite to trap ³He pointed out in [17]).

Acknowledgements: This work was supported by RFBR-DFG grant No. WO 1800/7-1.

References: [1] Pieters, C. M. et al. (2009) *Current Science* 96, 500-505; [2] Goswami, J. and Annadurai, M., (2009) *Current Science* 96, 486-491; [3] Pieters, C. M. et al. (2009) *Science* 326, 568-572; [4] Bandfield, J. L. et al. (2017) *LPSC XLVIII*, abstract #2083; [5] Wöhler, C. et al. (2017) *Sci. Adv.* 3, e1701286; [6] Sunshine, J. M. et al. (2017) *Science* 326, 565-568; [7] McCord, T. B. et al. (2011) *JGR* 116, E00G05; [8] Li, S. and Milliken, R. E. (2017) *Sci. Adv.* 3, e1701471; [9] Wöhler, C. et al. (2017) *Icarus* 285, 118-136; [10] Starukhina, L. (2001) *JGR* 106(E7), 14701-14710; [11] Farrell, W. M. et al. (2015) *Icarus* 255, 116-126; [12] Farrell, W. M. et al. (2017) *JGR* 122, 269-289; [13] Wöhler, C. et al. (2017) *Proc. ELS*; [14] Wöhler, C. et al. (2014) *Icarus* 235, 86-122; [15] Bhatt, M. et al. (2015) *Icarus* 248, 72-88; [16] Papike, J. et al. (1991) *Lunar Minerals*, in: Heiken, G. H. et al. (eds.), *Lunar Sourcebook*, Cambridge Univ. Press, pp. 121-181; [17] Shkuratov, Y. G. et al. (1999) *Solar Syst. Res.* 33, 409-420.

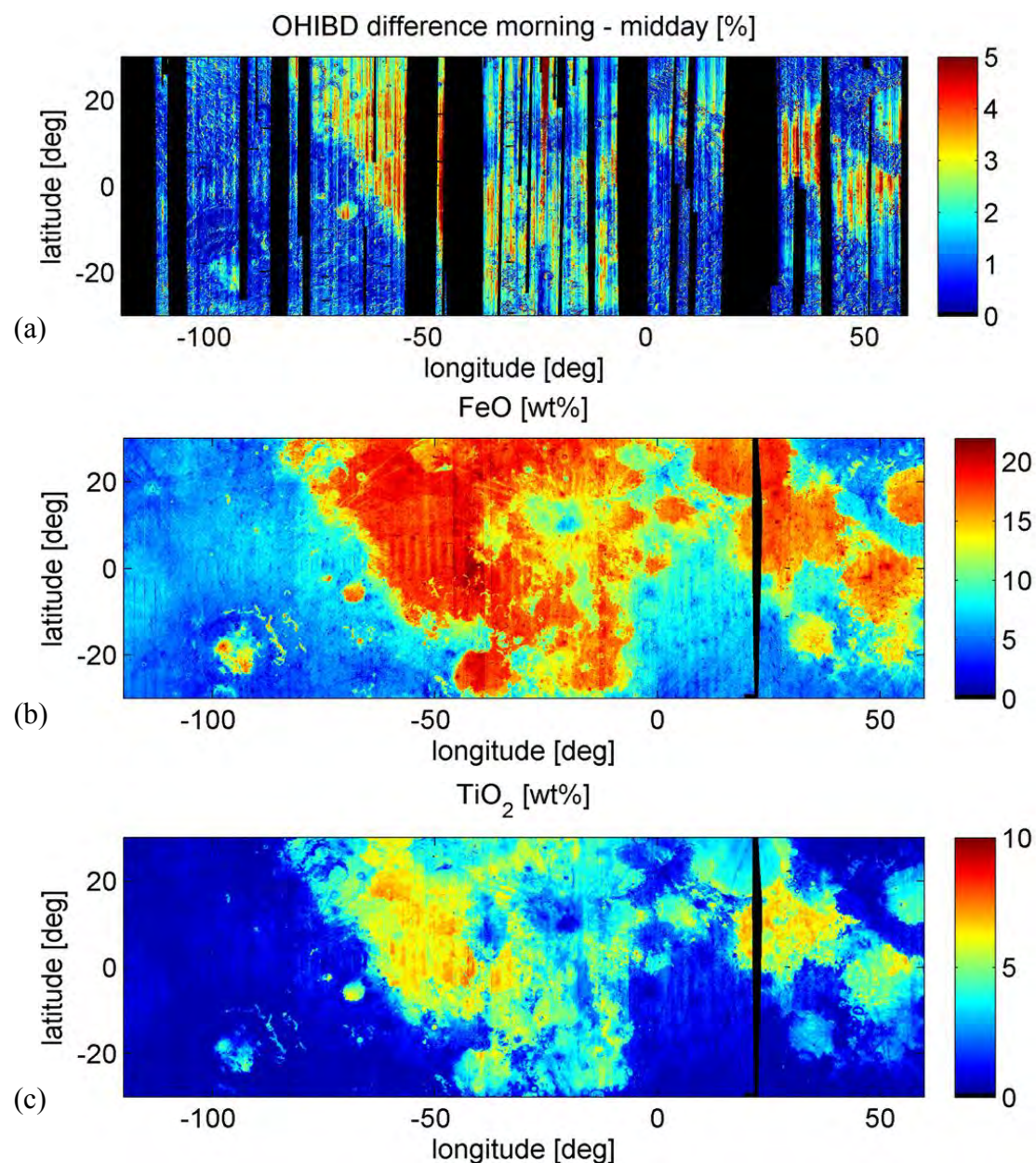


Fig. 1: (a) Map of the OHIBD difference between morning and midday. (b) FeO abundance map. (c) TiO₂ abundance map. Black denotes missing data.

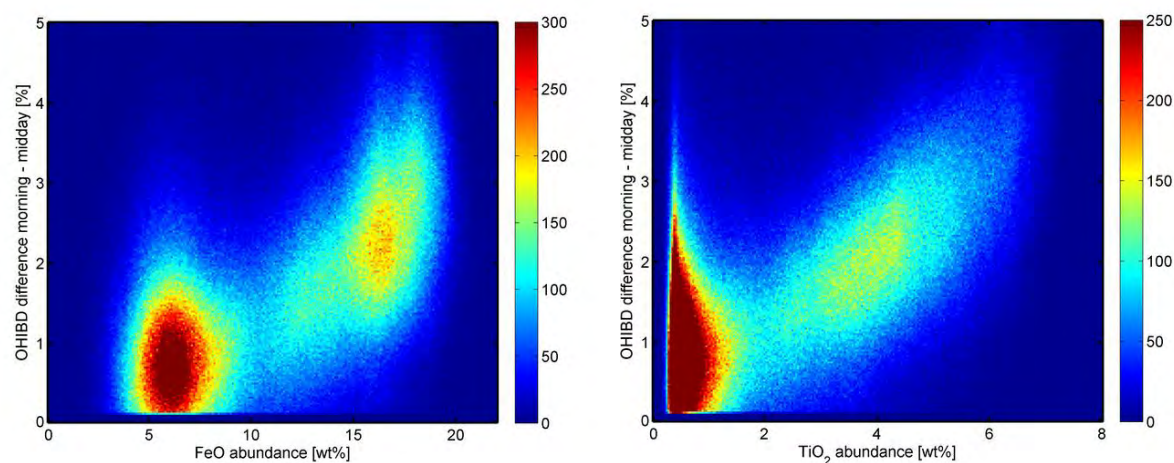


Fig. 2: Density plot of (a) OHIBD difference vs. FeO abundance and (b) OHIBD difference vs. TiO₂ abundance.

SIMULATION OF THE EFFECT OF SPACE WEATHERING ON THE 3-MICROMETER ABSORPTION BAND BASED ON MIE THEORY. K. Wohlfarth¹, C. Wöhler¹, A. Grumpe¹, A. Morlok², and H. Hiesinger², ¹Image Analysis Group, TU Dortmund University, 44227 Dortmund, Germany {kay.wohlfarth,christian.woehler,arne.grumpe}@tu-dortmund.de, ²Institut für Planetologie, Westfälische Wilhelms-Universität Münster, 48149 Münster, Germany {morlokan,hiesinger}@uni-muenster.de

Introduction: Space weathering processes cause the deposit of small spherical iron particles in the upper layers of a planetary regolith, termed sub-microscopic iron (SMFe) [1]. The presence of this iron results in considerable changes of the observed infrared spectra, i.e., darkening, reddening (increasing slope in the NIR) and flattening of spectral features. Space weathering also affects the depth of the absorption band around 2.8-3.0 μm . The 3- μm absorption feature indicates the presence of water (H_2O) and/or hydroxyl (OH) [2]. In [3], the relative integrated 3- μm band depth (OHIBD) is used as a measure for the strength of the 3- μm band. Larger OHIBD values indicate relatively deeper absorption bands and more lunar OH/ H_2O . Thus, it is of valuable interest to quantify the effects of space weathering on the OHIBD value. This work consists of three parts: At first, we employ our previously described method [4] to simulate space weathering of silicates based on Mie theory. Secondly, we examine the 2.5-4.0 μm range and analyse the effect of space weathering. At third, the simulation is compared to lunar OHIBD maps indicating the presence of surficial OH/ H_2O .

Method: Reflectance Modelling and Spectral Mixing. The works of [1] and [5] rely on the Maxwell-Garnett theory. Our analysis is based on our method presented in [4]. It employs the widely recognized reflectance theory of Hapke [6] which exhibits the useful property of linear mixing of the single scattering albedo w and the phase function $p(g)$ [7]. SMFe is included by explicitly modeling its behavior using Mie theory, allowing more flexibility. Our model requires the illumination conditions, the wavelength dependent single scattering albedo, and the phase function of a particulate material in Legendre representation. The Legendre coefficients are computed based on [8,9]. The scattering efficiencies and the albedo of iron are calculated following [10], requiring measurements of the refractive index.

Simulation. As described in [4], the mixing procedure comprises four steps: (1) The single scattering albedo w and the scattering efficiencies of a mineral are retrieved from laboratory measurements of reflectance and refractive index. The albedo and scattering efficiencies of SMFe are calculated from the complex refractive index of iron using Mie theory. (2) The albedo values of the mineral and the SMFe are mixed linearly. (3) The phase functions $p(g)$ of the mineral and the SMFe are developed in terms of Legendre coefficients and mixed linearly. (4) The

resulting albedo w and phase function $p(g)$ are fed into the Hapke model yielding the desired radiance spectra.

Results: Simulation of space weathering. We use a reflectance spectrum of olivine with an average particle radius of 47.5 μm measured with a VERTEX 70v spectrometer, and mix it with simulated SMFe of 0.5 μm , 0.1 μm , and 0.01 μm radius. The incidence angle is $i = 15^\circ$ and the emission angle is $e = 15^\circ$. We use the refractive index measurements of olivine [11] and iron [12] and simulate mixtures with 0-1 weight percent (wt %) of iron. This conforms with the range of lunar SMFe [1]. The spectra are normalized to the reflectance at 2.6 μm . Figure 1 shows space weathered spectra with a SMFe grain size of $r = 0.01 \mu\text{m}$, Figure 2 and Figure 3 show the spectra for grain sizes of $r = 0.1 \mu\text{m}$ and $r = 0.5 \mu\text{m}$, respectively. It can be observed that the relative absorption depth at 3 μm becomes smaller with an increase in SMFe. The relative depth of the pure olivine spectrum is 0.288 at 3 μm . The flattest absorption band at 3 μm occurs for 1 wt % of SMFe and a grain size of 0.1 μm (Figure 2). It has a relative depth of 0.109 which is only one third of the original spectrum. The grain size has only a minor influence on the relative depth of the band but alters the shape of the spectra with increasing wavelength. It can be concluded that space weathering has a significant influence on the relative depth of the 3 μm absorption band, regardless of the particle size of SMFe.

OHIBD map of mare surface east of the crater Lichtenberg. Figure 4 shows the reflectance map in the 1.579 μm band of the M³ instrument [13] and a map of the OHIBD at midday of a region east of the crater Lichtenberg. These maps were constructed using the framework in [2]. The bright spots indicate the ejecta of fresh impact craters (a,b,c in Figure 4). It can be seen that these small craters show increased OHIBD values (a,b,c in Fig. 4). A possible explanation is that these fresh craters had less exposure time to space weathering processes than the surrounding surface. This is in accordance with our simulation results. However, there are also larger craters (e.g., d in Figure 4) with locally decreased OHIBD values. This might be caused by the exposure of deeper regolith layers having a lower surficial OH/ H_2O content than the surrounding material.

Acknowledgement: This work has partially been supported by RFBR-DFG grant No. WO 1800/7-1.

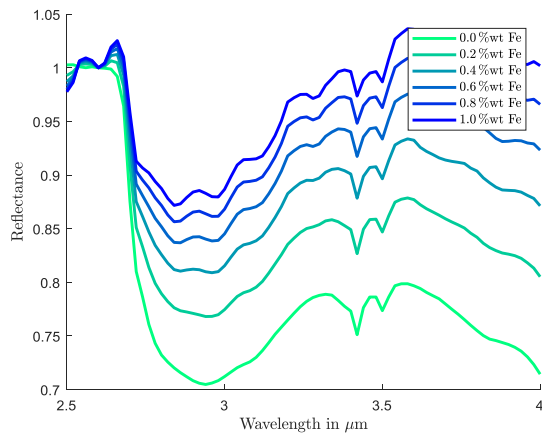


Figure 1. Normalized spectra of space weathered olivine (SMFe particle radius 0.01 μm).

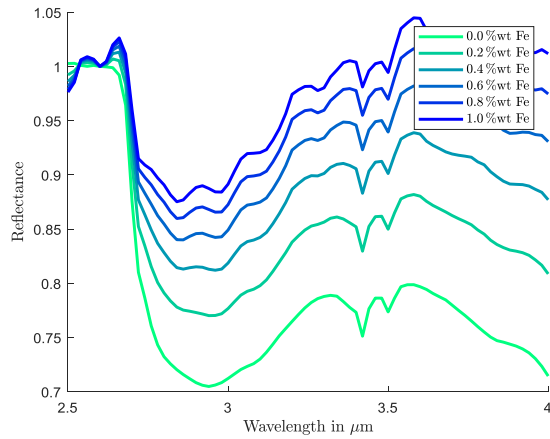


Figure 2. Normalized spectra of space weathered olivine (SMFe particle radius 0.1 μm).

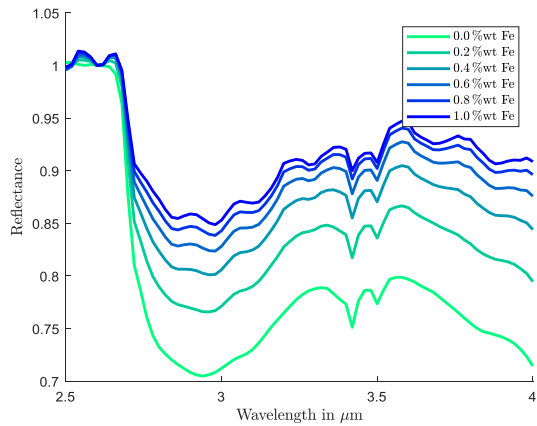


Figure 3. Normalized spectra of space weathered olivine (SMFe particle radius 0.5 μm).

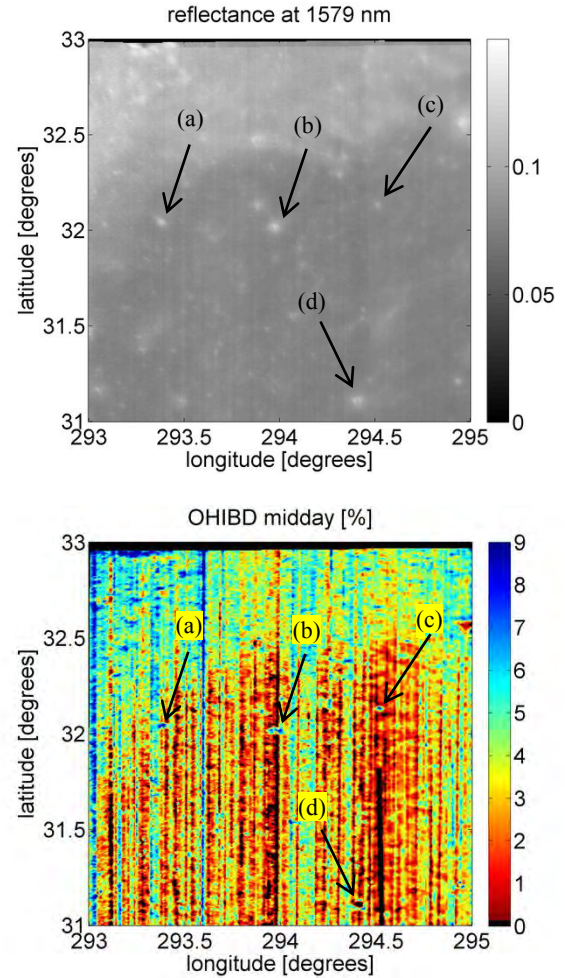


Figure 4. Reflectance at 1.579 μm (top) and OHIBD at midday (bottom) of a region east of the crater Lichtenberg in northwestern Oceanus Procellarum.

References: [1] Hapke B. (2001) *JGR*, 106, 10,039–10,073. [2] Pieters, C. M. et al. (2009) *Science* 326, 568–572. [3] Wöhler C. et al. (2017) *Sci. Adv.*, 3, 9, e1701286. [4] Grumpe A. et al. (2018) *LPSC XLIX*, #2533. [5] Warell, J. and Davidsson, B. J. R. (2010) *Icarus*, 209, 164–178. [6] Hapke B. (2002) *Icarus*, 157, 523–534. [7] Mustard, J. F. and Pieters, C. M. (1989) *JGR* 94(B10), 13619–13634. [8] Fowler B. (1983) *J. Opt. Soc. Am.*, 73, 19–22. [9] Mätzler C. (2002) *Research Report, Institute of Applied Physics*, University of Bern. [10] de Rooij W. A. et al. (1984) *A&A*, 131, 237–248. [11] Fabian et al. (2001) *A&A*, 378, 1, 228–238: <http://www.astro.uni-jena.de/Laboratory/OCDB/crsilicates.html> [12] Querry M.R. (1985) *Contractor Report CRDC-CR-85034* (1985): <https://refractiveindex.info/?shelf=main&book=Fe&page=Querry> [13] Pieters C. M. et al. (2009) *Curr. Sci.*, 96, 500–505.

Introduction: Additive Manufacturing (AM) is one of the feasible candidates for realising the construction of Moon village assets and other surface elements. Using In-Situ Resource Utilization (ISRU), the construction of structures and surface elements will be simplified, speeding up the colonization of the Moon and increasing humanity's capability to explore the Moon in a sustainable manner.

Sintering of lunar regolith in a layer-wise manner was demonstrated using laser melting [1] for relatively small scale products. Proof of concept of regolith melting has also been shown for other techniques, such as microwaving [2]. However, there is poor published information on the interaction of sintered regolith, acting as substrate, with the powder during the AM process. Regarding this, the contact angle and drop shape analysis enhance the understanding of this interaction and lead to optimization of different AM parameters such as temperature distribution, printing speed, layer thickness, particle size, etc. Following this idea, this project aims at studying different contact angle measurement techniques such as Hot Stage Microscopy (HSM) and sessile drop technique for on-site 3D printing applications. Contact angles are studied atop of different substrate under different working atmospheres.

HSM technique: HSM (Figure 1) technique is used to analysis the wetting behaviour of the regolith simulat (JSC-2A) as a function of temperature under atmospheric air condition. In HSM, JSC2-A powder is pressed in different sizes ranging from 3 mm to 20 mm (in diameter). Samples are placed atop of different substrates such as pre-sintered regolith as well as Zirconia (ZrO_2), and their drop shape is recorded using a CCD camera. HSM setup for analysing the JSC-2A simulat is shown in Figure 1. As Figure 1(A) shows, the setup consists of a thermal camera (a), a CCD camera (b) and, in-between, the oven with the sample (c).

As Figure 1(B) shows, sample is placed in the oven on top of the substrate. Transparent ceramic window allows for recording the specimen's shape versus temperature evolution during the sintering process. Analysing the recorded data using HSM leads in different contact angles at different viscosity temperatures. An example of drop shape evaluation of sintered regolith recorded using HSM is shown in Figure 2.

Sessile drop technique: The sessile drop technique is used to assess the contact angle under

vacuum condition. The equipment consists of a horizontal stage to mount a solid sample, a micrometre pipette to form a liquid drop, an illumination source and a device to record the drop shape [4]. Through drop shape analysis, the contact angle is obtained. This permits obtaining a value for the solid surface energy, thus the wettability of the substrate in relation to the liquid drop.

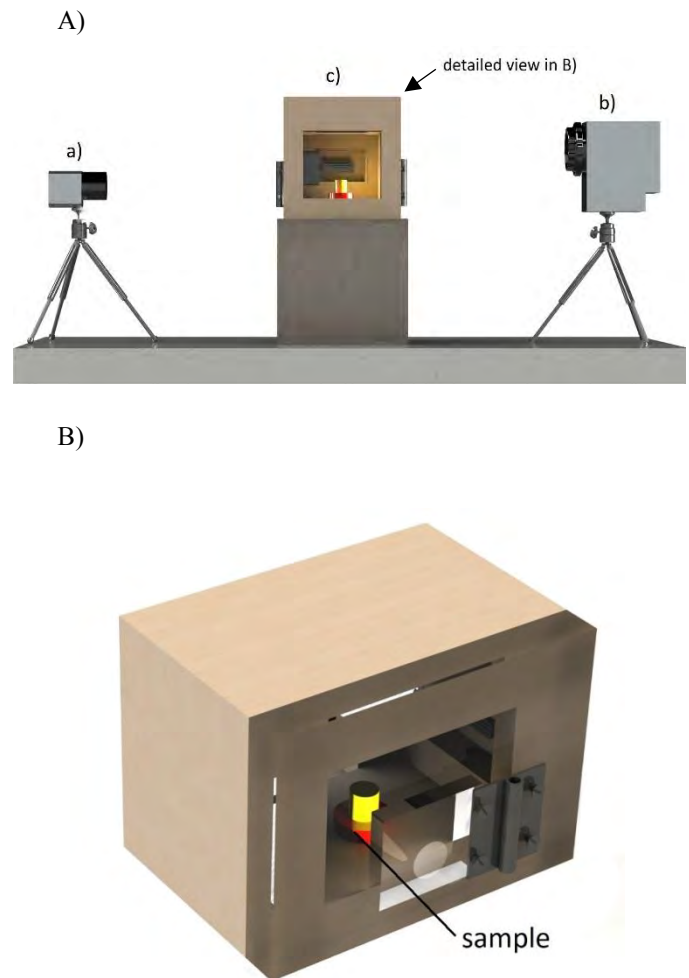


Figure 1: Illustration of HSM setup (A) and detailed view of the HSM oven (B).



Figure 2: Drop shape analysis of JSC-2A using HSM technique.

Acknowledgements:

This project is a result of collaboration between the Spaceship EAC initiative and the German Aerospace Center (DLR).

References:

[1] Fateri M. et al. (2015), *Int. J. Appl. Ceram. Technol.*, 12, 46–52. [2] Taylor L. A. and Meek T. T. (2005) *JAE*, 18, 3, 188–196. [3] W. Panna, P. Wyszomirski, and P. Kohut, *Application of hot stage microscopy to evaluating sample morphology changes on heating*, J. Therm. Anal. Calorim., vol. 125, no. 3, pp. 1–7, 2016. [4] Yuehua Yuan and T. Randall Lee, *Contact Angle and Wetting Properties*, Surface Science Techniques, Springer Series in Surface Sciences 51, DOI 10.1007/978-3-642-34243-1_1.

Developing Structures For An International Art Gallery on the Moon.

Alexander Zaklynsky. (affiliation MFA, KABK. azaklynsky@gmail.com - <http://AZ4D.com>),

Bernard Foing. (affiliation ESA Estec, ILEWG, VU Amsterdam, Artscience The Hague. bernard.Foing@esa.int)

Link to visual abstract / informational poster in development: <http://zaklynsky.com/MoonGalleryPosterSmall.png>

Introduction - A short History of Art on the Moon:

The Moon Museum is a small ceramic wafer three-quarters of an inch by half an inch in size, containing artworks by six prominent artists from the late 1960s. The artists with works in the "museum" are Robert Rauschenberg, David Novros, John Chamberlain, Claes Oldenburg, Forrest Myers and Andy Warhol.

- https://en.wikipedia.org/wiki/Moon_Museum

Fallen Astronaut: 8.5 cm aluminium sculpture by Paul Van Hoeydonck.
https://en.wikipedia.org/wiki/Fallen_Astronaut

A Gallery on the Moon project: Concept:

- An international collaborative art work and Moon village promotion structure.
- A crowd sourced online gallery of images created by an international group of participants.
- A 10 by 10 cm patch of Lunar Rover exterior paneling is one intended venue for this Gallery.
- A robust online presence, promotion structure and dissemination of information/teaching materials related to the program along with the potential of realising an art work on the moon.

Format:

A 10 x 10 cm square can be split into 100 cels of 1 cm x 1 cm. It can be split into even more equal sizes down to the pixel. A hi definition 10 x 10 cm printed image could have 1000 x 1000 pixels. That is 1 million pixels. The current initiative is to define and develop the aesthetic approach to this structure.

Digital Format:

Through an online interactive web platform individuals could input their designs into the grid. Over a set time period and with multiple submissions from the public a variation of designs could be collected into an archive representing a broad spectrum of aesthetic approaches to a set of guidelines

Project outline/structure:

- 1] Research , concept development, collection of informative materials.
- 2] Design & Implementation of website & international call for artistic proposals/submissions.
- 3] Selection Process of submitted works and management of aesthetic organism online.
- 4] Potential implementation of gallery on the moon via ESA lunar rover or other craft destined for the moon.

Project Abstract:

The Moon Gallery is a proposal for defining and promoting the evolution of an aesthetic organism. The three main components of this project are research , collaboration and archive. The Research component is directed toward the development of context , informative materials and structure for the promotion of a **call for artistic submissions**. The Collaboration component is the implementation of the online creative tool and website designed for collecting submissions and showing a realtime evolution of the 'aesthetic organism'. The Archive component is both the dissemination of an online resource of images and artist proposals along with a possibly random selection of proposals fabricated into an actual material installation on the moon surface in the 10 x 10 cm grid format.

What is an 'aesthetic organism'. A petri dish is good for growing bacteria cultures while a website is good at growing visual

cultures. The 10 cm x 10 cm grid structure along with an on-line sign up and submit image structure could develop a large amount of submissions over time with good promotion. Each section of the grid relates to both the biological concept of cells and the understanding of perspective. As the grid is filled with more and more input / imagery, the more it evolves. Over time an expanding stack of grids will create a 3d space of aesthetic intentions. What can we find out by such a construction of content. What is there to gain from studying the outcomes of such a visual social experiment? At the very least the intention of this endeavour is to raise awareness and interest in space and the moon village project along with attempting to develop a program which can have the potential to inspire new explorers of the imagination, perspective and space through a collaborative, interactive and evolving web project.

Additional Information:

This Initiative of implementing a strategy for an International Art Gallery on the Moon is in a preliminary phase of sketching out ideas and methods while building a resource of information and developing a platform on the web for an international call to participate. Connected to the research and conceptual development of this initiative I am producing a series of large scale 2 x 2 m paintings which utilise a custom built drawing machine. These paintings will show a study of the grid format mentioned previously in various abstractions. An Exhibition of this work along with a presentation on the initiatives development will be presented at Pulchri Studio in Den Haag on the 19th of May and run until June 20th, 2018. <http://pulchri.nl/>

Other inspirations / conceptual-structural guides:

The Magic Square - https://en.wikipedia.org/wiki/Magic_square

Map of the moon: - <https://moontrek.jpl.nasa.gov/>

Interactive Web Art Models: Generative & Crowdsourcing.

<http://www.thesheepmarket.com/> - <http://swarmsketch.com/>

Galileo experiment on the Moon: The Hammer Feather Drop.

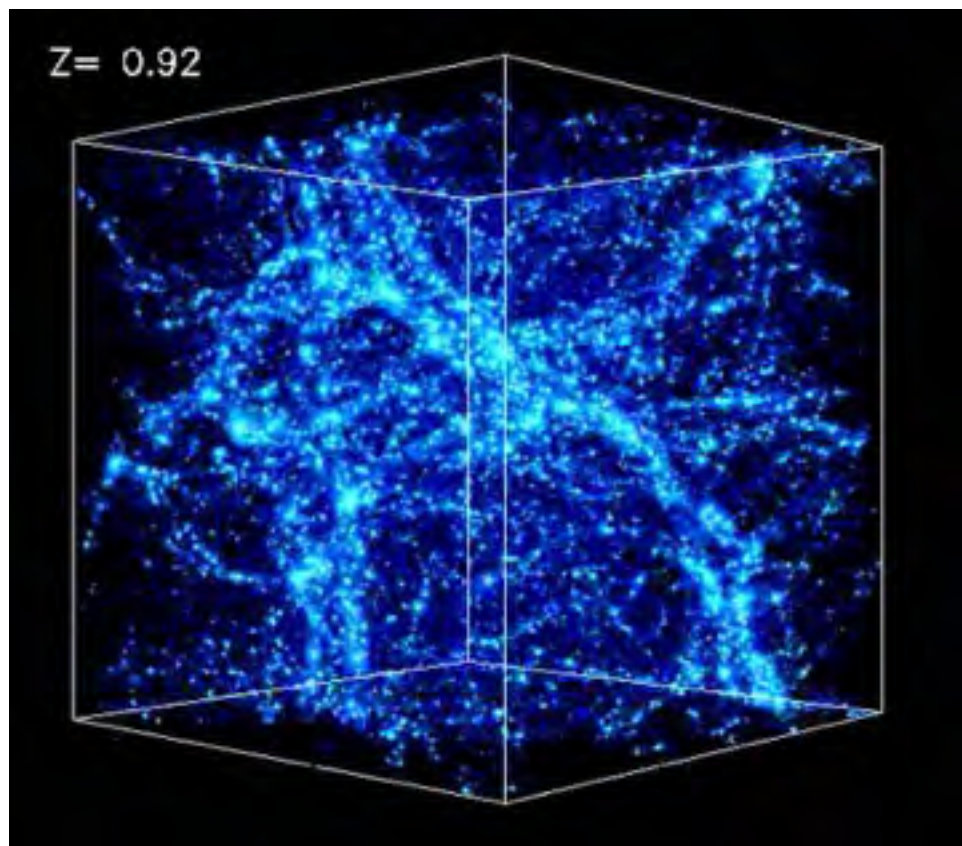
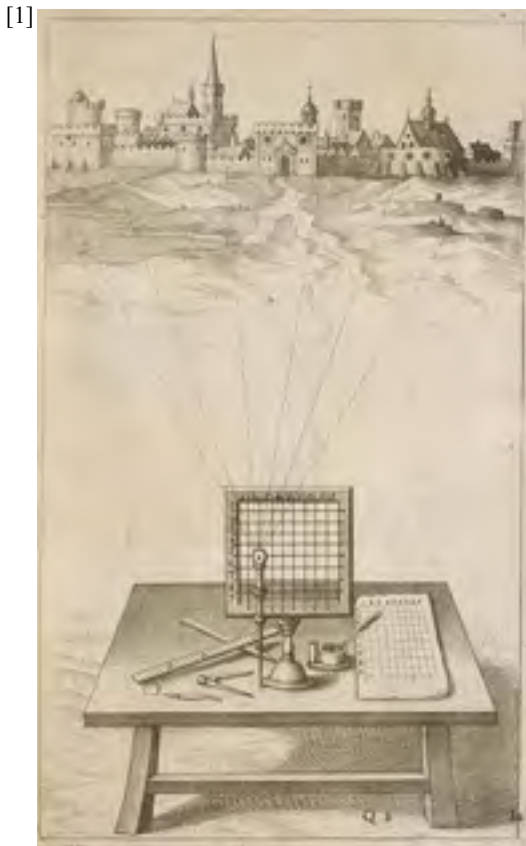
https://www.youtube.com/watch?v=4_rceVPVSY

References:

[1] The "Moon Village" Concept and Initiative.
<https://www.hou.usra.edu/meetings/leag2016/pdf/5084.pdf>

[2] Space is the Place – MoonVillage ArtScience Residency.
<http://meetingorganizer.copernicus.org/EPSC2017/EPSC2017-982.pdf>

[3] Launch Your Design With Cheops - Art&Science@ESA.
<http://blogs.esa.int/artscience/2017/11/02/launch-your-design-with-cheops/>



The above images and art work show an evolution in concepts of perspective and space. The invention of techniques to aid in the accurate reproduction of our landscape and environment led to philosophical advancements in concepts of our aesthetic and spiritual nature on one hand while on the other it led to the ability of our species to infer a map of the observable universe we exist in. Our perspective has taken us from the terrestrial to the celestial while solidifying the understanding of our place in between. The images aim to illustrate the evolution of our human perspective and our capacity for the exploration of the space within and around us.

[1]Brunelleschi's mirror. Filippo Brunelleschi was one of the founding fathers of the Renaissance and is generally known for developing this technique for linear perspective in art. https://en.wikipedia.org/wiki/Filippo_Brunelleschi

[2]Wassily Kandinsky (Russian, 1866-1944). Thirty (Trente), 1937. Oil on canvas. 31 7/8 x 39 5/16 in. (81 x 100 cm). Musée national d'art moderne, Centre Pompidou, Paris. <https://www.thoughtco.com/kandinsky-profile-4122945>

[3]Ellsworth Kelly, 1951. Spectrum Colors Arranged by Chance II, Collage on paper. https://en.wikipedia.org/wiki/Ellsworth_Kelly

[4]Sloan Digital Sky Survey map of the known universe. At this scale, no stars are visible. Individual galaxies like the Milky Way are also invisible. Only clusters of galaxies, super clusters and filaments containing millions of galaxies can be seen. <http://www.sdss.org/>

A SINGLE PLUME UPWELLING ON LUNAR NEAR SIDE THAT PROVIDES A SOURCE FOR TITANIUM-RICH VOLCANISM. Y. Zhao¹, Ana-Catalina Plesa², Doris Breuer², Matthieu Laneuville³, Arie P. van den Berg⁴, Wim van Westrenen¹, ¹Faculty of Science, Vrije Universiteit Amsterdam, the Netherlands, ²Department of Planetary Physics, German Aerospace Center (DLR), Berlin, Germany, ³Earth-Life Science Institute (ELSI), Tokyo Institute of Technology, Tokyo, Japan, ⁴Dept. Earth Sciences, Utrecht University, email y.zhao@vu.nl

Introduction: The most striking feature of the lunar surface is the dichotomy between the near side and the far side. The mare basalts that cover about a third of the near-side surface are present on only 1% of the far side. The Lunar Prospector mission discovered that the distribution of thorium on the lunar surface is concentrated in the Procellarum KREEP terrain (PKT), whose location strongly correlates to that of a nearside mare basalt region [1], and to a lesser extent in the far-side South Pole–Aitken basin. The lack of KREEP signatures in the material ejected from many large far-side impact basins implies that the source of KREEP is concentrated in the near-side hemisphere [2].

The asymmetrical distribution of mare basalts and KREEP on the lunar surface has been proposed to be due to a single-plume upwelling toward the near side. Zhong et al. [3] argued that this upwelling stems from dense ilmenite-bearing cumulates (IBC) that sank to the core-mantle boundary from under the crust where IBC crystallized in the late stages of lunar magma ocean solidification. The IBC contains high concentrations of heat-producing elements, making it thermally buoyant enough to rise after the initial sinking. Parmentier et al. [4] studied the Rayleigh-Taylor instability developed in a dense layer lying on top of another layer, simulating the gravitationally unstable IBC after the solidification of the lunar magma ocean. They suggested that spherical harmonic degree 1 is the fastest growing instability when the top layer is sufficiently thick, and when the viscosity of the top layer is ~ 4 orders of magnitude lower than the underlying mantle.

This study aims to investigate the possibility of localizing key ingredients for lunar volcanic activities, including sources for titanium and radioactive elements, to the near side of the Moon after solidification of the magma ocean, using numerical models that simulate both the downwelling of IBC and the upwelling that give rise to volcanism. In particular, we describe our preliminary results using asymmetrical crustal thickness and distribution of KREEP as an initial condition.

Numerical method: Our numerical models are performed in a 2-D cylindrical domain. The lunar mantle is simulated using the Boussinesq approximation as a fluid with infinite Prandtl number. Finite volume code Gaia [5] is used to solve the conservation equations of mass, momentum, and energy. The advection of chemical components is implemented

using the particle-in-cell method [6]. The mantle domain is heated from within by radioactive decay and from below by a cooling core. A reference viscosity of 1×10^{20} Pa s is used, resulting in a thermal Rayleigh number of 1×10^7 . We use a fine mesh with a radial resolution of 1.7 km throughout the domain. More than 90 million tracers are used to track various material properties, including density, viscosity and concentrations of heat-producing elements.

Our models start when the lunar magma ocean has solidified. The stratified cumulates are characterized by varying density, viscosity, and distribution of heat-producing elements [7]. Viscosity is computed by using a temperature- and pressure-dependent Arrhenius law for diffusion creep. In addition to that, IBC have their viscosities one order of magnitude lower than calculated from the Arrhenius model, taking into account the low viscosity of ilmenite [8]. For density and concentration of heat-producing elements, we use a weighted arithmetic average according to their concentration when different chemical components are mixed. Viscosity is combined to a product of the viscosity of all compositions to the power of their relative concentration.

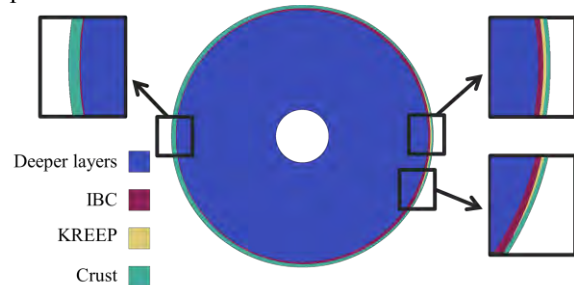


Figure 1. The asymmetrical distribution of crustal thickness, IBC, and KREEP in the initial condition.

The crust has a thermal conductivity of 1 W/m/K, taking into account the low thermal conductivity of plagioclase, and the porous top layers of the crust. The initial crustal thickness is a minimum of 20 km on the near side and a maximum of 40 km on the far side, and we use a sine function to model its variation. KREEP, having the same density and viscosity as IBC while containing higher concentrations of heat-producing elements, is localized in a cylindrical cap of 40 degrees, which mimics the PKT region subsurface. Its thickness is 20 km where crustal thickness is 20 km, and gradually decreases to 0

towards the PKT edge. Figure 1 shows these initial conditions.

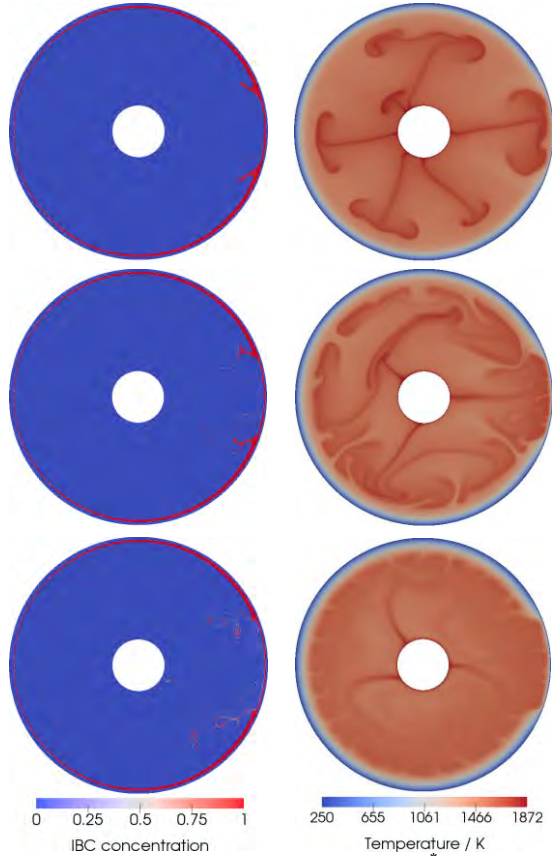


Figure 2. model results using $E^*=300$ kJ/mol. Here IBC concentration includes both the IBC and KREEP in Figure 1.

Results: Two sets of model results are shown in Figures 2 and 3, corresponding to activation energies E^* of 300 kJ/mol and 100 kJ/mol, respectively, in the Arrhenius viscosity model. Both models show the sinking of dense IBC in two diapirs that correspond to the edges of the PKT region. An upwelling remains under the PKT region, due to the region's high heat production, though the convective pattern evolves differently in the two models. We can see from Figure 2 that when $E^*=300$ kJ/mol, the onset of convection is driven by several upwellings at the core-mantle boundary (CMB). When $E^*=100$ kJ/mol, as shown in Figure 3, the onset of convection is driven by sinking IBC. During the sinking of IBC along the edges of PKT, an upwelling is formed underneath the PKT. Foundered IBC at the CMB are then brought up by the near-side upwelling, providing a source of titanium and heat-producing elements to the near side.

Discussion and conclusion: Our preliminary results show that the behavior of IBC overturn under an asymmetrical initial condition is sensitive to the temperature dependence of viscosity. When $E^*=100$ kJ/mol, foundered IBC is brought to the surface through a near-side single-plume upwelling.

This mechanism may explain titanium-rich sources for nearside volcanism. Our continued numerical experiments will further test the effects of a range of other parameters, including the reference viscosity, which may also play an important role in the convective pattern.

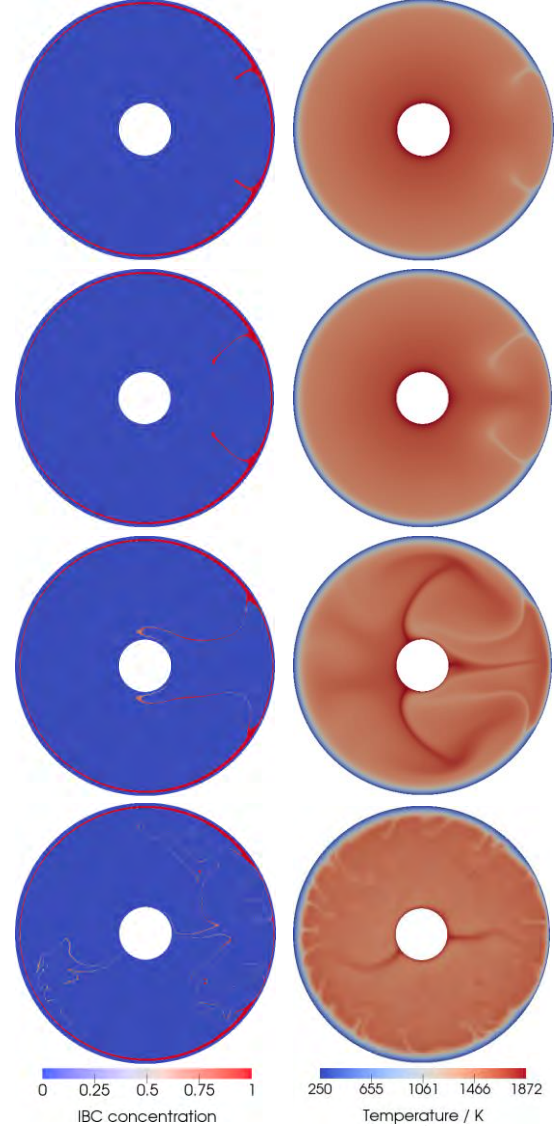


Figure 3. model results using $E^*=100$ kJ/mol. Here IBC concentration includes both the IBC and KREEP in Figure 1.

Acknowledgement: This work was carried out on the Dutch national e-infrastructure with the support of SURF Cooperative, and also the Cray XC30 system of the Earth-Life Science Institute in Tokyo.

References: [1] Jolliff B. L. et al. (2000) *JGR*, 105, 4197–4216 [2] Warren P. H. (2001) *GRL*, 28, 2565–2568 [3] Zhong S. et al. (2000) *EPSL*, 177, 131–140 [4] Parmentier E. M. et al. (2002) *EPSL*, 201, 473–480 [5] Plesa A.-C. et al., (2012) In: Rueckemann, C.-P. (Ed.), *IGI Global*, 302–323 [6] Hüttig C. et al. (2013) *PEPI*, 220, 11–18 [7] de Vries J. (2012) Chapter 5, *PhD diss*, Utrecht University. [9] Dygert N., et al. (2016) *GRL*, 43, 532–540